Design of oxide electrocatalysts for efficient conversion of CO2 into liquid fuels

Bhowmik, Arghya; Vegge, Tejs; Hansen, Heine Anton

Publication date:
2017

Document Version
Publisher's PDF, also known as Version of record

Citation (APA):
Bhowmik, A., Vegge, T., & Hansen, H. A. (2017). Design of oxide electrocatalysts for efficient conversion of CO2 into liquid fuels. Department of Energy Conversion and Storage, Technical University of Denmark.

Design of oxide electrocatalysts for efficient conversion of CO_2 into liquid fuels

PhD thesis

Arghya Bhowmik

May 2017

Department of Energy Conversion and Storage
Technical University of Denmark

Design of oxide electrocatalysts for efficient conversion of CO_2 into liquid fuels

Author

Arghya Bhowmik
E-mail: arbh@dtu.dk

Supervisors:

Tejs Vegge
Professor, Head of Section
Section of Atomic Scale Modelling and Materials
Department of Energy Conversion and Storage
Technical University of Denmark
E-mail: teve@dtu.dk

Heine Anton Hansen
Researcher
Section of Atomic Scale Modelling and Materials
Department of Energy Conversion and Storage
Technical University of Denmark
E-mail: heih@dtu.dk

Department of Energy Conversion and Storage:

Atomic Scale Modelling and Materials
Technical University of Denmark
Fysikvej 309
2800 Kgs. Lyngby
Denmark

www.energy.dtu.dk
Tel: +45 46 77 58 00
E-mail: info@energy.dtu.dk

Preface

This thesis is submitted in candidacy for a Ph.D. degree from the Technical University of Denmark (DTU). The work has been conducted between June 2014 and May 2017 at the section of Atomistic Scale Modelling and Materials, at the Department of Energy Conversion and Storage supervised by Prof. Tejs Vegge and Dr. Heine Anton Hansen.

Lundbeck Foundation financially supported the work via grant no.R141-2013-A13204.

Arghya Bhowmik
May 2017
Lyngby

Acknowledgements

I am thankful to many people around me for whom PhD years ended up being a very fulfilling journey both professionally and personally.

I cannot imagine a better guide for this journey than Tejs. The enormous amount of trust he places on all of us, providing with the intellectual freedom and space to grow. I always appreciated and tried to learn, how he comes out with patterns in seemingly random set of numbers. I also want to emulate his leadership style, of which I am a benefactor. I have much gratitude for Heine, who has always made himself available for my random questions and scientific discussions. His wide spread knowledge in theoretical electrocatalysis helped me immensely.

The ASC group has a wonderful, supportive and collaborative environment that I benefited from every day. Rune and Simon have become friends without any reservation. The coffee room discussion with Mateusz, Marko, Juanma, Vladimir, Niels, Steen, Jin, Nicolai brightens my day. I thank many other colleagues with whom I shared good time. Thanks to Henrik, Mateusz, Simon, Rune, Murat and Jin for proof reading this manuscript.

I would like to thank Thomas Bligaard and Maxx Hoffmann who made my stay at SUNCAT center fruitful and enriching.

Experts maintaining Niflheim provided a stable computing environment to make this work possible. I also thank administrative staffs Karina, Lene and Annette for being helpful always.

I am blessed for having parents who inculcated the spirit of scholarship from childhood and a wife who always stands by my side. Jaysree, you left your PhD midway to be with me – I promise to force you to finish the PhD as well.

Abstract

Electrochemical conversion of CO_2 into high energy density liquid fuels utilizing renewable electricity can usher in a carbon neutral society without limiting the energy consumption. Lack of active and efficient electrocatalysts for this reaction remains a challenge. Research efforts towards catalyst development have obtained limited success due to adsorbate scaling relations on metallic surfaces. Preliminary experimental results indicate rutile oxide catalysts are active at very low overpotential, although the scientific understanding is missing. This thesis aims at delivering knowledge of atomic scale reaction thermodynamic needed to engineer efficient and active oxide electrocatalysts.

Rutile oxides are explored for CO_2 reduction reaction (CO2RR) through density functional theory based simulation of reaction thermodynamics. Oxygen atom coordinated intermediates constitute the reaction mechanism active on such catalysts, annulling the scaling laws that limit metallic catalysts. Utilizing model rutile oxide surfaces, trends and limitations of CO2RR on oxide catalysts are analyzed. OH* binding energy is established as the descriptor for CO2RR activity on oxide surfaces. Scaling law based thermodynamic volcano relation for CO2RR is constructed. Guidelines for H* and OH* binding energy range for good activity and selectivity of oxide CO2RR catalysts is proposed. This provides guidance to future development of oxide CO2RR catalysts.

The key role of CO* spectators on reaction onset potential and product selectivity of RuO_2 electrocatalyst is elucidated through simulations of CO2RR pathway with varying CO* coverage level. The effect of adsorbate-adsorbate interaction in CO2RR activity is significant. Steric effects from spectator coverage also play a role by altering binding geometry of adsorbates. It is concluded that under experimental condition, CO* coverage is necessary for methanol evolution from RuO2 electrocatalyst, but very high coverage lead to evolution of formic acid and hydrogen together.

Building on the understanding of descriptors for CO2RR activity and CO* spectator effects, a new method of further enhancing the oxide electrocatalyst activity is proposed utilizing ligand effects in mixed oxide systems. Such effects in CO2RR catalysts can produce striking behaviours for adsorbate binding and catalytic properties. Detailed study of such properties for Ru/Ir mixed oxide surfaces with varying metal atom composition as well as different CO* coverages is done. It is identified that monolayer or lesser amount of iridium oxide on RuO_2 catalyst can have a methanol onset potential of -0.2 V below RHE. This is attributed to a combination of ligand effect and adsorbate interaction. Through thermodynamic and kinetic barrier calculations, the possibility of 2C products is explored.

Resume

Elektrokemisk omdannelse af CO_2 til flydende brændstoffer med høj massefylde ved hjælp af vedvarende elektricitet kan understøtte et kulstofneutralt samfund uden at begrænse energiforbruget. Mangel på aktive og effektive elektrokatalysatorer til denne reaktion forbliver dog en udfordring. Forskningsindsatsen med katalysator udvikling har haft begrænset succes på grund af skaleringslove mellem bindingsstyrken af molekyler på metaloverflader. Foreløbige eksperimentelle resultater indikerer, at rutil oxid katalysatorer er aktive ved meget lavt overpotentiale, selv om den videnskabelige forståelse mangler. Denne afhandling har til formål at levere termodynamisk viden på atomart niveau om de reaktioner, der er nødvendige for at konstruere effektive og aktive oxid elektrokatalysatorer.

CO_2 reduktionsreaktionen (CO2RR) på rutiloxider undersøges gennem tæthedsfunktionalteori baseret simulering af reaktion termodynamik. Oxygenkoordinerede mellemprodukter udgør den aktive reaktionsmekanisme på sådanne katalysatorer og annullerer de skaleringslove, som begrænser metalliske katalysatorer. Ved udnyttelse af rutiloxid modeloverflader analyseres tendenser og begrænsninger af CO2RR på oxidkatalysatorer. OH* bindingsenergien er etableret som estimater for CO2RR-aktivitet på oxidoverflader og skaleringsbaserede termodynamiske relationer for CO2RR er konstrueret. Retningslinjer for bindingsenergien af H* og OH*, hvor der kan opnås god aktivitet og selektivitet af oxid-CO2RR-katalysatorer, foreslås. Dette giver vejledning til fremtidig udvikling af oxid CO2RR katalysatorer.

Co-adsorberet CO* spiller en nøglerolle med hensyn til reaktionsstartpotentiale og produktselektivitet af RuO_2-elektrokatalysator. Dette er belyst ved simuleringer af CO2RR-reaktionsvejen med varierende CO* dækningsgrad. Betydningen af adsorbat-adsorbat interaktioner i CO2RR-aktiviteten er signifikant. Steriske effekter fra dækningsgraden spiller også en rolle ved at ændre geometrien for bindende adsorbater. Det konkluderes at under eksperimentelle betingelser er en hvis CO* dækning nødvendig for methanol udvikling fra RuO_2 elektrokatalysator, men meget høj dækningsgrad fører til udvikling af myresyre og hydrogen.

På baggrund af forståelsen for OH* som estimator for CO2RR-aktiviteten og CO* tilskuer-effekter foreslås en ny metode til yderligere at forøge oxid elektrokatalysator aktiviteten ved anvendelse af ligandvirkninger i blandede oxidsystemer. Sådanne virkninger i CO2RR-katalysatorer kan frembringe slående adfærd for adsorbatbinding og katalytiske egenskaber. Detaljerede undersøgelser af sådanne egenskaber for Ru/Ir blandede oxidoverflader med varierende metalkomposition samt forskellige CO* dækningsgrader udføres. Det er identificeret at et monolag eller mindre iridiumoxid på RuO_2-katalysatorer kan have et methanol-startpotentiale på -0,2 V under RHE. Dette tilskrives en kombination af ligand effekter og adsorbat interaktioner. Gennem termodynamiske og kinetiske barriereberegninger undersøges muligheden for 2C-produkter.

Table of Contents

Table of figures

List of Tables

1.Introduction

1.1. Why sustainable energy

Rise of humankind as the sole species with the power to reshape the face of earth is a fascinating story. The expanding ability to harness and utilize energy, created the pace of this progress. All basic necessities as well as luxuries of modern life like a protein rich diet, climate controlled homes, traveling for vacation to places of great distance – are viable all due to enormous amount of energy resources accessible to us. For a pre-industrial era person, our life is nothing but fiction. Extending the quality of life available to the richest one billion, to the rest of the human population means increasing our current energy demand by many fold. Although this is a wishful thinking, we must consider how it is achieved and the cost involved.

It is estimated that we rely on the energy equivalent of 25 billion horses to get by in our day-to-day life[1]. Our present day method of energy harvesting and usage also has polluting equivalent of horse excreta. The great horse manure crisis of 1894[2] made government and innovators put effort in all directions to solve the looming catastrophe, which could have drowned all major cities with droppings. The Times reported, “In 50 years, every street in London will be buried under nine feet of manure.” Henry Ford’s invention of building affordable motor cars alleviated the problem in the next few decades.

A century later, we are again at a juncture where we need to innovate our way out of an environmental disaster, which has already reached our doorstep (Figure 1-1). Estimated energy budget for all humans was around 500 Mt.o.e. in 1900 and have since grown to 12 Bt.o.e. in recent years. Booming petroleum and natural gas industry enabled this growth along with increased coal production. As the billions of citizens in low income countries improve upon their living condition, this is expected to grow to ~18 Bt.o.e. by 2035 spewing out 43 Gton CO_2 per year[3]. To achieve a sustainable environment, we not only need to reverse this trend, but go altogether CO_2 neutral and sequester some of the CO_2 already emitted.

Figure 1-1: after effects on our dependence on unsustainable energy sources for fueling higher quality life – (a) London streets filled with horse manure in 1894 (Photographer G.E. Waring) (b) Beijing air is a health hazard for its residents (CNN news agency, 2006)

So far, in most countries policy makers have done little to significantly change the energy mix towards energy sources with lower environmental impact. However, the stakes are higher this time. Atmospheric CO_2 levels have not seen such rapidly increasing CO_2 level since 23 million years ago[4]. Current rate of CO_2 build up (2.32 ppm) far exceeds the previous geophysical occurrences and thus very much uncharted territory. We have little capability to foresee all the effects on climate, ecology, human habitat and physiology due to the complexities and uncertainties involved. The most often discussed effect is changing weather patterns which is affecting the poorer 2 billion hardest. Every year central India sees tens of thousands die from water and food scarcity caused by draught, and a hundred thousand lose their home from rising sea level and salinity in Sundarbans. While the mainstream media tries to inform people of future bad effects of climate change, this is a present day scenario for millions in Asia and Africa.

The ray of hope is that we already are working on the innovations required to move towards sustainable energy production with great successes. The price of solar power modules have plunged to 0.50 US\$ W^{-1} in 2016 and full levelized cost of electricity (LCOE) for location like Dubai have reached 0.03 US\$ kWh^{-1}. This success story is repeated in wind energy generation as well. The latest LAZARD report[5] on LCOE remarkably found that wind energy cost now undercuts all fossil fuel based energy sources even without any subsidy. On 22nd February 2017, wind farms in Denmark generated all the electricity needed for the whole country. Costa Rica, Iceland, Portugal, Paraguay and Uruguay also have achieved long term renewable only electricity grid operation.

1.2. Benefits of electrochemical conversion of CO_2 to fuel

Electricity produced from wind and solar energy show fluctuations at different time scales due to weather conditions, but the energy supply from the grid needs to be reliable and predictable. This is easy to manage when the share of renewables in the grid is much smaller than coal or gas turbine based generation. We can easily ramp up or drive down the fossil fuel based units quickly to compensate for the variations in solar/wind power available. This becomes impossible to achieve without additional grid scale storage options once the peak generation capacity of all renewable sources exceeds that of sources manageable at discretion. Along with the favourable economics of renewable power generation, eventually large scale energy storage capability would be crucial for proliferation of renewable energy as the sole electrical energy source. Both mechanical (e.g. pumped hydro storage) and chemical (e.g. batteries, electrolyzer/fuel cells) have been studied as probable storage options for the grid[6,7]. The key deciding factor for grid scale energy storage is low cost and scalability to TWh scale. Hydroelectric or compressed air energy storages are very cost effective but dependent on geographical location and often have damaging effect upon the ecology. Various types of batteries, e.g. sodium-sulfur, vanadium redox flow, etc. provide quick response time and flexibility of integration, while missing long-term storage cost[8]. However, electrochemical systems like batteries and fuel cells can provide the required portability to enable integration into the transport sector, which amount to more than one fourth of total energy utilization. Even with already existing technology, the very limited employment of electric vehicles comes from the cost of overhauling the infrastructure and limited production capacity. On the technology side, batteries suffer from lower than ideal gravimetric and volumetric energy density. Traditional petroleum fuel delivers orders of magnitude higher energy density and fast refueling. For fuel cell powered cars, safe storage of hydrogen inside the vehicle with smaller volume is a challenge.

The electrochemical reduction of CO_2 to liquid fuels addresses many of the shortcomings of aforementioned technologies both from grid storage perspective as well as mobility applications. The despised byproduct of fossil fuel can become an opportunity as an energy carrier – a route plants have already taken. Capture and conversion of CO_2 effluence into useful chemicals closes the carbon transfer loop and makes the continued usage of carbon based chemical energy flow system inherently carbon neutral and sustainable[10–12]. If liquid fuels like methanol, ethanol, formic acid etc. are obtained from the electrochemical processing, both fuel cells as well as conventional engines can utilize them (Figure 1-2). Possibility of continued usage of existing infrastructure and equipment helps quick penetration of such sustainable fuels without monumental capital investment. Carbon based liquid fuels are very easy to store and transport and possess no safety issues unlike hydrogen. Hence, it can enable cheaper sustainable energy transport quickly compared to fuel cell or battery powered cars. It is also a superior technology for grid energy storage. Excess production from renewable sources can be converted into chemical energy inside liquid fuels and can be stored for an indefinite period with little added cost. This is in contrast with battery technologies where long term energy storage is economically not viable.

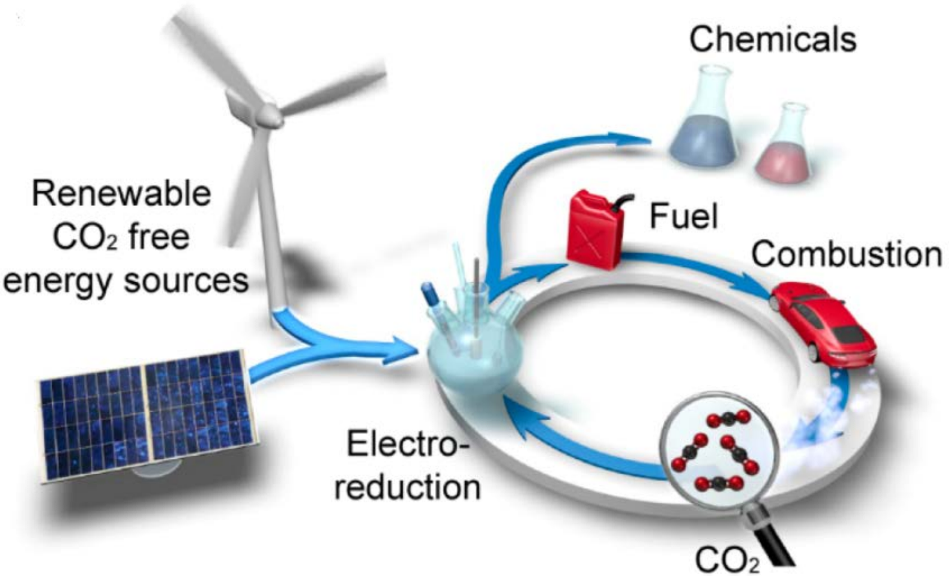

Figure 1-2: The carbon neutral energy cycle utilizing renewable electricity sources and electrochemical synthesis of fuel and chemical from CO_2. Obtained from .[9]

1.3. State of the art in CO_2 reduction electrocatalyst

An ideal catalyst would execute the CO_2 reduction reaction at very low overpotential and with very high selectivity towards a single fuel molecule and not be active for byproducts like hydrogen evolution. Seminal work by Hori[13–15] summarized that among single metal catalysts, only copper produces a mixture of hydrocarbons and alcohols from CO_2 only at high overpotential of ~1V. All other metals are more active towards evolution of hydrogen, formate or CO. The high overpotential requirement for such catalysts renders them impractical for efficient energy conversion purposes.

The unique activity of copper for CO_2 reduction and the overpotential limitations were later explained by atomic scale simulation of the reduction mechanism[17]. Extensive experimental and theoretical studies on various types of copper electrocatalysts suggested that facet engineering might help with better selectivity towards a particular product[18–22]. Theoretical models also predict that a lowest overpotential of -0.68 V with respect to the reversible hydrogen electrode (V-RHE) is achievable on copper (211) stepped surface[16]. CO_2 reduction on metallic catalysts involve two key reaction intermediates – CO* and CHO*. These adsorbates binds to the active site through the carbon atom. This leads to a strong adsorption energy scaling between these two intermediates. The scaling line is such that the electrochemical potential required to drive protonation of CO* to CHO* does not change significantly on changing the binding strength of the catalyst surface (Figure 1-3). Formation of COOH* intermediate limits the CO_2 reduction reaction on surfaces with weaker binding than copper. Copper shows close to optimal adsorbate binding energy for reaction pathway involving CO*/CHO* intermediate[16]. Further improvement in overpotential requirement would require breaking the scaling relation between CO* and CHO*.

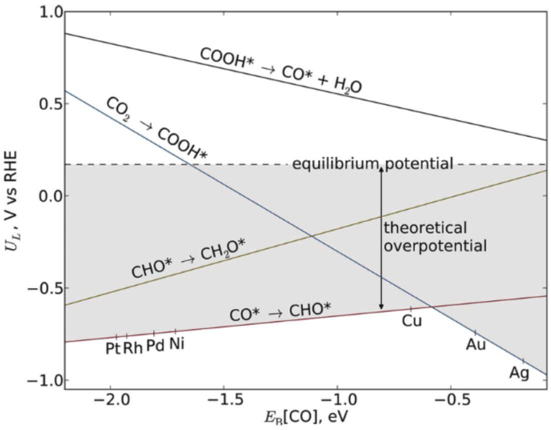

Figure 1-3: Strong CO/CHO* scaling relation dictates the onset for CO_2 reduction to methane/methanol on metallic (211) surfaces. Obtained from* [16]

Alternatively, new class of material with different scaling relation can alleviate the issue. For example doped MoS_2 has been shown to bind CO* significantly weaker than COOH*, CHO* and COH*, relative to transition metal surfaces[23,24]. CO* binding happens on the doped metal atom site and COOH*, CHO* and COH* on the sulphur site. Binding in different sites results in an overall deviation from transition metal scaling lines. Theoretical predictions suggests Ni doped MoS2 can reduce CO_2 to methane with onset potential of -0.28 V-RHE[23]. For two electron transfer products like formate, the binding energy of the 1st electron transfer product determines the thermodynamics of the reaction steps. Thus, it is easier to optimize catalysts for very low overpotential operation. Pt-Pd nanoparticles[25] and CoO_x catalysts[26] have recently been discovered to be very good formic acid evolution electrocatalysts. Oxide derived Cu, has been demonstrated by Kanan and coworkers[27] to exhibits the lowest overpotential for converting CO into methanol at an overpotential of -0.5 V. This provides a possibility of tandem electrocatalysis with optimum CO evolution catalyst along with oxide derived copper[28,29] for liquid fuel production.

Remarkably, a different class of material – metal dioxides, rarely studied as a CO_2 reduction electrocatalyst, has been observed to be active at much lower overpotential of ~0.1-0.3 V-RHE[30–34]. Experimental studies were conducted for pure and mixed oxides of molybdenum, ruthenium, titanium and tin. The catalyst composition, preparation methods and reaction conditions changed the products obtained during these studies. Up to 76% faradic efficiency for methanol was obtained with mixed ruthenium-titanium oxide electrocatalyst at pH 4 and -0.32 V-RHE[31]. In addition, RuO_2 electrocatalyst on boron doped diamond substrate faradic efficiency of ~40% towards formic acid evolution at similar pH and -0.12 V-RHE[33]. These results are strikingly better off than metallic catalysts for methanol or formic acid evolution from CO_2. Exceptional behaviour of oxide catalysts compared to metallic electrocatalysts for CO_2 conversion to liquid fuel indicates possible different reaction mechanism or disparate scaling laws governing the reactions. With only few experimental studies described in the existing literature and large variations in their experimental methods and results, make it difficult to create mechanistic understanding. This thesis explores avenues of understanding distinctive features of CO_2 reduction reaction on oxide surfaces, factors governing activity and propose guidelines for optimized design of oxide electrocatalysts for energy efficient conversion of CO_2 to liquid fuel.

1.4. Computational catalyst design

Design of functional materials based on atomic scale simulations is the penultimate goal of computational materials science[35–38]. Computational materials science is the third pillar that connects experiments and theory. Exponential improvement in available computing power and better algorithms for numerical techniques helped computational science to become an equally powerful tool in discovering new materials. Based on the length and the time scale at which important physical phenomena occur computational materials science uses different physical and chemical models. The less approximate model used, the better portrayal of the actual physical phenomenon is possible. Thus simulation based materials design are becoming more reliable as well. Now it is possible to perform a large set of first principles based in silico experiments to create the theoretical understanding about materials behaviour, which would otherwise need years of carefully controlled experimental work. Such theoretical understanding is then used to design high performance materials to be tested in actual laboratory experiments (Figure 1-4).

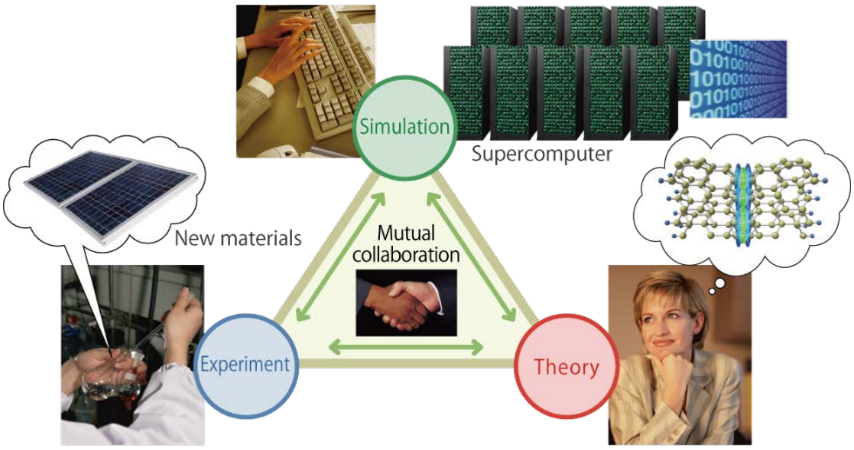

Figure 1-4: Simulations leading the formulation of theoretical understating needed for designer materials, finally to be tested in laboratory. (Image courtesy tohoku.ac.jp)

In the case of catalyst design, predicting the thermodynamics and kinetics of reaction steps at the molecular level and linking them to the observable reaction rate using statistical physics has been used as a theoretical route[37,39]. The electrochemical phenomenon at the catalyst surface are often extremely complex and difficult to portray using atomistic models. Several well accepted and simplified models developed during the last decade have made quantum mechanical simulations of electrochemical reaction feasible. The computational hydrogen electrode[40] concept is one of them. Development of faster, efficient and more accurate density functional theory (DFT) based simulation technique and improvement on computer hardware also helped. It is now possible to describe heterogeneous electrochemical reactions at surfaces with the accuracy required for computational results to compare favorably with experiments. Successful design of electrocatalysts using density functional theory based modelling and consequent validation with experiments further aided in establishing in silico design as a viable alternative to traditional experimental methods[41,42]. Atomic scale simulations also have the added advantage of having a clear picture of electronic level description of the reaction process. It helps in further refining the catalytic activity bottom up. Trend analysis using electronic descriptors like d-band center[43–45] have helped predict the optimal catalyst composition without performing simulation of a very large number of possible catalyst surfaces and reactions on those. Development of basic understanding of defining processes is the key scientific goal, and DFT based simulation is a very capable research tool for that. This thesis primarily relies on computational surface science to come up with important scientific conclusions related to CO_2 electro reduction on oxide electrocatalysts.

1.5. Thesis outline

The PhD work explores a few directions in modelling of CO_2 electro reduction on oxide catalyst surfaces. Rutile oxide surfaces are studied in depth to understand key factors like reaction mechanism, selectivity, onset potential, adsorbate interaction effects and ligand effects. The goal is to create an understanding of how CO_2 reduction reaction (CO2RR) works on oxide electrocatalysts and how one can control the activity to aid further development of oxide catalysts as an alternative of metallic catalysts. The following chapter are included:

- Chapter 1: Introduction
  The critical need for development of efficient electrocatalyst for CO_2 reduction to liquid fuel is explained. Limitations of metallic catalysts and opportunities in exploring oxide based catalyst are indicated.
- Chapter 2: Theoretical background
  Density functional theory based total energy calculations, nudged elastic band method for barriers and catalyst modelling concepts like the computational hydrogen electrode model and scaling relations are briefly introduced.
- Chapter 3: Trends in CO2RR on rutile structured oxide surfaces
  Utilizing model surfaces with varying adsorbate binding characteristics, established reaction mechanisms and activity descriptor. Design guidelines for effective oxide CO2RR electrocatalysts are developed.
- Chapter 4: CO* spectator effects in CO2RR
  Thermodynamics of elementary steps of CO2RR process are studied on RuO_2 (110) surface under variety of CO* coverage and distribution to identify the effects of CO* spectator on reaction mechanism, selectivity and activity.
- Chapter 5: CO2RR on $Ru_xIr_{1-x}O_2$ surfaces
  Behaviour of CO2RR in presence of CO* spectator coverages is presented to understand characteristics of mixed oxide electrocatalyst. Importance of optimum composition and segregation is highlighted.
- Chapter 6: C-C coupling on $Ru_xIr_{1-x}O_2$ surfaces
  Possibility of C-C coupling on mixed oxide surfaces explored leading to CO2RR products with more than one carbon atom.
- Chapter 7: Conclusion and outlook
  Key findings from the PhD project are summarized and possible future research directions suggested.

2.Theoretical background

Recent developments in computational catalysis have been able to link the catalyst performance to the energetics of reaction intermediate binding to the catalyst surface and that of the kinetics of elementary reaction steps. The physics based models used for this PhD project to understand those reaction intermediates and reactions rates at atomic scale, rely on tremendous development of computational electronic structure theory. Basic concepts in density functional theory and computational electrocatalysis are briefly mentioned here.

Activity of chemical reactions on catalyst surfaces are linked to the adsorption strength of reaction intermediates, which in turn depends on the electronic structure of the catalyst surface. The catalyst electronic structure can be described by using computational methods utilizing the theory of quantum mechanics. The reaction thermodynamics and kinetics can be predicted from ab-initio simulations if one can calculate the total energy of catalyst with reaction intermediates. Of many approaches towards electronic structure simulation most widely used one is density functional theory (DFT). This approach has helped us during the last two decades to gain insight into chemical reactions on surfaces[37]. It is possible to evaluate the complete thermodynamic and kinetics for chemical reactions based solely on DFT calculations.

2.1. Electronic structure problem

All material properties can be in principal obtained by solving the time dependent Schrödinger equation[46] for the electronic wavefunction of the system:

$$\hat{H}\psi = i\frac{\partial}{\partial t}\psi \qquad 2\text{-}1$$

Where $\hat{H}$ is the Hamiltonian operator and ψ is the electronic wavefunction which is dependent on nuclear and electronic coordinates and time. No closed form analytical exact solution exists for two or more interacting particles. So judicious approximations and numerical techniques are needed to obtain solutions for system size of engineering consequence. Simulations related to electrocatalysis do not require time dependency as no optical excitations are utilized as in photocatalysis. Assuming time invariant orbitals, the N-electron time independent Schrödinger equation is obtained.

$$\hat{H}\psi = E\psi \qquad 2\text{-}2$$

Now ψ is the N electron wavefunction without time variation and E is the total energy of the system.

As the nuclei are many orders of magnitude heavier than the electrons, the Born-Oppenheimer approximation[47] can be applied to decouple the motion of nuclei and electrons. Electrons are assumed to follow nuclear movement instantaneously i.e. any nuclear motion follows instantaneous electronic transfer. Adopting atomic units the Hamiltonian can be written as

$$\hat{H} = -\frac{1}{2}\sum_{i=1}^{N}\nabla_i^2 + \sum_{i=1}^{N}\upsilon_{ext}(r_i) + \frac{1}{2}\sum_{i\neq j}^{N}\frac{1}{\left|r_i - r_j\right|} \qquad 2\text{-}3$$

The first term is the kinetic energy operator for the electrons ($\hat{T}$). The middle term is the external potential acting on electrons due to the nuclei ($\hat{V}_{ext}$). The last term is the electron-electron coulomb interaction ($\hat{V}_{\mathrm{int}}$). Terms from nuclear-nuclear interaction is trivial and nuclear kinetic energy operator are ignored from Born Oppenheimer approximation. The Hamiltonian can be written as

$$\hat{H} = \hat{T} + \hat{V}_{ext} + \hat{V}_{\mathrm{int}} \qquad 2\text{-}4$$

2.1.1. Density functional theory

Density functional theory translates the 3N variable wavefunction problem to one related to electronic charge density, which is a three spatial coordinate based variable. This allows electronic scale simulation at the scale of actual engineering importance. In the DFT scheme, all operators in the Hamiltonian are function of charge density ρ which is spatially (r) dependent. The Hohenberg Kohn theorems[48] linked the charge density distribution to the electronic wavefunction and thus all ground state properties. 1st Hohenberg and Kohn theorem proves that the ground state density ρ(r) uniquely determine the external potential and the total energy of the ground state wave function. Now the energy of the system can be written as

$$E[\rho] = T[\rho] + V_{ext}[\rho] + \int d^3V_{ext}(r)\rho(r) \qquad 2\text{-}5$$

The 2nd Hohenberg Kohn theorem states that the ground state energy can be obtained variationally i.e. the density that minimizes the total energy is the exact ground state density. Later on, Kohn and Sham[49] proposed a scheme to map a system of interacting particles located in an external potential onto a system of non-interacting particles in an effective potential V_{eff}, which has the same ground state density. The 2nd Hohenberg Kohn theorem dictates that the total energy of these two systems will be same. In the Kohn Sham scheme, the total energy is written as

$$E[\rho(r)] = T_s[\rho(r)] + V_H[\rho(r)] + E_{xc}[\rho(r)] + V_{ext}[\rho(r)] \qquad 2\text{-}6$$

T_S is the kinetic energy of the non-interacting electron gas, V_H is the Hartree energy. E_{xc} is a concept introduced to incorporate the electron exchange and correlation. The exact form of it makes result from DFT based simulations exact. However, currently only approximate forms are known and this is an active area of research to develop an accurate and efficient approximation to the E_{xc}.

The T_s part is obtained by iterative solution of Kohn Sham equations (2-7 and 2-8) relating charge density and effective potential starting from an approximate charge density until satisfactory convergence is reached.

$$[-\frac{1}{2}\nabla^2 + V_{eff}(r)]\psi_i = \varepsilon\psi_i \quad while \quad \rho(r) = \sum_{i \in occupied} |\psi_i|^2 \tag{2-7}$$

$$V_{eff}(r) = V_{ext} + \int \frac{\rho(r')}{|r - r'|}dr + \frac{\delta E_{xc}[\rho(r)]}{\delta\rho(r)} \tag{2-8}$$

In this project density functional theory based iterative total energy calculation method has been used as implemented in Vienna ab-initio simulation package (VASP).

2.1.2. Exchange correlation functional

Electron exchange energy comes from Pauli exclusion principle and correlation term is non-zero due to the dependency of electron-electron interaction on the presence of other electrons. The accuracy of Kohn Sham scheme of iterative solution for ground state energy depends on how close is the exchange correlation functional E_{xc} approximation is to the exact one. Often the simplest approximation from the homogeneous electron gas model with only local charge density dependent[50] exchange and correlation (local density approximation (LDA)) works well.

$$E_{xc}^{LDA}[\rho] = \int \varepsilon_{xc}^{LDA}[\rho(r)]dr \tag{2-9}$$

Where ε_{xc} is the functional. Simple models as this enables quick large scale simulation, but are low on accuracy. Solids are well represented by this model, but for molecular and surface system (important for catalysis) with large variation in charge density require approximations that are more sophisticated. The approximations introducing gradient of charge density (generalized gradient approximation (GGA)) in the model[51] together with the local density are most popular now.

$$E_{xc}^{GGA}[\rho] = \int \varepsilon_{xc}^{GGA}[\rho(r), \nabla\rho(r)]dr \tag{2-10}$$

Optimized flavours for GGA functionals have been developed like RPBE[52] and BEEF[53,54] for good accuracy in atomistic catalysis process simulation. BEEF functional along with vdW-DF2[55] nonlocal correlation energy and potential function have been used throughout this work. Often non-local interactions like hydrogen bonding are key to the behaviour of molecular systems like large adsorbate on catalysts surface. Such interactions can be captured by special exchange correlation functional like vdW-DF2.

2.1.3. Plane wave basis

In VASP the Kohn-Sham wave functions are described by a set of plane wave basis functions. This choice of plane waves as a basis requires the system to be solved in a cell with periodic boundary conditions. This, however, makes the code well suited for investigating bulk crystal structures, which are periodic in all three dimensions. By introducing vacuum regions, 2D systems like surfaces can also be calculated. In this case, a slab with a reasonable number of

atomic layers with vacuum in both sides, is built in order to simulate the surface. In addition, molecules can be calculated by introducing vacuum in all three dimensions.
Larger number of plane waves lead to better description of the wave functions. An energy cutoff E_{cut} is used based on the required accuracy. 500 eV have been chosen as E_{cut} in simulations done for this thesis based on reproducibility of key material parameters. In addition, the reciprocal space (first Brillouin zone) has to be sampled densely with wave vectors (k-points) for correct wave function approximation. Here the k-points are sampled with a Monkhorst-Pack grid[56]. To reduce the computational load, with Projector Augmented Method (PAW) utilized in VASP, one can model the tightly bound core electrons of an atom as frozen and outer electrons are represented by soft pseudo valence projector functions.

2.2. Free energy of molecules and reaction intermediates

One can estimate the binding free energy of a reaction intermediate on a catalyst surface from free energy estimates of the surface without the adsorbate, that of the surface with the adsorbate and free energy of reference molecules. For example, the binding free energy of OCHO* (ΔG_{OCHO*}) will be

$$\Delta G_{OCHO*} = G_{OCHO*} - G_{*} - G_{CO_2} - \frac{1}{2} G_{H_2} \qquad 2\text{-}11$$

where, G_{OCHO*} is the free energy of the surface with the OHCO* adsorbate, G_{*} is that of the surface only, G_{CO2} and G_{H2} are the free energy of CO_2 and H_2 molecules. * denotes a empty active site and A* denotes an adsorbate A bound to that active site.

2.2.1. Free energy corrections

To estimate the free energy of an adsorbate configuration, ground state energy from DFT simulations is done at 0K. Finite temperature energy contributions from heat capacity (C_p), entropy (TS) as well as zero point energy (E_{ZPE}) are calculated by treating the adsorbate degrees of freedom as independent quantum mechanical harmonic oscillators within the harmonic approximation.

$$G = E_{DFT} + E_{ZPE} + \int C_p dT - TS \qquad 2\text{-}12$$

Normal mode calculations using a two-point finite difference approximation with small displacements of 0.01 Å along all three axis for each atom in the adsorbate and spectator species are done. Atoms in the catalyst surface are not vibrated in calculations during the course of this project. Verification were made that vibrating surface atoms with adsorbates lead to negligible changes in free energy corrections. The free energies of molecules are calculated within the ideal gas approximation assuming vibrational, rotational and translational modes are decoupled. The total energies of molecules are calculated with a cell such that at least 12 Å of vacuum is present between periodic images. Vibrational modes and their free energy contributions are calculated and analyzed using the Atomistic Simulation Environment (ASE)[57]. The energies of molecular CO_2 and H_2 are corrected by +0.3 eV and +0.1 eV respectively to correct for the systematic DFT errors that originate from inaccurate descriptions of carbon-oxygen double bonds[58] and observed shift in describing hydrogen bond energy in BEEF ensemble. $CO_2(g)$, $H_2O(l)$ and $H_2(g)$ free energies are used as references for reaction free energy and adsorbate binding free energy calculations. Species and products like CH_4, HCOOH, CH_3OH etc. are either in a liquid state or in solution. Fugacity value reported in articles on theoretical CO_2 electroreduction[17,59] is used. Experimentally, CO2RR is typically done in a 0.1 to 0.5 M solution of $KHCO_3$ or $NaHCO_3$ [15,22,27,32]. Such solutions allow dilute (0.01M considered here) formic acid to exist in a hydrated anion form ($HCOO^-$). A free energy correction of -0.19 eV for deprotonation and solvation has therefore been included[18]. The free energy of $H_2C(OH)_2(aq)$ is obtained from previous theoretical work[59]. Much lower fugacity value of 0.003 Pa for methanol is used in chapter 3 and 4 to match experimentally observed methanol concentration in CO2RR condition.

2.3. Computational hydrogen electrode model

The presence of electrolyte molecules and electric field makes estimation of free energy of adsorption for electrochemical reaction intermediates, a complex task. It is computationally very demanding to systematically simulate a large number of adsorbate/catalyst surface configurations with the full details of the electrified electrolyte-catalyst interface. The computational hydrogen electrode (CHE) model allows approximating the reaction free energy of an electrochemical reaction[60] at a certain applied potential from the reaction free energy calculated without explicitly considering the potential or the electrolyte. The model links the reaction free energy of each step involving a coupled electron proton transfer (ΔG_{step}) to the applied potential (U) by a simple linear relation

$$\Delta G_{step}(U) = \Delta G_{step}(U = 0) + eU \qquad \text{2-13}$$

where e is the elementary charge. Thus, for any such elementary step, one can calculate the free energy change associated with the transformation at U=0 V and predict the electrochemical potential required to drive the reaction step forward. ΔG_{step} for any reaction step is estimated as the difference between the binding free energy of the final and the initial adsorbates for the reaction step. For example, $\Delta G_{OCHO*\rightarrow HCOOH*}$ is defined as

$$\Delta G_{OHCO*\rightarrow HCOOH*} = \Delta G_{HCOOH*} - \Delta G_{OCHO*}$$

If the potential is chosen to be on a reversible hydrogen electrode (RHE) scale, where the following reaction is reversible at 0 V vs RHE (V-RHE)

$$\frac{1}{2}H_2 = H^+ + e^- \qquad \text{2-14}$$

In CHE model, the free energy of an adsorbate (e.g. ΔG_{HCOOH*}) is estimated with respect to hydrogen gas. Utilizing the adsorbate binding free energies for calculation of ΔG_{step}, at U = 0 V, the energies for the proton and electron gets included implicitly.

For the overall reaction to happen at an appreciable rate, all such steps must have $\Delta G_{step}<0$. The reaction step requiring the largest negative potential for making the forward reaction feasible is called the potential limiting step and the required potential is the limiting potential for the overall reaction.

2.4. Scaling relations

The thermodynamics of reactions on electrocatalyst surfaces depends on binding energy of intermediate molecules on the catalyst surface. Density functional theory based simulations have shown that[61] the adsorption energy of any of the molecules considered scales approximately with the adsorption energy of the central, C, N, O, or S atom. This behaviour comes from the fact that the central atom participates in direct chemical bonding with the catalyst surface. These observed linear relations between binding energy of adsorbates, which connects to the surface with the same atom, is popularly known as scaling relations within the field of theoretical catalysis[616263]. For example, OH* and OCHO* intermediates binds to the surface through oxygen atoms and their binding energies should scale with that of O*, i.e. they should also scale with each other.

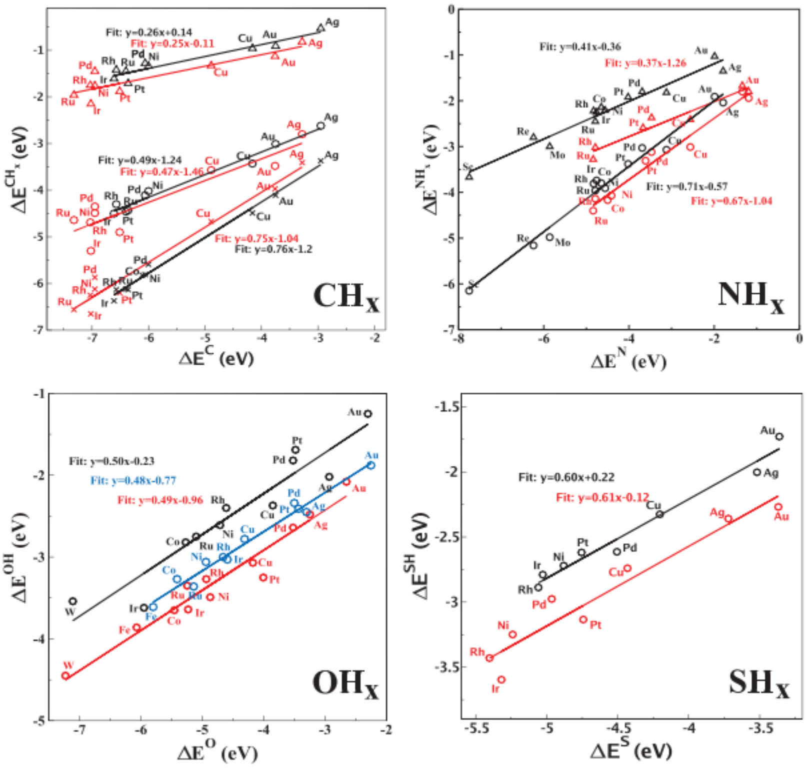

2-15: Linear scaling between adsorption energy of adsorbates, which bind through the same atom on metallic surfaces. Obtained from [61]

2.4.1. Volcano relation in multistep reaction

Sabatier's empirical law states that for a reaction, there is an optimum binding energy for an intermediate where both stronger and weaker binding leads to lower activity. This volcano shaped relationship between activity and binding energy is straightforward to understand for a simple reaction like HER[64]. If the hydrogen atom binds too weakly to the surface then it is inefficient to create H*, and if it binds too strongly then removal of H* to make hydrogen gas takes too much energy. However, the relationship between adsorbate binding energies and overall activity is non-intuitive for a complex reaction like CO2RR due to the large number of adsorbates and possible pathways. Simple linear relations based on scaling laws help reducing this complexity. Utilizing correlation between the binding energy of different adsorbates, the activity can be modelled as a function of only one or two binding energy parameters. Finally, this simplification lead to a volcano like binding energy – activity relation similar to Sabatier's volcano concept. The binding energy to which one can correlate all other binding energy parameters and activity, is often termed as the descriptor for the catalytic process.

2.5. Nudged elastic band method

The slowest reaction step is a rare event in comparison to other fast reaction steps or molecular vibrations. For calculation of kinetic barrier of elementary reaction steps, which are rate limiting, transition state theory, can be used due to the difference in timescale. Key to this is finding the saddle point, which is the lowest possible peak in energy landscape along a trajectory between the initial and the final atomic configuration of the reaction step. Being a saddle point on the potential energy landscape, the reaction rate is maximum through this path.

In the nudged elastic band (NEB) method[65], an preliminary guess for a path between two stable states is mapped out with several images. To search for a minimum energy path between the initial and final state and to keep the images evenly distributed along the path an effective spring force is applied between consecutive images along the path. While minimizing, the tangential component of the spring force and the perpendicular component of the real force is used. To force one of the images at the saddle point, the image with the highest energy is released from the spring system and relaxed with a reversal of the force component along the direction of the path. This trick is known as climbing image NEB[66].

3.Trends in CO2RR on rutile structured oxide surfaces

Atomistic mechanisms for CO_2 reduction reactions on oxides surfaces can be much different from mechanisms on metallic catalyst surfaces and exhibit different thermodynamic limitations. In this chapter, the mechanistic specialties of CO2RR to 1C products (molecules containing a single carbon atom) on model rutile oxide overlayer structures are explored. Trend analysis enunciates OH* binding as the key descriptor. Activity volcanos are created for CO2RR on oxide surfaces using scaling relations. In addition, a guideline for important binding energy parameters for oxide surfaces is derived, which will allow good activity, and selectivity for CO2RR.

3.1. Introduction

Experimental research in catalysts for electrochemical conversion of CO_2 to reduced energy rich molecules dates back almost four decades[67]. The first comprehensive work on metallic catalysts for CO2RR was done by Hori[13,15]. Density functional theory based modelling of the reaction process at the atomic level has recently helped[16] understand the limitations met while optimizing metallic catalysts for methane and methanol evolution from CO_2. Reduction of CO* to CHO* is an essential step in methane and methanol evolution on metallic catalyst surfaces. The scaling relation between CO* and CHO* adsorbates is such that modification in binding energy of the catalyst surfaces do not significantly improve upon the onset potential requirement. Theoretical analysis based on scaling relations leads to a best-case scenario of ~-0.65 V-RHE as the onset potential at the top of the activity volcano. This limitation can be overcome by breaking the scaling relation or by promoting for a path that is not limited by this scaling. Metal di-chalcogenides have been shown to achieve this by binding CO* and CHO* at different sites[23]. Scientific literature suggest rutile-structured oxide catalysts can reduce CO_2 to 1C liquid products at low overpotential potential with good faradic efficiency[30–34,68]. This opens up the possibility that either the CO*/CHO* scaling relation is different on such oxides or CO* reduction is not part of the path. Recent computational research by Karamad et.al. suggested that on the RuO_2 (110) surface, CO_2 proceeds through a HCOOH* intermediate[69] instead of a CO* intermediate at the 2nd electron/proton transfer step. HCOOH* binds through an oxygen atom to the active site unlike CO* and CHO* which binding through the carbon atom. Scaling relations are often valid for similar adsorbates which binding through the same atom[61]. Correlation has also been observed between COOH* and H* adsorbates on metallic surfaces[70] but not between OH* and CO*[71]. Thus the CO2RR reaction mechanism utilizing O-atom coordinated adsorbates like HCOOH* is expected to be bound by different scaling relations. The activity volcano will thus be different. The main goal of this part of the PhD project is to establish the active reaction mechanism in a wide range of rutile structured oxide surfaces and to look for scaling relations for this class of materials. Such understanding will allow defining an activity volcano for CO2RR on such oxide surfaces and create design guidelines for efficient oxide catalysts.

3.2. Computational approach

3.2.1. Simulation details

In this part of the project, the Vienna Ab-initio Simulation Package[72] (VASP) with plane wave basis sets and the projector-augmented wave based DFT implementation has been used. Details of the theoretical methods and exchange correlation functional used have already been discussed in chapter 2. Parameters specific to the work presented in this chapter are mentioned here. The bulk RuO_2 unit cell Brillouin zone is sampled with a 5×5×7 Monkhorst-Pack k-point mesh. For oxide catalyst surface slab a mesh of 4×4×1 is used. A 500 eV plane wave energy cutoff is used for all simulations. Systems studied here are conducting by nature as needed for electron transport for electrocatalysis. A Gaussian smearing of 10 meV is used for the electronic states in all calculations. Optimizations of atomic structures are performed until forces acting on non-constrained atoms are less than 0.003 eV/Å. As explained in chapter 2, BEEF-vdW[54] exchange correlation functional is used as needed for atomistic CO2RR simulation.

3.2.2. Simulation model for catalysts

Experimental results showing encouraging results for oxide electrocatalysts towards CO2RR, often employ RuO_2 as the main component for the catalyst[30–34,73]. Thus, this analysis builds upon the recent experimental and theoretical work[69]. RuO_2 is a rutile (tetragonal) structured dioxide with a unit cell consisting of two metal and four oxygen atoms (Figure 3-1). RuO_2 bulk properties like lattice parameters are reproduced with DFT simulations within acceptable accuracy. Calculated RuO_2 lattice parameters are a = 4.537 Å and c = 3.135 Å. These are less than 2% different from the experimentally observed lattice parameters of a = 4.491 Å and c = 3.106 Å. GGA type xc-functional often overestimate lattice parameter of bulk oxides by a few percentage points[74].

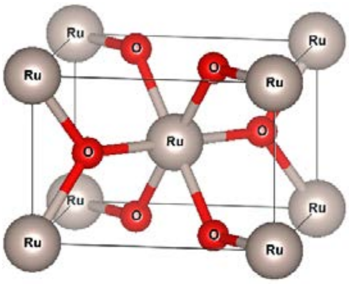

Figure 3-1: Atoms in the unit cell of bulk RuO_2

Among low index surfaces of rutile structures metal dioxides like TiO_2, RuO_2, IrO_2, VO_2 etc., the (110) surface has been shown to be the most stable surface[75–77]. The (110) surface is thus expected to be widely available among open facets in catalyst nanoparticles of such oxides.

The RuO_2 (110) surface is used as a template for catalysts in this part of the project. As a model of a RuO_2 (110) surface with available active sites, a 2×2 slab is created consisting of four metal atom layers (Figure 3-2). This surface has two types of sites – bridge and coordinated unsaturated sites (cus)[78]. Bridge sites are between two metal atoms and are occupied by oxygen atom in oxidizing condition. CO2RR needs reducing condition and thus these bridge site oxygen atoms are expected to be removed making the bridge site available for reaction intermediates or spectators to occupy[79]. Cus sites are on-top sites above a metal atom. In the simulation cell two bridge and two cus sites are accessible. Due to the periodic boundary condition imposed in the plane wave basis, catalyst surface is modeled with a slab. To manage the computational complexity, catalysis process simulation is done on one surface and the other surface is kept empty. Two atomic layers at the bottom forming the second surface, is kept fixed to the structure of bulk materials. This is to imitate a semi-infinite bulk. Any rearrangement in atomic position due to adsorbates is minimal beyond the first two atomic layers. Atoms in the top two layers as well as any adsorbate present are optimized to minimize forces.

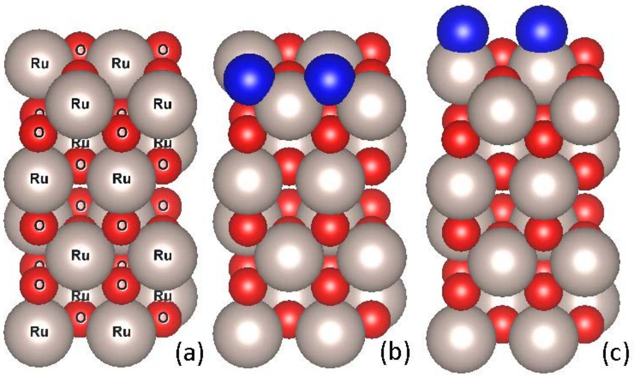

Figure 3-2: simulation model for RuO_2 (110) surface (a) bare surface with bridge and cus sites empty (b) blue sphere coordinated with two ruthenium atoms show the location of bridge sites (c) blue spheres on top of ruthenium atom locate the coordinated unsaturated sites.

To create generalized understanding of trends in CO2RR activity on oxides surfaces, CO2RR needs to be simulated on catalytic surfaces with widely varying adsorbate binding characteristics. Weak binding surfaces might allow a different reaction mechanism than strong binding surfaces. Many different parameters like strain[80,81], substitution[82,83], active site geometry[84,85], ligand effect[86–88], lattice structure[89] etc. can affect the catalytic reaction besides adsorbate binding energy. Both experimentally and theoretically researcher often use model hetero-structures to produce a set of results on catalyst activity and other chemical properties from which statistical inferences can be drawn on the underlying trends[90–94]. A number of over-layer structures have been taken as examples for oxides surfaces with a large spread in binding energy. To simplify the analysis, these overlayer are created as a monolayer of rutile structured metal oxide (other than RuO_2) on top of a 3-layer RuO_2 (110) slab (Figure 3-3(a)). Considering different metal atoms the top layer, the binding energy is changed. The presence and availability of bridge and cus sites remain the same as the RuO_2 (110) model surface. The monolayer oxide structure conforms to the RuO_2 (110) substrate. Thus the simulation box and lattice structure of the bottom two fixed layer is also kept unchanged. To assert the feasibility of actually fabricating such oxide hetero-structures and stability, ruthenium in the top layer has been replaced with metals that have an ionic radius very similar to ruthenium in RuO_2 (+4 oxidation state and octahedral coordination). Goldschmidt's rule proposes up to 15% variation in ionic radius and equivalent oxidations state likely replacement of the cation in oxide crystals. Maximum difference of 10% has been used to choose the metals atoms in the top layer in the model oxide catalyst surfaces. Chosen overlayer contain Ru, Ir, Mo, Nb, Pd, Pt, Re, Sn, Ta, Ti and W atom in the top layer. All oxides - RuO_2, IrO_2, MoO_2, NbO_2, PdO_2, PtO_2, ReO_2, SnO_2, TaO_2, TiO_2 and WO_2 are available in rutile structure[95]. Thus, precise atomic scale epitaxial growth techniques like reflection high energy electron diffraction (RHEED) controlled molecular beam epitaxy (MBE)[96] is anticipated to be able to reproduce oxide hetero-structures studied here.

Surfaces in electrochemical environment are expected to have species like H*, OH*, O* adsorbed at the active site if the free energy for formation of such adsorbates are negative. In CO2RR condition a small amount of CO molecules might evolve along with fuel molecules like methanol methane etc. and stay at the active site. Evolution of CO, its binding strength to the active site and possible coverage on the surfaces depend upon the catalyst surface. Adsorbates interaction can happen via modification of electronic structure[97,98] as well steric and hydrogen bond effects[99] creating promotion and poisoning. Spectator CO* species also have been observed to modify catalytic behaviour of metal surfaces[100,101]. So to included CO* coverage effect in the study and at the same time maintain comparability, one CO* spectator molecule is considered (Figure 3-3(b)) in the simulation box at one of the bridge site. This 25% surface CO* coverage leaves one bridge site and two cus site for reaction in the model catalyst slab.

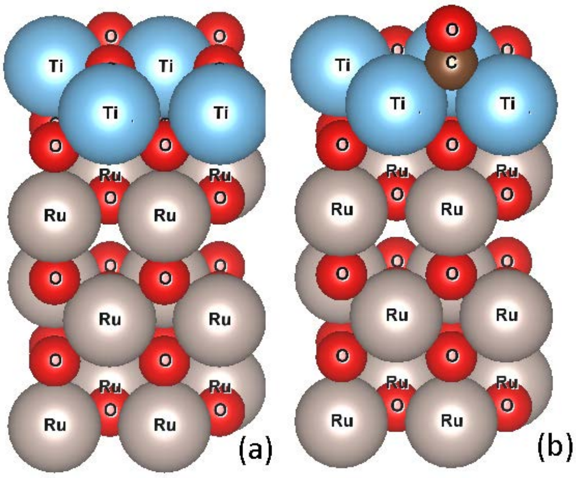

Figure 3-3: Simulation model for TiO_2 on RuO_2 over-layer structure (a) all active sites empty (b) oen bridge site occupied by CO molecule*

3.3. Results and discussion

3.3.1. CO* adsorption

The bridge site binds adsorbates stronger than the cus site for a pure RuO_2 (110) surface[102]. Binding energy of a CO* adsorbate at the bridge site (on overlayer surfaces without any other adsorbates) vary remarkably for different oxide hetero-structures (Table 3-1). The free energy change from binding a CO molecule to the surfaces is notably large on oxide surfaces with rhenium and molybdenum. On such surfaces, the CO* adsorbate shorten the CO-metal bond distance, indicating strong bonding. This effect reduces the symmetry of the top oxide layer as some metal-metal atomic distances decrease and others increase.

Table 3-1: CO binding energy on different overlayer at the bridge site (at bridge site on empty oxide surface w.r.t. gas molecule).*

Top oxide layer metal atom	CO* binding energy (eV)
Ru	-1.34
Ir	-1.61
Mo	-2.09
Nb	-1.48
Pd	-0.23
Pt	-1.00
Re	-3.61
Sn	0.24
Ta	-1.45
Ti	-0.48
W	-1.93

3.3.2. CO* spectator effect on competing HER

Hydrogen evolution reaction is the main competing reaction for CO2RR. If active sites preferentially bind H* and available protons have a small barrier towards forming hydrogen gas from H* and large barrier towards combining with CO_2 molecule, carbonaceous products are not produced. Thus, it is crucial to suppress hydrogen evolution to obtain good faradic efficiency from CO2RR. For example, Ni catalyst in CO2RR condition makes primarily hydrogen[15], although it has a similar methane onset potential as Cu[16], which evolves a mixture of CO_2 reduction products at high overpotential[17]. Presence of CO* spectator has been proven to affect hydrogen evolution[100]. It can either promote or prevent HER. Weakening of H* binding on the catalyst surface due to interaction with CO* spectator causes this[100].

Table 3-2: Effect of CO spectator on binding free energy of H* (ΔG[H]) adsorbate in the bridge site and HER onset potential.*

Top layer metal atom	ΔG[H] on empty surface (eV)	ΔG[H] with CO* spectator (eV)	Change in binding free energy (eV)	HER onset without CO* spectator (V-RHE)	HER onset with CO* spectator (V-RHE)	Effect of CO* spectator
Ru	-0.49	-0.31	0.18	-0.49	-0.31	promotion
Ir	-0.75	-0.15	0.60	-0.75	-0.15	promotion
Mo	-0.99	-0.17	0.82	-0.99	-0.17	promotion
Nb	-0.89	-0.95	-0.06	-0.89	-0.95	poisoning
Pd	0.24	0.42	0.18	-0.24	-0.42	poisoning
Pt	-0.48	-0.19	0.29	-0.48	-0.19	promotion
Re	-1.08	0.95	2.03	-1.08	-0.95	promotion
Sn	0.09	0.27	0.18	-0.09	-0.27	poisoning
Ta	0.05	-0.85	-0.90	-0.05	-0.85	poisoning
Ti	-0.13	0.18	0.31	-0.13	-0.18	poisoning
W	-0.79	-1.15	-0.36	-0.79	-1.15	poisoning

Here the impact of CO* spectators on H* binding is studied. Oxide overlayers with Mo/Ir/Re/Ta metal atoms observed to show large modification in H* binding energy due to CO* spectators. Adsorbate-adsorbate interaction between CO* and H* can be both attractive (Ta/W/Nb-oxide overlayer) and repulsive (rest of the surfaces). The magnitude of changes in H* binding energy is much larger than that observed on metals[100]. CO* spectators can be used as a tool to optimize selectivity of CO2RR over HER on oxides. However, lack of systemic behaviour means once a suitable oxide for CO2RR is found, CO* coverage effects must be studied for that oxide in details.

3.3.3. Hydroxylation of the active site

OH^- radicals present in the aqueous electrolyte can populate the active site[103]. The free energy associated with this reaction is often negative (Table 3-3), making the process spontaneous. Large reducing potential need to be applied to remove the hydroxyl as water and make the active site available for reaction intermediates. Thus hydroxylation can become a limitation for CO2RR, especially if it is difficult to remove the OH* from the active site. CO* presence in the neighbouring bridge site can alter the potential for dihydroxylation. For molybdenum and rhenium oxide over-layers, CO* can significantly weaken OH* binding. On ruthenium and tantalum oxide over-layer the opposite effect is observed (Table 3-3). Given the importance of CO* spectator interaction on the adsorption energy, CO2RR reaction path analysis is done with CO* coverage. One of the bridge sites in the simulation model is always occupied yielding 25% CO* spectator coverage consistently for all surfaces.

Table 3-3: Hydroxyl binding energy at the bridge site, in absence and presence of spectator CO.*

Top oxide layer metal atom	OH* binding energy without CO* spectator (eV)	OH* binding energy with CO* spectator (eV)	Change in binding free energy (eV)
Ru	-0.32	-0.64	-0.32
Ir	-0.76	-0.49	0.27
Mo	-1.63	-0.86	0.77
Nb	-1.73	-1.90	-0.17
Pd	0.42	0.78	0.36
Pt	-0.34	0.02	0.36
Re	-1.65	-0.63	1.02
Sn	-0.67	-0.51	0.16
Ta	-1.47	-2.03	-0.56
Ti	-1.45	-0.95	0.50
W	-1.90	-1.70	0.20

3.3.4. CO_2 activation

CO2RR can proceed through a myriad of multi-electron electron transfer processes. It is initiated through an electrochemical step of protonating a CO_2 molecule to make an adsorbed reaction intermediate. It leads to carboxyl (COOH*) intermediate or formate (OCHO*) intermediate. Carboxyl is attached to the active site via the carbon atom. OCHO* binds through both the oxygen atoms. In the simulation model for CO2RR, one bridge site is occupied by a CO* spectator. COOH* is adsorbed at the other bridge site. OCHO* is a bidentate adsorbate. OCHO* utilized both a bridge site and the nearest cus site. Despite the large spread in the binding characteristic of the simulated surfaces, OCHO* is stronger bound to the surface compared to COOH* by 0.14 eV to 1.79 eV (Figure 3-4). Elementary symbols for metal atom in the top layer are used for oxide overlayer nomenclature. Henceforth, such naming convention will be used in figures and tables of this chapter. Platinum and palladium are the most non-reactive surfaces and prone to HER. These surfaces also show little preference towards formation of OCHO* over COOH*. Over-layers with Nb/Ta/W atoms show strong OH* binding in presence of CO* adsorbate. The same set of surfaces also bind OCHO* strongest with a binding free energy <-1.5 eV. Generally surfaces with strong OH* binding show higher preference for OCHO* than COOH* characterized by the large difference in binding free energy (Figure 3-4). Preferential formation of OCHO* is crucial for selectivity and the overpotential needed. COOH* adsorbates can get further reduced to adsorbed CO* or CO molecule as product[104]. CHO* formation from CO* and further to methane or methanol would be have the CO*/CHO* scaling law limitations as has been discussed previously (chapter 1.3). CO gas evolution is not the goal of this project as effective metallic catalysts exist for that.

Favourable OCHO* intermediate formation free energy is not only important for the selectivity of liquid fuel as CO2RR product over CO; but also to improve selectivity of CO2RR compared to HER. HER is a simple two electron process and have lower overpotential on surfaces studied here than the typical CO2RR onset potential of <-0.5 V-RHE. Thus, hydrogen can be a major product if formation of OCHO* or COOH* is less favourable than H*. However very stable OCHO* intermediate translates to selectivity towards CO2RR as the active site is preferentially occupied by OCHO* over H*. OCHO* can be further reduced to energetic molecules like formic acid, methanol, methane etc.

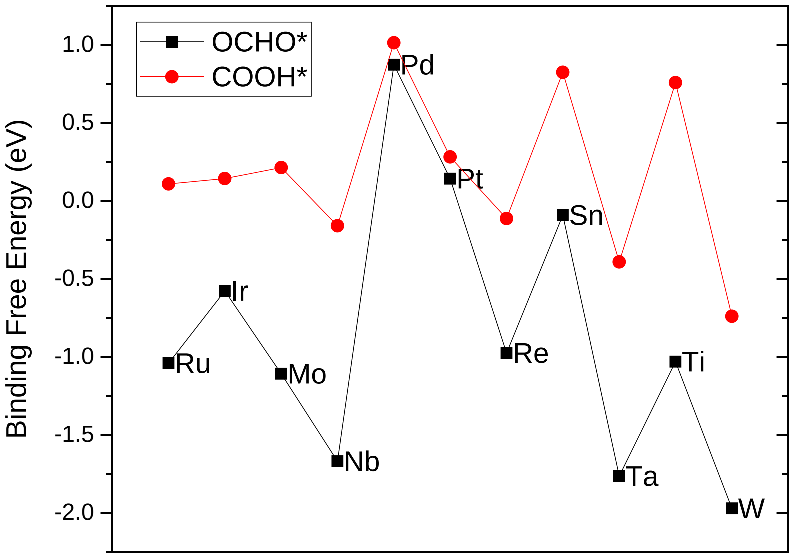

Figure 3-4: Binding free energy of COOH and OCHO* on oxide over-layer surfaces with 25% CO* spectator present.*

3.3.5. CO2RR pathway

In this part of the project reaction mechanisms have been studied pertaining to reaction products with only one carbon atom (C1). The OCHO* intermediate can lead to formic acid, methanediol, methanol and methane via 2e$^-$, 4e$^-$, 6e$^-$, 8e$^-$ transfer reaction mechanisms. At every electron transfer step, more than one reaction intermediate can form, implying a reaction network with many possible reaction mechanisms to the same product. Relative adsorption energy of intermediates at a particular reaction step on a surface can determine the active reaction mechanism on that surface. Knowledge of the stability of oxygen coordinated OCHO* intermediates over carbon coordinate COOH* intermediates helps limit the reaction tree to a manageable size consisting of oxygen coordinated intermediates only (Figure 3-5). All reaction step thermodynamic analysis is done with 25% CO* spectator.

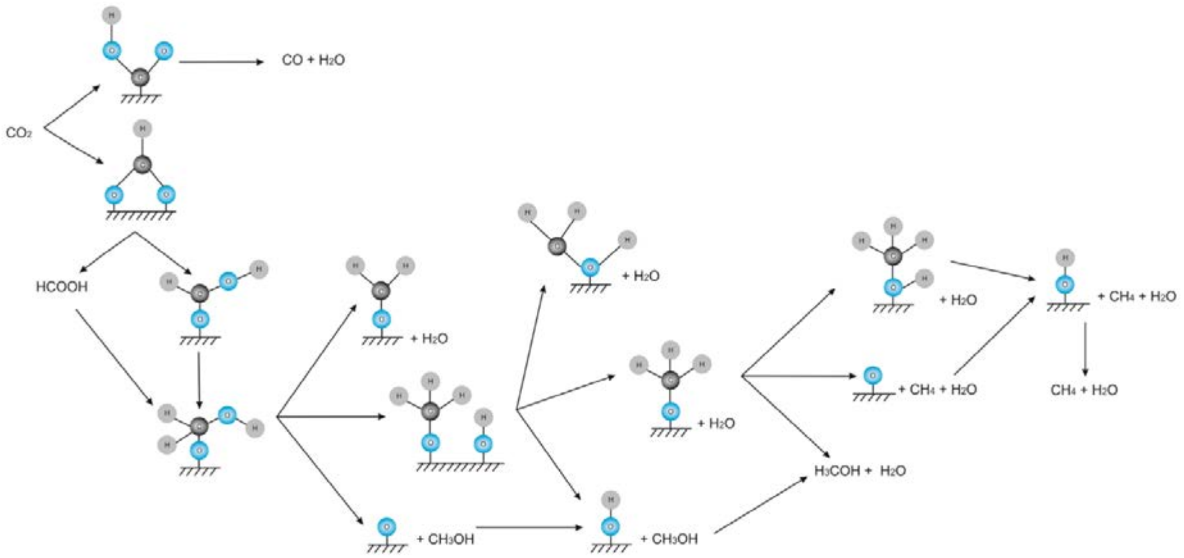

Figure 3-5: CO2RR reaction network studied for the preferred reaction mechanism over all eleven oxide-overlayers.

3.3.6. Formic acid evolution

The 2nd proton/electron transfer step reduces the OCHO* intermediate to a HCOOH* adsorbate or HCOOH (aq) molecule. Often formic acid in the electrolyte is deprotonated as $HCOO^-$ and in a solvated state. If the active sites can not bind HCOOH* intermediate, it leaves the surface as formic acid. As 2nd electron transfer product, formic acid is preferred over CO molecule as the precursor to CO molecules (COOH* intermediate) is difficult to form on oxide surfaces.

The overall reaction consist of the following two electrochemical steps where * denotes available bridge site with spectator CO*

$CO_2(aq) + H^+ + e^- + * \rightarrow OCHO*$

$OCHO* + H^+ + e^- \rightarrow HCOOH\ (aq)$

Figure 3-6 summarizes the thermodynamics of these two steps at 0 V-RHE. If the step has a positive free energy change, reducing potential needs to be applied to make the proton transfer occur. A negative free energy change amounts to a facile forward reaction. Formation of OCHO* from CO_2 molecule is downhill in free energy on all surfaces except the very weak binding Pt and Pd-oxide overlayers. The equilibrium potential of formic acid evolution is -0.06 V-RHE based on free energy of molecules used here. If OCHO* binds too strong to the active site, removing it as a formic acid molecule becomes thermodynamically limiting and thus requires large reducing potential to drive the reaction forward (Figure 3-6). On the contrary, on the Pd-oxide overlayer, OCHO* cannot form and HER will be the preferred reaction. The Pt-oxide overlayer binds OCHO* optimal and predicted onset potential is -0.14 V-RHE. However, H* is more stable than OCHO* on the Pt-oxide overlayer, leading to hydrogen evolution only. The Sn-oxide over layer is expected not to prefer HER to CO2RR as OCHO* is significantly more stable than H*. The Sn-oxide overlayer also has advantageous OCHO* binding (Figure 3-6) such that the onset potential is close to ideal (~0.01 V-RHE). Hydroxylation can possess as a limit towards the onset of formic acid evolution. A reducing potential of -0.51 V-RHE is needed to remove every hydroxyl adsorbed at the bridge site in presence of 25% CO* coverage.

For potentials above this, only limited number of active sites will be available for formic acid evolution. If empty bridge sites are accessible, the Sn-oxide overlayer can evolve formic acid very efficiently. Indeed tin oxide has been recently observed to produce formic acid at near ideal potential[105].

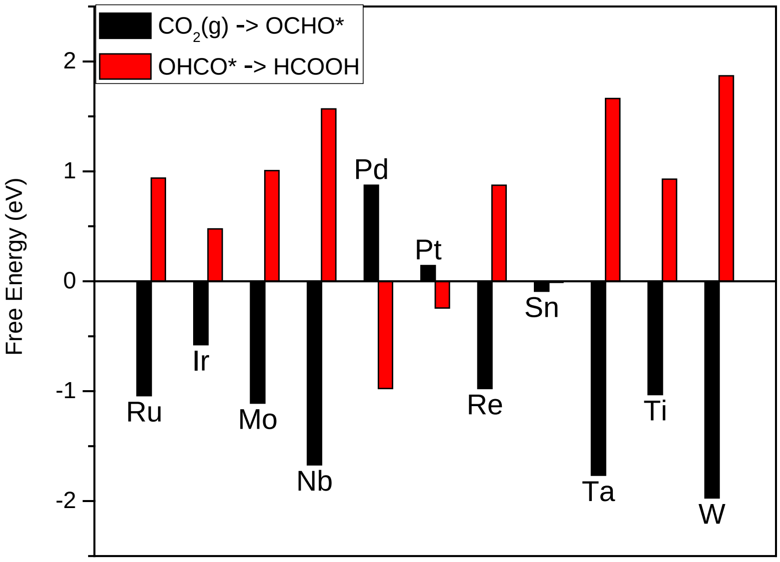

Figure 3-6: Free energy changes for the two elementary step in formic acid evolution on all oxide surfaces.

The key adsorbate in formic acid evolution determining the thermodynamics of elementary steps is OCHO*. It is noteworthy that the trends in binding free energy of OCHO* is correlated with that of OH*. OH* binding energy also gives the limitation for hydroxyl poisoning. The correlation between OH* binding energy and formic acid onset potential is evident from Figure 3-7. The formic acid onset potential for different surfaces follow roughly a Sabatier volcano in relation to OH* binding energy with Sn-oxide overlayer at the top. This behaviour emerges due to the following reason. Strong OH* binding surfaces also have very stable OCHO* intermediates. So the second reaction step i.e. release of a formic acid molecule requires large reducing potential. Weaker OCHO* adsorption allows formic acid to be releases at less reducing potential. If OCHO* adsorption is too weak (right of the top of the volcano), for CO_2 activation reducing potential is needed and overall onset potential increases with weaker OH* binding. The Sn-oxide overlayer has OCHO* binding energy such that the two reaction steps have negligible free energy change at 0 V-RHE. Surfaces with predicted formic acid onset potential above the OH* removal potential line (red) might require more reducing potential than the predicted onset potential due to OH* poisoning.

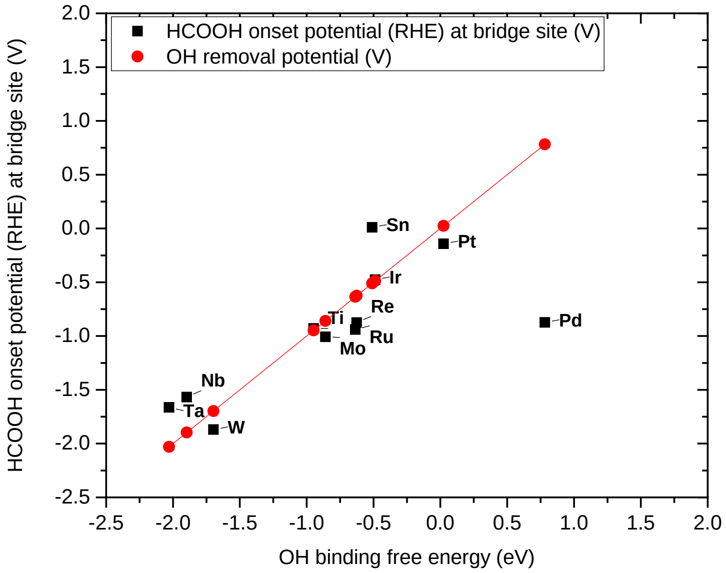

Figure 3-7: correlation between formic acid onset potential for oxide surfaces and OH binding energies. Redline shows the dihydroxylation potential required.*

3.3.7. Methanediol evolution

Methanediol ($H_2C(OH)_2$) is a product formed from CO_2 after transfer of four protons. Pd/Pt/Sn-oxide overlayers do not bind HCOOH* at the active site. Instead, formic acid molecules are released in the electrolyte. However high concentration of formic acid in the solution and a downhill thermodynamics for the creation of further reduced reaction intermediate can facilitate the evolution of methanediol, methanol etc. The reaction mechanism analysis for methanediol constitutes either HCOOH* or HCOOH(aq) as the 2nd electron transfer intermediate. The four-electron transfer reaction mechanism is as follows:

$CO_2(aq) + H^+ + e^- + * \rightarrow OCHO^*$

$OCHO^* + H^+ + e^- \rightarrow HCOOH^*$ or $OCHO^* + H^+ + e^- \rightarrow HCOOH\ (aq)$

$HCOOH^* + H^+ + e^- \rightarrow H_2COOH^*$ or $HCOOH(aq) + H^+ + e^- \rightarrow H_2COOH^*$

$H_2COOH^* + H^+ + e^- \rightarrow H_2C(OH)_2$

Due to the aqueous nature of the electrolyte, a methanediol molecule is not expected to form the anhydrous formaldehyde. The binding energy

ies of OCHO*, HCOOH* and H_2COOH^* determine the thermodynamic onset of methanediol evolution. H_2COOH^* species is bidentate through O-atom in a fashion similar to OCHO*. Thus formation of H_2COOH^* is energetically downhill at 0 V-RHE on surfaces with strong affinity of oxygen atom (Figure 3-8). On weak binding surfaces, H_2COOH^* formation requires highest negative potential as H_2COOH^* is difficult to form. On Ti-oxide overlayer, reduction of OCHO* shows a large increase in free energy at 0 V-RHE, comparable to methanediol release step. 4th elementary step leading to methanediol release is the thermodynamic limiting step for all strong binding oxide overlayers (Figure 3-8). The correlation on OH* binding strength and methanediol onset potential is evident from Figure 3-9. The left leg consists of strong binding surfaces with the limiting step being the reduction of H_2COOH^*, which involves bearing metal-oxygen bonds. Right leg consists of very weak binding surfaces where creation of metal oxygen bond (the step of HCOOH (aq) → H_2COOH^*) is limiting.

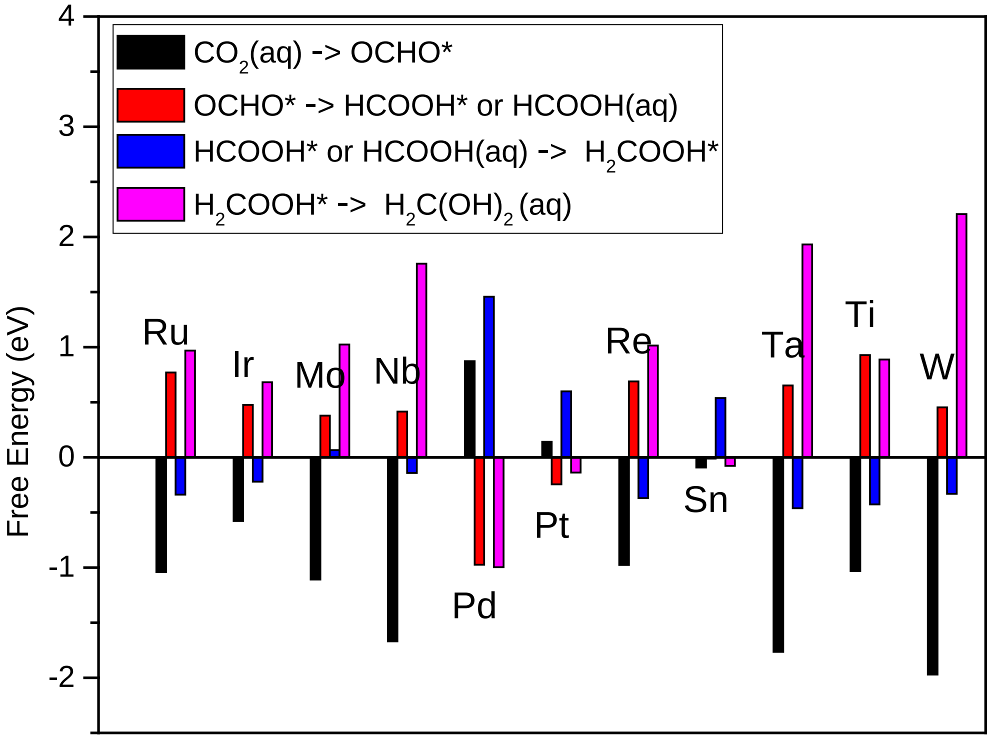

Figure 3-8: Free energy change for the four elementary steps to methanediol evolution on all oxide surfaces at 0 V-RHE. Highest positive step requires the most reducing potential for being thermodynamically feasible.

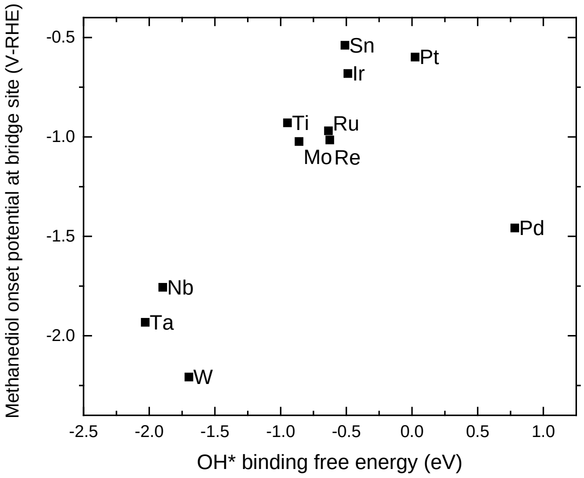

Figure 3-9: Correlation of individually calculated methanediol onset potential and OH binding energy for oxide overlayers.*

3.3.8. Methanol evolution pathways

Methanol evolution from CO2RR requires six electron transfer steps. This is the most widely reported liquid product from CO2RR on ruthenium dioxide electrocatalysts [31,32,34]. Previous theoretical work on methanol evolution mechanism on RuO_2 (110) have proposed a mechanism involving OCHO*, HCOOH*, H_2COOH*, H3CO* and OH* intermediates in low CO* coverage condition. In the reaction network considered here (Figure 3-5), methanol evolution can proceed through a variety of paths. Protonation of H_2COOH^* may lead to combination of H3CO*(bridge) + OH*(cus) intermediates or H_2CO^* intermediate or release of a methanol molecule while O* is left at the bridge site. Cus site OH* is easily removed via a protonation step as a water molecule. The O* intermediate is reduced to water through two hydrogen transfer steps. H_2CO^* intermediate in hydrogenated to form H_3CO^* intermediate. H_3CO^* formed in either way is released as methanol at the 6th electron transfer step.

Preference of intermediates and the pathways are dependent on the relative stability of adsorbates on a particular oxide overlayer and the reaction barrier for formation. Under the computational hydrogen electrode model, it can be assumed that either the reaction barriers are small or they scale with the thermodynamic barrier itself. This simplifies the choice of a reaction pathway to the most stable intermediate at any given electron transfer step. Similar to methanediol evolution analysis, aqueous formic acid molecule released by reduction of OCHO* intermediate on weak binding surfaces is considered as a possible 2nd electron step and further reduction of H_2COOH^* is allowed. Thus, all reaction paths considered here have the following three initial electron transfers steps common:

$CO_2(aq) + H^+ + e^- + * \rightarrow OCHO^*$

$OCHO^* + H^+ + e^- \rightarrow HCOOH^*$ or $OCHO^* + H^+ + e^- \rightarrow HCOOH\ (aq)$

$HCOOH^* + H^+ + e^- \rightarrow H_2COOH^*$ or $HCOOH(aq) + H^+ + e^- \rightarrow H_2COOH^*$

Furthermore, five different routes to release of a methanol and a water molecule are possible. They are:

I. Reaction path A
   $H_2COOH^* + H^+ + e^- \rightarrow H_3CO^*\ (bridge) + OH^*\ (cus)$
   $H_3CO^*\ (bridge) + OH^*\ (cus) + H^+ + e^- \rightarrow H_3CO^* + H_2O(l)$
   $H_3CO^* + H^+ + e^- \rightarrow H_3COH\ (aq)$
II. Reaction path B
   $H_2COOH^* + H^+ + e^- \rightarrow H_2CO^* + H_2O(l)$
   $H_2CO^* + H^+ + e^- \rightarrow H_3CO^*$
   $H_3CO^* + H^+ + e^- \rightarrow H_3COH\ (aq)$
III. Reaction path C
   $H_2COOH^* + H^+ + e^- + \rightarrow H_3COH\ (aq) + O^*$
   $O^* + H^+ + e^- \rightarrow OH^*$
   $OH^* + H^+ + e^- \rightarrow H_2O(l)$
IV. Reaction path D
   $H_2COOH^* + H^+ + e^- \rightarrow H_2CO^* + H_2O(l)$
   $H_2CO^* + H^+ + e^- \rightarrow H_2COH^*$
   $H_2COH^* + H^+ + e^- \rightarrow H_3COH\ (aq)$
V. Reaction path E
   $H_2COOH^* + H^+ + e^- \rightarrow H_3CO^*\ (bridge) + OH^*\ (cus)$
   $H_3CO^*\ (bridge) + OH^*\ (cus) + H^+ + e^- \rightarrow OH^* + H_3COH\ (aq)$
   $OH^* + H^+ + e^- \rightarrow H_2O(l)$

3.3.8.1. Methanol evolution on RuO_2 (110) surface

Reaction mechanism A is followed on the RuO_2 (110) surface. OCHO* is a very stable bidentate adsorbate on this surface. A reducing potential of -0.77 V-RHE is needed to reduce OHCO* to HCOOH* with 25% CO* coverage while reduction of HCOOH* is downhill in free energy. Protonation of H_2COOH* yields H_3CO* at bridge site and OH* at the cus site. OH* is removed as water from the cus site first before the final proton transfer releases methanol as a product. Previous theoretical modelling work suggested that methanol is released first and OH* adsorbate moves to bridge site at the 5th electron transfer step. This is disputed, as this is actually a combination of two elementary reaction steps, one electrochemical step of methanol release and a chemical step of OH* migration. Validity of computational hydrogen electrode model requires only elementary electrochemical step to be considered for free energy calculations at finite applied potential. Figure 3-10 summarizes that reduction of OCHO* and release of methanol from H_3CO* are the two uphill steps at 0 V-RHE. The onset potential is predicted to be -0.77 V-RHE at which all are energetically favourable.

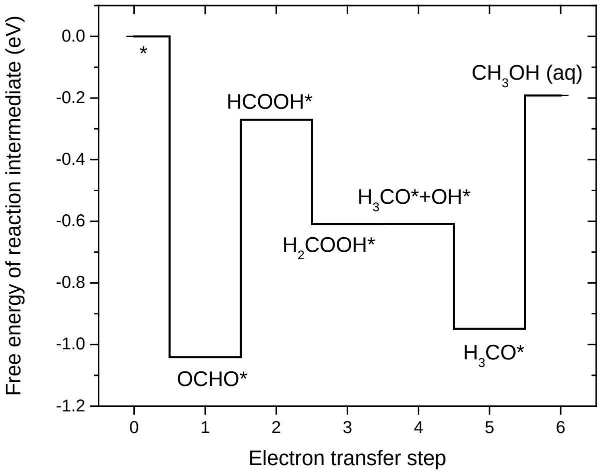

Figure 3-10: Thermodynamic path for methanol evolution on RuO_2 (110) surface at 0 V-RHE.

3.3.8.2. Methanol evolution on Ir-oxide overlayer

The reaction mechanism on the Ir-oxide overlayer on ruthenium oxide substrate also follow reaction path A like the pure ruthenium oxide surface. This overlayer however cannot bind formic acid molecules at the bridge site in the presence of 25% CO* coverage and thus the reaction goes through an aqueous formic acid intermediate. As H_2COOH* is stable (~-0.3 eV binding free energy) formation of H_2COOH* and further reduction to methanol is possible. Reduction of OCHO* and release of methanol from H_3CO* are the steps which requires large increase in free energy at 0 V-RHE (Figure 3-11). The 6th electron transfer to methanol formation is most difficult and requires at least -0.57 V-RHE to become free energy neutral. Mixed iridium-ruthenium oxide catalysts have been observed to evolve methanol at -0.65 V-RHE along with ethanol (2C) as primary product[73].

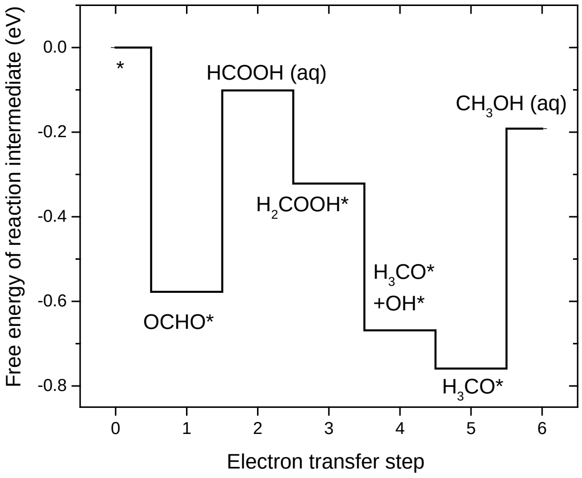

Figure 3-11: Reaction path for methanol evolution on the Ir-oxide overlayer (110) surface at 0 V-RHE

3.3.8.3. Methanol evolution on Mo-oxide overlayer

Mo-oxide overlayer binds OH* much stronger than Ru/Ir-oxide surfaces. Formation of the O* intermediate becomes more stable than the combination of methoxy and hydroxyl intermediates. Thus, reaction path C is followed on this surface. H_2COOH* on protonation releases methanol molecule by breaking a C-O bond. An O* atom at the bridge site is removed as water after two consecutive protonations. Strong bonding between surface and OH* leads to large reducing potential requirement for dihydroxylation. This is also the 6th step on the methanol evolution reaction mechanism. -0.86 V-RHE is needed for methanol formation. Other steps like OCHO* reduction, which have positive free energy change at 0 V-RHE, can progress at less reducing potential.

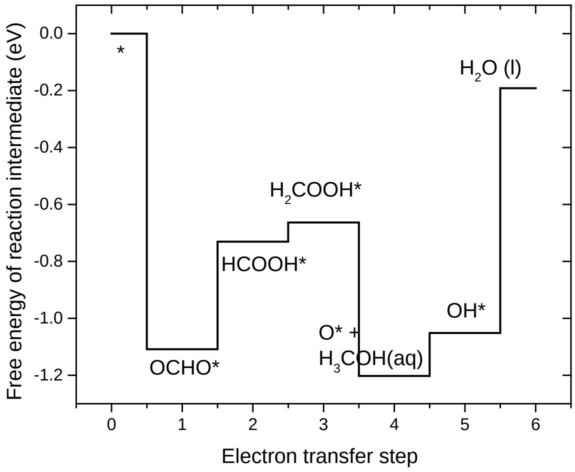

Figure 3-12: Free energies of reaction intermediates for methanol evolution on Mo-oxide overlayer at 0 V-RHE

3.3.8.4. Methanol evolution on Nb-oxide overlayer

Analogous to the Mo-oxide overlayer, the Nb-oxide overlayer binds oxygen-coordinated adsorbates very strong. Therefore, breaking of metal-oxygen bond is difficult. Reaction path C is preferred on this surface for methanol evolution. Like other strong binding surfaces, it binds HCOOH* to the bridge site with no applied potential, allowing further reduction to methanol. Due to the binding characteristics of the surfaces, OH* removal requires the largest applied potential of -1.9 V-RHE, of all the six elementary steps.

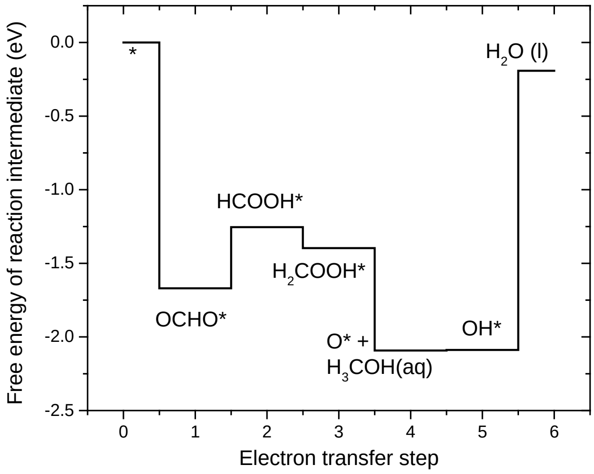

Figure 3-13: Reaction path for methanol evolution on Nb-oxide overlayer at 0 V-RHE.

3.3.8.5. Pd-oxide overlayer for methanol evolution

The Pd-oxide overlayer provides an opportunity to understand the CO2RR reaction mechanism behaviours at the other end of binding characteristics of the Nb-oxide overlayer. This surface has the weakest OH* adsorption of all surfaces studied here. Thus adsorbates like OCHO* or H_2COOH^* are not stable without applied reducing potential and the HCOOH* intermediate escapes from the surfaces to the electrolyte. Reaction mechanism D is predicted to be most accessible on this surface.

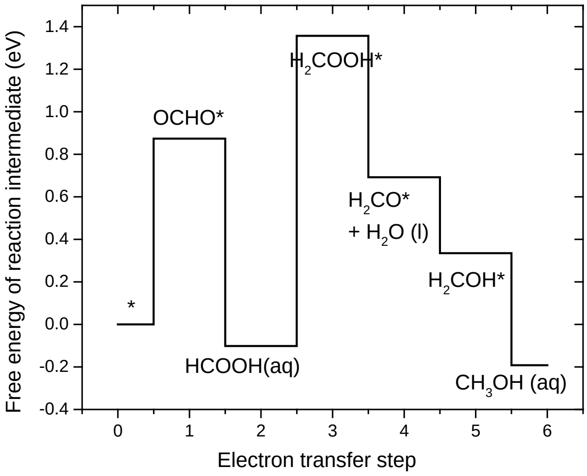

Figure 3-14: Free energies of reaction intermediates for methanol evolution on Pd-oxide overlayer at 0V-RHE.

H_2CO* and H_2COH* are reaction intermediates from 4th and 5th elementary step. Proton transfer for formation of OCHO* or H_2COOH* need -0.87 V-RHE and -1.47 V-RHE respectively for the reaction to go forward. 3rd proton transfer is especially difficult as solvated formic acid molecules can not be protonated readily. Palladium oxide is not expected to be stable under reducing condition and hydrogen would be the only observable product as CO_2 activation to OHCO* is very difficult. However, this surface illustrates the path and intermediates pertaining to CO2RR on very weak binding surfaces.

3.3.8.6. Pt-oxide overlayer for methanol evolution

The Pt-oxide overlayer is a weak binding surfaces but it is feasible to form OCHO* under a small reducing potential (-0.14 V-RHE). Reaction mechanism B is preferred on this surface for CO2RR to methanol. 1st, 5th and 6th steps are uphill in free energy change at 0 V-RHE, but -0.2 V-RHE is sufficient to drive those steps forward. However it is difficult to reduce the formic acid (which desorbs from surface) to H_2COOH*. It necessitates a reducing potential of -0.6 V-RHE, which is predicted to be the onset potential for methanol on this surfaces.

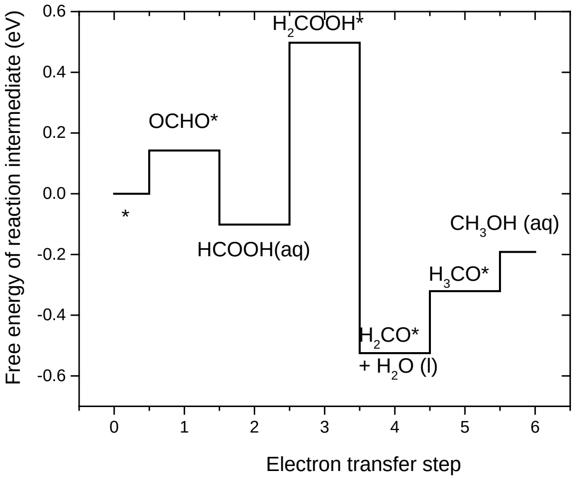

Figure 3-15: Free energies of reaction intermediates for methanol evolution on Pt-oxide overlayer at 0V-RHE.

3.3.8.7. Methanol evolution on Re-oxide overlayer

Re-oxide overlayer is a unique surface among those studied in this project. With 25% CO* coverage, it has an OH* binding energy similar to the pure ruthenium oxide surface but H* is very unstable with a binding free energy of +0.95 eV. On the contrary, protonation of CO_2 to form OCHO* releases ~1eV at no applied potential. This creates the probability of very good selectivity of CO2RR over HER.

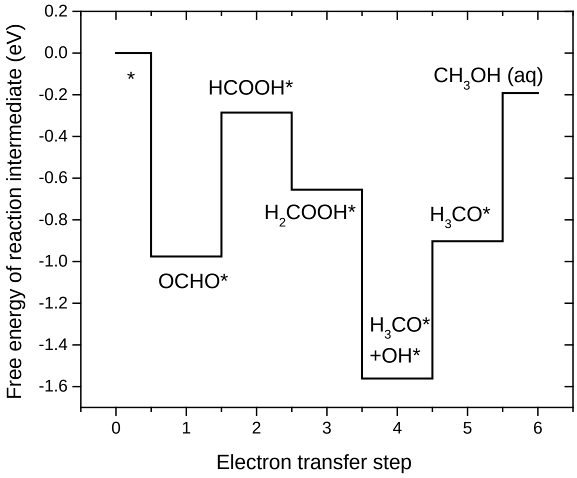

Figure 3-16: Reaction path for methanol evolution on Re-oxide overlayer at 0V-RHE

Similar to pure ruthenium oxide surfaces, reaction mechanism A is preferred for methanol evolution on this surface. It is uphill in free energy to reduce OCHO* to HCOOH* intermediate and HCOOH* stay adsorbed at the bridge site. Reduction of H_2COOH^* leads to H_3CO^* and OH* adsorbates, both of which are strongly adsorbed on the surface. OH* removal as water and release of methanol from H_3CO^* require -0.66 V-RHE and -0.71 V-RHE respectively. Overall -0.71 V-RHE is the onset potential for methanol evolution. This is not an improvement over a pure ruthenium surface but considering the selectivity of CO2RR over HER, this surface could be worth exploring experimentally as an effective CO2RR catalyst.

3.3.8.8. Methanol evolution on tin-oxide overlayer

The Tin-oxide overlayer is well suited for formic acid evolution as discussed in previous chapter. However adequate reducing potential and plentiful availability of formic acid molecules close to reaction site can activate formic acid from the electrolyte to form H_2COOH^* intermediate. Reaction mechanism C is suggested to be active for methanol evolution. The thermodynamics of the methanol evolution path on the Sn-oxide overlayer is interesting due to the presence of two uphill steps, each characterizing a different binding energy regime. Formation of a H_2COOH^* intermediate from solvated a formic acid molecule is uphill by +0.54 eV at 0 V-RHE. The onset potential of methanol evolution is thus -0.54 V-RHE. Very weak binding surfaces like Pt/Pd-oxide overlayers show large free energy increases for this step. Also OH* is bound moderately strong and the dihydroxylation potential is -0.51 V-RHE. This is reminiscent of stronger binding surfaces. It indicate a regime change at the binding strength shown by Sn-oxide overlayer. This is further supported by the fact that this surface sits close to the top of the volcano like behaviour observed in formic acid and methanediol onset potential plot.

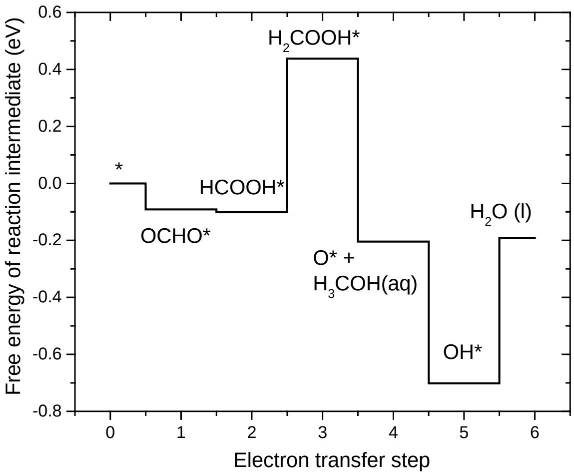

Figure 3-17: Reaction path for methanol evolution on Sn-oxide overlayer at 0V-RHE.

3.3.8.9. Methanol evolution on Ta-oxide overlayer

The Ta-oxide overlayer has the strongest OH* adsorption (with 25% CO* coverage) among the surfaces studied in this chapter. Methanol evolution follow reaction mechanism C on this surface and it is released after 4th electron transfer step, leaving an O* intermediate at the bridge site. Removal of OH* formed after protonation of O*, requires -2.03 V-RHE potential. This surface is unlikely to show significant activity towards CO2RR. However methanol evolution paths computed on such strong binding surfaces help make the hypothesis that on strong binding surfaces, OH* removal would be the step dictating the onset potential.

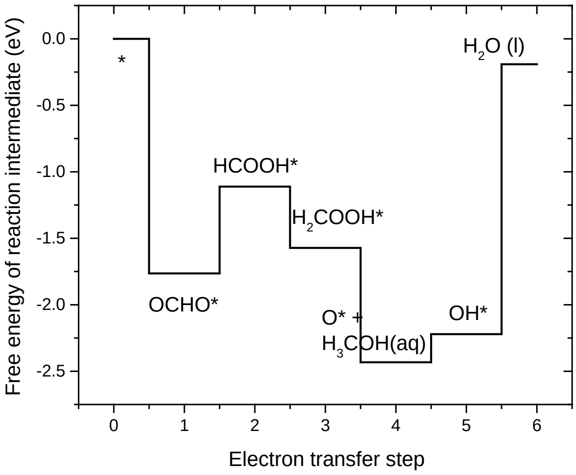

Figure 3-18: Reaction path for methanol evolution on Ta-oxide overlayer at 0V-RHE.

3.3.8.10. Methanol evolution on Ti-oxide overlayer

Ti-Ru mixed oxide catalysts have been shown to successfully evolve methanol at moderate reducing potential[31]. Pure TiO_2 (110) surface binds OH* stronger than RuO_2 or IrO_2 surfaces. This holds true for the Ti-oxide overlayer as well. Strong OH* adsorption means large reducing potential is required for removing OH* as water. Similar to other strong binding surfaces, reaction mechanism C is most probable here. OCHO* and OH* intermediates being very stable, protonation of these two adsorbates is comparably difficult (~-0.9 V-RHE). OH* removal determines the onset potential at -0.95 V-RHE. Interestingly, even with strong OH* adsorption, HCOOH* desorbs as formic acid to the electrolyte. Formation of H_2COOH^* is downhill in free energy at 0 V-RHE.

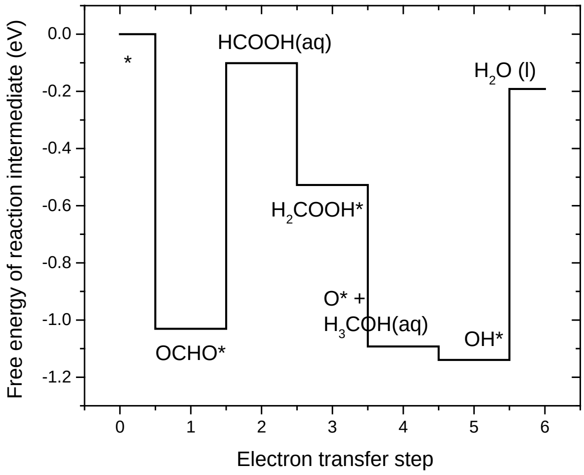

Figure 3-19: CO2RR pathway to methanol production on Ti-oxide overlayer at 0V-RHE

3.3.8.11. Methanol evolution on W-oxide overlayer

Reaction mechanism A is followed on the W-oxide overlayer surface. Protonation of H_2COOH^* leads to H_3CO^* in bridge site and OH* at the cus site. Removal of OH* by protonation requires relatively small reducing potential compared to release of methanol from protonation of H_3CO^* (-1.81 V-RHE). The 6th elementary step is the most uphill step at 0 V-RHE and determines the onset potential. This is more reducing than dihydroxylation potential of -1.7 V-RHE.

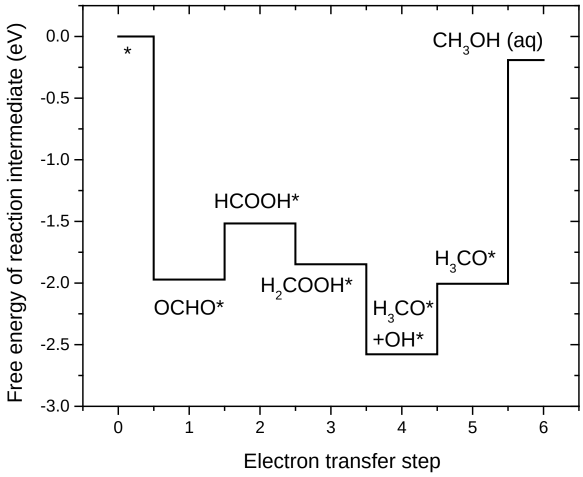

Figure 3-20: CO2RR pathway to methanol production on W-oxide overlayer at 0V-RHE and 25% CO coverage.*

3.3.8.12. Trends in methanol evolution mechanism on oxide overlayers

Four different reaction paths are active on the 11 oxide surfaces studied here. Surfaces with OH* adsorption energy <-0.4 eV, forms H_3CO*+OH* adsorbates on protonation of H_2COOH*. The weakest binding surfaces e.g. Pt/Pd-oxide overlayers form a H_2CO* intermediate and a water molecule is released. Elementary step determining the onset potential also portray the binding characteristics of the surface. Strong binding surfaces are limited by reaction step where a metal-oxygen bond is severed. OCHO* is a bidentate adsorbate. Protonation of OCHO* leads to HCOOH* adsorbate, which is monodentate. On a pure ruthenium oxide surface, this step is potential limiting. On Mo-/Nb-/Ta-/Ti-oxide overlayers splitting of metal-oxygen bond in OH* removal is linked to the highest free energy increment at 0 V-RHE. Ir/Re/W-oxide surfaces following reaction mechanism A, are limited by breaking of M-O bond to release methanol from the methoxy intermediate. Surfaces on the weaker side of the adsorption energy spectrum have weaker metal oxygen bonds and HCOOH* adsorbate desorbs from the surfaces as a formic acid molecule. Large reducing potential is required to activate formic acid molecules and form surfaces bound H_2COOH* intermediates. Formation of bidentate H_2COOH* is the thermodynamic limiting step on such surfaces. Sn-oxide overlayer have comparable uphill free energy steps for OH* removal and H_2COOH* formation, which convey a change of regime. Onset potentials for methanol evolution and OH* removal potentials for surfaces are listed in Table 3-4.

Table 3-4: Onset potentials estimated for overlayers and the potential for OH removal*

Metal atom at the top layer	Methanol onset potential (V-RHE)	OH* removal potential (V-RHE)
Ru	-0.77	-0.64
Ir	-0.57	-0.49
Mo	-0.86	-0.86
Nb	-1.90	-1.90
Pd	-1.46	0.78
Pt	-0.60	0.02
Re	-0.71	-0.63
Sn	-0.54	-0.51
Ta	-2.03	-2.03
Ti	-0.95	-0.95
W	-1.81	-1.70

3.3.9. Methane evolution pathways

Methane is the most reduced C1 product from CO2RR. It takes eight electron/proton transfer step to convert CO_2 into methane and involves cleaving of both C-O bonds. Within the reaction network studied here with O-coordinated intermediates, methane can be obtained by four different mechanisms. The first three elementary steps are similar to the methanol reaction pathways. They involve OCHO*, HCOOH* (or formic acid released in electrolyte) and H_2COOH*.

$CO_2(aq) + H^+ + e^- + * \rightarrow OCHO*$

$OCHO* + H^+ + e^- \rightarrow HCOOH*$ or $OCHO* + H^+ + e^- \rightarrow HCOOH (aq)$

$HCOOH* + H^+ + e^- \rightarrow H_2COOH*$ or $HCOOH(aq) + H^+ + e^- \rightarrow H_2COOH*$

After the 4th electron transfer step, either a $H_3CO*+OH*$ adsorbate pair is formed (strong binding surfaces) or a H_2CO* adsorbate. H_2CO* is preferred only on the weakest binding surfaces Pt-/Pd-oxide overlayers and gets further reduced to either H_3CO* or H_2COH*. OH* removal on strong binding surfaces also leave a H3CO* adsorbate after 5th elementary step. Protonation at the oxygen atom of H_2COH* or H_3CO* intermediate either produces H_3COH* intermediate or releases methanol. On Ru/Mo/Nb/Ta/W-oxide overlayer, a H_3COH* intermediate is more stable than methanol in the electrolyte. However, this is dependent on the free energy for methanol in aqueous solution. Lower concentration in electrolyte would make it easier to desorb from the catalyst surface. Further hydrogenation (7th step) at the carbon atom cleaves a C-O bond to release methane. Methane release can happen in 6th chemical step as well. H_3CO* intermediate can be hydrogenated at the carbon atom, concerted with a splitting of C-O bond releasing methane. A O* intermediate is left if methane release occurs after the 6th electron transfer step and OH* is left if H_3COH* is formed before methane evolution. The O*/OH* intermediates are removed as water through hydrogenation. The final five steps from the four possible reaction mechanisms are summarized below:

Reaction path F:

$H_2COOH* + H^+ + e^- \rightarrow H_3CO* \text{ (bridge)} + OH* \text{ (cus)}$

$H_3CO* \text{ (bridge)} + OH* \text{ (cus)} + H^+ + e^- \rightarrow H_3CO* + H_2O \text{ (l)}$

$H_3CO* + H^+ + e^- \rightarrow O* + CH_4 \text{ (aq)}$

$O* + H^+ + e^- \rightarrow OH*$

$OH* + H^+ + e^- \rightarrow H_2O(l)$

Reaction path G:

$H_2COOH* + H^+ + e^- \rightarrow H_2CO* \text{ (bridge)} + H_2O \text{ (l)}$

$H_2CO* + H^+ + e^- \rightarrow H_3CO*$

$H_3CO* + H^+ + e^- \rightarrow O* + CH_4 \text{ (aq)}$

$O* + H^+ + e^- \rightarrow OH*$

$OH* + H^+ + e^- \rightarrow H_2O(l)$

Reaction path H:

$H_2COOH* + H^+ + e^- \rightarrow H_2CO* \text{ (bridge)} + H_2O \text{ (l)}$

$H_2CO* + H^+ + e^- \rightarrow H_3CO*$

$H_3CO* + H^+ + e^- \rightarrow H_3COH*$

$H_3COH* + H^+ + e^- \rightarrow OH* + CH_4 \text{ (aq)}$

$OH* + H^+ + e^- \rightarrow H_2O \text{ (l)}$

Reaction path I:

$H_2COOH* + H^+ + e^- \rightarrow H_2CO* \text{ (bridge)} + H_2O \text{ (l)}$

$H_2CO* + H^+ + e^- \rightarrow H_2COH*$

$H_2COH* + H^+ + e^- \rightarrow H_3COH*$

$H_3COH* + H^+ + e^- \rightarrow OH* + CH_4 \text{ (aq)}$

$OH* + H^+ + e^- \rightarrow H_2O \text{ (l)}$

Analysis based on adsorbate binding free energies of the different elementary reaction steps asserts that reaction mechanism F is most feasible on all surfaces except the two weakest binding – Pt/Pd oxide overlayers. On Pd-oxide overlayer reaction mechanism I and on Pt-oxide overlayer, reaction mechanism G is predicted.

3.3.9.1. Methane evolution on strong bonding overlayers

Among the nine oxide overlayers, where methane evolution pathway F is expected to be active, all surfaces except Sn-oxide overlayer have OCHO* activation and OH* removal as steps with positive free energy change at 0 V-RHE (Figure 3-21, Figure 3-22, Figure 3-23). On pure ruthenium oxide and Re-oxide overlayer, protonation of bidentate OCHO* leading to a monodentate HCOOH* intermediate requires the most reducing potential for being thermodynamically feasible. The other six surfaces of this set, i.e. Ir/Mo/Nb/Ta/Ti/W-oxide overlayers need larger reducing potential for OH* removal than OCHO* activation. Sn-oxide overlayer, along with OH* removal, have H2COOH* formation as an elementary step with comparable increase in free energy at 0 V-RHE. While tin-oxide overlayer has one of the smallest overpotentials for methane evolution, it is more active towards formic acid production from CO2RR. Thus, surfaces, which bind adsorbates marginally stronger than this overlayer, would be a better methanation electrocatalyst. For such surfaces, OCHO* activation and OH* removal would be decisive factor for onset potential.

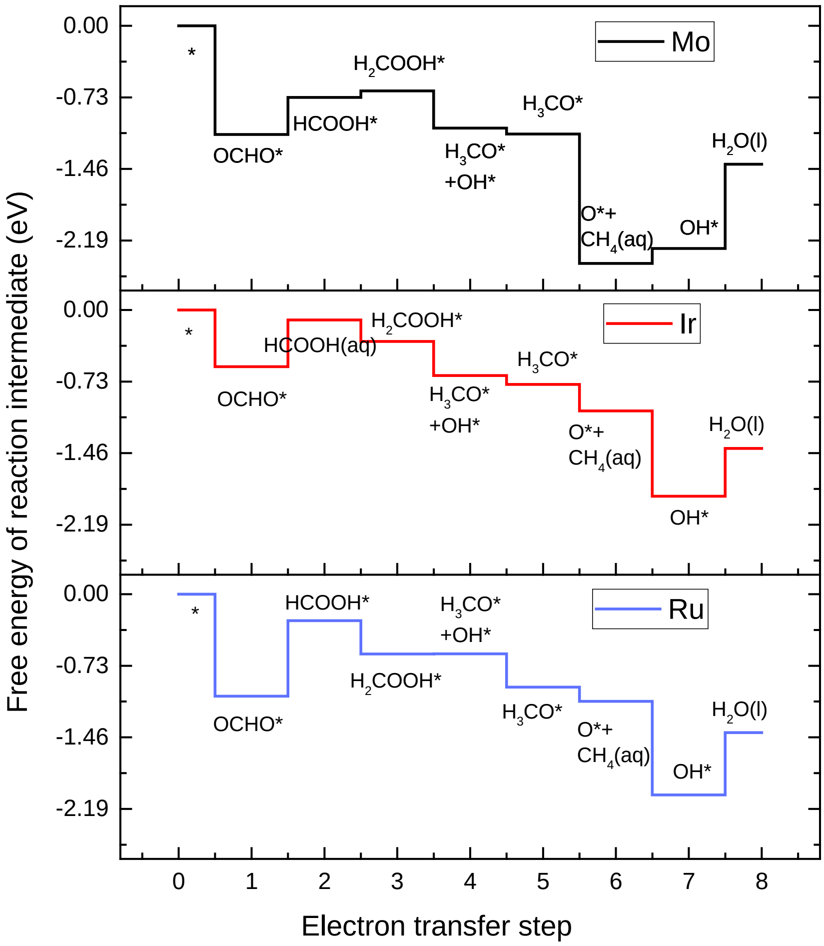

Figure 3-21: Thermodynamic of reaction path F to methane on Ru/Ir/Mo-oxide overlayers at 0 V-RHE

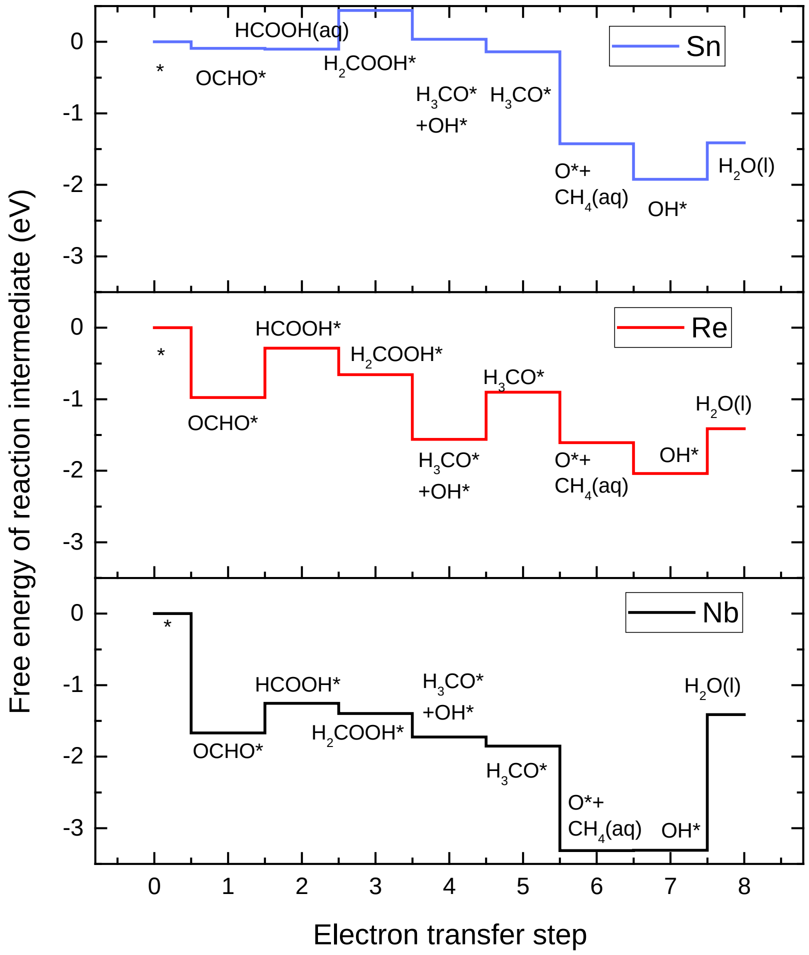

Figure 3-22: Thermodynamic of reaction path F to methane on Nb/Re/Sn-oxide overlayers at 0 V-RHE

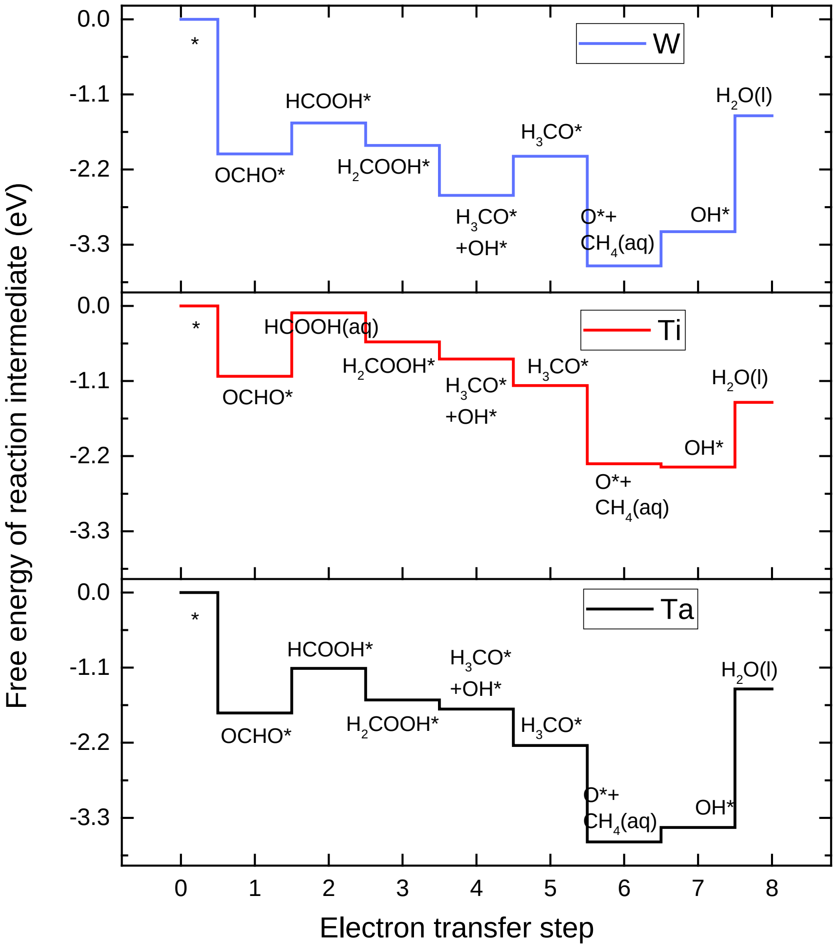

Figure 3-23: Thermodynamic of reaction path F to methane on Ta/Ti/W-oxide overlayers at 0 V-RHE

3.3.9.2. Methane evolution on weak binding overlayers

Binding free energy analysis of adsorbates on Pd-oxide and Pt-oxide overlayer reveals that the 4th electron transfer intermediate is H_2CO^* (unlike other surfaces). H_2CO^* hydrogenates further to H_2COH^* and H_3CO^* on Pd- and Pt-oxide overlayers respectively. These two surfaces bind O-coordinated adsorbates very weakly. HCOOH* desorbs as formic acid and formation of OCHO* and H_2COOH^* are uphill in free energy at 0 V-RHE. Protonating formic acid from the electrolyte takes the largest reducing potential of all steps to become feasible.

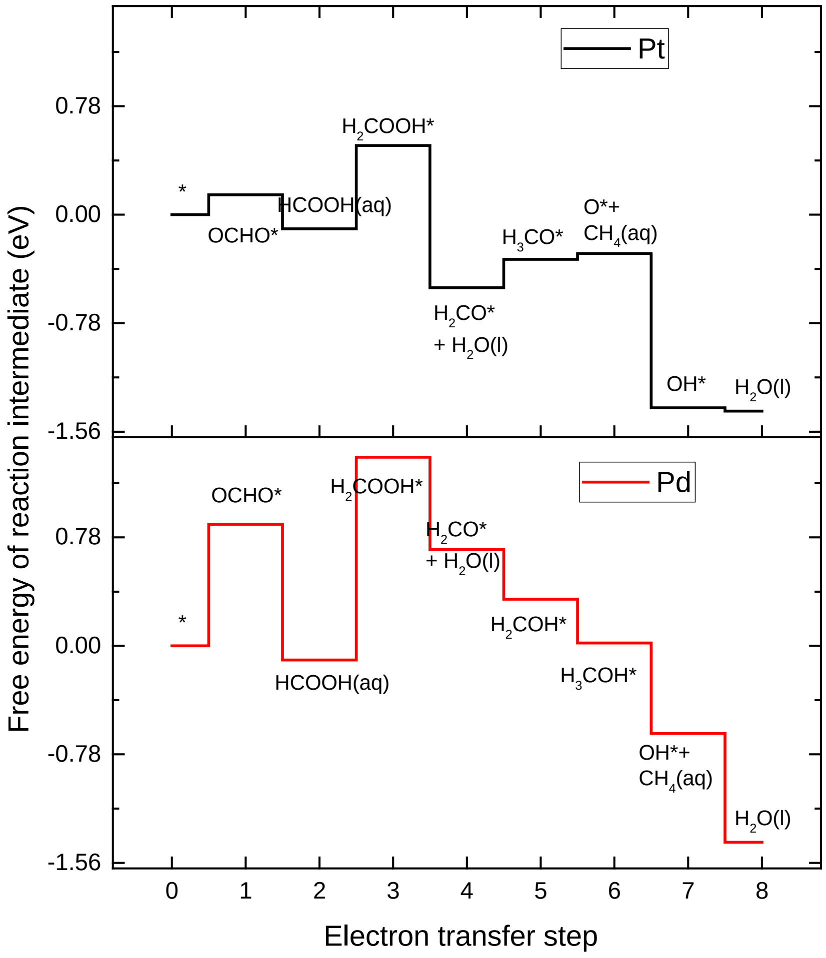

Figure 3-24: Thermodynamics of methane evolution pathway I on Pd-oxide overlayer and pathway G on Pt-oxide overlayer at 0 V-RHE

3.3.10. Selectivity of products during CO2RR

Surfaces which do not bind OCHO* preferentially over H* (e.g. Pt-/Pd-oxide overlayers) would produce only hydrogen and are not anticipated to be active towards CO2RR. Also for surfaces which do not bind the HCOOH* intermediate such that further reduction to H_2COOH^* requires a large reducing potential (e.g. Sn-oxide overlayer), CO2RR is limited to the 2nd electron transfer step, i.e. formic acid evolution. For stronger biding surfaces, evolution of methane and methanol is predicted. However, calculated onset potential for methanol and methane evolution are often identical or different (on Ir-/Re-/W-oxide overlayers) by a maximum of ~0.1 V-RHE (Table 3-5). In addition, usually the thermodynamically limiting step in the reaction mechanism for the two products are identical as well It is thus difficult to suggest any possible preference of methane or methanol simply based on onset potential analysis.

Selectivity might arise from barriers for elementary steps where a C-O or a Metal-O bond dissociates. Scrutiny of the reaction mechanism itself provides better insight into probable product selectivity for strong binding surfaces. Ru/Ir/Re/W-oxide surfaces employ mechanism A for methanol evolution and mechanism F for methane evolution. Methane evolution is preferred if the C-O bond in H_3CO^* is easier to break by hydrogenation at C-atom. Methanol evolution is preferred if metal-O bond in H_3CO^* is easily broken by hydrogenation at the O-atom. Mo/Nb/Ta/Ti-oxide overlayers follow C mechanism for methanol evolution and F mechanism for methane evolution. If protonation is preferred at the carbon atom of H_2COOH^*, methanol is released and protonation at the oxygen atom leads to eventual methane evolution.

Table 3-5: methanol and methane onset potentials and limiting steps on oxide overlayers

Metal atom the top layer	Step limiting onset potential for methanol evolution	Onset potential for methanol evolution (V-RHE)	Step limiting onset potential for methane evolution (V-RHE)	Onset potential for methane evolution (V-RHE)
Ru	$OHCO^* \rightarrow HCOOH^*$	-0.77	$OHCO^* \rightarrow HCOOH^*$	-0.77
Ir	$H_3CO^* \rightarrow CH_3OH(aq)$	-0.57	$OH^* \rightarrow H_2O(l)$	-0.49
Mo	$OH^* \rightarrow H_2O(l)$	-0.86	$OH^* \rightarrow H_2O(l)$	-0.86
Nb	$OH^* \rightarrow H_2O(l)$	-1.90	$OH^* \rightarrow H_2O(l)$	-1.90
Pd	$HCOOH(aq) \rightarrow H_2COOH^*$	-1.46	$HCOOH(aq) \rightarrow H_2COOH^*$	-1.46
Pt	$HCOOH(aq) \rightarrow H_2COOH^*$	-0.60	$HCOOH(aq) \rightarrow H_2COOH^*$	-0.60
Re	$H_3CO^* \rightarrow CH_3OH(aq)$	-0.71	$OHCO^* \rightarrow HCOOH^*$	-0.69
Sn	$HCOOH(aq) \rightarrow H_2COOH^*$	-0.54	$HCOOH(aq) \rightarrow H_2COOH^*$	-0.54
Ta	$OH^* \rightarrow H_2O(l)$	-2.03	$OH^* \rightarrow H_2O(l)$	-2.03
Ti	$OH^* \rightarrow H_2O(l)$	-0.95	$OH^* \rightarrow H_2O(l)$	-0.95
W	$H_3CO^* \rightarrow CH_3OH(aq)$	-1.81	$OH^* \rightarrow H_2O(l)$	-1.70

3.3.11. Adsorbate scaling relations

The key difference between CO2RR mechanism on metallic catalysts and oxide catalyst surfaces studied here is the atom through which key reaction intermediates bind to the surfaces. On metal surfaces, the binding free energy of CO* and CHO* adsorbates determine the onset potential. On oxide overlayers, OCHO*, HCOOH*, OH* and H_3CO^* are key towards predicting the thermodynamic limiting potential. In the $2e^-$, $4e^-$, $6e^-$ and $8e^-$ reaction mechanisms discussed here, trends in binding free energy of intermediates can be used to develop general understanding of the reaction mechanism and onset potentials. Ideally a set of most optimal free energy for each reaction intermediate exist that leads to zero overpotential[40]. Presence of scaling relations between reaction intermediates makes it unrealistic to have such optimal binding energy for all reaction intermediates. Deviation of the adsorbate binding energy from the ideal due to the adsorption scaling laws give rise to overpotential in chemical reactions. Understanding the scaling laws present between reaction intermediates in the reaction of interest gives a tool to create a simple analytical model for catalyst activity with few variables and provide clues on how to improve catalyst activity under given constraints[37,106].

Onset potential analysis done on oxide overlayers give a indication that the OH* binding free energy can be a descriptor of activity on such surfaces. This hypothesis is further supported by the fact that reaction intermediate for CO2RR on oxide surfaces bind to the active site via oxygen atom like OH*. Adsorbates binding through oxygen atoms often have adsorption energy scaling with one another[61,62,107]. OH* adsorption free energy is taken here as independent variable among other adsorbate binding free energies due to the widely varying utilization as a descriptor for properties of oxides[108–111] like ionic conductivity and methanol oxidation catalyst activity. Also OH* removal is potential limiting step for many oxide surfaces for methane and methanol evolution.

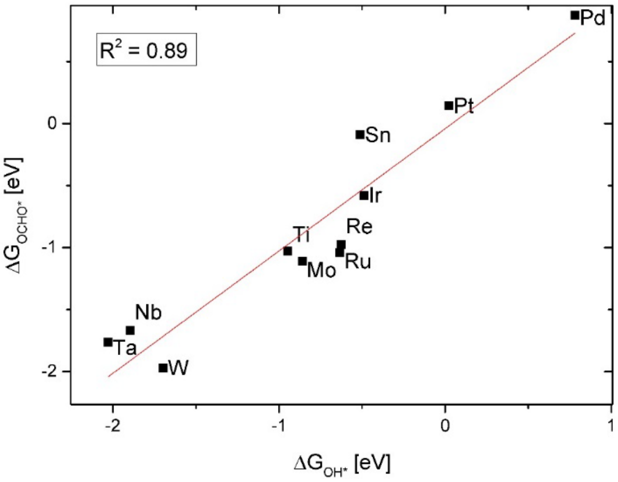

(a) OH* and OCHO* binding free energy

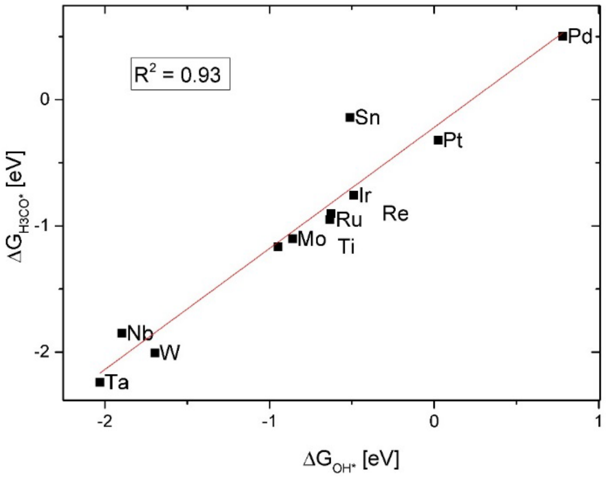

(b) OH* and H_3CO* binding free energy

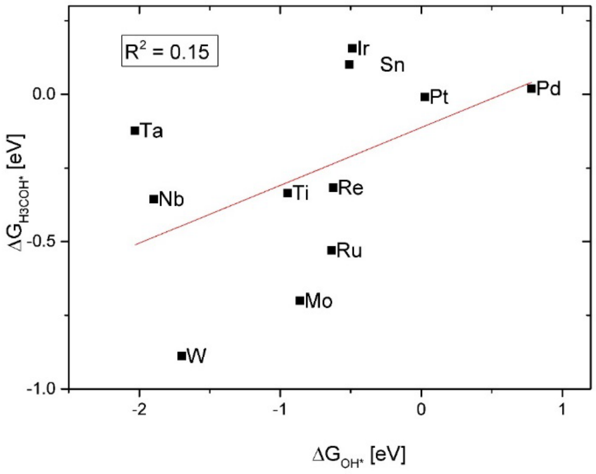

(c) OH* and H_3COH* binding free energy

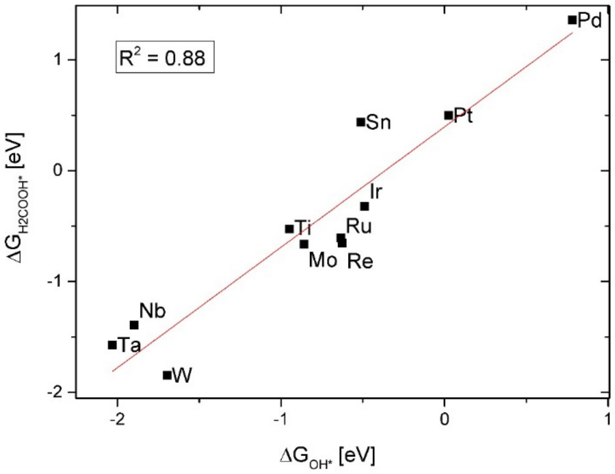

(d) OH* and H_2COOH* binding free energy

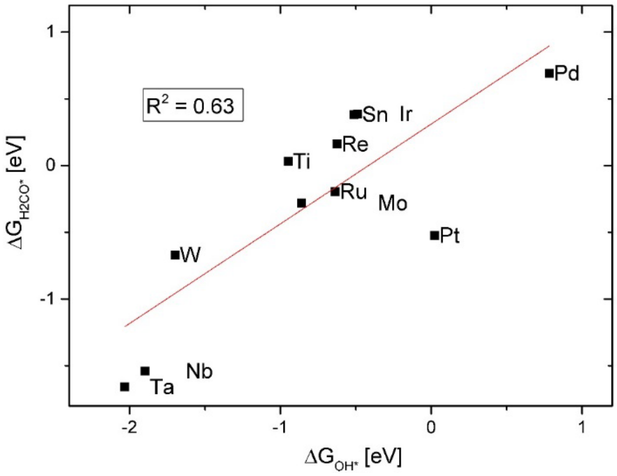

(e) OH* and H_2CO* binding free energy

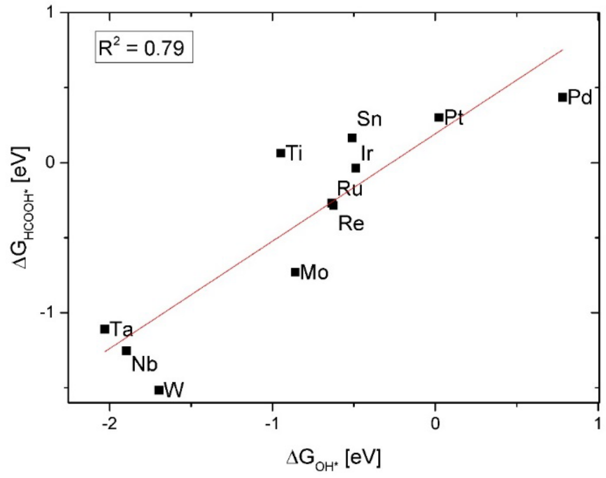

(f) OH* and H_2COOH* binding free energy

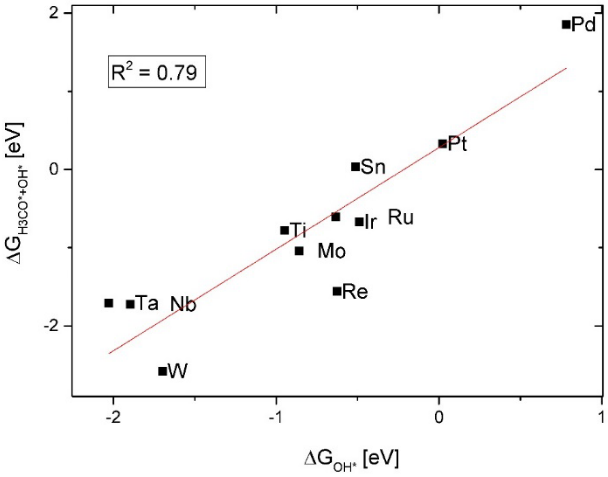

(g) OH* and H_3CO*+OH* (aggregate) binding free energy

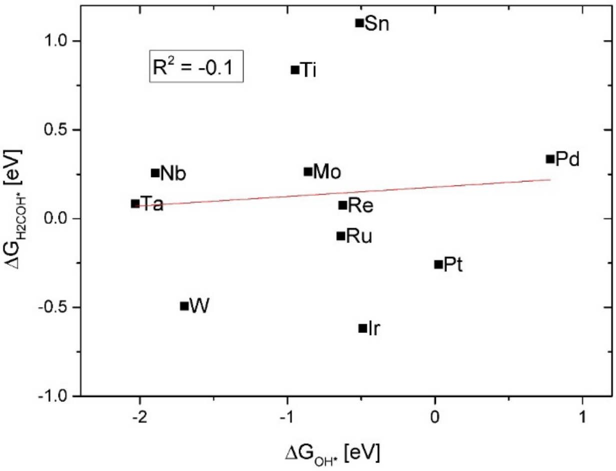

(h) OH* and H_2COH* binding free energy

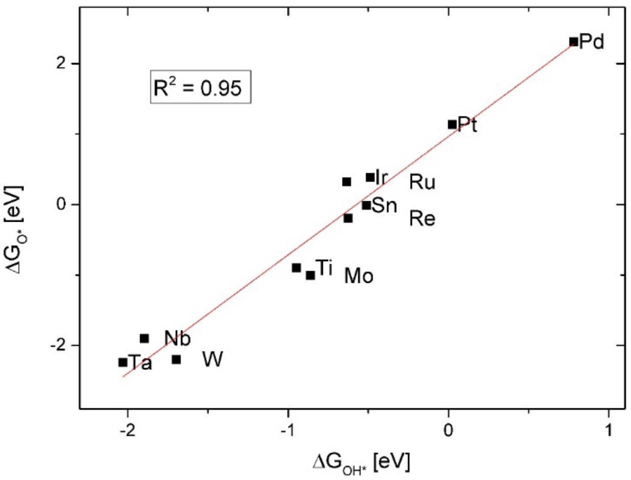

(i) OH* and O* binding free energy

Figure 3-25: Linear fit between binding free energy of OH and nine CO2RR intermediate on oxide overlayers.*

Scaling relations, popularized by Nørskov and co-workers over the last two decades for simplified analysis of catalytic activity based on binding energy descriptors, have traditionally used simple linear fitting. Linear fitting between adsorption free enrgy of OH* and the adsorption free energy of other CO2RR intermediates with CO* coverage are presented in Figure 3-25. Small scatter ($R^2 \approx 1$) means the linear scaling is reliable and large scatter ($R^2 < 0.7$) makes analysis based on such scaling laws questionable. Scaling lines obtained for $H_2COH^*/H_2CO^*/H_3COH^*$ intermediates are used in further analysis with necessary caution. Fortunately these adsorbates either not a part of the reaction mechanisms active on the studied surfaces or do not define the onset limiting step. Hence, errors in these few scaling lines do not affect the quality of the activity volcano analysis done. The linear binding free energy relations based on OH* binding free energy descriptor ($\Delta G_B[OH]$) is provided below:

$$\Delta G_B[OCHO] = 0.99 \Delta G_B[OH] - 0.04\ \text{eV} \tag{3-1}$$

$$\Delta G_B[HCOOH] = 0.72\ \Delta G_B[OH] + 0.19\ \text{eV} \tag{3-2}$$

$$\Delta G_B[H_2COOH] = 1.09\ \Delta G_B[OH] + 0.40\ \text{eV} \tag{3-3}$$

$$\Delta G_B[H_3CO{+}OH] = 1.30\ \Delta G_B[OH] + 0.28\ \text{eV} \tag{3-4}$$

$$\Delta G_B[H_3CO] = 0.96\ \Delta G_B[OH] - 0.22\ \text{eV} \tag{3-5}$$

$$\Delta G_B[O] = 1.68\ \Delta G_B[OH] + 0.96\ \text{eV} \tag{3-6}$$

$$\Delta G_B[H_2CO] = 0.75\ \Delta G_B[OH] + 0.31\ \text{eV} \tag{3-7}$$

$$\Delta G_B[H_3COH] = 0.20\ \Delta G_B[OH] - 0.11\ \text{eV} \tag{3-8}$$

$$\Delta G_B[H_2COH] = 0.05\ \Delta G_B[OH] + 0.18\ \text{eV} \tag{3-9}$$

3.3.12. Construction of theoretical activity volcano

The reaction mechanism consist of a number of single electron/proton transfer step. The free energy change for such steps depend on the intrinsic binding free energy of the intermediate before protonation and the one after. Furthermore, the free energy change is modified with applied electrochemical potential – which is modeled by the computational hydrogen electrode model here. From binding energy calculation provides free energy needed to be supplied for an elementary reaction step and predicts the potential at which the step can go forward. By using linear scaling relations, the biding free energies of the adsorbates are parametrized as a function of OH* binding energy. This allows writing the limiting potential for each possible electrochemical step as a linear function of OH* binding energy. Two pivotal decision can be made out of these. One is the selection of the intermediate formed from an elementary step where multiple intermediate can form. For example, from intermediate H_2COOH^*, 4th electron transfer lead to three possible reaction intermediates (Figure 3-5). Free energy change for elementary step leading to each of these intermediates are accessible as a function of OH* binding energy. At a given ΔG_B[OH], the step requiring the least reducing potential will be active. Analogous investigation performed over the whole OH* binding spectrum, provide information on the reaction mechanism active at different binding regimes. This leads to the second part of the interpretation. In a spread of ΔG_B[OH] with specific reaction mechanism, the line segment(s) pertaining to the step(s) with the largest onset potential requirement defines the overall reaction onset potential in that ΔG_B[OH] range.

3.3.12.1. Formic acid activity volcano

Formic acid evolution is a simple two-step process and involves only one surface bound intermediate OHCO*. Its linear scaling relation with OH* binding is used to parametrize the onset potential of the two elementary steps. The slope of the OH*-OCHO* linear correlation is almost unity. Weaker OH* adsorption means it is easier to protonate OHCO* than to release formic acid. Left side of the volcano plot is defined by 2nd electron transfer step of formic acid release. Strong bonding surfaces fall on this part of the volcano and weaker OH* adsorption links to smaller overpotential. When the OH*/OCHO* binding free energy becomes positive, extra energy need to be supplied for activating a CO_2 molecule to OCHO*. Thus, further weaker binding surfaces need larger overpotential. The 1st proton transfer is limiting for such surfaces. Right side of the volcano is defined by the CO_2 activation step. As previously discussed, OH* blocking of the active site can limit formic acid evolution activity. This is especially true for Sn-oxide overlayer. Tin oxide catalyst has been observed to have a very low onset potential (-0.2 V-RHE). Useful current density can be obtained only at ~-0.5 V-RHE. Hydroxylation of the active sites is probable cause behind this[105]. The onset potential for the 2nd electron transfer step as a function of ΔG_B[OH], almost coincides with the OH* removal potential line. Thus the OH* removal leg can be used to represent both the dihydroxylation step and OHCO* activation step. The top of the volcano touches the equilibrium potential line. A catalyst surface with ~0 eV binding free energy at 0 V-RHE for OH* and OCHO* would sit at the top of the volcano. Such an ideal surface would evolve formic acid with no overpotential and would not suffer any OH* poisoning. In principle, this volcano construction points to formic acid as a CO2RR product, theoretically which can be used to store energy with almost perfect round trip efficiency.

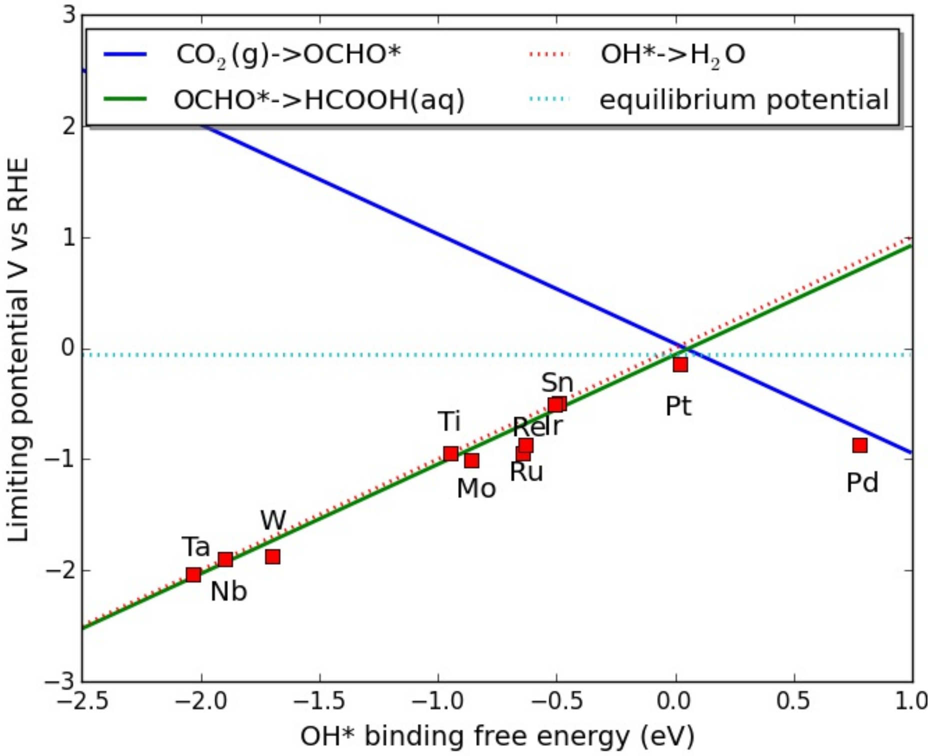

Figure 3-26: Theoretical onset potential volcano for formic acid. Actual onset potentials calculated for oxide overlayers considering OH poisoning is included for comparison.*

3.3.12.2. Activity volcano for methanediol

Methanediol is produced from CO_2 reduction by a 4-electron transfer reaction. The reaction steps involve OCHO*/HCOOH*/H_2COOH* adsorbates on surfaces which bind HCOOH* to the surface. Surfaces with weak OH* adsorption (ΔG_B[OH]> -0.25 eV) do not bind HCOOH* from scaling relation analysis. Thus, six possible reaction steps are part of the volcano construction along with hydroxyl removal reaction (Figure 3-27).

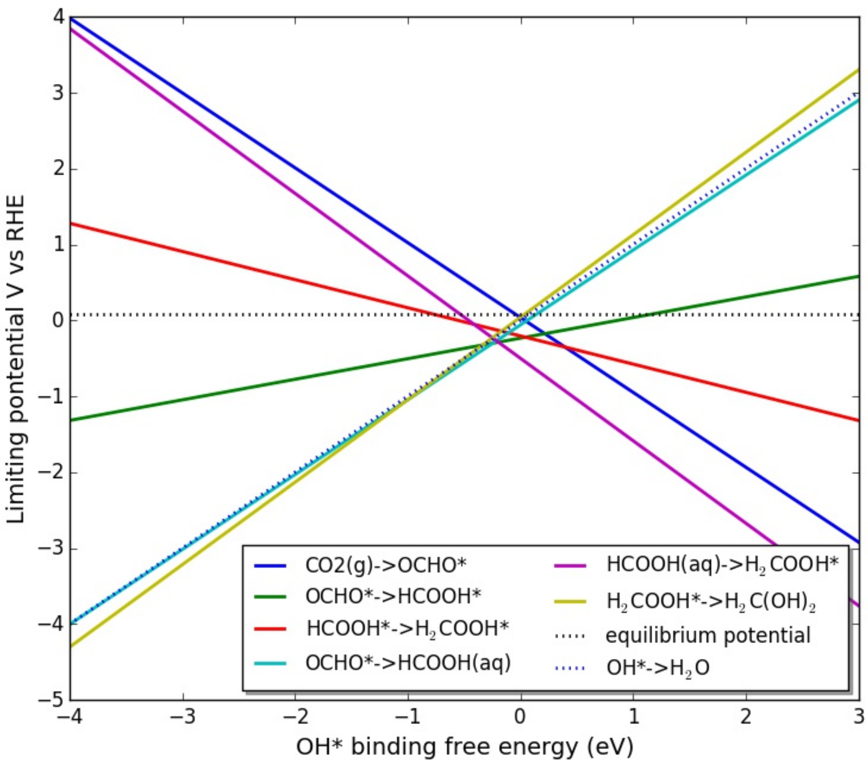

Figure 3-27: Scaling relation based thermodynamics of steps for methanediol evolution on oxide surfaces

On oxide surfaces which bind OH strongly (ΔG_B[OH] < - 0.25 eV), among different reaction steps, release of methanediol by H_2COOH* activation requires the most negative potential. However, in the range -0.8 eV < ΔG_B[OH] < - 0.25 eV, keeping active sites hydroxyl free requires more reducing potentials than reaction steps. Hence, it becomes the limiting reaction. For weak binding surfaces, protonating a solvated formic acid molecule determines the onset potential. Consequently, the activity volcano is comprised of HCOOH* activation for ΔG_B[OH] < -0.8 eV and OH* removal for -0.8 eV < ΔG_B[OH] < - 0.25 eV on the left side; protonation of formic acid to H_2COOH* on the right side. The top of the volcano is at ΔG_B[OH] = - 0.25 eV with a limiting potential of -0.25 V RHE. In the range -0.8 eV < ΔG_B[OH] < - 0.25 eV, OH* removal steps and methanediol release steps are different by less than 0.03 eV in free energy change. Therefore, further simplification of the volcano can be done to include only OH* removal and formic acid activation as left and right leg of the volcano respectively (Figure 3-28).

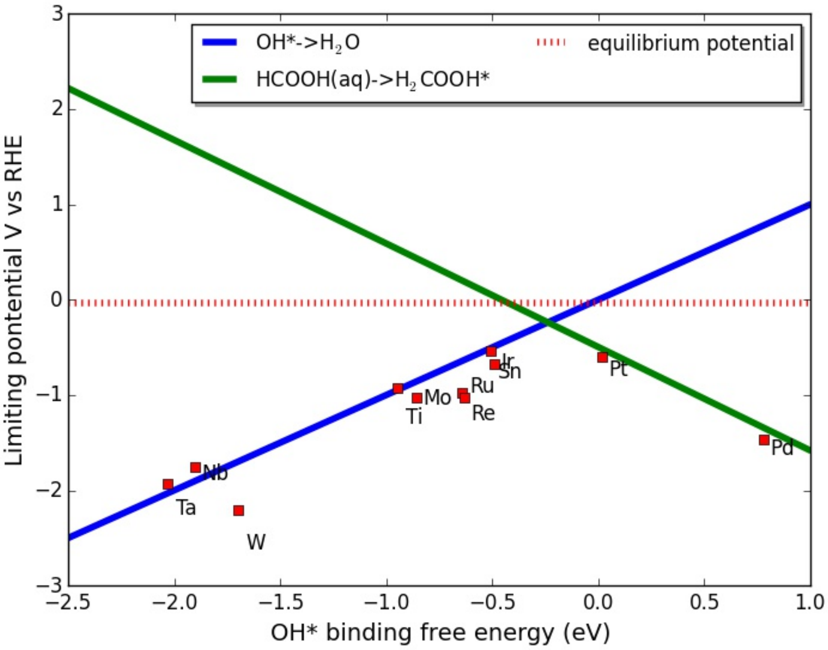

Figure 3-28: Methanediol evolution thermodynamic volcano. Specific onset potential of oxide surfaces (demarcated by top layer metal atom) are provided for comparison.

3.3.12.3. Methanol evolution volcano

The volcano plot can be divided into binding energy ranges based on the dominant reaction mechanism in that range. Scaling relations show that at $\Delta G_B[OH] < -1.30$ eV; the 4th electron transfer step i.e. H_2COOH^* activation leads to formation of O* at a bridge site along with the release of one methanol molecule. In this strong binding regime (reaction mechanism C), OH* removal demands the most reducing potential. For, $-1.30 \text{ eV} < \Delta G_B[OH] < 0.05$ eV; H_2COOH^* activation leads to H_3CO^*(bridge) + OH*(cus) intermediates. In this interval, the free energy change predicted (from scaling relations) for either the release of methanol from protonation of H_3CO^* or the release of water by protonation of OH* are almost degenerate for free energy change. Thus, oxide surfaces with OH* binding free energy in this range produces methanol through either reaction mechanism A or E. The top of the methanol activity volcano is at $\Delta G_B[OH] = -0.25$ eV. The predicted lowest possible negative potential required for methanol evolution on oxide surfaces is -0.25 V-RHE. The left side of this volcano is defined by activation of H_3CO^* to methanol. Scaling relations predict that this step is energetically close to OH* removal. Hence, OH* blocking of the active site is not a deterrent. One can also simply take OH* removal line as the left leg of the thermodynamic volcano. The right side of the volcano is defined by protonation of a formic acid molecule to H_2COOH^*. For $-0.25 \text{ eV} < \Delta G_B[OH] < 0.05$ eV reaction mechanism A is followed but with a formic acid intermediate. For $\Delta G_B[OH] > 0.05$ eV H_2COOH^* activation leads to H_2CO^*. Further reduction produces H_3CO^* in the binding energy interval $0.05 \text{ eV} < \Delta G_B[OH] < 0.43$ eV and reaction mechanism B is followed for methanol evolution. For weakest binding surfaces ($\Delta G_B[OH] > 0.43$ eV) H_2CO^* protonation gives H_2COH^*. For such weakly binding surfaces (e.g. Pd-oxide overlayer) reaction mechanism D is active for methanol evolution. HCOOH(aq) → H_2COOH* is the thermodynamic limiting step for both B and D reaction mechanisms.

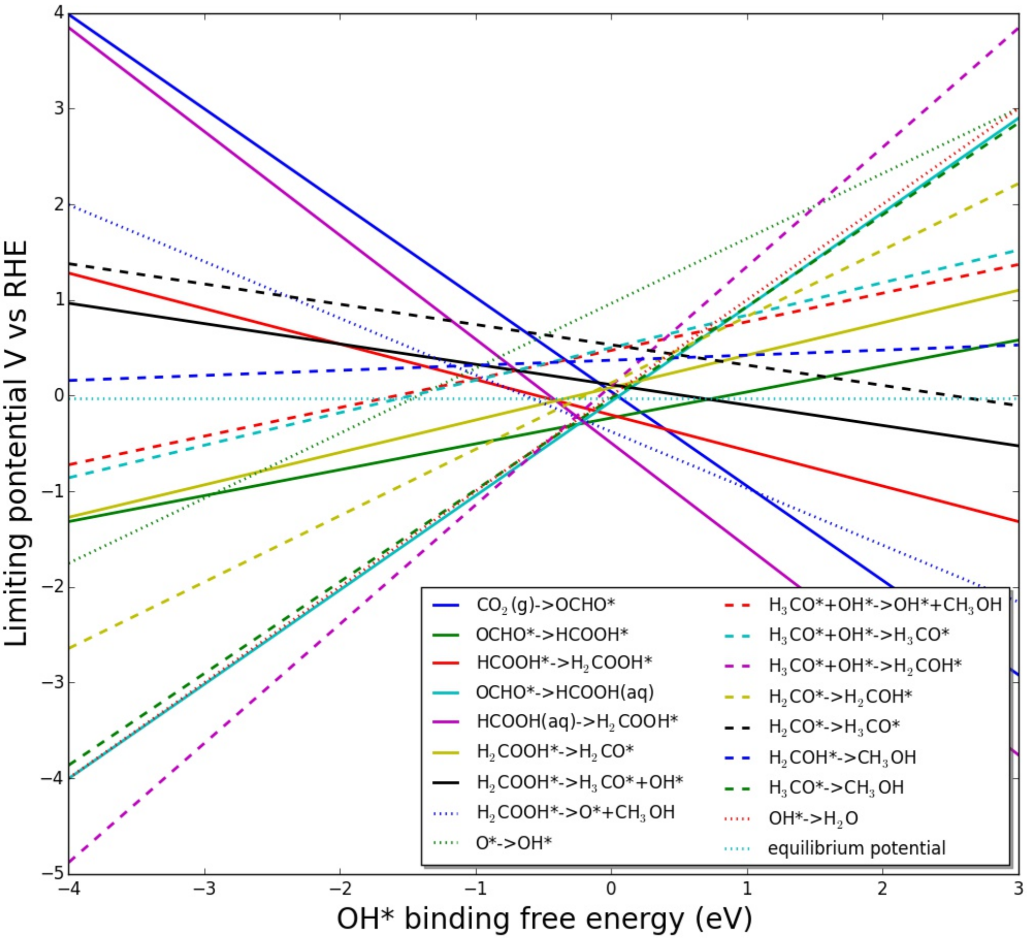

Figure 3-29: Thermodynamic of all elementary steps of methanol evolution reaction network as function of OH binding energy*

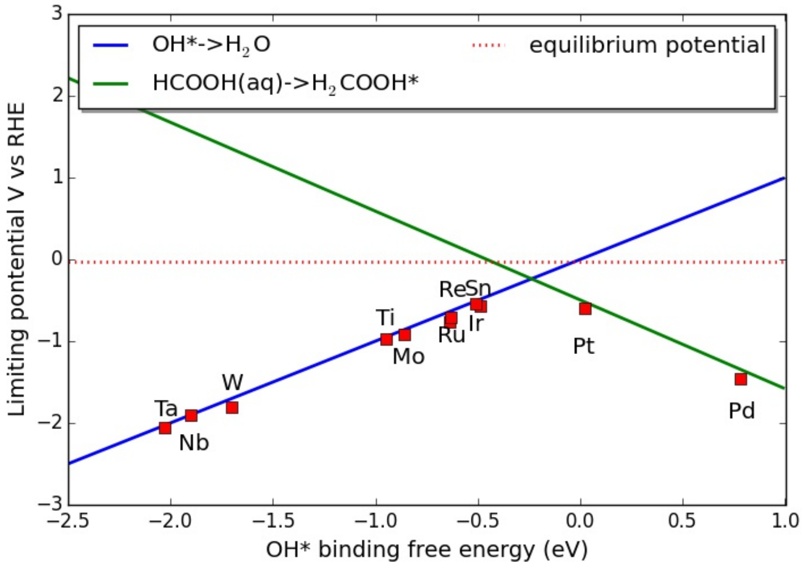

Figure 3-30: Thermodynamic volcano for methanol evolution. Symbols of top layer metals atoms for oxide surfaces for which calculations were done individually.

Despite a number of reaction mechanism being active in different OH* binding energy intervals, only two reaction steps suffice to define the limiting onset potential. Similar to methanediol, OH* removal and protonation of aqueous formic acid to H_2COOH* defines the left and right leg of the activity volcano. This simplification from the large number of reaction steps and mechanisms, capture the trend in onset potential, such that individually calculated data points agree very well with the proposed volcano (Figure 3-30).

3.3.12.4. Methane evolution volcano

The methane evolution reaction proceeds through a HCOOH* intermediate for ΔG_B[OH] < -0.25 eV and through a formic acid molecule for weaker binding surfaces (Figure 3-31). Protonation of H_2COOH* yields H_3CO* (bridge) + OH* (cus) intermediates for ΔG_B[OH] < 0.05 eV and H2CO* for ΔG_B[OH] > 0.05. H_3CO* intermediate is protonated at the carbon atom for methane release if 0.05 eV < ΔG_B[OH] < 0.21 eV and protonated at the oxygen atom for H_3COH* intermediate formation for 0.21 eV < ΔG_B[OH] < 0.43 eV. H_2CO* protonates to H_2COH* for ΔG_B[OH] > 0.43 eV.

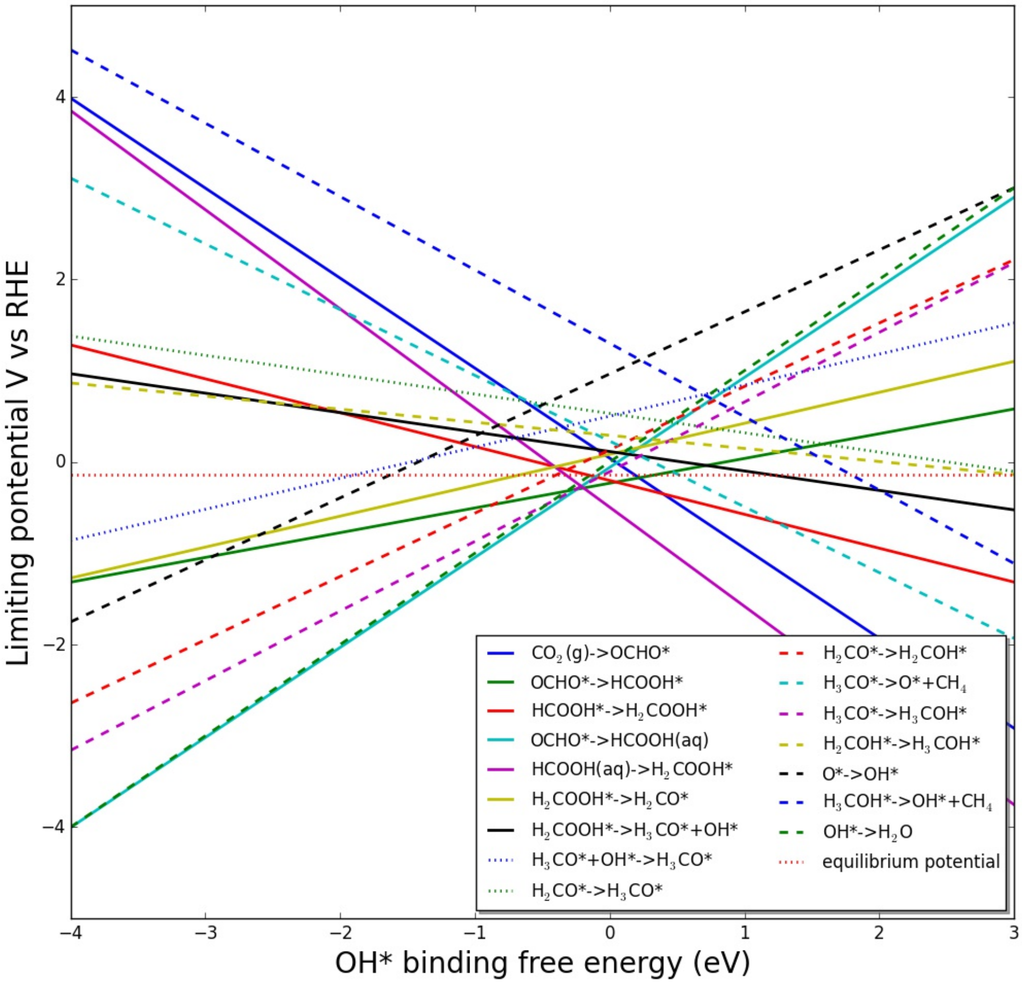

Figure 3-31: Thermodynamic of all elementary steps of methane evolution reaction network as function of OH binding energy*

Effectively, methane evolution reaction mechanism F is followed via the HCOOH* intermediate for $\Delta G_B[OH] < -0.25$ eV and via a formic acid molecule for -0.25 eV $< \Delta G_B[OH] < 0.05$ eV. Mechanism G is followed for 0.05 eV $< \Delta G_B[OH] < 0.21$ eV. Further weak binding surfaces with 0.05 eV $< \Delta G_B[OH] < 0.21$ eV follows mechanism H. Weakest OH* binding surfaces ($\Delta G_B[OH] > 0.43$ eV) might make methane by reaction mechanism I through the H_2COH^* intermediate. For reaction mechanism F with HCOOH* intermediate in $\Delta G_B[OH] < -0.25$ eV range, OH* removal determine the onset potential (Figure 3-31). For surfaces with weaker OH* binding, irrespective of reaction mechanism, formation of H_2COOH^* from solvated formic acid require most negative potential to be applied to proceed. This simplifies the methane evolution thermodynamic volcano to the same as discussed for methanol and methanediol (Figure 3-32).

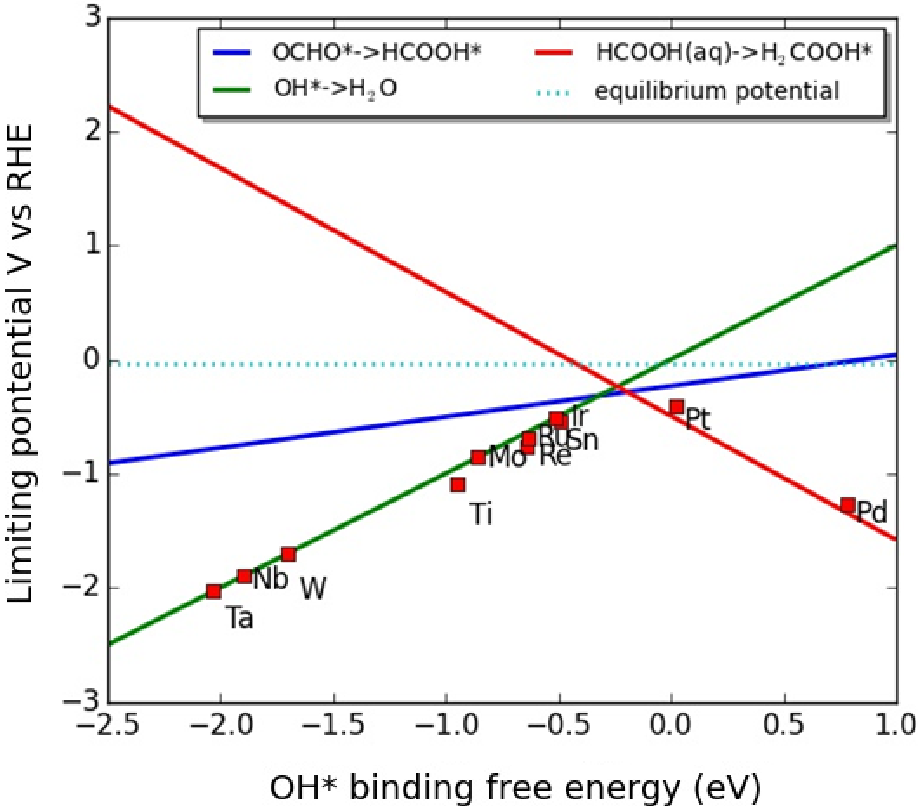

Figure 3-32: Methane evolution thermodynamic volcano with data from individual oxide-surface calculations.

3.4. Designing rutile oxide electrocatalysts for CO2RR

Oxide electrocatalysts following three rules are expected to show good selectivity towards liquid fuel products over hydrogen or CO.

(a) As the first proton transfer product, OCHO* must be more stable than H*

(b) OCHO* binding should not be too strong, or protonation to HCOOH* will be too difficult

(c) To limit CO* formation COOH* intermediate should not bind to the surface. CO as a product is not intended and further reduction of CO* intermediate would require high onset potential due to CO*/CHO* scaling.

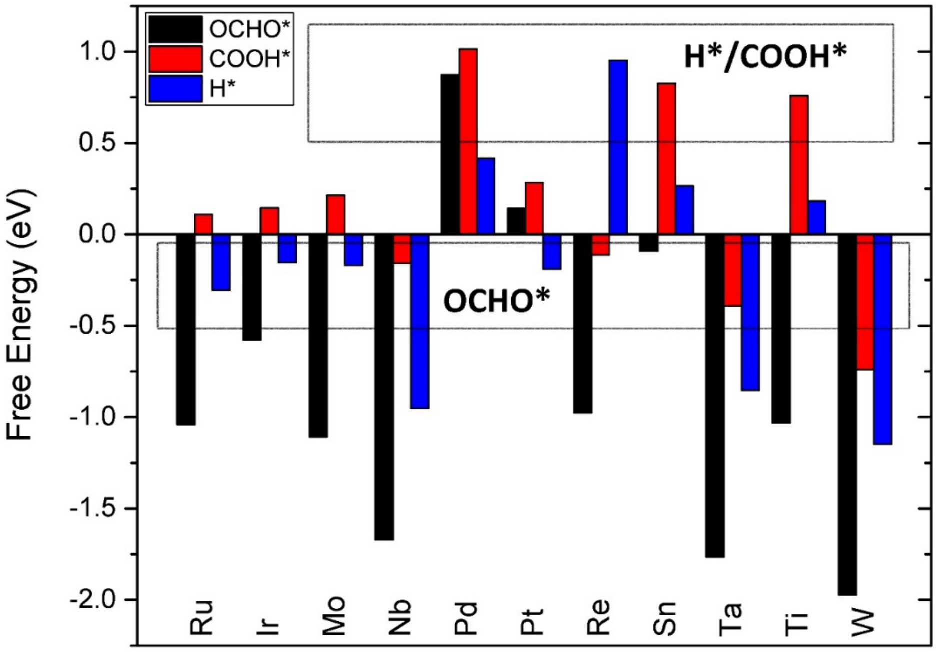

Figure 3-33: Binding free energy of the H, OCHO*, and COOH*. The suitable H*/COOH*/OCHO* binding free energy for selective CO2RR is marked with boxes.*

Across different binding energy regime, all oxide overlayers studied here binds OCHO* stronger than COOH* (Figure 3-33). This indicates the robustness of the assumption taken that reaction network for CO2RR does not go through CO* adsorbate but make use of O-coordinated adsorbates. It validates the volcano analysis done.

In summary, H* and COOH* having large positive binding energies ($\Delta G < 0.5$ eV) at 0 V-RHE and OCHO* adsorbing with moderate strength (-0.5 eV $< \Delta G[OCHO] < 0$ eV) links to good selectivity. The Re-oxide overlayer shows a uniquely large destabilization of the H* adsorbate while OCHO* is very stable. The binding free energy order is $\Delta G[H] > \Delta G[COOH] > \Delta G[OCHO]$. This indicates a high selectivity of $HCOOH/CH_3OH/CH_4$ formation with very little hydrogen evolution. Excluding Re-oxide overlayer, adsorption free energies of COOH* and H* scales linearly (Figure 3-34). This behaviour is similar to that observed on metallic catalysts[70]. The H* and OH* binding energies show little correlation, i.e. for any given OH* binding energy it is possible to find surfaces with widely varying H* binding energy. H*/COOH* scaling law helps in binding energy based criterion for active and selective oxide CO2RR catalysts in the H*/OH* binding energy scatter plot. Once a suitable oxide surface with OH* adsorption strength close to the top of the volcano and very weak H* adsorption free energy is found, it is expected to not bind COOH* due to the scaling relation. A quick check of oxide catalysts for CO2RR activity and selectivity can be done following the map provided in Figure 3-35. This selection incorporates that the top of the volcano for formic acid is at $\Delta G[OH] \approx 0$ eV and that for other C1 products are at $\Delta G[OH] \approx -0.25$ eV as well as the weak binding of H*/COOH* and their scaling reactions.

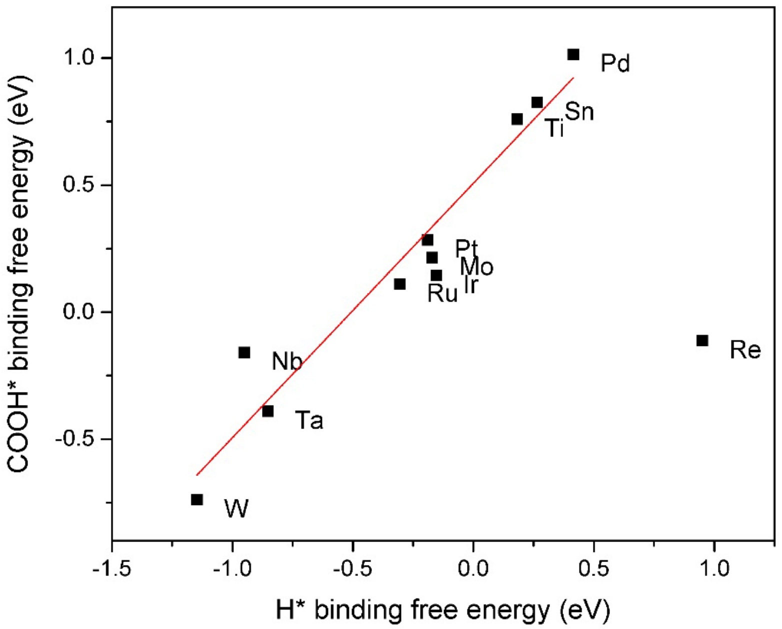

Figure 3-34: scaling relation between H and COOH* adsorbates (with 25% CO* coverage). Re-oxide overlayer showing disparate behaviour is not included in the scaling. Data points indexed by metal atoms at the top of the oxide overlayer.*

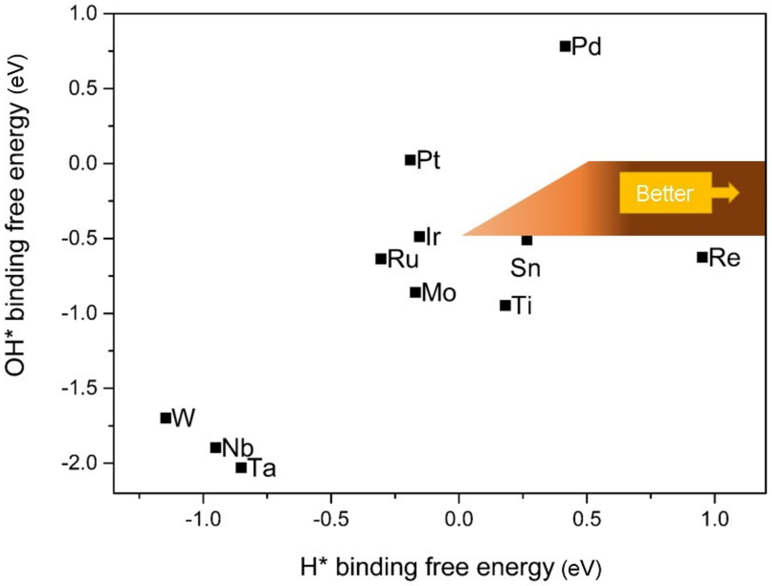

Figure 3-35: Suggested area in H/OH* binding free energy scatter plot for best CO2RR activity and selectivity.*

3.5. Conclusions

Thermodynamic volcano analysis for methane and methanol suggest that it is possible to design oxide electrocatalysts with optimum OH* binding, which can significantly lower the overpotential requirement from contemporary metal catalysts. While the volcano for metallic catalysts indicates that at least a reducing potential of -0.68 V-RHE is needed for methanation, the volcano for oxides, presented here hint to a best case scenario of -0.25 V-RHE. This is due to differences in reaction pathway and onset limiting steps in these reaction pathways. Unlike metals, CO2RR on oxide do not proceed through a CO* intermediate but a HCOOH* intermediate. The limiting step on metal CO* protonation cannot be engineered to have smaller onset potential by choice of a surface with different binding characteristics due to scaling relations. On the contrary, OH* removal as water or H_3CO* hydrogenation to release of methane or methanol can have very different onset potential on different oxide surfaces.

The left side of the thermodynamic volcano for CO2RR to methanol/methane evolution on oxide surfaces is defined by OH* removal and right side is defined by the H_2COOH* formation step. For formic acid evolution, the left and right side of the volcano is defined by OCHO* activation and OCHO* formation, respectively. OH* poisoning can be a constraint for oxide surfaces producing formic acid efficiently. Due to scaling relations, lines depicting onset potential for OH* removal and OCHO* protonation to formic acid overlap. Considering this, OH* removal can be considered as left leg of a universal CO2RR volcano. For $\Delta G[OH] > -0.25$ eV, HCOOH* do not bind to the surface and formic acid is the major reaction product. Reduction of formic acid to H_2COOH* is difficult and onset potential limiting for surfaces binding weaker than this. For such surfaces, the formic acid volcano can be used to construct the universal CO2RR volcano. OH* removal and CO_2 activation to OCHO* characterize the left and right segment of the universal volcano (Figure 3-36). For $\Delta G[OH] < -0.25$ eV, methane and methanol are primary product and for $\Delta G[OH] > -0.25$ eV, formic acid is dominant. Selectivity of methane over methanol can not be predicted from this thermodyanamic analysis as it depends on the kinetic barrier of protonation at carbon or oxygen atom of the H_3CO* intermediate.

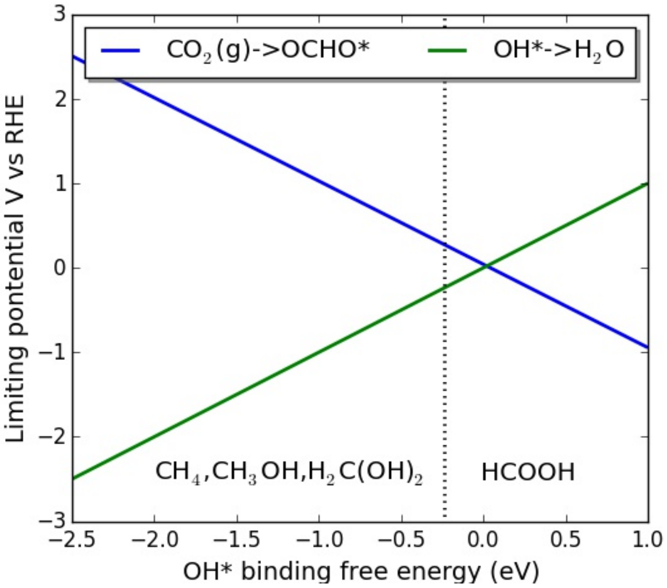

Figure 3-36: thermodynamic volcano for CO2RR on oxide surfaces considering all C1 products.

This portion of the PhD project successfully created first mechanistic understanding or CO2RR on oxide surfaces, defined scaling relations, thermodynamic descriptors and onset potential limits. Design principles for selectivity over HER and CO evolution is also charted. The general materials design principles developed in this chapter will aid in future development of efficient selective oxide catalysts for CO2RR. Specifically, Ir/Re-oxide overlayers are worth studying experimentally for methanol evolution. Ir-oxide overlayer is predicted to be more active than a pure Ru-oxide surface. Overlayers considered here consist of well studied oxides that are lattice matched and it is energetically favourable to form this overlayer[112]. Re-oxide overlayer is promising due to exceptional selectivity over HER. Formic acid is economically most valuable among C1 products and can be produced with low over potential on Tin oxide derived catalysts.

4.CO* spectator effects on CO2RR

4.1. Introduction

Molecular adsorbates are often present on the catalysts surface without taking part in the reaction. Such adsorbates are called spectator species. Interaction between spectators and reaction intermediates affect the binding energy changing the thermodynamics of reaction steps. The presence of spectator species on the catalyst surface can enhance or poison electrocatalyst activity, as have been studied theoretically and experimentally[113–117]. COOH* intermediate being much less stable than the OCHO* intermediate on rutile oxide surfaces. However, a small amount of COOH* might form on CO_2 activation. Further reduction is expected to leave adsorbed CO* from this spurious reaction[33]. CO* spectators interact with other adsorbed reaction intermediates and alter their binding energy. In chapter 3 it was discussed that spectator CO* species can have large effect on H* binding free energy, potentially promoting/poisoning HER. Interaction between CO* and H* weakens the H* adsorptions and HER is either improves of slows down HER based on which side of the volcano the catalyst surfaces is[100]. It is expected OH* binding energy to be affected by spectator CO*. Intermediates formed during CO2RR to methanol on the RuO_2 catalyst surface are bound to the surface by oxygen atoms and their binding energy is correlated with the OH* binding energy. Thus a strong effect of CO* spectators on the onset potential for methanol production and selectivity over HER is conceivable. Shift in the reaction site of CO2RR due to blockade of more favourable sites by CO* spectator can have very large effect on the thermodynamics of elementary reaction steps. For example, under reducing conditions the RuO_2 (110) surface can have both strong biding bridge sites and weak binding coordinated unsaturated (cus) sites available for intermediates. If all bridge sites (br) are occupied by spectator CO* species, then the reaction can only proceed through cus sites. To understand how CO* spectators changes CO2RR pathway on RuO_2 (110) surface, reaction intermediate and paths to formic acid, methanol and methane in the presence of many different concentrations of CO* spectators as well as variation in the spatial distribution is studied here. Also the importance of local pH and mass transfer conditions are discussed as key parameters to successful CO2RR on ruthenium oxide electrocatalysts.

4.2. Computational methods

Maintaining conformity with simulation model and techniques used in chapter 3, VASP[72] package for DFT based simulation tool is used here for modelling catalyst surfaces with spectators and adsorbed reaction intermediates. BEEF-vdW[54] exchange correlation functional with 500 eV wave function cutoff is used as well. Atomic structure of the bare RuO2 (110) slab is identical to that used in chapter 3, where top two layers are relaxed along with the adsorbates and spectators. The bridge site is considered vacant due to reducing environment during CO2RR. Thus, the model has two bridge and two cus sites available for reaction intermediates and spectator CO* molecules. During simulation, a 4x4x1 k-point mesh and 16 Å of vacuum in the z-direction and Gaussian electronic smearing is used. Optimization of atomic positions are done until forces on atoms in top two layers and adsorbates are lower than 0.003 eV/Å. Vibrational modes for adsorbed molecules are also analyzed to enable finite temperature free energy estimates by approximating adsorbate degrees of freedom as independent quantum mechanical harmonic oscillators. Unlike the surfaces studied in chapter 3, only pure ruthenium oxide surfaces if studied here. Therefore, the finite temperature free energy corrections for the same adsorbate is considered invariant for all spectator coverage configurations. In addition, the experimental studies of CO2RR on ruthenium oxide electrocatalysts report very low methanol concentration in the electrolyte along with high faradic efficiency for conversion. To better represent the experimental condition in the free energy estimation, a methanol fugacity value of 0.003 is used (estimated from concentration provided by [31,32]). This is much lower than the methanol fugacity value 6079 used in chapter 3. Binding free energy of adsorbates, elementary reaction step energy and their dependency on applied electrochemical potential are evaluated by models and methods explained in chapter 2 and exemplified in chapter 3.

4.3. Results and discussions

4.3.1. CO* coverage on RuO_2 (110) surface

With four adsorption site in the simulation model, CO* coverage can be 0%, 25%, 50%, 75% or 100%. With full CO* coverage CO2RR or HER cannot advance due to unavailability of active sites. Each additional CO* spectator in the simulation model amount to 25% added CO* coverage. Two different types of active site being present and considering symmetry of relative positions of the CO* adsorbates, 25% and 75% coverage can be represented in two different manner, while 50% coverage leads to four difference representations (Figure 4-1). All such different coverages are inspected for relative stability. On the bare surface, 1st CO* adsorption at the bridge site (Figure 4-1b) is favourable compared to cus site (Figure 4-1c) by 0.18 eV. With respect to CO molecule, binding free energy of CO* at the bridge site of the bare surfaces is -1.34 eV. Two cus sites and one bridge site is accessible for catalysis with 25% CO* coverage. For 50% CO* coverage, putting all adsorbates in the bridge site (Figure 4-1d) is most stable. All cus configuration (Figure 4-1e) for 50% CO* coverage is less stable by 0.28 eV. The adsorption free energy for the two 50% CO* coverage configuration with combination of bridge and cus occupancy are less stable than the all bridge configuration by 0.08 eV (while neighbouring bridge and cus sites have CO* (Figure 4-1f)) and 0.1 eV (occupied bridge and cus sites are far apart (Figure 4-1g)). With both bridge site CO* covered, catalysis can proceed through the cus sites available. On the other hand, if 50% CO* coverage is mixed site (bridge+cus), both bridge and cus sites are available for CO2RR. At 75% CO* coverage, the adsorbate configuration with 2*bridge+cus sites (Figure 4-1h) is more stable than bridge+2*cus (Figure 4-1i) by ~0.2 eV. These two configurations are fundamentally different as the first allows catalysis through the cus sites and the latter requires the reaction to take place at the bridge site. The free enrgy of CO* covered surfaces with w.r.t. bare surfaces and CO molecule is given in Figure 4-2. Due to repulsive CO*-CO* interactions, incremental biding energy for CO* decrease. At 75% CO* coverage reduction of surfaces bound CO* starts at -0.77 V-RHE leading to lower CO* coverage.

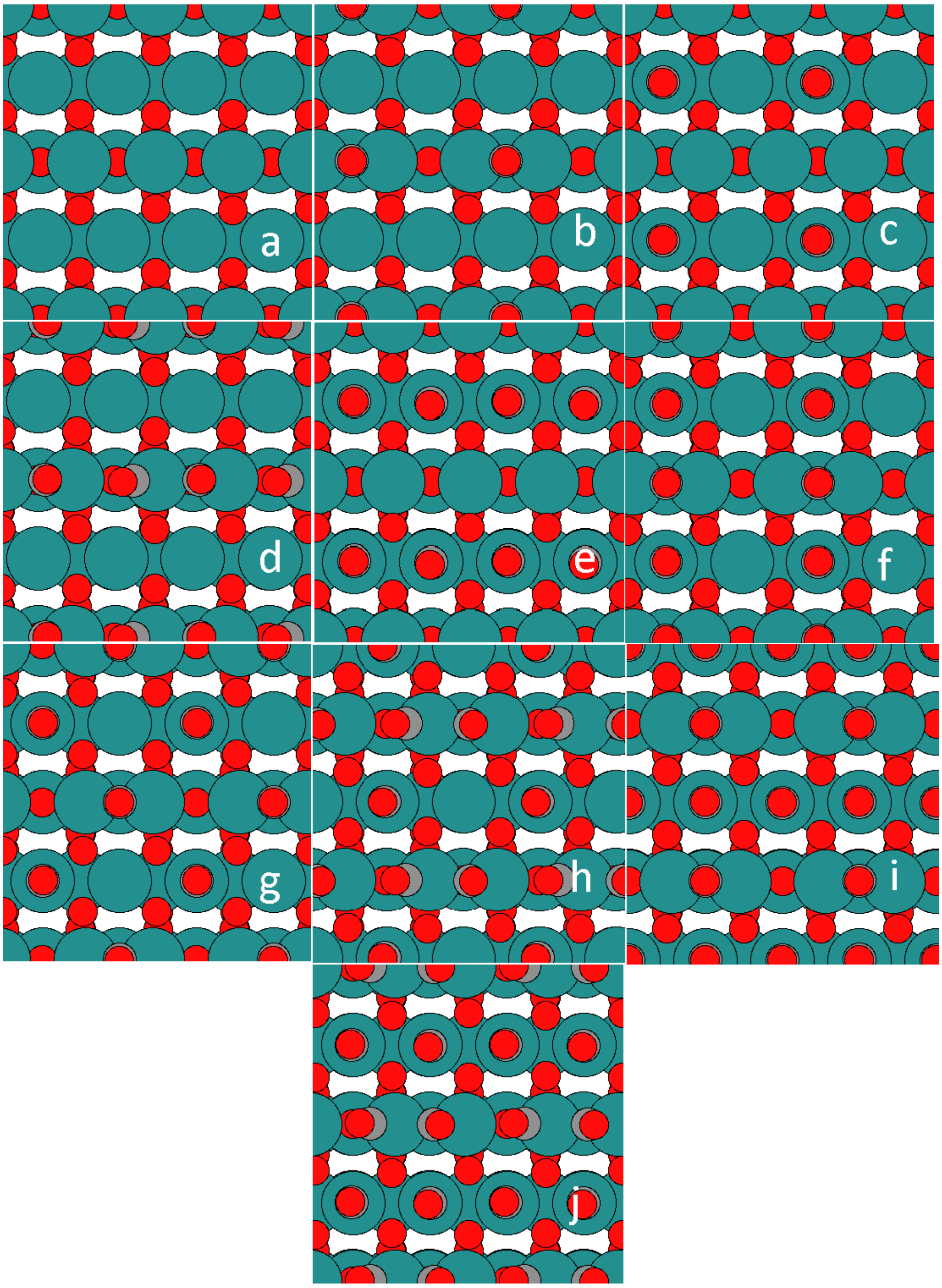

Figure 4-1: all possible spatially distinct CO spectator coverage within the simulation slab with two bridge and two cus sites. (a) no CO* coverage (b) 25% CO* coverage (bridge site) (c) 25% CO* coverage (cus sites) (d) 50% CO* coverage (all bridge sites) (e) 50% CO* coverage (all cus sites) (f) 50% CO* coverage (adjoining bridge and cus sites) (g) 50% CO* coverage (distant bridge and cus sites (h) 75% CO* coverage (all bridge sites and half cus sites) (i) 75% CO* coverage (all cus sites and half bridge sites) (j) 100% CO* coverage. Green, red, black spheres are Ru, O, C atoms respectively.*

Some adsorbates like OCHO* and H_2COOH* can attach to the catalyst surface through one or two active sites due to the molecular geometry, as observed with surfaces studied in chapter 3. Such bidentate adsorbates are allowed to remain so for 0-50% CO* coverage. Lack of multiple neighbouring vacant active site forces them to be monodentate for 75% CO* coverage. Six of the following CO* configurations are picked for CO2RR reaction mechanism analysis – 0% CO* coverage, 25% CO* coverage (bridge site), 50% CO* coverage (all bridge sites). 50% CO* coverage (neighbouring bridge and cus sites), 75% CO* coverage (2*bridge+cus sites), 75% CO* coverage (bridge+2*cus sites).

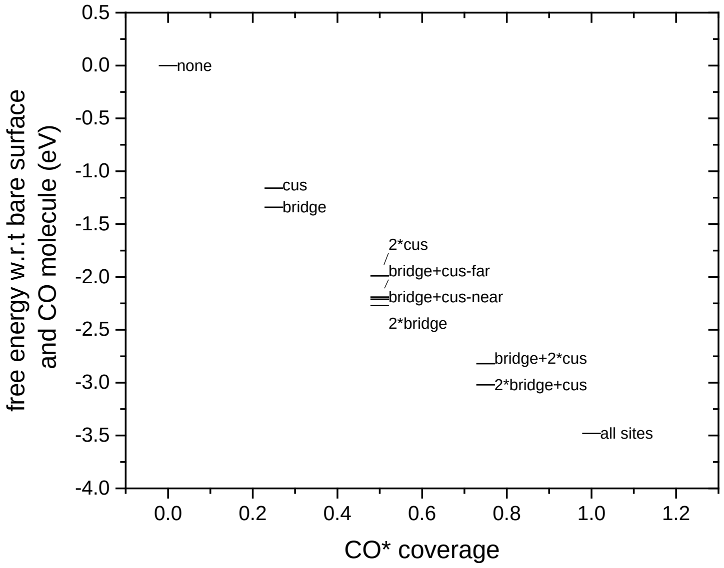

Figure 4-2: free energy of CO covered surfaces relative to bare RuO_2 (110) surfaces and CO molecule.*

Investigation of adsorbate binding free energy on the RuO_2 (110) surface at bridge and cus sites reveals that oxygen coordinated adsorbates bind significantly stronger to the bridge sites compared to cus sites. The relative preference for bridge site is less pronounced for CO*. For example, the binding energy of OH* at bridge and cus sites are -0.32 eV and +0.08 eV, respectively, while these values for CO* are -1.34 eV and -1.16 eV (w.r.t. CO molecule). This observation helps understand the distribution of spectating CO* in bridge and cus sites under reaction conditions. As CO2RR intermediates are O-coordinated, if a mixture of CO* and O-coordinated intermediates are present at the catalyst surface, CO2RR intermediates would preferentially occupy the bridge sites. For example, three CO* and one OH* adsorbate can be distributed such that OH* can occupy a bridge site or it can occupy a cus site. The configuration with OH* in bridge site have 0.77 eV lower free energy than the configuration with OH* in cus site. This is critical in effective CO2RR catalysis on the RuO_2 (110) surface. Reaction path thermodynamics shows that bridge site CO2RR is not only energetically preferred but also has lower thermodynamic onset potential.

4.3.2. HER with CO* spectator

Effect of 25% CO* spectator on adsorption free energy of H* at bridge site have been studied in chapter 3. However HER can progress via the cus site and in reaction condition, CO* coverage might vary. Without large reducing potential, hydroxylation of the active site can happen spontaneously as well as H* can be a spectator. Considering several spectator cases analysis is done for H* binding free energy. RuO_2 (110) bridge sites, when vacant, are hydroxylated in aqueous solution due to negative binding free energy of OH* at the bridge site at 0 V-RHE. Hydroxylation of cus sites is not energetically favourable at 0 V-RHE. If CO* spectators are absent at the bridge site, OH* might occupy those sites and HER can proceed at the cus site.

For 0% CO* coverage and hydroxylated bridge sites, H* binding free energy at the cus site is +0.33 eV. Hence, bridge site filled with OH* spectators, HER requires a reducing potential of -0.33 V-RHE. However, the OH* removal potential for clean RuO_2 (110) surface bridge site is -0.32 V-RHE and the H* binding free energy at the same site is -0.49 eV. For an empty surface, the H* binding free energy at the cus site is +0.22 eV and that at cus site (with H* spectators at all bridge site) is +0.41 eV. With 75% OH* coverage and only cus site availability, H* binding at cus site is -0.56 eV due to attractive interaction with hydroxyl spectators. Without any CO* coverage, with gradual lowering of applied potential, at -0.32 V-RHE RuO_2 (110) would start evolving hydrogen.

For 25% CO* coverage (bridge site) in absence of any other spectator, H* binding free energy is -0.31 eV at the bridge site and +0.26 eV in the cus site. OH* binding energy with 25% CO* coverage is -0.64 eV. Hydroxylation of the remaining bridge site can force H* to bind at cus site. H* binding energy at cus site, with all bridge sites filled by CO* and OH*, is +0.39 eV. OH* being strongly binding at bridge site, HER would begin at -0.39 V-RHE with 25% CO* coverage. If both the bridge sites are filled with CO* i.e. 50% coverage, at cus site $\Delta G[H]$ is +0.41 eV. If 50% CO* is distributed between bridge and cus sites, $\Delta G[H]$ is -0.29 eV at bridge site and -0.22 eV at cus site. Bridge site $\Delta G[OH]$ for 50% CO* coverage (bridge + cus) is -0.48 eV. With 50% CO* and 25% OH* coverage, HER starts only at -0.56 V-RHE. Due to OH* poisoning, at least -0.42 V-RHE is needed for HER for 50% CO* coverage. With 75% CO* coverage, $\Delta G[OH]$ at the bridge site is -0.13 eV and at the cus site, +0.63 eV. Bridge site is only accessible after OH* removal at -0.49 V-RHE, limiting the HER to this potential.

*Table 4-1: Calculated thermodynamic onset potential [V vs RHE] for HER at bridge and cus sites with different spectator species on RuO_2 (110); yellow represents a cus site and green represents a bridge site. OH, CO, H are possible spectators and X is absence of any of them. * is the site considered for HER.*

Configurations															
cus	X	*		CO	*		X	*		X	*		CO	*	
bridge	OH	OH		CO	OH		H	H		CO	X		CO	X	
HER onset [V-RHE]	-0.33			-0.56			-0.41			-0.26			-0.22		
Cus	X	*		*	X		X	X		*	X		OH	*	
Bridge	OH	CO		X	X		CO	*		CO	CO		OH	OH	
HER onset [V-RHE]	-0.39			-0.22			-0.31			-0.41			-0.56		
Cus	X	X		CO	X		CO	*		CO	CO				
Bridge	*	X		CO	*		CO	CO		*	CO				
HER onset [V-RHE]	-0.49			-0.29			-0.63			-0.13					

4.3.3. CO2RR reaction mechanism

An analysis of relative binding energies of adsorbates and products formed at different electron transfer steps at 0 V-RHE helps investigating the modifications in CO2RR pathway and onset potential as well as selectivity over HER due to adsorbate interactions with CO*. All reaction intermediates are considered with six possible CO* coverage condition. 75% CO* coverage do not allow multi-adsorbate intermediates like $H_3CO^*+OH^*$.

Table 4-2: Reaction intermediates considered for CO2RR and HER on RuO_2 (110) surface with different CO coverage*

$0e^-$	$1\ e^-$	$2\ e^-$	$3\ e^-$	$4\ e^-$
*	$OHCO^*$, H^*, $COOH^*$	$HCOOH^*$, $CO^*+H_2O(l)$, $HCOOH(aq)$, $H_2(aq)$	H_2COOH^*	$H_3CO^*+OH^*$, $H_2CO+H_2O(l)$, $O^*+CH_3OH(aq)$
$5\ e^-$	$6\ e^-$	$7\ e^-$	$8\ e^-$	
$H_3CO^*+H_2O(l)$, $H_2COH^*+H_2O(l)$, $OH^*+CH_3OH(aq)$	$O^*+CH_4(aq)+H_2O(l)$, $CH_3OH^*+H_2O(l)$, $CH_3OH(aq)+H_2O(l)$	$OH^*+CH_4(aq)+H_2O(l)$	$CH_4(aq)+H_2O(l)$	

4.3.4. CO2RR: no CO* spectator

CO_2 activation leads to OCHO* intermediate which binds through a cus site and a bridge site. OCHO* is significantly more stable than COOH*. Without CO* spectator RuO_2 (110), due to lower adsorbate binding, ensuing protonation releases formic acid molecule to electrolyte. Bidentate adsorbate H_2COOH* being very stable, it is thermodynamic downhill to protonate formic acid molecule. 4th reaction intermediate in CO2RR is a pair of adsorbate H_3CO*+OH*. Both bridge site being available, these adsorbate occupy bridge site. OH* is removed as water. H_3CO* is either protonation at oxygen atom to form methanol or at carbon atom for release methane. For all the CO2RR products protonation of OCHO* to formic acid is onset limiting at -0.71 V-RHE. Without any CO* coverage, hydrogen is expected to dominate products obtained due to cus site HER although at bridge site OCHO* is favoured.

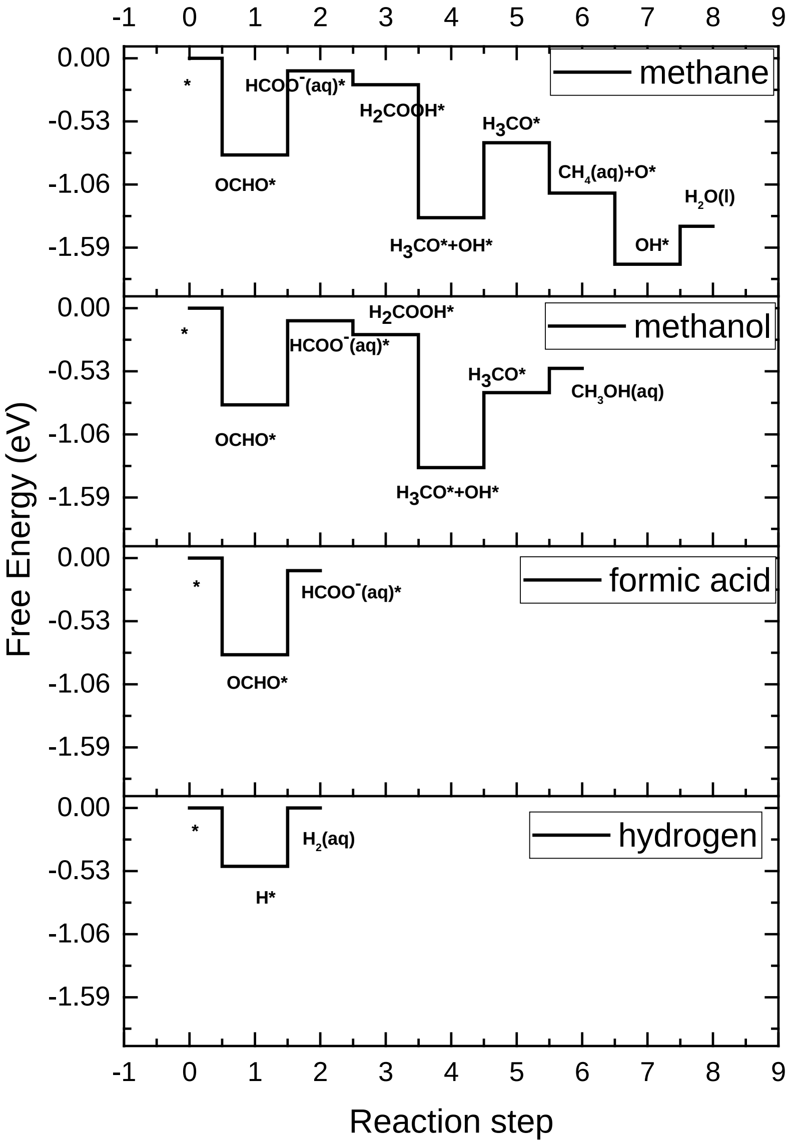

Figure 4-3: Thermodynamics of elementary electron transfer steps leading to evolution of methane, methanol, formic acid and hydrogen on the RuO_2 (110) surface with no CO coverage.*

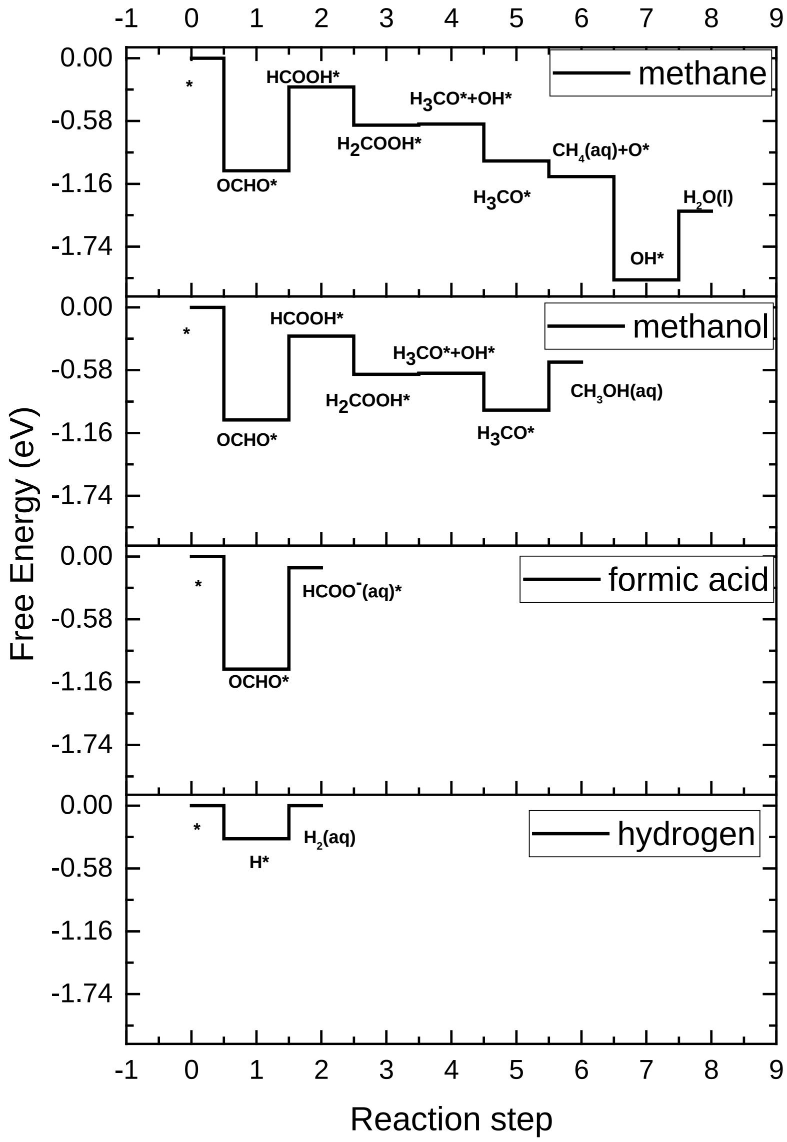

Figure 4-4: Thermodynamics of elementary electron transfer steps leading to evolution of methane, methanol, formic acid and hydrogen on the RuO_2 (110) surface with 25% CO coverage (bridge site).*

4.3.5. CO2RR: 25% CO* spectator (bridge)

Due to attractive adsorbate adsorbate interaction from CO* spectator, OCHO* binds stronger with 25% CO* coverage than no CO*. It is also true for HCOOH* adsorbate and CO2RR proceed through surface bound species only. The reaction mechanism stays unchanged from 0% CO* coverage analysis. However, $H_3CO^*+OH^*$ intermediate binds through bridge and cus site respectively. Thus OH* removal from cus site is easier. Form OCHO*, protonation to HCOOH* is very demanding and onset potential is -0.78 V-RHE. Formic acid molecules being less stable than HCOOH*, onset for it is even more reducing at 0.94 V-RHE. With 25% CO* coverage, RuO2 (110) is not expected to evolve formic acid but prefer methane or methanol.

4.3.6. CO2RR: 50% CO* spectator (bridge + cus)

With two CO* adsorbates in bridge and cus sites, lead to more optimal binding energy for reaction intermediates while keeping the reaction mechanism same as 25% CO* coverage – as observable with the smaller positive steps (Figure 4-5). Weakening of OCHO* (which still binds through a bridge and a cus site) makes formation of HCOOH* easier with onset on -0.4 V-RHE. This is also the overall onset potential for methanol formation. Formic acid molecule stays bound to the surface, giving access to higher reduction product like methane and methanol. At this CO* coverage, the onset potential for methane and methanol evolution come from different reactions steps. Last reaction step of OH* removal from the bridge site for methane evolution needs slightly more reducing potential at -0.48 V-RHE.

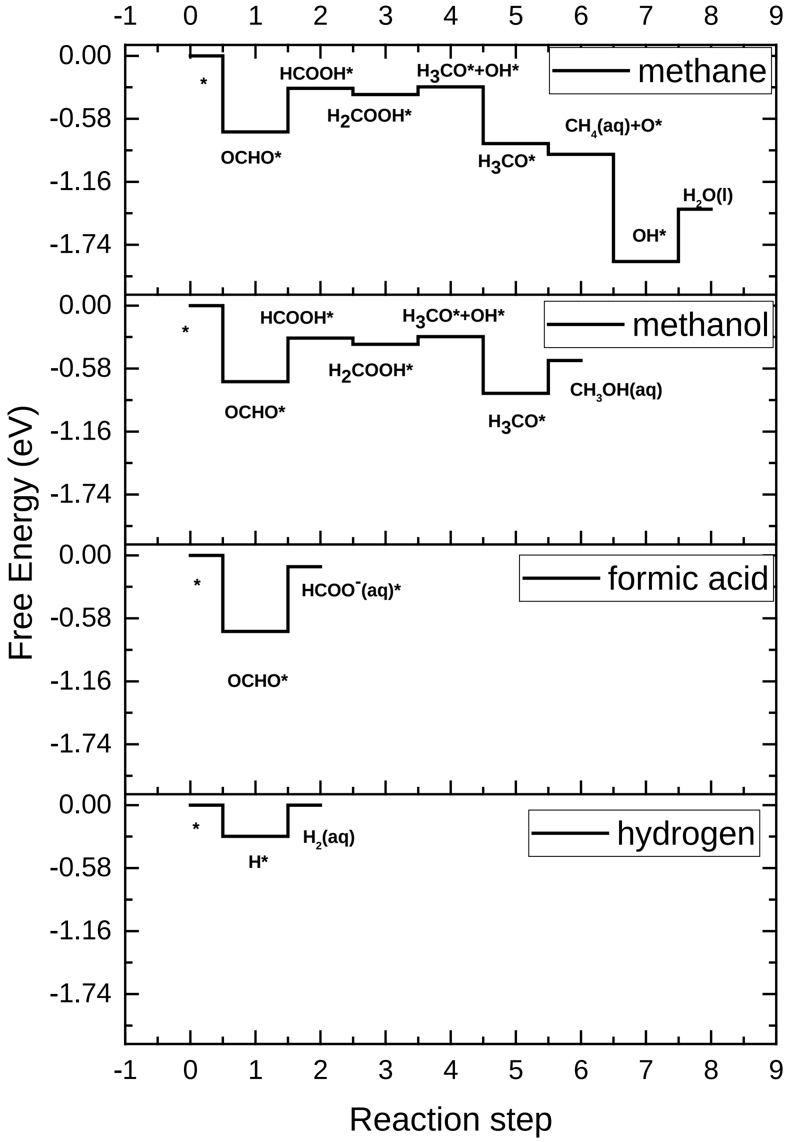

Figure 4-5: Thermodynamics of elementary electron transfer steps leading to evolution of methane, methanol, formic acid and hydrogen on the RuO_2 (110) surface with 50% CO coverage (bridge + cus sites).*

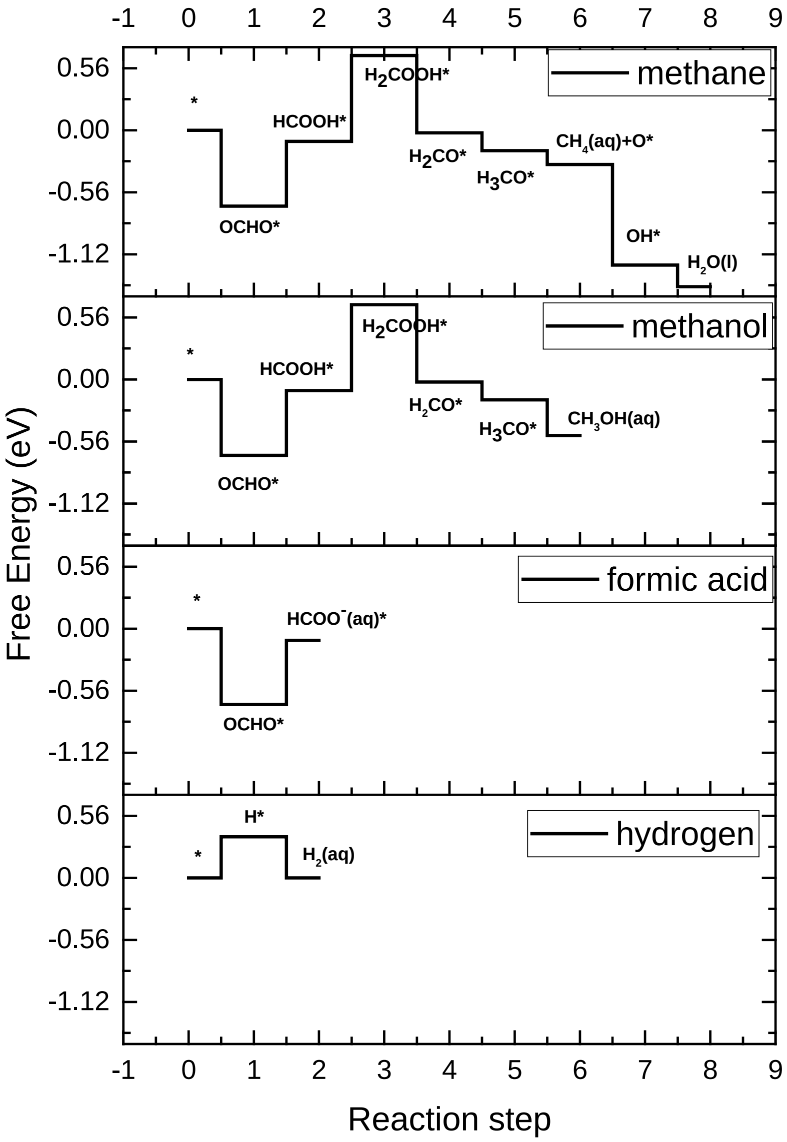

Figure 4-6: Thermodynamics of elementary electron transfer steps leading to evolution of methane, methanol, formic acid and hydrogen on the RuO2 (110) surface with 50% CO coverage (two bridge sites).*

4.3.7. CO2RR: 50% CO* coverage (2×bridge)

All bridge sites being filled with CO* spectators, CO2RR intermediates and hydrogen bind at cus site. OCHO* is still a bidentate adsorbate binding through two cus sites and its downhill to protonate CO_2 to form OCHO* at 0 V-RHE. But reduction of OCHO* to formic acid have an onset potential of -0.58 V-RHE. HCOOH* and formic acid molecule are energetically degenerate. H_2COOH* do not bind at cus site without applied potential. HCOOH* reduction needs -0.78 V-RHE onset potential. 4th electron transfer intermediate is H_2CO* for both methane and methanol evolution, which further reduces to H_3CO*. Henceforth, the reaction mechanism is similar to previously discussed coverage situations. HCOOH* reduction defines the onset potential for methane and methanol evolution. H* have a positive binding energy at 0 V-RHE, while OCHO* is very stable. This is supportive of CO2RR selectivity, but this particular CO* configuration might not be experimentally accessible as bridge + cus configuration is preferred energetically with oxygen-bound adsorbates as discussed previously.

4.3.8. CO2RR: 75% CO* coverage (2×bridge+cus)

With a lone cus site available for reaction intermediate, bidentate adsorbates like OCHO* and H_2COOH* are forced to be monodentate. Cus site binds oxygen coordinates adsorbates very weak, thus formation of OCHO* and H_2COOH* require very reducing potential. HCOOH* escapes to electrolyte due to non-binding nature of the cus site. H_2COOH* requires -1.33 V-RHE to be formed. OCHO* is less stable than H* ruling out any CO2RR activity. HER also needs high overpotential of -0.63 V-RHE. Presence OH* however can modify the CO* configuration to free up one bridge site – which is discussed later.

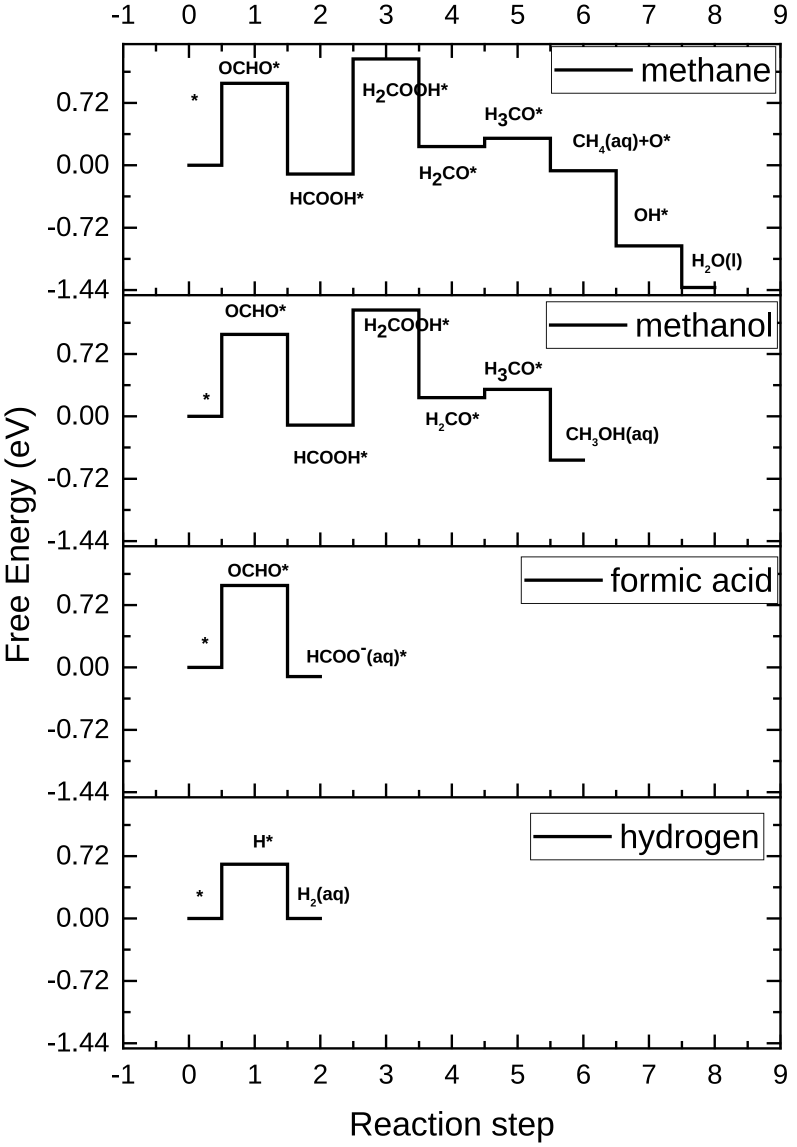

Figure 4-7: Thermodynamics of elementary electron transfer steps leading to evolution of methane, methanol, formic acid and hydrogen on the RuO_2 (110) surface with 75% CO coverage (two bridge + one cus site).*

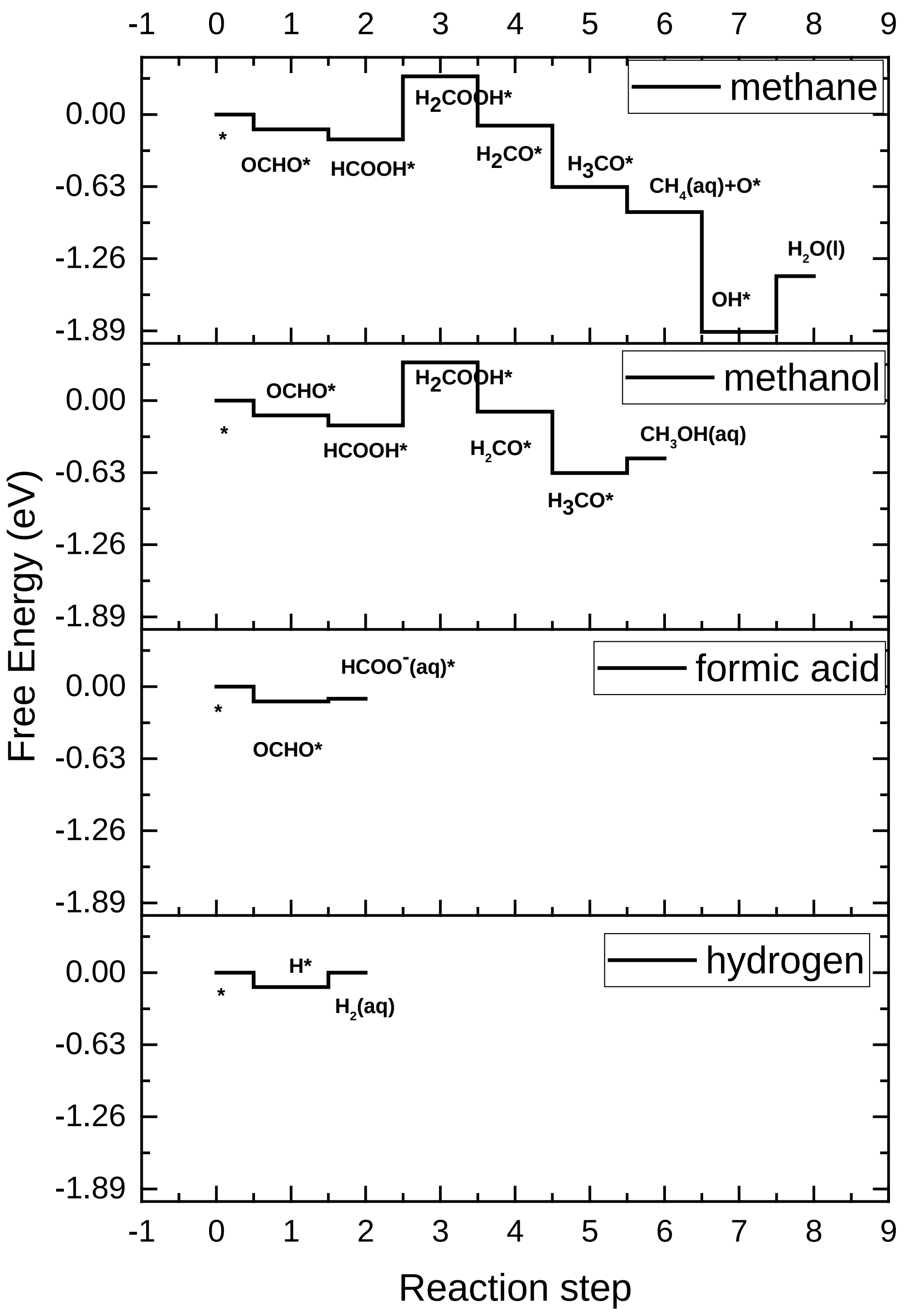

Figure 4-8: Thermodynamics of elementary electron transfer steps leading to evolution of methane, methanol, formic acid and hydrogen on RuO_2 (110) surface with 75% CO coverage (two cus + one bridge site).*

4.3.9. CO2RR: 75% CO* coverage (2×cus + bridge)

All reaction intermediates are forcibly single adsorbate and monodentate. OCHO* binds stronger than 2*bridge + cus configuration CO* coverage case, but it is very close to H* adsorption energy. Onset potential for formic acid and hydrogen evolution are -0.02 V-RHE and -0.13 V-RHE. This coverage configuration being more stable than other configuration with 75% coverage, it can be suggested that 75% coverage would lead to evolution of a mixture of hydrogen and formic acid at low overpotential. HCOOH* is bound to the bridge site, and further reduction is possibility. However, very weak binding H_2COOH* adsorbate leads to onset potential of 0.55 V-RHE.

4.3.10. Binding energy modification and product selectivity due to CO* coverage

To draw parallel to experimental observations, in this subsection, only four of six configurations considered are taken into account based on their stability in presence of CO2RR intermediate co-adsorption. Among 50% and 75% CO* coverage configurations, bridge + cus and 2*cus + bridge configuration are taken respectively. On all six CO* coverage configurations, OCHO* is more stable than COOH* at 0 V-RHE. OCHO* is a bidentate adsorbate if adjacent sites are available. At 0% and 25% CO* coverage, OCHO* binds through one bridge and one cus site. Presence of CO* in an adjacent bridge site strengthens the OCHO* binding at low (25%) CO* coverage compared to bare catalyst surface. at 50% CO* coverage also OCHO* is bidentate but 75% CO* coverage compel OCHO* to be mono-dentate, reducing the binding free energy significantly. It is to be noted that trends in COOH* and OCHO* binding free energy at different CO* adsorbate configuration are similar and maintain their relative position. (Even for cus site adsorption, OCHO* intermediate is much stronger bound to the active site than COOH*). Consequently, the CO2RR pathway proceed preferentially through OCHO* and other O-coordinated adsorbates at all CO* coverages. The other intermediate after the 1st proton transfer step is H*. Substantially weaker binding of H* than OHCO* facilitate selectivity of CO2RR over HER. For CO* coverages 0-50%, OCHO* is stronger bound to the catalyst surface than H* by 0.31-0.73 eV. For high (75%) CO* coverage, owing to the aforementioned destabilization of OCHO*, H* is either equally probable at bridge site (binding energy difference of 0.004 eV). Effectively OCHO* is no longer preferred over H* and CO2RR is not selective (Figure 4-9). The best selectivity for CO2RR at around 50% CO* coverage. At high CO* coverage, RuO_2 electrocatalysts should therefore show less selectivity towards CO2RR and evolve significant amount of hydrogen.

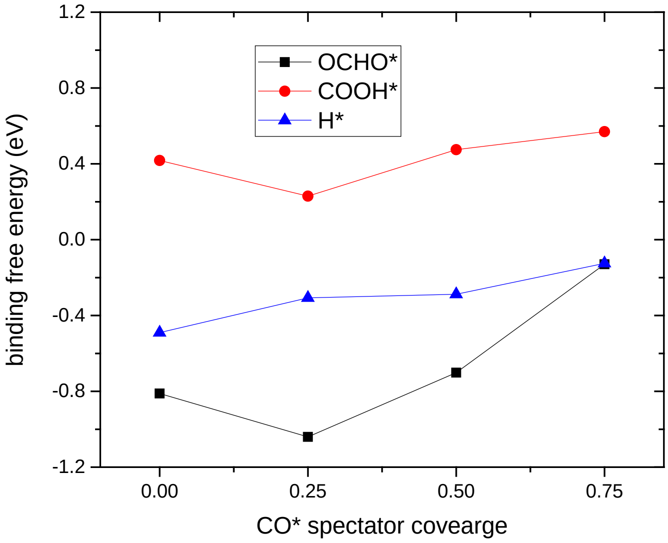

Figure 4-9: Effect of CO coverage on binding energy of intermediates formed by the 1st proton transfer H*/OCHO*/COOH* at the bridge site*

With CO* coverage, the attractive adsorbate-adsorbate interaction between CO* and OH* at bridge site makes OH* removal from bridge much more difficult compared to that in absence of CO* (Figure 4-10). This effectively stops absorbing H* and thus HER until onset for OH* removal. Once active sites are empty, OCHO* is preferred over H*. Lack of CO* leaves active site open for HER even after OCHO* adsorption. HER being active at less reducing potential than CO2RR, dominates. While up to 50% CO* coverage is expected to allow only limited HER activity if OCHO* forms rapidly. For the 2*cus + bridge configuration, H* binding free energy is near ideal at +0.03 eV and OCHO* at -0.13 eV. This leads to loss of selectivity and the catalyst evolves both formic acid and hydrogen. Thus, hydrogen is the main product without CO* coverage, methane and methane for intermediate coverage; formic acid and hydrogen for o high CO* coverage.

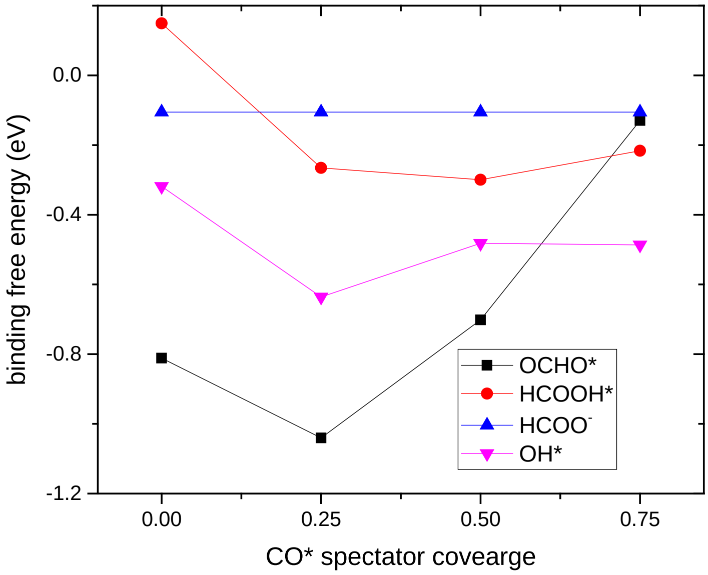

Figure 4-10: Effect of CO coverage on binding energy of OCHO*/HCOOH*/OH* at the bridge site along with free energy of deprotonated formic acid.*

Both methane and methanol have thermodynamic onset potential (Figure 4-12) either same (0%, 25% and 75% coverage) or less than 0.1 V-RHE different (50%coverage). Thus, it is difficult to predict selectivity between these two products from this analysis. However both are formed from H_3CO* adsorbate protonation. Barrier for protonation at oxygen atom (methanol evolution) and carbon atom (methane evolution) might hold clue to any selectivity observed. Experimental evidence[31,32] points to methanol formation having a smaller barrier, as methanol has been observed to be produced in much larger quantities than methane[32–34].

The H*/OCHO* binding free energy correlation helps in understanding the HER/CO2RR selectivity; the HCOOH* binding free energy w.r.t solvated formic acid in solution dictates whether formic acid is the major product or higher proton transfer products like methanol and methane can be formed. If the catalyst surface fails to bind formic acid molecules to the active site, it will escape to solution in a solvated form, rendering further hydrogenation difficult. HCOOH* being O-coordinated like OH*, the trend in the binding free energy variation at different CO* coverage are similar for these adsorbates (Figure 4-10). Adsorbate-adsorbate interaction effects inducing stronger OH* binding can open up the possibility of methanol/methane as product as seen in the case of partial CO* coverage. If the formic acid molecule fails to bind at the catalyst site, H_2COOH* is only expected to form by application of an additional electrochemical driving force and in solution saturated with formic acid to supply protonated formic acid molecules. Nevertheless, the downhill nature of protonation of formic at 0% CO* coverage and 0 V-RHE, opens up the possibility of further reduction.

For CO* coverages of up to 50%, protonation of OCHO* is energetically uphill (Figure 4-10) forming HCOOH* on CO* covered surfaces and formic acid in the absence of CO*. This large increase in free energy requires proportionately large reducing potential to be applied for the reaction to proceed and to free up active site. So OCHO* formation without at 0 V-RHE can reduce the HER activity simply by blocking the active sites. If only a single site is available (75% CO* coverage), OCHO* is adsorbed in the less stable mono-dentate configuration, while HCOOH* is inherently mono-dentate. Therefore, the formation of HCOOH* from OCHO* is downhill in energy for 75% coverage. For 75% CO* coverage binding free energy of HCOOH* w.r.t. solvated formic acid in liquid water is ~0.1 eV, which is small enough for a large fraction of adsorbates to escape into solution instead of forming HCOOH*. Weakening of the OCHO* adsorbate binding reduces the thermodynamic onset potential requirement to only –0.02 V-RHE (Figure 4-12). Therefore, at this CO* coverage, a high turnover of formic acid is expected at very low over potential.

Key adsorbates determining the onset potential for CO2RR products included OH*, OCHO*, H_2COOH* as HO* removal, OCHO* protonation and H_2COOH* formation have the most demanding onset potential at different CO* coverage level. OCHO*, H_2COOH* are oxygen atom coordinated like OH*. Thus due to adsorbate scaling law effects, along with changes in OH* removal, OCHO* protonation and H_2COOH* formation also change in onset potential requirement as CO* coverage changes (Figure 4-11). This enables the improvement of methanol onset potential at 50% CO* coverage and that of formic acid at 75% CO* coverage.

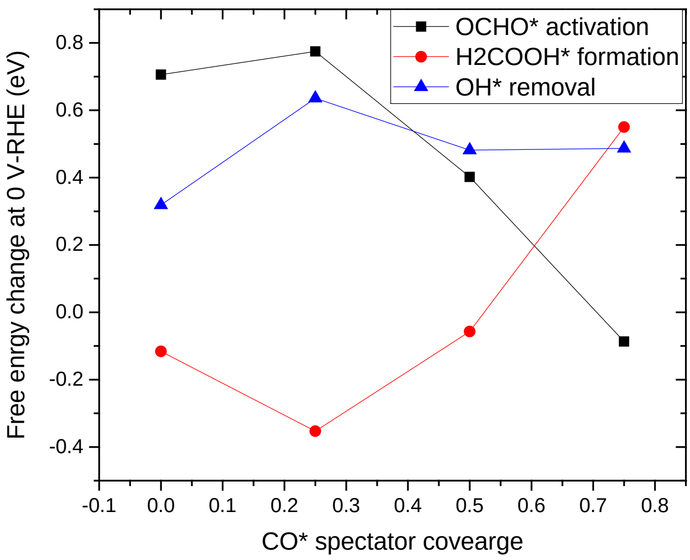

Figure 4-11: The free energy change associated with few key elementary reaction steps for CO2RR change with different CO spectator coverage. The largest positive step at 0 V-RHE would define the onset potential.*

Experimental studies by Popic et. al and Qu et. al employing pure ruthenium oxide electrocatalyst[32,34] did not report any CO detected as product. It can be deducted that these experimental results observing methanol as the primary product, might have clean catalyst surface without any CO* coverage or medium CO* coverage if only very small quantity of CO is produced and stays bound to the active site[32,34]. On the contrary, experiments by Spataru et al.[33] observe hydrogen and formic acid as dominant products along with methanol, methane and CO. It can be contemplated that the presence of CO ~30-200 ppm[33] level in the solution comes from CO escaping catalyst surface after high CO* coverage is reached. These experimental results matches well with conclusions from current thermodynamic analysis that low to moderate CO* coverage leads to methanol/methane formation and high CO* coverage induce evolution of hydrogen and formic acid together (Figure 4-12).

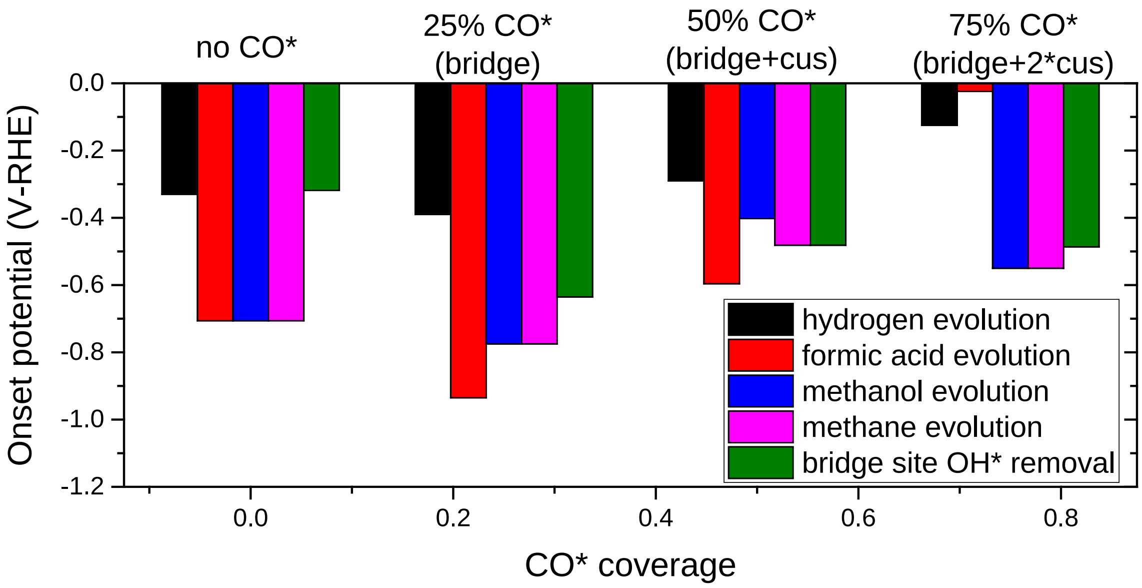

Figure 4-12: Onset potentials for hydrogen, formic acid, methanol, methane evolution at different CO spectator coverage. OH* removal potential at bridge site included to provide information about possible OH* blockage.*

Within the catalyst surface model with two bridge and 2 cus sites, the incremental free energy changes for adsorbing from the 1st to the 4th CO molecule are -1.34 eV, -0.93 eV, -0.75 eV and -0.46 eV respectively with respect to CO molecule. It is striking that at 0 V-RHE and 75% CO* coverage, OH* binds stronger to the empty fourth site than CO*. Evidently, under aqueous solution, RuO_2 (110) will not be fully poisoned by CO* but have high CO* coverage with few sites available for HER/CO2RR if plenty of CO_2 is available. Transient formation of CO* and slow transport of CO away from the catalyst will eventually leave the catalyst surface with high CO* coverage[102] as might be the case in a previous experimental study[33].

4.3.11. Effect of reaction condition on selectivity

Activity and selectivity of CO2RR on RuO_2 surfaces depend on ease of formation of OCHO* intermediate compared to H*. Plentiful availability of CO_2 molecules in the electrochemical layer close to the catalysts surface is necessary. CO2RR experiments are often done in a bicarbonate buffer solution[13,15,30,32]. Bicarbonate ion is in equilibrium with the free CO_2 molecules in the electrolyte. If the concentration of OH^- increases sufficiently, most of free CO_2 molecules react to form HCO_3^-. Based on pH-potential diagram (Figure 4-13) provided by Hori[15], free CO_2 molecules might not be available for CO2RR if close to catalyst surface, local pH increases beyond 7.8.

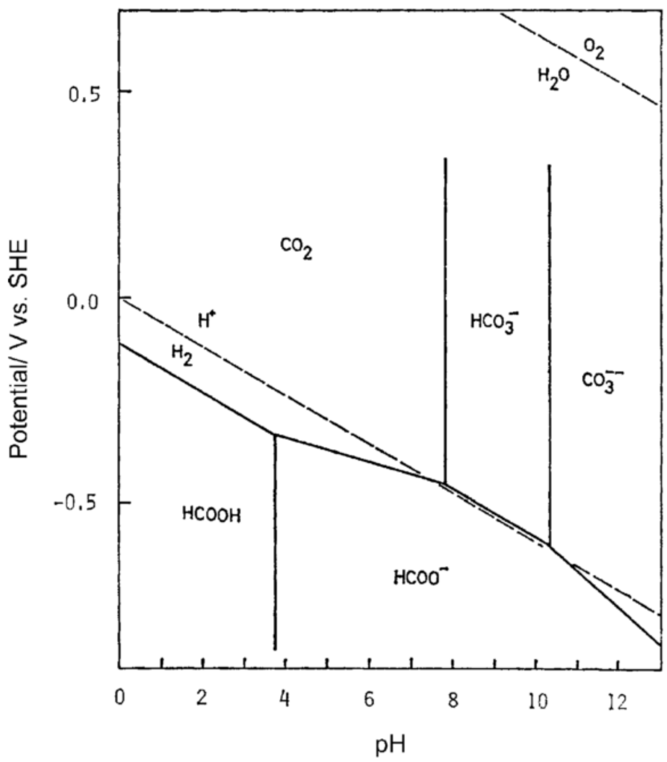

Figure 4-13: Stability diagram for CO_2 in bicarbonate solution as a function of potential and pH. Taken from [15]

During electrochemical reaction, neutral buffer solution loses H^+ to HER and CO2RR. Higher current rate, slow buffer action and slower mass transport aids to accumulation of OH^- in the reaction layer pushing the pH very high locally even though bulk pH is close to neutral (Figure 4-14). For example, a 0.1 mm diffusion layer and 50 Am^{-2} current density a buffer solution of 0.5M NaHCO3 would show a bulk pH of 6.82 but it is as high as ~9.3 pH in the diffusion layer. The availability of CO_2 close to the reaction site is affected by the conversion of CO_2 to HCO_3^- , formation of OCHO* on surface and CO_2 diffusivity as well. Slow CO_2 diffusion rate in the electrolyte and thick diffusion layer would aid conversion to bicarbonate through buffer reaction. A smaller diffusion layer thickness, slow buffer reaction and large forward reaction rate for OCHO* formation is needed for successful CO2RR. Diffusivity of CO_2 at infinite dilution is 1.91E-9 m2s-1. Expected time needed for a CO2 molecule to traverse diffusion layer of δ=1.0E-4 m is ~2.5 s. A reaction condition like this and a higher forward rate constant for HCO_3^- formation from CO_2 than OCHO* formation would lead to few OHCO* and help evolve only hydrogen. The trend is unchanged with higher buffer concentration or with a narrower diffusion layer (0.01 mm). This problem can be alleviated by using a very low current density (~0.5 Am-2) as used in previous experimental reports[30,32]. Higher concentration of OH- close to reactions surface increase the forward rate of reaction for bicarbonate formation. Fast mass transport (e.g. fast rotating disk electrode) effectively reduces the diffusion layer thickness and can help in CO2RR selectivity.

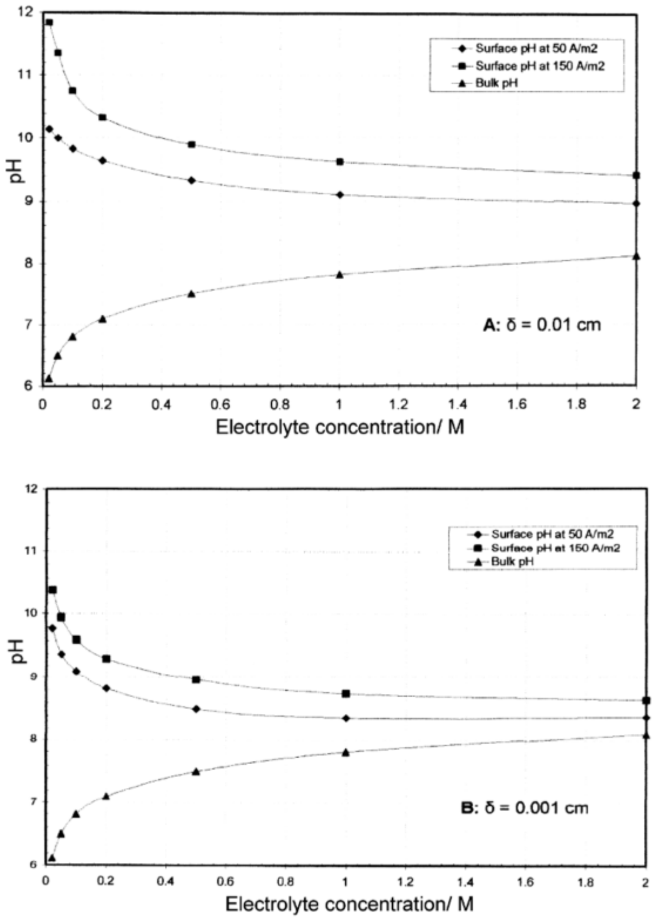

Figure 4-14: Calculated pH at the cathode vs. electrolyte HCO3 concentration with the diffusion layer thickness δ = 0.01 cm and 0.001 cm for 2 different current densities (taken from Hori[15])

4.4. Conclusion

CO* coverage can be crucial in selectivity of CO2RR over HER. Without CO* coverage, RuO_2 (110) is expected to start producing hydrogen at cus site (-0.33 V-RHE) with hydroxylated or OCHO* blocked bridge sites. The large reducing potential required (-0.71 V-RHE) to activate OCHO* leads to negligible CO2RR activity at lower potentials. With 25% CO* coverage, CO2RR products (methane/methanol) have an onset potential of -0.78 V-RHE, but HER onset potenail is -0.39 V-RHE, utilizing cus sites with bridge sites occupied by OH*and CO*. 50% CO* coverage is predicted to provide the best activity towards methane/methanol as CO2RR products. At this CO* coverage, HER cannot start above -0.48 V-RHE due to surface hydroxylation and both methanol and methane evolution becomes active at that potential. If availability of CO_2 in the reaction layer and kinetic barriers for CO_2 activation are not limiting, OCHO* is preferred over H* as the 1st proton transfer product from purely thermodynamic perspective. So, at sufficiently high reducing potential, the CO2RR pathway is expected to show significant activity in conjunction with hydrogen evolution especially with moderate CO* coverage. 75% CO* coverage, on the contrary, have close to ideal onset potential for formic acid due to weak OCHO* binding. Once OH* is removed from the active site, both hydrogen and formic acid are expected to form. Suppression of HER at 50% or lower CO* coverage by formation of OCHO* at the active sites is critically dependent on availability of CO_2 in close proximity to the active site.

The availability of CO_2 close to the reaction site is important for CO2RR. Reaction layer pH must nor increase much to avoid conversion of CO_2 molecule to bicarbonate ion. Without readily available CO_2 reactant, hydrogen would be only observable product. A smaller diffusion layer thickness (quick CO_2 replenishment), low current density, and large forward reaction rate for OCHO* formation is needed for successful CO2RR. The concentration of methanol in the solvent can also affect the reaction thermodynamics of methanol production. With higher concentration, free energy of methanol increases and release of methanol from H_3CO* intermediate needs larger reducing potential.

Binding energy alteration of both H* and CO2RR intermediates emerging from adsorbate interaction with CO* drive switching of CO2RR/HER activity at optimal CO* coverage as well as the product selectivity (formic acid vs methanol). The absence of CO* or low accessibility of CO_2 near the active site will result in hydrogen as the only observable product. RuO_2 based electrocatalysts have been shown experimentally to hold great promise for direct conversion of CO_2 to methanol. It is shown here that optimization of reaction environment, i.e. CO* coverage, pH, current density, product removal is also needed to achieve high activity and selectivity for methanol.

5.CO2RR on $Ru_xIr_{1-x}O_2$ surfaces

In this chapter CO* coverage dependent CO2RR mechanism is modelled on a well studied and easy to synthesize class of rutile structured mixed oxide catalysts. Work presented here gives general direction on how to optimize the CO2RR efficiency and selectivity by tuning the composition and adsorbate interaction effects. Specific suggestions are made for experimental validation.

5.1. Introduction

Alloying and substation are tools for optimization of oxide electrocatalyst activity [118–125]. Alloying modifies the binding energy of reaction intermediates by means of strain and ligand effects. Key adsorbate binding energies for metallic alloy catalysts often fall between the pure metal components. This gives rise to an interesting approach to catalyst design. Combining two metals: one with too strong adsorption (left side of volcano) and one with too weak adsorption (right side of volcano) one can create a catalyst surface with optimum reaction intermediate binding energy to be at the top of the volcano curve. This principle has been successfully implemented to create new highly active catalysts for nitrogen reduction to ammonia[126] and CO_2 reduction to methanol[127]. Validity of this proposition relates to the d-band theory for adsorbate interaction on metal surfaces. Electronic structure (d-band position) of alloys often can be estimated from simple interpolation of d-band position of constituent elements[37]. Correlation of electronic structure of oxides and the binding strength are often less straight forward than metals. A volcano-shaped dependence has been observed for oxygen evolution activity (O-coordinated adsorbates) and the occupancy of the 3d electron with an e_g symmetry of surface transition metal cations in an oxide[118]. For complex electronic structure parameters like this, simple interpolation from that of component oxides does not provide the descriptor parameter for a mixed oxide. Also segregation effects are very prominent for oxide catalyst surfaces[128]. Hence, reliable theoretical prediction of catalytic property of mixed oxide must involve rigorous modelling of various active site configuration, cation ordering, surface coverage etc.

Optimization of activity, stability and selectivity in tandem is critical for effective and useful catalyst design[129]. Such principles must be incorporated while designing oxide catalysts for CO2RR. Results described in chapter 3 indicate that activity of oxide CO2RR catalysts can be tuned by optimizing the OH* binding energy. Hence it is worth studying OH* binding charades of mixed oxides. Understanding modification in binding strength of CO2RR intermediates due to composition on mixed oxide surfaces can help identify catalysts, which can convert CO_2 into liquid fuel at low overpotential. Thermodynamic volcano analysis suggests surface binding OH* slightly weaker than RuO_2 (110) has lower overpotential. IrO_2 binds OH* stronger than RuO_2 [130]. However, Ir-oxide overlayer on RuO_2 has weaker OH* binding energy than pure RuO_2. This behaviour cannot be predicted by simple mixing rule for OH* binding energy of pure ruthenium and iridium oxide. This mixed oxide system has been repeatedly shown to be excellent catalyst for oxygen evolution reaction [131–135].

$Ru_xIr_{1-x}O_2$ (110) surfaces are excellent models of mixed oxide surfaces for studying catalytic properties. RuO_2 and IrO_2 have been widely studied as catalysts for various reactions[33,116,119,131–145]. Both oxides are good band conductors[146] as required for electrocatalysis. IrO_2 and RuO_2 in pure form have similar crystals structure and matching lattice parameters[147]. Especially for the (110) surface, the change in composition is not expected to bring any lateral strain, which can affect the binding energy of adsorbates. Lattice parameter *a* (defining the in place strain in (110) plane) is less than 0.3% percent higher for IrO_2 than RuO_2. Simulation optimized lattice parameter *a* (details presented later in this chapter) for IrO_2 differ by 0.5% from that of RuO_2. This is much lower than the 1-4% strain needed to have any significant modification in catalytic activity[45,80,148,149]. Thus, any modification of binding energy due to composition differences emerges from the chemical nature, i.e. the presence of Ir and Ru atoms in the neighbourhood of the active site.

$Ru_xIr_{1-x}O_2$ mix oxide system is also an ideal electrocatalyst from a stability point of view. This system is miscible for a wide range of composition[150]. Segregation can be a challenge for long lifetime of electrocatalyst as structural evolution changes the catalytic property[151–156]. Bulk mixing energy as well as overlayer adhesion is exothermic in nature for $Ru_xIr_{1-x}O_2$[112] – supporting the excellent stability of the system. Indeed the mixed oxide has been shown to be more stable and suitable for long-term operations as an electrocatalyst[135].

It is important to systematically study the binding energy and reaction path on such catalysts surfaces for check in suitability for CO2RR. $Ru_xIr_{1-x}O_2$ mixed oxide system can be active at moderate over-potentials if the trend observed for Ir-oxide overlayer holds for other mixed structures. While single metal atom doped oxide catalysts have been studied theoretically[122,157,158], methodical study of catalytic properties for compositional variance in any mixed oxide system is absent. This study aims to investigate how the key adsorbates like H*/OH*/CO* binds to mixed Ru-Ir-oxide surface with different Ru-Ir characteristics.

Furthermore, the results discussed in chapter 3 and 4 reveal that CO* coverage can drastically modify the adsorbate binding, affecting both the CO2RR onset potential as well as selectivity over HER. Small amount of spurious CO evolution can alter the CO* surface coverage. Consequently, CO* coverage effects on mixed oxide surfaces are also studied simultaneously for the entire composition range.

5.2. Computational details

5.2.1. Simulation parameters

Similar to computational parameters utilized in previous two chapters, Vienna Ab-initio Simulation Package[72] (VASP) is used with 500 eV wave function cutoff. Bulk IrO_2/RuO_2 unit cell Brillouin zone is sampled with 5×5×7 Monkhorst-Pack k-point mesh and oxide catalyst surface slab with 4×4×1. Due to finite electronic occupation at Fermi energy, a Gaussian smearing of 10 meV is used for the electronic states in all calculations. Optimizations of atomic structures are performed until forces of the free atoms are less than 0.003 eV/Å. For bulk IrO_2 and RuO_2, cell parameter optimization is also done. As explained in previous chapter, BEEF-vdW[54] exchange correlation functional with the vdW-DF2[55] nonlocal correlation energy and potential is used as needed for atomistic CO2RR simulation. The minima hopping technique is used to obtain most energetically favourable adsorption geometry for the catalyst site and adsorbate combinations when catalyst site (bridge) involves different metal atoms or the adsorbate binds through multiple atoms.

5.2.2. Catalyst surface model

Density functional theory based study of CO2RR thermodynamic process (as presented in chapter 3 and 4) is complex and computationally demanding. Modelling the mixed oxide system $Ru_xIr_{1-x}O_2$ can be equally complicated due to the statistical nature of cation ordering. To avoid such complexity of cation distribution, previous theoretical study involved either substitution of a single atom in a RuO_2 or IrO_2 bulk/surface; or replacement of all the top layer cations in the simulation slab keeping the bottom layers fixed to the bulk lattice structure[112]. Such simplification of the mixed oxide system needs to be considered, especially if the complete reaction pathway for CO2RR need to be analysed on each model oxide surfaces. In the absence of strain effects, adsorption energy variation in mixed oxides with different composition is expected to come from the geometry of the active site and the chemical behaviour of the atoms surrounding it. Cation substitution closest to the active site would impact the binding energy more than a substitution in a different atomic layer. Thus by following the substitution modelling strategy of Novell-Leruth[112] et.al. but doing so at a different position with respect to the active site, range of mixed oxide catalytic behaviours can be represented.

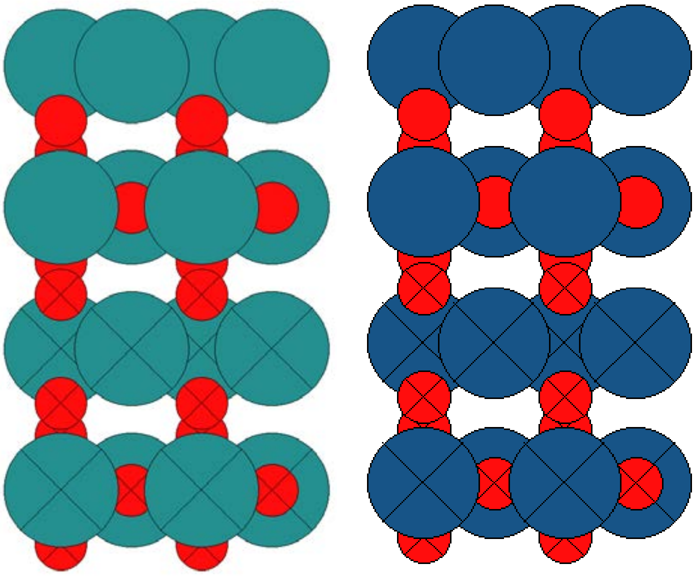

(a) (b)

Figure 5-1: Pure (a) RuO_2 and (b) IrO_2 (110) surfaces with bridge oxygens removed

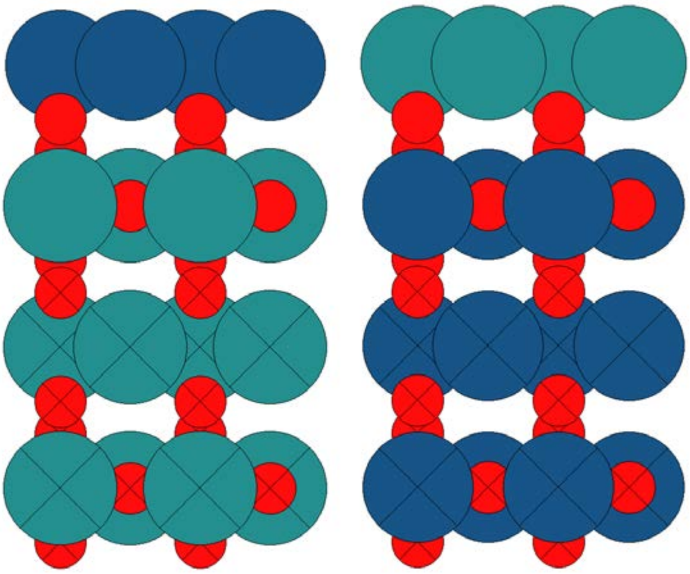

(a) (b)

Figure 5-2: All cations in the top atomic layer have been replaced for (a) RuO_2 and (b) IrO_2 (110) surfaces

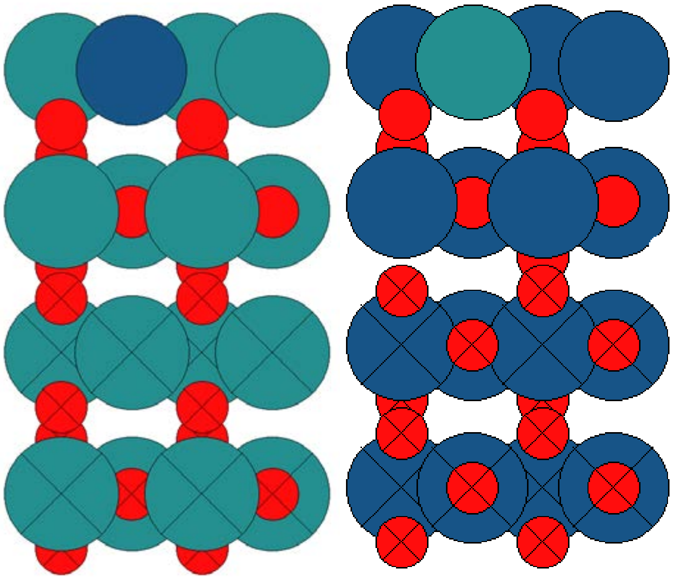

(a) (b)

Figure 5-3: One of the two metal atoms making the bridge site is replaced in (a) RuO_2 and (b) IrO_2 (110) surface

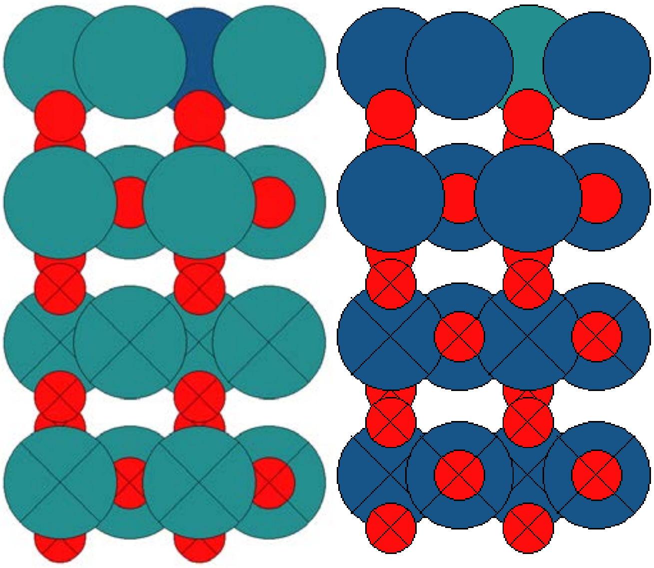

(a) (b)

Figure 5-4: Cation at the neighbouring cus site is substituted in (a) RuO_2 and (b) IrO_2 (110) surface

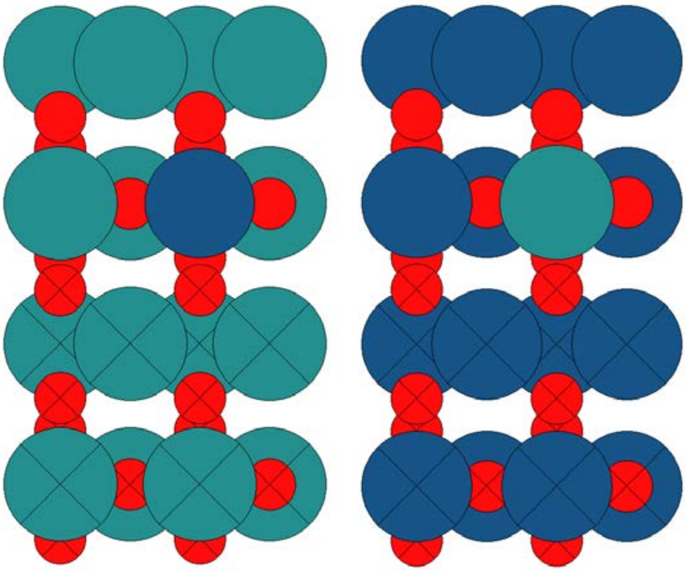

(a) (b)

Figure 5-5: Cation below the bridge site is replaced in (a) RuO_2 and (b) IrO_2 (110) surface

Therefore, to understand the differences emanating from different configuration of Ir/Ru cation distribution near active site, 10 different model rutile (110) surfaces of these oxides considered starting from pure RuO_2 to pure IrO_2 surface (Figure 5-1). Each surface is considered as a slab with four atomic layers. Top two layers are relaxed along with any adsorbate present. The bottom two layers are kept fixed to bulk structure. For bare surfaces, here are 16 cations and 32 oxygen atoms. Bridge oxygens were removed due to reducing environment for CO2RR. The surface slabs are prepared in the same manner as described in chapter 3 and 4. RuO_2 and IrO_2 surface are made based on optimized bulk structure of the respective oxides and cations are substituted to make mixed oxide model.

The bridge site has been identified as the active site for CO2RR. All the cations in the top layer can be replaced following previous theoretical work on mixed rutile oxide[112]. Single cation replacement can be done at one of the metal sites supporting the bridge site (Figure 5-3), at the cus site in the top atom layer (Figure 5-4) or below the bridge site in the 2nd atomic layer (Figure 5-5). Each of these cation substitutions due to position with respect to the adsorption site and symmetry would render different effects on the adsorption characteristics. Also due to periodic boundary condition, an adsorbate would have a certain cation distribution order around it.

Surfaces need to be assigned numerical values to represent how much Ir/Ru-character an adsorbate feels while attached to an active site. This would serve as a surrogate variable for mapping binding characteristics and catalytic properties to mixed oxide systems with variable composition. This is incepted as follows. A hydrogen atom is adsorbed at the bridge site (preferred adsorption site for CO2RR intermediates) of the bare oxide surface. Geometry optimization is done for the adsorbate along with top two atomic layers. Consequently centered around the optimized coordinates of the hydrogen atom the partial radial distribution function for Ir and Ru atoms are computed upto 12 Å, which is approximately the thickness of the simulation slab. Periodic boundary conditions are assumed along the slab unit vectors (xy plane). The Ir distribution curve is denoted $\mathrm{Ir_{rdf}(r)}$ and that of Ru atoms as $\mathrm{Ru_{rdf}(r)}$. Furthermore a proxy variable describing abundance of Ir and Ru atoms ($\mathrm{Ir_{index}}$ and $\mathrm{Ru_{index}}$) close to the adsorption site is defined as

$$\mathrm{Ru_{index}} = \int_0^{12} (12 - \mathrm{r})\mathrm{Ru_{rdf}}(\mathrm{r})\,dr$$

$$\mathrm{Ir_{index}} = \int_0^{12} (12 - \mathrm{r})\mathrm{Ir_{rdf}}(\mathrm{r})\,dr$$

Using these indexes a single unbiased parameter ranging from 0 to 1 is created

$$\eta = \frac{\mathrm{Ir_{index}}}{\mathrm{Ir_{index}} + \mathrm{Ru_{index}}}$$

This number η indicate how IrO_2 –like is the character of the active site. Pure RuO_2 surface has $\eta = 0$ and pure IrO_2 has $\eta = 1$. Surfaces and their η values are listed in Table 5-1.

Table 5-1: Model surfaces of mixed Ru-Ir oxide (110). Index for Ir-character observed at the active site.

Surface construction	η	Figure no.
Pure RuO_2 slab	0.0	Figure 5-1
In a RuO_2 slab, one Ru atom replaced with Ir atom in 2nd atom layer below bridge site	0.05	Figure 5-5
In a RuO_2 slab One Ru atom at the cus site replaced with Ir atom	0.11	Figure 5-4
In a RuO_2 slab One Ru atom at the bridge site replaced with Ir atom	0.29	Figure 5-3
In a RuO_2 slab All Ru atoms in the top layer replaced with Ir atoms	0.75	Figure 5-2
In a IrO2 slab All Ir atoms in the top layer replaced with Ru atoms	0.25	Figure 5-2
In a IrO_2 slab One Ir atom at the bridge site replaced with Ru atom	0.79	Figure 5-3
In a IrO_2 slab One Ir atom at the cus site replaced with Ru atom	0.90	Figure 5-4
In a IrO_2 slab, one Ir atom replaced with Ru atom in 2nd atom layer below bridge site	0.95	Figure 5-5
Pure IrO_2 slab	1.0	Figure 5-1

These model surfaces have two bridge sites and two cus sites in the repeating unit cell. Three possible CO* coverage conditions are considered. (a) no CO* spectator (b) one CO* spectator at one bridge site (c) two CO* spectator, one at bridge site and the other at the cus site next to it. These correspond to 0%, 25% and 50% CO* coverage. Choice of thee CO* coverage models were done based on the analysis in chapter 4.

5.3. Results and discussion

5.3.1. Composition and spectator effects on adsorbate binding

The adsorption free energies of H*, OH* (Figure 5-6) and CO* (Table 5-3) are studied to understand how the Ir/Ru ratio near the adsorption site and CO* coverage affects the binding energy of key reaction intermediates and subsequently the catalytic activity. Surfaces with mostly Ir-character, binds H* much stronger than those with more Ru-character across different CO* spectator coverage. The surface binding H* the strongest is the IrO_2 surfaces with single Ru atom at the cus site for 25% or 50% CO* coverage. Without any CO* coverage, an Ir-oxide overlayer on Ru-oxide shows the strongest H* binding. The presence of up to 50% CO* spectator coverage weakens the H* binding by 0.2 eV or less for surfaces rich in ruthenium. On the contrary, surfaces rich in Ir shows a slight increase in the H* binding strength. Surfaces with mixed character, e.g. an Ir adsorption site with a Ru neighbour (a monolayer Ir-oxide overlayer on Ru-oxide (β=0.75) or single Ir-atom at the bridge site of RuO_2 slab (β=0.29)), shows a strong repulsive adsorbate-adsorbate interaction and the H* binding decreases by up to 0.65 eV. Although weak binding H* leads to low overpotential for HER, H* fails to bind to the surface as strong binding OH* and other CO2RR intermediates have a thermodynamic preference, effectively blocking HER.

A similar contradictory effect is observed on surfaces with β=0.29, 0.75, 0.79 for OH*-CO* adsorbate-adsorbate interaction. OH* is much stronger bound to surfaces with Ir atoms than Ru rich surfaces. The presence of CO* spectators makes OH* bind stronger than without CO* coverage on Ru or Ir rich surfaces (β = 0, 0.5, 0.11, 0.25 and β = 0.9, 0.95, 1.0). On a few surfaces with intermediate β=0.29, 0.75, 0.79 the CO* adsorbate interaction is repulsive for OH* binding and OH* is thus destabilized by up to 0.4 eV. Based on thermodynamic volcano interpretation of CO2RR on oxide catalysts, the weakening of OH* binding should lead to a lower overpotential for CO2RR.

The 1st CO* binding at the bare surface bridge site is favourable by 1 eV or more for all surfaces(Table 5-3). The 1st CO* molecule is more stable on surfaces with β≈0 than β≈1. This is a contradiction to the behaviour observed for H* and OH* adsorbates. E observe an exceptionally high stability of the 1st CO* adsorbate on surfaces with an active site with at least one coordinating Ir atom having Ru neighbours (β=0.29, 0.75, 0.79). For surfaces with mainly Ru character, the CO*-CO* adsorbate interaction is repulsive, whereas it is strongly repulsive for intermediate compositions (0.25 < β < 0.8) and attractive for Ir-rich surfaces (β > 0.8). On surfaces with a single Ir atom close to the bridge site of a RuO_2 slab, such CO*-CO* interaction will limit the CO* coverage and provide sufficient active sites for CO2RR with favourable OH* binding associated. Vice-versa, Ir-rich surfaces (β=0.9, 0.95, 1.0) will accumulate high CO* coverage, due to the attractive CO*-CO* interaction and fail to activate CO_2.

Under reaction conditions, adsorbates like O* [159], H* [160] and CO* [161] have been shown to create preferential conditions for one metal to segregate at the surface over the other metal. Stronger adsorption of the species on one type of metal over another causes this segregation. Segregation happens in presence of the large thermodynamic driving force if the barrier for atom migration is surmountable. Replacement of a ruthenium atom by an iridium atom in a bare RuO_2 (110) slab is most favourable at the subsurface layer and least favourable at the cus site. However, the energy difference between these two configurations is only 0.12 eV. Replacement of one iridium atom by a ruthenium atom in a bare IrO_2 (110) slab, is most favourable at the bridge site and least favourable at the subsurface layer. The energy difference between these two configurations is even smaller at 0.06 eV. Due to the very limited thermodynamic driving force for adsorbate induced surface segregation, such substitution is expected to be limited and occur nearly randomly between these three sites. With H*, OH* and CO* adsorbates, some sites are better suited for cation substation than others sites (Table 5-2). For Ir atoms doping in RuO_2 (110) surface, all substation close to bridge site is preferred in presence of H* or OH* or CO* adsorbates. For Ru doping in IrO_2 (110) slab, in presence of H*/OH* adsorbates, cus site substation is preferred. CO* presence imparts large thermodynamic preference towards bridge site substitution. It can be suggested that CO* spectators may induce bridge site segregation for the small amount of cation doping in IrO_2/RuO_2 surface if kinetic barriers are surmountable. This leads to bridge sites coordinated with one Ir and one Ru atom. Thus CO* spectator should enhance the possibility of exhibiting ligand effects based modifications in catalyst properties.

Table 5-2: Adsorbate induced preference for cation substation position

	Energy difference of Ir atom substitution position in RuO$_2$ slab w.r.t. bridge site substitution			Energy difference of Ru atom substitution position in IrO$_2$ slab w.r.t. bridge site substitution		
adsorbate	Bridge β=0.29	Cus β=0.11	Subsurface β=0.05	Bridge β=0.79	Cus β=0.9	Subsurface β=0.95
None	0.00	0.03	-0.09	0.00	0.06	0.00
H*	0.00	0.19	0.10	0.00	-0.07	-0.02
OH*	0.00	0.39	0.23	0.00	-0.23	0.04
CO*	0.00	0.32	0.27	0.00	0.45	0.19

Table 5-3: Variation of CO binding free energy at bridge site due to Ir/Ru mixed oxide composition and CO* spectator. Lightest share means highest value and darkest is the lowest value*

β	0.00	0.05	0.11	0.25	0.29	0.75	0.79	0.90	0.95	1.00
CO* spectator coverage	CO* adsorption free energy at bridge site (eV)									
0%	-1.34	-1.23	-1.29	-1.15	-1.58	-1.62	-1.56	-1.17	-0.98	-1.1
25%	-0.9	-1.06	-0.84	-0.99	-0.72	-0.71	-0.53	-1.34	-1.42	-1.42
50%	-0.77	-0.9	-0.77	-0.83	-0.51	-0.64	-0.32	-1.26	-1.36	-1.33

A thermodynamic volcano for CO2RR activity on rutile oxide surfaces based on the OH* binding energy descriptor has been established in chapter 3. OH* binding energies between -0.25 eV and 0.25 eV were considered very favourable for CO2RR activity. Weakening of the OH* binding energy on partially CO* covered surfaces with mixed Ir-Ru characteristics compared to pure IrO$_2$ or RuO$_2$ surfaces, moves the investigated mixed oxide surfaces closer to top of the activity volcano. Additionally, a weak H* binding on these partially CO* covered surfaces support selectivity by promoting OCHO* formation at the active site instead of H*. Fundamentally different behaviour of adsorbate binding and strong CO* spectator interaction on surfaces where the bridge site has an Ir atom which in turn have ruthenium as cation neighbour, is striking and key to the suitable binding energy behaviour.

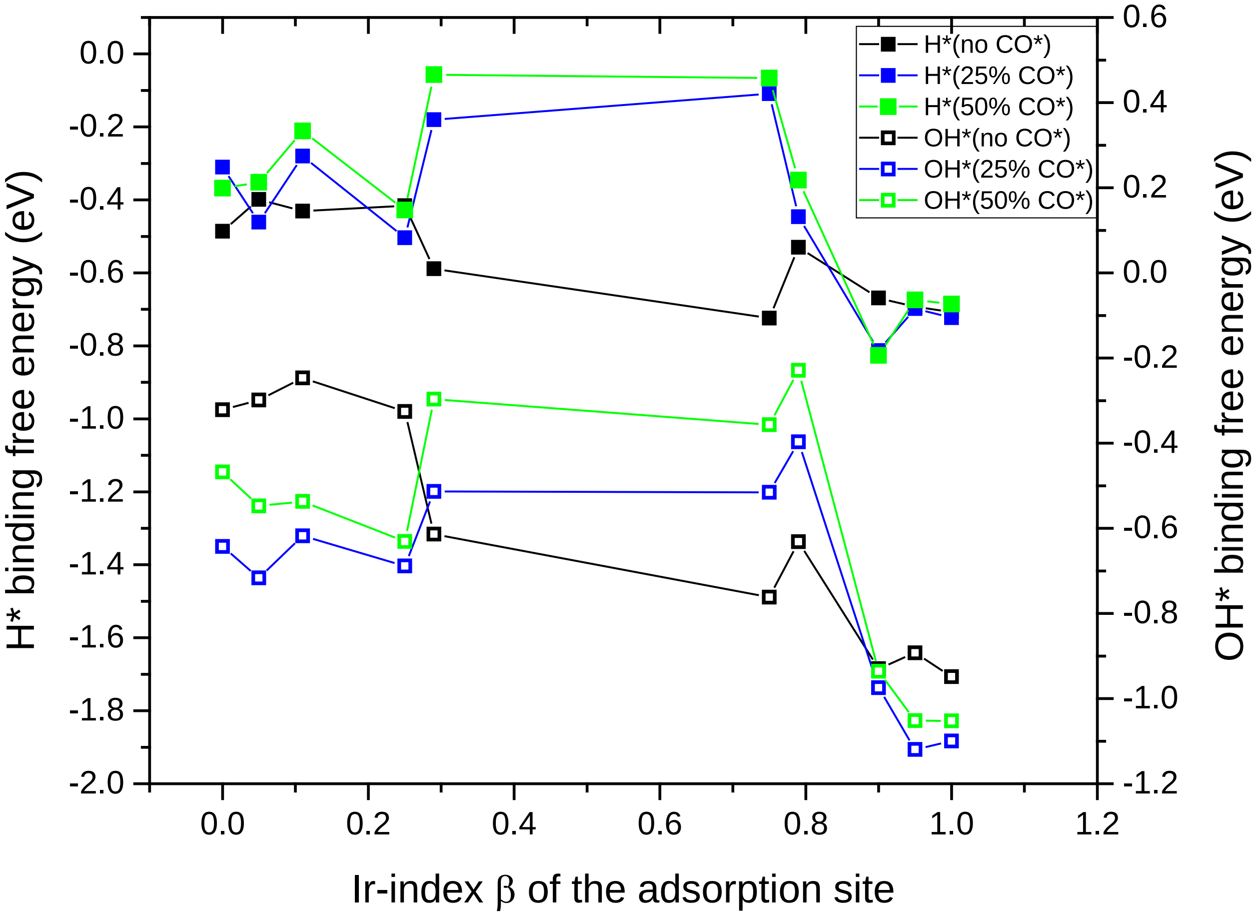

Figure 5-6: H/OH* binding energy on Ru-Ir mixed oxide surfaces at varying CO* spectator coverage.*

5.3.2. CO_2 activation

The first reaction step in CO2RR leads to formation of OCHO* or COOH* from protonation of CO_2 . H* can form if CO_2 molecules are not available at the vicinity of the reaction site or the CO_2 activation barrier is very high (>1 eV). Reported values for proton transfer to COOH* formation on Pt[162] (0.55 eV), OCHO* formation on Pb[163] (0.25 eV) suggest the CO_2 activation barrier to be small enough to be surmountable at room temperature. The kinetic barriers are assumed to be small and proportional to the free energy change of the reactions step. Thus reaction intermediates that are more stable are readily formed. On pure RuO_2 (110) and Ir-oxide overlayer on RuO_2, the stability order for the 1st electron transfer products is ΔG[OCHO] < ΔG[H] < ΔG[COOH][164]. This relative ordering of stability holds true for all surfaces studied here. Thus, with good availability of CO_2 molecules and protons in the electrolyte layer close to catalyst surface, CO2RR activity is expected to dominate over HER on this class of mixed oxides. OCHO* binds strongest on Ir-rich surfaces and ruthenium rich surfaces with 25% CO* coverage (Table 5-4). Although COOH* adsorbates are less stable than OCHO* in the absence of CO* spectators, or on Ir-rich surfaces with any CO* coverage, the formation of COOH* is downhill in free energy at 0 V-RHE and thus side reactions can proceed through this intermediate. Further protonation of COOH* leaves another CO* adsorbate as product. This suggest that bare Ir-Ru mixed oxide surface would develop a ~25% CO* coverage over time under CO2RR conditions. Only on Ir-rich surfaces (β≥0.9) can further COOH* intermediates form even with higher CO* coverage and increase the CO* coverage. The thermodynamics of high CO* coverage on Ir-rich surfaces is discussed in the previous section.

Table 5-4: Binding free energy of COOH and OCHO* intermediates formed from CO$_2$ activation. Lightest shade means highest value and darkest is the lowest value*

β	0.00	0.05	0.11	0.25	0.29	0.75	0.79	0.90	0.95	1.00
CO* spectator coverage	COOH* binding free energy (eV)									
0%	0.27	-0.17	-0.02	0.11	-0.35	-0.43	-0.34	-0.71	-0.58	-0.64
25%	0.08	0.02	0.13	0.05	0.41	0.11	0.13	-0.23	-0.39	-0.29
50%	0.31	0.23	0.29	0.13	0.71	0.21	0.29	-0.02	-0.21	-0.16

β	0.00	0.05	0.11	0.25	0.29	0.75	0.79	0.90	0.95	1.00
CO* spectator coverage	OCHO* binding free energy (eV)									
0%	-0.81	-0.81	-0.8	-0.89	-0.95	-1.1	-1.15	-1.33	-1.25	-1.28
25%	-1.04	-1.07	-1	-1.13	-0.71	-0.55	-0.65	-1.23	-1.27	-1.24
50%	-0.71	-0.75	-0.78	-0.88	-0.3	-0.29	-0.54	-1.03	-1.2	-1.16

5.3.3. CO2RR pathway

One of the main challenges in simulating CO2RR at the atomic scale is the complexity of the possible reaction network. Restricting the intermediates to those with a single carbon atom is a reasonable assumption as the reported products from rutile oxide CO2RR catalysts are primarily 1C type[30,32–34]. Previous theoretical studies of CO2RR on oxide surface did not include C-coordinated reaction intermediates like CHO*, COH*, C*, CH*, CH$_2$*, CH$_3$*, due to the higher stability of O-coordinated intermediate for similar electron transfer step. Here such intermediates have been included to confirm that O-coordinated intermediates are indeed preferred as reaction intermediates in all relevant scenarios.

All the reaction intermediate steps (involving adsorbates and free molecules) simulated on the mixed oxide surfaces are listed in Table 5-5. This reaction network is sufficient to understand the reaction mechanism and onset potential limitations of formic acid, methanol and methane production. All intermediates are simulated with 3 difference configurations of spectator CO* coverage. All adsorbates are bound to the bridge site and OCHO*/ H$_2$COOH* being bidentate also occupy a cus site along with the bridge site. The thermodynamic free energy diagram for all surfaces and CO* coverage configurations with all 26 reaction intermediates are provided as appendix.

Table 5-5: Adsorbate/product cases examined at electron transfer step from 0e^- to 8e^-

1 e^-	2 e^-	3 e^-	4 e^-
OHCO*, H*, COOH*	HCOOH*, CO*+**H_2O(l)**, **HCOOH(aq)**, **H_2(aq)**	H_2COOH*, CHO*+**H_2O(l)**, COH*+**H_2O(l)**	H_3CO*+OH*, H_2CO+ **H_2O(l)**, O*+**CH_3OH(aq)**, CHOH*+**H_2O(l)**, C*+**2H_2O(l)**
5 e^-	6 e^-	7 e^-	8 e^-
H_3CO*+ **H_2O(l),** H_2COH*+ **H_2O(l),** OH*+**CH_3OH(aq)**, CH*+**2H_2O(l)**	O*+**CH_4(aq)+ H_2O(l)**, CH_3OH*+ **H_2O(l),** **CH_3OH(aq)+H_2O(l)** , CH_2*+**2H_2O(l)**	OH*+**CH_4(aq)+ H_2O(l)** , CH_3*+**2H_2O(l)**	**CH_4(aq)+ 2H_2O(l)**

5.3.4. Formic acid evolution

Formic acid evolution is a simple two step reaction with OCHO*, which is studied here as one of the surface bound species after 1st proton transfer on oxide surfaces. Rutile oxide surfaces follow the pathway with OCHO* due to higher stability of OHCO* compared to COOH*. On metals both OCHO* mediated and COOH* mediate pathways are observed[70]. OCHO* binds very strongly to all the oxide surfaces studied here protonating to release formic acid requires applied reducing potential. The Ru-Ir mixed oxide system is on the left leg (strong binding) of the formic acid volcano and weaker binding surfaces are thus better at evolving formic acid. On pure RuO_2 surface, it was predicted that very high CO* coverage weakens the OCHO* binding and produces formic acid at low overpotential[165]. At such high CO* coverage, H* and OCHO* have similar binding free energies and HER dominates.

OCHO* binding free energy close to zero at 0 V-RHE leads to lower thermodynamic barrier for formic acid evolution. Utilizing the peculiar adsorbate binding behaviour on surfaces with an active site based on an Ir atom but with Ru neighbours (discussed above), such optimal OCHO* binding is accessible with only 50% CO* coverage. On a surface with single one Ir atom next to the bridge site in a pure RuO_2 surfaces (β=0.29), with 50% CO* overage, OCHO* is 0.25 eV more stable than H* and the formic acid onset potential is -0.2 V-RHE. Similar enhancements in the evolution of formic acid is observed for Ir-oxide overlayers on RuO_2 oxide slab (β = 0.25). Thus small amount of Ir substitution can make RuO_2 evolve formic acid with better selectivity and lower CO* coverage.

Table 5-6: Formic acid evolution onset potential as a function of Ir-character of the oxide surface and CO coverage. Lightest shade means highest value and darkest is the lowest value*

β	0.00	0.05	0.11	0.25	0.29	0.75	0.79	0.90	0.95	1.00
CO* spectator coverage	Onset potential for formic acid evolution (V-RHE)									
0%	-0.71	-0.7	-0.7	-0.78	-0.84	-1	-1.05	-1.23	-1.14	-1.17
25%	-0.93	-0.97	-0.9	-1.02	-0.6	-0.45	-0.55	-1.13	-1.17	-1.13
50%	-0.6	-0.64	-0.67	-0.77	-0.2	-0.19	-0.44	-0.92	-1.09	-1.06

5.3.5. Methanol evolution

Pure RuO_2 (110) surface reduces CO_2 to methanol by the following six electron pathway for 0% to 50% CO* coverage.

$CO_2(aq) + H^+ + e^- + * \rightarrow OCHO*$

$OCHO* + H^+ + e^- \rightarrow HCOOH*$ or $OCHO* + H^+ + e^- \rightarrow HCOOH\ (aq)$

$HCOOH* + H^+ + e^- \rightarrow H_2COOH*$ or $HCOOH(aq) + H^+ + e^- \rightarrow H_2COOH*$

$H_2COOH* + H^+ + e^- \rightarrow H_3CO* + OH*$

$H_3CO* + OH* + H^+ + e^- \rightarrow H_3CO* + H_2O(l)$

$H_3CO* + H^+ + e^- \rightarrow H_3COH\ (aq)$

For the Ir-Ru mixed oxide surfaces studied here, the 25% and 50% CO* coverage follows the same reaction pathway. Without CO* spectator, Ir-rich surfaces ($\beta \geq 0.75$) prefer a methanol evolution pathway involving C-coordinated intermediates like CHO*/CHOH*.

For example, on IrO_2 monolayer on RuO_2 slab the methane evolution pathway is as follows

$CO_2(aq) + H^+ + e^- + * \rightarrow OCHO*$

$OCHO* + H^+ + e^- \rightarrow HCOOH*$

$HCOOH* + H^+ + e^- \rightarrow CHO* + H_2O\ (l)$

$CHO* + H^+ + e^- \rightarrow CHOH*$

$CHOH* + H^+ + e^- \rightarrow H_2COH*$

$H_2COH* + H^+ + e^- \rightarrow H_3COH\ (aq)$

However, a detailed analysis of the potential determining step reveals that protonation of OCHO* to HCOOH* or an aqueous formic acid molecule, HCOOH(aq), has the largest increase in free energy on most surfaces and most CO* coverages (Table 5-7) . OCHO* is a very stable adsorbate and protonating it involves metal-oxygen bond breaking. A few Ir-rich surfaces (β=0.95, 1.0) also show OH* removal or protonation of H_3CO* as onset potential determining step under CO* coverage conditions of 25-50% and 25% respectively. These surfaces need very high reducing potential due to the strong OH* binding nature of the Ir-rich surfaces. OH*, OCHO*, H_3CO* binding energies are correlated with each other as all three intermediates bind to the surface through oxygen atoms. Weak binding surfaces might not bind HCOOH* and the formic acid molecules escape. However, the most active surfaces (e.g. Ir-oxide overlayer on RuO_2 and Ir-substitution near bridge site) studied here binds H_2COOH*

strongly and thus formation of H_2COOH* from formic acid molecules is an energetically downhill process at 0 V-RHE.

With sufficient formic acid molecules present in electrolyte, methanol evolution is expected to occur. For example, with 50% CO* coverage, Ir-overlayers and Ir substitution at bridge sites in the RuO_2 slab are predicted to evolve methanol at only -0.2 V-RHE, which is better than RuO_2 surface with optimized CO* coverage and any known metal catalyst[9,166]. In essence, using the surprising surface chemistry of the mixed Ir/Ru oxides and adsorbate-adsorbate interaction from CO* spectator, highly efficient oxide based methanol evolution catalysts can be designed.

Table 5-7: Methanol evolution onset potential as a function of Ir-character of the oxide surface and CO coverage. Lightest shade means highest value and darkest is the lowest value. The 2nd table provides the onset potential limiting step for each surface and CO* coverage combination.*

β	0.00	0.05	0.11	0.25	0.29	0.75	0.79	0.90	0.95	1.00
CO* spectator coverage	Onset potential for methanol evolution (V-RHE)									
0%	-0.71	-0.7	-0.7	-0.78	-0.78	-0.79	-1.05	-0.93	-0.83	-0.81
25%	-0.77	-0.75	-0.75	-0.8	-0.6	-0.45	-0.55	-0.82	-0.93	-0.93
50%	-0.46	-0.46	-0.54	-0.54	-0.2	-0.2	-0.44	-0.92	-0.92	-1.07

β	0.00	0.05	0.11	0.25	0.29	0.75	0.79	0.90	0.95	1.00
CO* spectator coverage	Potential determining step for methane evolution									
0%	OCHO* protonation	OCHO* protonation	OCHO* protonation	OCHO* protonation	OCHO* protonation	OCHO* protonation	OCHO* protonation	OCHO* protonation	OCHO* protonation	OCHO* protonation
25%	OCHO* protonation	OCHO* protonation	OCHO* protonation	OCHO* protonation	OCHO* protonation	OCHO* protonation	OCHO* protonation	H3CO* protonation	OH* removal	OH* removal
50%	OCHO* protonation	OCHO* protonation	OCHO* protonation	OCHO* protonation	OCHO* protonation	OCHO* protonation	OCHO* protonation	OCHO* protonation	OH* removal	OCHO* protonation

5.3.6. Methane evolution

With some CO* coverage, all mixed oxide surfaces follow a methane evolution path consisting of oxygen coordinated intermediates as follows:

$CO_2(aq) + H^+ + e^- + * \rightarrow OCHO*$
$OCHO* + H^+ + e^- \rightarrow HCOOH*$ or $OCHO* + H^+ + e^- \rightarrow HCOOH\ (aq)$
$HCOOH* + H^+ + e^- \rightarrow H_2COOH*$ or $HCOOH\ (aq) + H^+ + e^- \rightarrow H_2COOH*$
$H_2COOH* + H^+ + e^- \rightarrow H_3CO* + OH*$
$H_3CO* + OH* + H^+ + e^- \rightarrow H_3CO* + H_2O\ (l)$
$H_3CO* + H^+ + e^- \rightarrow O* + CH_4\ (aq)$
$O* + H^+ + e^- \rightarrow OH*$
$OH* + H^+ + e^- \rightarrow H_2O(l)$

For this pathway, OH* removal or OCHO* protonation require the largest onset potential. After the 5th reaction step H_3CO* intermediate is formed. At 6th electron transfer step, protonation at carbon atom in H_3CO* intermediate, lead to release of methane.

In the absence of CO* spectators, Ir-rich surfaces (β=0.9, 0.95, 1.0) bind carbon coordinated adsorbates very strong. Thus, on such surfaces, adsorbates like CH*, CHOH*, CHO*, CH_2*, CH_3* are part of the reaction mechanism. For example on pure IrO_2 (110) surface the methane evolution mechanism is

$CO_2(aq) + H^+ + e^- + * \rightarrow OCHO*$
$OCHO* + H^+ + e^- \rightarrow HCOOH*$
$HCOOH* + H^+ + e^- \rightarrow CHO* + H_2O\ (l)$
$CHO* + H^+ + e^- \rightarrow CHOH*$
$CHOH* + H^+ + e^- \rightarrow CH* + H_2O\ (l)$
$CH* + H^+ + e^- \rightarrow CH_2*$
$CH_2* + H^+ + e^- \rightarrow CH_3*$
$CH_3* + H^+ + e^- \rightarrow CH_4\ (aq)$

Despite such difference in actual reaction mechanism, OCHO* protonation remains the most energetically difficult reactions step. The OCHO* adsorption energy scales with the OH* binding energy and the weakest OH* binding surfaces i.e. $\beta = 0.29$ or $\beta = 0.79$, shows the lowest methane evolution potential at 50% CO* coverage.

Ir-oxide overlayers on RuO_2 display a methanol onset potential of -0.45 V-RHE with only 25% CO* coverage. For pure RuO_2 surface, with 50% CO* coverage a similar onset potential of -0.46 V-RHE is predicted. The difference between methanol onset potential computed in this work for Ir-oxide overlayers on RuO_2 with 25% CO* coverage and that from previous chapter emanates from the difference in free energy of methanol molecule considered. A lower concentration of methanol in electrolyte (300 ppm following Popic et al.[32]) lead to a smaller thermodynamic barrier (0.29 eV at 0 V-RHE) for H3CO* protonation to release of methanol molecule. Thus OCHO* protonation step dictate the onset potential to be -0.45 V-RHE.

Table 5-8: Methane evolution onset potential as a function of Ir-character of the oxide surface and CO coverage. Lightest share means highest value and darkest is the lowest value. The 2nd table provides the onset potential limiting step for each surface and CO* coverage combination.*

β	0.00	0.05	0.11	0.25	0.29	0.75	0.79	0.90	0.95	1.00
CO* spectator coverage	Onset potential for methane evolution (V-RHE)									
0%	-0.71	-0.7	-0.7	-0.79	-0.78	-0.79	-1.05	-0.93	-0.89	-0.81
25%	-0.77	-0.75	-0.75	-0.8	-0.6	-0.52	-0.55	-0.97	-1.12	-1.1
50%	-0.47	-0.57	-0.54	-0.63	-0.3	-0.36	-0.44	-0.94	-1.05	-1.07

β	0.00	0.05	0.11	0.25	0.29	0.75	0.79	0.90	0.95	1.00
CO* spectator coverage	Potential determining step for methane evolution									
0%	OCHO* protonation	OCHO* protonation	OCHO* protonation	OH* removal	OCHO* protonation	OCHO* protonation	OCHO* protonation	OCHO* protonation	OH*removal	OCHO* protonation
25%	OCHO* protonation	OCHO* protonation	OCHO* protonation	OCHO* protonation	OCHO* protonation	OH*removal	OCHO* protonation	OH*removal	OH*removal	OH*removal
50%	OH*removal	OH*removal	OCHO* protonation	OH*removal	OH*removal	OH*removal	OCHO* protonation	OH*removal	OH*removal	OCHO* protonation

5.3.7. Scaling of binding energies with CO* spectator coverage

CO* spectator interaction with CO2RR adsorbates are found to be both attractive and repulsive as exemplified through the binding energy variation of OH*/H*/CO* in presence of CO* spectator coverages. A thermodynamic analysis of the active reaction pathways on various surfaces and CO* coverages, reveal that OH* removal, OCHO* activation or H_3CO*

protonation to methanol determine the onset potential of the CO2RR reaction. All these adsorbates are bound to the surfaces via oxygen atom. It is thus expected that a decrease in the binding free energy of OH* would lead to stronger OCHO* and H_3CO* adsorption as well. Indeed, when the binding energy of OHCO* (Figure 5-7) and H_3CO* (Figure 5-8) is plotted, a strong interdependency is observed. Interestingly, for H3CO* vs. OH* adsorbate binding free energy correlation, the three scaling lines drawn based on linear fitting of data points from three different CO* coverage, follows each other closely and all displaying a slope of 1 (slope m=1.02, 1.11, 1.08 for 0%, 25%, 50% CO* coverage respectively), but with a CO* coverage dependent offset. This result is in good agreement with previously reported H3CO*-OH* scaling line on rutile oxides with slope of 0.96[164].

For OCHO* vs. OH* scaling line, computed slopes are m=1.29, 0.84, 0.89 respectively for 0%, 25%, 50% CO* coverage, indicating that the chemical nature of the scaling relation changes if CO* coverage is considered. OCHO* is bidentate and binds through one bridge and one cus site. Different CO* spectator effect at the bridge site and the cus site can possibly cause this difference in slopes of scaling lines. The scaling line slope for 25% CO* coverage is deviant from the slope of 0.99 suggested in section 3 which considers 25% CO* coverage. The slope of 0.99 was derived from binding energies observed on rutile oxide surfaces with a much wider variety of binding characteristics[164]. The rather small variation in chemical nature of the surfaces considered here compared to those studied previously might result in skewed data and wrong estimation of the slope. The standard error in current analysis of OCHO*-OH* scaling line is 0.17. Even with the variation in scaling line from CO* coverage effects, the fundamental behaviour remain unperturbed. This suggests that a universal adsorbate scaling relations for O-coordinates adsorbates on rutile oxide surface exist, which holds irrespective of CO* coverage, but with a CO* coverage dependent offset. This unification can help to model CO2RR activity on oxide catalysts without simulating full thermodynamic path. The OH* binding energy at different CO* coverage can provide onset potential for the key reaction steps.

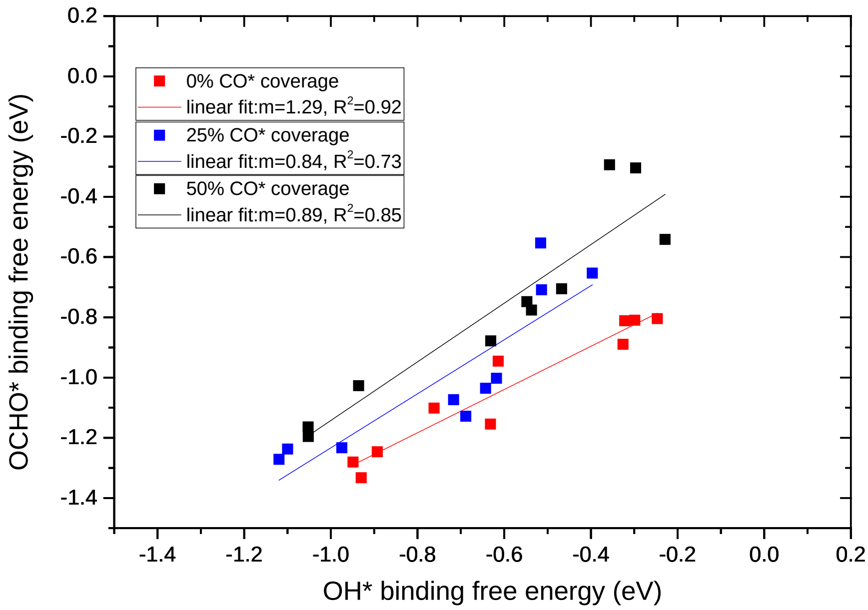

Figure 5-7: OCHO-OH* binding free energy scaling relation at three different CO* coverage with slope m and coefficient of determination* R^2

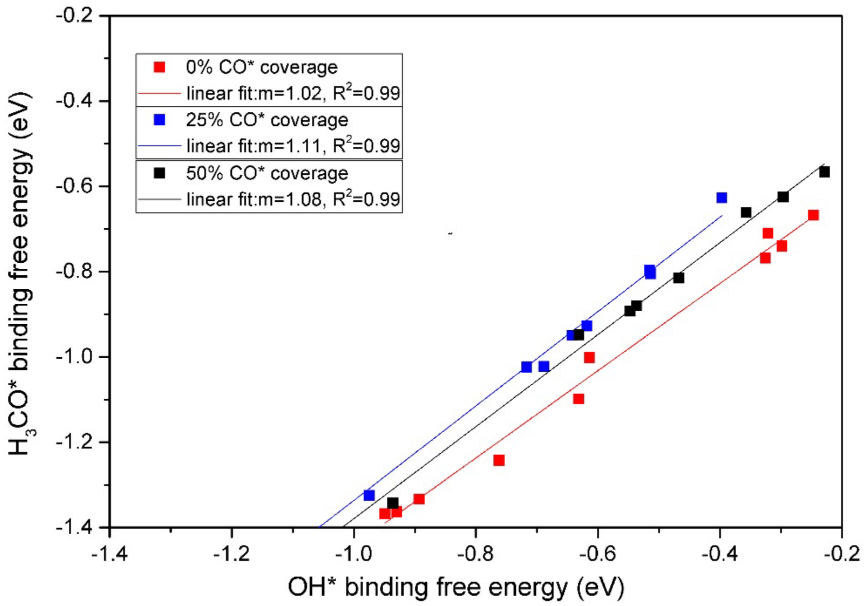

Figure 5-8: H_3CO^* - OH binding free energy scaling relation at three different CO* coverages with slope m and coefficient of determination R^2*

5.3.8. Electronic structure effects in mixed oxide surfaces

Adsorbate binding properties and thus the catalytic activities of oxides have been shown to be dependent on the oxygen atom *p*-band position[167,168] and the metal atom *d*-band configuration[169,170]. RuO_2, IrO_2 and their mixed oxides show strong metal oxygen overlap covalency[171,172] and any modification in the atomistic constituent will thus affect both the O-*p* and metal-*d* band. The effects of such changes on adsorbate binding are therefore expectedly coupled.

Here, the *d*-band center is computer for the two metal atoms closest to the bridge site on all surfaces and coverages (Figure 5-10). The calculation is also done for the average *p*-band center for the O atoms in the top layer of catalyst surfaces, for a trend analysis. A Bader charge[173] analysis of these metal and oxygen atoms reveals that oxidation number of oxygen does not significantly depend on change in the type of metal atom and CO* coverage (Table 5-9). In comparison to Ru atom close to bridge site in pure RuO_2 surface, similar Ru atoms in mixed oxide surfaces with Ir atoms as neighbours do not show large deviation in oxidation number. On the contrary, Ir atoms close to the bridge site that have ruthenium neighbours (β= 0.29, 0.75, 0.79) show markedly reduced oxidation number especially with CO* spectators (Table 5-9). This might partly explain the weaker OH* binding on these surfaces. OH* is an electron donating adsorbate. Lower oxidation state of the metal atom would prevent strong bond formation via electron exchange mechanism. The correlation between charge state of the metal atoms closest to the bridge site and OH* binding energy is evident from the correlation plot. Two distinct regime of correlation emerge (Figure 5-9). CO* adsorbates transfers charge to the metal atom while adsorbing onto an oxide surface[174]. Surfaces with low or high β change regime whenever oxidation number increase due to electron doping by CO* spectator. Surfaces with β= 0.29, 0.75, 0.79, continue on the same correlation regime of OH* binding and Bader charge dependency even with electron donation from CO* spectator, leading to weaker OH* binding.

Even in the absence of any strain effect and without any CO* spectators, a wide variation in band centers (Figure 5-10) are observed for both Ir and Ru atoms next to the bridge site and the oxygen atoms close to them. The range of band positions observed in the mixed oxide surfaces range both above and below the band position of metal-*d* band and O-*p* band of pure IrO_2 and RuO_2, indicating that complex and non-linear ligand effects are in play. It is clear that ligand effects between the chemically similar Ir and Ru atoms are strong and result in electronic structure modification leading to anomalous behaviour in the mixed oxides. The presence of CO* spectators further enhance this unexpected behaviour. These findings show that mixed oxide catalyst design should include the unexpected electronic structure effects due to ligand interaction through the oxygen *p*-band.

Iridium in IrO_2 have five electron in t_{2g} orbitals leading to four paired and one unpaired electron[175]. The unpaired electron engages in Kramers–Anderson super-exchange coupling with neighbouring Ir t_{2g} orbital unpaired electron via oxygen p-orbital (Figure 5-11). Ruthenium in IrO_2 have four electron in t_{2g} orbitals leading to two paired and two unpaired electron. This configuration allows intra-atomic triplet coupling due to presence of two unpaired electron in the t_{2g} orbital[142]. Special situation arises when Ir atom has Ru neighbours. Intra-atomic coupling is not possible with single triplet electron and inter-atomic exchange coupling is limited due to unavailability of uncoupled triplet in neighbouring Ru atom. This leads to increase in band energy. Ir atom close to bridge site in IrO_2 monolayer on RuO_2 structure (β=0.75) have some Ir atom neighbours and some Ru atom as neighbours. Its t_{2g} orbital shifts towards positive direction. For a single Ir atom close to bridge site in RuO2 slab, the Ir atom has only Ru neighbours. The positive shift is even stronger (Figure 5-12).

Due to strong covalency in the system, oxygen p-orbital gets affected as well. Differences originating from both the oxygen and metal atom electronic structure parameters affects the adsorbate binding energy. The intricacy of the intermingled effects make it impossible to establish simple linear model for describing changes in adsorbate binding energy. The lack of correlation of binding energy with either metal-d or oxygen-p band center position parameter is evident.

Table 5-9: Oxidation number of metal atom 1 (ON1) and atom 2 (ON2) that make up the bridge site and average oxidation number of oxygen atoms in the top layers calculated from Bader charges. Yellow boxes for Ru-atom and green boxes for Ir atom.

	0% CO* coverage			25% CO* coverage			50% CO* coverage		
β	ON1	ON2	ON-oxygen	ON1	ON2	ON-oxygen	ON1	ON2	ON-oxygen
0	1.19	1.21	-0.87	1.3	1.3	-0.85	1.33	1.33	-0.84
0.05	1.18	1.2	-0.87	1.28	1.29	-0.85	1.32	1.32	-0.84
0.11	1.2	1.2	-0.86	1.3	1.3	-0.84	1.31	1.3	-0.84
0.25	1.19	1.19	-0.86	1.29	1.29	-0.85	1.32	1.31	-0.85
0.29	1.2	1.12	-0.86	1.32	1.02	-0.85	1.36	1.01	-0.84
0.75	1.16	1.16	-0.85	1.28	1.06	-0.85	1.29	1.06	-0.85
0.79	1.22	1.11	-0.85	1.33	1.03	-0.85	1.35	1.0	-0.87
0.9	1.16	1.16	-0.86	1.23	1.23	-0.84	1.23	1.22	-0.84
0.95	1.16	1.16	-0.85	1.21	1.21	-0.85	1.2	1.21	-0.86
1	1.14	1.14	-0.85	1.21	1.21	-0.85	1.21	1.21	-0.87

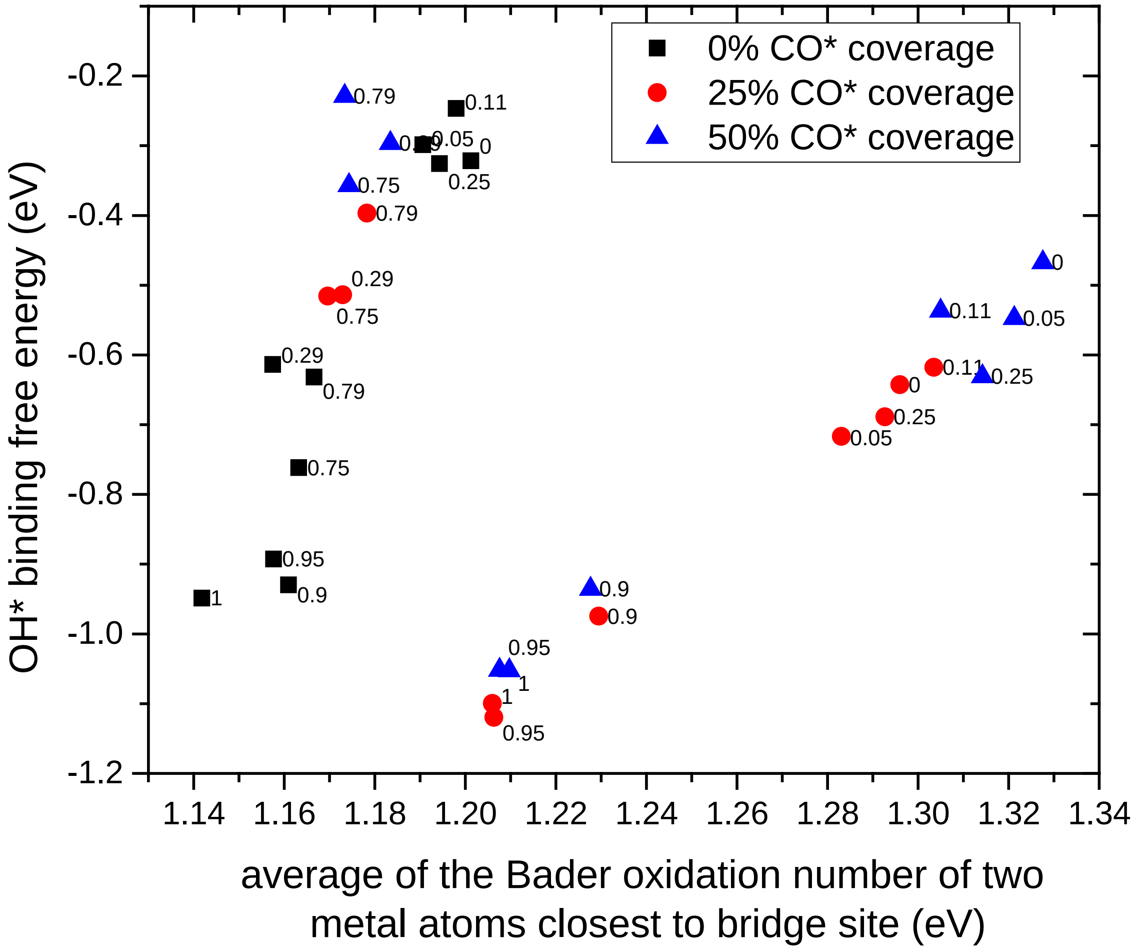

Figure 5-9: Correlation of OH binding free energy with average Bader oxidation number of the two metal atoms closest to the bridge site. Labels indicate the β value of the surface for which the data point.*

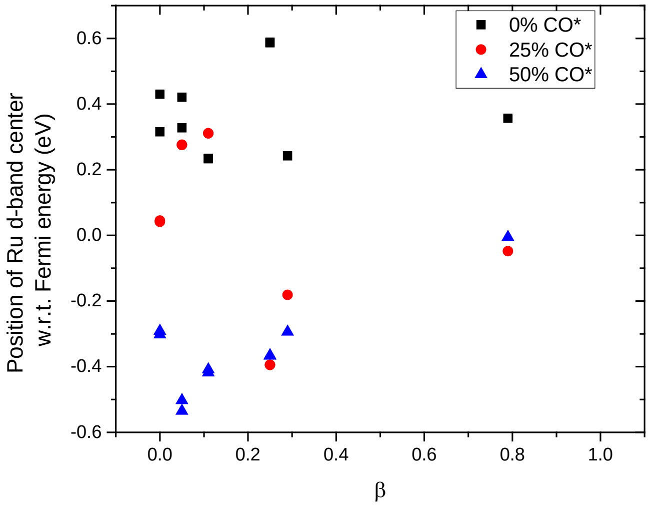

(a)

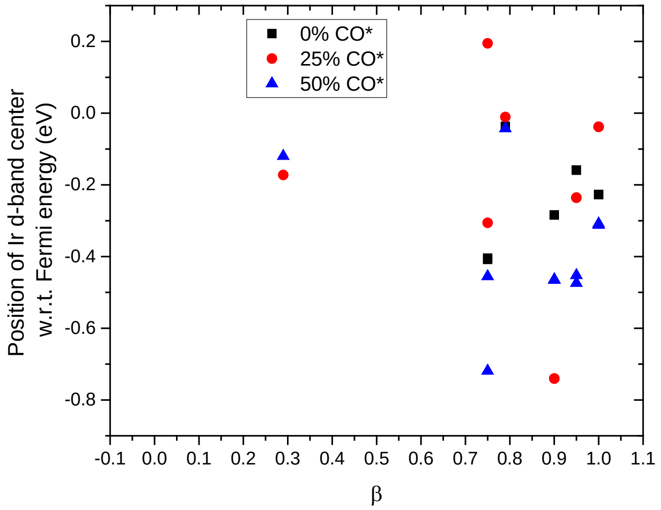

(b)

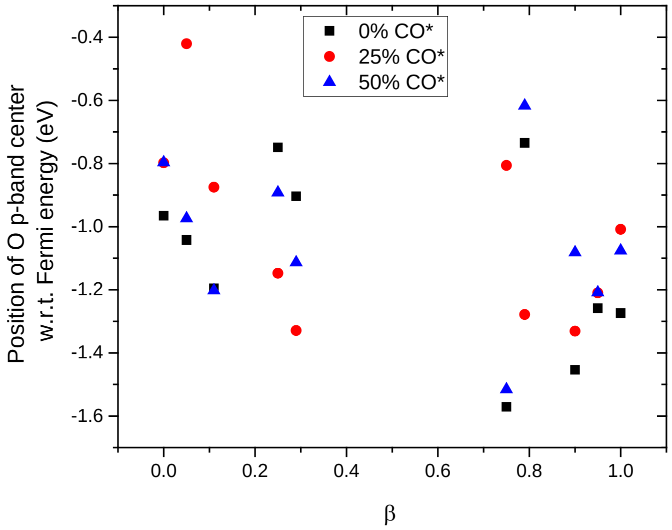

(c)

Figure 5-10: Modification in the band center for (a) Ru-d electrons (b) Ir d-electrons (c) O-p electrons, due to ligand effects and CO coverage.*

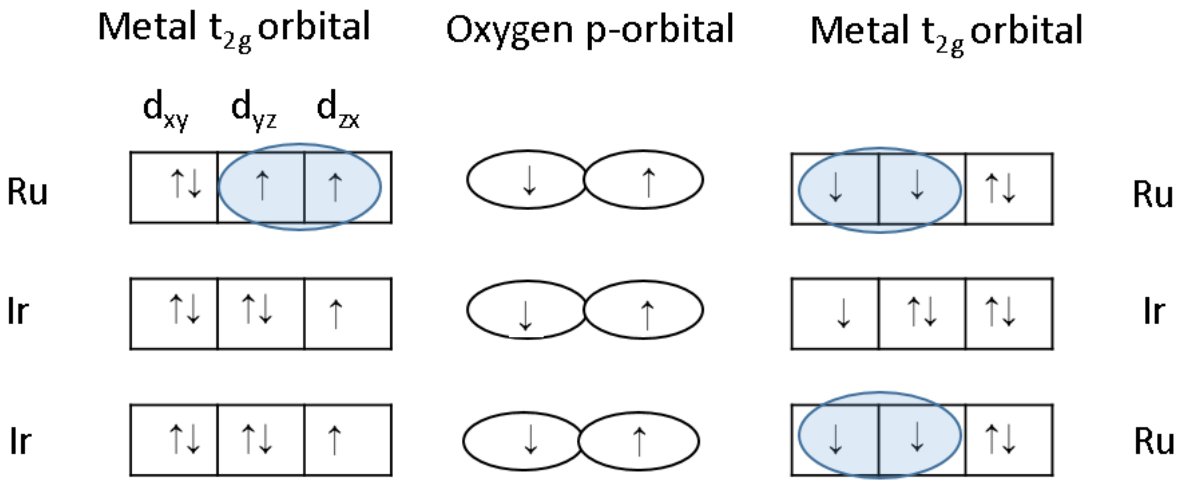

Figure 5-11: Ligand effect from metal atom neighbours is established via Kramers–Anderson super-exchange coupling. Onsite triplet pairing in neighbouring Ru-t_{2g} orbital limits such exchange coupling for Ir atoms as well. Blue ring denote intra-atomic triplet pairing

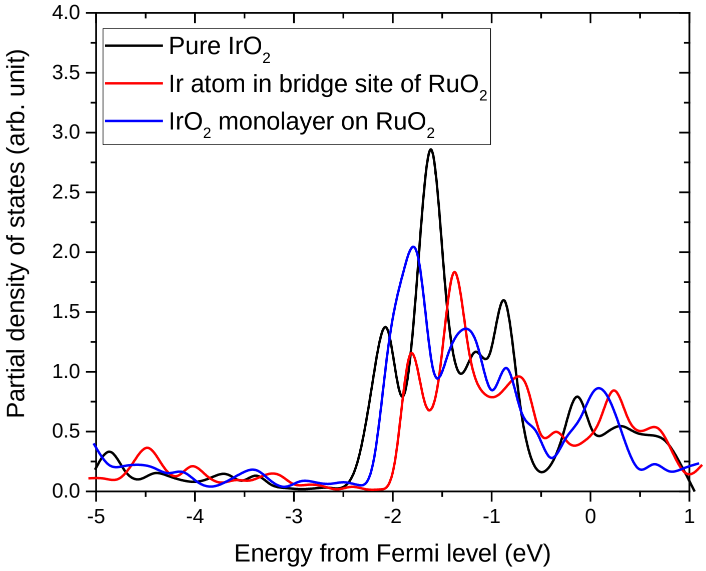

Figure 5-12: shift in t_{2g} orbital of Ir atom from reduced super-exchange related stability due to intra-atomic triplet paring in neighbouring ruthenium atoms.

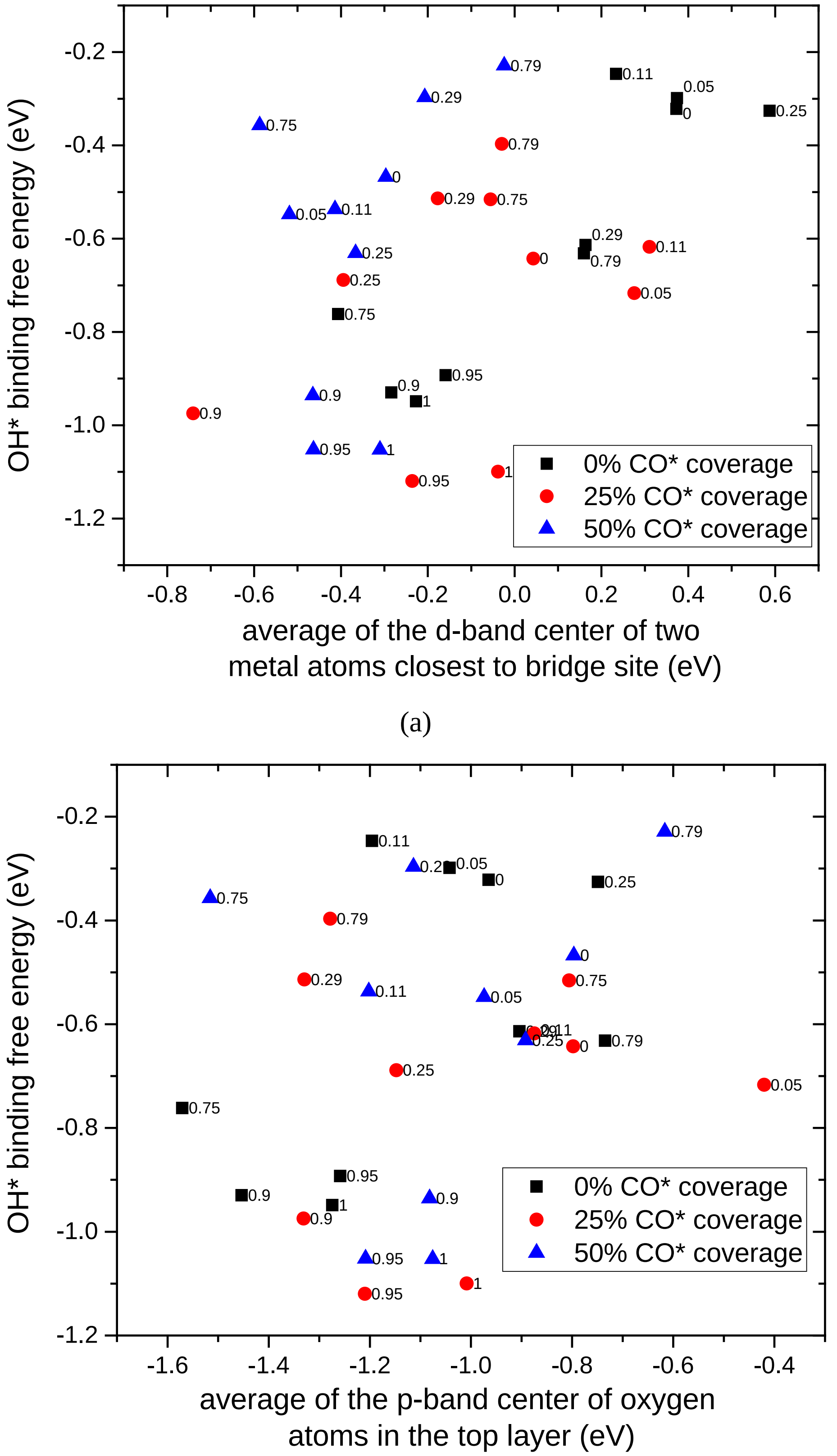

(a)

(b)

Figure 5-13: correlation of OH binding free energy with (a) average d-band position of the two metal atoms closest to the bridge site (b) average p-band position of oxygen atoms in the top layer of the catalyst surfaces. Labels indicate the β value of the surface for which the data point.*

5.4. Conclusion

RuO_2-based CO2RR electrocatalysts hold great promise. Overpotential requirement and selectivity of these catalyst can be further enhanced through control of the CO* coverage effects and more importantly through doping with Ir. In the presence of CO* and OH* spectators (often present in CO2RR environment), small amounts of Ir substituents are predicted to segregate near the bridge position in rutile (110) surface. Bridge sites coordinated with Ir and Ru atoms on a RuO_2/IrO_2 bulk catalyst or IrO_2 monolayer on RuO_2 shows unexpected non-linear adsorbate binding energies, due to strong ligand effects from neighbouring Ru atoms onto the coordinating Ir atom. CO* binds much stronger on surfaces with such bridge sites than on the pure oxides. The CO* adsorbate interaction effects are also more influential for these mixed oxide surfaces, where, e.g., the CO* interaction leads to weaker OCHO* and OH* binding on these surfaces. Thermodynamic reaction pathway analysis shows two elementary steps determine the onset potential for CO2RR regardless of the chemical nature of the bridge site and CO* spectator coverage - (a) OCHO* protonation (b) OH* removal. The CO* interaction weakens the binding energy of RuO_2 catalyst with a monolayer of IrO_2 on top (β=0.75) or Ir substituted at a bridge site (β=0.29) such that an onset potential for methanol of -0.2 V-RHE is predicted.

It is also shown the universality of OH*/OCHO* and OH*/H_3CO* scaling relations regardless of CO* coverage, simplifying the analysis of CO2RR activity on CO* coverage mixed oxide systems. Enhancements of the catalytic activity in mixed oxides comes from a concerted ligand and spectator effects, where mixing of oxides with strong covalent character can lead to remarkable electronic structure effects and binding energy behaviour.

Unlike metals, where simple extrapolation techniques often provide good approximation of key adsorbate binding energies, mixed oxides are much more complex for the electronic structure variations. The increased complexity also provides a unique possibility to design very active catalysts with low levels of cation substitution. Specifically, a monolayer or less of IrO_2 deposited on RuO_2 (110) surface is suggested to be very good CO2RR catalyst for formic acid and methanol evolution with moderate CO* coverage.

6. C-C coupling on $Ru_xIr_{1-x}O_2$ surfaces

6.1. Introduction

Metallic catalyst especially copper is known to evolve 2C product during CO and CO_2 electroreduction[29,166,176]. Computational studies have confirmed that C-C coupling happens on copper facets through CO-CO dimer formation with a very small kinetic barrier of only 0.33 eV[177]. Recent experimental studies on Ru/Ir mixed oxide electrocatalysts for CO_2 reduction also observed considerable ethanol formation during CO2RR experiments[73]. Utilizing the Ru/Ir-mixed oxide simulation models developed in chapter 5, the thermodynamic and kinetic feasibilities of C-C coupling reaction on such oxide electrocatalysts are assessed.

6.2. Computational details

Evaluation of binding free energy of reaction adsorbates and thermodynamic of reaction steps are done following DFT simulations methods described in chapter 5. The mixed oxide surface models and their indexing based on Ir character are exactly followed as well. Both chemical and electrochemical steps towards C-C bond formation of CO and few other reaction intermediates are followed using the computational hydrogen electrode model. Finite temperature free energy corrections are considered unchanged from the coupling reaction. During electrochemical reaction steps, loss of entropy of hydrogen molecules is considered. In the surface simulation model, two bridge sites are available for reaction. Before coupling adsorbates occupy these two sites and coupled product bind through only one bridge site (Figure 6-1). On some surfaces, C-C coupled intermediates are not stable and relaxes back to original position during optimizing. Chemical and electrochemical steps considers here on all surfaces are listed in (Table 6-1 and Table 6-2)

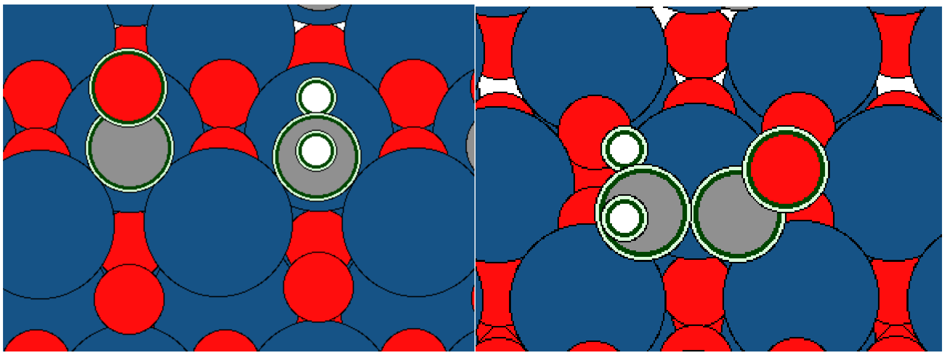

Figure 6-1: Chemical coupling of CO^* and CH_2^* in to a single bridge site adsorbate $COCH_2^*$ on pure IrO_2 (110) surface.

6.3. Thermodynamics of C-C coupling as a chemical step

CO-CO dimerization is either not possible or energetically extremely difficult on all Ru/Ir-mixed oxide surfaces. Coupling between CO* and a further reduced adsorbate like C* or CH_2^*

appears to be more feasible thermodynamically. Energetics of C-C coupling between CO* and CH_x* adsorbates is more favourable on surfaces with high Ru character than surfaces with Ir character. Even for the most favourable cases for C-C coupling, the increase in energy is significantly more than that observed for C-C coupling on copper facets[177,178]. Unless the kinetics barriers are of comparable to this increase in total energy, C-C coupling on Ru/Ir-mixed oxides is not expected.

Table 6-1: electronic energy change due to chemical C-C coupling on $Ru_xIr_{1-x}O_2$ surfaces. Ir character of the surfaces represented by β as explained in previous chapter. Darker colour means smaller increase in electronic energy.

β→	0.00	0.05	0.11	0.25	0.29	0.75	0.79	0.90	0.95	1.00
Coupling reaction	Change in electronic energy from coupling (eV)									
CO*+CO*→COCO*	2.25	X	X	2.23	X	2.09	X	X	X	X
CO*+CHO*→COCHO*	X	X	X	1.74	X	X	2.10	1.73	X	1.27
CO*+COH*→COCOH*	1.49	1.52	1.47	1.93	1.67	1.66	1.73	1.40	1.57	1.63
CO*+C*→COC*	0.62	0.65	0.41	0.62	0.45	0.43	0.43	0.62	0.57	0.61
CO*+CH*→COCH*	0.48	0.53	0.45	0.68	1.26	0.92	1.05	1.30	1.39	1.34
CO*+CH_2*→$COCH_2$*	0.65	0.65	0.63	0.52	0.80	0.92	0.70	1.10	0.98	0.99
CO*+CH_3*→$COCH_3$*	0.47	0.38	0.48	X	0.97	0.77	X	X	X	X

6.4. Kinetic barriers for C-C coupling

To examine the kinetic barrier associated with C-C coupling on Ru/Ir-mixed oxides a few chemical C-C coupling cases were selected with a comparatively smaller increase in energy ranging from 0.41 eV to 0.68 eV. Kinetic barriers are evaluated using a climbing nudged elastic band method. The forward reaction barrier for C-C coupling ranges from 1.19 eV to 1.63 eV. No correlation is observed between the kinetic barrier and energy increment from the reaction step. The forward reaction barriers are too large to be surmountable at room temperature. Interestingly the backward reaction barriers are also high ranging from 0.7 to 1.2 eV. This indicates that C-C coupling through chemical steps is not possible on Ru/Ir mixed oxide catalysts. However, if 2C intermediates are formed by other means (e.g. electrochemical mechanism) then the large barrier will prohibit dissociation.

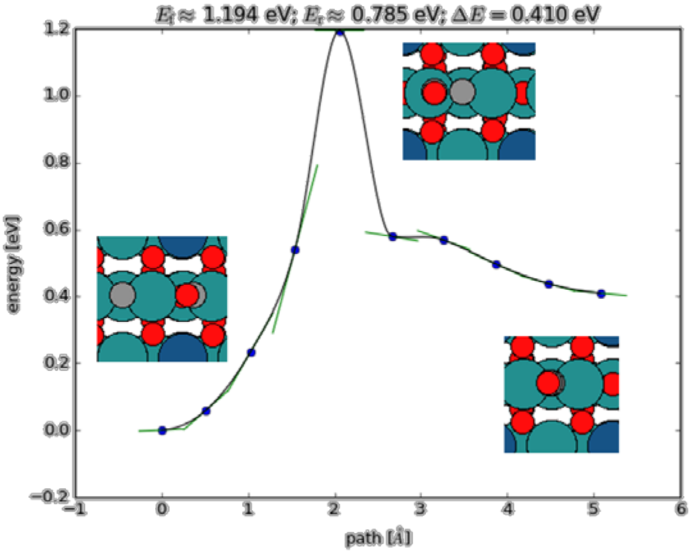

Figure 6-2: kinetic barrier for CO and C* coupling on RuO_2 surface with one Ir atom doped at cus site. (β=0.11)*

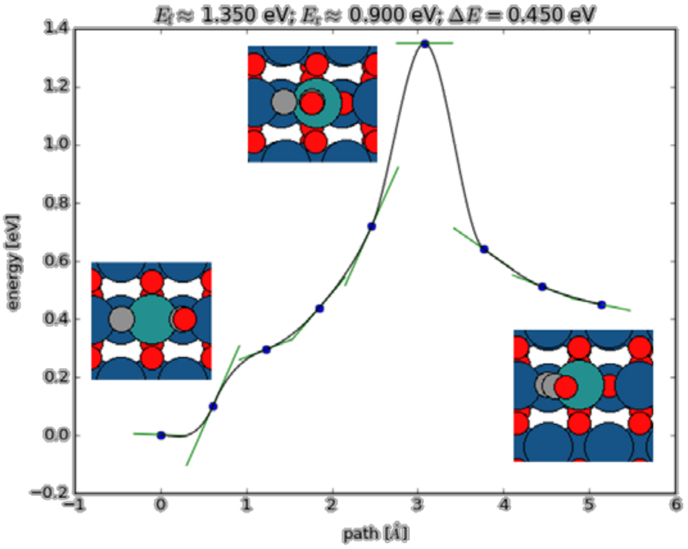

Figure 6-3: kinetic barrier for CO and C* coupling on IrO_2 surface with one Ru atom doped near bridge site. (β=0.79)*

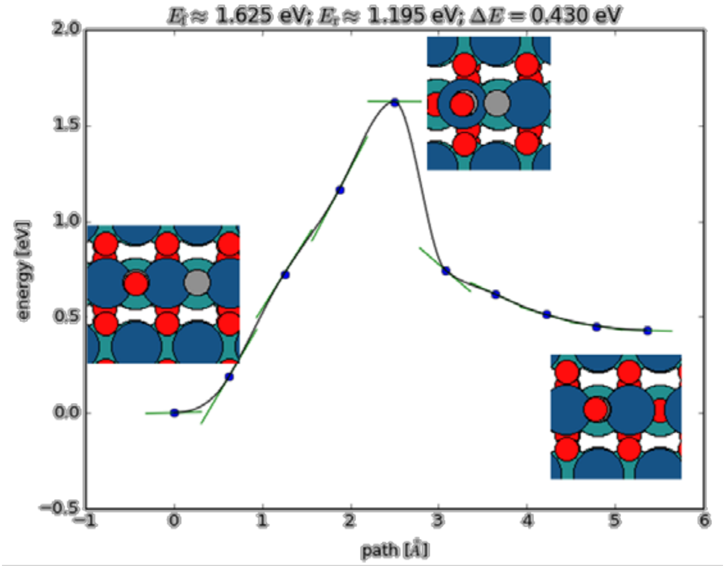

Figure 6-4: kinetic barrier for CO and C* coupling on IrO_2 monolayer on RuO_2 (β=0.75)*

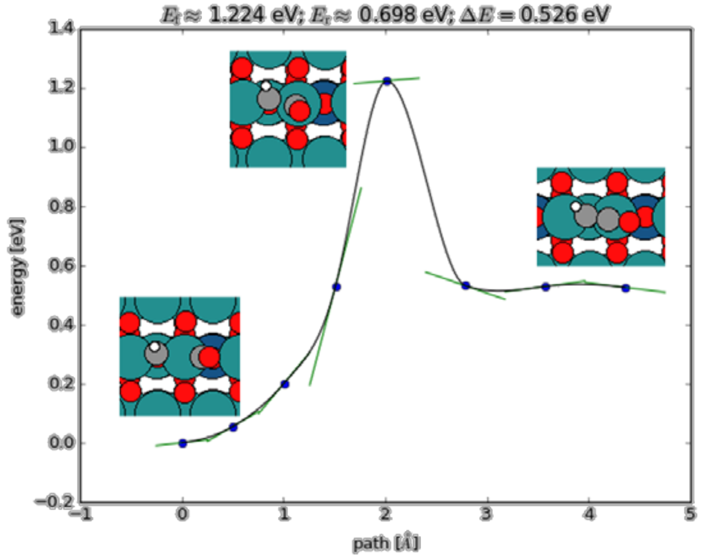

Figure 6-5: kinetic barrier for CO and CH* coupling on RuO_2 surface with one Ir atom in the subsurface layer. (β=0.05)*

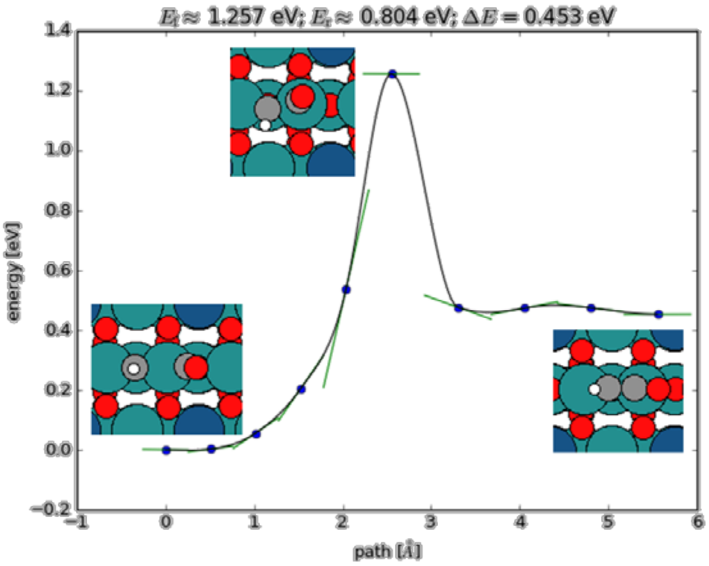

Figure 6-6: kinetic barrier for CO and CH* coupling on RuO₂ surface with one Ir atom doped below cus site. (β=0.11)*

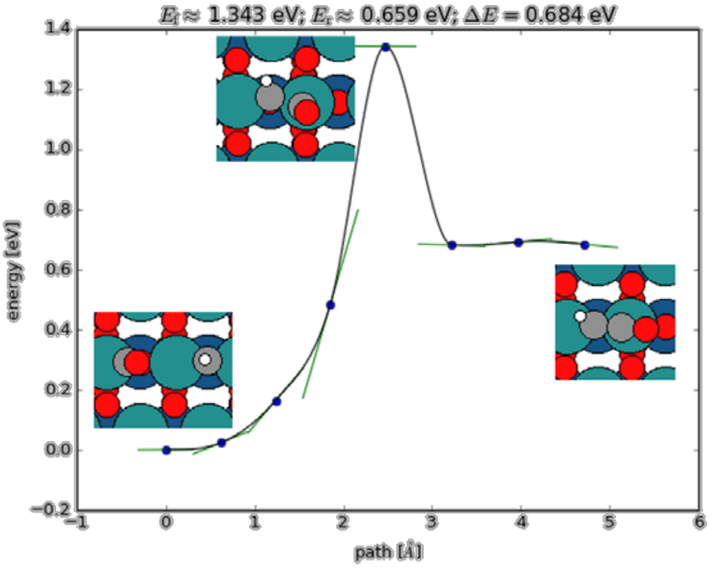

Figure 6-7: kinetic barrier for CO and CH* coupling on RuO₂ monolayer on IrO₂ (β=0.25)*

6.5. Thermodynamic of C-C coupling as a electrochemical step

Free energy change as well as the kinetic barriers can be controlled for a proton transfer mediated C-C coupling in an electrochemical environment by application of potential[179]. Even at 0 V-RHE, formation of $COCH_x$* intermediates through a proton transfer reaction mechanism have either small increase in free in free energy or it is downhill (Table 6-2). This is in stark contrast to chemical C-C coupling steps. Thermodynamic is especially favourable for C-C coupling on ruthenium rich surfaces and formation of COCH* and $COCH_2$*. Any kinetic barrier for these electrochemical steps will get smaller with applied potential and provide a possibility of 2C products on further reduction of the C-C coupled intermediate. The large kinetic barrier for chemical step of C-C bond breaking helps in stability the 2C intermediate.

Table 6-2: Free energy change due to electrochemical C-C coupling on $Ru_xIr_{1-x}O_2$ surfaces. Ir character of the surfaces represented by β as explained in previous chapter. Darker colour means smaller increase in electronic energy.

β→	0.00	0.05	0.11	0.25	0.29	0.75	0.79	0.90	0.95	1.00
Coupling reaction	Change in free energy at 0 V-RHE (eV)									
$CO^*+CO^*+H^++e^-\rightarrow COCOH^*$	2.43	2.48	2.43	2.67	2.14	1.76	2.04	1.60	1.62	1.66
$CO^*+CO^*+H^++e^-\rightarrow COCHO^*$	X	X	X	2.04	X	X	1.87	1.83	X	1.38
$CO^*+C^*+H^++e^-\rightarrow COCH^*$	-0.05	0.04	-0.09	-0.13	0.58	0.33	0.36	0.92	0.94	0.95
$CO^*+CH^*+H^++e^-\rightarrow COCH_2^*$	-0.30	-0.28	-0.34	0.25	0.52	0.41	0.16	0.32	0.23	0.37
$CO^*+CH_2^*+H^++e^-\rightarrow COCH_3^*$	0.16	0.12	0.15	X	-0.01	0.46	X	X	X	X

6.6. Conclusion

C-C coupling among CO2RR reaction intermediates is possible on Ru rich Ru/Ir-oxides via electrochemical mechanism. However it involves CH_x^* intermediates with CO*, unlike CO*-CO* coupling observed on copper surfaces. A large kinetic barrier for chemical step of C-C coupling as well as C-C bond breaking is expected to help with the stability of the 2C intermediates once formed by an electrochemical route. Further reduction of these $COCH_x^*$ intermediates might lead to ethanol evolution as observed in experimetns[68].

7.Conclusion and outlook

7.1. Conclusion

The main achievement of this PhD research lies in the identification of promise in oxide electrocatalysts and ways to engineer them. Worldwide, the research on CO2RR electrocatalysts has focused on metallic systems and measures to break the scaling law limitations in them. By providing mechanistic understanding of reaction mechanism, thermodynamic limits, descriptors and chemical factors determining activity, this thesis aims to reignite experimental and theoretical research activity in oxide CO2RR electrocatalyst area. The key scientific knowledge developed here is summarized

A. Fundamental difference in reaction mechanism and intermediates in CO2RR on metallic and oxide catalysts explained. OH* binding energy is identified as an activity descriptor.
B. Identification of onset limiting reaction steps and environmental constraints like hydroxylation and local pH effects for CO2RR on oxides.
C. Scaling law based volcano construction for CO2RR on oxide surfaces constructed. Mapping of OH*/H* suitable for CO2RR activity and selectivity (over HER and CO evolution) is done. This provides rules for quick identification of oxides as a probable CO2RR catalysts candidate
D. Large effects of spectator species CO* on reaction mechanism, thermodynamics and product selectivity explained. Difference in experimental observations of product selectivity on RuO2 based electrocatalysts is clarified using adsorbate interaction models. For RuO_2 based electrocatalysts the requirement for moderate CO* coverage for effective CO2RR is found out.
E. Extraordinary adsorbate binding behaviour in Ru/Ir-oxides is investigated. Strong ligand effect of Ru neighbours on Ir atom close to the active site shows anomalous behaviour for adsorbate binding and large CO* spectator interaction effects on binding energy. This lead to methanol onset potential of -0.2 V-RHE on 50% CO* covered monolayer of IrO_2 on RuO_2 (110) surface.
F. Opening the opportunity for binding energy modulation without strain effect but utilizing ligands effects. Further development of this method of mixed oxide engineering can yield new stable yet more efficient electrocatalysts
G. Possibility of 2C products on Ru/Ir-mixed oxides is explored. Advantageous thermodynamic of electrochemical C-C coupling between CO* and CH_x* and large barrier for C-C bond breaking through a chemical step might lead to methanol as a product.

7.2. Outlook

Electrocatalyst compositions and CO* coverage conditions that are predicted to be very active for CO2RR, need to be tested experimentally. Especially tin oxide and iridium oxide doped

RuO2 for formic acid and methanol evolution respectively. Rhenium oxide based catalysts would be very interesting to study for good selectivity over HER. It is crucial to control reaction environment and spectator coverage for obtaining desirable CO2RR activity from oxide catalysts due to very strong adsorbate interaction effects present.

Scaling laws established on rutile oxide surfaces need to be tested for applicability on other class of oxides like perovskite, spinel or rocksalt structured ones. Variability of reaction mechanism and thermodynamics of reaction steps also should be studied on such oxides to prove universality of volcano and activity – selectivity map created in this work.

As the broad-based fundamental study, this thesis looked into mainly the thermodynamic of CO2RR reaction steps on oxide surfaces the create the generative oxide CO2RR catalyst design ideas. In future specific catalysts can be designed using the chemical principals suggested here. When determining the suitability of a specific catalyst for CO2RR, calculation of electrochemical reaction barrier with explicit electrolyte effects would be needed. However a high throughput search for quick identification of possible good candidates can also be done.

References

(1) Chu, S.; Cui, Y.; Liu, N. The Path towards Sustainable Energy. *Nat. Mater.* **2016**, *16* (1), 16–22.

(2) Davies, S. The Great Horse-Manure Crisis of 1894. **2004**, 32–33.

(3) Chu, S.; Majumdar, A. Opportunities and Challenges for a Sustainable Energy Future. *Nature* **2012**, *488* (7411), 294–303.

(4) Reichgelt, T.; D'Andrea, W. J.; Fox, B. R. S. Abrupt Plant Physiological Changes in Southern New Zealand at the Termination of the Mi-1 Event Reflect Shifts in Hydroclimate and pCO2. *Earth Planet. Sci. Lett.* **2016**, *455*, 115–124.

(5) LAZARD'S LEVELIZED COST OF ENERGY ANALYSIS 10.0. *www.lazard.com* **2016**, *10.0* (December 2016), 1–21.

(6) U.S. Department of Energy. Grid Energy Storage. **2013**, No. December, 67.

(7) Pedersen, A. S.; Elmegaard, B.; Christensen, C. H.; Kjøller, C.; Elefsen, F.; Hansen, J. B.; Sørensen, P. A.; Hvid, J.; Kær, S. K.; Vangkilde-Pedersen, T.; et al. Status and Recommendations for RD & D on Energy Storage Technologies in a Danish Context. **2014**, No. February, 64.

(8) Dunn, B.; Kamath, H.; Tarascon, J.-M. Electrical Energy Storage for the Grid: A Battery of Choices. *Science (80-.).* **2011**, *334* (6058), 928–935.

(9) Kuhl, K. P.; Hatsukade, T.; Cave, E. R.; Abram, D. N.; Kibsgaard, J.; Jaramillo, T. F. Electrocatalytic Conversion of Carbon Dioxide to Methane and Methanol on Transition Metal Surfaces. *J. Am. Chem. Soc.* **2014**, *136* (40), 14107–14113.

(10) Centi, G.; Perathoner, S. Opportunities and Prospects in the Chemical Recycling of Carbon Dioxide to Fuels. *Catal. Today* **2009**, *148* (3–4), 191–205.

(11) Olah, G. A.; Goeppert, A.; Prakash, G. K. S. Beyond Oil and Gas: The Methanol Economy: Second Edition. *Beyond Oil Gas Methanol Econ. Second Ed.* **2009**, 1–334.

(12) Ganesh, I. Conversion of Carbon Dioxide into Methanol - A Potential Liquid Fuel: Fundamental Challenges and Opportunities (a Review). *Renew. Sustain. Energy Rev.* **2014**, *31* (2014), 221–257.

(13) Hori, Y.; Kikuchi, K.; Suzuki, S. Production of CO and CH4 in Electrochemical Reduction of CO2 at Metal Electrodes in Aqueous Hydrogencarbonate Solution. *Chem. Lett.* **1985**, *14* (11), 1695–1698.

(14) Hori, Y.; Murata, A.; Takahashi, R. Formation of Hydrocarbons in the Electrochemical Reduction of Carbon Dioxide at a Copper Electrode in Aqueous Solution. *J. Chem. Soc. Faraday Trans. 1 Phys. Chem. Condens. Phases* **1989**, *85* (8), 2309.

(15) Hori, Y. Electrochemical CO2 Reduction on Metal Electrodes. In *Modern Aspects of Electrochemistry*; Springer New York: New York, NY, 2008; Vol. 42, pp 89–189.

(16) Peterson, A. A.; Nørskov, J. K. Activity Descriptors for CO 2 Electroreduction to Methane on Transition-Metal Catalysts. *J. Phys. Chem. Lett.* **2012**, *3* (2), 251–258.

(17) Peterson, A. A.; Abild-Pedersen, F.; Studt, F.; Rossmeisl, J.; Nørskov, J. K.; Lewis, N. S.; Nocera, D. G.; Hori, Y.; Kikuchi, K.; Murata, A.; et al. How Copper Catalyzes the Electroreduction of Carbon Dioxide into Hydrocarbon Fuels. *Energy Environ. Sci.* **2010**, *3* (9), 1311.

(18) Hansen, H. A.; Shi, C.; Lausche, A.; Peterson, A.; Nørskov, J. K. Bifunctional Alloys for the Electroreduction of CO_2 and CO. *Phys. Chem. Chem. Phys.* **2016**, *18* (111), 9194–9201.

(19) Wang, Z.; Yang, G.; Zhang, Z.; Jin, M.; Yin, Y. Selectivity on Etching: Creation of High-Energy Facets on Copper Nanocrystals for CO2 Electrochemical Reduction. *ACS Nano* **2016**, *10* (4), 4559–4564.

(20) Luo, W.; Nie, X.; Janik, M. J.; Asthagiri, A. Facet Dependence of CO2 Reduction Paths

on Cu Electrodes. *ACS Catal.* **2016**, *6* (1), 219–229.

(21) Durand, W. J.; Peterson, A. A.; Studt, F.; Abild-Pedersen, F.; Nørskov, J. K. Structure Effects on the Energetics of the Electrochemical Reduction of CO2 by Copper Surfaces. *Surf. Sci.* **2011**, *605* (15–16), 1354–1359.

(22) Ren, D.; Deng, Y.; Handoko, A. D.; Chen, C. S.; Malkhandi, S.; Yeo, B. S. Selective Electrochemical Reduction of Carbon Dioxide to Ethylene and Ethanol on Copper(I) Oxide Catalysts. *ACS Catal.* **2015**, *5* (5), 2814–2821.

(23) Hong, X.; Chan, K.; Tsai, C.; N??rskov, J. K. How Doped MoS2 Breaks Transition-Metal Scaling Relations for CO2 Electrochemical Reduction. *ACS Catal.* **2016**, *6* (7), 4428–4437.

(24) Chan, K.; Tsai, C.; Hansen, H. A.; Nørskov, J. K. Molybdenum Sulfides and Selenides as Possible Electrocatalysts for CO 2 Reduction. *ChemCatChem* **2014**, *6* (7), 1899–1905.

(25) Kortlever, R.; Shen, J.; Schouten, K. J. P.; Calle-Vallejo, F.; Koper, M. T. M. Catalysts and Reaction Pathways for the Electrochemical Reduction of Carbon Dioxide. *J. Phys. Chem. Lett.* **2015**, *6* (20), 4073–4082.

(26) Parajuli, R.; Gerken, J. B.; Keyshar, K.; Sullivan, I.; Sivasankar, N.; Teamey, K.; Stahl, S. S.; Cole, E. B. Integration of Anodic and Cathodic Catalysts of Earth-Abundant Materials for Efficient, Scalable CO2 Reduction. *Top. Catal.* **2015**, *58* (1), 57–66.

(27) Li, C. W.; Ciston, J.; Kanan, M. W. Electroreduction of Carbon Monoxide to Liquid Fuel on Oxide-Derived Nanocrystalline Copper. *Nature* **2014**, *508* (7497), 504–507.

(28) Bertheussen, E.; Verdaguer-Casadevall, A.; Ravasio, D.; Montoya, J. H.; Trimarco, D. B.; Roy, C.; Meier, S.; Wendland, J.; Nørskov, J. K.; Stephens, I. E. L.; et al. Acetaldehyde as an Intermediate in the Electroreduction of Carbon Monoxide to Ethanol on Oxide-Derived Copper. *Angew. Chemie - Int. Ed.* **2016**, *55* (4), 1450–1454.

(29) Schouten, K. J. P.; Calle-Vallejo, F.; Koper, M. T. M. A Step Closer to the Electrochemical Production of Liquid Fuels. *Angew. Chemie - Int. Ed.* **2014**, *53* (41), 10858–10860.

(30) Bandi, A.; Kiihne, H. Electrochemical Reduction of Carbon Dioxide in Water: Analysis of Reaction Mechanism on Ruthenium-Titanium-Oxide. *J. Electrochem. Soc.* **1992**, *139* (6), 1605.

(31) Bandi, A. Electrochemical Reduction of Carbon Dioxide on Conductive Metallic Oxides. *J. Electrochem. Soc.* **1990**, *137* (7), 2157.

(32) Popic, J. P.; Avramov-Ivic, M. L.; Vukovic, N. B.; Popić, J.; Avramov-Ivić, M.; Vuković, N.; Popic, J. P.; Avramov-Ivic, M. L.; Vukovic, N. B.; Popić, J.; et al. Reduction of Carbon Dioxide on Ruthenium Oxide and Modified Ruthenium Oxide Electrodes in 0.5 M NaHCO 3. *J. Electroanal. …* **1997**, *421*, 105–110.

(33) Spataru, N.; Tokuhiro, K.; Terashima, C.; Rao, T. N.; Fujishima, A. Electrochemical Reduction of Carbon Dioxide at Ruthenium Dioxide Deposited on Boron-Doped Diamond. *J. Appl. Electrochem.* **2003**, *33* (12), 1205–1210.

(34) Qu, J.; Zhang, X.; Wang, Y.; Xie, C. Electrochemical Reduction of CO2 on RuO2/TiO 2 Nanotubes Composite Modified Pt Electrode. *Electrochim. Acta* **2005**, *50* (16–17), 3576–3580.

(35) Meng, Y. S.; Arroyo-de Dompablo, M. E. First Principles Computational Materials Design for Energy Storage Materials in Lithium Ion Batteries. *Energy Environ. Sci.* **2009**, *2* (6), 589.

(36) Norskov, J. K.; Abild-Pedersen, F.; Studt, F.; Bligaard, T. Density Functional Theory in Surface Chemistry and Catalysis. *Proc. Natl. Acad. Sci.* **2011**, *108* (3), 937–943.

(37) Norskov, J. K.; Bligaard, T.; Rossmeisl, J.; Christensen, C. H. Towards the Computational Design of Solid Catalysts. *Nat Chem* **2009**, *1* (1), 37–46.

(38) Hafner, J.; Wolverton, C. T Oward Computational Materials Design : The Impact of Density Functional. *MRS Bull.* **2006**, *31* (September), 659–668.

(39) Greeley, J.; Mavrikakis, M. Alloy Catalysts Designed from First Principles. *Nat. Mater.* **2004**, *3* (11), 810–815.

(40) Nørskov, J. K.; Rossmeisl, J.; Logadottir, A.; Lindqvist, L.; Kitchin, J. R.; Bligaard, T.; Jónsson, H. Origin of the Overpotential for Oxygen Reduction at a Fuel-Cell Cathode. *J. Phys. Chem. B* **2004**, *108* (46), 17886–17892.

(41) Greeley, J.; Stephens, I. E. L.; Bondarenko, a S.; Johansson, T. P.; Hansen, H. a; Jaramillo, T. F.; Rossmeisl, J.; Chorkendorff, I.; Nørskov, J. K. Alloys of Platinum and Early Transition Metals as Oxygen Reduction Electrocatalysts. *Nat. Chem.* **2009**, *1* (7), 552–556.

(42) Greeley, J.; Jaramillo, T. F.; Bonde, J.; Chorkendorff, I. B.; Nørskov, J. K. Computational High-Throughput Screening of Electrocatalytic Materials for Hydrogen Evolution. *Nat. Mater.* **2006**, *5* (11), 909–913.

(43) Hammer, B.; Nørskov, J. K. Theoretical Surface Science and Catalysis-Calculations and Concepts. *Adv. Catal.* **2000**, *45*, 71–129.

(44) Hammer, B.; Nørskov, J. K. Electronic Factors Determining the Reactivity of Metal Surfaces. *Surf. Sci.* **1995**, *343* (3), 211–220.

(45) Mavrikakis, M.; Hammer, B.; Nørskov, J. Effect of Strain on the Reactivity of Metal Surfaces. *Phys. Rev. Lett.* **1998**, *81* (13), 2819–2822.

(46) Schrödinger, E. An Undulatory Theory of the Mechanics of Atoms and Molecules. *Phys. Rev.* **1926**, *28* (6), 1049–1070.

(47) Born, M.; Oppenheimer, R. Zur Quantentheorie Der Molekeln. *Ann. Phys.* **1927**, *389* (20), 457–484.

(48) Hohenberg, P.; Kohn, W. Inhomogeneous Electron Gas. *Phys. Rev.* **1964**, *136* (3B), B864–B871.

(49) Kohn, W.; Sham, L. J. Self-Consistent Equations Including Exchange and Correlation Effects. *Phys. Rev.* **1965**, *140* (4A), A1133–A1138.

(50) Ceperley, D. M.; Alder, B. J. Ground State of the Electron Gas by a Stochastic Method. *Phys. Rev. Lett.* **1980**, *45* (7), 566–569.

(51) Perdew, J. P.; Yue, W. Accurate and Simple Density Functional for the Electronic Exchange Energy: Generalized Gradient Approximation. *Phys. Rev. B* **1986**, *33* (12), 8800–8802.

(52) Hammer, B.; Hansen, L. B.; Nørskov, J. K. Improved Adsorption Energetics within Density-Functional Theory Using Revised Perdew-Burke-Ernzerhof Functionals. *Phys. Rev. B* **1999**, *59* (11), 7413–7421.

(53) Mortensen, J.; Kaasbjerg, K.; Frederiksen, S.; Nørskov, J.; Sethna, J.; Jacobsen, K. Bayesian Error Estimation in Density-Functional Theory. *Phys. Rev. Lett.* **2005**, *95* (21), 216401.

(54) Wellendorff, J.; Lundgaard, K. T.; Møgelhøj, A.; Petzold, V.; Landis, D. D.; Nørskov, J. K.; Bligaard, T.; Jacobsen, K. W. Density Functionals for Surface Science: Exchange-Correlation Model Development with Bayesian Error Estimation. *Phys. Rev. B - Condens. Matter Mater. Phys.* **2012**, *85* (23), 235149.

(55) Lee, K.; Murray, É. D.; Kong, L.; Lundqvist, B. I.; Langreth, D. C. Higher-Accuracy van Der Waals Density Functional. *Phys. Rev. B - Condens. Matter Mater. Phys.* **2010**, *82* (8), 3–6.

(56) Pack, J. D.; Monkhorst, H. J. “Special Points for Brillouin-Zone Integrations”—a Reply. *Phys. Rev. B* **1977**, *16* (4), 1748–1749.

(57) Bahn, S. R.; Jacobsen, K. W. An Object-Oriented Scripting Interface to a Legacy Electronic Structure Code. *Comput. Sci. Eng.* **2002**, *4* (3), 56–66.

(58) Christensen, R.; Hansen, H. A.; Vegge, T. Identifying Systematic DFT Errors in Catalytic Reactions. *Catal. Sci. Technol.* **2015**, *5* (11), 4946–4949.

(59) Hansen, H. A.; Montoya, J. H.; Zhang, Y. J.; Shi, C.; Peterson, A. A.; Nørskov, J. K. Electroreduction of Methanediol on Copper. *Catal. Letters* **2013**, *143* (7), 631–635.

(60) Nørskov, J. K.; Rossmeisl, J.; Logadottir, A.; Lindqvist, L.; Kitchin, J. R.; Bligaard, T.; Jónsson, H. Origin of the Overpotential for Oxygen Reduction at a Fuel-Cell Cathode. *J. Phys. Chem. B* **2004**, *108* (46), 17886–17892.

(61) Abild-Pedersen, F.; Greeley, J.; Studt, F.; Rossmeisl, J.; Munter, T. R.; Moses, P. G.; Sk??lason, E.; Bligaard, T.; N??rskov, J. K. Scaling Properties of Adsorption Energies for Hydrogen-Containing Molecules on Transition-Metal Surfaces. *Phys. Rev. Lett.* **2007**, *99* (1), 16105.

(62) Man, I. C.; Su, H. Y.; Calle-Vallejo, F.; Hansen, H. A.; Martínez, J. I.; Inoglu, N. G.; Kitchin, J.; Jaramillo, T. F.; Nørskov, J. K.; Rossmeisl, J. Universality in Oxygen Evolution Electrocatalysis on Oxide Surfaces. *ChemCatChem* **2011**, *3* (7), 1159–1165.

(63) Jones, G.; Bligaard, T.; Abild-Pedersen, F.; Nørskov, J. K. Using Scaling Relations to Understand Trends in the Catalytic Activity of Transition Metals. *J. Phys. Condens. Matter* **2008**, *20* (6), 64239.

(64) Laursen, A. B.; Varela, A. S.; Dionigi, F.; Fanchiu, H.; Miller, C.; Trinhammer, O. L.; Rossmeisl, J.; Dahl, S. Electrochemical Hydrogen Evolution: Sabatiers Principle and the Volcano Plot. *J. Chem. Educ.* **2012**, *89* (12), 1595–1599.

(65) Mills, G.; J??nsson, H. Quantum and Thermal Effects in H2 Dissociative Adsorption: Evaluation of Free Energy Barriers in Multidimensional Quantum Systems. *Phys. Rev. Lett.* **1994**, *72* (7), 1124–1127.

(66) Henkelman, G.; Uberuaga, B. P.; Jónsson, H. Climbing Image Nudged Elastic Band Method for Finding Saddle Points and Minimum Energy Paths. *J. Chem. Phys.* **2000**, *113* (22), 9901–9904.

(67) Russell, P. G. The Electrochemical Reduction of Carbon Dioxide, Formic Acid, and Formaldehyde. *J. Electrochem. Soc.* **1977**, *124* (9), 1329.

(68) Ullah, N.; Ali, I.; Jansen, M.; Omanovic, S. Electrochemical Reduction of CO2 in an Aqueous Electrolyte Employing an Iridium/ruthenium-Oxide Electrode. *Can. J. Chem. Eng.* **2015**, *93* (1), 55–62.

(69) Karamad, M.; Hansen, H. A.; Rossmeisl, J.; N??rskov, J. K. Mechanistic Pathway in the Electrochemical Reduction of CO2 on RuO2. *ACS Catal.* **2015**, *5* (7), 4075–4081.

(70) Yoo, J. S.; Christensen, R.; Vegge, T.; N??rskov, J. K.; Studt, F. Theoretical Insight into the Trends That Guide the Electrochemical Reduction of Carbon Dioxide to Formic Acid. *ChemSusChem* **2016**, *9* (4), 358–363.

(71) Rossmeisl, J.; Ferrin, P.; Tritsaris, G. a.; Nilekar, A. U.; Koh, S.; Bae, S. E.; Brankovic, S. R.; Strasser, P.; Mavrikakis, M. Bifunctional Anode Catalysts for Direct Methanol Fuel Cells. *Energy Environ. Sci.* **2012**, *5* (8), 8335.

(72) Kresse, G. From Ultrasoft Pseudopotentials to the Projector Augmented-Wave Method. *Phys. Rev. B* **1999**, *59* (3), 1758–1775.

(73) Ullah, N.; Ali, I.; Jansen, M.; Omanovic, S. Electrochemical Reduction of CO2 in an Aqueous Electrolyte Employing an Iridium/ruthenium-Oxide Electrode. *Can. J. Chem. Eng.* **2015**, *93* (1), 55–62.

(74) Haas, P.; Tran, F.; Blaha, P. Calculation of the Lattice Constant of Solids with Semilocal Functionals. *Phys. Rev. B - Condens. Matter Mater. Phys.* **2009**, *79* (8), 1–10.

(75) Beltrán, a; Andrés, J.; Sambrano, J. R.; Longo, E. Density Functional Theory Study on the Structural and Electronic Properties of Low Index Rutile Surfaces for TiO2/SnO2/TiO2 and SnO2/TiO2/SnO2 Composite Systems. *J. Phys. Chem. A* **2008**, *112* (38), 8943–8952.

(76) Hansen, H. a; Man, I. C.; Studt, F.; Abild-Pedersen, F.; Bligaard, T.; Rossmeisl, J. Electrochemical Chlorine Evolution at Rutile Oxide (110) Surfaces. *Phys. Chem. Chem. Phys.* **2010**, *12* (1), 283–290.
(77) Mellan, T. a; Grau-Crespo, R. Density Functional Theory Study of Rutile VO2 Surfaces. *J. Chem. Phys.* **2012**, *137* (15), 154706.
(78) Over, H.; Kim, Y. D.; Seitsonen, A. P.; Wendt, S.; Lundgren, E.; Schmid, M.; Varga, P.; Morgante, A.; Ertl, G. Atomic-Scale Structure and Catalytic Reactivity of the RuO2(110) Surface. *Science (80-.).* **2000**, *287* (5457), 1474–1476.
(79) Rochefort, D.; Dabo, P.; Guay, D.; Sherwood, P. M. A. XPS Investigations of Thermally Prepared RuO2 Electrodes in Reductive Conditions. *Electrochim. Acta* **2003**, *48* (28), 4245–4252.
(80) Strasser, P.; Koh, S.; Anniyev, T.; Greeley, J.; More, K.; Yu, C.; Liu, Z.; Kaya, S.; Nordlund, D.; Ogasawara, H.; et al. Lattice-Strain Control of the Activity in Dealloyed Core–shell Fuel Cell Catalysts. *Nat. Chem.* **2010**, *2* (6), 454–460.
(81) Zhang, J.; Vukmirovic, M. B.; Xu, Y.; Mavrikakis, M.; Adzic, R. R. Controlling the Catalytic Activity of Platinum-Monolayer Electrocatalysts for Oxygen Reduction with Different Substrates. *Angew. Chemie - Int. Ed.* **2005**, *44* (14), 2132–2135.
(82) Vojvodic, a.; Norskov, J. K. Optimizing Perovskites for the Water-Splitting Reaction. *Science (80-.).* **2011**, *334* (6061), 1355–1356.
(83) Grimaud, A.; May, K. J.; Carlton, C. E.; Lee, Y.-L.; Risch, M.; Hong, W. T.; Zhou, J.; Shao-Horn, Y. Double Perovskites as a Family of Highly Active Catalysts for Oxygen Evolution in Alkaline Solution. *Nat. Commun.* **2013**, *4* (May), 2439.
(84) Zhao, Z.-J.; Kulkarni, A.; Vilella, L.; Norskov, J. K.; Studt, F. Theoretical Insights into the Selective Oxidation of Methane to Methanol in Copper-Exchanged Mordenite. *ACS Catal.* **2016**, acscatal.6b00440.
(85) Liu, H.; An, W.; Li, Y.; Frenkel, A. I.; Sasaki, K.; Koenigsmann, C.; Su, D.; Anderson, R. M.; Crooks, R. M.; Adzic, R. R.; et al. In Situ Probing of the Active Site Geometry of Ultrathin Nanowires for the Oxygen Reduction Reaction. *J. Am. Chem. Soc.* **2015**, *137* (39), 12597–12609.
(86) Liu, P.; Nørskov, J. K. Ligand and Ensemble Effects in Adsorption on Alloy Surfaces. *Phys. Chem. Chem. Phys.* **2001**, *3* (17), 3814–3818.
(87) Kitchin, J. R.; N??rskov, J. K.; Barteau, M. A.; Chen, J. G. Role of Strain and Ligand Effects in the Modification of the Electronic and Chemical Properties of Bimetallic Surfaces. *Phys. Rev. Lett.* **2004**, *93* (15), 156801.
(88) Davies, J. C.; Bonde, J.; Logadóttir, Á.; Nørskov, J. K.; Chorkendorff, I. The Ligand Effect: CO Desorption from Pt/Ru Catalysts. *Fuel Cells* **2005**, *5* (4), 429–435.
(89) Zhang, J.; Zhou, P.; Liu, J.; Yu, J. New Understanding of the Difference of Photocatalytic Activity among Anatase, Rutile and Brookite TiO2. *Phys. Chem. Chem. Phys.* **2014**, *16* (38), 20382–20386.
(90) Bandarenka, A. S.; Varela, A. S.; Karamad, M.; Calle-Vallejo, F.; Bech, L.; Perez-Alonso, F. J.; Rossmeisl, J.; Stephens, I. E. L.; Chorkendorff, I. Design of an Active Site towards Optimal Electrocatalysis: Overlayers, Surface Alloys and near-Surface Alloys of Cu/Pt(111). *Angew. Chemie - Int. Ed.* **2012**, *51* (47), 11845–11848.
(91) Knudsen, J.; Nilekar, A. U.; Vang, R. T.; Schnadt, J.; Kunkes, E. L.; Dumesic, J. A.; Mavrikakis, M.; Besenbacher, F. A Cu / Pt Near-Surface Alloy for Water - Gas Shift Catalysis. *J. Am. Chem. Soc.* **2007**, *129* (3), 6485–6490.
(92) Reske, R.; Duca, M.; Oezaslan, M.; Schouten, K. J. P.; Koper, M. T. M.; Strasser, P. Controlling Catalytic Selectivities during CO2 Electroreduction on Thin Cu Metal Overlayers. *J. Phys. Chem. Lett.* **2013**, *4* (15), 2410–2413.
(93) Kelly, T. G.; Chen, J. G. Metal Overlayer on Metal Carbide Substrate: Unique Bimetallic

Properties for Catalysis and Electrocatalysis. *Chem. Soc. Rev.* **2012**, 8021–8034.

(94) Hikita, Y.; Nishio, K.; Seitz, L. C.; Chakthranont, P.; Tachikawa, T.; Jaramillo, T. F.; Hwang, H. Y. Band Edge Engineering of Oxide Photoanodes for Photoelectrochemical Water Splitting: Integration of Subsurface Dipoles with Atomic-Scale Control. *Adv. Energy Mater.* **2016**, *6* (7), 1–7.

(95) Romanov, D. P.; Skrobot, V. N. Distortions of Octahedra in Rutile-Type Structures of Transition Element Dioxides. *Glas. Phys. Chem.* **2009**, *35* (5), 518–524.

(96) Nie, Y. F.; Zhu, Y.; Lee, C.-H.; Kourkoutis, L. F.; Mundy, J. a; Junquera, J.; Ghosez, P.; Baek, D. J.; Sung, S.; Xi, X. X.; et al. Atomically Precise Interfaces from Non-Stoichiometric Deposition. *Nat. Commun.* **2014**, *5*, 4530.

(97) Hyldgaard, P.; Persson, M. Long-Ranged Adsorbate-Adsorbate Interactions Mediated by a Surface-State Band. *J. Phys. Condens. Matter* **1999**, *12* (1), L13–L19.

(98) Lang, N. D.; Holloway, S.; Nørskov, J. K. Electrostatic Adsorbate-Adsorbate Interactions: The Poisoning and Promotion of the Molecular Adsorption Reaction. *Surf. Sci.* **1985**, *150* (1), 24–38.

(99) Karlberg, G. S.; Wahnström, G. An Interaction Model for OH+H2O -Mixed and Pure H2O Overlayers Adsorbed on Pt(111). *J. Chem. Phys.* **2005**, *122* (19).

(100) Zhang, Y. J.; Sethuraman, V.; Michalsky, R.; Peterson, A. A. Competition between CO2 Reduction and H2 Evolution on Transition-Metal Electrocatalysts. *ACS Catal.* **2014**, *4* (10), 3742–3748.

(101) Shi, C.; Hansen, H. a; Lausche, A. C.; Nørskov, J. K. Trends in Electrochemical CO2 Reduction Activity for Open and Close-Packed Metal Surfaces. *Phys. Chem. Chem. Phys.* **2014**, *16* (10), 4720–4727.

(102) Reuter, K.; Scheffler, M. Composition and Structure of the RuO2 (110) Surface in an O2 and CO Environment: Implications for the Catalytic Formation of CO2 Karsten. *Phys. Rev. B* **2001**, *65* (3), 35406.

(103) Lindan, P. J. D.; Harrison, N. M.; Gillan, M. J. Mixed Dissociative and Molecular Adsorption of Water on the Rutile (110) Surface. *Phys. Rev. Lett.* **1998**, *80* (4), 762–765.

(104) Hansen, H. A.; Varley, J. B.; Peterson, A. A.; Nørskov, J. K. Understanding Trends in the Electrocatalytic Activity of Metals and Enzymes for CO2 Reduction to CO. *J. Phys. Chem. Lett.* **2013**, *4* (3), 388–392.

(105) Lee, S.; Ocon, J. D.; Son, Y. Il; Lee, J. Alkaline CO2 Electrolysis toward Selective and Continuous HCOO- Production over SnO2 Nanocatalysts. *J. Phys. Chem. C* **2015**, *119* (9), 4884–4890.

(106) Greeley, J. Theoretical Heterogeneous Catalysis: Scaling Relationships and Computational Catalyst Design. *Annu. Rev. Chem. Biomol. Eng.* **2016**, *7* (1), 605–635.

(107) Montemore, M. M.; Medlin, J. W. Scaling Relations between Adsorption Energies for Computational Screening and Design of Catalysts. *Catal. Sci. Technol.* **2014**, *4* (11), 3748–3761.

(108) Shin, S.; Huang, H. H.; Ishigame, M.; Iwahara, H. Protonic Conduction in the Single Crystals of SrZrO3 and SrCeO3 Doped with Y2O3. *Solid State Ionics* **1990**, *40–41* (PART 2), 910–913.

(109) Ferrin, P.; Nilekar, A. U.; Greeley, J.; Mavrikakis, M.; Rossmeisl, J. Reactivity Descriptors for Direct Methanol Fuel Cell Anode Catalysts. *Surf. Sci.* **2008**, *602* (21), 3424–3431.

(110) Bork, N.; Bonanos, N.; Rossmeisl, J.; Vegge, T. Simple Descriptors for Proton-Conducting Perovskites from Density Functional Theory. *Phys. Rev. B - Condens. Matter Mater. Phys.* **2010**, *82* (1), 1–6.

(111) Viswanathan, V.; Hansen, H. A.; Rossmeisl, J.; Nørskov, J. K. Unifying the 2e

- and 4e - Reduction of Oxygen on Metal Surfaces. *J. Phys. Chem. Lett.* **2012**, *3* (20), 2948–2951.

(112) Novell-Leruth, G.; Carchini, G.; López, N. On the Properties of Binary Rutile MO2 Compounds, M = Ir, Ru, Sn, and Ti: A DFT Study. *J. Chem. Phys.* **2013**, *138* (19), 17886–17892.

(113) An, W.; Xu, F.; Stacchiola, D.; Liu, P. Potassium-Induced Effect on the Structure and Chemical Activity of the CuxO/Cu(1 1 1) (X ≤ 2) Surface: A Combined Scanning Tunneling Microscopy and Density Functional Theory Study. *ChemCatChem* **2015**, *7* (23), 3865–3872.

(114) Cui, C.; Han, J.; Zhu, X.; Liu, X.; Wang, H.; Mei, D.; Ge, Q. Promotional Effect of Surface Hydroxyls on Electrochemical Reduction of CO2 over SnOx/Sn Electrode. *J. Catal.* **2016**, *343*, 257–265.

(115) Marshall, S. T.; Medlin, J. W. Surface-Level Mechanistic Studies of Adsorbateadsorbate Interactions in Heterogeneous Catalysis by Metals. *Surf. Sci. Rep.* **2011**, *66* (5), 173–184.

(116) Wang, H. Y.; Schneider, W. F. Comparative Chemistries of CO and NO Oxidation over RuO2(110): Insights from First-Principles Thermodynamics and Kinetics. *Mol. Simul.* **2012**, *38* (8–9), 615–630.

(117) Tang, D. C.; Hwang, K. S.; Salmeron, M.; Somorjai, G. A. High Pressure Scanning Tunneling Microscopy Study of CO Poisoning of Ethylene Hydrogenation on Pt(111) and Rh(111) Single Crystals. *J. Phys. Chem. B* **2004**, *108* (35), 13300–13306.

(118) Suntivich, J.; May, K. J.; Gasteiger, H. A.; Goodenough, J. B.; Shao-Horn, Y. A Perovskite Oxide Optimized for Oxygen Evolution Catalysis from Molecular Orbital Principles. *Science (80-.).* **2011**, *334* (6061), 1383–1385.

(119) Angelinetta, C.; Trasatti, S.; Atanasoska, L. D.; Minevski, Z. S.; Atanasoski, R. T. Effect of Preparation on the Surface and Electrocatalytic Properties of RuO2 + IrO2 Mixed Oxide Electrodes. *Mater. Chem. Phys.* **1989**, *22* (1–2), 231–247.

(120) Yuan, C.; Wu, H. Bin; Xie, Y.; Lou, X. W. Mixed Transition-Metal Oxides: Design, Synthesis, and Energy-Related Applications. *Angew. Chemie - Int. Ed.* **2014**, *53* (6), 1488–1504.

(121) Raghuveer, V.; Ravindranathan Thampi, K.; Xanthopoulos, N.; Mathieu, H. J.; Viswanathan, B. Rare Earth Cuprates as Electrocatalysts for Methanol Oxidation. *Solid State Ionics* **2001**, *140* (3–4), 263–274.

(122) García-Mota, M.; Vojvodic, A.; Metiu, H.; Man, I. C.; Su, H. Y.; Rossmeisl, J.; Nørskov, J. K. Tailoring the Activity for Oxygen Evolution Electrocatalysis on Rutile TiO2(110) by Transition-Metal Substitution. *ChemCatChem* **2011**, *3* (10), 1607–1611.

(123) Velichenko, A. B.; Amadelli, R.; Zucchini, G. L.; Girenko, D. V.; Danilov, F. I. Electrosynthesis and Physicochemical Properties of Fe-Doped Lead Dioxide Electrocatalysts. *Electrochim. Acta* **2000**, *45* (25–26), 4341–4350.

(124) Malkhandi, S.; Yang, B.; Manohar, A. K.; Manivannan, A.; Prakash, G. K. S.; Narayanan, S. R. Electrocatalytic Properties of Nanocrystalline Calcium-Doped Lanthanum Cobalt Oxide for Bifunctional Oxygen Electrodes. *J. Phys. Chem. Lett.* **2012**, *3* (8), 967–972.

(125) Tavares, A. C.; Cartaxo, M. A. M.; Da Silva Pereira, M. I.; Costa, F. M. Effect of the Partial Replacement of Ni or Co by Cu on the Electrocatalytic Activity of the NiCo2O4 Spinel Oxide. *J. Electroanal. Chem.* **1999**, *464* (2), 187–197.

(126) Jacobsen, C. J. H.; Dahl, S.; Clausen, B. S.; Bahn, S.; Logadottir, A.; Nørskov, J. K. Catalyst Design by Interpolation in the Periodic Table: Bimetallic Ammonia Synthesis Catalysts. *J. Am. Chem. Soc.* **2001**, *123* (34), 8404–8405.

(127) Studt, F.; Sharafutdinov, I.; Abild-Pedersen, F.; Elkjær, C. F.; Hummelshøj, J. S.; Dahl,

S.; Chorkendorff, I.; Nørskov, J. K. Discovery of a Ni-Ga Catalyst for Carbon Dioxide Reduction to Methanol. *Nat. Chem.* **2014**, *6* (4), 320–324.

(128) Wachs, I. E.; Routray, K. Catalysis Science of Bulk Mixed Oxides. *ACS Catal.* **2012**, *2* (6), 1235–1246.

(129) Bandarenka, A. S.; Ventosa, E.; Maljusch, A.; Masa, J.; Schuhmann, W. Techniques and Methodologies in Modern Electrocatalysis: Evaluation of Activity, Selectivity and Stability of Catalytic Materials. *Analyst* **2014**, *139* (6), 1274.

(130) Rossmeisl, J.; Qu, Z. W.; Zhu, H.; Kroes, G. J.; Nørskov, J. K. Electrolysis of Water on Oxide Surfaces. *J. Electroanal. Chem.* **2007**, *607* (1–2), 83–89.

(131) Cheng, J.; Zhang, H.; Chen, G.; Zhang, Y. Study of IrxRu1-xO2 Oxides as Anodic Electrocatalysts for Solid Polymer Electrolyte Water Electrolysis. *Electrochim. Acta* **2009**, *54* (26), 6250–6256.

(132) Marshall, A. T.; Haverkamp, R. G. Electrocatalytic Activity of IrO2-RuO2 Supported on Sb-Doped SnO2 Nanoparticles. *Electrochim. Acta* **2010**, *55* (6), 1978–1984.

(133) Lyons, M. E. G.; Floquet, S. Mechanism of Oxygen Reactions at Porous Oxide Electrodes. Part 2--Oxygen Evolution at RuO2, IrO2 and Ir(x)Ru(1-x)O2 Electrodes in Aqueous Acid and Alkaline Solution. *Phys. Chem. Chem. Phys.* **2011**, *13* (12), 5314–5335.

(134) Lee, Y.; Suntivich, J.; May, K. J.; Perry, E. E.; Shao-Horn, Y. Synthesis and Activities of Rutile IrO $_2$ and RuO $_2$ Nanoparticles for Oxygen Evolution in Acid and Alkaline Solutions. *J. Phys. Chem. Lett.* **2012**, No. pH 1, 399–404.

(135) Kötz, R.; Stucki, S. Stabilization of RuO2 by IrO2 for Anodic Oxygen Evolution in Acid Media. *Electrochim. Acta* **1986**, *31* (10), 1311–1316.

(136) Stoerzinger, K. A.; Qiao, L.; Biegalski, M. D.; Shao-Horn, Y. Orientation-Dependent Oxygen Evolution Activities of Rutile IrO2 and RuO2. *J. Phys. Chem. Lett.* **2014**, *5* (10), 1636–1641.

(137) Siahrostami, S.; Vojvodic, A. Influence of Adsorbed Water on the Oxygen Evolution Reaction on Oxides. *J. Phys. Chem. C* **2015**, *119* (2), 1032–1037.

(138) Over, H.; Seitsonen, A. P.; Lundgren, E.; Schmid, M.; Varga, P. Direct Imaging of Catalytically Important Processes in the Oxidation of CO over RuO2(110) [6]. *J. Am. Chem. Soc.* **2001**, *123* (47), 11807–11808.

(139) Lister, T. E.; Tolmachev, Y. V.; Chu, Y.; Cullen, W. G.; You, H.; Yonco, R.; Nagy, Z. Cathodic Activation of RuO2 Single Crystal Surfaces for Hydrogen-Evolution Reaction. *J. Electroanal. Chem.* **2003**, *554–555* (1), 71–76.

(140) Doyle, A. D.; Montoya, J. H.; Vojvodic, A. Improving Oxygen Electrochemistry through Nanoscopic Confinement. *ChemCatChem* **2015**, *7* (5), 738–742.

(141) Toftelund, A.; Man, I. C.; Hansen, H. A.; Abild-Pedersen, F.; Bligaard, T.; Rossmeisl, J.; Studt, F. Volcano Relations for Oxidation of Hydrogen Halides over Rutile Oxide Surfaces. *ChemCatChem* **2012**, *4* (11), 1856–1861.

(142) Torun, E.; Fang, C. M.; De Wijs, G. A.; De Groot, R. A. Role of Magnetism in Catalysis: RuO2 (110) Surface. *J. Phys. Chem. C* **2013**, *117* (12), 6353–6357.

(143) Gutsche, C.; Moeller, C. J.; Knipper, M.; Borchert, H.; Parisi, J.; Plaggenborg, T. Synthesis, Structure, and Electrochemical Stability of Ir-Decorated RuO2 Nanoparticles and Pt Nanorods as Oxygen Catalysts. *J. Phys. Chem. C* **2016**, *120* (2), 1137–1146.

(144) Wang, J.; Fan, C. Y.; Jacobi, K.; Ertl, G. Adsorption and Reaction of CO on RuO2(110) Surfaces. *Surf. Sci.* **2001**, *481* (1–3), 113–118.

(145) Karlsson, R. K. B.; Cornell, A.; Pettersson, L. G. M. Structural Changes in RuO 2 during Electrochemical Hydrogen Evolution. *J. Phys. Chem. C* **2016**, *120* (13), 7094–7102.

(146) Xu, J. H.; Jarlborg, T.; Freeman, A. J. Self-Consistent Band Structure of the Rutile Dioxides NbO2, RuO2, and IrO2. *Phys. Rev. B* **1989**, *40* (11), 7939–7947.

(147) Butler, S. R.; Gillson, J. L. Crystal Growth, Electrical Resistivity and Lattice Parameters of RuO2 and IrO2. *Mater. Res. Bull.* **1971**, *6* (2), 81–89.

(148) María Escudero-Escribano, 1, 2* Paolo Malacrida, 1 Martin H. Hansen, 3, 4 Ulrik G. Vej-Hansen, 1, 3 Amado Velázquez-Palenzuela, 1 Vladimir Tripkovic, 3, 5 Jakob Schiøtz, 1, 3 Jan Rossmeisl, 3, 4 Ifan E. L. Stephens, 1, 6* Ib Chorkendorff1. Tuning the Activity of Pt Alloy Electrocatalysts by Means of the Lanthanide Contraction. *Science (80-.).* **2016**, *352* (6281), 73–76.

(149) Wang, H.; Xu, S.; Tsai, C.; Li, Y.; Liu, C.; Zhao, J.; Liu, Y.; Yuan, H.; Abild-pedersen, F.; Prinz, F. B.; et al. Direct and Continuous Strain Control of Catalysts with Tunable Battery Electrode Materials. *Science (80-.).* **2016**, *354* (6315), 1031–1036.

(150) Balko, E. N.; Davidson, C. R. Solid Solutions of RuO2 and IrO2. *J. Inorg. Nucl. Chem.* **1980**, *42* (12), 1778–1781.

(151) Wanjala, B. N.; Luo, J.; Loukrakpam, R.; Fang, B.; Mott, D.; Njoki, P. N.; Engelhard, M.; Naslund, H. R.; Wu, J. K.; Wang, L.; et al. Nanoscale Alloying, Phase-Segregation, and Core-Shell Evolution of Gold-Platinum Nanoparticles and Their Electrocatalytic Effect on Oxygen Reduction Reaction. *Chem. Mater.* **2010**, *22* (14), 4282–4294.

(152) Liao, H.; Fisher, A.; Xu, Z. J. Surface Segregation in Bimetallic Nanoparticles: A Critical Issue in Electrocatalyst Engineering. *Small* **2015**, *11* (27), 3221–3246.

(153) Tang, X.; Li, Y.; Huang, X.; Xu, Y.; Zhu, H.; Wang, J.; Shen, W. MnOx-CeO2 Mixed Oxide Catalysts for Complete Oxidation of Formaldehyde: Effect of Preparation Method and Calcination Temperature. *Appl. Catal. B Environ.* **2006**, *62* (3–4), 265–273.

(154) Di Cosimo, J. I.; Díez, V. K.; Xu, M.; Iglesia, E.; Apesteguía, C. R. Structure and Surface and Catalytic Properties of Mg-Al Basic Oxides. *J. Catal.* **1998**, *178* (2), 499–510.

(155) Schoeb, A. M.; Raeker, T. J.; Yang, L.; Wu, X.; King, T. S.; Depristo, A. E. Driving Force for Surface Segregation in Bimetallic Catalysts. **1992**, *278*, 2–7.

(156) Christoffersen, E.; Liu, P.; Ruban, A.; Skriver, H. .; Nørskov, J. . Anode Materials for Low-Temperature Fuel Cells: A Density Functional Theory Study. *J. Catal.* **2001**, *199* (1), 123–131.

(157) Kim, H. Y.; Lee, H. M.; Pala, R. G. S.; Shapovalov, V.; Metiu, H. CO Oxidation by Rutile TiO2(110) Doped with V, W, Cr, Mo, and Mn. *J. Phys. Chem. C* **2008**, *112* (32), 12398–12408.

(158) He, H.; Zapol, P.; Curtiss, L. a. Computational Screening of Dopants for Photocatalytic Two-Electron Reduction of CO2 on Anatase (101) Surfaces. *Energy Environ. Sci.* **2012**, *5* (3), 6196.

(159) Zafeiratos, S.; Piccinin, S.; Teschner, D. Alloys in Catalysis: Phase Separation and Surface Segregation Phenomena in Response to the Reactive Environment. *Catal. Sci. Technol.* **2012**, *2* (9), 1787.

(160) Hoffmannová, H.; Okube, M.; Petrykin, V.; Krtil, P.; Mueller, J. E.; Jacob, T. Surface Stability of Pt3Ni Nanoparticulate Alloy Electrocatalysts in Hydrogen Adsorption. *Langmuir* **2013**, *29* (29), 9046–9050.

(161) Mayrhofer, K. J. J.; Juhart, V.; Hartl, K.; Hanzlik, M.; Arenz, M. Adsorbate-Induced Surface Segregation for Core-Shell Nanocatalysts. *Angew. Chemie - Int. Ed.* **2009**, *48* (19), 3529–3531.

(162) Shi, C.; O'Grady, C. P.; Peterson, A. a; Hansen, H. a; Nørskov, J. K. Modeling CO2 Reduction on Pt(111). *Phys. Chem. Chem. Phys.* **2013**, *15* (19), 7114–7122.

(163) Back, S.; Kim, J.-H.; Kim, Y.-T.; Jung, Y. On the Mechanism of High Product Selectivity for HCOOH Using Pb in CO $_2$ Electroreduction. *Phys. Chem. Chem. Phys.* **2016**, *18* (14), 9652–9657.

(164) Bhowmik, A.; Vegge, T.; Hansen, H. A. Descriptors and Thermodynamic Limitations of Electrocatalytic Carbon Dioxide Reduction on Rutile Oxide Surfaces. *ChemSusChem*

2016, *9* (22), 3230–3243.
(165) Bhowmik, A.; Hansen, H. A.; Vegge, P. T. The Role of CO* as a Spectator in CO2 Electro-Reduction on RuO2. 1–29.
(166) Jovanov, Z. P.; Hansen, H. A.; Varela, A. S.; Malacrida, P.; Peterson, A. A.; N??rskov, J. K.; Stephens, I. E. L.; Chorkendorff, I. Opportunities and Challenges in the Electrocatalysis of CO2 and CO Reduction Using Bifunctional Surfaces: A Theoretical and Experimental Study of Au???Cd Alloys. *J. Catal.* **2016**, *343*, 215–231.
(167) Lee, Y.-L.; Kleis, J.; Rossmeisl, J.; Shao-Horn, Y.; Morgan, D. Prediction of Solid Oxide Fuel Cell Cathode Activity with First-Principles Descriptors. *Energy Environ. Sci.* **2011**, *4* (10), 3966.
(168) Han, B.; Risch, M.; Lee, Y.-L.; Ling, C.; Jia, H.; Shao-Horn, Y. Activity and Stability Trends of Perovskite Oxides for Oxygen Evolution Catalysis at Neutral pH. *Phys. Chem. Chem. Phys.* **2015**, *17* (35), 22576–22580.
(169) Suntivich, J.; May, K. J.; Gasteiger, H. A.; Goodenough, J. B.; Shao-Horn, Y. A Perovskite Oxide Optimized for Oxygen Evolution Catalysis from Molecular Orbital Principles. *Science (80-.).* **2011**, *334* (6061), 1383–1385.
(170) Calle-Vallejo, F.; Inoglu, N. G.; Su, H.-Y.; Martínez, J. I.; Man, I. C.; Koper, M. T. M.; Kitchin, J. R.; Rossmeisl, J. Number of Outer Electrons as Descriptor for Adsorption Processes on Transition Metals and Their Oxides. *Chem. Sci.* **2013**, *4* (3), 1245.
(171) Mattheiss, L. Electronic Structure of RuO_{2}, OsO_{2}, and IrO_{2}. *Phys. Rev. B* **1976**, *13* (6), 2433–2450.
(172) Daniels, R. R.; Margaritondo, G.; Georg, C. A.; Lévy, F. Electronic States of Rutile Dioxides: RuO2, IrO2, and RuxIr1-xO2. *Phys. Rev. B* **1984**, *29* (4), 1813–1818.
(173) Tang, W.; Sanville, E.; Henkelman, G. A Grid-Based Bader Analysis Algorithm without Lattice Bias. *J. Phys. Condens. Matter* **2009**, *21* (8), 84204.
(174) Kim, Y. D.; Seitsonen, A. P.; Over, H. Adsorption Characteristics of CO and N2 on RuO2 (110). *Phys. Rev. B* **2001**, *63* (11), 115419.
(175) Ping, Y.; Galli, G.; Goddard, W. A. Electronic Structure of IrO $_2$: The Role of the Metal D Orbitals. *J. Phys. Chem. C* **2015**, *119* (21), 11570–11577.
(176) Schouten, K. J. P.; Kwon, Y.; van der Ham, C. J. M.; Qin, Z.; Koper, M. T. M. A New Mechanism for the Selectivity to C1 and C2 Species in the Electrochemical Reduction of Carbon Dioxide on Copper Electrodes. *Chem. Sci.* **2011**, *2* (10), 1902.
(177) Montoya, J. H.; Shi, C.; Chan, K.; Nørskov, J. K. Theoretical Insights into a CO Dimerization Mechanism in CO2 Electroreduction. *J. Phys. Chem. Lett.* **2015**, *6* (11), 2032–2037.
(178) Montoya, J. H.; Peterson, A. A.; Nørskov, J. K. Insights into C-C Coupling in CO2 Electroreduction on Copper Electrodes. *ChemCatChem* **2013**, *5* (3), 737–742.
(179) Goodpaster, J. D.; Bell, A. T.; Head-Gordon, M. Identification of Possible Pathways for C-C Bond Formation during Electrochemical Reduction of CO2: New Theoretical Insights from an Improved Electrochemical Model. *J. Phys. Chem. Lett.* **2016**, *7* (8), 1471–1477.

Appendix

Free energy plot of reaction intermediates and products from CO2RR on Ru/Ir mixed oxide surfaces with 0%, 25%, 50% CO* coverage.

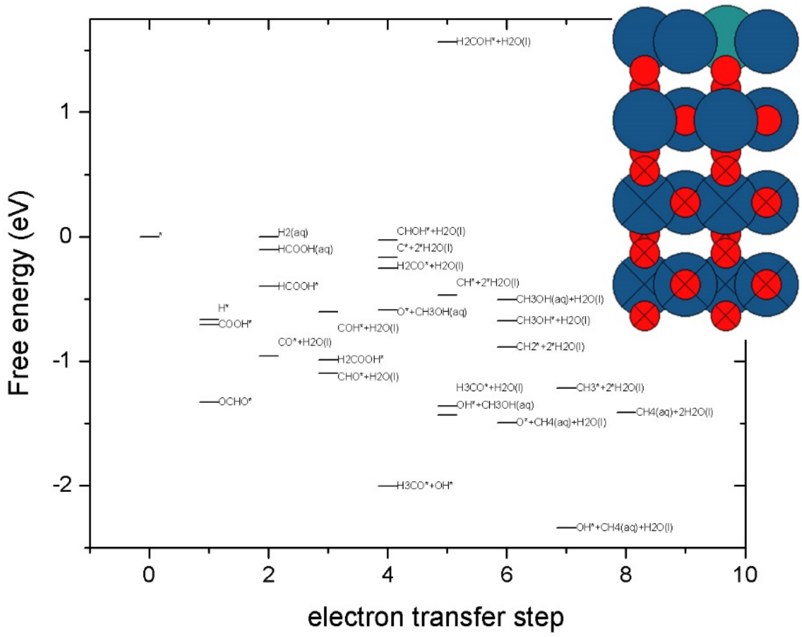

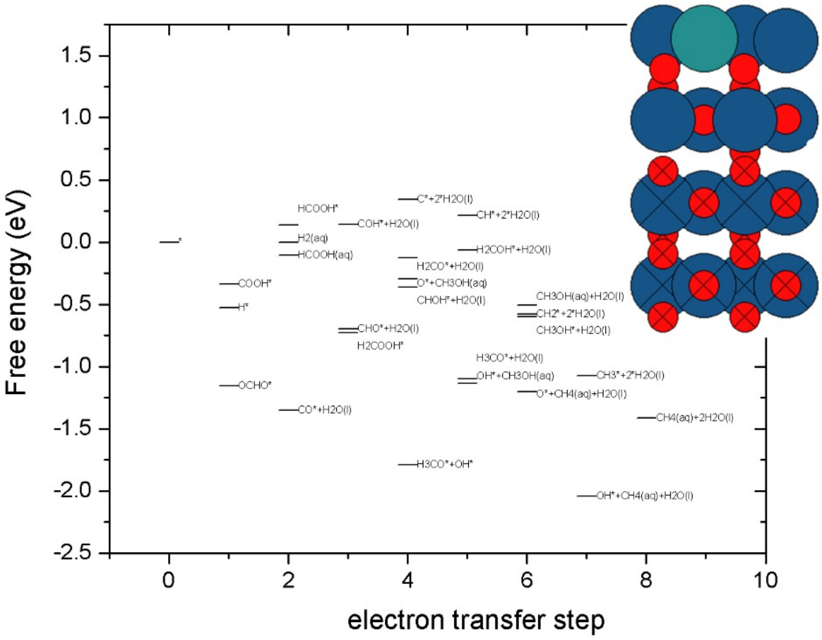

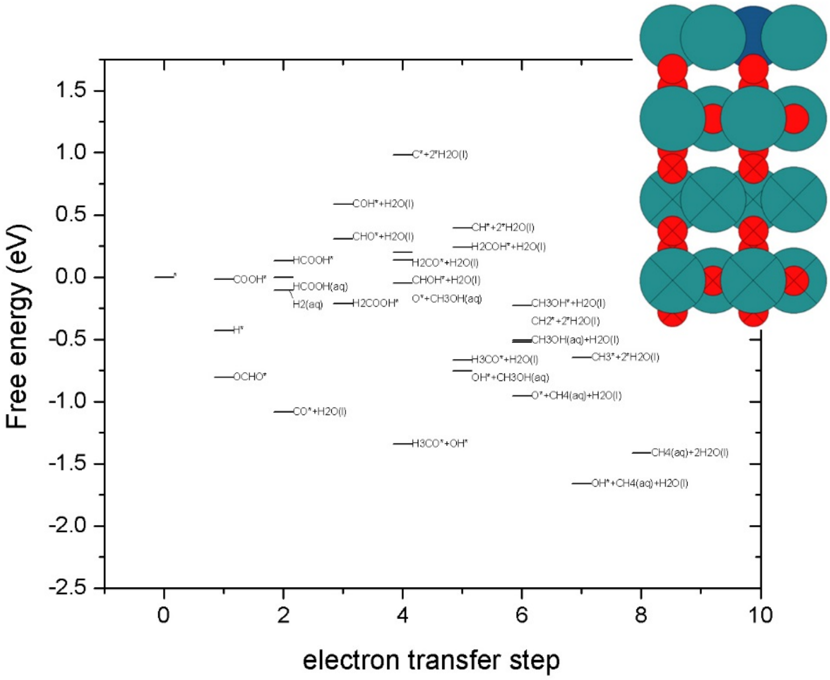
Free energy (eV)
1.5
1.0
0.5
0.0
-0.5
-1.0
-1.5
-2.0
-2.5
electron transfer step
0
2
4
6
8
10
*
COOH*
H*
OCHO*
HCOOH*
HCOOH(aq)
H2(aq)
CO*+H2O(l)
COH*+H2O(l)
CHO*+H2O(l)
H2COOH*
C*+2*H2O(l)
H2CO*+H2O(l)
CHOH*+H2O(l)
O*+CH3OH(aq)
H3CO*+OH*
CH*+2*H2O(l)
H2COH*+H2O(l)
H3CO*+H2O(l)
OH*+CH3OH(aq)
CH3OH*+H2O(l)
CH2*+2*H2O(l)
CH3OH(aq)+H2O(l)
O*+CH4(aq)+H2O(l)
CH3*+2*H2O(l)
OH*+CH4(aq)+H2O(l)
CH4(aq)+2H2O(l)

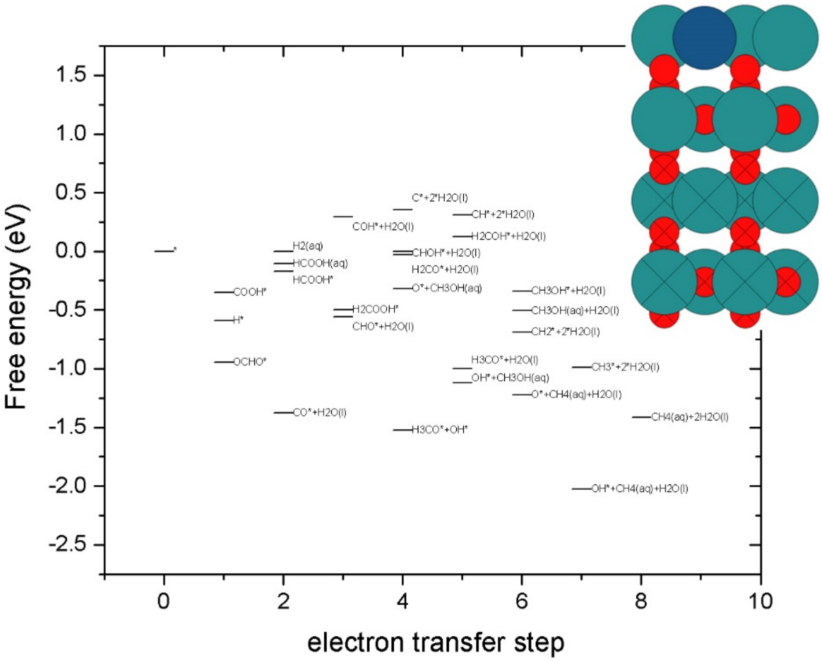
Free energy (eV)
1.5
1.0
0.5
0.0
-0.5
-1.0
-1.5
-2.0
-2.5
electron transfer step
0
2
4
6
8
10
*
COOH*
H*
OCHO*
H2(aq)
HCOOH(aq)
HCOOH*
CO*+H2O(l)
COH*+H2O(l)
H2COOH*
CHO*+H2O(l)
C*+2*H2O(l)
CHOH*+H2O(l)
H2CO*+H2O(l)
O*+CH3OH(aq)
H3CO*+OH*
CH*+2*H2O(l)
H2COH*+H2O(l)
H3CO*+H2O(l)
OH*+CH3OH(aq)
CH3OH*+H2O(l)
CH3OH(aq)+H2O(l)
CH2*+2*H2O(l)
O*+CH4(aq)+H2O(l)
CH3*+2*H2O(l)
OH*+CH4(aq)+H2O(l)
CH4(aq)+2H2O(l)

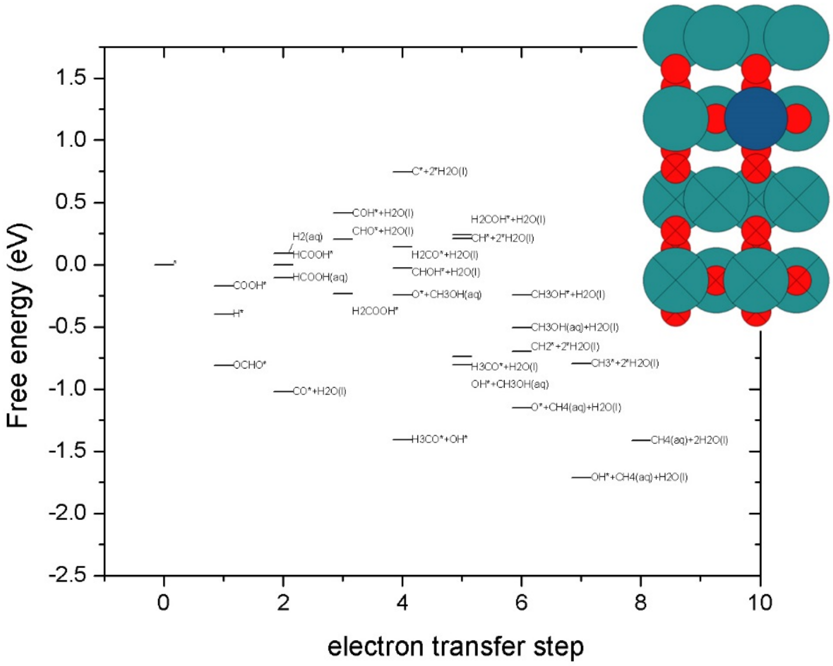
Free energy (eV)
1.5
1.0
0.5
0.0
-0.5
-1.0
-1.5
-2.0
-2.5
0
2
4
6
8
10
electron transfer step
*
COOH*
H*
OCHO*
H2(aq)
HCOOH*
HCOOH(aq)
CO*+H2O(l)
COH*+H2O(l)
CHO*+H2O(l)
H2COOH*
C*+2*H2O(l)
H2CO*+H2O(l)
CHOH*+H2O(l)
O*+CH3OH(aq)
H3CO*+OH*
H2COH*+H2O(l)
CH*+2*H2O(l)
H3CO*+H2O(l)
OH*+CH3OH(aq)
CH3OH*+H2O(l)
CH3OH(aq)+H2O(l)
CH2*+2*H2O(l)
O*+CH4(aq)+H2O(l)
CH3*+2*H2O(l)
OH*+CH4(aq)+H2O(l)
CH4(aq)+2H2O(l)

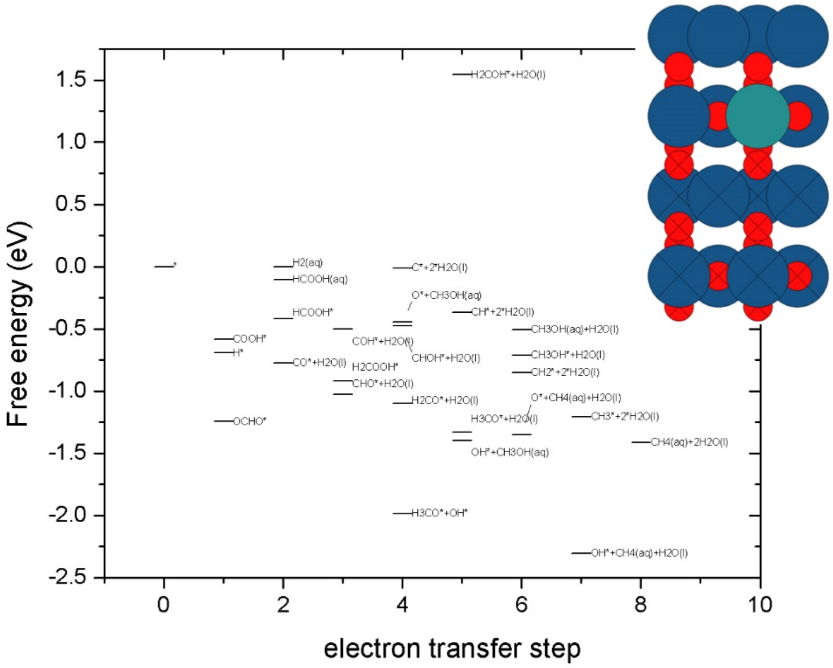
Free energy (eV)
1.5
1.0
0.5
0.0
-0.5
-1.0
-1.5
-2.0
-2.5
0
2
4
6
8
10
electron transfer step
*
COOH*
H*
OCHO*
H2(aq)
HCOOH(aq)
HCOOH*
CO*+H2O(l)
COH*+H2O(l)
H2COOH*
CHO*+H2O(l)
C*+2*H2O(l)
O*+CH3OH(aq)
CHOH*+H2O(l)
H2CO*+H2O(l)
H3CO*+OH*
H2COH*+H2O(l)
CH*+2*H2O(l)
H3CO*+H2O(l)
OH*+CH3OH(aq)
CH3OH(aq)+H2O(l)
CH3OH*+H2O(l)
CH2*+2*H2O(l)
O*+CH4(aq)+H2O(l)
CH3*+2*H2O(l)
OH*+CH4(aq)+H2O(l)
CH4(aq)+2H2O(l)

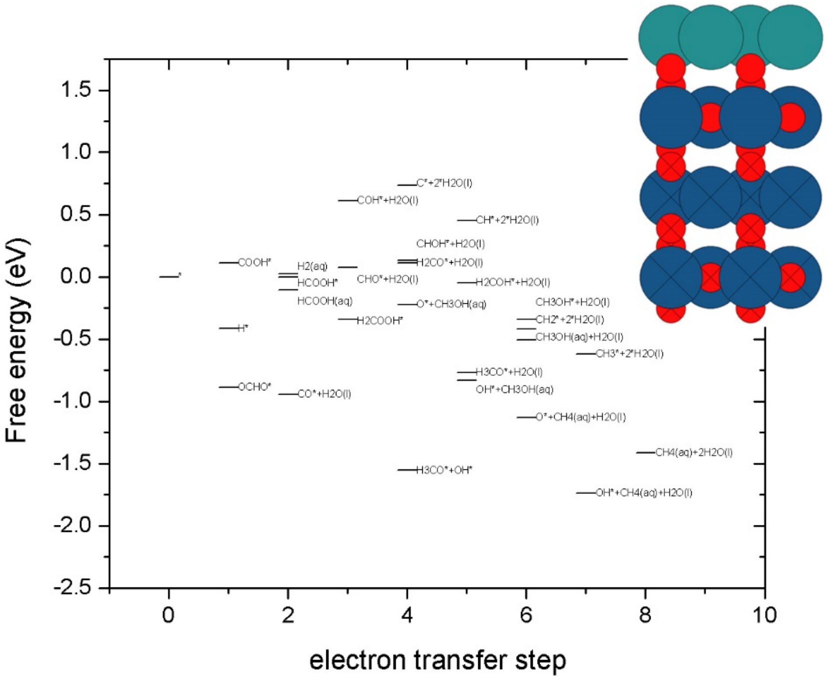
Free energy (eV)
1.5
1.0
0.5
0.0
-0.5
-1.0
-1.5
-2.0
-2.5
0
2
4
6
8
10
electron transfer step
*
COOH*
H*
OCHO*
H2(aq)
HCOOH*
HCOOH(aq)
CO*+H2O(l)
COH*+H2O(l)
CHO*+H2O(l)
H2COOH*
C*+2*H2O(l)
CHOH*+H2O(l)
H2CO*+H2O(l)
O*+CH3OH(aq)
H3CO*+OH*
CH*+2*H2O(l)
H2COH*+H2O(l)
H3CO*+H2O(l)
OH*+CH3OH(aq)
CH3OH*+H2O(l)
CH2*+2*H2O(l)
CH3OH(aq)+H2O(l)
O*+CH4(aq)+H2O(l)
CH3*+2*H2O(l)
OH*+CH4(aq)+H2O(l)
CH4(aq)+2H2O(l)

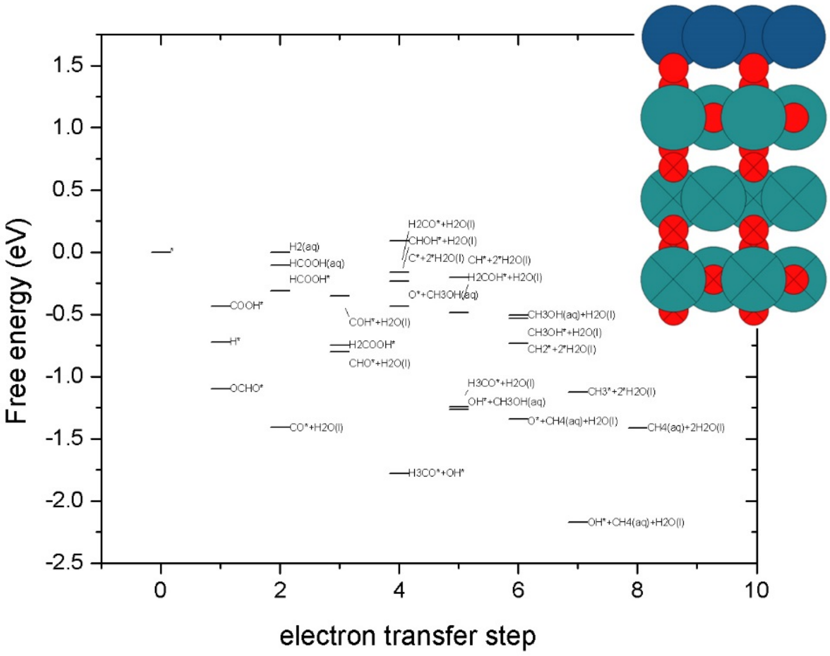
Free energy (eV)
1.5
1.0
0.5
0.0
-0.5
-1.0
-1.5
-2.0
-2.5
0
2
4
6
8
10
electron transfer step
*
COOH*
H*
OCHO*
H2(aq)
HCOOH(aq)
HCOOH*
CO*+H2O(l)
COH*+H2O(l)
H2COOH*
CHO*+H2O(l)
H2CO*+H2O(l)
CHOH*+H2O(l)
C*+2*H2O(l)
O*+CH3OH(aq)
H3CO*+OH*
CH*+2*H2O(l)
H2COH*+H2O(l)
H3CO*+H2O(l)
OH*+CH3OH(aq)
CH3OH(aq)+H2O(l)
CH3OH*+H2O(l)
CH2*+2*H2O(l)
O*+CH4(aq)+H2O(l)
CH3*+2*H2O(l)
OH*+CH4(aq)+H2O(l)
CH4(aq)+2H2O(l)

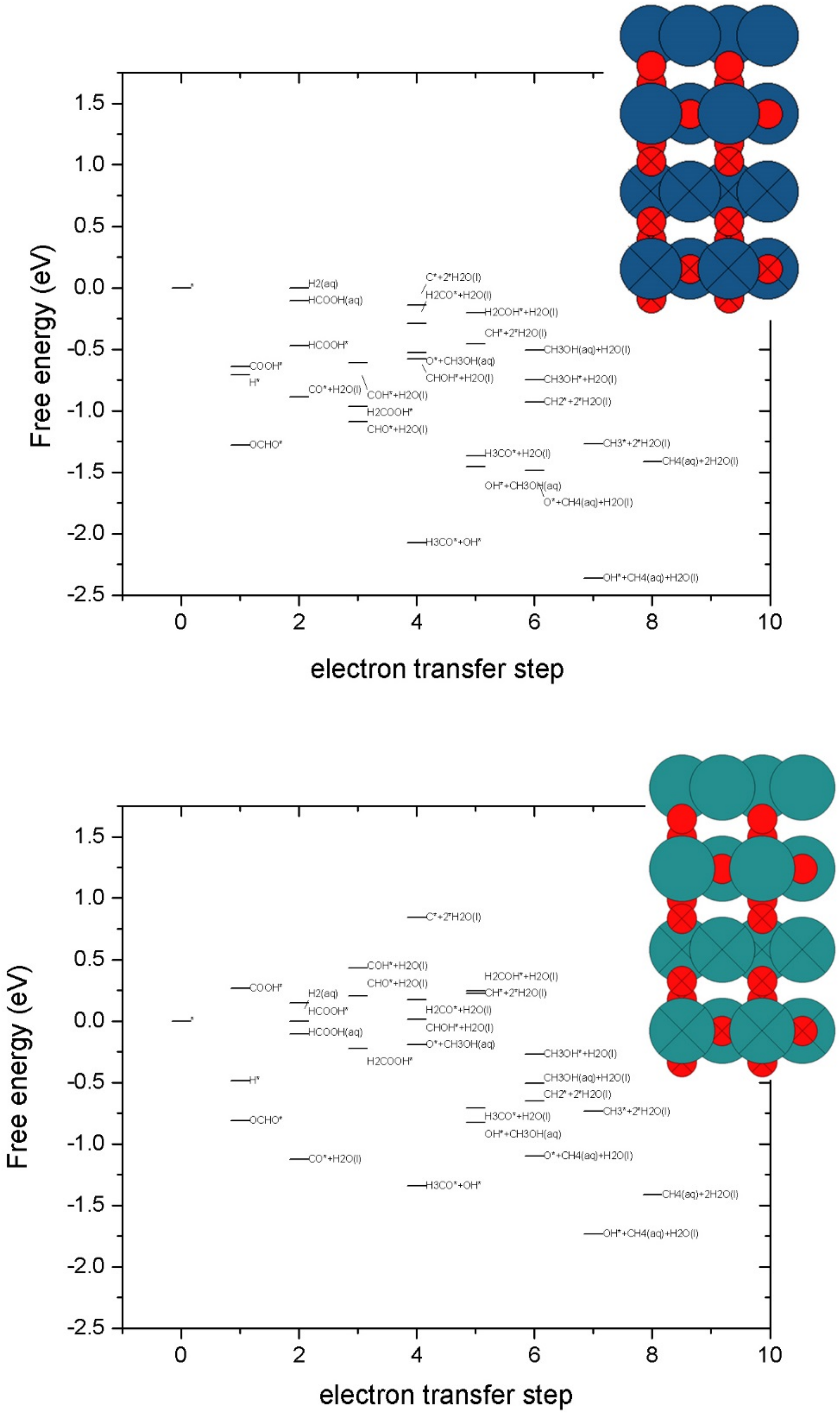

Figure S0-1: free energy of reaction intermediates and products with reference to CO_2, H_2 and H_2O at 0 V-RHE on all 10 surfaces models with no CO coverage*

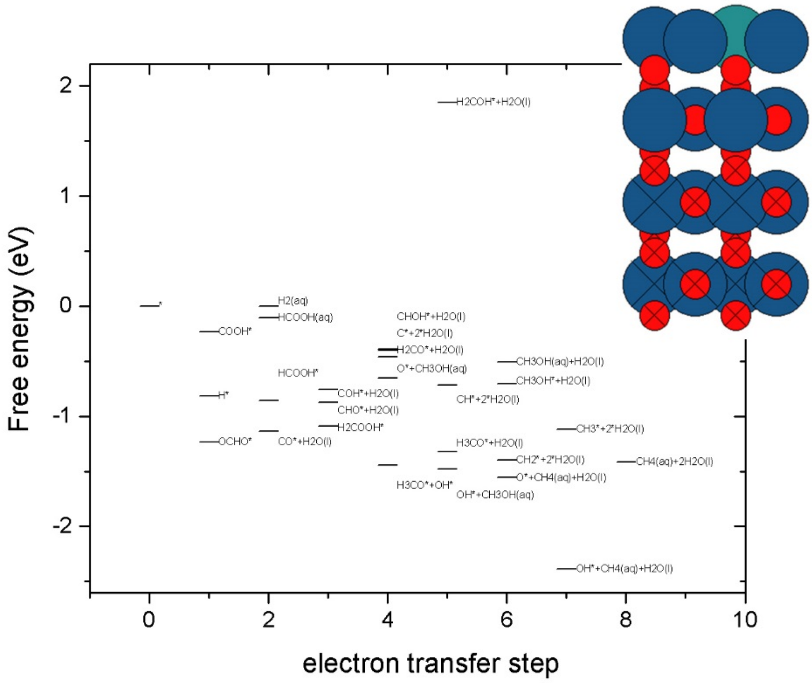
Free energy (eV)
2
1
0
-1
-2
electron transfer step
0
2
4
6
8
10
*
COOH*
H*
OCHO*
H2(aq)
HCOOH(aq)
HCOOH*
CO*+H2O(l)
COH*+H2O(l)
CHO*+H2O(l)
H2COOH*
CHOH*+H2O(l)
C*+2*H2O(l)
H2CO*+H2O(l)
O*+CH3OH(aq)
H3CO*+OH*
H2COH*+H2O(l)
CH*+2*H2O(l)
H3CO*+H2O(l)
OH*+CH3OH(aq)
CH3OH(aq)+H2O(l)
CH3OH*+H2O(l)
CH2*+2*H2O(l)
O*+CH4(aq)+H2O(l)
CH3*+2*H2O(l)
OH*+CH4(aq)+H2O(l)
CH4(aq)+2H2O(l)

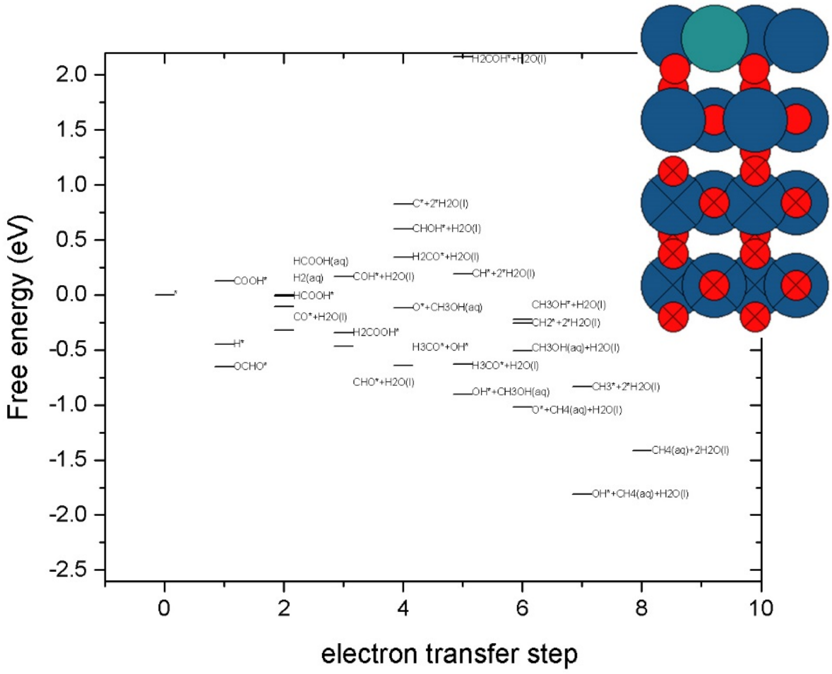
Free energy (eV)
2.0
1.5
1.0
0.5
0.0
-0.5
-1.0
-1.5
-2.0
-2.5
electron transfer step
0
2
4
6
8
10
*
COOH*
H*
OCHO*
HCOOH(aq)
H2(aq)
HCOOH*
CO*+H2O(l)
COH*+H2O(l)
H2COOH*
CHO*+H2O(l)
C*+2*H2O(l)
CHOH*+H2O(l)
H2CO*+H2O(l)
O*+CH3OH(aq)
H3CO*+OH*
H2COH*+H2O(l)
CH*+2*H2O(l)
H3CO*+H2O(l)
OH*+CH3OH(aq)
CH3OH*+H2O(l)
CH2*+2*H2O(l)
CH3OH(aq)+H2O(l)
O*+CH4(aq)+H2O(l)
CH3*+2*H2O(l)
OH*+CH4(aq)+H2O(l)
CH4(aq)+2H2O(l)

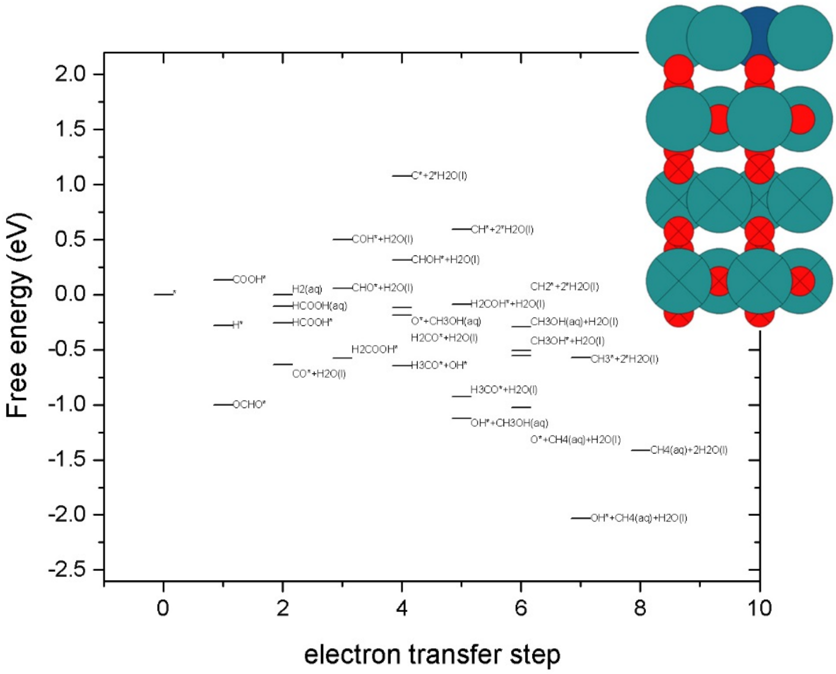
Free energy (eV)
2.0
1.5
1.0
0.5
0.0
-0.5
-1.0
-1.5
-2.0
-2.5
0
2
4
6
8
10
electron transfer step
*
COOH*
H*
OCHO*
H2(aq)
HCOOH(aq)
HCOOH*
CO*+H2O(l)
COH*+H2O(l)
CHO*+H2O(l)
H2COOH*
C*+2*H2O(l)
CHOH*+H2O(l)
O*+CH3OH(aq)
H2CO*+H2O(l)
H3CO*+OH*
CH*+2*H2O(l)
H2COH*+H2O(l)
H3CO*+H2O(l)
OH*+CH3OH(aq)
CH2*+2*H2O(l)
CH3OH(aq)+H2O(l)
CH3OH*+H2O(l)
O*+CH4(aq)+H2O(l)
CH3*+2*H2O(l)
OH*+CH4(aq)+H2O(l)
CH4(aq)+2H2O(l)

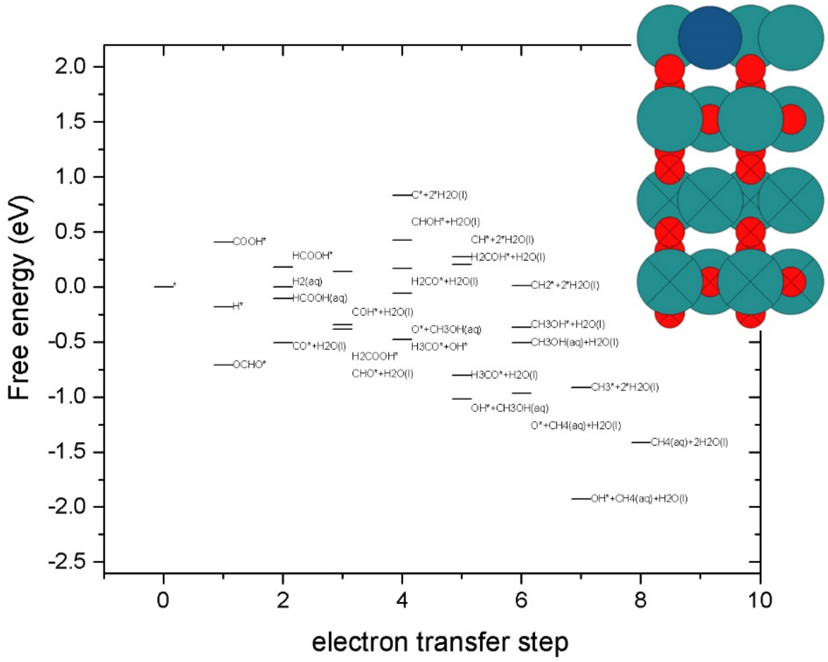
Free energy (eV)
2.0
1.5
1.0
0.5
0.0
-0.5
-1.0
-1.5
-2.0
-2.5
0
2
4
6
8
10
electron transfer step
*
COOH*
H*
OCHO*
HCOOH*
H2(aq)
HCOOH(aq)
CO*+H2O(l)
COH*+H2O(l)
H2COOH*
CHO*+H2O(l)
C*+2*H2O(l)
CHOH*+H2O(l)
H2CO*+H2O(l)
O*+CH3OH(aq)
H3CO*+OH*
CH*+2*H2O(l)
H2COH*+H2O(l)
H3CO*+H2O(l)
OH*+CH3OH(aq)
CH2*+2*H2O(l)
CH3OH*+H2O(l)
CH3OH(aq)+H2O(l)
O*+CH4(aq)+H2O(l)
CH3*+2*H2O(l)
CH4(aq)+2H2O(l)
OH*+CH4(aq)+H2O(l)

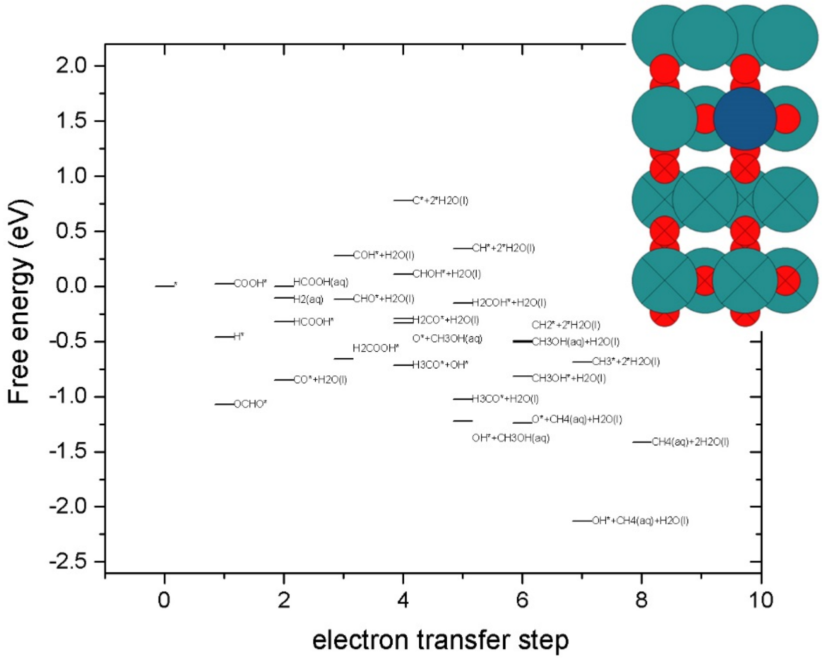
Free energy (eV)
2.0
1.5
1.0
0.5
0.0
-0.5
-1.0
-1.5
-2.0
-2.5
0
2
4
6
8
10
electron transfer step
*
COOH*
H*
OCHO*
HCOOH(aq)
H2(aq)
HCOOH*
CO*+H2O(l)
COH*+H2O(l)
CHO*+H2O(l)
H2COOH*
C*+2*H2O(l)
CHOH*+H2O(l)
H2CO*+H2O(l)
O*+CH3OH(aq)
H3CO*+OH*
CH*+2*H2O(l)
H2COH*+H2O(l)
H3CO*+H2O(l)
OH*+CH3OH(aq)
CH2*+2*H2O(l)
CH3OH(aq)+H2O(l)
CH3OH*+H2O(l)
O*+CH4(aq)+H2O(l)
CH3*+2*H2O(l)
OH*+CH4(aq)+H2O(l)
CH4(aq)+2H2O(l)

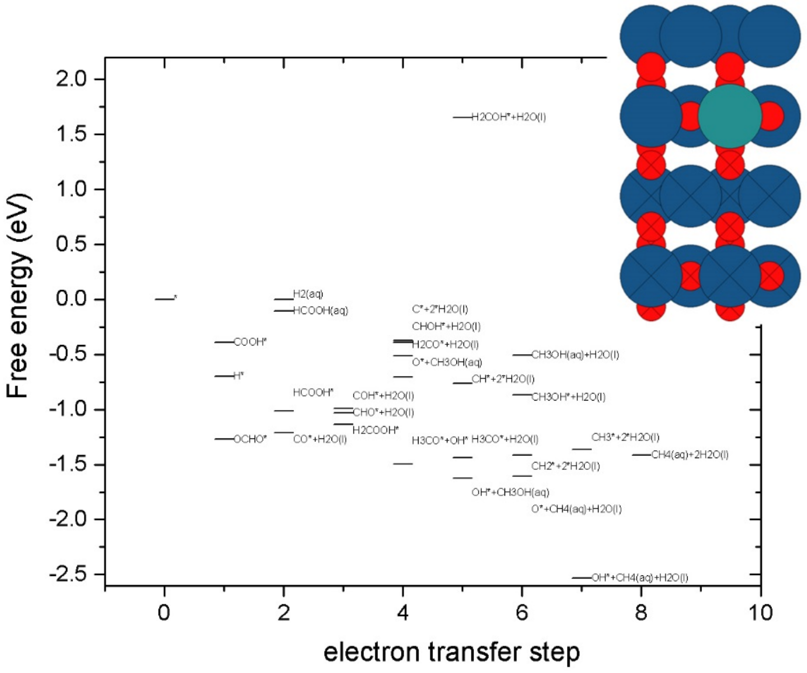
Free energy (eV)
2.0
1.5
1.0
0.5
0.0
-0.5
-1.0
-1.5
-2.0
-2.5
0
2
4
6
8
10
electron transfer step
H2COH*+H2O(l)
*
H2(aq)
HCOOH(aq)
COOH*
H*
HCOOH*
OCHO*
CO*+H2O(l)
COH*+H2O(l)
CHO*+H2O(l)
H2COOH*
C*+2*H2O(l)
CHOH*+H2O(l)
H2CO*+H2O(l)
O*+CH3OH(aq)
H3CO*+OH*
CH*+2*H2O(l)
H3CO*+H2O(l)
OH*+CH3OH(aq)
CH3OH(aq)+H2O(l)
CH3OH*+H2O(l)
CH2*+2*H2O(l)
O*+CH4(aq)+H2O(l)
CH3*+2*H2O(l)
CH4(aq)+2H2O(l)
OH*+CH4(aq)+H2O(l)

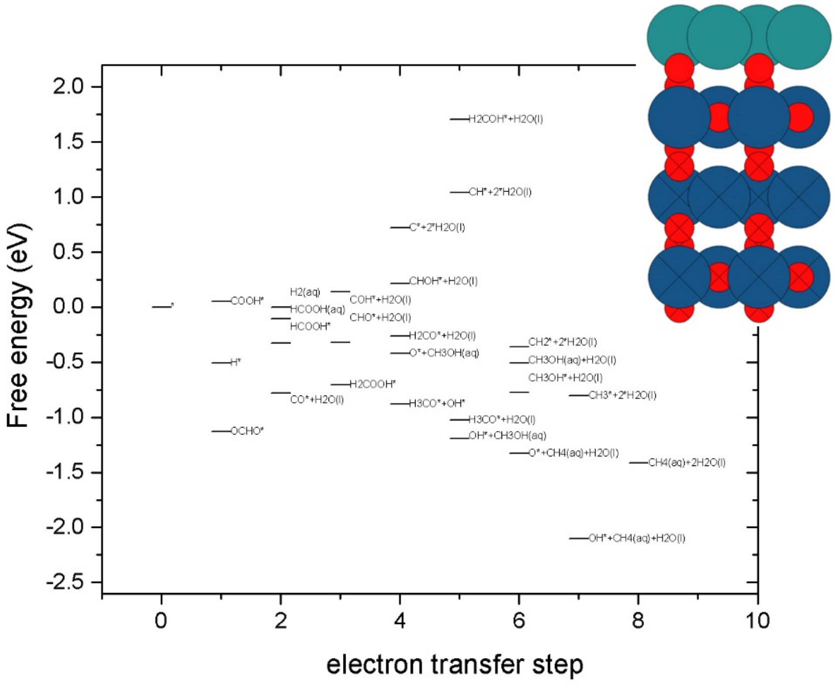
2.0
1.5
1.0
0.5
0.0
-0.5
-1.0
-1.5
-2.0
-2.5
Free energy (eV)
0
2
4
6
8
10
electron transfer step
H2COH*+H2O(l)
CH*+2*H2O(l)
C*+2*H2O(l)
CHOH*+H2O(l)
*
COOH*
H2(aq)
HCOOH(aq)
HCOOH*
COH*+H2O(l)
CHO*+H2O(l)
H2CO*+H2O(l)
O*+CH3OH(aq)
CH2*+2*H2O(l)
CH3OH(aq)+H2O(l)
CH3OH*+H2O(l)
H*
H2COOH*
CO*+H2O(l)
CH3*+2*H2O(l)
H3CO*+OH*
H3CO*+H2O(l)
OCHO*
OH*+CH3OH(aq)
O*+CH4(aq)+H2O(l)
CH4(aq)+2H2O(l)
OH*+CH4(aq)+H2O(l)

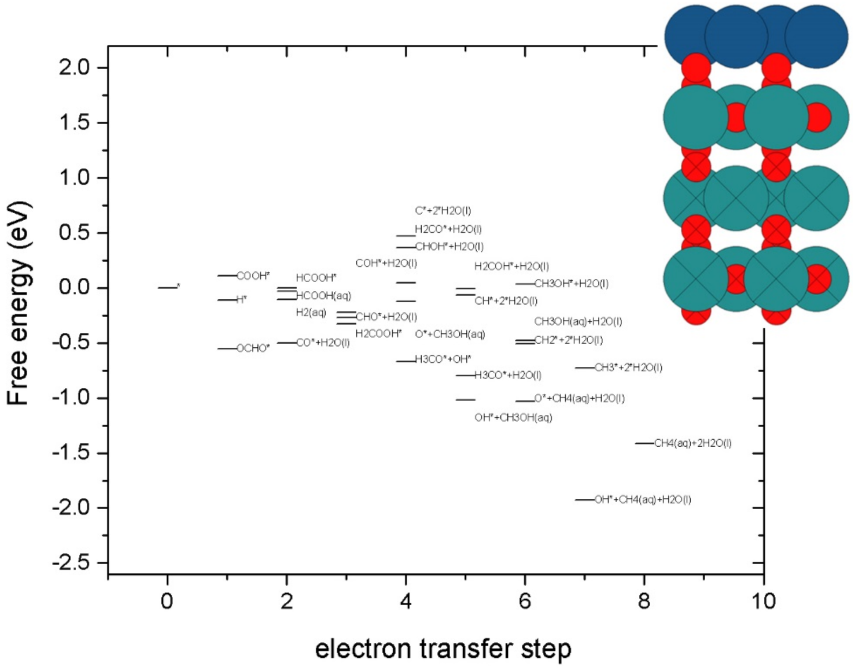
2.0
1.5
1.0
0.5
0.0
-0.5
-1.0
-1.5
-2.0
-2.5
Free energy (eV)
0
2
4
6
8
10
electron transfer step
C*+2*H2O(l)
H2CO*+H2O(l)
CHOH*+H2O(l)
COH*+H2O(l)
H2COH*+H2O(l)
COOH*
HCOOH*
*
CH3OH*+H2O(l)
HCOOH(aq)
H*
CH*+2*H2O(l)
H2(aq)
CHO*+H2O(l)
CH3OH(aq)+H2O(l)
H2COOH*
O*+CH3OH(aq)
CO*+H2O(l)
CH2*+2*H2O(l)
OCHO*
H3CO*+OH*
CH3*+2*H2O(l)
H3CO*+H2O(l)
O*+CH4(aq)+H2O(l)
OH*+CH3OH(aq)
CH4(aq)+2H2O(l)
OH*+CH4(aq)+H2O(l)

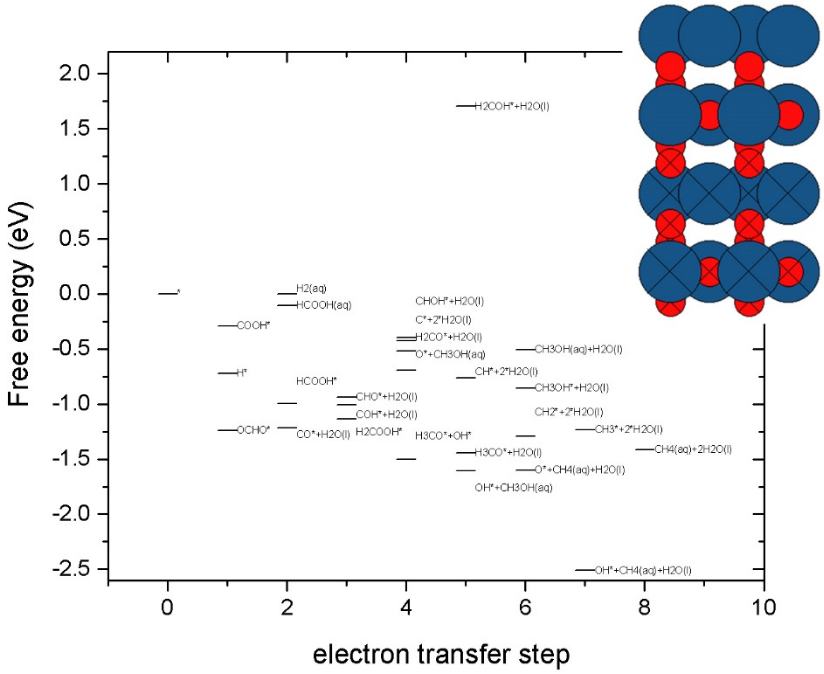

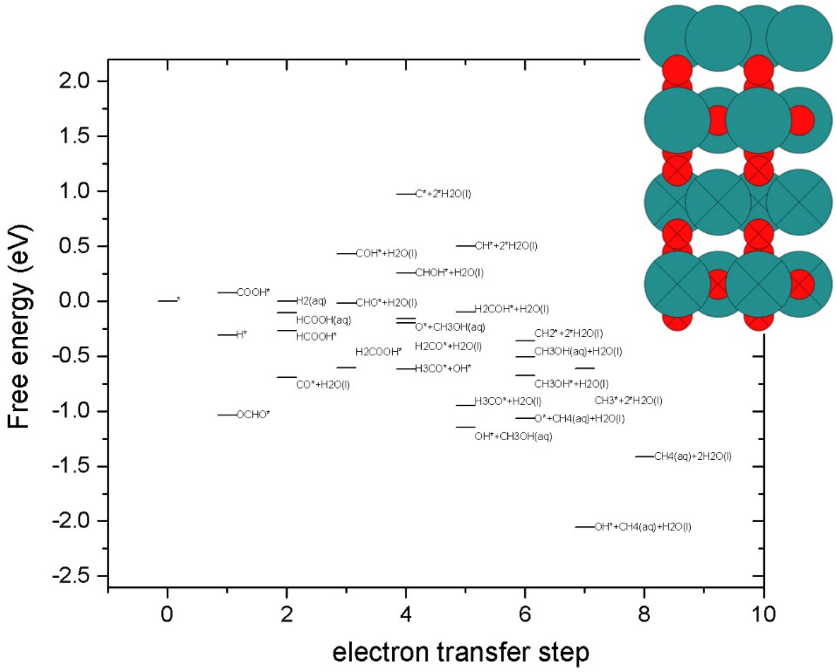

Figure S0-2: free energy of reaction intermediates and products with reference to CO_2, H_2 and H_2O at 0 V-RHE on all 10 surfaces models with 25% CO coverage*

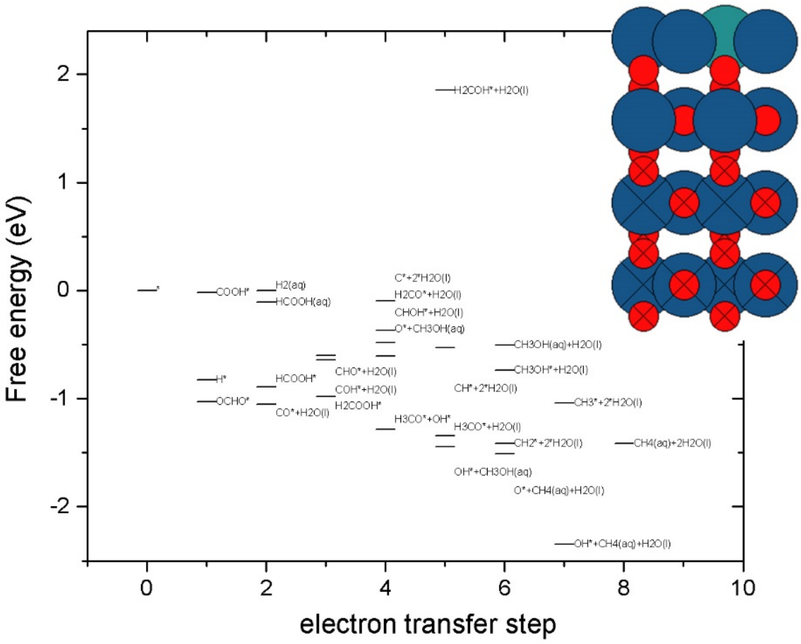
Free energy (eV)
2
1
0
-1
-2
electron transfer step
0
2
4
6
8
10
*
COOH*
H2(aq)
HCOOH(aq)
H*
OCHO*
HCOOH*
CO*+H2O(l)
CHO*+H2O(l)
COH*+H2O(l)
H2COOH*
H2COH*+H2O(l)
C*+2*H2O(l)
H2CO*+H2O(l)
CHOH*+H2O(l)
O*+CH3OH(aq)
H3CO*+OH*
CH*+2*H2O(l)
H3CO*+H2O(l)
OH*+CH3OH(aq)
CH3OH(aq)+H2O(l)
CH3OH*+H2O(l)
CH2*+2*H2O(l)
O*+CH4(aq)+H2O(l)
CH3*+2*H2O(l)
OH*+CH4(aq)+H2O(l)
CH4(aq)+2H2O(l)

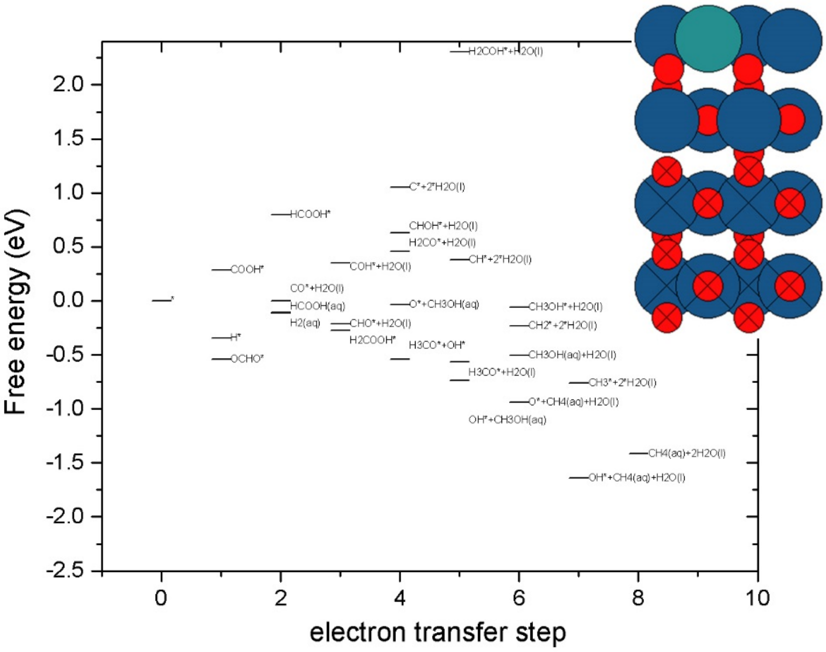
Free energy (eV)
2.0
1.5
1.0
0.5
0.0
-0.5
-1.0
-1.5
-2.0
-2.5
electron transfer step
0
2
4
6
8
10
H2COH*+H2O(l)
C*+2*H2O(l)
HCOOH*
CHOH*+H2O(l)
H2CO*+H2O(l)
CH*+2*H2O(l)
COOH*
COH*+H2O(l)
CO*+H2O(l)
*
HCOOH(aq)
H2(aq)
O*+CH3OH(aq)
CH3OH*+H2O(l)
CHO*+H2O(l)
CH2*+2*H2O(l)
H*
H2COOH*
H3CO*+OH*
OCHO*
CH3OH(aq)+H2O(l)
H3CO*+H2O(l)
CH3*+2*H2O(l)
O*+CH4(aq)+H2O(l)
OH*+CH3OH(aq)
CH4(aq)+2H2O(l)
OH*+CH4(aq)+H2O(l)

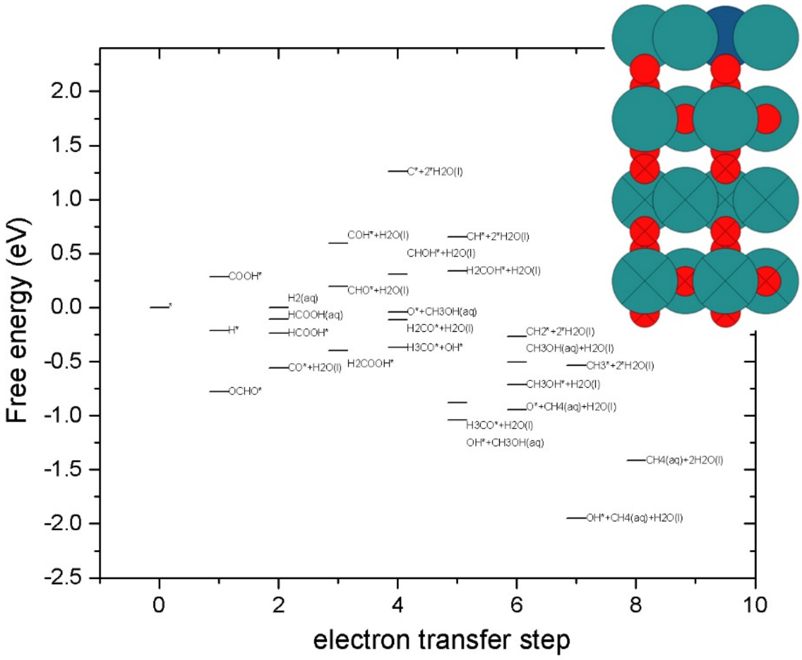
Free energy (eV)
2.0
1.5
1.0
0.5
0.0
-0.5
-1.0
-1.5
-2.0
-2.5
0
2
4
6
8
10
electron transfer step
*
COOH*
H*
OCHO*
H2(aq)
HCOOH(aq)
HCOOH*
CO*+H2O(l)
COH*+H2O(l)
CHO*+H2O(l)
H2COOH*
C*+2*H2O(l)
CHOH*+H2O(l)
O*+CH3OH(aq)
H2CO*+H2O(l)
H3CO*+OH*
CH*+2*H2O(l)
H2COH*+H2O(l)
H3CO*+H2O(l)
OH*+CH3OH(aq)
CH2*+2*H2O(l)
CH3OH(aq)+H2O(l)
CH3OH*+H2O(l)
O*+CH4(aq)+H2O(l)
CH3*+2*H2O(l)
OH*+CH4(aq)+H2O(l)
CH4(aq)+2H2O(l)

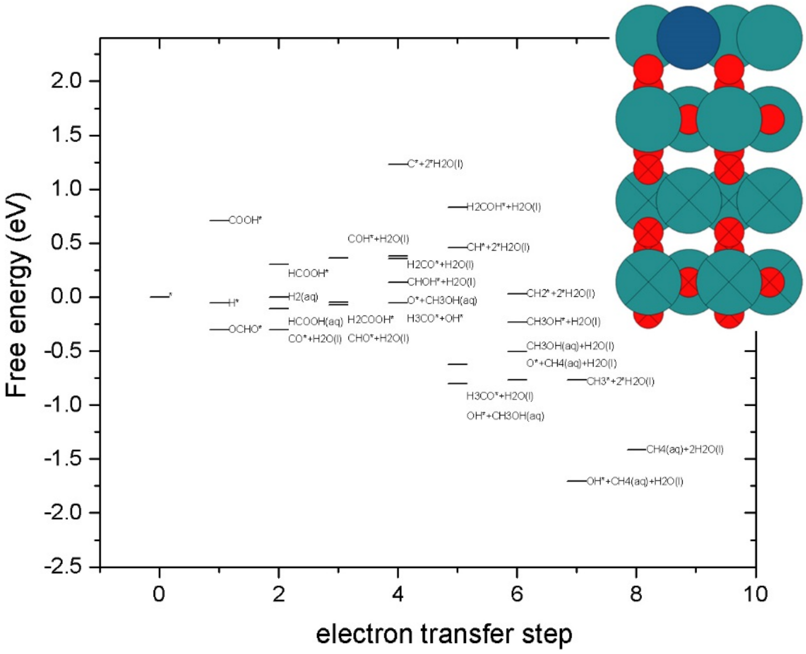
Free energy (eV)
2.0
1.5
1.0
0.5
0.0
-0.5
-1.0
-1.5
-2.0
-2.5
0
2
4
6
8
10
electron transfer step
*
COOH*
H*
OCHO*
HCOOH*
H2(aq)
HCOOH(aq)
CO*+H2O(l)
COH*+H2O(l)
H2COOH*
CHO*+H2O(l)
C*+2*H2O(l)
H2CO*+H2O(l)
CHOH*+H2O(l)
O*+CH3OH(aq)
H3CO*+OH*
H2COH*+H2O(l)
CH*+2*H2O(l)
H3CO*+H2O(l)
OH*+CH3OH(aq)
CH2*+2*H2O(l)
CH3OH*+H2O(l)
CH3OH(aq)+H2O(l)
O*+CH4(aq)+H2O(l)
CH3*+2*H2O(l)
CH4(aq)+2H2O(l)
OH*+CH4(aq)+H2O(l)

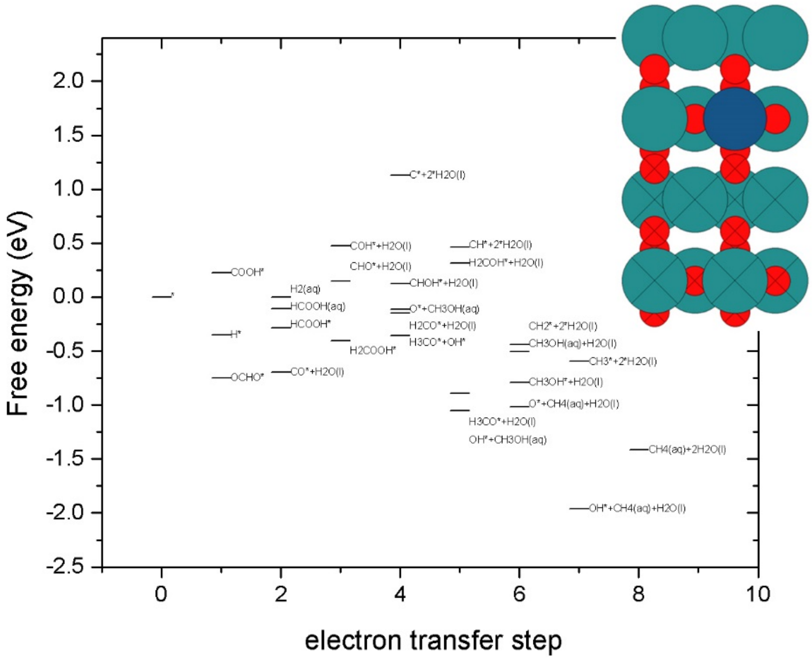
Free energy (eV)
2.0
1.5
1.0
0.5
0.0
-0.5
-1.0
-1.5
-2.0
-2.5
0
2
4
6
8
10
electron transfer step
*
COOH*
H*
OCHO*
H2(aq)
HCOOH(aq)
HCOOH*
CO*+H2O(l)
COH*+H2O(l)
CHO*+H2O(l)
H2COOH*
C*+2*H2O(l)
CHOH*+H2O(l)
O*+CH3OH(aq)
H2CO*+H2O(l)
H3CO*+OH*
CH*+2*H2O(l)
H2COH*+H2O(l)
H3CO*+H2O(l)
OH*+CH3OH(aq)
CH2*+2*H2O(l)
CH3OH(aq)+H2O(l)
CH3OH*+H2O(l)
O*+CH4(aq)+H2O(l)
CH3*+2*H2O(l)
OH*+CH4(aq)+H2O(l)
CH4(aq)+2H2O(l)

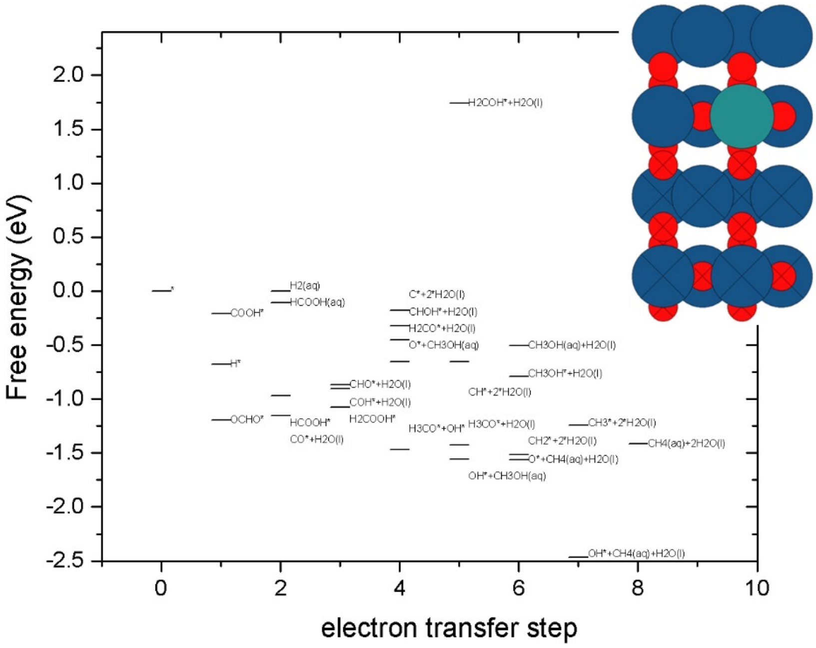
Free energy (eV)
2.0
1.5
1.0
0.5
0.0
-0.5
-1.0
-1.5
-2.0
-2.5
0
2
4
6
8
10
electron transfer step
*
COOH*
H*
OCHO*
H2(aq)
HCOOH(aq)
HCOOH*
CO*+H2O(l)
CHO*+H2O(l)
COH*+H2O(l)
H2COOH*
H2COH*+H2O(l)
C*+2*H2O(l)
CHOH*+H2O(l)
H2CO*+H2O(l)
O*+CH3OH(aq)
H3CO*+OH*
CH*+2*H2O(l)
H3CO*+H2O(l)
OH*+CH3OH(aq)
CH3OH(aq)+H2O(l)
CH3OH*+H2O(l)
CH2*+2*H2O(l)
O*+CH4(aq)+H2O(l)
CH3*+2*H2O(l)
CH4(aq)+2H2O(l)
OH*+CH4(aq)+H2O(l)

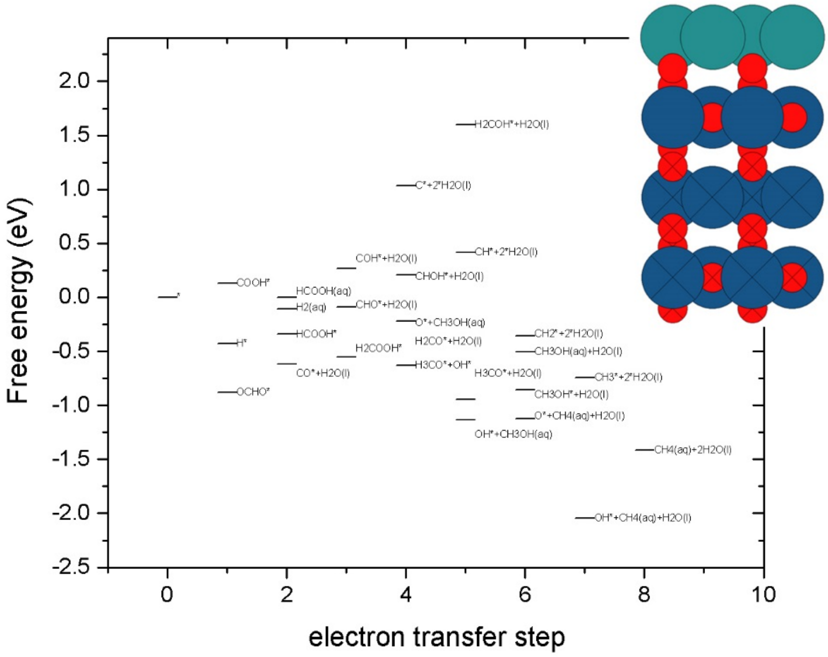
2.0
1.5
1.0
0.5
0.0
-0.5
-1.0
-1.5
-2.0
-2.5
Free energy (eV)
0
2
4
6
8
10
electron transfer step
*
COOH*
H*
OCHO*
HCOOH(aq)
H2(aq)
HCOOH*
CO*+H2O(l)
COH*+H2O(l)
CHO*+H2O(l)
H2COOH*
C*+2*H2O(l)
CHOH*+H2O(l)
O*+CH3OH(aq)
H2CO*+H2O(l)
H3CO*+OH*
H2COH*+H2O(l)
CH*+2*H2O(l)
H3CO*+H2O(l)
OH*+CH3OH(aq)
CH2*+2*H2O(l)
CH3OH(aq)+H2O(l)
CH3OH*+H2O(l)
O*+CH4(aq)+H2O(l)
CH3*+2*H2O(l)
OH*+CH4(aq)+H2O(l)
CH4(aq)+2H2O(l)

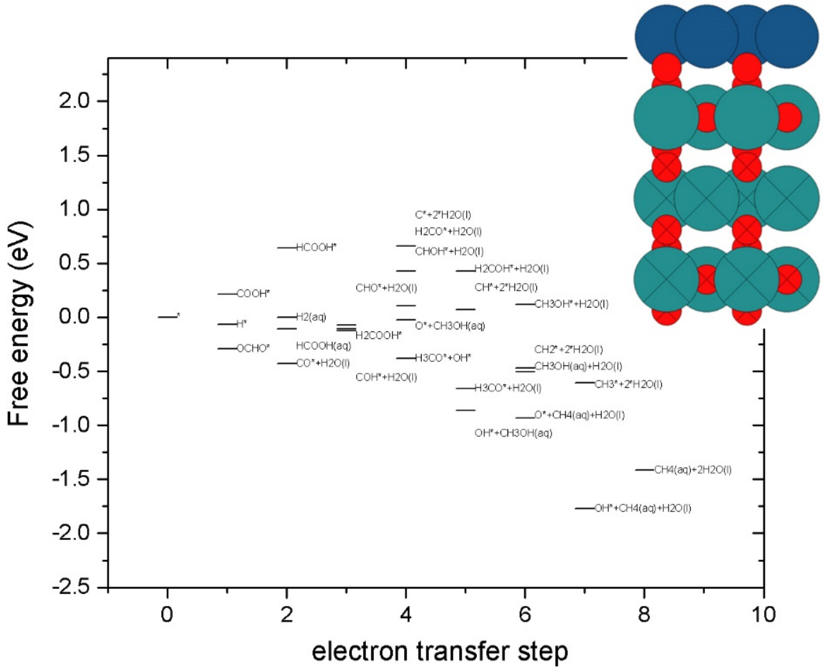
2.0
1.5
1.0
0.5
0.0
-0.5
-1.0
-1.5
-2.0
-2.5
Free energy (eV)
0
2
4
6
8
10
electron transfer step
*
COOH*
H*
OCHO*
HCOOH*
H2(aq)
HCOOH(aq)
CO*+H2O(l)
CHO*+H2O(l)
H2COOH*
COH*+H2O(l)
C*+2*H2O(l)
H2CO*+H2O(l)
CHOH*+H2O(l)
O*+CH3OH(aq)
H3CO*+OH*
H2COH*+H2O(l)
CH*+2*H2O(l)
H3CO*+H2O(l)
OH*+CH3OH(aq)
CH3OH*+H2O(l)
CH2*+2*H2O(l)
CH3OH(aq)+H2O(l)
O*+CH4(aq)+H2O(l)
CH3*+2*H2O(l)
CH4(aq)+2H2O(l)
OH*+CH4(aq)+H2O(l)

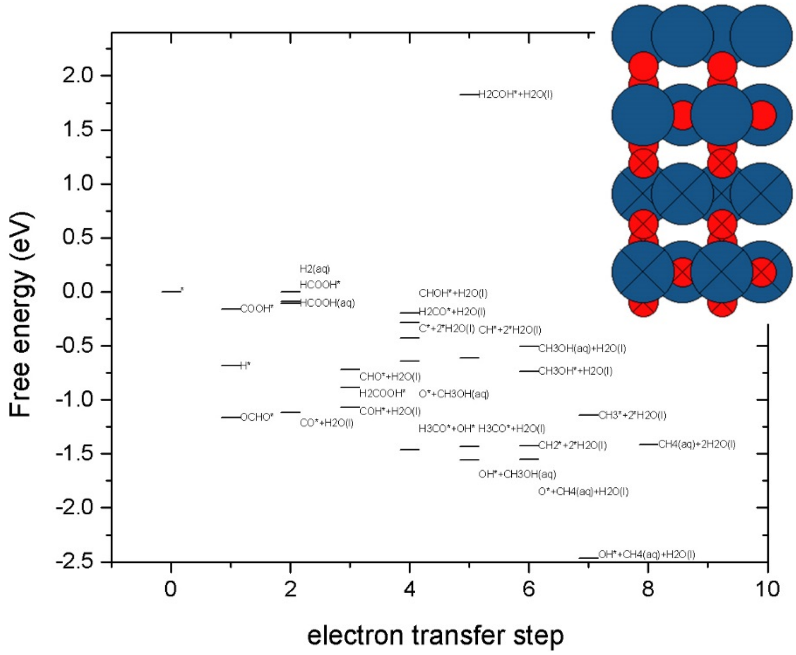

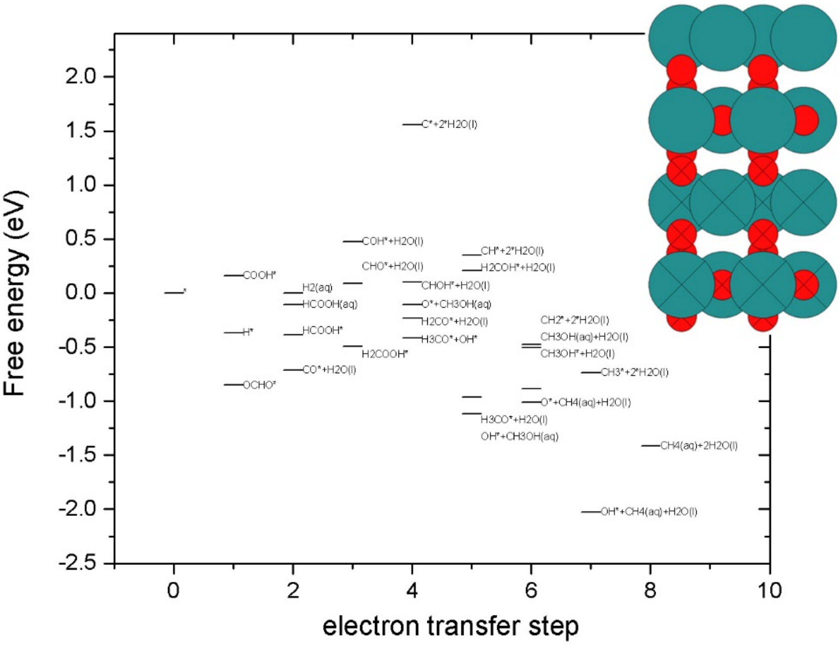

Figure S0-3: free energy of reaction intermediates and products with reference to CO_2, H_2 and H_2O at 0 V-RHE on all 10 surfaces models with 50% CO coverage*

Included publications

Paper I

Descriptors and Thermodynamic Limitations of Electrocatalytic Carbon Dioxide Reduction on Rutile Oxide Surfaces
Arghya Bhowmik, Tejs Vegge, and Heine A. Hansen
ChemSusChem, 2016, 9(22), pp 3230-3243

Paper II

Role of CO* as a spectator in CO2 electro-reduction on RuO_2
Arghya Bhowmik, Heine A. Hansen and Tejs Vegge
The Journal of Physical Chemistry C, 2017, DOI: 10.1021/acs.jpcc.7b04242

Paper III

Electrochemical reduction of CO2 on $Ir_xRu_{(1-x)}O_2$ (110) surfaces
Arghya Bhowmik, Heine A. Hansen and Tejs Vegge
Submitted

ChemPubSoc Europe

DOI: 10.1002/cssc.201600845

CHEMSUSCHEM
Full Papers

Descriptors and Thermodynamic Limitations of Electrocatalytic Carbon Dioxide Reduction on Rutile Oxide Surfaces

Arghya Bhowmik, Tejs Vegge, and Heine A. Hansen*[a]

A detailed understanding of the electrochemical reduction of CO_2 into liquid fuels on rutile metal oxide surfaces is developed by using DFT calculations. We consider oxide overlayer structures on $RuO_2(110)$ surfaces as model catalysts to elucidate the trends and limitations in the CO_2 reduction reaction (CO2RR) based on thermodynamic analysis. We aim to specify the requirements for CO2RR catalysts to establish adsorbate scaling relations and use these to derive activity volcanoes. Computational results show that the OH* binding free energy is a good descriptor of the thermodynamic limitations and it defines the left leg of the activity volcano for CO2RR. HCOOH* is a key intermediate for products formed through further reduction, for example, methanediol, methanol, and methane. The surfaces that do not bind HCOOH* are selective towards formic acid (HCOOH) production, but hydrogen evolution limits their suitability. We determine the ideal binding free energy for H* and OH* to facilitate selective CO2RR over H_2/CO evolution to be $\Delta G_B[H] > 0.5$ eV and $-0.5\text{ eV} < \Delta G_B[OH] < 0.1$ eV. The Re-containing overlayers considered in this work display excellent promise for selectivity, although they are active at a highly reducing potential.

Introduction

The surge in atmospheric CO_2 levels and the ensuing impact on the climate has intensified research activities in carbon-neutral energy technologies. If we use CO_2 as an energy carrier, for example, in the glucose synthesis in plants, we can achieve sustainability without limiting our energy use,[1,2] which is a key indicator of technological and economic growth. Fuel produced from renewable electricity is essential for a carbon-neutral energy cycle. Unlike hydrogen, carbonaceous fuel can be integrated seamlessly into the existing transportation system, which accounts for $\approx 30\%$ of our total energy consumption, without major new investments in infrastructure. It may also circumvent some of the drawbacks, for example, in battery-based electricity storage:[3] a) feasibility and cost of TW-scale energy storage to smooth out hourly fluctuation as well as seasonal variation in renewable power generation, and b) high-energy-density storage for transport applications. Sustainable synthetic fuels can be produced electrochemically in both centralized and distributed systems. It is also safe and cheap to store and transport; a trait very difficult to achieve if pure hydrogen is used as an energy carrier.

Of the many metals and alloys that have been investigated as catalysts for the efficient and selective electroreduction of CO_2 to liquid fuels, Cu is the only metal that produces hydrocarbons with reasonable Faradaic efficiency,[4,5] whereas most metallic catalysts tend to produce CO or hydrogen as the main products. The effectiveness and selectivity of Cu has been elucidated by theoretical modeling,[5,6] and thermodynamic models have been able to explain the difficulty to design better metallic electrocatalysts for methane production catalysts that originates from a scaling relation between CO* and CHO* adsorbates. The difference in the binding free energy between these adsorbates is almost invariant to changes in the CO* binding energy on different metal surfaces.[6] However, theoretical estimates also predict that products with more than one C atom can be obtained on Cu surfaces.[7–9] Ethylene has been observed by Schouten et al.[10] as the dominant C_2 product along with a smaller amount of methane at -0.6 V vs. a reversible hydrogen electrode (RHE) for Cu catalysts. Also, ethanol can be obtained at -0.3 V vs. RHE by CO reduction on oxide-derived Cu.[11] At this potential, oxide-derived Cu shows a current density in the range of a few $\mu A\,cm^{-2}$ and a Faradic efficiency of $\approx 50\%$. For industrial-scale deployment, new catalysts must operate at less reducing potentials, display a high rate capability (above 0.1 $A\,cm^{-2}$), and limit the hydrogen evolution reaction (HER).

In the last two decades, research in the computational description of surface reactions for heterogeneous catalysis have led to an improved accuracy and predictive power, which can be used for new catalyst design.[12] The development of fundamental concepts such as "scaling relations" has created a new era of the molecular-level understanding of catalytic activities. The binding energies of adsorbates, which bind through the same type of atom (e.g., C*, CH*, CH_2* binding through a C atom) scale linearly with one another.[13] We can use these

---

[a] A. Bhowmik, Prof. Dr. T. Vegge, Dr. H. A. Hansen
Department of Energy Conversion and Storage
Technical University of Denmark
Fysikvej Bldg. 309, 2800 Kgs. Lyngby (Denmark)
Fax: (+45) 46 77 57 58
E-mail: heih@dtu.dk

Supporting Information for this article can be found under: http://dx.doi.org/10.1002/cssc.201600845.

linear relations to express the energetics of the elementary steps of a chemical reaction pathway using a few binding energies as descriptors. This facilitates the modeling of the catalytic activity with fewer parameters, the understanding of why some catalysts are better than others, and allows us to narrow the search window for good catalysts.[12] Importantly, we can identify fundamental thermodynamic limits on catalyst refinement through changes in the chemical composition and structure.[14–16] Specifically for fuel-cell electrocatalysts, the identification of scaling relations[13] and the construction of theoretical activity volcanoes have been used to establish why overpotentials exist.[17] These concepts have been used to predict highly active electrocatalysts.[18,19] Although studies like these have been very successful in the design and prediction of metal and oxide catalysts for the oxygen evolution reaction (OER) and the oxygen reduction reaction (ORR), similar studies for the electrocatalytic reduction of CO_2 to fuels have been limited to metal catalysts.[20–23]

These studies have shown that it is challenging to find a good metal electrocatalyst for the CO_2 reduction reaction (CO2RR). The overall thermodynamic limiting potential for the reaction is decided by the step with the largest positive change in free energy at zero applied bias. A large reducing potential needs to be applied to compensate for this free energy change before the CO_2 reduction can proceed at appreciable rates. The potential limiting step on metal catalysts is the activation of CO* to CHO*. The binding free energy of CO* and CHO* adsorbates are correlated in such a way that the difference in binding energy of CO* and CHO* (i.e., ΔG of CO* activation) stays largely unchanged if the CO* binding energy is varied. This limits the possibility to find an efficient metal catalyst, which follows the scaling relation between CO* and CHO*.[6] However, oxide catalysts might open up new avenues for efficient liquid fuel production from CO_2. Ruthenium dioxide and its mixtures with iridium and titanium dioxides have been shown experimentally to be active towards CO_2 electroreduction.[24–28] Recent theoretical studies[29] indicate that methanol and methane are produced through a different pathway that involves an HCOOH* intermediate on RuO_2 catalysts. Although the reaction intermediates involved in the thermodynamically limiting step on metal surfaces, that is, CO* and CHO*, bind through the C atom to the active site, the expected intermediates on oxide surfaces are coordinated through an O atom. Consequently, the scaling laws that govern the thermodynamically limiting potential are expected to be different, which may allow better catalysts to be found among oxides than metals. A pathway to methanol that involves formic acid and three tandem catalysts[30] has been proposed as an additional route, which can be optimized more readily than the direct six-electron reduction of CO_2 to methanol.

Here, we first perform detailed DFT calculations to establish free energy diagrams for CO_2 reduction intermediates on a range of oxide model surfaces. This allows us to explore which pathways are active on different surfaces and to determine the limiting thermodynamic steps. We then establish scaling relations and construct activity volcanoes to derive trends in the CO_2 reduction on oxides. In addition, we propose a binding energy range for H* and OH* on oxide surfaces for the selectivity of CO2RR over HER. This work identifies the thermodynamic limitations of CO2RR on oxide surfaces and identifies the “materials genome” required for good oxide CO2RR electrocatalysts, which will set the ground for further exploration.

Theoretical Details

Thermodynamic principles

The thermodynamics of reactions on electrocatalyst surfaces depend on the binding energy of intermediate molecules on the catalyst surface. DFT-based simulations were used to show that the adsorption energy of any of the molecules considered scales approximately with the adsorption energy of the central, C, N, O, or S atom.[13] This behavior comes from the fact that the central atom participates in direct chemical bonding with the catalyst surface. These observed linear relations between the binding energy of adsorbates, which connect to the surface with the same atom, are known popularly as scaling relations in the field of theoretical catalysis.[13,31,32] For example, OH* and OCHO* intermediates bind to the surface through O atoms and their binding energies should scale with that of O*, that is, they should also scale with each other.

Sabatier’s empirical law states that for a reaction there is an optimum binding energy for an intermediate in which both stronger and weaker binding leads to lower activity. This volcano-shaped relationship between the activity and binding energy is straightforward to understand for a simple reaction such as the HER.[33] If the H atom binds too weakly to the surface then it is inefficient to create H* and if it binds too strongly then the removal of H* to make H_2 takes too much energy. However, the relationship between adsorbate binding energies and overall activity is not intuitive for a complex reaction such as CO2RR because of the large number of adsorbates and possible pathways. Simple linear relations based on scaling laws help us to reduce this complexity. We can use the correlation between the binding energies of different adsorbates to model the activity as a function of only one or two binding energy parameters. Finally, this simplification leads to a volcano-like binding energy–activity relation similar to Sabatier’s volcano concept. The binding energy to which we can correlate all other binding energy parameters and activity is often termed as the descriptor for the catalytic process.

We can estimate the binding free energy of a reaction intermediate (without electric field and electrolyte effects) on a catalyst surface from estimates of the free energy of the surface without the adsorbate, that of the surface with the adsorbate, and the free energy of reference molecules. For example, the binding free energy of OCHO* with a CO* spectator (ΔG_{OCHO*}) will be [Eq. (1)]:

$$\Delta G_{OCHO*} = G_{OCHO*} - G_{*} - G_{CO_2} - \frac{1}{2} G_{H_2} \quad (1)$$

in which G_{OCHO*} is the free energy of the surface with the OHCO* adsorbate and a CO* spectator, G_* is that with only the CO* spectator, and G_{CO_2} and G_{H_2} are the free energies of CO_2 and H_2. For O, OH, and H adsorbates, we can use H_2 and H_2O free energies as a reference. In this study, we calculate the thermodynamics of CO2RR in the presence of a CO* spectator as this species is expected to be present under CO2RR conditions and affect the thermodynamics through adsorbate–adsorbate interactions.

The presence of electrolyte molecules and the electric field makes the estimation of the free energy of adsorption for electrochemical reaction intermediates a complex task. It is computationally very demanding to simulate a large number of adsorbate–catalyst surface configurations systematically with the full details of the electrified electrolyte–catalyst interface. The computational hydrogen electrode (CHE) model allows us to approximate the reaction free energy of an electrochemical reaction[17] at a certain applied potential from the reaction free energy calculated without the explicit consideration of the potential or the electrolyte. The model links the reaction free energy of each step that involves a coupled electron proton transfer ($\Delta G_{a\rightarrow b}$) to the applied potential (U) by a simple linear relation [Eq. (2)]:

$$\Delta G_{a\rightarrow b}(U) = \Delta G_{a\rightarrow b}(U=0) + eU \qquad (2)$$

in which e is the elementary charge and U is the potential relative to a suitable reference electrode. We chose the potential to be on a RHE scale, for which the following reaction is reversible [Eq. (3)]:

$$\frac{1}{2}H_2 \rightarrow H^+ + e^- \qquad (3)$$

at 0 V vs. the reversible hydrogen electrode (V-RHE). Under this choice of potential, the chemical potential of pairs of protons (at some pH) and electrons (at 0 potential) equals the chemical potential of $^1/_2$ H_2.

Thus, for any elementary step, we can calculate the free energy change associated with the transformation at $U = 0$ V and predict the electrochemical potential required to drive the reaction step forward. $\Delta G_{a\rightarrow b}$ for any reaction step is estimated as the difference between the binding free energy [obtained using Eq. (2)] of the final and the initial adsorbates for the reaction step. For example, $\Delta G_{OCHO*\rightarrow HCOOH*}(U=0)$ is defined as [Eq. (4)]:

$$\Delta G_{OHCO*\rightarrow HCOOH*} = \Delta G_{HCOOH*} - \Delta G_{OCHO*} \qquad (4)$$

in which ΔG_{HCOOH*} and ΔG_{HCOOH*} are binding free energies calculated with respect to H_2 gas from equations similar to Equation (1).

For the overall reaction to happen at an appreciable rate, all such steps must have $\Delta G_{a\rightarrow b} < 0$ eV. The reaction step that requires the highest negative potential to make the forward reaction feasible is called the potential limiting step, and the required potential is the limiting potential for the overall reaction.

The model only provides access to the thermodynamic contribution to the onset potential and assumes implicitly that the kinetic barriers for proton transfer are surmountable at room temperature. This is expected to be valid at room temperature as barriers for the CO_2 reduction reaction steps on a Pt(111) surface are $\approx$0.55 eV or lower.[34]

To estimate the free energy of an adsorbate configuration, we calculate the ground state energy from DFT simulations at 0 K. Finite temperature energy contributions from heat capacity (C_p), entropy, and zero point energy (E_{ZPE}) are calculated by treating the adsorbate degrees of freedom as independent quantum mechanical harmonic oscillators within the harmonic approximation [Eq. (5)]:

$$G_a = E_{DFT} + E_{ZPE} + \int C_p dT - TS \qquad (5)$$

Normal-mode calculations are performed using a two-point finite difference approximation of the Hessian matrix by displacements of 0.01 Å along all three axes for each atom in the adsorbate and spectator species. Atoms in the catalyst surface are not vibrated in our calculations. The free energies of molecules are calculated within the ideal gas approximation assuming that the vibrational, rotational, and translational modes are decoupled. The total energies of molecules are calculated with a cell such that at least 12 Å of vacuum is present between periodic images. Vibrational modes and their free energy contributions are calculated and analyzed by using the Atomistic Simulation Environment (ASE)[35] and given in the Supporting Information. The energies of molecular CO_2, CO, and H_2 are corrected by +0.3, +0.15, and +0.1 eV, respectively, to correct for the systematic DFT errors that originate from inaccurate descriptions of C=O double bonds[36] and the observed shift in the description of the hydrogen binding energy in the BEEF (Bayesian error estimation functional) ensemble. $CO_{2(g)}$, $H_2O_{(l)}$, and $H_{2(g)}$ free energies are used as references for reaction free energy and adsorbate binding free energy calculations. As these species and products such as CH_4, HCOOH, and CH_3OH are either in a liquid state or in solution, we used an appropriate fugacity value for CO_2 electroreduction.[5,37] Experimentally, CO2RR is performed typically in a 0.1–0.5 M solution of $KHCO_3$ or $NaHCO_3$.[4,11,28,38] Such solutions allow dilute (0.01 M considered here) formic acid to exist in a hydrated anion form ($HCOO^-$). We denote this species as $HCOOH_{(aq)}$. A free energy correction of −0.19 eV for deprotonation and solvation has, therefore, been included.[21] The free energy of $H_2C(OH)_{2(aq)}$ is obtained from previous theoretical work.[37]

Model system

To understand how the CO_2 electroreduction proceeds as the binding energies of key reaction intermediates to the catalyst surface vary, we need to study a range of comparable surfaces. As the RuO_2(110) surface has already been studied theoretically in the CO_2 electroreduction mechanism,[29] we use this as the basis of our study. RuO_2 is found in the rutile-type structure with lattice parameters $a = 4.491$ Å and $c = 3.106$ Å.[39] The lattice parameters estimated from our calculations are $a = 4.537$ Å and $c = 3.135$ Å. This small discrepancy emanates from our choice of the BEEF-vdW exchange correlation functional,[40] which belongs to the class of generalized gradient approximation (GGA) exchange correlation functionals with nonlocal correlation to account for van der Waals interactions, for which GGA functionals overestimate lattice parameters slightly.[41]

Following a previous study by Karamad et al.,[29] our supercell that represents the catalyst surface consists of a four trilayer thick 2×1 $RuO_2(110)$ surface. The bridge site O atoms are removed in this model because the surface is expected to be in a partially reduced state in an CO_2 electroreduction environment.[42] This leaves two bridge (br) and two coordinatively unsaturated (cus) Ru sites in the unit cell to be occupied by reaction intermediates or spectator species.

To look at the reaction thermodynamics for an array of weak and strong binding metal atoms at the catalyst site, we chose to replace the metal atoms in the top layer in our model with several different transition metals. Such overlayer structures have been studied numerous times to understand the parameters that govern activity and to engineer effective catalysts both experimentally and theoretically.[43–47]

The catalyst activity can be modified both by changing the local electronic structure by strain,[14,48] ligand,[49–51] substitution,[16,52] and alloying.[53] Such alteration leads to changes in the binding energy of the reaction intermediates. Here, we seek to develop a general understanding of how CO2RR proceeds on strong and weak binding oxide surfaces and we, therefore, chose to keep strain and ligand effects constant throughout our models. The modification of only the top layer allows us to simulate catalyst surfaces with fixed lattice parameters for the substrate, whereas the subsurface layer (ligand) stays the same. DFT-based theoretical modeling allows us to explore any metal as a substitute for Ru in the surface layer, but we select only the metals that have an ionic radius that varies by less than 10% from Ru in the +4 oxidation state under octahedral coordination. Thus, the catalyst surfaces considered in this work have one of the following metals in the top layer: Ru, Ir, Mo, Nb, Pd, Pt, Re, Sn, Ta, Ti, W (Figure 1a). This selection increases the feasibility of experimental synthesis of the overlayer structures and limits surface reconstruction in our simulations. For brevity, the symbol of the metal atom at the surfaces will be used to denote the surfaces henceforth. The overlayers show large variations in the CO binding energy and are expected to display different CO coverages under CO2RR conditions. Binding energies of reaction intermediates are not only decided by the intrinsic electronic structure of the catalyst but are also affected by other adsorbate species on the surface.[54,55] A species that does not actively take part in the reaction mechanism but influences the reaction thermodynamics by remaining on the catalyst surface is called a spectator. Spectator CO molecules are expected to affect the binding energy of other adsorbates and it has been reported to modify the catalytic behavior of certain metal surfaces.[56,57] To maintain uniformity in our analysis, we have populated one of the bridge sites with a CO molecule as a spectator species in all our simulations (Figure 1b). This corresponds to a CO* coverage of 1/4th monolayer on the surface. Unless specified otherwise, A* denotes the intermediate A at a bridge site with a CO spectator on another bridge site throughout this manuscript.

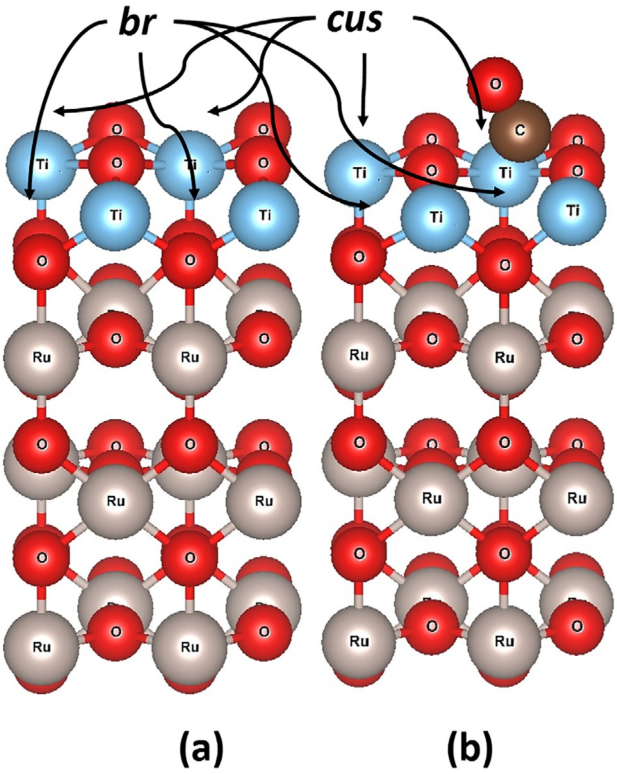

Figure 1. Model system structure a) of a reduced surface of $RuO_2(110)$ with Ti in the top layer. b) The same overlayer structure with $1/4_{th}$ monolayer CO coverage at the bridge site. Surfaces considered in this article will be denoted by the metal atom at the top layer (Ti for the surface in this figure).

Simulation Results

CO_2 activation and competition reactions

The first proton transfer step in the electrochemical conversion of CO_2 leads to two possible intermediates, namely, COOH* (carboxyl) or OCHO* (formate). On our model oxide surfaces, OCHO* is a bidentate adsorbate as it binds through two O atoms to a bridge site and the closest cus site, whereas COOH* is as a monodentate adsorbate that binds through the C atom (Figure 2). OCHO* is more stable than COOH* by 0.14–1.79 eV on the investigated surfaces. The formation of these intermediates is only feasible if the active site remains free from OH* adsorbates formed by water oxidation. The reaction will thus only proceed at an electrochemical potential that can remove OH* as a water molecule. The surfaces considered here show large variations in OH* binding energy that range from:

a) very strong binding ($\Delta G_{OH} < -1.5$ eV) such as Ta/Nb/W-terminated surfaces, to

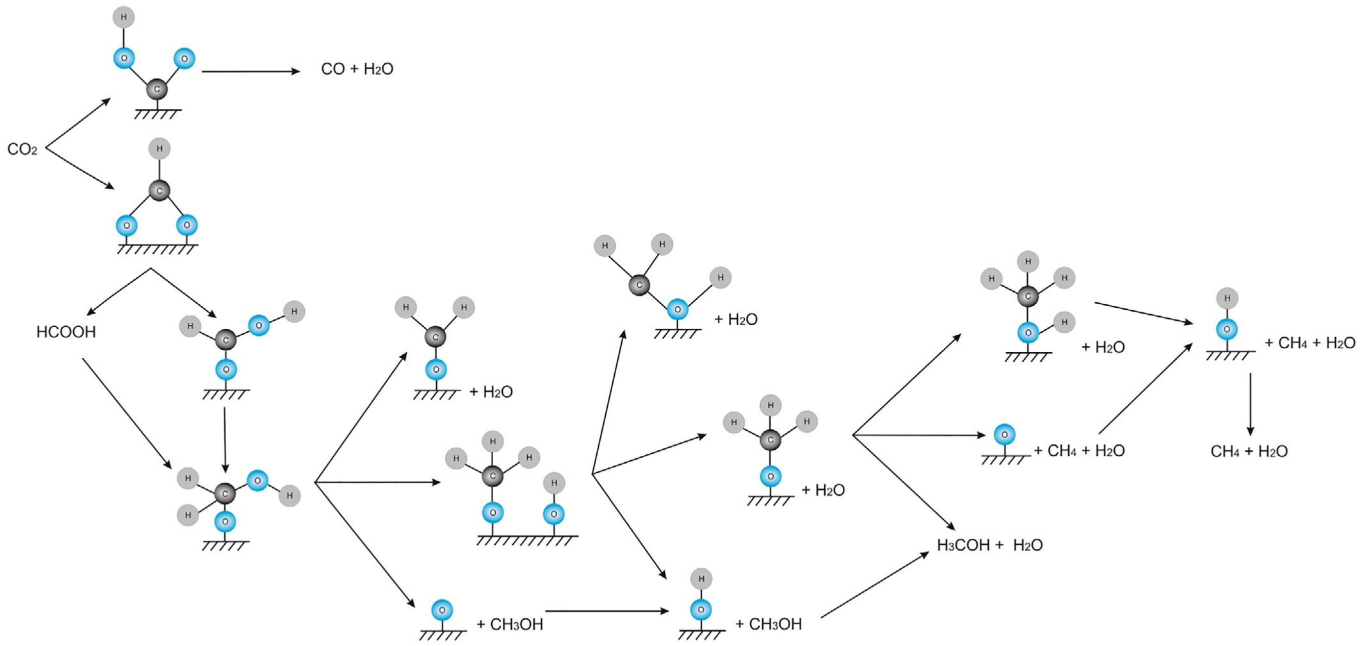

Figure 2. CO2RR reaction network explored in this computational study on 11 different surfaces.

b) moderate binding ($-1.5<\Delta G_{OH}<0$ eV) such as Mo/Re/Ti/Ru/Ir/Sn-terminated surfaces, and

c) surfaces that have positive binding free energy for OH* such as those with Pt/Pd in the top layer.

On strongly binding surfaces, OCHO* is significantly more stable than COOH*, whereas weakly binding surfaces show a relatively small difference in binding free energy of the OCHO* and COOH* adsorbates (Table S2 a–k). Nevertheless, OCHO* is the preferred adsorbate on all surfaces. The preferential formation of OCHO* over COOH* has a large impact on the selectivity of the CO_2 reduction product(s) formed because CO formation only happens through the COOH* intermediate.[22] As a result, the two-electron product formic acid is expected to be formed with high selectivity over CO. Reaction pathways for higher electron transfer products such as methanediol, methanol, and methane will involve a further reduction of HCOOH*.

The low overpotential for hydrogen production makes hydrogen a preferred product on most surfaces at CO2RR potentials (Table 1). Except for the palladium/platinum oxide overlayers, because of the relative stability of OCHO* over H*, CO_2 reduction (which involves the OCHO* intermediate) and HER occur in tandem. This has also been observed experimentally on RuO_2.[25,26] However, it has been suggested that metal catalysts can be selective for formic acid production over HER if OCHO* is the reaction intermediate instead of COOH* because of the lack of scaling between H* and OCHO*.[23] Our simulations (Table 1) also suggest that the presence of CO as a spectator species has a large effect on the HER onset potential as it can act as both a promoter and poison. This provides additional scope to suppress the HER activity over CO2RR on appropriate catalyst surfaces.

Table 1. Calculated onset potential for hydrogen formation and OH* removal at the bridge site. OH* removal potential is calculated with a CO* spectator at the other bridge site. The HER onset potential is evaluated with and without CO* spectator in the bridge site.

Metal at the top oxide layer	Onset potential for HER [V-RHE]		CO spectator effect on HER	OH* removal potential [V-RHE]
	with CO spectator	without CO spectator		
Ru	−0.31	−0.49	promotion	−0.64
Ir	−0.15	−0.75	promotion	−0.49
Mo	−0.17	−0.99	promotion	−0.86
Nb	−0.95	−0.89	poisoning	−1.90
Pd	−0.42	−0.24	poisoning	0.78
Pt	−0.19	−0.48	promotion	0.02
Re	−0.95	−1.08	promotion	−0.63
Sn	−0.27	−0.09	poisoning	−0.51
Ta	−0.85	−0.05	poisoning	−2.03
Ti	−0.18	−0.13	poisoning	−0.95
W	−1.15	−0.79	poisoning	−1.70

The other material limitation for oxides comes from the hydroxylation of active sites because the potential must be sufficiently reducing to remove OH* as water to make active sites available for CO2RR reaction. Thus, on oxides that bind OH* strongly, it is possible that OH* reduction limits the catalytic activity. Even if CO2RR is theoretically feasible at a low overpotential, the reaction must be run at more reducing potentials to remove OH*. Often at OH* removal potential, HER will happen very fast (if protons are readily available). Thus, it is advisable to run CO2RR experiments in neutral solution rather than an acidic medium. Our simulations suggest that water can be adsorbed at the active site and that the water binding energy scales weakly with the OH* binding energy (Figure S5).

CO_2 reduction pathway

CO_2 reduction products that contain a single C atom (C_1) can range from HCOOH (second electron transfer) to $H_2C(OH)_2$ (fourth electron transfer), CH_3OH (sixth electron transfer), and CH_4 (eighth electron transfer). This implies that the reaction can proceed through many possible paths that involve multiple intermediates and configurations. For a specific surface, the relative stability of the intermediates determines the most likely reaction path. Without prior knowledge, we have to explore a large number of possible pathways. Following previous theoretical work on the CO2RR mechanism for rutile oxide catalyst,[29] we limit our study to a reduced reaction network with only C_1 products and intermediates that bind through O. Our reaction network for CO2RR is shown in Figure 2.

In the second protonation step, the formed intermediate can be either an adsorbed HCOOH* species or $HCOOH_{(aq)}$. From here, the fourth and fifth steps can each create three different intermediates, which lead to different pathways to methanol and methane shown in Tables 2 and 3, respectively.

Formic acid production

As discussed in the previous section, $HCOOH_{(aq)}$ is the favored two-electron product because of the stability of the OCHO* intermediate compared to COOH*. At 0 V-RHE, only the weakly binding overlayers that contain Pt/Pd metals have positive binding free energies for the OCHO* adsorbate. The first proton transfer reaction is facile at 0 V-RHE for all other surfaces, and the further reduction to $HCOOH_{(aq)}$ requires an applied reducing potential, which makes OCHO* reduction thermodynamically limiting (Figure 3). For the platinum/palladium oxide overlayers, CO_2 activation requires a negative electrochemical potential.

OCHO* is an O-coordinated species, and the thermodynamically limiting step switches from the removal of OCHO* to the binding of OCHO* as the binding strength is reduced. This leads to a Sabatier volcano for the onset potential, which is shown in Figure 4 as a function of the OH* binding free

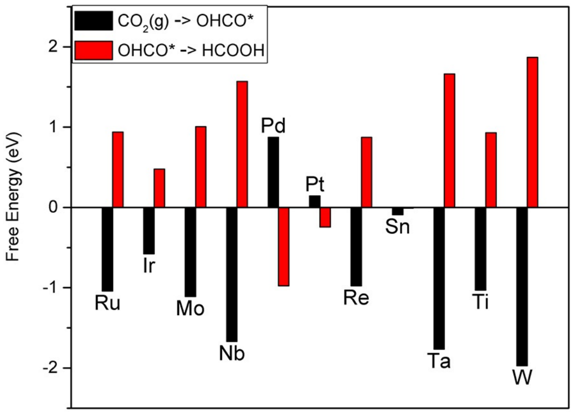

Figure 3. Free energy change associated with the elementary steps in the $HCOOH_{(aq)}$ pathway at 0 V-RHE for different surfaces. The higher positive value indicates the requirement of a larger reducing potential, that is, the thermodynamically limiting step.

Table 2. Intermediates and products in methanol production.

CH_3OH Path	Intermediate or product after combined electron proton transfer step number					
	first	second	third	fourth	fifth	sixth
A	OCHO*	HCOOH* or $HCOOH_{(aq)}$	H_2COOH*	H_3CO*(br)+OH*(cus)	H_3CO*+$H_2O_{(l)}$	$CH_3OH_{(aq)}$
B	OCHO*	HCOOH* or $HCOOH_{(aq)}$	H_2COOH*	H_2CO*+$H_2O_{(l)}$	H_3CO*	$CH_3OH_{(aq)}$
C	OCHO*	HCOOH* or $HCOOH_{(aq)}$	H_2COOH*	O*+$CH_3OH_{(aq)}$	OH*	$H_2O_{(l)}$
D	OCHO*	HCOOH* or $HCOOH_{(aq)}$	H_2COOH*	H_2CO*+$H_2O_{(l)}$	H_2COH*	$CH_3OH_{(aq)}$
E	OCHO*	HCOOH* or $HCOOH_{(aq)}$	H_2COOH*	H_3CO*(br)+OH*(cus)	OH*+$CH_3OH_{(aq)}$	$H_2O_{(l)}$

Table 3. Intermediates and products in methane evolution.

CH_4 Path	Intermediate or product after combined electron proton transfer step number							
	first	second	third	fourth	fifth	sixth	seventh	eighth
F	OCHO*	HCOOH* or $HCOOH_{(aq)}$	H_2COOH*	H_3CO*(br)+OH*(cus)	H_3CO*+$H_2O_{(l)}$	O*+$CH_{4(aq)}$	OH*	$H_2O_{(l)}$
G	OCHO*	HCOOH* or $HCOOH_{(aq)}$	H_2COOH*	H_2CO*(br)+$H_2O_{(l)}$	H_3CO*+$H_2O_{(l)}$	O*+$CH_{4(aq)}$	OH*	$H_2O_{(l)}$
H	OCHO*	HCOOH* or $HCOOH_{(aq)}$	H_2COOH*	H_2CO*(br)+$H_2O_{(l)}$	H_3CO*+$H_2O_{(l)}$	H_3COH*	OH*+$CH_{4(aq)}$	$H_2O_{(l)}$
I	OCHO*	HCOOH* or $HCOOH_{(aq)}$	H_2COOH*	H_2CO*(br)+$H_2O_{(l)}$	H_2COH*+$H_2O_{(l)}$	H_3COH*	OH*+$CH_{4(aq)}$	$H_2O_{(l)}$

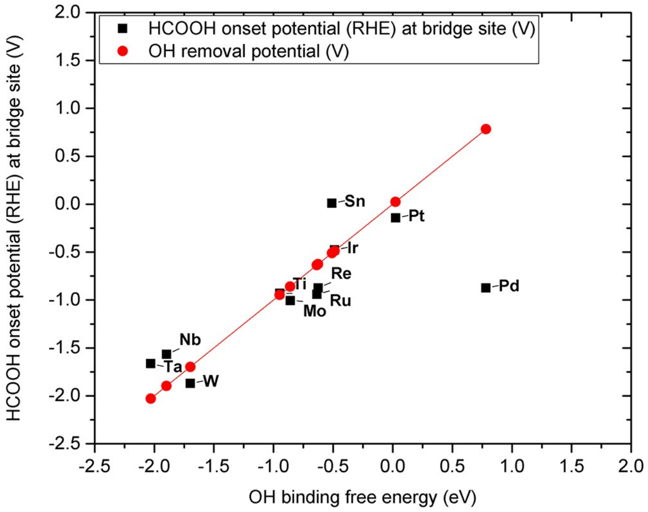

Figure 4. Calculated onset potential for $HCOOH_{(aq)}$ formation for overlayers (denoted by the metal at top layer) as a function of the OH binding free energy at the bridge site. The red line shows the reducing potential required to keep the bridge site free from OH blocking.

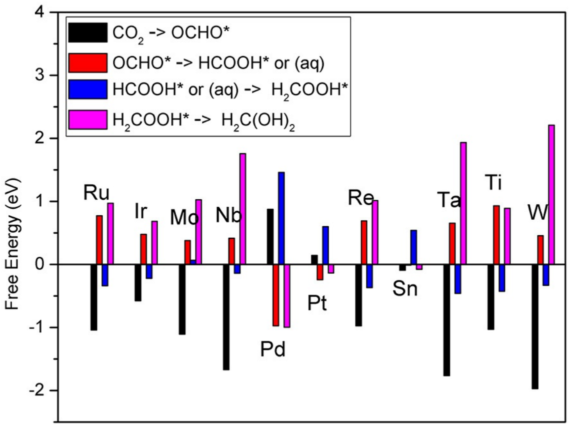

Figure 5. Free energy change associated with the elementary steps in the methanediol pathway at 0 V-RHE for different surfaces. A higher positive value indicates the requirement of a larger reducing potential, that is, the thermodynamically limiting step.

energy. Although overlayers at the top of the volcano (e.g., a tin oxide overlayer) are predicted to have the lowest onset potential (≈0.01 V-RHE), the reaction cannot proceed efficiently at this potential because of the blocking of the active site by OH* adsorbates formed by water oxidation on reactive surfaces.[58] For the Pt-containing overlayer, OH* poisoning is not a problem, but the high hydrogen evolution activity will decrease the Faradic efficiency of $HCOOH_{(aq)}$ production as explained previously. The results indicate that the tin oxide overlayer structure could be an effective $HCOOH_{(aq)}$ evolution catalyst with an onset potential of approximately −0.5 V-RHE, which originates from the reduction of surface OH*.

Four-electron methanediol reaction

We also consider the formation of methanediol by the further reduction of HCOOH. It is predicted that weakly O binding overlayers such as Sn, Pt, or Pd overlayers will produce more $HCOOH_{(aq)}$ than further reduced products because HCOOH does not bind to these surfaces. Pt/Sn overlayers are, therefore, not expected to produce significant quantities of methanediol even though the calculated onset potential is low (Figure 5). If the catalyst surface fails to bind HCOOH*, the protonation of OCHO* will release $HCOOH_{(aq)}$. Here, we also consider the possibility of $HCOOH_{(aq)}$ to be activated at a highly reducing potential. As we calculate the thermodynamic barrier for the third proton transfer step, we consider either the HCOOH* or $HCOOH_{(aq)}$; whichever has lower free energy as the second-step product. The third electron transfer reaction in the CO_2 reduction leads to the H_2COOH^* species at the bridge site, at which H_2COOH^* is then further reduced to form $H_2C(OH)_2$. On the investigated oxide overlayers, either $OCHO^* \rightarrow HCOOH^*$ or $HCOOH_{(aq)} \rightarrow H_2COOH^* \rightarrow H_2C(OH)_{2(aq)}$ is the preferred reaction pathway. The intermediates in this pathway bind through O. As expected, this is also the pathway for electrochemical methanediol synthesis on other oxides as oxides bind O more strongly than metals.[59,60] In this reaction mechanism, all strong binding surfaces are thermodynamically limited by the removal of H_2COOH^* to form methanediol, except for the Ti-containing overlayer. Structures with Sn, Pd, or Pt are limited by the formation of H_2COOH^* from $HCOOH_{(aq)}$. Interestingly, the titanium oxide overlayer needs a large negative potential to release $HCOOH_{(aq)}$ from strongly bound OCHO*. The titanium oxide overlayer is expected to produce methanediol at an onset potential −0.93 V-RHE, close to the potential needed for OH* removal (−0.95 V-RHE). Surfaces such as Ru/Ir/Mo have a surface-bound fourth protonation intermediate, which is more stable than the methanediol product. Thus, methanediol is not expected to be produced on these surfaces.

Methanol production

Methanol production from CO_2 involves six electron transfer steps (Figure 2). As oxide surfaces stabilize O-coordinated adsorbates, we consider different O-coordinated reaction intermediates formed through the further reduction of H_2COOH^*. Recent theoretical work on the CO_2 reduction mechanism of the $RuO_2(110)$ surface shows[29] that the thermodynamically favored intermediates are $CO_{2(g)} \rightarrow OCHO^* \rightarrow HCOOH^* \rightarrow H_2COOH^* \rightarrow H_3CO^*(br) + OH^*(cus) \rightarrow OH^* + CH_3OH \rightarrow H_2O + CH_3OH$ for low-CO-coverage conditions similar to this work. Experimental work on ruthenium/iridium/titanium oxides for CO_2 to methanol production[24–26] have shown activity towards methanol production at potentials of −0.5 to −1.0 V-RHE. Our simulations reveal that the thermodynamically limiting steps for these surfaces are the activation of OCHO* to HCOOH*, CH_3O^* hydrogenation to $CH_3OH_{(aq)}$, and the removal of OH*, respectively. For the very weak binding surfaces with Pt/Pd overlayers, H_2COOH^* formation requires the highest negative potential. The rhenium oxide overlayer requires −0.71 V-RHE for the removal of OCH_3^* as methanol. For the Mo/Nb/Sn/Ta/W-containing structures, OH* removal determines the onset potential in this reaction mechanism.

The oxide surfaces considered here display a broad range of binding energies. Based on the relative strength of the reaction intermediates, different reaction pathways to methanol formation are observed on different surfaces. If we use the CHE model, we assume that reaction barriers are either small or scale with the thermodynamic barrier such that activation energies mainly depend on the reaction free energies. Therefore, the relative stability of the adsorbates at a specific electron transfer step (the most stable intermediate) decides which reaction path will be active. At the fourth electron/proton transfer step, the protonation of H_2COOH^* leads to the following intermediates:

a) $H_3CO^*(br)+OH^*(cus)$ on Ir/Ru/Rh/W oxide overlayers,
b) $O^*+CH_3OH_{(aq)}$ on Mb/Nb/Sn/Ta/Ti oxide overlayers,
and c) H_2CO^* on Pt/Pd oxide overlayers.

The O^* intermediate leads to OH^* as the fifth reaction step. $H_3CO^*(br)+OH^*(cus)$ can make methanol and OH^*. Alternatively, $H_3CO^*(br)+OH^*(cus)$ may lead to either H_3CO^* or H_2COH^* with water removal. H_2CO^* adsorbates protonate to H_3CO^*. We predict the methanol evolution to take place following pathway A (Table 4) on the pure $RuO_2(110)$ surface with 1/4th CO coverage, whereas a previous study[29] suggested pathway E under these conditions. These two pathways differ by the fifth reaction intermediate of OH^* or H_3CO^*. H_3CO^* is more stable by 0.12 eV than OH^* on $RuO_2(110)$ in our calculation. The different order of adsorbate stability is expected because of the inclusion of van der Waals interactions in the BEEF-vdW functional and the explicit temperature corrections performed in this work. We calculated temperature corrections for all adsorbate phonon modes, which were not included previously.[29] For example, we have observed up to 0.18 eV variation in the entropic contribution in binding free energy of H_3CO^* on the surfaces under consideration (Table S2). The ease of the removal of OH^* as $H_2O_{(l)}$ leaves H_3CO^* as the favored fifth electron transfer intermediate. Binding free energies of OH^* at both the bridge and cus sites are tabulated in Table S1, in which the Re-containing oxide overlayer has a comparable binding energy to OH^* at the bridge and cus sites.

In summary, different mechanisms are active, which depend on the binding strength of the surfaces covered in this study. The active pathway and the onset potentials for methanol formation and OH^* reduction are summarized in Table 4. Here it is seen that the palladium/platinum oxide overlayer shows thermodynamically limited H_2COOH^* formation, whereas OH^* removal is limiting for the Mo/Nb/Ta/Ti-containing overlayers. For the Re/W/Ir surfaces, the H_3CO^* activation to methanol is limiting, that is, the sixth electron/proton transfer step, and on the pure RuO_2 surface, $OCHO^*$ activation is the most difficult. The latter result is in agreement with previous findings by Karamad et al.[29]

The calculated methanol onset potentials presented here take into account the potential requirement for OH^* removal needed to keep the active site available for CO_2 reduction. All the calculated onset potentials are lower than or equal to the OH^* removal potential for strongly binding surfaces.

Methane evolution

Similar to the methanol production reaction, methane evolution can occur through multiple paths that involve O-coordinated intermediates. If we start from the H_2COOH^* intermediate, the fourth electron/proton transfer step results in $H_3CO^*(br)+OH^*(cus)$ or H_2CO^* intermediates, which are subsequently reduced to H_3CO^* or H_2COH^*. On the weakly binding Pt/Pd surfaces, H_2CO^* intermediates form, whereas all other surfaces show a path that involves $H_3CO^*(br)+OH^*(cus)$ intermediates. Further reduction yields H_2COH^* on the Pd overlayer and H_3CO^* on all other surfaces. The sixth reaction intermediate is CH_3OH^* on the Pd overlayer, whereas all other surfaces form O^* with the evolution of methane. The Pd overlayer does not bind methanol and thus cannot produce methane by further reduction. The last two reaction steps involve the protonation of O^* to water on all surfaces.

If we evaluate the onset potential for methane production based on the calculated binding free energies we observe that the thermodynamic limitation originates from $HCOOH^*$ formation for the Ru/Re overlayers, OH^* removal for Ir/Mo/Nb/Sn/Ta/Ti/W-containing overlayers, and H_2COOH^* formation for tin/platinum/palladium oxide overlayers (Table 5). We also observe a Sabatier-like volcano relation for the methane and methanol onset potentials and the OH^* binding free energy, which will be discussed later.

Table 4. Predicted methanol production pathway, onset potentials, and OH^* removal potential on all overlayer surfaces.

Transition metal at top layer	Methanol production mechanism	Step requiring largest reducing potential for methanol path	Potential [V-RHE] methanol onset	OH* removal
Ru	A	$OHCO^* \rightarrow HCOOH^*$	−0.77	−0.64
Ir	A	$H_3CO^* \rightarrow CH_3OH_{(aq)}$	−0.57	−0.49
Mo	C	$OH^* \rightarrow H_2O_{(l)}$	−0.86	−0.86
Nb	C	$OH^* \rightarrow H_2O_{(l)}$	−1.90	−1.90
Pd	D	$HCOOH_{(aq)} \rightarrow H_2COOH^*$	−1.46	0.78
Pt	B	$HCOOH_{(aq)} \rightarrow H_2COOH^*$	−0.60	0.02
Re	A	$H_3CO^* \rightarrow CH_3OH_{(aq)}$	−0.71	−0.63
Sn	C	$HCOOH_{(aq)} \rightarrow H_2COOH^*$	−0.54	−0.51
Ta	C	$OH^* \rightarrow H_2O_{(l)}$	−2.03	−2.03
Ti	C	$OH^* \rightarrow H_2O_{(l)}$	−0.95	−0.95
W	A	$H3CO^* \rightarrow CH_3OH_{(aq)}$	−1.81	−1.70

Table 5. Predicted methane evolution pathways, onset potentials, and OH* removal potentials on all the investigated overlayer surfaces.

Transition metal at top layer	Methane evolution mechanism	Step requiring largest reducing potential for methane path	Potential [V-RHE] methane onset	methanol onset	OH* removal
Ru	F	$OHCO^* \rightarrow HCOOH^*$	−0.77	−0.77	−0.64
Ir	F	$OH^* \rightarrow H_2O_{(l)}$	−0.49	−0.57	−0.49
Mo	F	$OH^* \rightarrow H_2O_{(l)}$	−0.86	−0.86	−0.86
Nb	F	$OH^* \rightarrow H_2O_{(l)}$	−1.90	−1.90	−1.90
Pd	I	$HCOOH_{(aq)} \rightarrow H_2COOH^*$	−1.46	−1.46	0.78
Pt	G	$HCOOH_{(aq)} \rightarrow H_2COOH^*$	−0.60	−0.60	0.02
Re	F	$OHCO^* \rightarrow HCOOH^*$	−0.69	−0.71	−0.63
Sn	F	$HCOOH_{(aq)} \rightarrow H_2COOH^*$	−0.54	−0.54	−0.51
Ta	F	$OH^* \rightarrow H_2O_{(l)}$	−2.03	−2.03	−2.03
Ti	F	$OH^* \rightarrow H_2O_{(l)}$	−0.95	−0.95	−0.95
W	F	$OH^* \rightarrow H_2O_{(l)}$	−1.70	−1.81	−1.70

Discussion

Adsorbate scaling relations

The formation of the different C_1 products from the CO2RR investigated here proceeds through up to seven reaction intermediates (for the eighth electron reduction). The thermodynamic barriers for these reactions will be minimized if the intermediate binding free energies are tuned such that all reaction steps occur at the equilibrium potential. Our analysis of the reaction paths for different products suggests that the CO2RR on the investigated rutile oxide catalysts involves intermediates that interact with the catalyst through the O atoms. Previous theoretical studies on adsorption energy scaling relations[13,61,31] suggest that there might be a strong adsorption free energy correlation between the O-coordinated species. Indeed, we observe a linear correlation between the adsorption free energy of the different adsorbates included in our reaction mechanism analysis and the OH* adsorption energy. We apply the OH* binding energy as a descriptor as it has been used in the analysis of chemical properties of various energy materials.[62–65] For CO_2 reduction on rutile oxides, the removal of OH* from the active site is a potential limiting step. Some adsorbates such as H_2COH^* show a large deviation from this linear model (Figure S1). This, however, does not affect the results of the analysis as these intermediates are either not a part of the active pathways in the binding energy interval of interest or do not define the thermodynamic limiting step. Linear free energy relations (details in the Supporting Information) for different adsorbates are [Eqs. (6)–(14)]:

$$\Delta G_B[OCHO] = 0.99\,\Delta G_B[OH] - 0.04\text{ eV} \tag{6}$$

$$\Delta G_B[HCOOH] = 0.72\,\Delta G_B[OH] + 0.19\text{ eV} \tag{7}$$

$$\Delta G_B[H_2COOH] = 1.09\,\Delta G_B[OH] + 0.40\text{ eV} \tag{8}$$

$$\Delta G_B[H_3CO+OH] = 1.30\,\Delta G_B[OH] + 0.28\text{ eV} \tag{9}$$

$$\Delta G_B[H_3CO] = 0.96\,\Delta G_B[OH] - 0.22\text{ eV} \tag{10}$$

$$\Delta G_B[O] = 1.68\,\Delta G_B[OH] + 0.96\text{ eV} \tag{11}$$

$$\Delta G_B[H_2CO] = 0.75\,\Delta G_B[OH] + 0.31\text{ eV} \tag{12}$$

$$\Delta G_B[H_3COH] = 0.20\,\Delta G_B[OH] - 0.11\text{ eV} \tag{13}$$

$$\Delta G_B[H_2COH] = 0.05\,\Delta G_B[OH] + 0.18\text{ eV} \tag{14}$$

Theoretical activity volcanoes

To consider the possible reaction pathways at different OH* binding energies, we can construct activity volcanoes for all four CO2RR products at a low CO coverage (Figures S2–S4). To understand how well the scaling relation volcano predicts trends in the onset potential, we compare it with the explicitly calculated onset potentials for surfaces from full free energy diagrams. We observe that the volcanoes constructed using only thermodynamic considerations coincide for methanediol, methanol, and methane. If OH* removal is not part of the reaction path, it can become limiting if the onset potential is higher than the OH* removal potential. Thus, we can simply take OH* removal as the limiting step for $\Delta G_B[OH] < -0.24$ eV. For $\Delta G_B[OH] > -0.24$ eV, HCOOH* does not bind to the active site and stays in aqueous solution. It will require a large reduction potential to protonate $HCOOH_{(aq)}$ and form H_2COOH^*, which is key to the further reduction of $HCOOH_{(aq)}$. The right leg ($\Delta G_B[OH] > -0.24$ eV) of the volcano for the fourth, sixth, and eighth electron reductions is, therefore, defined by $HCOOH_{(aq)}$ activation to H_2COOH^*. A very high concentration of $HCOOH_{(aq)}$ can destabilize $HCOOH_{(aq)}$ in solution and facilitate the reduction of formic acid by binding HCOOH* to the active site. However, at a higher proton concentration, the HER might become more dominant.

The construction of these volcanoes reveals that these oxide catalysts can have a thermodynamic limit for liquid fuel production as high as −0.24 V-RHE. The scaling line for the reaction $OCHO^* \rightarrow HCOOH^*$ touches the top of the volcano (Figure S3). However, at this binding energy $HCOOH_{(aq)}$ is more stable than HCOOH*. The goodness of fit for the scaling relation between OH* and HCOOH* binding free energy is less than ideal at $R^2 = 0.79$. If we consider the uncertainty in the U_{step} for $OCHO^* \rightarrow HCOOH^*$, this step might become the thermodynamically limiting step for some of the most active surfaces.

Methanediol/methanol/methane volcano

The release of methanediol by H_2COOH^* activation is facile at the OH* removal potential for the left leg of the methanediol activity volcano (Figure S2). $HCOOH_{(aq)}$ protonation to H_2COOH^* is the thermodynamically limiting step for $\Delta G_B[OH] > -0.24$ eV. The top of the volcano is at $\Delta G_B[OH] = -0.24$ eV with a corresponding limiting potential of −0.24 V-RHE (Figure 6). Methanol and methane production can follow different electrochemical pathways based on the relative stability of the possible reaction intermediates. The scaling relations can help us to identify dominant pathways at different binding energy regimes. The scaling relations also suggest that methanol formation paths A and E (Table 2) are almost identical in terms of the onset potential requirement. On the strong binding leg, both elementary steps $OH^* \rightarrow H_2O$ and $H_3CO^* \rightarrow CH_3OH_{(aq)}$ are important and both can be thermodynamically limiting (Figure S3).

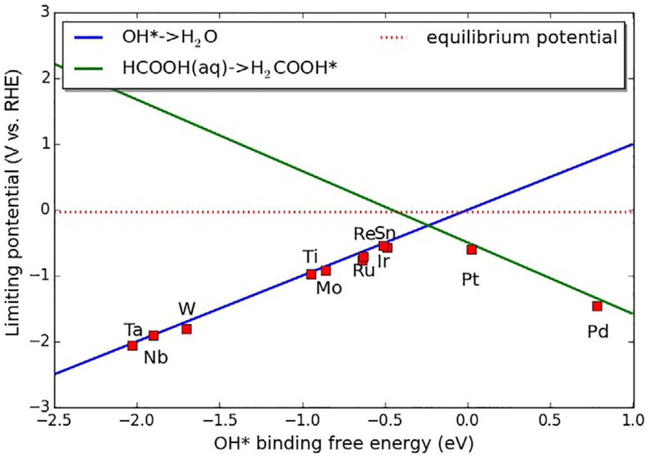

Figure 6. Thermodynamically limiting volcano for methanol production derived from OH* reduction, $HCOOH_{(aq)}$ activation, and scaling relations. The limiting potential for specific overlayers calculated without assumptions about scaling relations is also indicated. A similar volcano with all involved reaction steps is included in the Supporting Information.

Among the possible methanol reaction paths, we predict that at $\Delta G_B[OH] < -1.30$ eV; the fourth electron transfer step, that is, H_2COOH^* activation, leads to the formation of O* at a bridge site along with the release of a methanol molecule (Figure S3). In this strong binding regime, in which path C is preferred, OH* removal demands the largest reducing potential. For $-1.30 < \Delta G_B[OH] < 0.05$ eV, H_2COOH^* activation leads to $H_3CO^*(br)+OH^*(cus)$ intermediates. In this interval, the scaling lines for $H_3CO^*(br)+OH^*(cus) \rightarrow H_3CO^*+H_2O_{(l)}$ and $H_3CO^*(br)+OH^*(cus) \rightarrow OH^*+CH_3OH_{(aq)}$ steps are almost degenerate (Figure S3). The activation of H_3CO^* to methanol is energetically comparable to OH* removal. The top of the methanol activity volcano is at $\Delta G_B[OH] = -0.24$ eV as discussed previously.

The methane evolution reaction proceeds through the $H_3CO^*(br)+OH^*(cus)$ intermediates for $\Delta G_B[OH] < 0.05$ eV and through a H_2CO^* intermediate for weaker binding energies (Figure S4). The fifth electron transfer leads to H_3CO^* from both H_2CO^* and $H_3CO^*+OH^*$ intermediates for $\Delta G_B[OH] < 0.43$ eV. H_2COH^* is protonated to form H_3CO^* as well even for weaker binding surfaces. For $\Delta G_B[OH] < -0.24$ eV, OH* removal requires the largest negative potential, which defines the left leg of the methane volcano. Similar to methanol evolution, the formation of $HCOOH_{(aq)}$ for $-0.24 \text{ eV} < \Delta G_B[OH]$ makes the third protonation to H_2COOH^* difficult, and this step becomes thermodynamically limiting.

Formic acid volcano

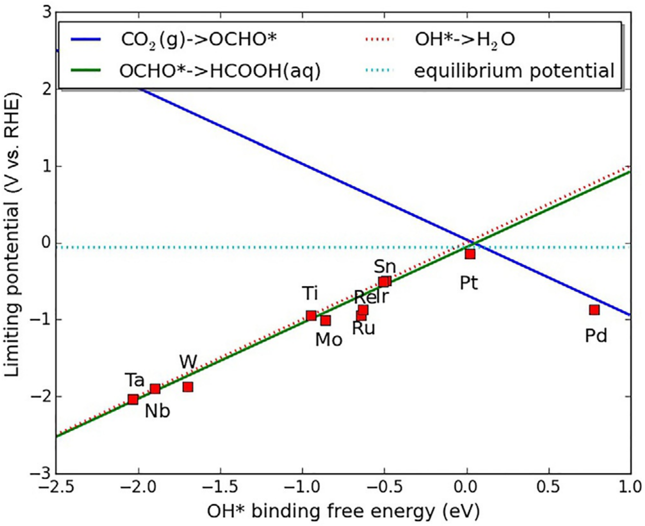

Figure 7. Activity volcano for the reduction of CO_2 to $HCOOH_{(aq)}$ constructed from the scaling relations established in this work. Limiting potentials for specific surfaces are calculated without assumptions of scaling relations. A few surfaces that include the tin oxide overlayer is limited by OH* poisoning.

The formation of $HCOOH_{(aq)}$ is a simple two-step reaction. The release of formic acid by the reduction of OCHO* defines the left leg of the volcano and OCHO* formation constitutes the right leg (Figure 7). The scaling relations suggest that the electrochemical potential required to drive the $OCHO^* \rightarrow HCOOH_{(aq)}$ step is also sufficient to free OH* from the active site. The calculated values for the different surfaces (Figure 7) take the potential required for OH* removal into account and the top of the volcano is at $\Delta G_B[OH] = 0.05$ eV with a limiting potential of −0.0 V-RHE. The equilibrium potential is, however, −0.05 V-RHE, and this discrepancy comes from the less-than-ideal fitting needed to obtain the scaling relations and the uncertainty that originates from this. Therefore, it is not unlikely that an oxide catalyst exists that can produce formic acid at a very low overpotential. Thus, formic acid is the most energy efficient fuel to be produced using oxide catalysts. An onset potential of −0.2 to −0.3 V-RHE has been observed for tin oxide catalyst for CO_2 conversion to $HCOOH_{(aq)}$.[66,67] Theoretical studies by Cui et al. suggested an $HCOOH_{(aq)}$ evolution onset potential of

−0.2 V-RHE on tin oxide.[68] Our calculations also suggest an oxide overlayer with Sn to be very efficient for this reaction.

Design of rutile oxide catalysts for selective CO2RR

The selectivity for liquid fuel products over HER during the electroreduction of CO_2 on rutile oxide overlayers on $RuO_2(110)$ can be assessed from the relative stability of intermediates formed after the first proton transfer step. If OCHO* binds moderately to the active site and H* has a large positive binding free energy, CO2RR will occur and the HER will be suppressed. The formation of COOH* is unfavorable compared to that of OCHO* on the investigated oxide overlayer surfaces. The analysis shows that the ordering of the binding free energy of these adsorbates is COOH* > H* > OCHO* for surfaces with strong oxygen affinity such as those that contain Ta/Ti/Nb and COOH* > OCHO* > H* for surfaces such as Pt/Pd, which do not bind O. Strong binding surfaces are, therefore, expected to display an inherently better selectivity for CO2RR over HER than weakly binding oxide surfaces. The overlayer structure that contains Re shows a uniquely large destabilization of H* adsorbate over OCHO* and a free energy order of H* > COOH* > OCHO*. This indicates a high selectivity of $HCOOH/CH_3OH/CH_4$ formation with very little hydrogen evolution. For rutile oxide surfaces, we propose a free energy order of COOH* > H* > OCHO* for the first electron/proton transfer step. A large positive binding energy for H*/COOH* (> 0.5 eV) and moderate binding of OCHO* ($-0.5 < \Delta G < 0$ eV) can be a good indicator of the selectivity (Figure 8).

Except for that of the Re overlayer, the COOH* binding free energy scales very well with the H* binding energy (Figure 9a). This behavior is similar to that observed on metals.[23] A weak binding energy for H*/COOH* and a moderate OH* binding energy is expected to lead to an efficient and selective CO2RR catalyst (Figure 9b). The H* and OH* binding free energies in the presence of a CO spectator are not well correlated on these oxide surfaces. This might allow us to design oxide catalysts with a high selectivity for CO2RR over the HER. Experimental results are currently available for certain oxides (i.e., Ti/Sn/Ir/Ru oxides) with H binding free energies of −0.25 to 0.25 eV based on our calculations on overlayers. A significant hydrogen evolution is, therefore, expected to take place as CO2RR takes place. The Faradic efficiency reported for carbonaceous products is 12–80%, and the rest is hydrogen.[24–26,28] Oxides with OH* binding energies similar to the Re overlayer can be highly selective for CO2RR as the HER is suppressed because of weak H* and COOH* binding.

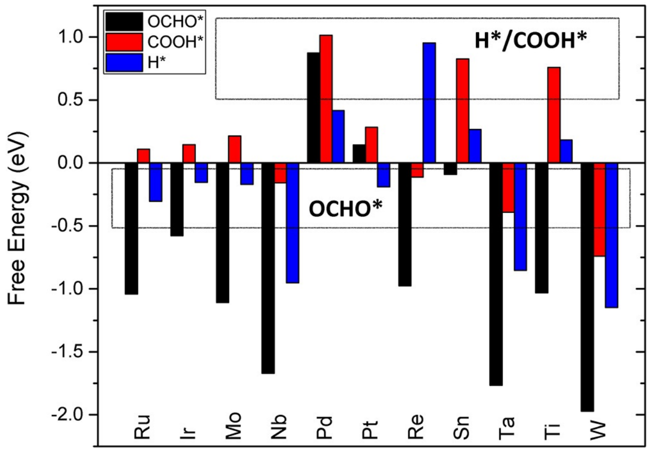

Figure 8. Binding free energy of the H*, OCHO*, and COOH* intermediates formed after the first proton transfer reaction with CO as a spectator in the bridge site. The suitable H*/COOH*/OCHO* binding free energy for selective CO2RR is marked with boxes.

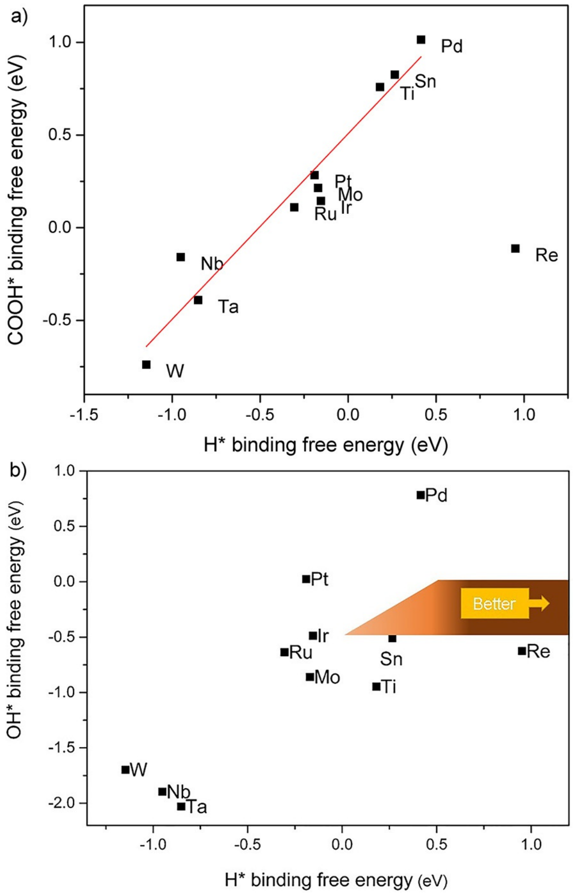

Figure 9. Binding free energy correlation between a) H*/COOH* and b) OH*/H* adsorbates. The red line denotes the linear scaling relation between H* and COOH* binding free energy. The scaling relation is fitted to all points except that for the rhenium oxide overlayer.

Although the Pourbaix diagram predicts that ruthenium oxide can be reduced under CO2RR conditions, thermodynamics is not the only parameter that governs the stability of materials in electrochemical environment. The surface can be stable because of kinetic/thermodynamic limitations. The CO/CO_2-rich environment might play a crucial role as well. Detailed X-ray photoelectron spectroscopy (XPS) studies that involve RuO_2 under reducing conditions show that RuO_2 maintains its chemical nature under reducing conditions.[42] The reduction of the oxide surface should proceed through the gradual removal of bridge site O and lattice O atoms. Although the removal of bridge site O or top-layer lattice O is calculated by us to be overall energetically favorable at 0 V-RHE, there is a thermodynamic barrier to both the two-electron O removal processes. In the case of bridge O, the barrier is identical to that of the removal of hydroxyl at the bridge site, that is, ΔG_B[OH] at the bridge site. This thermodynamic barrier requires -0.64 V-RHE to remove RuO_2(110) bridge O in presence of 1/4th monolayer CO. The thermodynamic barrier for lattice O removal comes from the hydrogenation of O, which is calculated to be -0.66 V-RHE for the first lattice layer O for RuO_2(110). Additional kinetic barriers are expected to be present over and above these kinetic barriers. Our analysis of CO2RR pathways shows that the onset potential is lower or comparable to ΔG_B[OH]. This confirms the theoretical basis of why rutile oxide catalysts are not reduced to metal at the CO2RR active potential region and remain active.

Conclusions

The thermodynamic activity volcanoes derived from the scaling relation analysis for different C_1 products in the CO_2 reduction reaction suggests that significant reduction in the overpotential is possible through the design of an oxide catalyst with an optimal OH* binding strength. Activity volcanoes show that for methane and methanol production, the investigated rutile oxide catalysts can reduce overpotentials by up to 0.35 V compared to metal catalysts.[6] On metal surfaces, the hydrogenation of CO* to CHO* is the most demanding step. Potential requirements for this step cannot be optimized much because of the strong scaling between CO* and CHO* intermediates. On oxide surfaces, we show that the primary descriptor and limiting step, OH* removal, can be modified easily. As the overpotential requirement is strongly dependent on this parameter, it is possible to tune the catalytic performance in an accessible fashion. This is achieved by different reaction pathways that involve O-coordinated adsorbates instead of C-coordinated ones.

The top of the volcano coinsides for methanediol, methanol, and methane evolution as the left (right) side is defined by OH* removal ($HCOOH_{(aq)}$ activation) for all products. For formic acid evolution, the left and right side of the volcano are defined by OCHO* activation and OCHO* formation, respectively. OH* removal occurs at a lower reducing potential than the release of $HCOOH_{(aq)}$ that results from OCHO* activation. For surfaces with $\Delta G_B[OH] < -0.24$ eV, the binding free energy of HCOOH* is negative, and further reduction can yield methane and methanol. For surfaces with weaker binding than this, $HCOOH_{(aq)}$ will be a major product as the reaction might not proceed further than the two-electron transfer to formic acid. Oxide surfaces with $-0.1 < \Delta G_B[OH] < 0.1$ eV are predicted to be very efficient and selective formic acid electrocatalysts. To produce methanol or methane, surfaces with $-0.3\text{ eV} < \Delta G_B[OH]$ (Figure 10) are expected to be the most effective.

As the potential limiting step for methanediol, methane, and methanol production is the same, a purely thermodynamic analysis is unable to predict the selectivity of one product over the other accurately. However, the selectivity of methanol over methane evolution might be observed[25] because the kinetic barriers are different for the methanol and methane evolution pathways. If selectivity is a requirement, it is possible to optimize the oxide surface for efficient $HCOOH_{(aq)}$ evolution. Bandi showed that Ag-doped Ru(Ti)O_2 can be very selective to produce formic acid.[24]

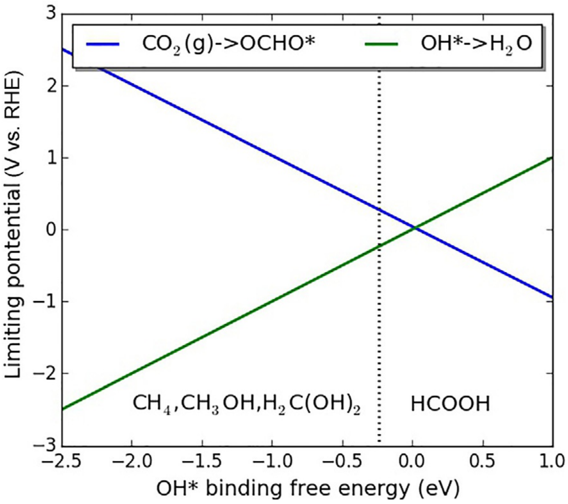

Figure 10. Volcano plot of the selectivity for formic acid and methanediol/methane/methanol formation. The dotted line denotes the ΔG_B[OH] value above which formic acid is not bound to the surface and $HCOOH_{(aq)}$ is the dominant product. The green line denotes the thermodynamically limiting potential on the stronger binding surfaces.

Our analysis (Figures 8 and 9b) can be used for the rule-of-thumb design of CO2RR catalysts. Among the overlayers considered here, those with Ir and Re atoms in the top layer are promising for experimental studies of CO2RR. We expect to observe an improved onset potential for liquid fuel production over the RuO_2(110) surface with the deposition of a single monolayer of IrO_2 on top of RuO_2. The deposition of a rhenium oxide monolayer should lead to a better selectivity for CO2RR than the HER. Conversely, the presence of a strongly binding metal oxide such as Ti-doped RuO_2 is expected to result in a higher overpotential. However, the selectivity of CO2RR over the HER is expected to be improved as on surfaces with Ti or Sn atoms, the formation of OCHO* is downhill and that of H* is uphill at 0 V-RHE (Figure 8), which leads to lower H* coverage and decreased HER. This work shows that the optimal mixture of COOH*/H*/OH* binding energies can lead to the suppression of CO and hydrogen evolution and efficient CO_2 reduction to liquid fuels on oxide surfaces. The wide variation in the binding energies of CO/H/OH species on the oxide surface compared to metals indicates that an oxide surface can be optimized for specific reactions, that is, with ΔG_B[COOH] and $\Delta G_B[H] > 0.5$ eV and $-0.5 < \Delta G_B[OH] < -0.3$ eV (for methane/methanol) or $-0.1 < \Delta G_B[OH] < 0.1$ eV (for $HCOOH_{(aq)}$).

Computational Methods

A plane wave basis set and projector-augmented wave based implementation of DFT, as implemented in VASP,[69] is used for total energy calculations. In the periodic repeating unit cell, 16 Å of vacuum is allowed in the direction normal to the catalytic surface to minimize any interaction under periodic boundary conditions.

The bottom two trilayers are fixed during atomic relaxations to represent the bulk structure, and 500 eV is used for the wavefunction cutoff. As ruthenium dioxide is a band conductor, a Gaussian smearing of 10 meV is used for the electronic states. The first Brillouin zone is sampled with a $4\times4\times1$ Monkhorst–Pack *k*-point mesh. The atoms in the top two trilayers are relaxed until forces on each atom are lower than 0.003 eV Å^{-1}. The same force criterion is used to determine the adsorbate configurations if placed on the top layer of the catalyst surface in bridge or cus sites, in which the top two trilayers are relaxed along with the adsorbates. We determine the contribution from the electrostatic dipole correction to be less than 10 meV for a number of investigated test cases including O*, OH*, OCHO*, HCOOH*, and H_2COOH* on pure $RuO_2(110)$ in the presence of a CO spectator. Therefore, we neglect the dipole correction in the following analysis. In our simulation, we use the BEEF-vdW[40] exchange correlation functional with the vdW-DF2[70] nonlocal correlation energy and potential. Although the RPBE functional was used in recent theoretical work on the CO_2 reduction mechanism over RuO_2 catalyst,[29] we use van der Waals correction to represent adsorbate interactions properly.[71,72] This is especially important for larger adsorbate molecules formed in CO_2 reduction. For the heterogeneous CO2RR, the BEEF-vdW functional has been shown to provide a better description of CO_2 reduction process than the RPBE functional.[73]

Acknowledgements

Funding from the Lundbeck foundation (R141-2013-A13204) and the Villum foundation (V-SUSTAIN) are gratefully acknowledged. The Niflheim supercomputer at DTU was used for the computations performed for this work.

Keywords: density functional calculations · electrochemistry · reduction · rutile oxide · thermodynamics

[1] H. B. Gray, *Nat. Chem.* **2009**, *1*, 7.
[2] S. Chu, A. Majumdar, *Nature* **2012**, *488*, 294–303.
[3] B. Dunn, H. Kamath, J.-M. Tarascon, *Science* **2011**, *334*, 928–935.
[4] Y. Hori, *Mod. Aspects Electrochem.* **2008**, *89*, 89–189.
[5] A. A. Peterson, F. Abild-Pedersen, F. Studt, J. Rossmeisl, J. K. Nørskov, *Energy Environ. Sci.* **2010**, *3*, 1311–1315.
[6] A. A. Peterson, J. K. Nørskov, *J. Phys. Chem. Lett.* **2012**, *3*, 251–258.
[7] J. H. Montoya, A. A. Peterson, J. K. Nørskov, *ChemCatChem* **2013**, *5*, 737–742.
[8] J. H. Montoya, C. Shi, K. Chan, J. K. Nørskov, *J. Phys. Chem. Lett.* **2015**, *6*, 2032–2037.
[9] F. Calle-Vallejo, M. T. M. Koper, *Angew. Chem. Int. Ed.* **2013**, *52*, 7282–7285; *Angew. Chem.* **2013**, *125*, 7423–7426.
[10] K. J. P. Schouten, Y. Kwon, C. J. M. van der Ham, Z. Qin, M. T. M. Koper, *Chem. Sci.* **2011**, *2*, 1902–1909.
[11] C. W. Li, J. Ciston, M. W. Kanan, *Nature* **2014**, *508*, 504–507.
[12] J. K. Nørskov, T. Bligaard, J. Rossmeisl, C. H. Christensen, *Nat. Chem.* **2009**, *1*, 37–46.
[13] F. Abild-Pedersen, J. Greeley, F. Studt, J. Rossmeisl, T. R. Munter, P. G. Moses, E. Skúlason, T. Bligaard, J. K. Nørskov, *Phys. Rev. Lett.* **2007**, *99*, 016105.
[14] P. Strasser, S. Koh, T. Anniyev, J. Greeley, K. More, C. Yu, Z. Liu, S. Kaya, D. Nordlund, H. Ogasawara, M. F. Toney, A. Nilsson, *Nat. Chem.* **2010**, *2*, 454–460.
[15] F. Calle-Vallejo, M. T. M. Koper, A. S. Bandarenka, *Chem. Soc. Rev.* **2013**, *42*, 5210–5230.
[16] A. Vojvodic, J. K. Nørskov, *Science* **2011**, *334*, 1355–1356.
[17] J. K. Nørskov, J. Rossmeisl, A. Logadottir, L. Lindqvist, J. R. Kitchin, T. Bligaard, H. Jónsson, *J. Phys. Chem. B* **2004**, *108*, 17886–17892.
[18] J. Greeley, I. E. L. Stephens, A. S. Bondarenko, T. P. Johansson, H. A. Hansen, T. F. Jaramillo, J. Rossmeisl, I. Chorkendorff, J. K. Nørskov, *Nat. Chem.* **2009**, *1*, 552–556.
[19] J. Greeley, T. F. Jaramillo, J. Bonde, I. B. Chorkendorff, J. K. Nørskov, *Nat. Mater.* **2006**, *5*, 909–913.
[20] M. Karamad, V. Tripkovic, J. Rossmeisl, *ACS Catal.* **2014**, *4*, 2268–2273.
[21] H. A. Hansen, C. Shi, A. Lausche, A. Peterson, J. K. Nørskov, *Phys. Chem. Chem. Phys.* **2016**, *18*, 9194–9201.
[22] H. A. Hansen, J. B. Varley, A. A. Peterson, J. K. Nørskov, *J. Phys. Chem. Lett.* **2013**, *4*, 388–392.
[23] J. S. Yoo, R. Christensen, T. Vegge, J. K. Nørskov, F. Studt, *ChemSusChem* **2016**, *9*, 358–363.
[24] A. Bandi, *J. Electrochem. Soc.* **1990**, *137*, 2157–2160.
[25] N. Spataru, K. Tokuhiro, C. Terashima, T. N. Rao, A. Fujishima, *J. Appl. Electrochem.* **2003**, *33*, 1205–1210.
[26] J. Qu, X. Zhang, Y. Wang, C. Xie, *Electrochim. Acta* **2005**, *50*, 3576–3580.
[27] N. Ullah, I. Ali, M. Jansen, S. Omanovic, *Can. J. Chem. Eng.* **2015**, *93*, 55–62.
[28] J. P. Popić, M. L. Avramovivić, N. B. Vuković, *J. Electroanal. Chem.* **1997**, *421*, 105–110.
[29] M. Karamad, H. A. Hansen, J. Rossmeisl, J. K. Nørskov, *ACS Catal.* **2015**, *5*, 4075–4081.
[30] E. E. Benson, C. P. Kubiak, A. J. Sathrum, J. M. Smieja, *Chem. Soc. Rev.* **2009**, *38*, 89–99.
[31] I. C. Man, H. Y. Su, F. Calle-Vallejo, H. A. Hansen, J. I. Martínez, N. G. Inoglu, J. Kitchin, T. F. Jaramillo, J. K. Nørskov, J. Rossmeisl, *ChemCatChem* **2011**, *3*, 1159–1165.
[32] G. Jones, T. Bligaard, F. Abild-Pedersen, J. K. Nørskov, *J. Phys. Condens. Matter* **2008**, *20*, 064239.
[33] A. B. Laursen, A. So, F. Dionigi, H. Fanchiu, C. Miller, O. L. Trinhammer, J. Rossmeisl, S. Dahl, *J. Chem. Educ.* **2012**, *89*, 1595–1599.
[34] C. Shi, C. P. O'Grady, A. A. Peterson, H. A. Hansen, J. K. Nørskov, *Phys. Chem. Chem. Phys.* **2013**, *15*, 7114–7122.
[35] S. R. Bahn, K. W. Jacobsen, *Comput. Sci. Eng.* **2002**, *4*, 56–66.
[36] R. Christensen, H. A. Hansen, T. Vegge, *Catal. Sci. Technol.* **2015**, *5*, 4946–4949.
[37] H. A. Hansen, J. H. Montoya, Y.-J. Zhang, C. Shi, A. A. Peterson, J. K. Nørskov, *Catal. Lett.* **2013**, *143*, 631–635.
[38] D. Ren, Y. Deng, A. D. Handoko, C. S. Chen, S. Malkhandi, B. S. Yeo, *ACS Catal.* **2015**, *5*, 2814–2821.
[39] S. R. Butler, J. L. Gillson, *Mater. Res. Bull.* **1971**, *6*, 81–89.
[40] J. Wellendorff, K. T. Lundgaard, A. Møgelhøj, V. Petzold, D. D. Landis, J. K. Nørskov, T. Bligaard, K. W. Jacobsen, *Phys. Rev. B* **2012**, *85*, 235149.
[41] P. Haas, F. Tran, P. Blaha, *Phys. Rev. B* **2009**, *79*, 085104.
[42] D. Rochefort, P. Dabo, D. Guay, P. M. A. Sherwood, *Electrochim. Acta* **2003**, *48*, 4245–4252.
[43] A. S. Bandarenka, A. S. Varela, M. Karamad, F. Calle-Vallejo, L. Bech, F. J. Perez-Alonso, J. Rossmeisl, I. E. L. Stephens, I. Chorkendorff, *Angew. Chem. Int. Ed.* **2012**, *51*, 11845–11848; *Angew. Chem.* **2012**, *124*, 12015–12018.
[44] J. Knudsen, A. U. Nilekar, R. T. Vang, J. Schnadt, E. L. Kunkes, J. A. Dumesic, M. Mavrikakis, F. Besenbacher, *J. Am. Chem. Soc.* **2007**, *129*, 6485–6490.
[45] R. Reske, M. Duca, M. Oezaslan, K. J. P. Schouten, M. T. M. Koper, P. Strasser, *J. Phys. Chem. Lett.* **2013**, *4*, 2410–2413.
[46] T. G. Kelly, J. G. Chen, *Chem. Soc. Rev.* **2012**, *41*, 8021–8034.
[47] Y. Hikita, K. Nishio, L. C. Seitz, P. Chakthranont, T. Tachikawa, T. F. Jaramillo, H. Y. Hwang, *Adv. Energy Mater.* **2016**, *6*, 1502154.
[48] J. Zhang, M. B. Vukmirovic, Y. Xu, M. Mavrikakis, R. R. Adzic, *Angew. Chem. Int. Ed.* **2005**, *44*, 2132–2135; *Angew. Chem.* **2005**, *117*, 2170–2173.
[49] P. Liu, J. K. Nørskov, *Phys. Chem. Chem. Phys.* **2001**, *3*, 3814–3818.
[50] J. R. Kitchin, J. K. Nørskov, M. A. Barteau, J. G. Chen, *Phys. Rev. Lett.* **2004**, *93*, 156801.
[51] J. C. Davies, J. Bonde, Á. Logadóttir, J. K. Nørskov, I. Chorkendorff, *Fuel Cells* **2005**, *5*, 429–435.
[52] A. Grimaud, K. J. May, C. E. Carlton, Y.-L. Lee, M. Risch, W. T. Hong, J. Zhou, Y. Shao-Horn, *Nat. Commun.* **2013**, *4*, 2439.
[53] M. K. Min, J. Cho, K. Cho, H. Kim, *Electrochim. Acta* **2000**, *45*, 4211–4217.
[54] J. J. Mortensen, B. Hammer, J. K. Nørskov, *Surf. Sci.* **1998**, *414*, 315–329.
[55] J. Neugebauer, M. Scheffler, *Phys. Rev. B* **1992**, *46*, 16067–16080.

[56] Y. J. Zhang, V. Sethuraman, R. Michalsky, A. A. Peterson, *ACS Catal.* **2014**, *4*, 3742 – 3748.
[57] C. Shi, H. A. Hansen, A. C. Lausche, J. K. Nørskov, *Phys. Chem. Chem. Phys.* **2014**, *16*, 4720 – 4727.
[58] P. J. D. Lindan, N. M. Harrison, M. J. Gillan, *Phys. Rev. Lett.* **1998**, *80*, 762 – 765.
[59] J. Rossmeisl, Z. W. Qu, H. Zhu, G. J. Kroes, J. K. Nørskov, *J. Electroanal. Chem.* **2007**, *607*, 83 – 89.
[60] J. Rossmeisl, A. Logadottir, J. K. Nørskov, *Chem. Phys.* **2005**, *319*, 178 – 184.
[61] M. M. Montemore, J. W. Medlin, *Catal. Sci. Technol.* **2014**, *4*, 3748 – 3761.
[62] S. Shin, H. H. Huang, M. Ishigame, H. Iwahara, *Solid State Ionics* **1990**, *40 – 41*, 910 – 913.
[63] P. Ferrin, A. U. Nilekar, J. Greeley, M. Mavrikakis, J. Rossmeisl, *Surf. Sci.* **2008**, *602*, 3424 – 3431.
[64] N. Bork, N. Bonanos, J. Rossmeisl, T. Vegge, *Phys. Chem. Chem. Phys.* **2011**, *13*, 15256 – 15263.
[65] V. Viswanathan, H. A. Hansen, J. Rossmeisl, J. K. Nørskov, *J. Phys. Chem. Lett.* **2012**, *3*, 2948 – 2951.
[66] S. Lee, J. D. Ocon, Y. I. Son, J. Lee, *J. Phys. Chem. C* **2015**, *119*, 4884 – 4890.
[67] C. Zhao, J. Wang, J. B. Goodenough, *Electrochem. Commun.* **2016**, *65*, 9 – 13.
[68] C. Cui, J. Han, X. Zhu, X. Liu, H. Wang, D. Mei, Q. Ge, *J. Catal.* **2016**, DOI: 10.1016/j.jcat.2015.12.001.
[69] G. Kresse, *Phys. Rev. B* **1999**, *59*, 1758 – 1775.
[70] K. Lee, E. D. Murray, L. Z. Kong, B. I. Lundqvist, D. C. Langreth, *Phys. Rev. B* **2010**, *82*, 081101.
[71] W. Liu, J. Carrasco, B. Santra, A. Michaelides, M. Scheffler, A. Tkatchenko, *Phys. Rev. B* **2012**, *86*, 245405.
[72] J. P. P. Ramalho, J. R. B. Gomes, F. Illas, *RSC Adv.* **2013**, *3*, 13085.
[73] F. Studt, F. Abild-Pedersen, J. B. Varley, J. K. Nørskov, *Catal. Lett.* **2013**, *143*, 71 – 73.

Received: June 24, 2016
Revised: August 9, 2016

CHEMISTRY & SUSTAINABILITY
CHEMSUSCHEM
ENERGY & MATERIALS

Supporting Information

Descriptors and Thermodynamic Limitations of Electrocatalytic Carbon Dioxide Reduction on Rutile Oxide Surfaces

Arghya Bhowmik, Tejs Vegge, and Heine A. Hansen*[a]

cssc_201600845_sm_miscellaneous_information.pdf

Table S1: Free energy calculation at 298.15 K for reactant and product molecules in this study. Fugacities, free energy corrections are also listed.

Species	Fugacity [Pa]	E_{elec} [eV]	ZPE [eV]	Heat capacity contribution [eV]	-TS [eV]	Correction [eV]
CO	5562	-12.07	0.13	0.09	-0.69	0.15
CO_2	101325	-18.4	0.31	0.1	-0.66	0.3
H_2	101325	-7.17	0.28	0.09	-0.4	0.1
H_2O	3534	-12.81	0.57	0.11	-0.67	0
HCOOH	2	-25.49	0.9	0.11	-1.05	0.15 and -0.19
CH_3OH	6079	-27.74	1.37	0.11	-0.81	0
CH_4	20467	-23.28	1.2	0.1	-0.62	0

* Free energy corrections of 0.15/0.3/0.1/0.15 eV respectively for CO/CO_2/H_2/HCOOH are obtained from [1]. HCOOH stays as a solvated ionic species $HCOO^-$ in solution, giving it extra stability. We estimate the free energy contribution of that to be -0.19 eV at pH 7 following [2]. The free energy of methanediol is calculated from $CO_2(g) + 2 H_2(g) \rightarrow H_2C(OH)_2(aq)$, which have a reaction free energy of 0.36 eV[3].

Table S2: Binding free energy calculation data for all surfaces

Table S2(a): Pure $RuO_2(110)$ surface

adsorbate	E_{elec} [eV]	ZPE [eV]	Heat capacity contribution [eV]	-TS [eV]
CO(br)	-251.79	0.2	0.07	-0.14
CO(br)+OCHO(br+cus)	-275.3	0.83	0.16	-0.29
CO(br)+O(br)	-257.2	0.29	0.09	-0.22
CO(br)+OH(br)	-262.02	0.57	0.11	-0.2
CO(br)+HCOOH(br)	-278.4	1.17	0.173	-0.33
CO(br)+H_2COOH(br)	-282.62	1.47	0.17	-0.3
CO(br)+H_2CO(br)	-272.5	1.01	0.14	-0.28
CO(br)+H_2COH(br)	-276.29	1.33	0.14	-0.26
CO(br)+H_3CO(br)	-277.1	1.32	0.16	-0.31
CO(br)+H_3COH(br)	-280.44	1.53	0.16	-0.32
CO(br)+H_3CO(br)+OH(cus)	-286.37	1.7	0.2	-0.37
CO(br)+H(br)	-255.85	0.41	0.07	-0.15
CO(br)+COOH(br)	-274.17	0.84	0.15	-0.29

Table S2(b): Ir over-layer

adsorbate	E_{elec} [eV]	ZPE [eV]	Heat capacity contribution [eV]	-TS [eV]
CO(br)	-246.56	0.22	0.06	-0.14
CO(br)+OCHO(br+cus)	-269.6	0.84	0.15	-0.3
CO(br)+O(br)	-251.94	0.28	0.09	-0.16

CO(br)+OH(br)	-256.67	0.6	0.1	-0.18
CO(br)+HCOOH(br)	-272.94	1.18	0.17	-0.33
CO(br)+H_2COOH(br)	-277.11	1.49	0.16	-0.29
CO(br)+H_2CO(br)	-266.71	1.03	0.13	-0.25
CO(br)+H_2COH(br)	-271.51	1.26	0.14	-0.25
CO(br)+H_3CO(br)	-271.72	1.34	0.14	-0.26
CO(br)+H_3COH(br)	-274.64	1.66	0.16	-0.32
CO(br)+H_3CO(br)+OH(cus)	-281.2	1.71	0.2	-0.37
CO(br)+H(br)	-250.42	0.38	0.07	-0.15
CO(br)+COOH(br)	-268.93	0.86	0.14	-0.26

Table S2(c): Mo over-layer

adsorbate	E_{elec} [eV]	ZPE [eV]	Heat capacity contribution [eV]	-TS [eV]
CO(br)	-266.21	0.21	0.06	-0.13
CO(br)+OCHO(br+cus)	-289.81	0.84	0.15	-0.28
CO(br)+O(br)	-272.98	0.29	0.09	-0.18
CO(br)+OH(br)	-276.65	0.57	0.11	-0.2
CO(br)+HCOOH(br)	-293.27	1.14	0.15	-0.3
CO(br)+H_2COOH(br)	-297.13	1.5	0.16	-0.28
CO(br)+H_2CO(br)	-286.99	1	0.15	-0.28
CO(br)+H_2COH(br)	-290.38	1.34	0.13	-0.22
CO(br)+H_3CO(br)	-291.7	1.32	0.14	-0.26
CO(br)+H_3COH(br)	-295.16	1.67	0.17	-0.33
CO(br)+H_3CO(br)+OH(cus)	-301.24	1.71	0.19	-0.35
CO(br)+H(br)	-270.18	0.42	0.05	-0.09
CO(br)+COOH(br)	-288.48	0.84	0.15	-0.28

Table S2(d): Nb over-layer

adsorbate	E_{elec} [eV]	ZPE [eV]	Heat capacity contribution [eV]	-TS [eV]
CO(br)	-270.27	0.22	0.05	-0.08
CO(br)+OCHO(br+cus)	-294.41	0.85	0.14	-0.25
CO(br)+O(br)	-277.91	0.29	0.08	-0.14
CO(br)+OH(br)	-281.76	0.6	0.09	-0.15
CO(br)+HCOOH(br)	-297.82	1.15	0.15	-0.29
CO(br)+H_2COOH(br)	-301.85	1.5	0.15	-0.3
CO(br)+H_2CO(br)	-292.28	1.02	0.13	-0.26
CO(br)+H_2COH(br)	-294.4	1.33	0.12	-0.2
CO(br)+H_3CO(br)	-296.43	1.33	0.15	-0.31
CO(br)+H_3COH(br)	-298.84	1.67	0.16	-0.31
CO(br)+H_3CO(br)+OH(cus)	-305.82	1.67	0.22	-0.44
CO(br)+H(br)	-274.97	0.41	0.05	-0.09
CO(br)+COOH(br)	-292.89	0.85	0.14	-0.26

Table S2(e): Pd over-layer

adsorbate	E_{elec} [eV]	ZPE [eV]	Heat capacity contribution [eV]	-TS [eV]
CO(br)	-230.29	0.19	0.07	-0.15
CO(br)+OCHO(br+cus)	-251.92	0.83	0.14	-0.26
CO(br)+O(br)	-233.76	0.28	0.1	-0.17
CO(br)+OH(br)	-239.16	0.6	0.1	-0.18
CO(br)+HCOOH(br)	-256.08	1.13	0.21	-0.45
CO(br)+H_2COOH(br)	-259.134	1.48	0.18	-0.35
CO(br)+H_2CO(br)	-250.12	0.94	0.1	-0.17
CO(br)+H_2COH(br)	-254.37	1.35	0.15	-0.29
CO(br)+H_3CO(br)	-254.2	1.34	0.14	-0.28
CO(br)+H_3COH(br)	-258.43	1.62	0.19	-0.41
CO(br)+H_3CO(br)+OH(cus)	-262.43	1.71	0.2	-0.36
CO(br)+H(br)	-233.6	0.36	0.08	-0.15
CO(br)+COOH(br)	-251.76	0.84	0.16	-0.32

Table S2(f): Pt over-layer

adsorbate	E_{elec} [eV]	ZPE [eV]	Heat capacity contribution [eV]	-TS [eV]
CO(br)	-234.42	0.21	0.06	-0.12
CO(br)+OCHO(br+cus)	-256.77	0.86	0.14	-0.26
CO(br)+O(br)	-239.06	0.3	0.08	-0.15
CO(br)+OH(br)	-244.05	0.63	0.09	-0.15
CO(br)+HCOOH(br)	-260.32	1.14	0.21	-0.45
CO(br)+H_2COOH(br)	-264.12	1.51	0.18	-0.35
CO(br)+H_2CO(br)	-255.56	1.07	0.1	-0.17
CO(br)+H_2COH(br)	-259.07	1.36	0.15	-0.28
CO(br)+H_3CO(br)	-259.14	1.37	0.15	-0.28
CO(br)+H_3COH(br)	-262.68	1.66	0.15	-0.27
CO(br)+H_3CO(br)+OH(cus)	-268.09	1.75	0.19	-0.34
CO(br)+H(br)	-238.31	0.37	0.07	-0.13
CO(br)+COOH(br)	-256.64	0.87	0.14	-0.26

Table S2(g): Re over-layer

adsorbate	E_{elec} [eV]	ZPE [eV]	Heat capacity contribution [eV]	-TS [eV]
CO(br)	-266.2	0.21	0.06	-0.12
CO(br)+OCHO(br+cus)	-289.66	0.85	0.15	-0.27
CO(br)+O(br)	-272.2	0.31	0.07	-0.13
CO(br)+OH(br)	-276.42	0.59	0.1	-0.19
CO(br)+HCOOH(br)	-292.79	1.17	0.15	-0.32
CO(br)+H_2COOH(br)	-297.1	1.5	0.15	-0.27
CO(br)+H_2CO(br)	-286.53	1.01	0.14	-0.28
CO(br)+H_2COH(br)	-290.53	1.34	0.13	-0.24
CO(br)+H_3CO(br)	-291.47	1.35	0.14	-0.29
CO(br)+H_3COH(br)	-294.79	1.68	0.16	-0.29
CO(br)+H_3CO(br)+OH(cus)	-301.73	1.73	0.2	-0.37
CO(br)+H(br)	-269.02	0.41	0.06	-0.09
CO(br)+COOH(br)	-288.81	0.86	0.14	-0.26

Table S2(h): Sn over-layer

adsorbate	E_{elec} [eV]	ZPE [eV]	Heat capacity contribution [eV]	-TS [eV]
CO(br)	-236.72	0.18	0.06	-0.12
CO(br)+OCHO(br+cus)	-259.3	0.84	0.15	-0.28
CO(br)+O(br)	-242.46	0.23	0.08	-0.15
CO(br)+OH(br)	-246.79	0.51	0.09	-0.15
CO(br)+HCOOH(br)	-262.77	1.12	0.21	-0.45
CO(br)+H_2COOH(br)	-266.46	1.47	0.18	-0.35
CO(br)+H_2CO(br)	-256.7	0.94	0.19	-0.4
CO(br)+H_2COH(br)	-259.98	1.3	0.16	-0.29
CO(br)+H_3CO(br)	-261.25	1.31	0.14	-0.26
CO(br)+H_3COH(br)	-264.79	1.59	0.16	-0.32
CO(br)+H_3CO(br)+OH(cus)	-270.61	1.69	0.21	-0.42
CO(br)+H(br)	-240.11	0.31	0.07	-0.15
CO(br)+COOH(br)	-258.34	0.81	0.17	-0.31

Table S2(i): Ta over-layer

adsorbate	E_{elec} [eV]	ZPE [eV]	Heat capacity contribution [eV]	-TS [eV]
CO(br)	-280.99	0.22	0.04	-0.07
CO(br)+OCHO(br+cus)	-305.22	0.86	0.14	-0.25
CO(br)+O(br)	-288.99	0.3	0.07	-0.12
CO(br)+OH(br)	-292.63	0.61	0.08	-0.14
CO(br)+HCOOH(br)	-308.41	1.17	0.15	-0.28
CO(br)+H_2COOH(br)	-312.78	1.5	0.15	-0.26
CO(br)+H_2CO(br)	-303.19	1.03	0.11	-0.17
CO(br)+H_2COH(br)	-305.3	1.34	0.12	-0.19
CO(br)+H_3CO(br)	-307.61	1.36	0.13	-0.24
CO(br)+H_3COH(br)	-309.33	1.67	0.15	-0.29
CO(br)+H_3CO(br)+OH(cus)	-316.55	1.7	0.22	-0.44
CO(br)+H(br)	-285.6	0.42	0.05	-0.08
CO(br)+COOH(br)	-303.86	0.86	0.14	-0.24

Table S2(j): Ti over-layer

adsorbate	E_{elec} [eV]	ZPE [eV]	Heat capacity contribution [eV]	-TS [eV]
CO(br)	-271.35	0.18	0.07	-0.18
CO(br)+OCHO(br+cus)	-294.85	0.81	0.18	-0.35
CO(br)+O(br)	-278.02	0.25	0.09	-0.18
CO(br)+OH(br)	-281.88	0.54	0.13	-0.26
CO(br)+HCOOH(br)	-297.67	1.15	0.17	-0.33
CO(br)+H_2COOH(br)	-302.12	1.46	0.18	-0.34
CO(br)+H_2CO(br)	-291.81	0.97	0.16	-0.33
CO(br)+H_2COH(br)	-294.89	1.29	0.16	-0.31
CO(br)+H_3CO(br)	-296.91	1.3	0.16	-0.31
CO(br)+H_3COH(br)	-299.93	1.64	0.18	-0.37
CO(br)+H_3CO(br)+OH(cus)	-306.04	1.66	0.23	-0.46
CO(br)+H(br)	-274.89	0.36	0.09	-0.21
CO(br)+COOH(br)	-293.08	0.81	0.17	-0.33

Table S2(k): W over-layer

adsorbate	E_{elec} [eV]	ZPE [eV]	Heat capacity contribution [eV]	-TS [eV]
CO(br)	-274.23	0.2	0.06	-0.14
CO(br)+OCHO(br+cus)	-298.72	0.85	0.15	-0.26
CO(br)+O(br)	-282.27	0.31	0.07	-0.12
CO(br)+OH(br)	-285.55	0.58	0.1	-0.19
CO(br)+HCOOH(br)	-302.13	1.17	0.15	-0.28
CO(br)+H_2COOH(br)	-306.41	1.51	0.13	-0.21
CO(br)+H_2CO(br)	-295.44	1	0.14	-0.25
CO(br)+H_2COH(br)	-299.18	1.35	0.12	-0.22
CO(br)+H_3CO(br)	-300.61	1.33	0.15	-0.31
CO(br)+H_3COH(br)	-303.41	1.67	0.16	-0.3
CO(br)+H_3CO(br)+OH(cus)	-310.73	1.71	0.18	-0.33
CO(br)+H(br)	-279.21	0.43	0.05	-0.07
CO(br)+COOH(br)	-297.5	0.85	0.14	-0.25

Table S3: OH* binding free energies for bridge and cus site for all over-layers

Transition metal at top layer	OH* binding free energy [eV]	
	Bridge (CO(br) spectator)	Cus (CO(br)+H_3CO(br) spectator)
Ru	-0.64	0.34
Ir	-0.49	0.09
Mo	-0.86	0.06
Nb	-1.90	0.13
Pd	0.78	1.35
Pt	0.02	0.65
Re	-0.63	-0.66
Sn	-0.51	0.18
Ta	-2.03	0.54
Ti	-0.95	0.39
W	-1.70	-0.57

Table S4: Data for calculation of HER onset potential without the presence of CO* spectator

Transition metal at top layer	E_{elec} [eV] for reduced surface	For 1/4th monolayer H* at bridge site			
		E_{elec} [eV]	ZPE [eV]	Heat capacity contribution [eV]	-TS [eV]
Ru	-237.86	-242.1	0.2	0	0
Ir	-232.35	-236.83	0.19	0	-0.01
Mo	-251.53	-256.28	0.21	0	0
Nb	-256.15	-260.77	0.19	0	-0.01
Pd	-217.49	-220.97	0.18	0	-0.01
Pt	-220.8	-225.03	0.2	0	0
Re	-249.98	-254.82	0.21	0	0
Sn	-224.38	-228.04	0.2	0	0
Ta	-266.89	-270.6	0.21	0	0
Ti	-258.33	-262.21	0.2	0	0
W	-259.72	-264.26	0.2	0	0

Scaling relations

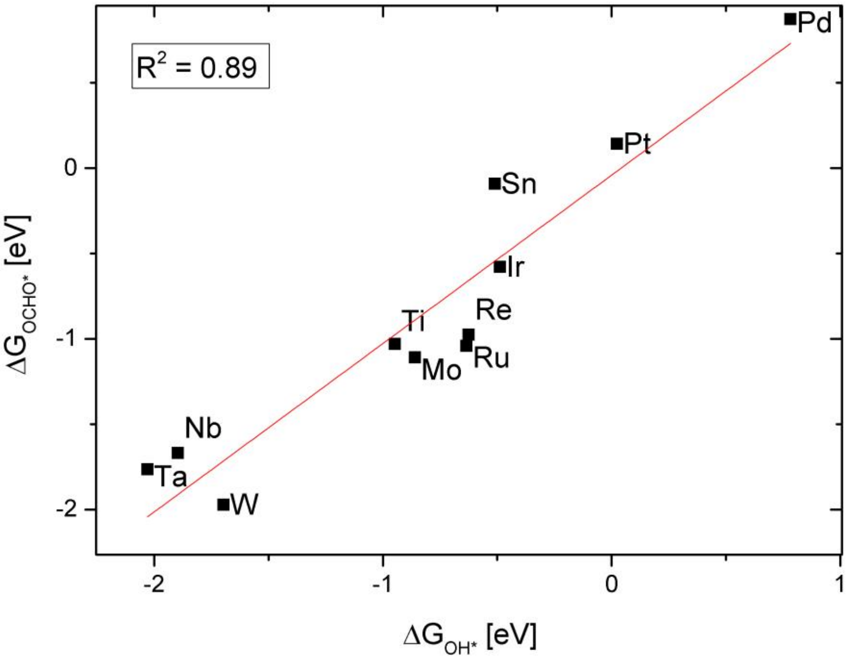

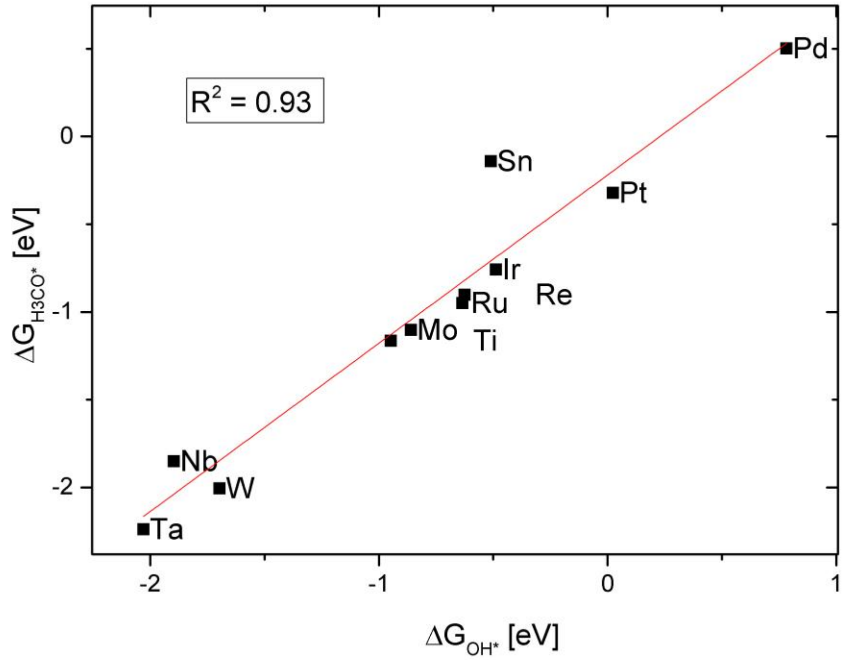

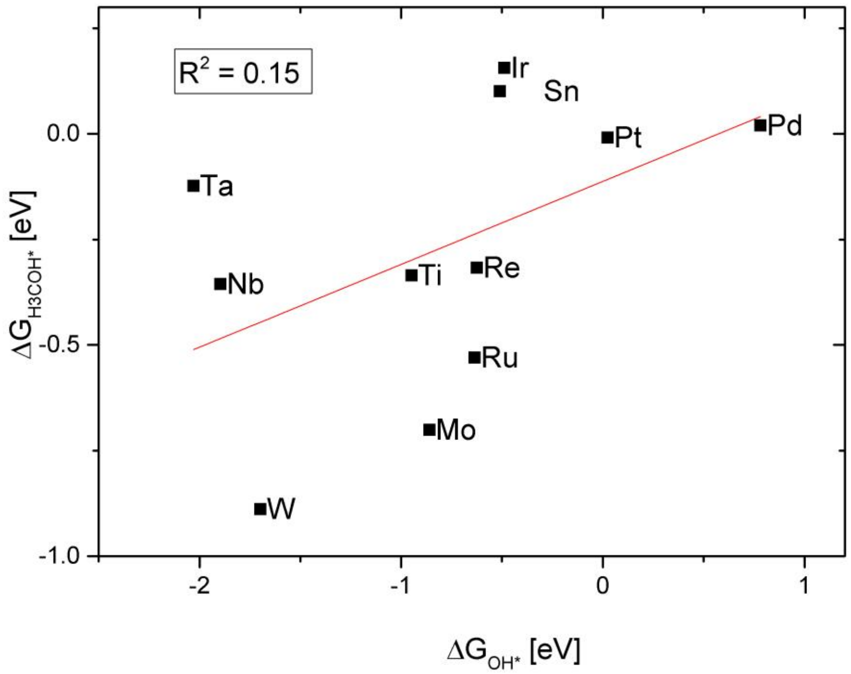

R^2 = 0.15
Ir
Sn
Pt
Pd
Ta
Nb
Ti
Re
Ru
Mo
W
0.0
-0.5
-1.0
-2
-1
0
1
ΔG$_{H3COH*}$ [eV]
ΔG$_{OH*}$ [eV]

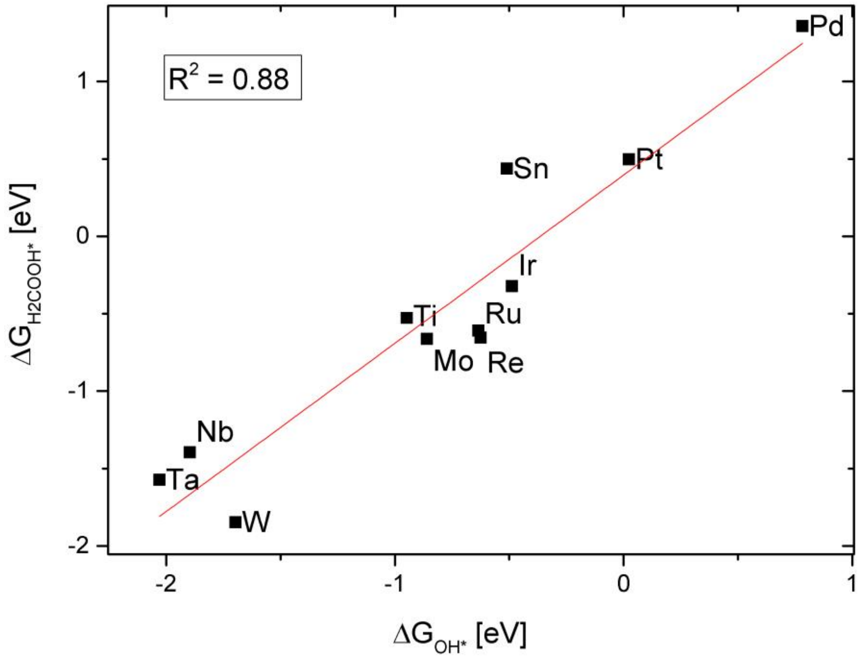

R^2 = 0.88
Pd
Sn
Pt
Ir
Ti
Ru
Mo
Re
Nb
Ta
W
1
0
-1
-2
-2
-1
0
1
ΔG$_{H2COOH*}$ [eV]
ΔG$_{OH*}$ [eV]

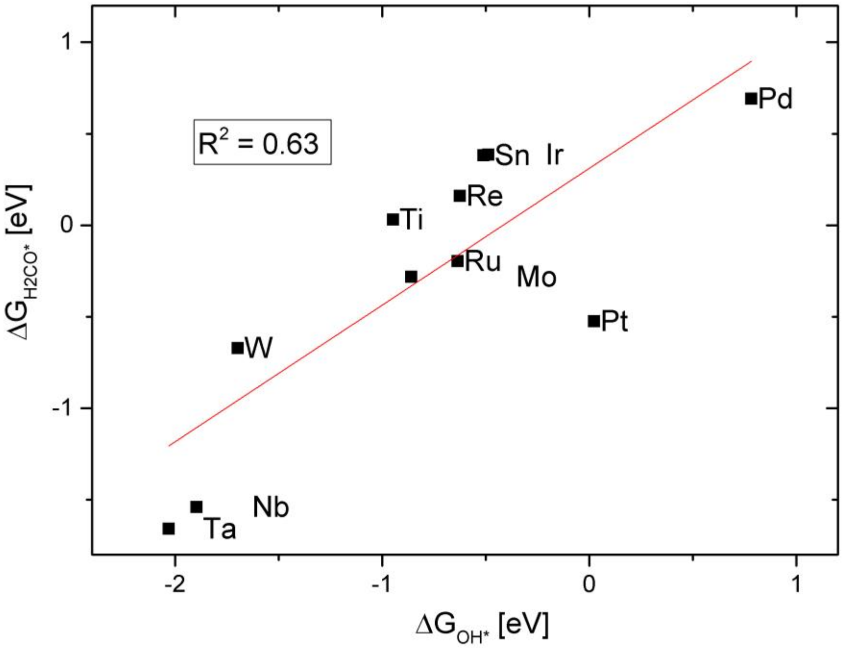
R^2 = 0.63
ΔG_{H2CO*} [eV]
ΔG_{OH*} [eV]
1
0
-1
-2
Pd
Sn
Ir
Re
Ti
Ru
Mo
Pt
W
Nb
Ta

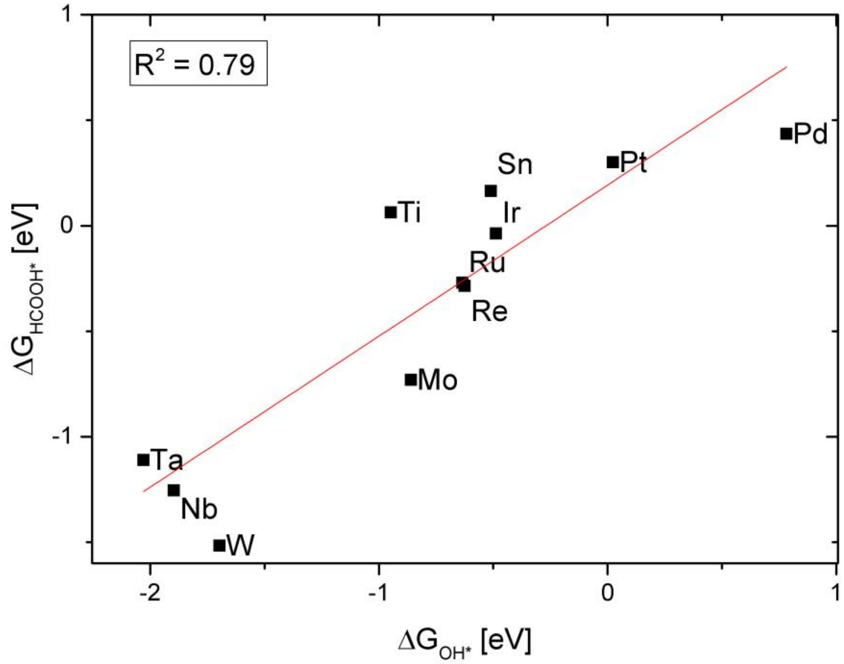
R^2 = 0.79
ΔG_{HCOOH*} [eV]
ΔG_{OH*} [eV]
1
0
-1
-2
Pd
Pt
Sn
Ir
Ti
Ru
Re
Mo
Ta
Nb
W

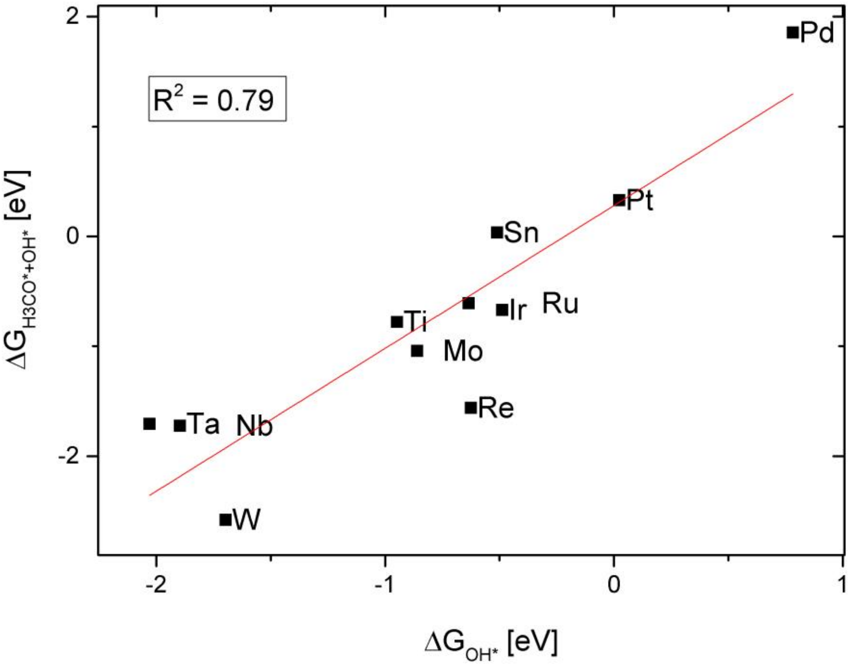

R² = 0.79
ΔG_H3CO*+OH* [eV]
ΔG_OH* [eV]
2
0
-2
-2
-1
0
1
Pd
Pt
Sn
Ru
Ir
Ti
Mo
Re
Ta
Nb
W

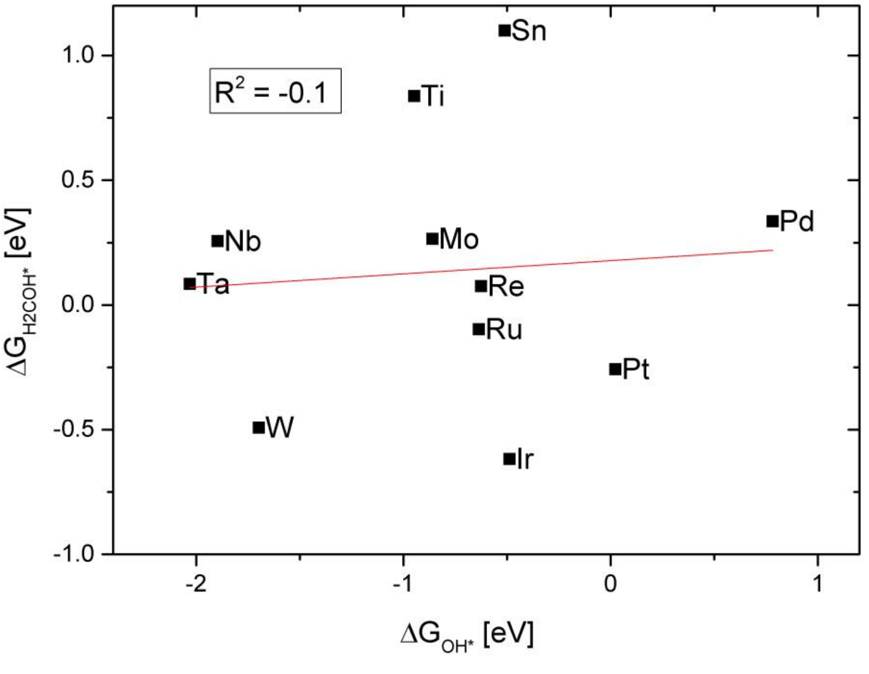

R² = -0.1
ΔG_H2COH* [eV]
ΔG_OH* [eV]
1.0
0.5
0.0
-0.5
-1.0
-2
-1
0
1
Sn
Ti
Pd
Nb
Mo
Ta
Re
Ru
Pt
W
Ir

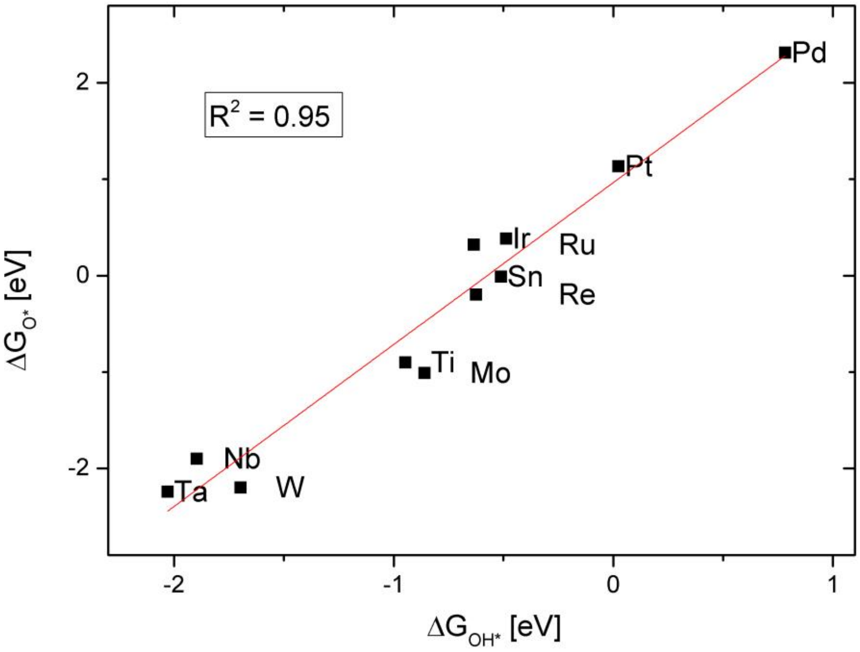

Figure S1: Scaling relations for CO2RR intermediates on oxide over-layers.

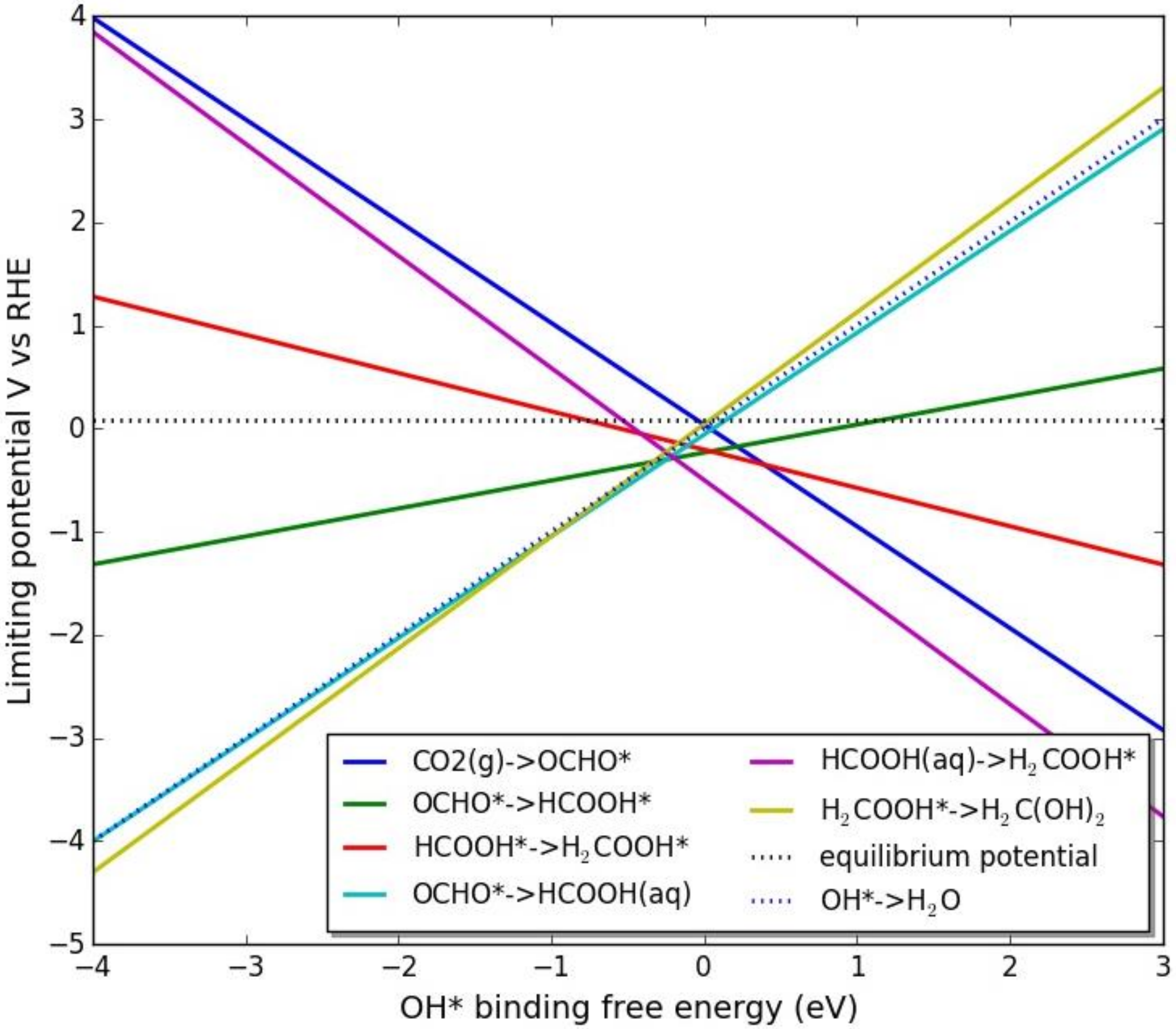

Figure S2: Volcano construction for methanediol production using free energy scaling relations.

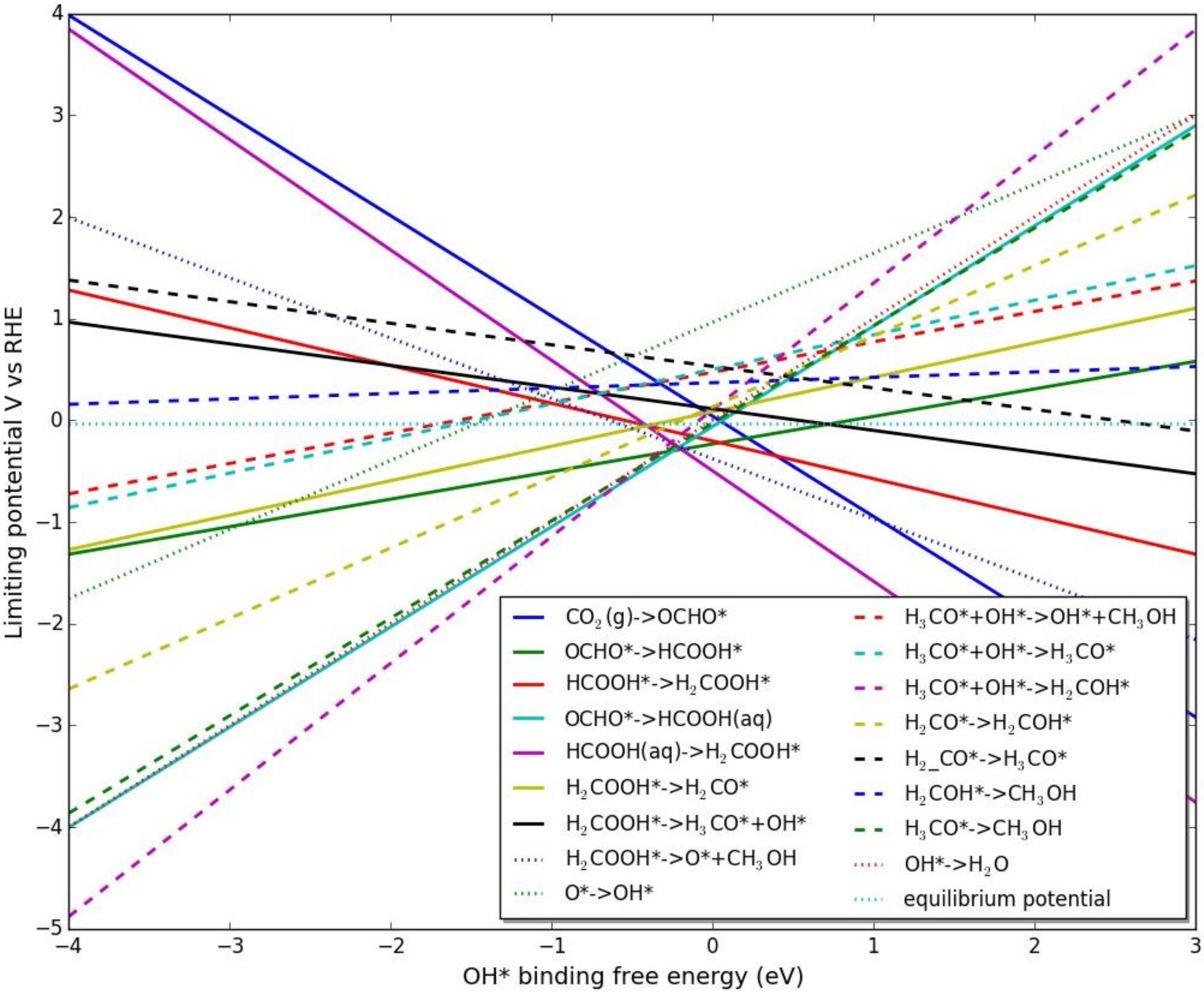

Figure S3: Volcano construction for methanol production using free energy scaling relations.

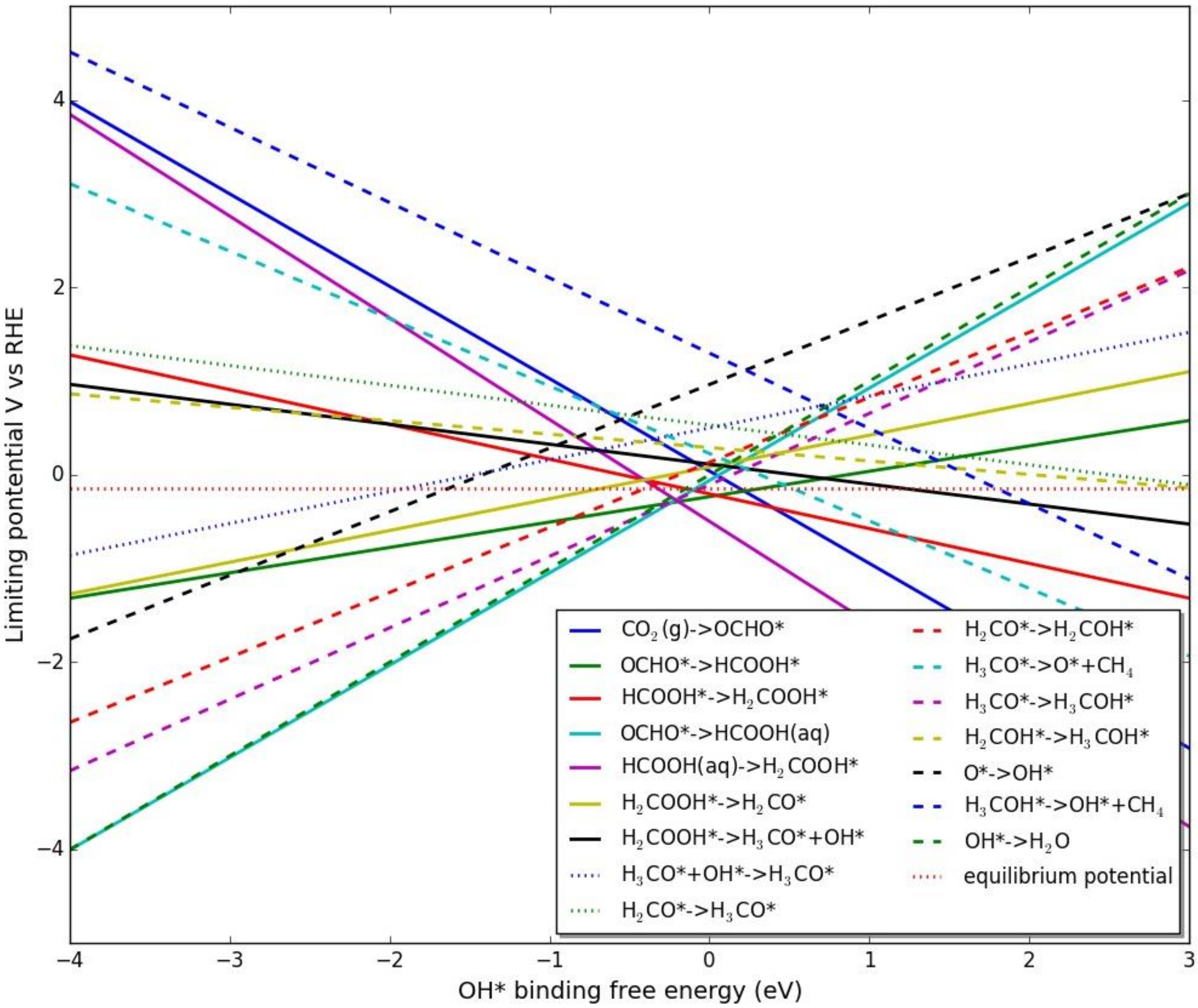

Figure S4: Volcano construction for methane production using free energy scaling relations.

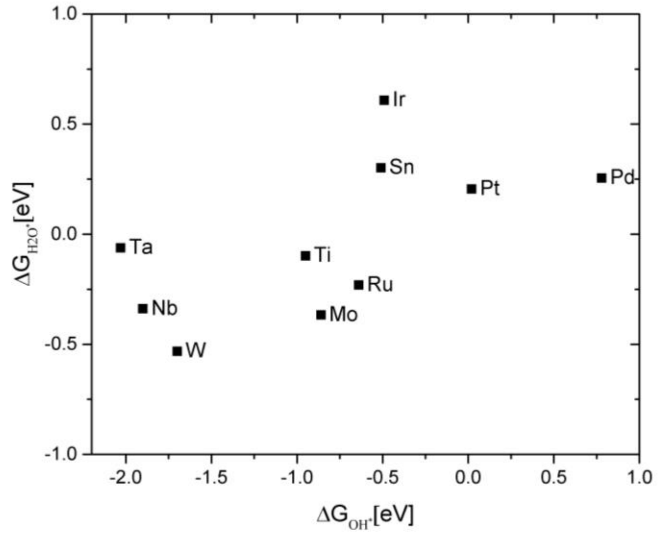

Figure S5: Binding free energy correlation between OH* and H_2O* at one bridge site with spectator CO* at the other bridge site.

References

[1] R. Christensen, H. A. Hansen, T. Vegge, *Catal. Sci. Technol.* **2015**, *5*, 4946–4949.

[2] H. A. Hansen, C. Shi, A. Lausche, A. Peterson, J. K. Nørskov, *Phys. Chem. Chem. Phys.* **2016**, *18*, 9194–9201.

[3] H. A. Hansen, J. H. Montoya, Y.-J. Zhang, C. Shi, A. A. Peterson, J. K. Nørskov, *Catal. Letters* **2013**, *143*, 631–635.

THE JOURNAL OF
PHYSICAL CHEMISTRY C

Article

pubs.acs.org/JPCC

Role of CO* as a Spectator in CO_2 Electroreduction on RuO_2

Arghya Bhowmik, Heine Anton Hansen, and Tejs Vegge*

Department of Energy Conversion and Storage, Technical University of Denmark, Fysikvej Bldg. 309, DK-2800 Kgs. Lyngby, Denmark

Supporting Information

ABSTRACT: RuO_2-based electrocatalysts are found to be active at low overpotential toward direct electrochemical reduction of CO_2 to formic acid and methanol. RuO_2 can circumvent the thermodynamic bottleneck resulting from the scaling relations observed on metallic electrocatalyst, by utilizing an alternate pathway through oxygen-coordinated intermediates. Employing density functional theory based computational electrocatalysis models we show adsorbate—adsorbate interaction effects for adsorbates and reaction intermediates on the $RuO_2(110)$ surface are large and impactful to the reaction thermodynamics. We studied binding energy amendment due to adsorbate interaction (steric and electronic) with varying coverage of CO* spectators on the catalyst surface. Implications on the reaction pathways help us rationalize differences in experimentally observed carbonaceous product mix and suppression of the hydrogen evolution reaction (HER). We show that a moderate CO* coverage (∼50%) is necessary for obtaining methanol as a product and that higher CO* coverages leads to very low overpotential for formic acid evolution. Our analysis also clarifies the importance of the reaction condition for CO_2 reduction to liquid fuels utilizing RuO_2-based electrocatalysts.

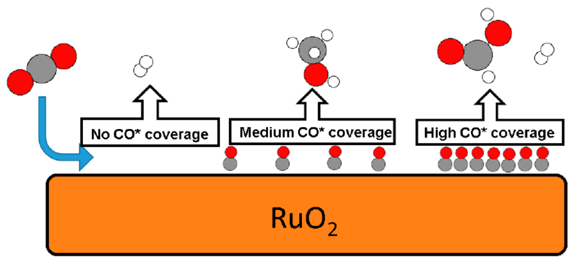

1. INTRODUCTION

The last hundred years of relentless human development have relied on fossil fuel based energy resources. To translate into a sustainable alternative course of long-term growth,[1] expanding renewable energy resources must be tapped at the earliest possible time. This is to mitigate limitations of fossil fuel as well as the inherent environmental problems emanating from increased anthropogenic emissions of CO_2. An electricity grid brimming with renewable electricity from wind and solar plants or cars propelled by renewable energy depends on inexpensive energy conversion and storage technologies.[2] Electrochemical reduction of carbon dioxide to liquid fuels is an appealing approach that could alleviate much of the CO_2 emission challenge, solve the bottleneck of cheap energy storage, and penetrate the fossil fuel dependent transport sector.[3]

The main challenge of direct electrochemical reduction of CO_2 to fuel molecules like formic acid, methanol, or methane is the absence of stable catalysts that can enable the CO_2 reduction reaction (CO2RR) at low overpotential and high selectivity over the hydrogen evolution reaction (HER).[4,5] The underlying chemistry limiting the effectiveness of metallic catalysts in CO2RR to methane or methanol was recently ascertained through density functional theory based modeling of the thermodynamics of reaction steps involved.[6] Adsorbed CO (CO*) is a crucial reaction intermediate in the CO2RR pathway on metallic catalysts. Strong correlation between the binding energy of key intermediates CO* and CHO* on metal catalyst surfaces enforces a large potential requirement for CO2RR to methane irrespective of the CO* binding energy of the metal.[7] Thus, further reduction of CO* remains a bottleneck for metal catalysts. Only copper produces mixtures of methane, ethane, and formic acid at high overpotential, owing to its favorable position in the theoretical activity volcano proposed in previous work. Ruthenium oxide based electrocatalysts have been repeatedly shown[8−10] to produce methanol from CO_2 with up to 60% Faradaic efficiency (FE) at low overpotential. Formic acid has been reported[11] to be the other major CO2RR product on RuO_2-based electrocatalysts. While experimental results have been very affirmative toward good CO2RR activity, oxide catalysts have largely been overlooked amidst the recent spurt in scientific activity pertaining to the electrocatalytic route to CO_2 reduction.[12−18] Our previous work on RuO_2-based electrocatalysts for CO_2 reduction[19] explained that a different reaction mechanism involving the HCOOH* intermediate instead of CO* is active on oxide electrocatalysts. We have also established[20] that different sets of scaling laws and resulting activity volcano lead to lower thermodynamic barriers for the CO_2 conversion reaction than their metal counterparts. This behavior emanates from the fundamentally different reaction path followed on oxide catalysts compared to metal catalysts. CO_2 activation on metals leads to COOH* intermediates and consecutive protonation to reaction intermediates like CO*, CHO*/COH*, and CHOH*/H_2CO* which tend to bind to the metal through the carbon atom.[21,22] On $RuO_2(110)$, CO_2 activation leads to OCHO*, which is further reduced to HCOOH*, H2COOH, etc., which bind to the catalyst through oxygen atoms.[19] The different reaction pathway signify that different scaling relations

Received: May 5, 2017
Revised: July 14, 2017
Published: August 2, 2017

DOI: 10.1021/acs.jpcc.7b04242
J. Phys. Chem. C 2017, 121, 18333−18343

govern CO2RR on oxide surfaces.[20] In particular, the limitation from the CO*/CHO* scaling is avoided.

The presence of spectator species on the catalyst surface can enhance or poison electrocatalyst activity, as has been studied theoretically and experimentally.[23−27] Despite the COOH* intermediate being much less stable than the OCHO* intermediate, a small amount of COOH* might form on CO_2 activation. Further reduction is expected to leave adsorbed CO* from this contingent reaction.[11] CO* spectators interact with other adsorbed reaction intermediates and alter their binding energy. We have observed that spectator CO* species can have a large effect on H* binding free energy, potentially promoting/poisoning HER.[20] Similar behavior has been observed for metallic catalysts.[28] We expect that a similar effect can be present for OH* binding free energy as well. Intermediates formed during CO2RR to methanol on the RuO_2 catalyst surface are bound to the surface by oxygen atoms, and their binding energy is correlated with the OH* binding energy. Thus, a strong effect of CO* spectators on the onset potential for methanol production and selectivity over HER is expected. A shift in the reaction site of CO2RR due to blockade of more favorable sites by the CO* spectator can have a very large effect on the thermodynamics of elementary reaction steps. For example, under reducing conditions the $RuO_2(110)$ surface can have both strong binding bridge sites and weak binding coordinated unsaturated (cus) sites available for intermediates. If all bridge sites (br) are occupied by spectator CO* species, then the reaction can only proceed through cus sites. To create a categorical understanding of CO* spectators on the CO2RR pathway on the $RuO_2(110)$ surface, we study the possible reaction intermediate and paths to formic acid, methanol, and methane in the presence of different concentrations of CO* spectators as well as variation in the br/cus sites occupied by spectator CO*. This work displays that weakening and strengthening of binding energies is of surprising importance toward both onset potential and possibly also the product selectivity for CO2RR on RuO_2. The outcome from this study is especially important to the understanding and development of oxide-based CO_2RR electrocatalyst, which may break the scaling relations. We show that high CO* coverage can render RuO_2-based catalysts very effective at formic acid evolution and lower selectivity toward HER, while a moderate coverage improves on methanol selectivity. Our results might give a clue to the widely varied product composition obtained from CO2RR with RuO_2-based electrocatalysts and highlight the importance of spectator coverage for successful CO2RR using RuO_2.

2. COMPUTATIONAL DETAILS

We utilize the VASP[29] package for density functional theory (DFT) based simulation of model catalyst surfaces with adsorbed reaction intermediates. Standard PBE−PAW potentials as distributed with VASP 5.3 are used with 500 eV wave function cutoff. A previous comparison study on convergence of chemisorption energy on the RuO_2 surface from VASP (PAW) and Wien2K (all electron) indicated that a 400 eV cutoff is sufficient for routine calculations. A 600 eV cutoff for standard PAW can provide accuracy of up to 10 meV.[30] Higher energy cutoff for this work is irrelevant as errors in the order of 0.1 eV are expected in GGA level theory.[31] Here the newly developed BEEF-vdW[32] exchange correlation functional is utilized. Our lattice parameter estimates are $a = 4.537$ Å and $c = 3.135$ Å for RuO_2, which agree well with experimental data.[33] Following our previous studies[19,20] the supercell representing the catalyst surface $RuO_2(110)$ consists of a four-layer thick slab with the lower two layers fixed at atomic positions identical to bulk RuO_2. The bridge site is considered vacant due to reducing environment during CO2RR (Figure SI1). This model has two bridge and two cus sites available for reaction intermediates and spectator CO* molecules. During simulation, we use a 4 × 4 × 1 k-point mesh and 16 Å of vacuum in the z-direction and Gaussian electronic smearing. Optimization of atomic positions is done until forces on atoms in the top two layers and adsorbates are lower than 0.003 eV/Å. Vibrational modes for adsorbed molecules are also analyzed to enable finite temperature free energy estimates by approximating adsorbate degrees of freedom as independent quantum mechanical harmonic oscillators (Table SI1).

Adsorbate binding free energies are estimated w.r.t. gas-phase free energies (Table SI2) of hydrogen, water, and CO_2.[20] Systematic DFT errors in total energy evaluation are corrected for H_2 (0.1 eV), CO_2 (0.3 eV), formic acid (0.15 eV), and COOH* (0.15 eV) following the approach by Christensen et al.[34] A stabilization of formic acid in solution[35] from deprotonation in neutral electrolyte (−0.19 eV) is also taken into account, and the experimentally observed reaction product concentrations were used for free energy estimation of methanol,[9] formic acid, and methane[11] free energies. The reaction thermodynamics calculations are susceptible to variation in reactant/product concentration in the electrolyte. High concentration of methanol in electrolyte leads to increased free energy (up to 0.2 eV), and release of methanol might become difficult. The low vapor pressure of formic acid means small variation in free energy from higher concentration. Thus, effects of concentration are minimal for formic acid evolution.

Vibrational modes of adsorbate molecules are used to estimate zero-point energy, heat capacity, and entropic contributions to the free energy at room temperature using the harmonic oscillator model as implemented in the atomistic simulation environment (ASE). Usage of the reversible hydrogen electrode (RHE) scale for electrochemical potential helps simplify onset potential estimation by considering reversible formation of a proton/electron pair from a hydrogen molecule as zero V-RHE at any given pH. Accordingly, the analysis becomes pH independent except for the free energy of formic acid in solution. We have employed the computational hydrogen electrode (CHE) model[36] to determine the thermodynamics of the electrochemical reaction steps involving single electron/proton transfer. The free energy of an adsorbate formed at the n^{th} proton transfer step is lowered by nU eV when a potential of -U vs RHE (V-RHE) is applied. Under the assumptions of the CHE model, a particular, elementary proton transfer step, requiring an increase in binding free energy, can be made free energy neutral by applying a negative potential, equivalent to the increase in free energy at 0 V-RHE. Hence, an analysis of relative binding energies of adsorbates formed at different electron transfer steps (Table 1) at 0 V-RHE allows us to investigate modifications in the CO2RR pathway and onset potential as well as selectivity over HER due to adsorbate interactions with CO*.

3. RESULTS AND DISCUSSION

3.1. Spectator Coverage. With four adsorption sites in the simulation model (Figure SI1), CO* coverage can be 0%, 25%, 50%, 75%, or 100%, respectively. Each CO* spectator in the

DOI: 10.1021/acs.jpcc.7b04242
J. Phys. Chem. C 2017, 121, 18333−18343

Table 1. Adsorbate/Product Cases Examined at the Electron Transfer Step from 0e$^-$ to 8e$^-$

0 e$^-$	1 e$^-$	2 e$^-$	3 e$^-$	4 e$^-$
*	OCHO*, H*, COOH*	HCOOH*, CO* + $H_2O(l)$, HCOOH(aq), $H_2(aq)$	H_2COOH*	H_3CO* + OH*, $H_2CO + H_2O(l)$, O* + $CH_3OH(aq)$
5 e$^-$	6 e$^-$	7 e$^-$	8 e$^-$	
H_3CO* + $H_2O(l)$, H_2COH* + $H_2O(l)$, OH* + $CH_3OH(aq)$	O* + $CH_4(aq)$ + $H_2O(l)$, CH_3OH* + $H_2O(l)$, $CH_3OH(aq)$ + $H_2O(l)$	OH* + $CH_4(aq)$ + $H_2O(l)$	$CH_4(aq)$ + $H_2O(l)$	

simulation model amounts to 25% added CO* coverage. With full CO* coverage, CO2RR or HER cannot advance due to unavailability of active sites, unless CO* is first reduced. Two different types of active site being present and considering symmetry of the relative positions of the CO* adsorbates, 25% and 75% coverage can be realized in two different ways, while 50% coverage leads to four different representations (Figure SI2). All such different CO* coverages are inspected for their relative thermodynamic stability (Figure SI3). Visual representations are provided in Figure SI2.

On the bare surface, the first CO* adsorption at the bridge site is favorable compared to the cus site by 0.18 eV (Figure SI3). With respect to the CO molecule, the binding free energy of CO* at the bridge site of the bare surfaces is −1.34 eV. Two cus sites and one bridge site are accessible for catalysis at 25% CO* coverage. With 50% CO* coverage, putting all adsorbates in the bridge site is the most stable configuration. All other cus configurations with 50% CO* coverage are less stable by 0.28 eV. The adsorption free energies for the two 50% CO* coverage configurations with a combination of bridge and cus occupancy are less stable than the all-bridge configuration by 0.08 eV (while neighboring bridge and cus sites have CO* (bridge + cus-near in SI3)) and 0.1 eV (occupied bridge and cus sites are far apart (bridge + cus-far in SI3)). With both bridge sites covered by CO*, catalysis can only occur on the cus sites available (Figure SI2). On the other hand, if CO at 50% CO* coverage occupies both bridge and cus sites, there are still bridge and cus sites available for CO2RR. At 75% CO* coverage, the adsorbate configuration with CO* on 2*bridge + cus sites is more stable than CO* on bridge + 2*cus by 0.2 eV (Figure SI3). These two configurations are fundamentally different, as the first allows catalysis through the cus sites and the latter requires the reaction to take place at the bridge site (Figure SI2). Due to repulsive CO*−CO* interactions, the incremental binding free energy for CO* decreases with CO* coverage (Figure SI3). The incremental binding free energies for four CO* molecules considering the most stable configurations are −1.34 eV, −0.93 eV, −0.75 eV, and −0.46 eV, respectively. Thus, the driving force for further CO* adsorption is smaller at high CO* coverage. It is striking that at 0 V-RHE and 75% CO* coverage OH* binds slightly stronger to the empty fourth site than CO* (by 0.02 eV). Thus, OH* can displace the fourth CO*.

The CO* spectator coverage at experimental conditions can also be limited due to reduction of CO* to CHO* or COH*, lowering the CO* coverage. CHO* is more stable than COH* on the $RuO_2(110)$ surface by 0.22−0.45 eV for different CO* coverages. At 0 V-RHE, the reduction of one of CO* to CHO* is energetically uphill by 1.34, 0.63, 0.73, and 0.03 eV for CO* coverage of 25%, 50%, 75%, and 100%, respectively. This indicates, that complete poisoning of the catalyst surfaces is not favorable. On the contrary, CO* spectators will not be removed by reduction even with application of moderate reducing potential if the coverage is low (∼25%). 50% and 75% CO* coverage might be observed under CO2RR conditions, due to kinetic barriers of CO* protonation and transient evolution of CO from CO2RR. Slow transport of CO away from the catalyst will eventually leave the catalyst surface with high CO* coverage[37] as might be the case in a previous experimental study.[11]

Previous studies by Popic et al. and Qu et al. employing pure ruthenium oxide electrocatalyst[9,10] have not reported any CO detected as a product. We deduce that these experimental results observing methanol as the primary product might have a catalyst surface with low to medium CO* coverage if only a very small quantity of CO is produced and stays bound to the active site.[9,10] On the contrary, experiments by Spataru et al.[11] observe hydrogen and formic acid as dominant products along with methanol, methane, and CO. It can be contemplated that the presence of CO at 30−200 ppm[11] in the solution comes from CO escaping the catalyst surface when a high CO* coverage is reached.

3.2. Hydroxylation with a CO* Spectator. CO_2 is often reduced in aqueous electrolytes. Hydroxylation of active sites is energetically downhill and spontaneous at the bridge site of the $RuO_2(110)$ surface (Figure 1). Any available bridge site is expected to be hydroxylated at 0 V-RHE. OH* needs to be removed from the active site for CO2RR to proceed. Thus, OH* removal can become a thermodynamic limiting step. Interactions between CO* and OH* are attractive for 25% to 50% CO* coverage, making OH* binding stronger in the presence of CO* spectators (Figure 1).

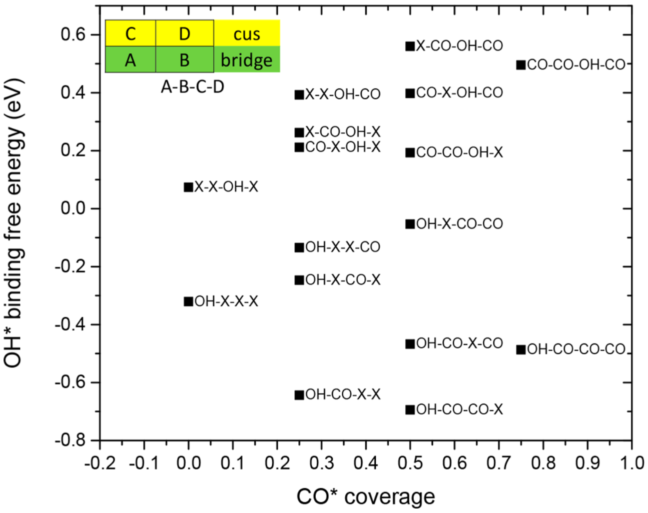

Figure 1. OH* binding energy as a function of CO* coverage and spatial distribution of CO* adsorbates. As depicted in the inset, the distributions of OH* and CO* at the two bridge and two cus sites consecutively are used as label, where X denotes an unoccupied site.

Investigations of the adsorbate binding free energy on the $RuO_2(110)$ surface at bridge and cus sites reveal that oxygen-coordinated adsorbates like OH* bind significantly stronger to the bridge sites compared to cus sites (Figure 1). The relative preference for bridge sites is less pronounced for CO* (Figure

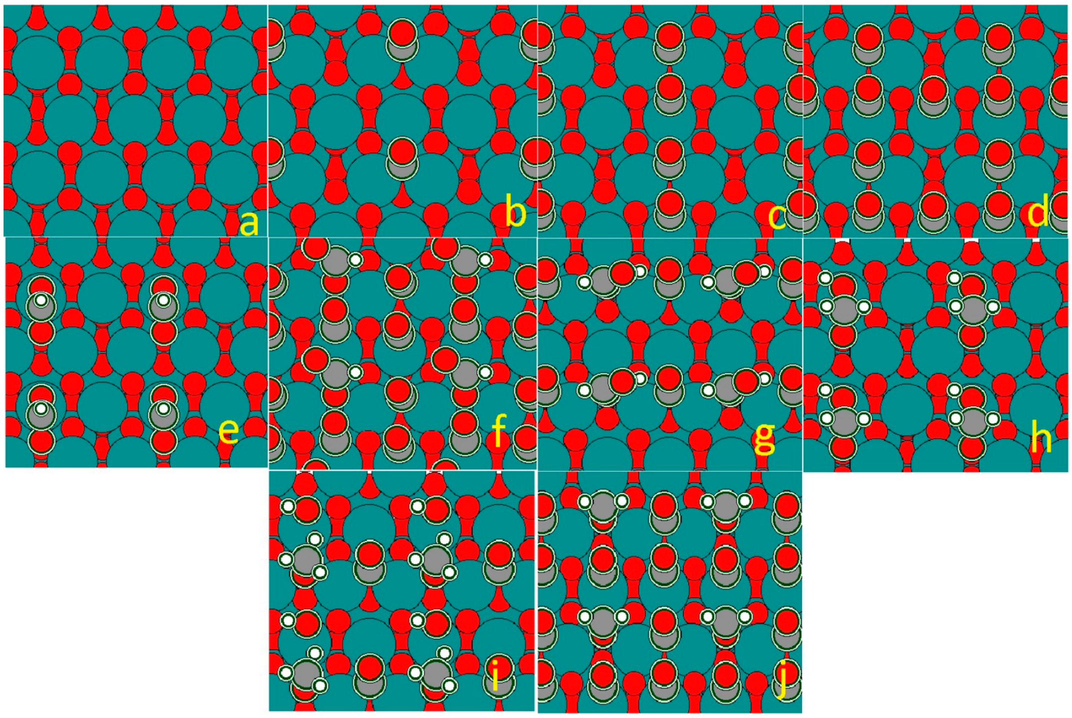

Figure 2. Simulated $RuO_2(110)$ surface with two bridge sites and two cus sites available. Bridge sites are coordinated to two ruthenium atoms, and cus sites are on top of ruthenium atoms. (a) All sites empty. (b) One bridge site has CO*. (c) One bridge site and one cus site have CO*. (d) One bridge site and two cus sites have CO*. (e) Bidentate OCHO* bound through one bridge and one cus site. (f) OCHO* in monodentate configuration in the bridge site with three CO* spectators occupying all the other sites. (g) HCOOH* at the bridge site with CO* in the other bridge site. (h) H_2COOH* in bidentate configuration. (i) H_3CO* + OH* intermediate with one bridge site CO* spectator. (j) H_2CO* in the bridge site with two cus site and one cus site CO* spectators. The actual unit cell in the simulation is given in Figure SI1.

SI3). The binding energies for OH* at different CO* spectator configurations and binding sites are presented in Figure 1 showing favored bridge site binding of OH* over cus site binding. For example, the binding energy of OH* at bridge and cus sites is −0.32 eV and +0.08 eV, respectively, while these values for CO* are −1.34 eV and −1.16 eV (w.r.t. the CO molecule). This observation helps to understand the distribution of spectating CO* in bridge and cus sites under reaction conditions. Key CO2RR intermediates on oxide surfaces like OCHO*/HCOOH*/H_2COOH*, etc., are all O-coordinated. If a mixture of CO*- and O-coordinated intermediates are present on the catalyst surface, CO2RR intermediates would preferentially occupy the bridge sites, and the bidentate coordination will be preferred over monodentate binding. For example, three CO* and one OH* adsorbate can be distributed such that OH* can occupy a bridge site, or it can occupy a cus site. The configuration with OH* in the bridge site has ~1 eV lower free energy than the configuration with OH* in the cus site (Figure 1). This is critical in effective CO2RR catalysis on the $RuO_2(110)$ surface.

Reaction path thermodynamics shows that bridge site CO2RR not only is energetically preferred but also has lower thermodynamic onset potential. For example, at 75% CO* coverage, OCHO* is unlikely to form at the cus site (binding free energy of +0.95 eV), but bridge site occupation as a monodentate adsorbate is feasible (binding free energy of −0.13 eV). The preferred CO* spectator configurations important for CO2RR at 0%, 25%, 50%, and 75% CO* coverage are given in Figure 2(a)−(d). Other free bridge sites and cus sites can be occupied by CO2RR/HER adsorbates as portrayed in Figure 2(e)−(i). OCHO* and H_2COOH* adsorbates bind as bidentate adsorbates if the adjoining bridge and cus sites are not occupied by CO* spectators (Figure 2(e) and (h)). These adsorbates are monodentate at high CO* coverage (Figure 2(f)). Adsorbates like H_2CO* (Figure 2(j)) and HCOOH* (Figure 2(g)) are always monodentate, but the reaction intermediate can consist of a pair of adsorbates like H_3CO* + OH* (Figure 2(i)). The priority of O atom coordinated CO2RR intermediates at the bridge site is not valid for HER. HER can proceed even at the cus site, while bridge sites are hydroxylated. Therefore, HER thermodynamic analysis is done for a variety of spectators.

3.3. CO_2 Activation: OCHO* vs COOH*. From a purely thermodynamic point of view, the free energy diagrams identify which reaction intermediate is most favorable at a particular electron transfer step. For example, if OCHO* is more stable than COOH* at 0 V-RHE, it will remain the preferred intermediate at an applied reducing potential (Figure 3(a)). A proton transfer to CO_2 molecules in the solvated phase creates both the intermediates. The free energy is lowered by the equal amount due to an applied reducing potential. OCHO* is a bidentate adsorbate if adjacent sites are available. At 0% and 25% CO* coverage, OCHO* binds through one bridge and one cus site (Figure 2(e)). The presence of CO* in an adjacent bridge site strengthens the OCHO* binding at low (25%) CO* coverage compared to the bare catalyst surface (Figure 3(a)). At 50% CO* coverage, OCHO* can bind through one bridge and one cus site or through two cus sites depending upon the CO* distribution. On a bare surface, OCHO* occupying the bridge + cus sites has a binding free energy of −0.81 eV. It is interesting to note that the configuration with bridge + cus distribution of CO* spectators continues to be more stable

DOI: 10.1021/acs.jpcc.7b04242
J. Phys. Chem. C 2017, 121, 18333−18343

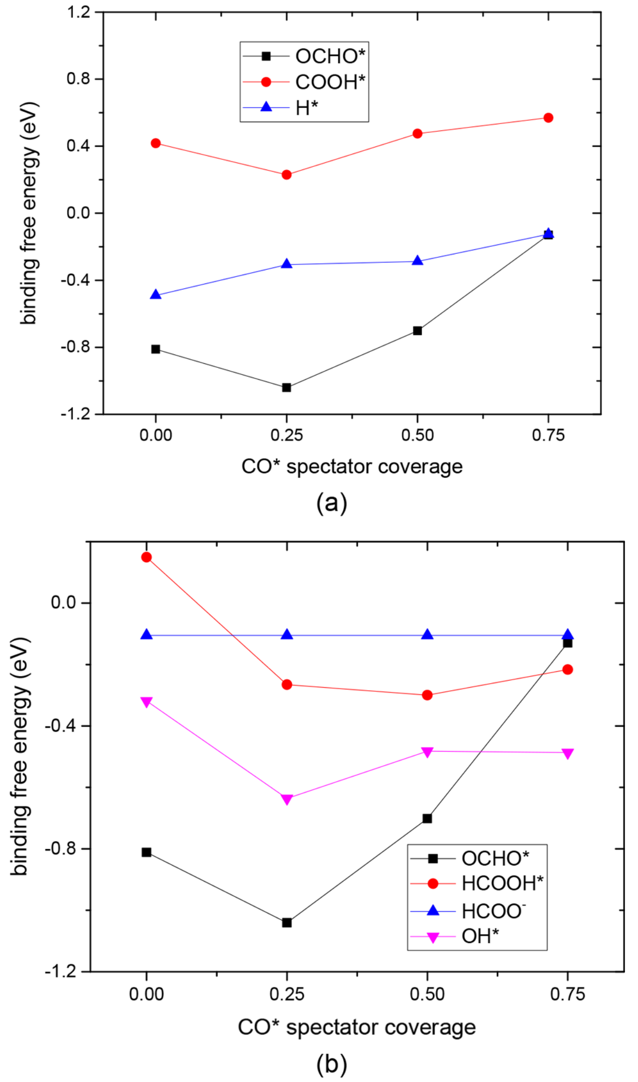

Figure 3. Effect of CO* coverage on binding energy of (a) intermediates formed by the 1st proton transfer*/OCHO*/COOH* and (b) HCOOH* and OH* at the available bridge site (or bridge + cus site for OCHO*) and free energy for deprotonated formic acid in solution.

than the bridge + bridge configuration when OH* or OCHO* is present on the surface. It can be argued that at a level of 50% coverage CO2RR will occur through a combination of bridge and cus sites, and OCHO* stays bidentate. 75% CO* coverage compels OCHO* to be monodentate (Figure 2(f)), reducing the binding free energy significantly. The 2*cus + bridge configuration of CO* adsorbates lets OCHO* adsorb at the bridge site, which is significantly more favorable than the cus site adsorption. Thus, in the presence of OCHO*, the 2*cus + bridge configuration of the CO* spectators is more stable.

It should be noted that trends in COOH* and OCHO* binding free energy at different CO* adsorbate configuration are similar and maintain their relative position in the free energy diagram. Figure 3(a) shows that the OCHO* intermediate is much more strongly bound to the active site than COOH*, regardless of spectator coverage. Consequently, the CO2RR pathway proceeds preferentially through OHCO* and other O-coordinated adsorbates at all CO* coverages. The other (unwanted) intermediate after the first proton transfer step is H* (Figure 3(a)).

3.4. Selectivity of CO2RR vs HER. The spectator adsorbate interaction between CO* and H* is repulsive, and H* binding weakens with higher CO* coverage (Figure 3(a)). Substantially weaker binding of H* than OCHO* facilitates selectivity of CO2RR over HER.[20] For CO* coverages 0−50%, OCHO* is more strongly bound to the catalyst surface than H* by 0.31−0.73 eV (Figure 2(a)). The binding free energy difference is over 1 eV for a coverage of 50% CO*, occupying all the bridge sites (Figure SI4). Because H* is a prerequisite for HER, we thus find the best selectivity for CO2RR at 50% CO* coverage. For high (75%) CO* coverage, owing to the aforementioned destabilization of OCHO*, H* is equally probable to form (Figure 3(a)) at bridge sites (binding energy difference of 4 meV between H* and OCHO*). For 75% coverage and cus site adsorption, H* is remarkably favored by 0.32 eV over OCHO* at cus sites (Figure SI5). At high CO* coverage, RuO_2 electrocatalysts should therefore show less selectivity toward CO2RR and evolve significant amounts of hydrogen.

RuO_2(110) bridge sites, when vacant, are hydroxylated in aqueous solution due to negative binding free energy of OH* at the bridge site at 0 V-RHE (Figure 1). Hydroxylation of cus sites is not energetically favorable at 0 V-RHE, and HER can proceed at the cus site. For 0% CO* coverage and hydroxylated bridge sites, the H* binding free energy at the cus site is +0.33 eV; i.e., HER requires a reducing potential of −0.33 V-RHE (Table 2). However, the OH* removal potential for the clean RuO_2(110) surface bridge site is −0.32 V-RHE. Once OH* is removed, on an otherwise empty surface, the H* binding free energy at the cus site is +0.22 eV. H* binding at the cus site (with H* spectators at all bridge sites) is +0.41 eV. The surface coverage, onset potential, and reaction site might vary, but these binding free energies suggest that at very low CO* coverage only HER is active at reducing potential up to −0.32 V-RHE utilizing both bridge and cus sites. Schematics of few such spectator configurations (within the 2 × 2-model catalyst surface) for HER mechanism and predicted onset potentials are provided in Table 2.

Table 2. Calculated Thermodynamic Onset Potential [V-RHE] for HER at Bridge and Cus Sites with Different Spectator Species on RuO_2 (110)[a]

	Configurations														
cus	X	*		CO	*		X	*		X	*		CO	*	
bridge	OH	OH		CO	OH		H	H		CO	X		CO	X	
HER onset [V-RHE]	-0.33			-0.56			-0.41			-0.26			-0.22		
cus	X	*		*	X		X	X		*	X		OH	*	
Bridge	OH	CO		X	X		CO	*		CO	CO		OH	OH	
HER onset [V-RHE]	-0.39			-0.22			-0.31			-0.41			-0.56		
cus	X	X		CO	X		CO	*		CO	CO				
Bridge	*	X		CO	*		CO	CO		*	CO				
HER onset [V-RHE]	-0.49			-0.29			-0.63			-0.13					

[a] Yellow represents a cus site, and green represents a bridge site. OH, CO, and H are possible spectators, and X is the absence of any of them. * is the site considered for HER.

Easy availability of CO_2 in the solution phase can prevent HER by formation of OCHO* in 2*cus or bridge + cus bidentate configuration due to higher stability than H* (Figure 3(a)). The binding free energy of OCHO* in weak binding cus site (2*cus configuration) with bridge sites filled by OH* is

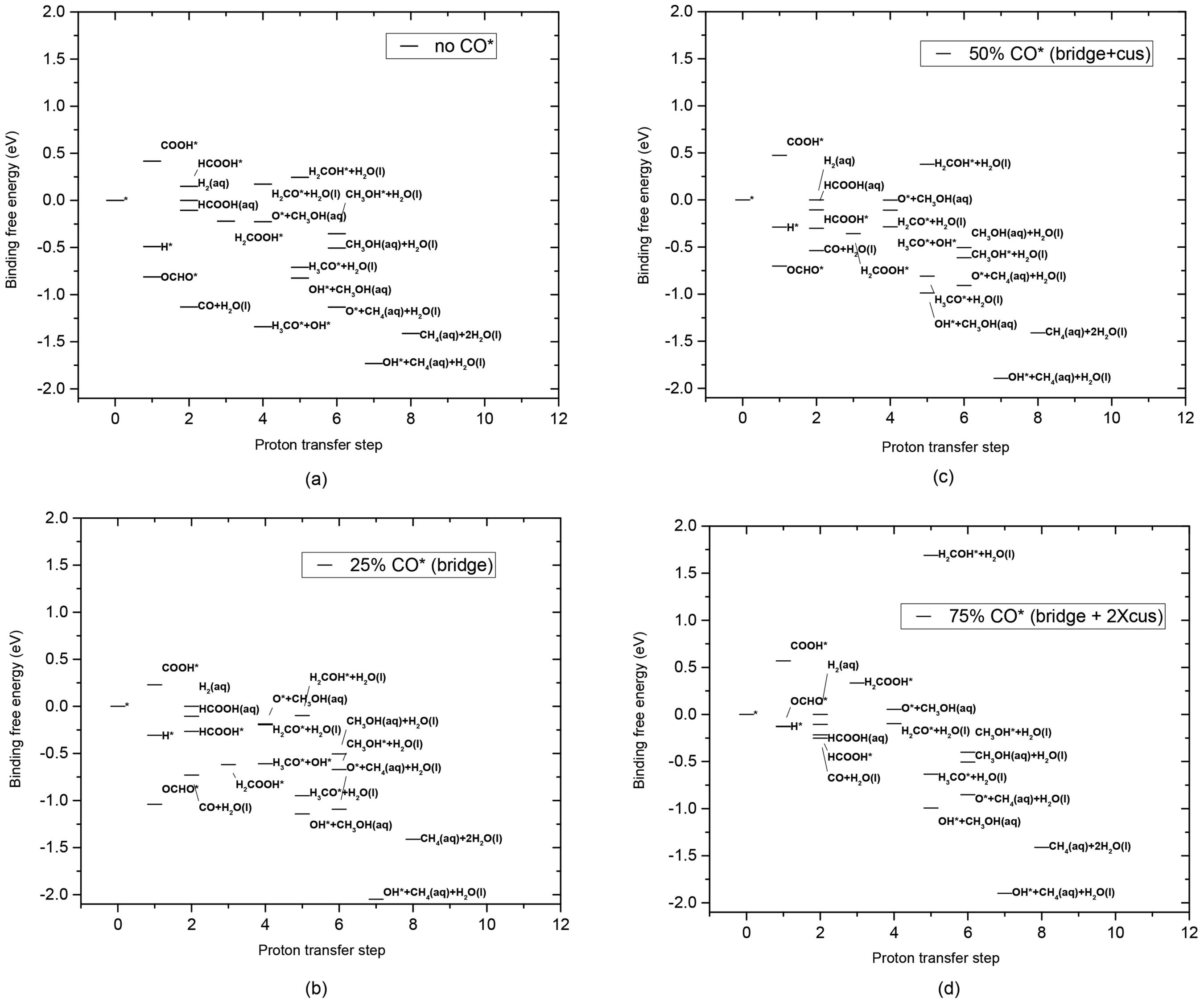

Figure 4. Free energy diagram of possible reaction intermediates for HER/CO2RR at four different coverages of CO* spectators: (a) 0%, (b) 25% utilizing bridge sites, (c) 50% utilizing half of bridge and cus sites, and (d) 75% utilizing all cus and half of bridge sites. The sites occupied by spectator CO* molecules are indicated. Adsorbate labels are on the right of the data point and adjusted in the *y*-direction to avoid superposition without changing the relative position between intermediates formed at the same electron transfer step.

−0.71 eV, and when bridge sites are filled with a mixture of OH* and CO*, the OCHO* binding free energy is −0.70 eV. In comparison, H* binding is +0.33 eV and +0.39 eV for similar bridge site spectator configuration, respectively.

For 25% CO* coverage, the attractive adsorbate−adsorbate interaction between CO* and OH* at bridge sites makes OH* removal from the bridge much more difficult (−0.64 V-RHE). Again bidentate OCHO* is very stable with a binding free energy of −1.04 eV at 25% CO* coverage. The H* binding free energy at the cus site (OH* and CO* being present at bridge sites) is +0.39 eV, canceling significant HER activity. A similar argument for subdued HER activity holds for 50% CO* coverage (all the bridge sites occupied (Figure SI4)), where all cus sites are available for adsorption. H* and OCHO* have binding free energy of +0.41 eV and −0.69 eV, respectively (Table SI4). On the other hand, in the more favorable configuration, the CO* adsorbates are distributed between bridge and cus sites, and the other bridge site is occupied by OH*. H* binding free energy at the cus site is +0.56 eV, but the bridge OH* removal is estimated at −0.48 V-RHE. H* binding free energy at a free bridge site with 50% CO* coverage is −0.29 eV, and that at the cus site is +0.26 eV. Consequently, HER can progress through bridge or cus sites at ∼−0.3 V-RHE (Table 2) except when OCHO* forms, occupying both the bridge and cus sites. This analysis shows that up to 50% CO* coverage is expected to allow little HER activity if OCHO* forms rapidly. For the 2*bridge + cus CO* configuration (75% coverage), H* binding is very weak (+0.63 eV), while for the 2*cus + bridge configuration, H* binding free energy is near ideal at +0.03 eV; however, hydroxylation of the active site blocks HER above −0.48 V-RHE.

3.5. Impact of CO* Coverage on CO2RR Intermediate Binding. Six of the CO* coverage configurations (Figure SI2) are picked for analysis of the CO2RR reaction mechanism: −0% CO* coverage, 25% CO* coverage (bridge site), 50% CO* coverage (all bridge sites), 50% CO* coverage (neighboring bridge and cus sites), 75% CO* coverage (2*bridge + cus sites), and 75% CO* coverage (bridge +

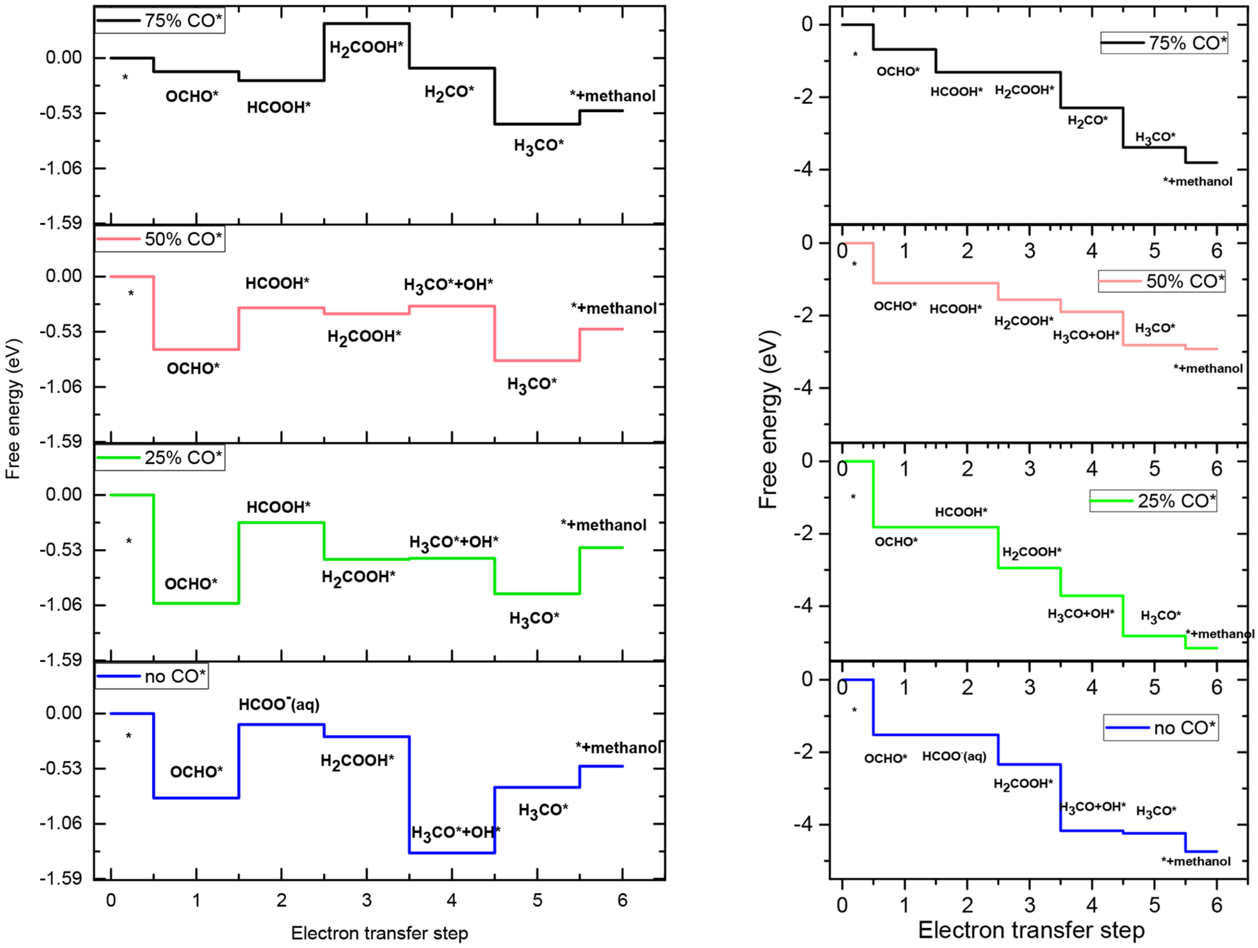

(a) (b)

Figure 5. Thermodynamic path for methanol evolution at bridge site with 0%, 25%, 50%, and 75% CO* spectator coverage at (a) 0 V-RHE and (b) at the respective methanol onset potential of −0.71, −0.78, −0.4, and −0.55 V-RHE. A downward step signifies no reducing potential required for forward reaction, and an upward step marks the need for proportional reducing potential for propelling the reaction step.

2*cus sites). Multisite adsorbates like H_3CO* + OH* occupy two bridge sites in the absence of CO* spectator and a combination of bridge + cus sites for 25% and 50% CO* coverage. 75% CO* coverage only allows single site adsorbates. Some CO2RR adsorbates like OCHO* and H_2COOH* can attach to the catalyst surface through one or two active sites, due to the molecular geometry. Such bidentate adsorbates are allowed to remain so for 0−50% CO* coverage. Lack of multiple neighboring vacant active sites forces them to be monodentate at 75% CO* coverage.

A previous study has shown that binding free energy of O atom coordinated CO2RR reaction intermediates scale with OH* binding free energy on oxide catalyst surfaces.[20] Hence the strong spectator adsorbate interaction between CO* and OH* is expected to be valid for other O atom coordinated CO2RR intermediates as well. Adsorbate binding energy diagrams at 0 V-RHE (Figure 4) for CO* configurations are dominant at 0%, 25% (bridge site), and 50% (bridge + cus sites), and 75% coverage (bridge + 2*cus sites) is used to obtain key conclusions here. Reaction intermediate free energy diagrams with two other CO* coverage configurations are provided in the Supporting Information (50% coverage with all bridge sites occupied (Figure SI4) and 75% coverage with the cus site free (Figure SI5)). Binding energy of an adsorbate can change from both electronic interaction with spectators as well as modifications in adsorption geometry.

3.6. Impact of CO* Coverage on CO2RR.

The free energy diagram of reaction intermediates helps to identify which reaction intermediate is most favorable at a particular electron transfer step and to determine the reaction mechanism. The H*/OCHO* binding free energy correlation helps us understand the HER/CO2RR selectivity; the HCOOH* binding free energy w.r.t. solvated formic acid in solution (Figure 3(b)) dictates whether formic acid is the major product or higher proton transfer products like methanol are dominant. If the catalyst surface fails to bind formic acid molecules to the active site, it will escape into solution in a solvated form, rendering further hydrogenation difficult. HCOOH* being O-coordinated like OH*, the trend in the binding free energy variation at different CO* coverage is similar for these adsorbates (Figure 3(b)). Adsorbate−adsorbate interaction effects inducing stronger OH* binding can open up the possibility of methanol/methane as product as seen in the case of partial CO* coverage.

If the formic acid molecule fails to bind at the catalyst site, H_2COOH* is expected to form by application of an additional electrochemical driving force (equivalent to the stability of deprotonated and solvated formic acid compared to surface-

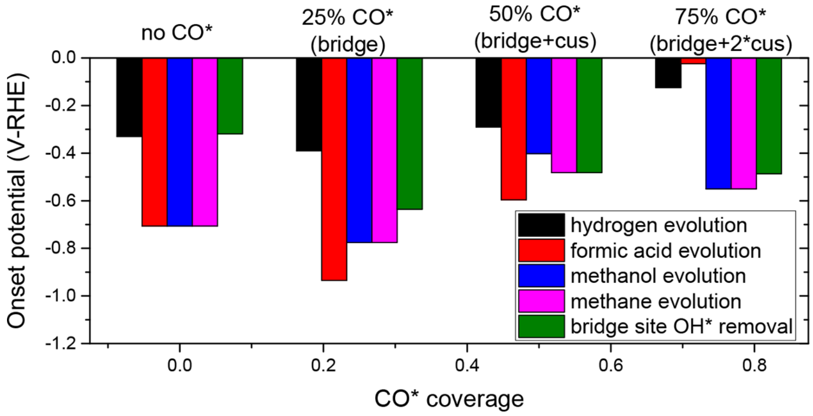

Figure 6. Onset potentials for hydrogen, formic acid, methanol, and methane evolution at different CO* spectator coverage. OH* removal potential at bridge site included to provide information about possible OH* blockage.

bound HCOOH*). However, the electrolyte needs to be saturated with formic acid to supply protonated formic acid molecules. Nevertheless, the accessibility requirement of solvated HCOO- and two protons close to the active site simultaneously suggests the kinetics will be extremely slow, stopping further reduction. The absence of any CO* coverage leads to release of formic acid in solution on hydrogenation of OCHO*.

We proceed to consider formic acid in solution as a possible intermediate/product formed on OCHO* activation (Figure 5). This step leads to either surface-bound HCOOH* or formic acid in solution. For CO* coverages of up to 50%, protonation of OCHO* is energetically uphill (Figure 3(b) and Figure 5(a)), forming HCOOH* on CO*-covered surfaces and formic acid in the absence of CO*. This large increase in free energy requires a proportionately large reducing potential to be applied for the reaction to proceed. So OCHO* formation can reduce the HER activity in the absence of CO* simply by blocking the active sites as previously discussed. At 75% CO* coverage, OCHO* and HCOOH* are both monodentate. The formation of HCOOH* from OCHO* is downhill in energy for 75% coverage (Figure 3(b)). Binding free energy of HCOOH* w.r.t. solvated formic acid in liquid water is ~0.1 eV, which is small enough for a large fraction of adsorbates to escape into solution instead of forming HCOOH* (Figure 3(b)). Weakening of the OCHO* adsorbate binding reduces the thermodynamic onset potential requirement to only −0.02 V-RHE. Therefore, at this CO* coverage, we expect a high turnover of formic acid at very low overpotential, in good agreement with Spataru et al., who observed this at only ~−0.13 V-RHE[11] and pH 3.9.

Investigations of the most probable methanol formation pathways at different CO* coverage using free energy diagrams enable us to identify the electron transfer steps requiring large reducing potentials to go forward. The preferred pathway has been established to be as follows for CO* coverage ≤50%.

$$* + CO_2(aq) + (H^+ + e^-) \rightarrow OCHO^* \tag{1}$$

$$OCHO^* + (H^+ + e^-) \rightarrow HCOOH^* \tag{2}$$

or

$$OCHO^* + (H^+ + e^-) \rightarrow HCOO^-(aq)$$

$$HCOOH^*(aq) + (H^+ + e^-) \rightarrow H_2COOH^* \tag{3}$$

or

$$HCOO^-(aq) + (H^+ + e^-) \rightarrow H_2COOH^*$$

$$H_2COOH^* + (H^+ + e^-) \rightarrow H_3CO^* + OH^* \tag{4}$$

$$H_3CO^* + OH^* + (H^+ + e^-) \rightarrow H_3CO^* + H_2O(l) \tag{5}$$

$$H_3CO^* + (H^+ + e^-) \rightarrow H_3COH(aq) \tag{6}$$

The lack of more than one active site for 75% CO* coverage forces the reaction pathway to go through H_2CO^* instead of H_3CO^* + OH^* adsorbates (Figure 5).

$$H_2COOH^* + (H^+ + e^-) \rightarrow H_2CO^* + H_2O(l) \tag{4a}$$

$$H_2CO^* + (H^+ + e^-) \rightarrow H_3CO^* + H_2O(l) \tag{5a}$$

Formation of OCHO* by CO_2 protonation is downhill at 0 V-RHE for all CO* coverages. Reduction of the H_2COOH^* intermediate (Figure 5 and Figure 4(a)) is either downhill or slightly uphill (0.07 eV for 50% bridge + cus CO* coverage). Formation of H_3CO^* is downhill, except in the absence of any CO* coverage. In the absence of any spectators, H_3CO^* and OH* can both occupy bridge sites. Stronger OH* binding energies require a large reducing potential for removal. Overall, OCHO* activation for 0% CO* coverage (0.71 eV), 25% CO* coverage (0.78 eV), and 50% CO* coverage (0.4 eV) and H_2COOH^* formation at 75% CO* coverage (0.55 eV) are the thermodynamically most difficult steps (Figure 4(a)). Thus, application of a reducing potential the same as the onset potential for these elementary steps automatically makes all other steps downhill as represented in Figure 4(b).

Similar to the OCHO* adsorbate, H_2COOH^* is also bidentate when two contiguous bridge and cus sites are available (Figure 2(e),(h)), as is the case for CO* coverages up to 50%. Forcing H_2COOH^* to be monodentate at 75% CO* coverage makes it difficult (free energy increase of 0.6 eV more than 50% CO* coverage) to reduce HCOOH*-forming H_2COOH^* (Figure 5(a)). Consequently, this becomes the elementary proton transfer step, necessitating the most reducing potential. Due to interactions with spectating CO*, the stability of different intermediates changes differently causing reaction step height (free energy change) to vary as well. The relative ΔG shift of these proton transfer steps from intermediate binding energy variation due to CO* spectator interaction is provided in Figure SI6. Changing the CO* coverage modifies the potential need to drive the elementary steps forward, but OCHO* activation remains the most difficult step for CO* coverage of 50% or lower (Figure 5(a)).

OH* removal is not a limitation for CO2RR for any CO* coverages, except 50% (Figure SI6), where OH* removal needs a reducing potential 80 meV lower than OCHO* protonation. For CO* spectator coverage of 25%−75%, methane and methanol evolution onset potential is close to OH* removal potential (Figure 6). The magnitude of change in overall onset potential for methanol is not as abrupt as that observed for formic acid and hydrogen evolution (75% coverage). Observable methanol evolution at different CO* coverages will therefore be dependent on kinetic barriers and competition from hydrogen and formic acid evolution. For methane evolution, the favored pathway is identical to methanol evolution until the fifth electron/proton transfer step, i.e., formation of H_3CO*, at all CO* coverages. At the sixth step, methane is released by protonation on the carbon atom of the H_3CO* adsorbate, leaving an oxygen atom at the bridge site, which is eventually removed as water through two protonation steps. The thermodynamic limiting steps are identical to methanol evolution, except at 50% coverage, where the onset potential predicted for methane evolution from thermodynamic analysis is different from methanol (Figure 6). From H_3CO*, methane evolution will be preferred if C−O bond cleaving has a smaller barrier than the detaching Ru−O bond.

Experimental evidence[8,9] points to methanol formation having a smaller barrier, as methanol has been observed to be produced in much larger quantities than methane.[9−11] Popic et al. observed up to 30.5% product efficiency for methanol at ∼−0.12 V-RHE, while no CO has been reported to be present. Conversely, Spataru et al. report excellent HCOOH/H_2 evolution with CO as the minority product at similar potential on the RuO_2 electrode. These experimental results directly correlate to our conclusion that moderate CO* coverage aids in methanol evolution and high CO* coverage leads to HCOOH/H_2 at very low potential.

Our simulation model does not explicitly consider pH effects. The discrepancy between observed and predicted methanol onset potential can originate from variations in CO* coverage, pH effects, or other differences like composition and surface structure. Preliminary work[8] by Bandi suggested strong dependence of methanol evolution efficiency on pH and observed a much better methanol efficiency in acidic solution than neutral electrolyte. The concentration of methanol in the solvent can also affect the reaction thermodynamics of methanol production. With higher concentration, free energy of methanol increases, and release of methanol from the H_3CO* intermediate needs larger reducing potential.

4. CONCLUSIONS

In summary, without CO* coverage, RuO_2(110) is expected to start producing hydrogen via the cus sites (−0.33 V-RHE) with hydroxylated bridge sites. Repulsive interactions with CO* spectators destabilize H*. If the availability of CO_2 in the reaction layer and the kinetic barriers for CO_2 activation are not limiting, OCHO* is preferred over H* as the first proton transfer product, as seen from a purely thermodynamic perspective. Transient formation of CO* from CO2RR leads to 25% to 75% CO* coverage. A large reducing potential is required to protonate stable bidentate OCHO* and break one Ru−O bond at 0−50% CO* coverage. At 25% CO* coverage, methanol is expected to be the main CO2RR product, with an onset potential of −0.78 V-RHE because HCOOH* is surface bound. 50% CO* coverage is predicted to provide the best activity toward methanol formation. At this CO* coverage, the HER cannot start above −0.56 V-RHE due to bridge site hydroxylation (Table 2), while methanol formation (onset of −0.4 V-RHE) is active at the OH* removal potential (−0.48 V-RHE). At a sufficient reducing potential, the CO2RR pathway to methanol is expected to show significant activity in conjunction with little hydrogen evolution for 25%−50% CO* coverage. The 75% CO*-covered surface, on the contrary, has close to ideal onset potential for formic acid production, due to weakly bound monodentate OCHO*. Once OH* is removed from the active site, both hydrogen and formic acid are expected to form. Suppression of HER at 50% or lower CO* coverage by formation of OCHO* at the active sites is critically dependent on fast reaction kinetics for OCHO* formation. Good activity and selectivity obtained for CO2RR on RuO_2 catalysts are highly dependent on the CO* coverage in the reaction environment. At high CO* coverages (75%), excellent availability of CO_2 is critical for formic acid evolution. If, however, CO_2 molecules are not readily available, hydrogen is expected to be the only observable product.

Binding energy alteration of both H* and CO2RR intermediates emerging from adsorbate interaction with CO* lets us observe switching of CO2RR/HER activity and CO2RR product selectivity at the optimal CO* coverage. 25%−50% CO* coverage is most conducive for methanol formation and higher CO* coverage for formic acid evolution.

RuO_2-based electrocatalysts have been shown experimentally to hold great promise for direct conversion of CO_2 to methanol and formic acid. Based on this theoretical exploration, we show that CO* spectators hold the key to good CO2RR activity and selectivity.

■ ASSOCIATED CONTENT

Ⓢ Supporting Information

The Supporting Information is available free of charge on the ACS Publications website at DOI: 10.1021/acs.jpcc.7b04242.

Additional visualizations of and explanation for CO* coverage configurations, adsorbate free energy diagrams, thermodynamic data for adsorbates and molecules, figure for methanol evolution elementary reaction step onset dependency on CO* coverage, free energy of CO* coverage configurations, and visualization for all possible CO* spectator models (PDF)

Atomic position data and visualization for all catalyst surface simulations (ZIP)

■ AUTHOR INFORMATION

Corresponding Author

*E-mail: teve@dtu.dk. Fax: +45 46 77 57 58. Tel.: +45 45 25 82 01.

ORCID

Arghya Bhowmik: 0000-0003-3198-5116

Notes

The authors declare no competing financial interest.

■ ACKNOWLEDGMENTS

Funding from the Lundbeck foundation (grant no. R141-2013-A13204) and The Velux Foundations through V-Sustain: The VILLUM Center for the Science of Sustainable Fuels and Chemicals (Grant no. 9455) is gratefully acknowledged. The

Niflheim supercomputer at DTU was used for the computations performed in this work.

REFERENCES

(1) Chu, S.; Majumdar, A. Opportunities and Challenges for a Sustainable Energy Future. *Nature* **2012**, *488* (7411), 294−303.

(2) Dunn, B.; Kamath, H.; Tarascon, J.-M. Electrical Energy Storage for the Grid: A Battery of Choices. *Science (Washington, DC, U. S.)* **2011**, *334* (6058), 928−935.

(3) Ganesh, I. Conversion of Carbon Dioxide into Methanol - A Potential Liquid Fuel: Fundamental Challenges and Opportunities (a Review). *Renewable Sustainable Energy Rev.* **2014**, *31* (2014), 221−257.

(4) Hori, Y. Electrochemical CO2 Reduction on Metal Electrodes. In *Modern Aspects of Electrochemistry*; Springer New York: New York, NY, 2008; Vol. *42*, pp 89−189.

(5) Kuhl, K. P.; Hatsukade, T.; Cave, E. R.; Abram, D. N.; Kibsgaard, J.; Jaramillo, T. F. Electrocatalytic Conversion of Carbon Dioxide to Methane and Methanol on Transition Metal Surfaces. *J. Am. Chem. Soc.* **2014**, *136* (40), 14107−14113.

(6) Peterson, A. A.; Abild-Pedersen, F.; Studt, F.; Rossmeisl, J.; Nørskov, J. K.; Lewis, N. S.; Nocera, D. G.; Hori, Y.; Kikuchi, K.; Murata, A.; et al. How Copper Catalyzes the Electroreduction of Carbon Dioxide into Hydrocarbon Fuels. *Energy Environ. Sci.* **2010**, *3* (9), 1311−1315.

(7) Peterson, A. A.; Nørskov, J. K. Activity Descriptors for CO_2 Electroreduction to Methane on Transition-Metal Catalysts. *J. Phys. Chem. Lett.* **2012**, *3* (2), 251−258.

(8) Bandi, A. Electrochemical Reduction of Carbon Dioxide on Conductive Metallic Oxides. *J. Electrochem. Soc.* **1990**, *137* (7), 2157.

(9) Popic, J. P.; Avramov-Ivic, M. L.; Vukovic, N. B.; Popić, J.; Avramov-Ivić, M.; Vuković, N.; Popic, J. P.; Avramov-Ivic, M. L.; Vukovic, N. B.; Popić, J.; et al. Reduction of Carbon Dioxide on Ruthenium Oxide and Modified Ruthenium Oxide Electrodes in 0.5 M NaHCO 3. *J. Electroanal.* **1997**, *421*, 105−110.

(10) Qu, J.; Zhang, X.; Wang, Y.; Xie, C. Electrochemical Reduction of CO_2 on RuO_2/TiO_2 Nanotubes Composite Modified Pt Electrode. *Electrochim. Acta* **2005**, *50* (16−17), 3576−3580.

(11) Spataru, N.; Tokuhiro, K.; Terashima, C.; Rao, T. N.; Fujishima, A. Electrochemical Reduction of Carbon Dioxide at Ruthenium Dioxide Deposited on Boron-Doped Diamond. *J. Appl. Electrochem.* **2003**, *33* (12), 1205−1210.

(12) Rasul, S.; Anjum, D. H.; Jedidi, A.; Minenkov, Y.; Cavallo, L.; Takanabe, K. A Highly Selective Copper-Indium Bimetallic Electrocatalyst for the Electrochemical Reduction of Aqueous CO_2 to CO. *Angew. Chem., Int. Ed.* **2015**, *54* (7), 2146−2150.

(13) Mistry, H.; Reske, R.; Zeng, Z.; Zhao, Z. J.; Greeley, J.; Strasser, P.; Cuenya, B. R. Exceptional Size-Dependent Activity Enhancement in the Electroreduction of CO_2 over Au Nanoparticles. *J. Am. Chem. Soc.* **2014**, *136* (47), 16473−16476.

(14) Li, Y.; Cui, F.; Ross, M. B.; Kim, D.; Sun, Y.; Yang, P. Structure-Sensitive CO_2 Electroreduction to Hydrocarbons on Ultrathin Five-Fold Twinned Copper Nanowires. *Nano Lett.* **2017**, *17* (2), 1312−1317.

(15) Varela, A. S.; Schlaup, C.; Jovanov, Z. P.; Malacrida, P.; Horch, S.; Stephens, I. E. L.; Chorkendorff, I. CO_2 Electroreduction on Well-Defined Bimetallic Surfaces: Cu Overlayers on Pt(111) and Pt(211). *J. Phys. Chem. C* **2013**, *117* (40), 20500−20508.

(16) Li, C. W.; Kanan, M. W. CO_2 Reduction at Low Overpotential on Cu Electrodes Resulting from the Reduction of Thick Cu_2O Films. *J. Am. Chem. Soc.* **2012**, *134* (17), 7231−7234.

(17) Jovanov, Z. P.; Hansen, H. A.; Varela, A. S.; Malacrida, P.; Peterson, A. A.; Nørskov, J. K.; Stephens, I. E. L.; Chorkendorff, I. Opportunities and Challenges in the Electrocatalysis of CO_2 and CO Reduction Using Bifunctional Surfaces: A Theoretical and Experimental Study of Au-Cd Alloys. *J. Catal.* **2016**, *343*, 215−231.

(18) Torelli, D. A.; Francis, S. A.; Crompton, J. C.; Javier, A.; Thompson, J. R.; Brunschwig, B. S.; Soriaga, M. P.; Lewis, N. S. Nickel-Gallium-Catalyzed Electrochemical Reduction of CO_2 to Highly Reduced Products at Low Overpotentials. *ACS Catal.* **2016**, *6* (3), 2100−2104.

(19) Karamad, M.; Hansen, H. A.; Rossmeisl, J.; Nørskov, J. K. Mechanistic Pathway in the Electrochemical Reduction of CO_2 on RuO_2. *ACS Catal.* **2015**, *5* (7), 4075−4081.

(20) Bhowmik, A.; Vegge, T.; Hansen, H. A. Descriptors and Thermodynamic Limitations of Electrocatalytic Carbon Dioxide Reduction on Rutile Oxide Surfaces. *ChemSusChem* **2016**, *9* (22), 3230−3243.

(21) Peterson, A. A.; Abild-Pedersen, F.; Studt, F.; Rossmeisl, J.; Nørskov, J. K.; Lewis, N. S.; Nocera, D. G.; Hori, Y.; Kikuchi, K.; Murata, A.; et al. How Copper Catalyzes the Electroreduction of Carbon Dioxide into Hydrocarbon Fuels. *Energy Environ. Sci.* **2010**, *3* (9), 1311.

(22) Back, S.; Kim, H.; Jung, Y. Selective Heterogeneous CO_2 Electroreduction to Methanol. *ACS Catal.* **2015**, *5* (2), 965−971.

(23) An, W.; Xu, F.; Stacchiola, D.; Liu, P. Potassium-Induced Effect on the Structure and Chemical Activity of the $Cu_xO/Cu(1\ 1\ 1)$ $(X \leq 2)$ Surface: A Combined Scanning Tunneling Microscopy and Density Functional Theory Study. *ChemCatChem* **2015**, *7* (23), 3865−3872.

(24) Cui, C.; Han, J.; Zhu, X.; Liu, X.; Wang, H.; Mei, D.; Ge, Q. Promotional Effect of Surface Hydroxyls on Electrochemical Reduction of CO_2 over SnO_x/Sn Electrode. *J. Catal.* **2016**, *343*, 257−265.

(25) Marshall, S. T.; Medlin, J. W. Surface-Level Mechanistic Studies of Adsorbate adsorbate Interactions in Heterogeneous Catalysis by Metals. *Surf. Sci. Rep.* **2011**, *66* (5), 173−184.

(26) Wang, H. Y.; Schneider, W. F. Comparative Chemistries of CO and NO Oxidation over $RuO_2(110)$: Insights from First-Principles Thermodynamics and Kinetics. *Mol. Simul.* **2012**, *38* (8−9), 615−630.

(27) Tang, D. C.; Hwang, K. S.; Salmeron, M.; Somorjai, G. A. High Pressure Scanning Tunneling Microscopy Study of CO Poisoning of Ethylene Hydrogenation on Pt(111) and Rh(111) Single Crystals. *J. Phys. Chem. B* **2004**, *108* (35), 13300−13306.

(28) Zhang, Y. J.; Sethuraman, V.; Michalsky, R.; Peterson, A. A. Competition between CO_2 Reduction and H_2 Evolution on Transition-Metal Electrocatalysts. *ACS Catal.* **2014**, *4* (10), 3742−3748.

(29) Kresse, G. From Ultrasoft Pseudopotentials to the Projector Augmented-Wave Method. *Phys. Rev. B: Condens. Matter Mater. Phys.* **1999**, *59* (3), 1758−1775.

(30) Kiejna, A.; Kresse, G.; Rogal, J.; De Sarkar, A.; Reuter, K.; Scheffler, M. Comparison of the Full-Potential and Frozen-Core Approximation Approaches to Density-Functional Calculations of Surfaces. *Phys. Rev. B: Condens. Matter Mater. Phys.* **2006**, *73* (3), 6−9.

(31) Norskov, J. K.; Bligaard, T.; Rossmeisl, J.; Christensen, C. H. Towards the Computational Design of Solid Catalysts. *Nat. Chem.* **2009**, *1* (1), 37−46.

(32) Wellendorff, J.; Lundgaard, K. T.; Møgelhøj, A.; Petzold, V.; Landis, D. D.; Nørskov, J. K.; Bligaard, T.; Jacobsen, K. W. Density Functionals for Surface Science: Exchange-Correlation Model Development with Bayesian Error Estimation. *Phys. Rev. B: Condens. Matter Mater. Phys.* **2012**, *85* (23), 235149.

(33) Butler, S. R.; Gillson, J. L. Crystal Growth, Electrical Resistivity and Lattice Parameters of RuO_2 and IrO_2. *Mater. Res. Bull.* **1971**, *6* (2), 81−89.

(34) Christensen, R.; Hansen, H. A.; Vegge, T. Identifying Systematic DFT Errors in Catalytic Reactions. *Catal. Sci. Technol.* **2015**, *5* (11), 4946−4949.

(35) Hansen, H. A.; Shi, C.; Lausche, A.; Peterson, A.; Nørskov, J. K. Bifunctional Alloys for the Electroreduction of CO_2 and CO. *Phys. Chem. Chem. Phys.* **2016**, *18* (111), 9194−9201.

(36) Nørskov, J. K.; Rossmeisl, J.; Logadottir, A.; Lindqvist, L.; Kitchin, J. R.; Bligaard, T.; Jónsson, H. Origin of the Overpotential for Oxygen Reduction at a Fuel-Cell Cathode. *J. Phys. Chem. B* **2004**, *108* (46), 17886−17892.

(37) Reuter, K.; Scheffler, M. Composition and Structure of the RuO_2 (110) Surface in an O_2 and CO Environment: Implications for

the Catalytic Formation of CO_2 Karsten. *Phys. Rev. B* **2001**, *65* (3), 045407.

Supplementary Information for “Role of CO* as a Spectator in CO_2 Electroreduction on RuO_2”

Arghya Bhowmik, Heine Anton Hansen and Tejs Vegge*

Department of Energy Conversion and Storage, Technical University of Denmark, Fysikvej Bldg. 309,

DK-2800 Kgs. Lyngby, Denmark.

E-mail: teve@dtu.dk; Fax: +45 46 77 57 58; Tel: +45 45 25 82 01

Table SI1: Free energy (eV) including zero point, heat capacity and entropy contributions at 298.15 K for adsorbed species on the model catalyst surface (and any product molecule released in the concerned electron/proton transfer step), with respect to CO_2, H_2O and H_2 molecules.

e^- / H^+ transfer step	Adsorbate and (or) product	Free energy of catalyst surface with intermediates and products released [eV] (and unused CO_2 for HER intermediates)					
		0CO	1CO-b	2CO-bc	2CO-bb	3CO-bbc	3CO-bcc
0	*	-237.86	-251.66	-265.06	-264.97	-278.26	-278.06
1	OCHO*	-260.59	-274.61	-287.67	-287.57	-299.22	-300.10
2	HCOOH*	-263.18	-277.39	-290.82	-290.54	-303.73	-303.74
3	H_2COOH*	-267.10	-281.29	-294.43	-293.31	-306.05	-306.74
4	H_3CO*+OH*	-271.77	-284.84	-297.91	-297.16		
4	H_2CO*+H_2O(l)	-270.26	-284.42	-297.73	-297.56	-310.61	-310.73
5	H_3CO*+H_2O(l)	-274.69	-288.73	-301.98	-301.28	-314.07	-314.82
6	O*+CH_4(aq)+H_2O(l)	-278.67	-292.42	-305.63	-304.95	-317.99	-318.59
7	OH*+CH_4(aq)+H_2O(l)	-282.82	-296.93	-310.17	-309.41	-322.41	-323.18
8	CH_4(aq)+2H_2O(l)	-286.05	-299.85	-313.24	-313.16	-326.45	-326.25
4	O*+CH_3OH(aq)	-270.75	-284.51	-297.72	-297.04	-310.08	-310.67
5	H_2COH*+H_2O(l)	-273.74	-287.88	-300.80	-300.72	-312.67	-312.49
5	OH*+CH_3OH(aq)	-274.90	-289.02	-302.26	-301.50	-314.50	-315.27
6	CH_3OH*+H_2O(l)	-277.99	-291.87	-305.34	-305.19	-318.08	-318.11
6	CH_3OH(aq)+H_2O(l)	-278.14	-291.93	-305.33	-305.25	-318.53	-318.34
2	HCOOH(aq)	-263.43	-277.23	-290.63	-290.54	-303.83	-303.63
1	COOH*	-259.36	-273.34	-286.49	-286.33	-298.22	-299.40
2	CO+H_2O(l)	-264.46	-277.85	-291.06	-291.06	-303.78	-303.78
1	H*	-260.26	-273.88	-287.26	-286.51	-299.54	-300.10
2	H_2(aq)	-263.33	-277.12	-290.52	-290.44	-303.72	-303.53

Table SI1: Free energy calculation at 298.15 K for reactant and product molecules in this study. Fugacities and free energy corrections are also listed. Fugacity values for methanol and formic acid are calculated from product concentration observed[1,2]. That for other reactants/products are from previous theoretical literature[3].

Species	Fugacity [Pa]	E_{elec} [eV]	ZPE [eV]	Heat capacity contribution [eV]	-TS [eV]	Correction [eV]
CO	5562	-12.07	0.14	0.09	-0.61	-
CO_2	101325	-18.4	0.31	0.1	-0.66	0.3
H_2	101325	-7.17	0.28	0.09	-0.4	0.1
H_2O	3534	-12.81	0.57	0.11	-0.67	0
HCOOH	2	-25.49	0.9	0.11	-1.05	0.15 (C=O bond) and -0.19 ($HCOO^-$ (aq))
CH_3OH	0.003	-27.74	1.37	0.12	-1.22	0
CH_4	20467	-23.28	1.2	0.11	-0.62	0

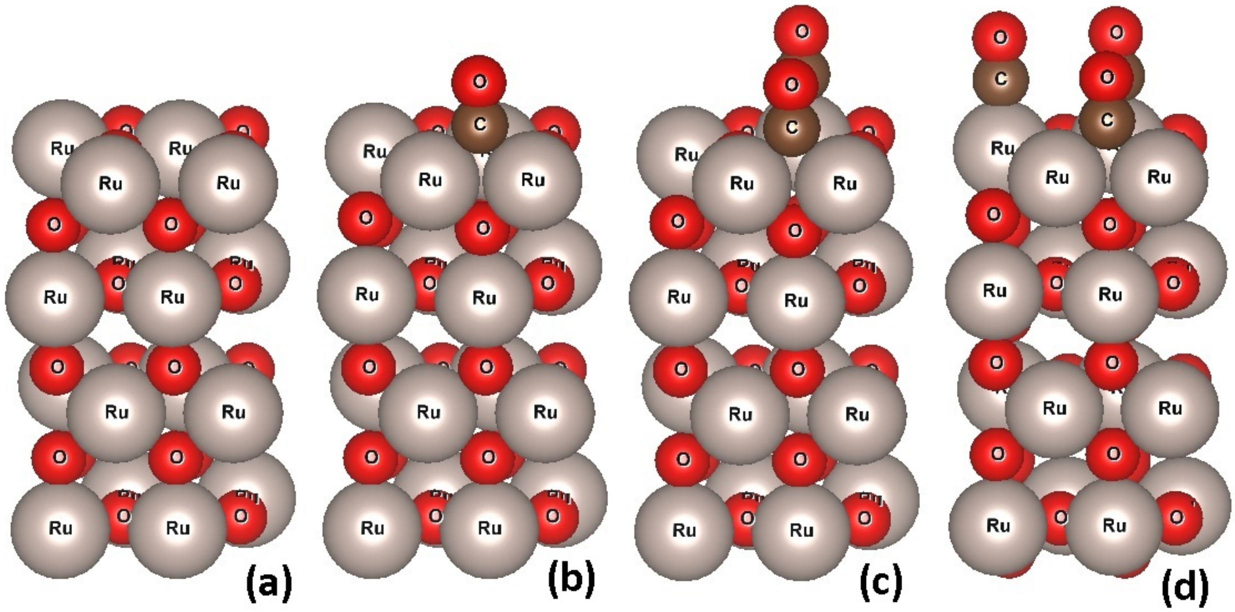

cus	X	X
bridge	X	X

cus	X	X
bridge	CO	X

cus	CO	X
bridge	CO	X

cus	CO	CO
bridge	CO	X

Figure SI1: The simulated cell for the RuO_2 (110) surface with two bridge (site coordinating between two Ru atoms) and two cus sites (on top position on a Ru atom). The four sites are occupied by (a) no spectator: all four active sites can take part in the catalysis, (b) one bridge site blocked by CO*, (c) one bridge site and one cus site (closer to the bridge site), and (d) two cus sites and one bridge site filled with CO*. Schematic representation of the active site occupation by CO* spectators is given below the molecular model, where X denotes an empty site. cus sites are yellow and bridge sites are green. Further, other CO* configurations were also studied as follows:

cus	CO	X
bridge	X	X

cus	X	CO
bridge	CO	X

cus	X	X
bridge	CO	CO

cus	CO	X
bridge	CO	CO

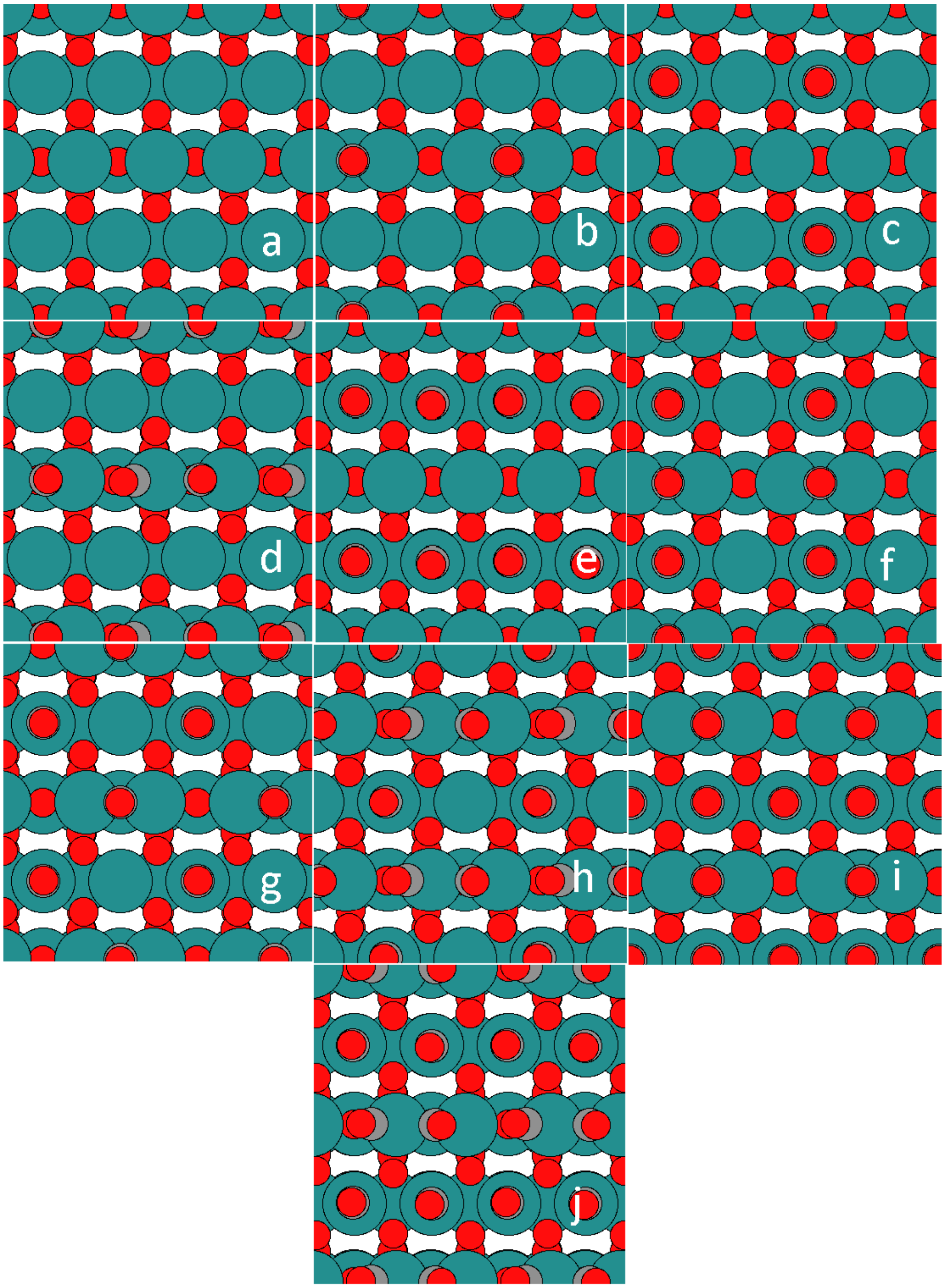

Figure SI2: all possible spatially distinct CO* spectator coverage within the simulation slab with two bridge and two cus sites. (a) no CO* coverage. (b) 25% CO* coverage (bridge site). (c) 25% CO* coverage (cus sites). (d) 50% CO* coverage (all bridge sites). (e) 50% CO* coverage (all cus sites). (f) 50% CO* coverage (adjoining bridge and cus sites i.e. near). (g) 50% CO* coverage (distant bridge and cus sites i.e. far). (h) 75% CO* coverage (all bridge sites and half cus sites). (i) 75% CO* coverage (all cus sites and half bridge sites). (j) 100% CO* coverage.

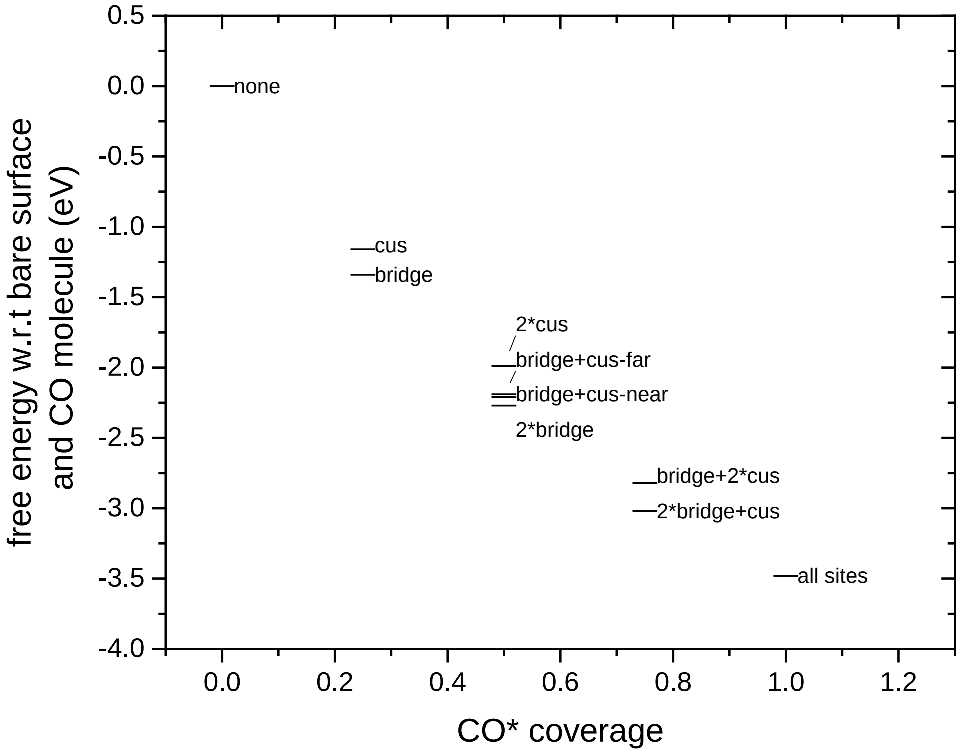

Figure SI3: free energy of CO* covered surfaces relative to bare RuO_2 (110) surfaces and CO molecule. (all surfaces mentioned in Figure SI2)

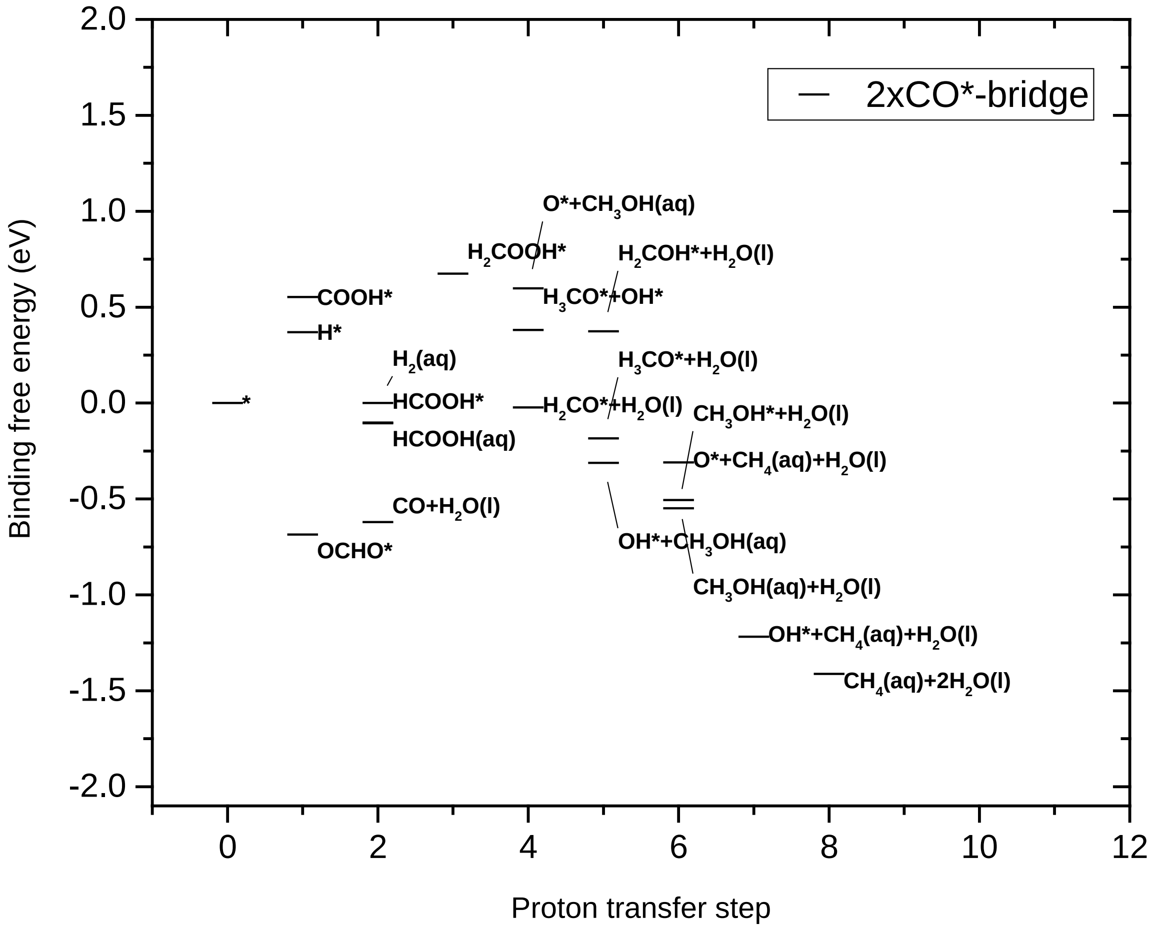

Figure SI4: Free energy diagram of possible reaction intermediates for HER/CO2RR and CO evolution from CO_2 with all bridge sites filled with spectator CO* and all cus sites empty.

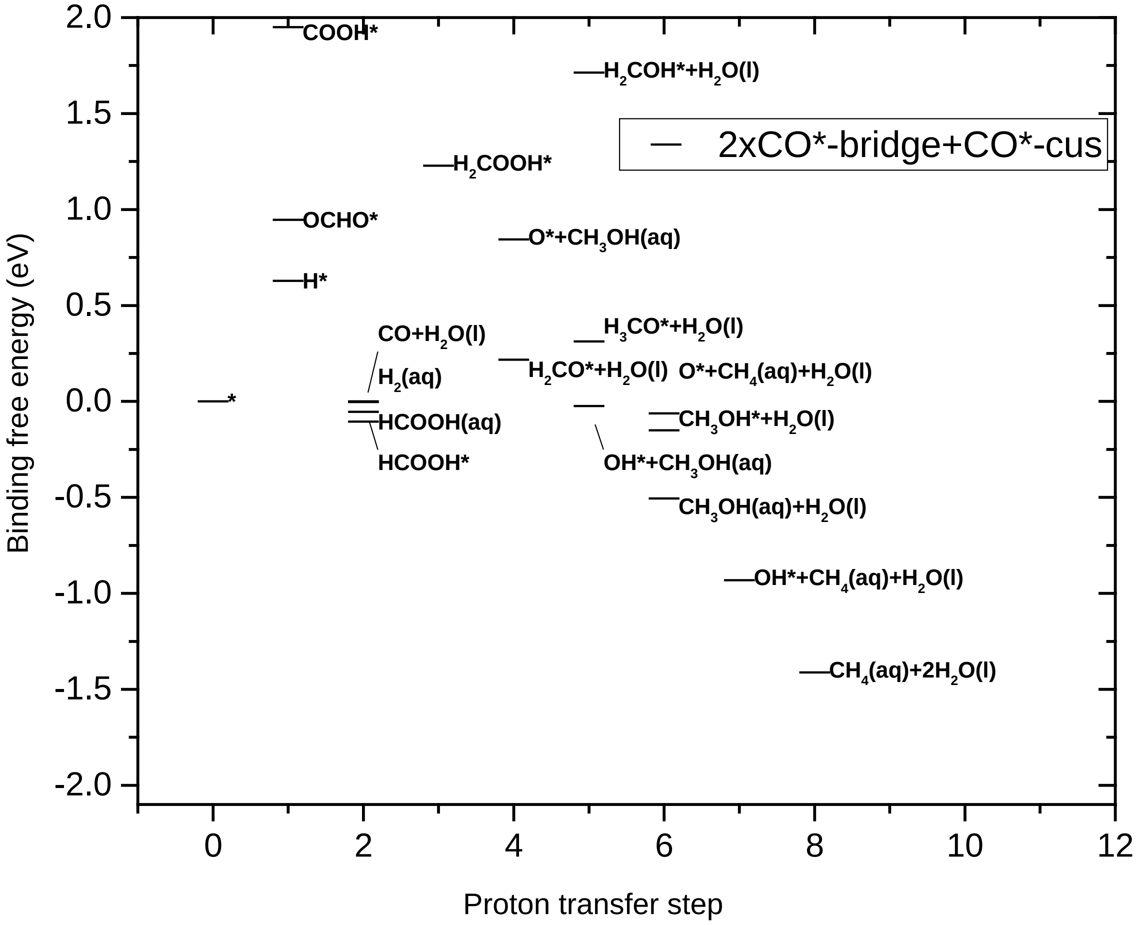

Figure SI5: Free energy diagram of possible reaction intermediates for HER/CO2RR and CO evolution from CO_2 with all bridge sites and half of the cus sites (total 75% sites) filled with spectator CO*.

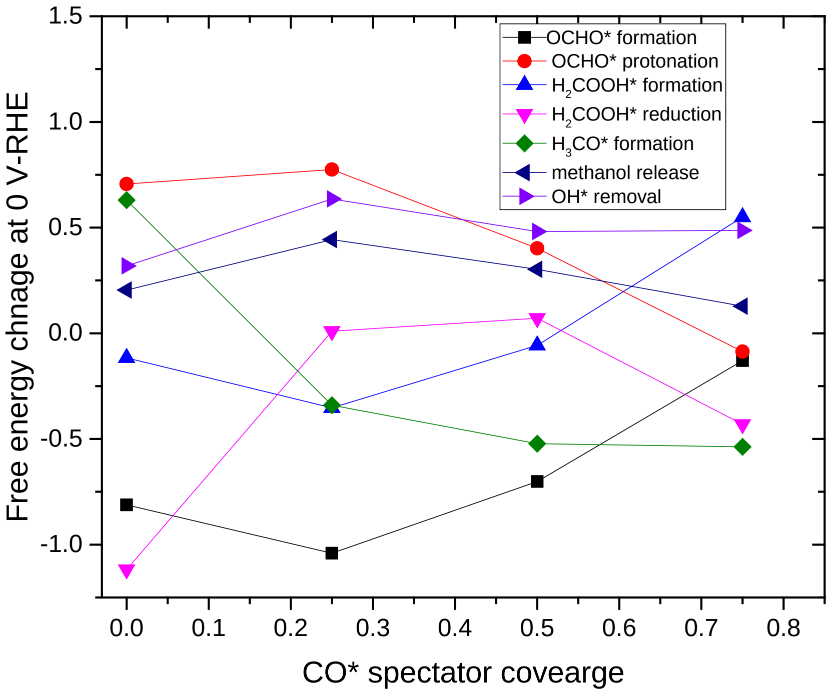

Figure SI6: The free energy change associated with an elementary step for methanol evolution is found to change with different CO* spectator coverage. The largest positive step at 0 V-RHE would require the most reducing condition to proceed. Steps showing negative free energy change are assumed to occur spontaneously.

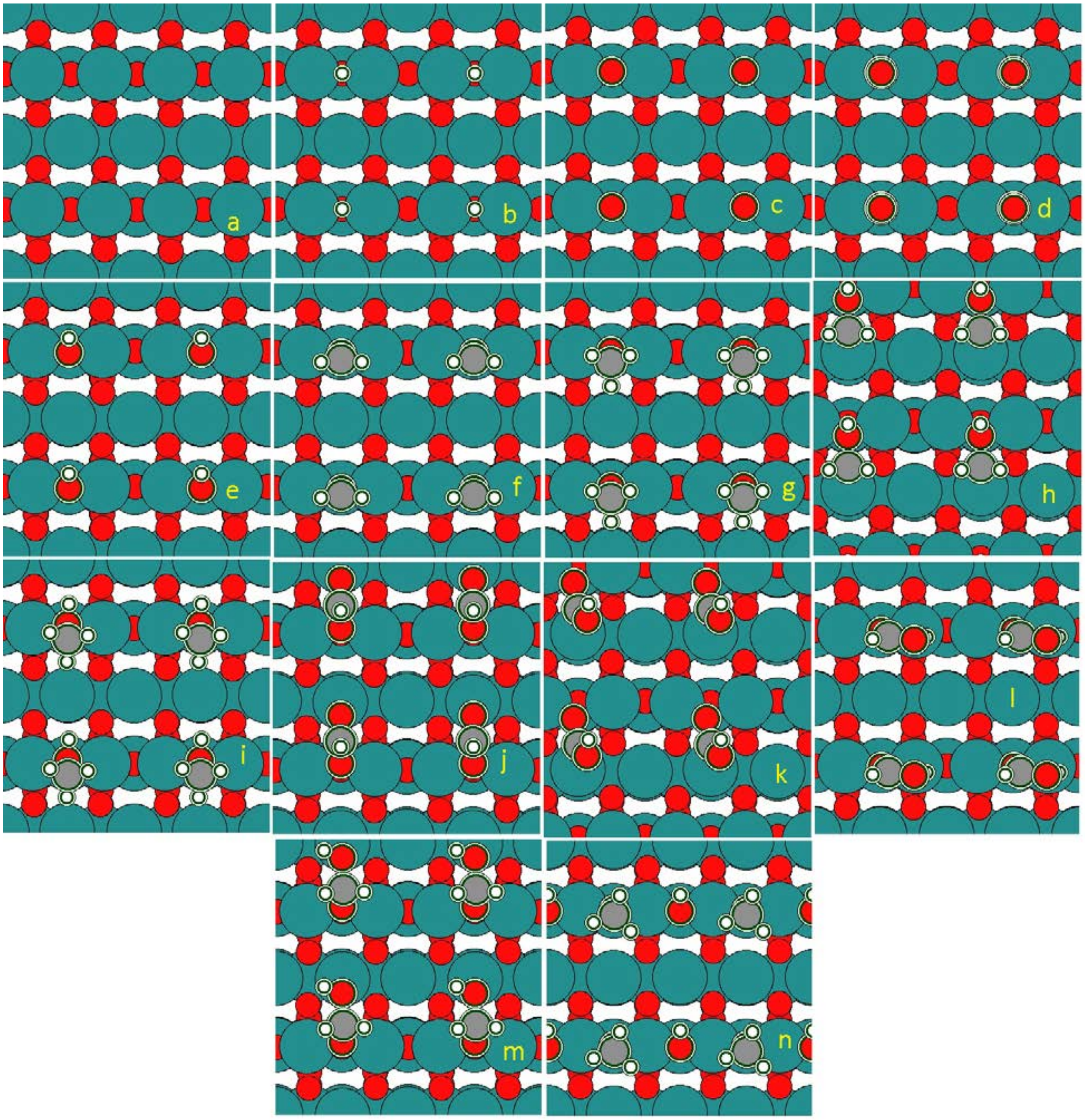

Figure S7: visualization of reaction intermediates with 0% CO* coverage (a) empty active site (b) H* (c) O* (d) CO* (e) OH* (f) H_2CO* (g) H_3CO* (h) H_2COH* (i) CH_3OH* (j) OCHO* (k) COOH* (l) HCOOH* (m) H_2COOH* (n) H_3CO*+OH*

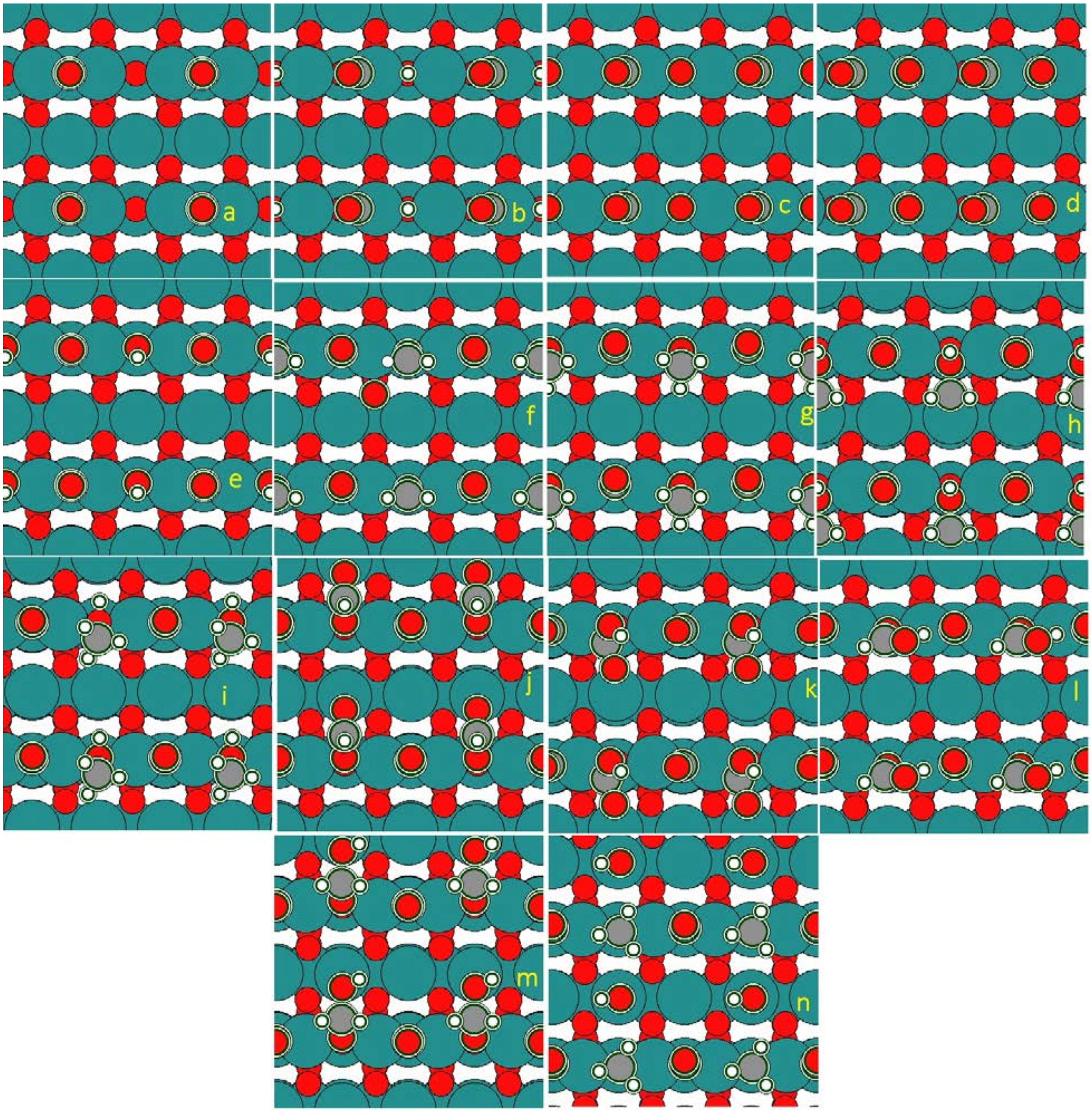

Figure S8: visualization of reaction intermediates with 25% CO* (bridge site) coverage (a) empty active site (b) H* (c) O* (d) CO* (e) OH* (f) H_2CO* (g) H_3CO* (h) H_2COH* (i) CH_3OH* (j) OCHO* (k) COOH* (l) HCOOH* (m) H_2COOH* (n) H_3CO*+OH*

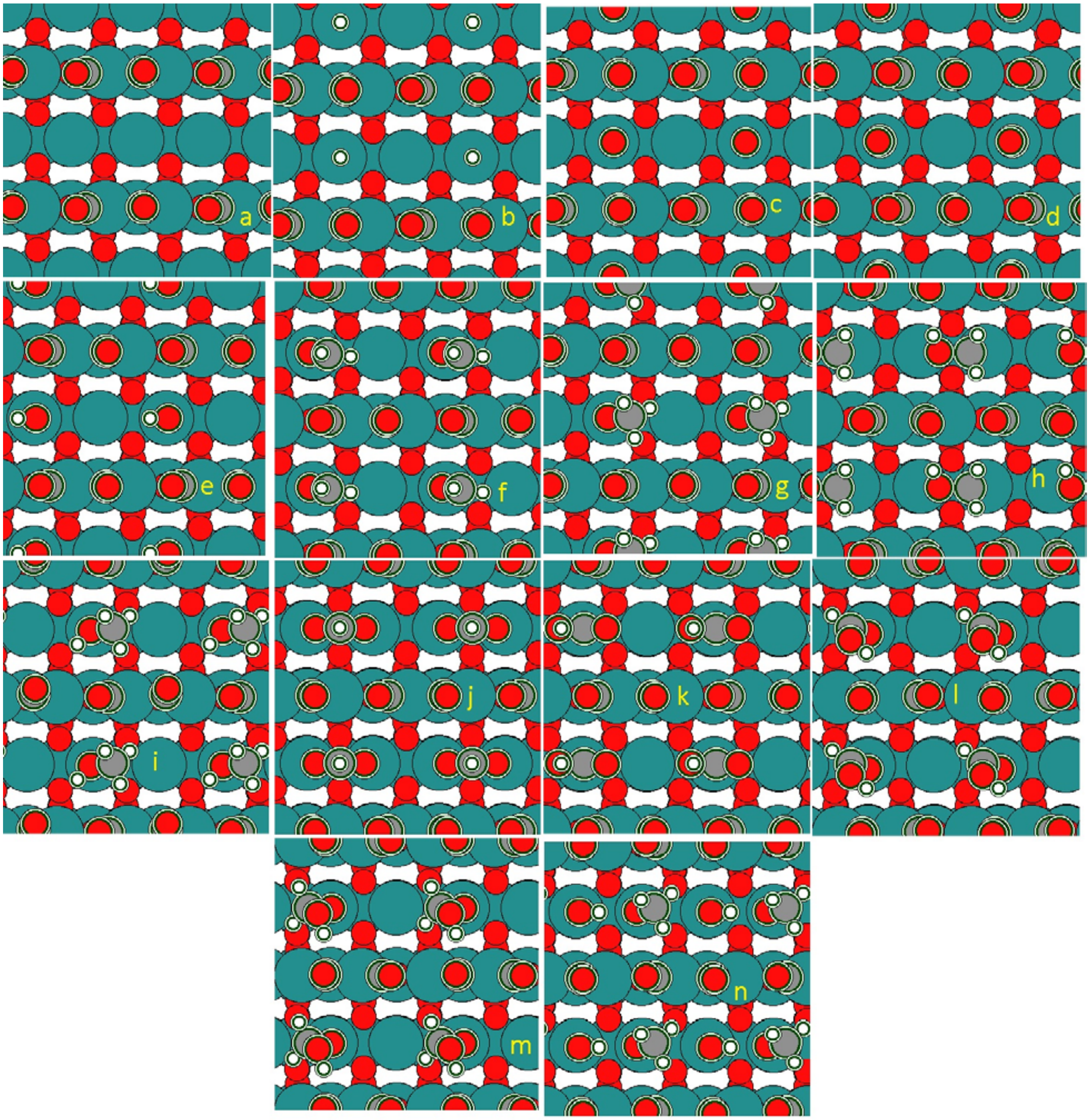

Figure S9: visualization of reaction intermediates with 50% CO* (bridge + bridge site) coverage (a) empty active site (b) H* (c) O* (d) CO* (e) OH* (f) H_2CO* (g) H_3CO* (h) H_2COH* (i) CH_3OH* (j) OCHO* (k) COOH* (l) HCOOH* (m) H_2COOH* (n) H_3CO*+OH*

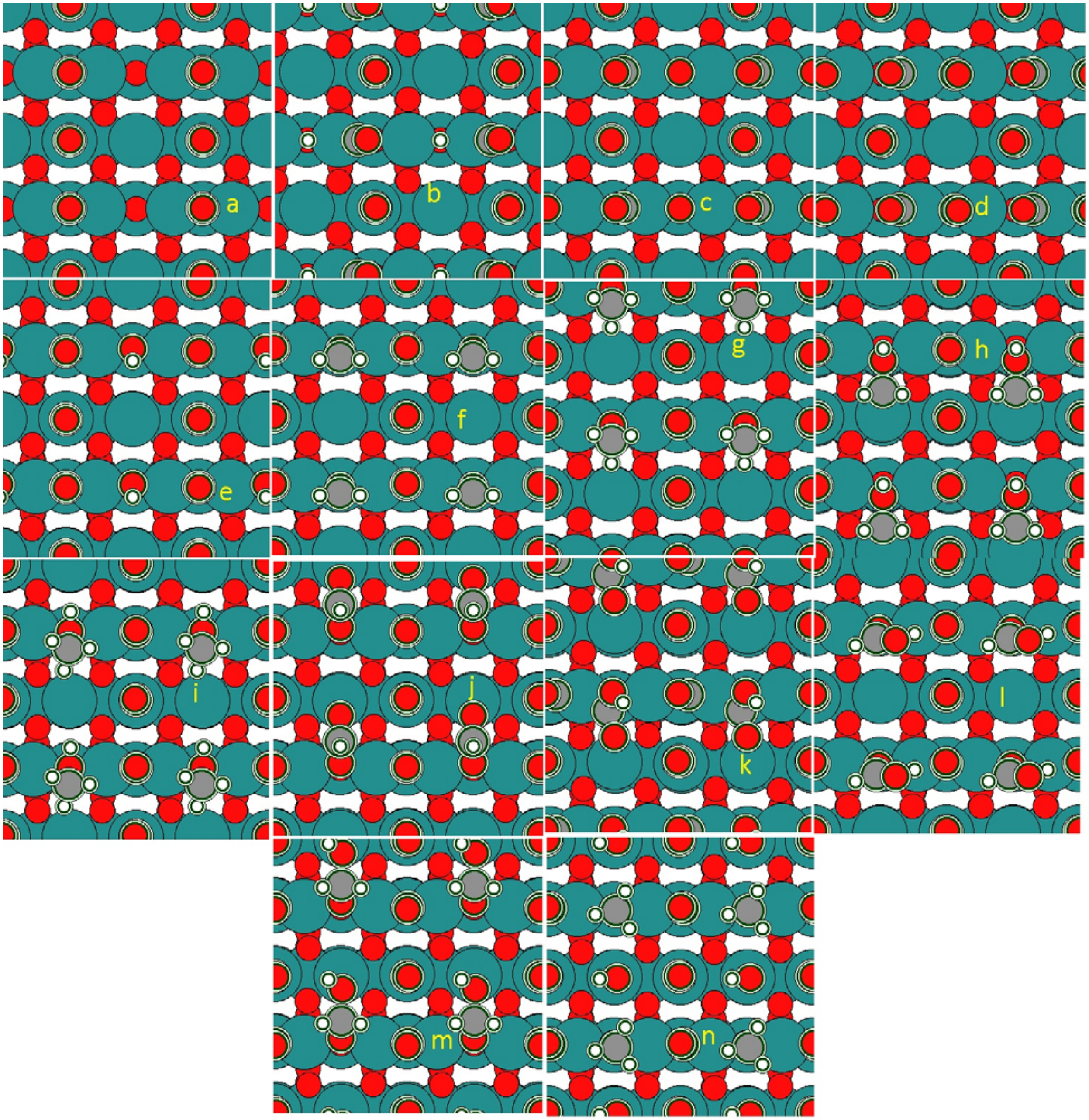

Figure S10: visualization of reaction intermediates with 50% CO* (bridge + adjacent cus site) coverage (a) empty active site (b) H* (c) O* (d) CO* (e) OH* (f) H_2CO* (g) H_3CO* (h) H_2COH* (i) CH_3OH* (j) OCHO* (k) COOH* (l) HCOOH* (m) H_2COOH* (n) H_3CO*+OH*

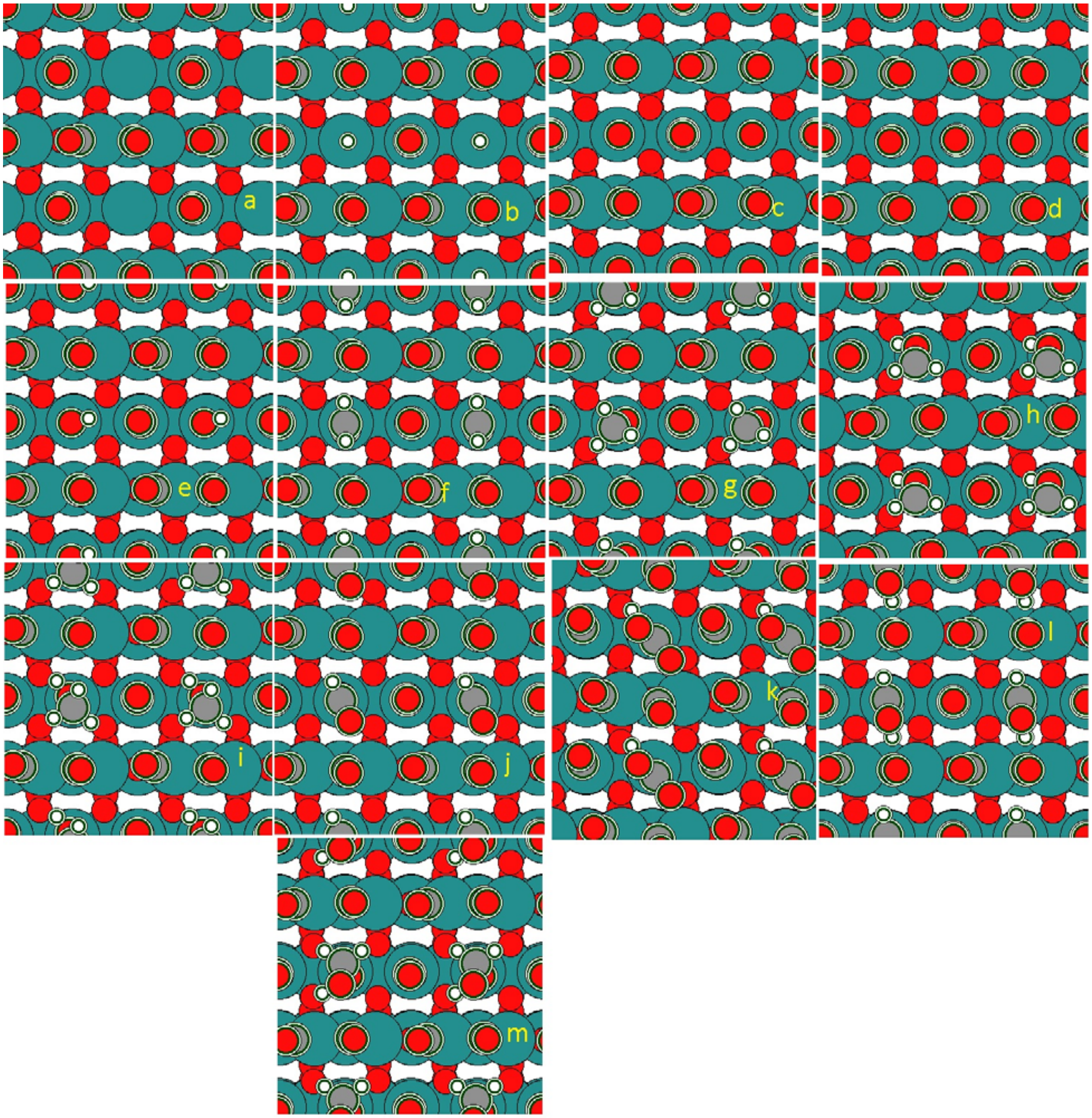

Figure S11: visualization of reaction intermediates with 75% CO* (bridge + bridge + cus site) coverage (a) empty active site (b) H* (c) O* (d) CO* (e) OH* (f) H_2CO* (g) H_3CO* (h) H_2COH* (i) CH_3OH* (j) OCHO* (k) COOH* (l) HCOOH* (m) H_2COOH*

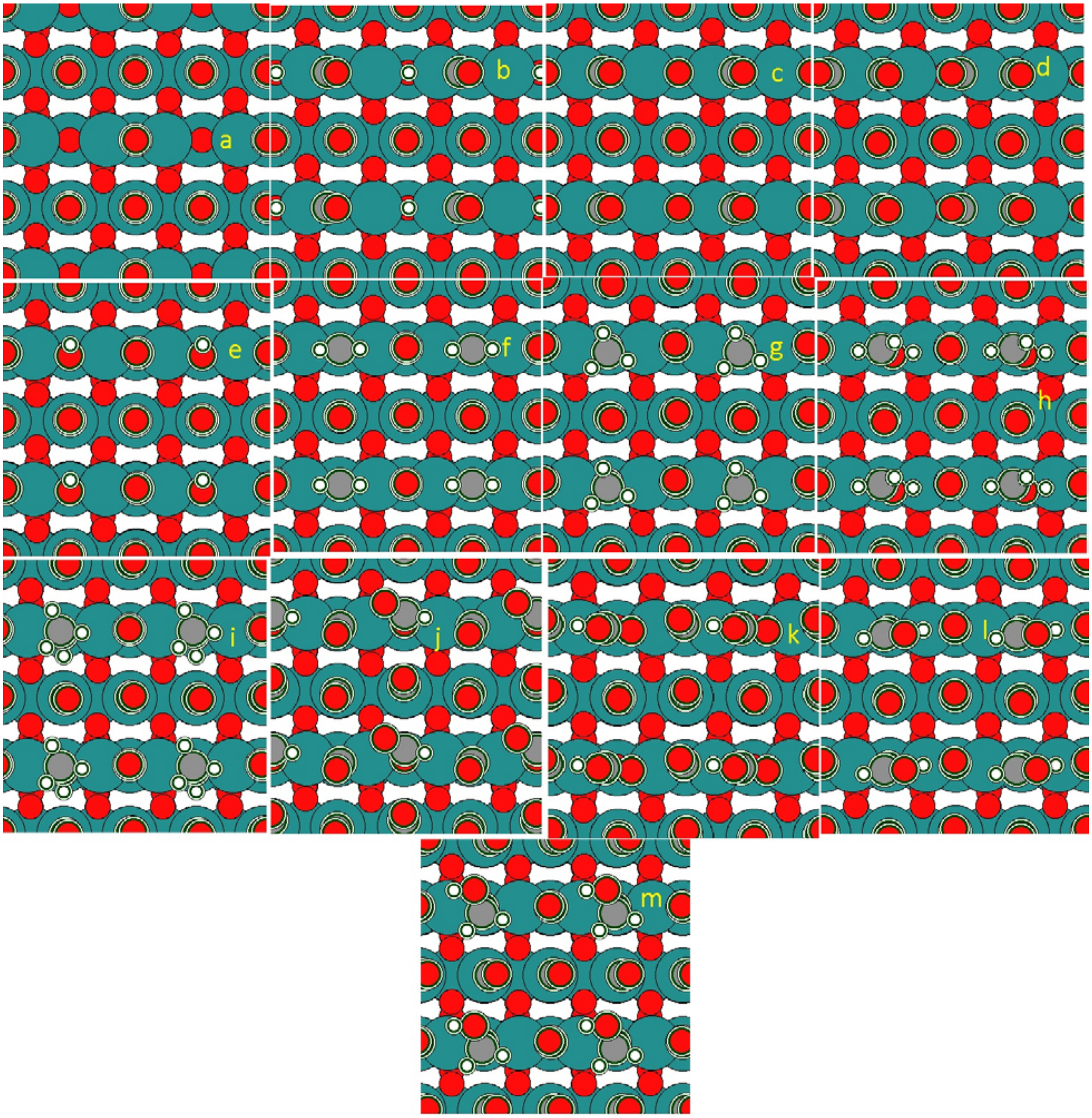

Figure S11: visualization of reaction intermediates with 75% CO* (bridge + cus + cus site) coverage (a) empty active site (b) H* (c) O* (d) CO* (e) OH* (f) H_2CO* (g) H_3CO* (h) H_2COH* (i) CH_3OH* (j) OCHO* (k) COOH* (l) HCOOH* (m) H_2COOH*

References:

(1) Popic, J. P.; Avramov-Ivic, M. L.; Vukovic, N. B.; Popić, J.; Avramov-Ivić, M.; Vuković, N.; Popic, J.

P.; Avramov-Ivic, M. L.; Vukovic, N. B.; Popić, J.; et al. Reduction of Carbon Dioxide on Ruthenium Oxide and Modified Ruthenium Oxide Electrodes in 0.5 M NaHCO 3. *J. Electroanal.* **1997**, *421*, 105–110.

(2) Spataru, N.; Tokuhiro, K.; Terashima, C.; Rao, T. N.; Fujishima, A. Electrochemical Reduction of Carbon Dioxide at Ruthenium Dioxide Deposited on Boron-Doped Diamond. *J. Appl. Electrochem.* **2003**, *33* (12), 1205–1210.

(3) Peterson, A. A.; Abild-Pedersen, F.; Studt, F.; Rossmeisl, J.; Nørskov, J. K.; Lewis, N. S.; Nocera, D. G.; Hori, Y.; Kikuchi, K.; Murata, A.; et al. How Copper Catalyzes the Electroreduction of Carbon Dioxide into Hydrocarbon Fuels. *Energy Environ. Sci.* **2010**, *3* (9), 1311-1315.

ACS Catalysis
Research Article
Cite This: ACS Catal. 2017, 7, 8502-8513
pubs.acs.org/acscatalysis

Electrochemical Reduction of CO_2 on $Ir_xRu_{(1-x)}O_2(110)$ Surfaces

Arghya Bhowmik, Heine Anton Hansen,* and Tejs Vegge

Department of Energy Conversion and Storage, Technical University of Denmark, Fysikvej Bldg. 309, DK-2800 Kgs. Lyngby, Denmark

Supporting Information

ABSTRACT: High overpotentials and low faradic efficiencies plague metal catalysts for direct conversion of CO_2 to methanol and other liquid fuels. RuO_2-based electrocatalysts have been observed to evolve methanol at low overpotentials, which has been attributed to an alternative reaction mechanism with oxygen-coordinated intermediates that can circumvent the limitations imposed by the scaling relations on metal catalysts. Here, we introduce an innovative concept of ligand effects in oxide catalysts. Both IrO_2 and RuO_2 binds OH* and other intermediates from the electrochemical reduction of CO_2 (CO2RR) strongly, but the stable and miscible system $Ir_xRu_{(1-x)}O_2$ exhibits anomalous weaker binding energy in the presence of CO* spectators, because of Ru−Ir ligand effects. The weakened adsorbate binding leads to a very low CO2RR onset potential (methanol evolution at −0.2 V RHE). An Ir atom at the bridge site with Ru neighbors binds intermediates such as OH* and OCHO* much weaker, because of synergistic ligand effects and adsorbate−adsorbate interactions. Consequently, a RuO_2 surface doped with Ir move close to the top of the predicted CO2RR volcano for oxides, which offers a significant improvement over state-of-the-art electrocatalysts for conversion of CO_2 into methanol. Analysis of electronic structure parameters with adsorbate binding energies indicates the ligand effect depletes electrons from the Ir atom and shifts the t_{2g} orbitals. The lack of electron donation from CO* spectators to Ir at the active site cause favorable adsorbate binding.

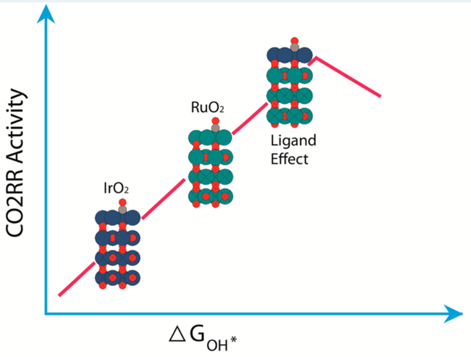

KEYWORDS: *computational catalysis, density functional theory, electrochemical CO_2 reduction, rutile oxide, ligand effect, adsorbate interaction*

INTRODUCTION

As consensus builds regarding the role of anthropogenic CO_2 emission as a fundamental cause behind increasing weather anomalies and global warming, the need to develop new technologies to enable growth without the associated CO_2 emissions becomes ever clearer.[1−3] Mankind has already mastered the art of harnessing electrical energy from renewable sources like solar and wind in an inexpensive manner, but challenges remain within the fossil-fuel-dependent transport sector and in large-scale energy storage, which deters the transition to a carbon neutral society.[2,4−6] Electrochemical reduction of CO_2 (CO2RR) into fuels and chemicals using renewable electricity can be proven to be a key technology, because it can provide inexpensive long-term mobile energy storage while being carbon neutral. Efficient electrochemical conversion of CO_2 directly to energy carriers such as methanol or ethanol is not yet feasible at high current densities, because of the lack of electrocatalysts, which can activate such reaction at low overpotentials and high product selectivity by suppressing the parasitic hydrogen evolution reaction (HER). Most single-metal catalysts produce either mostly hydrogen, CO, or formic acid,[7−9] with the exception being copper, which produces hydrocarbons at moderate faradic efficiency but requires an overpotential of $\eta > 1.0$ V for a modest current density of 1 mA/cm^2, reducing the energy storage efficiency.[10] Density functional theory (DFT)-based computational studies on the CO2RR pathway and thermodynamic barriers have been done previously for metal catalysts.[11,12] Such analyses have illustrated that, on metal catalysts, the reduction of adsorbed CO (CO*) to formyl (CHO*) is the thermodynamically limiting step in the reduction of CO_2 to hydrocarbons. The linear scaling relationship between the adsorption energies of the two critical reaction intermediates CO* and CHO* makes it difficult to improve the overpotential by choosing stronger- or weaker-binding single-metal catalysts.[11] Since the binding energy difference between CO* and CHO* remains similar for different metal surfaces, the potential required to reduce CO* to CHO* remains unchanged. Similarly, the reduction of CO_2 to CO on metal catalysts proceed through a COOH* intermediate, whose binding energy is strongly correlated with CO*. Thus, the most suitable binding energy combination of CO* and COOH* (leading to best activity) is not accessible together by choice of a different metal catalyst.[12,13] A class of sparingly studied rutile structured oxide materials has been observed to convert CO_2 to methanol at low overpotential.[14−18] Pourbaix diagrams suggest that IrO_2 and RuO_2 at neutral pH and under reducing conditions are eventually reduced to metals. However, X-ray photoelectron spectroscopy

Received: August 28, 2017
Revised: October 25, 2017
Published: November 1, 2017

DOI: 10.1021/acscatal.7b02914

(XPS) studies show that RuO_2 maintains its oxidized state under reducing conditions.[19] This kinetic stability can be attributed to a large kinetic barrier for leaching subsurface oxygen out. In an electrochemical environment, IrO_2 shows even greater stability than RuO_2[20] and will remain as an oxide under reducing conditions.

Recent theoretical studies have established that the different catalytic behaviors of such oxide catalysts, compared to metal catalysts, originate from differences in the CO2RR pathway.[21,22] The O-coordinated reaction intermediates dominate the pathway on oxide surfaces and obey different scaling relationships,[21] thereby circumventing the limitations of the metal electrocatalysts. The OH* binding energy is proven to be a good (single) descriptor for such catalyst activity, because it scales with the binding energy of other reaction intermediates in CO2RR. Therefore, engineering the OH* binding strength on oxide surfaces provides a handle toward optimizing CO2RR catalyst performance.[21]

Metal alloys often show intermediate adsorbate binding energies, compared to the constituent metals. This gives rise to an interesting approach to catalyst design. Combining two metals—one with too strong adsorption (left leg of the activity volcano) and one with too weak adsorption (right leg of the volcano)—one can create a catalyst surface with an optimum reaction intermediate binding energy to be at the top of the volcano curve. This interpolation principle has been successfully implemented to create new highly active catalysts for nitrogen reduction to ammonia[23] and CO_2 reduction to methanol.[24] Another approach for CO2RR electrocatalyst design is alloying with a metal with high oxygen affinity so that it interacts with some adsorbates through the oxygen atom. This would lead to a two-descriptor scenario, effectively breaking the CO*/CHO* binding scaling limitation.[11]

A study of the OH* binding on mixed oxides can equip us to fine-tune catalyst activity for CO2RR. $Ru_xIr_{(1-x)}O_2$ mixed oxide systems provide an excellent possibility to explore the adsorbate binding energy landscape. Lattice parameters for the rutile IrO_2 and RuO_2 oxides are well-matched and, for both oxides, the (110) surface has the lowest energy and is thus predominantly accessible for catalysis.[25,26] Based on the CO2RR reaction mechanism and analysis of the adsorbate binding energy scaling relations, the left leg of the CO2RR activity volcano on rutile oxide surfaces is limited by OH* removal.[21] RuO_2 falls on the left of the volcano. Thus, surfaces with OH* adsorption slightly weaker than that of $RuO_2(110)$ should have a lower overpotential. IrO_2 binds OH* stronger than RuO_2.[27] However, an Ir-oxide overlayer on RuO_2 has weaker OH* binding energy than pure RuO_2, thereby apparently violating the interpolation principle. Hence, unlike some metal alloys, detailed simulations are necessary to predict the catalytic properties of mixed oxides.

Adsorbate binding energies are sensitive to strain as well as ligand effects originating from variations in the nature of elements in the vicinity of the adsorption site. Alloyed catalysts with large strain are prone to degradation because of leaching and segregation. Utilizing ligand effects for modulating the OH* binding energy in mixed oxides is a better strategy to maintain catalyst stability. $Ru_xIr_{1-x}O_2(110)$ surfaces are excellent model mixed-oxide surfaces for studying catalytic properties. RuO_2 and IrO_2 have been widely researched as catalysts.[18,25,28−43] Both oxides are good band conductors,[44] as required for electrocatalysis. IrO_2 and RuO_2 are both found in the rutile-type crystal structure in pure form and the lattice parameters match closely.[45] Especially for the (110) surface, the change in composition would not bring forth any lateral strain, which can affect the binding energy for adsorbates. Lattice parameter *a* (defining the in-plane strain in the (110) plane) is <0.3% percent higher for IrO_2 than RuO_2. This is much lower than the 1%−4% strain needed to have any significant modification in catalytic activity.[46−49] Thus, ligand effects will dominate variations in binding energies on $Ru_xIr_{1-x}O_2(110)$ surfaces.

The close match in crystal structure and unit-cell parameters helps the $Ru_xIr_{1-x}O_2$ mixed oxide system to be stable over long periods of time. This system is miscible for a wide range of composition.[50] Segregation can otherwise be a challenge for the long lifetime of electrocatalysts as structural evolutions change the catalytic properties.[51−56] The bulk mixing energy as well as overlayer adhesion is exothermic[57] for $Ru_xIr_{1-x}O_2$, supporting the excellent stability of the system. Indeed, the mixed oxide has been shown to be more stable than pure RuO_2 and suitable for long-term operation as an electrocatalyst.[31]

Here, we systematically study the binding energy and reaction path on $Ru_xIr_{1-x}O_2$ catalyst surfaces to explore their suitability for CO2RR. $Ru_xIr_{1-x}O_2$ mixed-oxide systems can be active at moderate overpotential if the trend observed for the Ir-oxide overlayer on RuO_2 holds for other mixed-oxide structures.[21] While single-metal-atom-doped oxide catalysts have been studied theoretically,[58−61] a methodical study of the catalytic pathway under compositional variation in any mixed oxide system is absent. Our study also elucidates how key adsorbates such as H*/OH*/CO* binds to mixed Ru−Ir-oxides with varying Ru−Ir characteristics.

Previous work[21,62] has revealed that the CO* coverage can drastically modify the adsorbate binding, affecting both the CO2RR onset potential as well as selectivity over HER, where a small amount of spurious CO evolution can alter the CO* surface coverage. Consequently, CO* coverage effects on mixed oxide surfaces are also studied simultaneously for a wide range of Ir/Ru-mixed oxide surfaces. The CO* adsorption behavior is nonlinear as the composition changes from pure RuO_2 to pure IrO_2 and the adsorbate interaction has pronounced effects, especially for the intermediate composition range. Finally, a large reaction network for CO2RR consisting of 27 possible reaction intermediates with oxygen- and carbon-coordinated adsorbates and various products are explored on a range of $Ru_xIr_{1-x}O_2(110)$ mixed oxide surfaces, to create an understanding of composition and CO* coverage effects for efficient CO2RR to liquid fuel conversion.

■ COMPUTATIONAL METHOD

The density functional theory (DFT)-based simulation tool Vienna ab initio simulation package (VASP),[63] is used here along with Atomistic Simulation Environment (ASE)[64] to simulate model catalyst surfaces with and without adsorbates. The BEEF-vdW[65] exchange correlation functional with the vdW-DF2[66] nonlocal correlation energy and potential is used here to properly represent adsorbate interactions.[67,68] Details of molecular and adsorbate free-energy calculations and error correction schemes[69] are reported in the Supporting Information. To estimate the change in free energy under an applied potential for elementary proton transfer steps, the reaction thermodynamic are calculated using the computational hydrogen electrode (CHE) model.[70]

A comprehensive DFT-based study of the CO2RR thermodynamic process is complex and computationally demanding, because of the multiple reaction pathways possible.

DOI: 10.1021/acscatal.7b02914
ACS Catal. 2017, 7, 8502−8513

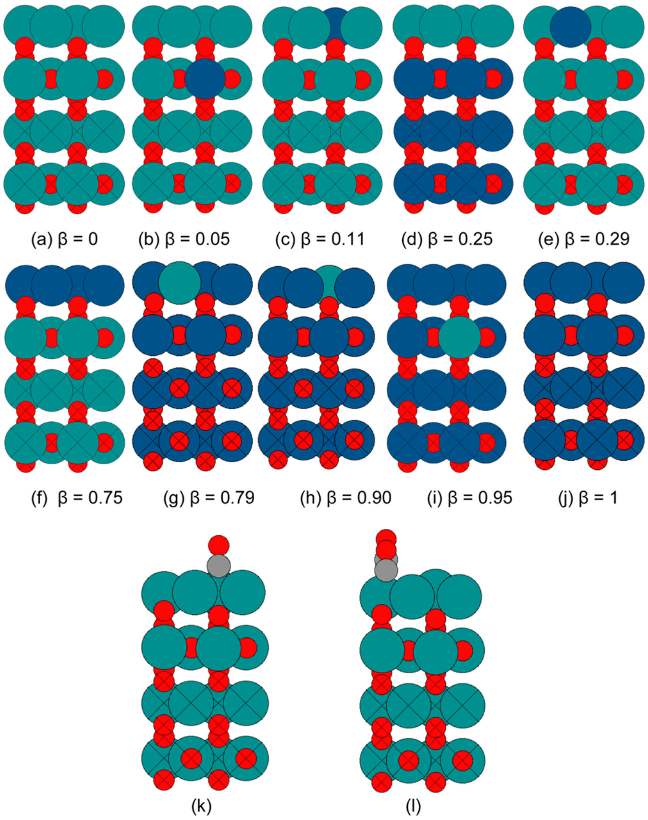

Figure 1. (a) Pure RuO_2 slab. (b) In a RuO_2 slab, one Ru atom replaced with Ir atom in the second atomic layer below the bridge site. (c) In a RuO_2 slab, one Ru atom at the coordinately unsaturated (cus) site replaced with Ir. (d) In an IrO_2 slab, all Ir atoms in the top layer replaced with Ru. (e) In a RuO_2 slab, one Ru atom at the bridge site replaced with Ir. (f) In a RuO_2 slab, all Ru atoms in the top layer replaced with Ir. (g) In an IrO_2 slab, one Ir atom at the bridge site replaced with Ru. (h) In an IrO_2 slab One Ir atom at the cus site replaced with Ru. (i) In an IrO_2 slab, one Ir atom replaced with a Ru atom in the second atomic layer below the bridge site. (j) Pure IrO_2 slab. (k) RuO_2 slab with 25% CO* coverage (bridge site). (l) RuO_2 slab with 50% CO* (bridge and cus site). Green, blue, and red spheres represent Ru, Ir, and O atoms, respectively. The β index is a measure of Ir character (between 0 and 1) of the bridge site based on the partial radial distribution of Ru and Ir atoms around the bridge site. All surfaces are (110).

Modeling the mixed oxide system $Ru_xIr_{1-x}O_2$ can be further complicated by many conceivable cation distributions. To avoid such complexity of cation distribution, previous theoretical studies involved either the substitution of a single atom in a RuO_2 or IrO_2 bulk/surface or the replacement of all the top layer cations in the simulation slab, keeping the bottom layers fixed to the bulk lattice structure.[57] Such simplification of the mixed oxide system must be considered, especially if the complete reaction pathway for CO2RR must be simulated on each model oxide surface.

In the absence of strain, adsorption energy variation in mixed oxides with composition will come from the geometry of the active site and the chemical environment of the atoms surrounding it. Cation substitution closest to the active site would impact the binding energy more than a substitution in a different atomic layer further away. Thus, by single-cation substitution at different positions relative to the active site, a range of mixed oxide catalytic behaviors can be represented.

To understand the differences emanating from the different configurations of Ir/Ru cation distributions near the active site, we consider 10 different model rutile(110) surfaces of these oxides starting from pure RuO_2 to pure IrO_2 surface (Figure 1). Surface slabs are prepared with four cation layers following previous theoretical work.[21,22] Bridging oxygen atoms were removed to model the reducing environment during the CO2RR. RuO_2 and IrO_2 surfaces are based on the optimized bulk structure of the respective oxides and cations are substituted to make mixed oxides. Each surface is given an index β, based on the Ru or Ir character of the bridge site. The procedure is detailed in the Supporting Information section.

The bridge site has been identified as the active site for the CO2RR.[21,22,62] Comprehensive DFT-based theoretical study has been done on the energetics of cation replacement in the (110) surface of IrO_2 and RuO_2.[57] This indicates that the replacement of Ru atoms in RuO_2 with Ir atoms and Ir atoms in IrO_2 with Ru atoms is favorable. The formation of a full overlayer is stable for the (110) surfaces of these oxides.[57] Single cation replacement can be done at one of the metal sites supporting the bridge site, at the coordinately unsaturated (cus) site in the top atom layer or below the bridge site in the second atomic layer (Figure 1).

These model surfaces have two bridge sites and two cus sites in the repeating unit cell. In our simulations, we consider three possible CO* spectator configurations: (a) no CO* spectator, (b) one CO* spectator at one bridge site, (c) two CO* spectators, one at bridge site and the other at the cus site next to it (Figures 1k and 1l)). This corresponds to 0%, 25% and 50% CO* coverage, respectively. The selection of these representative CO* coverage models was done based on our analysis of CO* coverage effects on CO2RR for RuO_2 catalyst.[62] We have studied the effects of CO* spectator coverage/ordering and found that oxygen-coordinated reaction intermediates such as OH* (based on binding free energy calculations) prefer to occupy bridge sites of the (110) surface rather than cus sites. The same preference is much less prominent for CO* adsorbate. Thus, a (110) surface with both the type of adsorbates would preferentially have OH* at the bridge site and CO* occupying other bridge and cus sites.

■ RESULTS AND DISCUSSION

Composition and Spectator Effects on Adsorbate Binding. The adsorption free energies of H*, OH* (Figure 2), and CO* (Table 1) are calculated to understand how composition and spectators affect the binding energy of key reaction intermediates and, subsequently, the catalytic activity. Surfaces with high Ir character bind H* much stronger than those with high Ru character across different CO* spectator coverage. The surface binding H* the strongest is the IrO_2 surface with a single Ru atom at the cus site for 25% or 50% CO* coverage. Without any CO* coverage, an Ir-oxide overlayer on Ru oxide shows the strongest H* binding. The presence of up to 50% CO* spectator coverage weakens the H* binding by 0.2 eV or less for surfaces rich in ruthenium. In contrast, surfaces rich in Ir show a slight increase in the H* binding strength.

Surfaces with mixed character, e.g., β = 0.75 or β = 0.29, show a strong repulsive adsorbate−adsorbate interaction and the H* binding decreases by up to 0.65 eV. Although weak binding H* leads to low overpotential for the HER, H* fails to bind to the surface, because strong binding OH* and other CO2RR intermediates have a thermodynamic preference, effectively blocking HER.

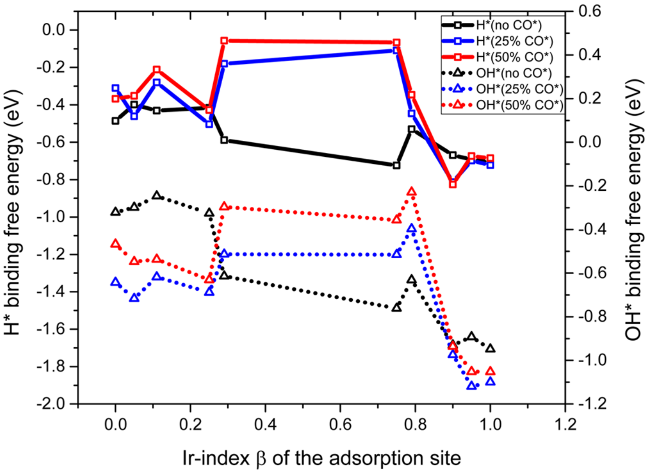

Figure 2. H*/OH* binding energy on Ru−Ir mixed oxide surfaces at varying CO* spectator coverages.

Table 1. Variation of CO* Binding Free Energy at the Bridge Site due to Ir/Ru Mixed Oxide Composition and CO* Spectators[a]

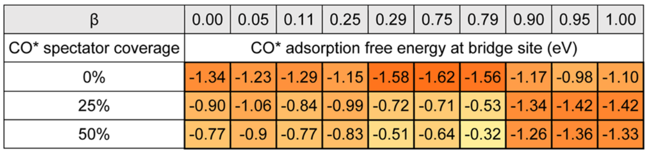

β	0.00	0.05	0.11	0.25	0.29	0.75	0.79	0.90	0.95	1.00
CO* spectator coverage	CO* adsorption free energy at bridge site (eV)									
0%	-1.34	-1.23	-1.29	-1.15	-1.58	-1.62	-1.56	-1.17	-0.98	-1.10
25%	-0.90	-1.06	-0.84	-0.99	-0.72	-0.71	-0.53	-1.34	-1.42	-1.42
50%	-0.77	-0.9	-0.77	-0.83	-0.51	-0.64	-0.32	-1.26	-1.36	-1.33

[a] Lightest shade means the highest value, and darkest shade represents the lowest value.

A similarly opposing adsorbate−adsorbate interaction effect is observed on intermediate index surfaces with β = 0.29, 0.75, 0.79 for the OH*−CO* interaction. OH* is bonded much more strongly to the surfaces with Ir atoms than Ru-rich surfaces. The presence of CO* spectators makes OH* bind stronger than without CO* coverage on Ru or Ir-rich surfaces (β = 0, 0.5, 0.11, 0.25 and β = 0.9, 0.95, 1.0). On the intermediate surfaces β = 0.29, 0.75, 0.79, the CO* adsorbate interaction is repulsive for OH* binding and OH* is therefore destabilized by up to 0.4 eV. Based on the thermodynamic volcano for CO2RR on oxide catalysts, this weakening of OH* binding should lead to equal amounts of lower overpotential for CO2RR as OH* removal forms the left leg of the volcano.[21]

The first CO* binding at the bare surface bridge site is favorable by 1 eV or more for all surfaces (see Table1). The first CO* molecule is more stable on surfaces with $\beta \approx 0$ than those with $\beta \approx 1$. This is opposite to the behavior observed for H* and OH* adsorbates. However, more striking is the exceptionally high stability of the first CO* adsorbate on surfaces with an active site that has at least one coordinating Ir atom, which has Ru neighbors (β = 0.29, 0.75, 0.79). For surfaces with mainly Ru character, the CO*−CO* adsorbate interaction is repulsive; it is strongly repulsive for intermediate compositions ($0.25 < \beta < 0.8$), but attractive for Ir-rich surfaces ($\beta > 0.8$). On surfaces with a single Ir atom close to the bridge site of a RuO_2 slab, such CO*−CO* interaction will limit the CO* coverage and provide sufficient active sites for CO2RR with favorable OH* binding associated. Vice versa, Ir-rich surfaces (β = 0.9, 0.95, 1.0) can accommodate high CO* coverage, because of the attractive CO*−CO* interaction and fail to activate CO_2.

Under reaction conditions, adsorbates such as O*,[71] H*,[72] and CO*[73] have been shown to create preferential conditions for one metal to segregate at the surface over the other metal. Stronger adsorption of the species on one type of metal over another causes this segregation. Replacement of a Ru atom by an Ir atom in a bare $RuO_2(110)$ slab is most favorable at the subsurface layer. Replacement is less favorable at the cus site (+0.11 eV with respect to the subsurface) or next to a bridge site (+0.09, with respect to the subsurface). Replacement of one Ir atom by a Ru atom in a bare $IrO_2(110)$ slab is most favorable at the bridge site and least favorable at the subsurface layer. The energy difference between these two configurations is even smaller at 0.06 eV. The thermodynamic driving force is very small for adsorbate-induced surface segregation. Thus, for sufficiently large kinetic barriers (limiting diffusion), substitution will occur nearly randomly between these three sites. With H*, OH*, and CO* adsorbates, some sites are better-suited for cation substitution than others (see Table 2). For the Ir-doped $RuO_2(110)$ surface, Ir is preferred close to the bridge site in the presence of H*, OH*, or CO* adsorbates. For the Ru-doped $IrO_2(110)$ slab, the Ru dopant is preferred at the cus site in the presence of H*/OH* adsorbates, while the Ru dopant prefers the bridge site in the presence of CO*. CO* spectators can induce bridge site segregation at low cation doping in IrO_2/RuO_2 surfaces if the kinetic barriers are surmountable. This leads to bridge sites coordinated with one Ir atom and one Ru atom. Thus, the CO* spectator also enhances the ligand effects in catalyst properties.

We have previously established a thermodynamic volcano for CO2RR activity on RuO_2-based rutile oxide surfaces with the OH* binding energy as the descriptor.[21] Here, OH* binding energies between −0.25 eV and 0.25 eV were found to be very favorable for CO2RR activity. The weakening of the OH* binding energy on partially CO* covered surfaces with mixed Ir−Ru characteristics, compared to pure IrO_2 or RuO_2 surfaces, moves the investigated mixed oxide surfaces closer to top of the activity volcano. In addition, a weak H* binding on these partially CO*-covered surfaces support selectivity by promoting OCHO* formation at the active site, instead of H*. The fundamentally different behavior of adsorbate binding and

Table 2. Adsorbate-Induced Preference for Cation Substitution Position

	Energy Difference of Ir Atom Substitution Position in RuO_2 Slab w.r.t. Bridge Site Substitution (eV)			Energy Difference of Ru Atom Substitution Position in IrO_2 Slab w.r.t. Bridge Site Substitution (eV)		
	Bridge	Cus	Subsurface	Bridge	Cus	Subsurface
adsorbate	β = 0.29	β = 0.11	β = 0.05	β = 0.79	β = 0.9	β = 0.95
none	0.00	0.02	−0.09	0.00	0.06	0.00
H*	0.00	0.19	0.10	0.00	−0.07	−0.02
OH*	0.00	0.39	0.23	0.00	−0.23	0.04
CO*	0.00	0.32	0.27	0.00	0.45	0.19

strong CO* spectator interaction on surfaces where the bridge site has an Ir atom, which, in turn, have Ru as cation neighbor, is striking and the key to the suitable binding energy behavior.

CO_2 Activation. The first reaction step in CO2RR leads to the formation of OCHO* or COOH* from the protonation of CO_2. H* can form if CO_2 molecules are not available close to the reaction site or the CO_2 activation barrier is very high (>1 eV). Reported values for proton transfer to COOH* formation on Pt[74] (0.55 eV), as well as OCHO* formation on Pb[75] (0.25 eV), suggest that the CO_2 activation barrier may be small enough to be surmountable at room temperature. We assume that the kinetic barriers are small and proportional to the free-energy change of the reactions step. Thus, reaction intermediates that are more stable are readily formed. On pure RuO_2 (110) and Ir-oxide overlayer on RuO_2(110), the stability order for the first electron transfer products is $\Delta G[\mathrm{OCHO}] < \Delta G[\mathrm{H}] < \Delta G[\mathrm{COOH}]$.[21] This relative ordering of stability holds true for all surfaces studied here. Thus, with good availability of CO_2 molecules and protons in the electrolyte layer close to catalyst surface, CO2RR activity dominates over HER on this class of mixed oxides. OCHO* binds strongest on Ir-rich surfaces and Ru-rich surfaces with 25% CO* coverage (see Table 3). Although COOH* is less stable than OCHO* in the absence of CO* spectators and on Ir-rich surfaces with any CO* coverage, the formation of COOH* is downhill in free energy at 0 V RHE and, thus, side reactions can proceed through this intermediate. Further protonation of COOH* forms H_2O and leaves another CO* adsorbate as products.

Table 3. Binding Free Energy of COOH* and OCHO* Intermediates Formed from CO_2 Activation[a]

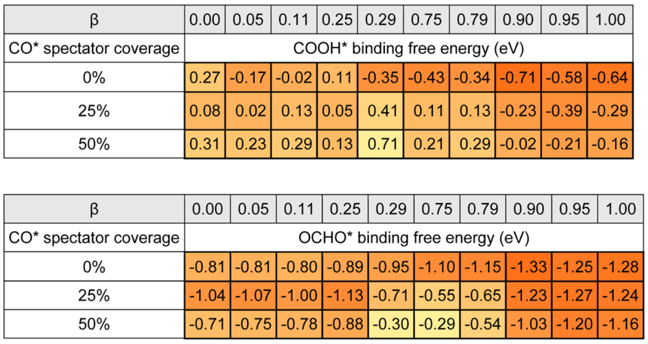

β	0.00	0.05	0.11	0.25	0.29	0.75	0.79	0.90	0.95	1.00
CO* spectator coverage	COOH* binding free energy (eV)									
0%	0.27	-0.17	-0.02	0.11	-0.35	-0.43	-0.34	-0.71	-0.58	-0.64
25%	0.08	0.02	0.13	0.05	0.41	0.11	0.13	-0.23	-0.39	-0.29
50%	0.31	0.23	0.29	0.13	0.71	0.21	0.29	-0.02	-0.21	-0.16

β	0.00	0.05	0.11	0.25	0.29	0.75	0.79	0.90	0.95	1.00
CO* spectator coverage	OCHO* binding free energy (eV)									
0%	-0.81	-0.81	-0.80	-0.89	-0.95	-1.10	-1.15	-1.33	-1.25	-1.28
25%	-1.04	-1.07	-1.00	-1.13	-0.71	-0.55	-0.65	-1.23	-1.27	-1.24
50%	-0.71	-0.75	-0.78	-0.88	-0.30	-0.29	-0.54	-1.03	-1.20	-1.16

[a] Lightest shade means the highest value, and darkest shade represents the lowest value.

Thus, a bare Ir–Ru mixed-oxide surface would develop ~25% CO* coverage over time, under CO2RR conditions. Only on Ir-rich surfaces ($\beta \geq 0.9$) can COOH* intermediates form spontaneously at 0 V RHE, even with higher CO* coverage, and increase the CO* coverage on further reduction. The relative stability of OCHO* intermediate, with respect to COOH* intermediate, is provided in Table S2 in the Supporting Information. The thermodynamics of high CO* coverage on Ir-rich surfaces has been discussed in the previous section.

CO2RR Pathway. One of the main challenges in simulating CO2RR at the atomic scale is the complexity of the possible reaction network. Restricting the intermediates to those with a single carbon atom is a reasonable assumption, because the reported products from rutile oxide CO2RR catalysts are primarily C_1 type.[14,16−18] Our previous theoretical studies of CO2RR on oxide overlayers on RuO_2(110) surface did not include C-coordinated reaction intermediates such as CHO*, COH*, C*, CH*, CH_2*, and CH_3*, because of the higher stability of O-coordinated intermediates on RuO_2(110).[21,22] Here, we have included such intermediates to confirm that O-coordinated intermediates are indeed preferred reaction intermediates as the surface composition is varied.

All the reaction intermediates (involving adsorbates and free molecules) simulated on the mixed-oxide surfaces are listed in Table S1 in the Supporting Information. This reaction network is sufficient to understand the reaction mechanism and onset potential limitations of formic acid, methanol, and methane production. All intermediates are simulated with three different configurations of spectator CO* coverage. All adsorbates are bound to the bridge site, and OCHO*/H_2COOH*, being a bidentate (see Figure S1 in the Supporting Information) also occupy a cus site along with the bridge site. The thermodynamic free-energy diagrams for all surfaces and CO* configurations with all 26 reaction intermediates are provided in the Supporting Information. The full reaction network considered is depicted in Figure 3.

Formic Acid. The formation of formic acid is a simple two-step reaction with OCHO* as the surface-bound species after the first proton transfer on oxide surfaces studied here. Rutile oxide surfaces follow the pathway with OCHO*, because of the higher stability of OCHO*, compared to COOH*. On metals, both the OCHO*- and COOH*-mediated pathways are observed.[76] OCHO* binds very strongly to all the oxide surfaces studied here and protonating it to release formic acid requires a reducing potential. The Ru–Ir mixed oxide system is on the left leg of the formic acid volcano and weaker binding surfaces are thus generally better at evolving formic acid. On the pure RuO_2(110) surface, it was predicted that very high CO* coverage weakens the OCHO* binding and produces formic acid at low overpotential.[62] However, at 75% CO* coverage, H* and OCHO* have similar binding free energies and the HER dominate.

An OCHO* binding free energy close to zero at 0 V RHE leads to a low thermodynamic barrier for the evolution of formic acid. We find such optimal OCHO* binding with only 50% CO* coverage on surfaces with an active site based on an Ir atom but with Ru neighbors (discussed above), because of distinctive adsorbate binding behavior. On $\beta = 0.29$ surface, with 50% CO* coverage, OCHO* is 0.25 eV more stable than H* and the formic acid onset potential is −0.2 V RHE (Table 4). Similar enhancement in the evolution of formic acid is observed for $\beta = 0.75$. Thus, small amounts of Ir doping can enhance formic acid formation on RuO_2 and lowers the CO* coverage needed for moderate CO2RR onset potentials.

Methanol. A pure RuO_2(110) surface reduces CO_2 to methanol by the following six electron pathways for 0% to 50% CO* coverage:

$$CO_2(aq) + H^+ + e^- + * \rightarrow OCHO^* \qquad (1)$$

$$\begin{aligned} &OCHO^* + H^+ + e^- \rightarrow HCOOH^* \text{ or} \\ &OCHO^* + H^+ + e^- \rightarrow HCOOH(aq) + * \end{aligned} \qquad (2)$$

$$\begin{aligned} &HCOOH^* + H^+ + e^- \rightarrow H_2COOH^* \text{ or} \\ &HCOOH(aq) + H^+ + e^- \rightarrow H_2COOH^* \end{aligned} \qquad (3)$$

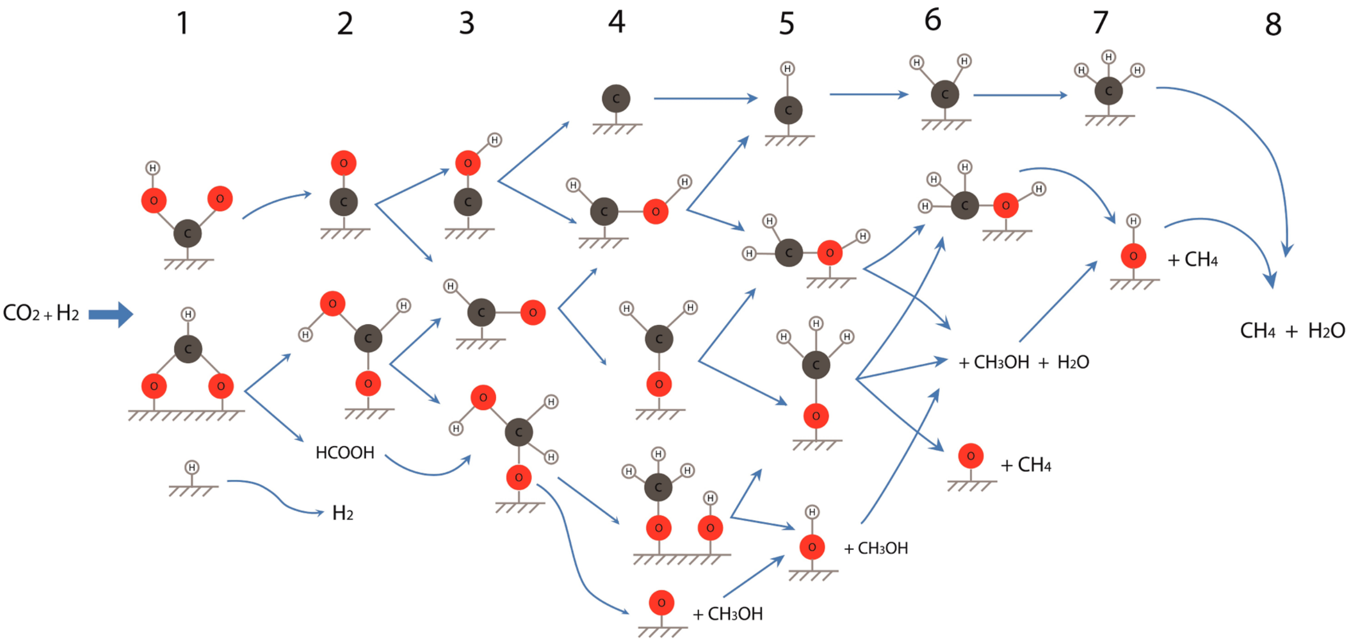

Figure 3. CO2RR reaction network for 1C products. Electron transfer steps are indicated at the top.

Table 4. Formic Acid Onset Potential as a Function of Ir Character of the Oxide Surface and CO* Coverage[a]

β	0.00	0.05	0.11	0.25	0.29	0.75	0.79	0.90	0.95	1.00
CO* spectator coverage	Onset potential for formic acid evolution (V-RHE)									
0%	-0.71	-0.70	-0.70	-0.78	-0.84	-1.00	-1.05	-1.23	-1.14	-1.17
25%	-0.93	-0.97	-0.90	-1.02	-0.60	-0.45	-0.55	-1.13	-1.17	-1.13
50%	-0.60	-0.64	-0.67	-0.77	-0.20	-0.19	-0.44	-0.92	-1.09	-1.06

[a] Lightest shade means the highest value, and darkest shade represents the lowest value.

$$H_2COOH^* + H^+ + e^- \rightarrow H_3CO^* + OH^* \qquad (4)$$

$$H_3CO^* + OH^* + H^+ + e^- \rightarrow H_3CO^* + H_2O(l) \qquad (5)$$

$$H_3CO^* + H^+ + e^- \rightarrow H_3COH(aq) + * \qquad (6)$$

For the Ir−Ru mixed oxide surfaces studied here, the 25% and 50% CO* coverage follows the same reaction pathway. Without the CO* spectator, Ir-rich surfaces ($\beta \geq 0.75$) prefer a methanol evolution pathway involving C-coordinated intermediates such as CHO* and CHOH*. However, an analysis of the potential determining step reveals that protonation of OCHO* to HCOOH* or an aqueous formic acid molecule, HCOOH(aq), still has the largest increase in free energy on most surfaces and most CO* coverages (Table 5). OCHO* is a very stable adsorbate, and protonating it involves metal−oxygen bond breaking.

A few Ir-rich surfaces (β = 0.95, 1.0) also show OH* removal or protonation of H_3CO^* as the onset potential-determining step at CO* coverages of 25%−50% and 25%, respectively. These surfaces need very high reducing potential, because of the strong OH* binding nature of these Ir-rich surfaces. OH*, OCHO*, H_3CO^* binding energies are correlated with each other as all three intermediates bind to the surface through oxygen atoms. Weak binding surfaces fail to bind HCOOH* and the formic acid molecules escape. However, the most active surfaces (e.g., β = 0.29, 0.75) studied here bind H_2COOH^* strongly and, thus, the formation of H_2COOH^* from formic acid molecules is an energetically downhill process at 0 V RHE. The quick removal of formic acid molecules will result in a greater production of formic acid. However, with sufficient formic acid molecules present in the electrolyte, methanol evolves. Thus, the final product mix would dependent explicitly on the reaction conditions.

With 50% CO* coverage, Ir overlayers and Ir substitution at bridge sites in the RuO_2 slab are predicted to evolve methanol at only −0.2 V RHE, which is better than RuO_2 surface with optimized CO* coverage and any known metal catalyst.[77,78] In essence, using the surprising surface chemistry of the mixed Ir/Ru oxides and adsorbate−adsorbate interaction from CO* spectator, we can design very efficient oxide-based methanol evolution catalysts.

Methane. With some CO* coverage, all mixed-oxide surfaces follow a methane evolution path that consists of the following oxygen-coordinated intermediates:

$$CO_2(aq) + H^+ + e^- + * \rightarrow OCHO^* \qquad (7)$$

$$\begin{aligned} &OCHO^* + H^+ + e^- \rightarrow HCOOH^* \text{ or} \\ &OCHO^* + H^+ + e^- \rightarrow HCOOH(aq) + * \end{aligned} \qquad (8)$$

$$\begin{aligned} &HCOOH^* + H^+ + e^- \rightarrow H_2COOH^* \text{ or} \\ &HCOOH(aq) + H^+ + e^- \rightarrow H_2COOH^* \end{aligned} \qquad (9)$$

$$H_2COOH^* + H^+ + e^- \rightarrow H_3CO^* + OH^* \qquad (10)$$

$$H_3CO^* + OH^* + H^+ + e^- \rightarrow H_3CO^* + H_2O(l) \qquad (11)$$

$$H_3CO^* + H^+ + e^- \rightarrow O^* + CH_4(aq) \qquad (12)$$

$$O^* + H^+ + e^- \rightarrow OH^* \qquad (13)$$

$$OH^* + H^+ + e^- \rightarrow H_2O(l) + * \qquad (14)$$

For this pathway, OH* removal or OCHO* protonation requires the largest onset potential (see Table 6). After the fifth

Table 5. Methanol Evolution Onset Potential as a Function of Ir Character of the Oxide Surface and CO* Coverage[a]

β	0.00	0.05	0.11	0.25	0.29	0.75	0.79	0.90	0.95	1.00
CO* spectator coverage	Onset potential for methanol evolution (V-RHE)									
0%	-0.71	-0.70	-0.70	-0.78	-0.78	-0.79	-1.05	-0.93	-0.83	-0.81
25%	-0.77	-0.75	-0.75	-0.80	-0.60	-0.45	-0.55	-0.82	-0.93	-0.93
50%	-0.46	-0.46	-0.54	-0.54	-0.20	-0.20	-0.44	-0.92	-0.92	-1.07

B	0.00	0.05	0.11	0.25	0.29	0.75	0.79	0.90	0.95	1.00
CO* spectator coverage	Potential determining step for methane evolution									
0%	OCHO* protonation	OCHO* protonation	OCHO* protonation	OCHO* protonation	OCHO* protonation	OCHO* protonation	OCHO* protonation	OCHO* protonation	OCHO* protonation	OCHO* protonation
25%	OCHO* protonation	OCHO* protonation	OCHO* protonation	OCHO* protonation	OCHO* protonation	OCHO* protonation	OCHO* protonation	H3CO* protonation	OH* removal	OH* removal
50%	OCHO* protonation	OCHO* protonation	OCHO* protonation	OCHO* protonation	OCHO* protonation	OCHO* protonation	OCHO* protonation	OCHO* protonation	OH* removal	OCHO* protonation

[a] Lightest shade means the highest value, and darkest represents the lowest value. The second table provides the onset potential limiting step for each surface and CO* coverage combination.

Table 6. Methane Evolution Onset Potential as a Function of Ir Character of the Oxide Surface and CO* Coverage[a]

β	0.00	0.05	0.11	0.25	0.29	0.75	0.79	0.90	0.95	1.00
CO* spectator coverage	Onset potential for methane evolution (V-RHE)									
0%	-0.71	-0.70	-0.70	-0.79	-0.78	-0.79	-1.05	-0.93	-0.89	-0.81
25%	-0.77	-0.75	-0.75	-0.80	-0.60	-0.52	-0.55	-0.97	-1.12	-1.10
50%	-0.47	-0.57	-0.54	-0.63	-0.30	-0.36	-0.44	-0.94	-1.05	-1.07

β	0.00	0.05	0.11	0.25	0.29	0.75	0.79	0.90	0.95	1.00
CO* spectator coverage	Potential determining step for methane evolution									
0%	OCHO* protonation	OCHO* protonation	OCHO* protonation	OH* removal	OCHO* protonation	OCHO* protonation	OCHO* protonation	OCHO* protonation	OH*removal	OCHO* protonation
25%	OCHO* protonation	OCHO* protonation	OCHO* protonation	OCHO* protonation	OCHO* protonation	OH*removal	OCHO* protonation	OH*removal	OH*removal	OH*removal
50%	OH*removal	OH*removal	OCHO* protonation	OH*removal	OH*removal	OH*removal	OCHO* protonation	OH*removal	OH*removal	OCHO* protonation

[a] Lightest shade means the highest value, and darkest shade represents the lowest value. The second table provides the onset potential-determining step for each surface and CO* coverage combination.

reaction step, a H_3CO* intermediate is formed. At the sixth electron transfer step, protonation at the C atom in the H_3CO* intermediate leads to the release of methane.

In the absence of CO* spectators, Ir-rich surfaces (β = 0.9, 0.95, 1.0) bind carbon-coordinated adsorbates very strongly. Thus, on such surfaces, adsorbates such as CH*, CHOH*, CHO*, CH_2*, CH_3* participates in the reaction mechanism. Despite this, OCHO* protonation remains the most energetically difficult reaction step. The OCHO* adsorption energy scales with the OH* binding energy and the weakest OH* binding surfaces, β = 0.29 or β = 0.75, shows the lowest methane evolution overpotential at 50% CO* coverage.

Ir-oxide overlayers on RuO_2 display a methanol onset potential of −0.45 V RHE with only 25% CO* coverage. For the pure RuO_2 surface, with 50% CO* coverage, a similar onset potential of −0.46 V RHE is predicted (methanol onset potential computed in this work can change due to the difference in assumed concentration of methanol in solution[62]). Thus, the OCHO* protonation step dictates the onset potential to be −0.45 V RHE.

Scaling of Binding Energies with CO* Spectator Coverage. The CO* spectator interactions with CO2RR adsorbates are found to be both attractive and repulsive, as exemplified through the binding energy variation of OH*/H*/CO* with CO* coverage. A thermodynamic analysis of the reaction pathways reveals that OH* removal, OCHO* activation, or H_3CO* protonation to methanol determine the onset potential of the CO2RR reaction for different composition and CO* coverages. Because all these adsorbates are bound to the surfaces through oxygen, an increase in the OH* binding strength leads to stronger OCHO* and H_3CO* binding as well. Indeed, when we plot the binding energy of OCHO* and H_3CO* (Figure 4), a strong interdependency is observed.

Adsorbates, which have common central atom engaging in chemical bond formation with catalyst surface, often have binding energy, which correlates strongly with each other. These observed linear relationships between the binding energy of such adsorbates are known as scaling laws in catalysis.[79] Because of the similarity in chemical nature of RuO_2 and IrO_2, the spread in binding energy observed for the 10 model surfaces is narrow and lead to a large error in linear fit for scaling laws with data presented in this work.

Interestingly, for the H3CO*−OH* adsorbate binding free-energy correlation, the three scaling lines drawn based on linear fitting of data points from three different CO* coverages follow each other closely with a slope of 1 (slope m = 1.02, 1.11, and 1.08 for 0%, 25%, and 50% CO* coverage, respectively) and an offset depending on the CO* coverage. This result is in good agreement with previously reported H3CO*−OH* scaling line on rutile oxides with a slope of m = 0.96.[21]

For the OCHO*−OH* scaling, computed slopes are m = 1.29, 0.84, and 0.89, respectively, for 0%, 25%, and 50% CO* coverage, indicating that the chemical nature of the scaling relation changes if CO* coverage is considered. OCHO* is bidentate and binds through one bridge site and one cus site. The scaling line slope for 25% CO* coverage deviates from the slope of 0.99 calculated in previous theoretical work, which considers 25% CO* coverage. The slope of 0.99 was derived from binding energies observed on rutile oxide surfaces with identical bridge and cus elements and a much wider variety of binding characteristics.[21] The rather small variation in chemical nature of the surfaces considered here, compared to those studied previously, result in skewed data and a different estimate of the slope. The quality of fit for scaling lines is better for OH*/H_3CO* binding free-energy correlation than between OH*/OCHO*. The chemical origin of observed scaling relationship between two adsorbates is based on the similar nature of bonding with the catalyst surface, where OH* and H_3CO* binding through one O atom to the bridge site, OCHO* binding through two O atoms at one bridge site and an adjoining cus site. Thus, it is possible to have different coordinating metal atoms at the cus site, while bridge site character remains unchanged on a mixed-oxide surface. Also, CO* adsorbates affect cus and bridge site binding differently. Disparate effects at bridge and cus site create larger scatter in the OH*/OCHO* scaling line.

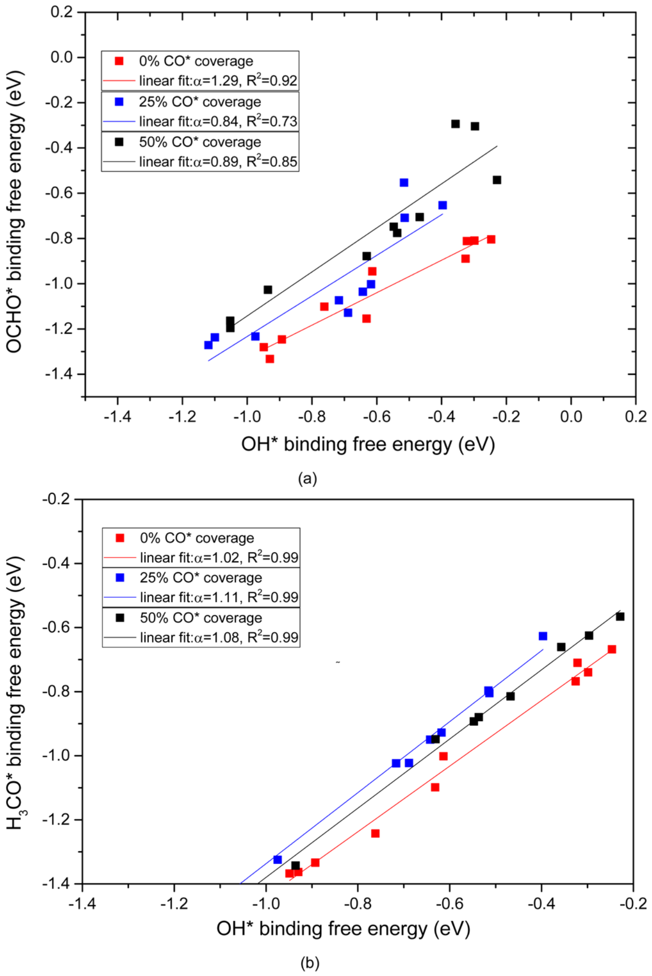

Figure 4. (a) OCHO*−OH* and (b) H_3CO*−OH* binding free-energy scaling relation at three different CO* coverages with slope α and coefficient of determination R^2.

Even with the variation in scaling line from CO* coverage effects, the fundamental behavior remains unperturbed. This indicates that a universal adsorbate scaling relationship for O-coordinate adsorbates on the rutile oxide surface exist, which holds, irrespective of the CO* coverage, but with a CO* coverage dependent offset. This unification can help to model CO2RR activity on oxide catalysts without simulating the full thermodynamic path. The OH* binding energy at different CO* coverage can provide onset potential for the key reaction steps.

Table 7. Oxidation Number of Metal Atom 1 (ON1) and Atom 2 (ON2) That Comprise the Bridge Site and Average Oxidation Number of Oxygen Atoms in the Top Layers Calculated from Bader Charges[a]

	0% CO* coverage			25% CO* coverage			50% CO* coverage		
β	ON1	ON2	ON-oxygen	ON1	ON2	ON-oxygen	ON1	ON2	ON-oxygen
0.00	1.19	1.21	-0.87	1.30	1.30	-0.85	1.33	1.33	-0.84
0.05	1.18	1.20	-0.87	1.28	1.29	-0.85	1.32	1.32	-0.84
0.11	1.20	1.20	-0.86	1.30	1.30	-0.84	1.31	1.30	-0.84
0.25	1.19	1.19	-0.86	1.29	1.29	-0.85	1.32	1.31	-0.85
0.29	1.20	1.12	-0.86	1.32	1.02	-0.85	1.36	1.01	-0.84
0.75	1.16	1.16	-0.85	1.28	1.06	-0.85	1.29	1.06	-0.85
0.79	1.22	1.11	-0.85	1.33	1.03	-0.85	1.35	1.00	-0.87
0.9	1.16	1.16	-0.86	1.23	1.23	-0.84	1.23	1.22	-0.84
0.95	1.16	1.16	-0.85	1.21	1.21	-0.85	1.20	1.21	-0.86
1.00	1.14	1.14	-0.85	1.21	1.21	-0.85	1.21	1.21	-0.87

[a] Yellow boxes represent data for the Ru atom, and green boxes represent data for the Ir atom.

Electronic Structure Effects in Mixed-Oxide Surfaces. Adsorbate binding properties and, thus, the catalytic activities of oxides have previously been shown to be dependent on the O atom *p*-band position[80,81] and the metal atom *d*-band configuration.[82,83] RuO_2, IrO_2, and their mixed oxides show strong metal oxygen overlap covalency[84,85] and any modification in the atomistic constituent will thus affect both the O *p*-band and the metal-*d*-band. Therefore, the effects of such changes on adsorbate binding are, expectedly, also coupled.

Here, we have computed the *d*-band center for the two metal atoms constituting the bridge site on all surfaces and with all coverages (see Figures S5 and S6 in the Supporting Information). The calculation is also done for the average *p*-band center for the O atoms in the top layer of the catalyst surfaces, for a trend analysis (Figures S5 and S6). Here, the binding energy of the key adsorbate OH* (activity descriptor) is found to be not correlated singularly with either the metal d-band position or the O *p*-band position (Figure S5).

A Bader charge[86] analysis for these metal and O atoms reveals that the oxidation number of oxygen does not change significantly with the metal atom present or with the CO* coverage (see Table 7). In comparison with Ru atoms at the bridge site in the pure RuO_2 surface, the Ru atoms at the bridge site in mixed-oxide surfaces with Ir atoms as neighbors do not show large deviation in oxidation number. In contrast, bridge site constituting Ir atoms that have Ru neighbors (β = 0.29, 0.75, 0.79) show markedly reduced oxidation number, especially with CO* spectators (Table 7), compared to surfaces with $\beta \geq 0.8$. OH* is an electron-accepting adsorbate. A lower oxidation state of the metal atom would prevent the formation of a strong bond to OH via electron exchange. The correlation between the charge state of the metal atoms closest to the bridge site and OH* binding energy is evident from the correlation plot in Figure 5, where two distinct correlations emerge. Up to a Bader oxidation number of 1.2 for metal atoms constituting bridge site, OH* binding strength weakens sharply with increases in oxidation number. This regime correlation is populated by all surfaces without CO* coverage and CO* covered surfaces with β = 0.29, 0.75, 0.79. Beyond a value of 1.2, OH* binding weakens slowly with higher oxidation number starting from OH* binding free energy of −1.15 eV. This regime is populated by CO* covered surfaces with β = 0.0, 0.11, 0.25, 0.90, 0.95, and 1.0.

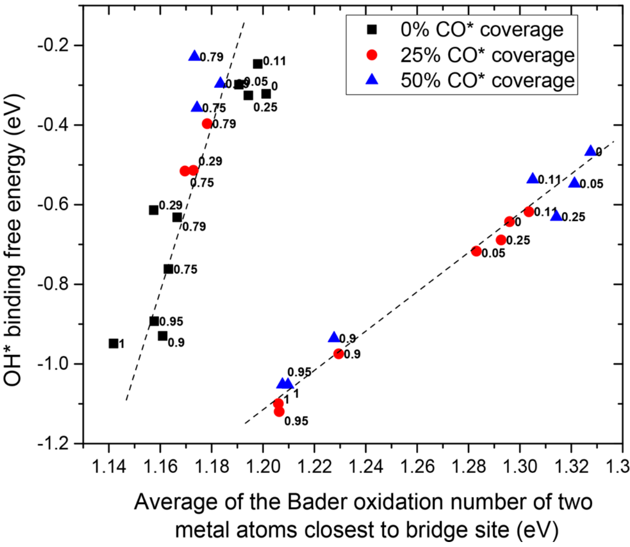

Figure 5. Correlation of OH* binding free energy with the average Bader oxidation number of the two metal atoms at the bridge site. Labels indicate the β value of the surface for which the data point.

CO* adsorbates transfer charge to the metal atom through covalent bonding when adsorbing onto an oxide surface.[87] Surfaces with low or high β change regime with an increase in oxidation number, because of electron doping by the CO* spectators. It is striking to notice that Ru−Ir ligand interaction in surfaces with β = 0.29, 0.75, and 0.79 prevents electron donation from CO* to increase metal oxidation number significantly. These surfaces remain on the same correlation regime of OH* binding and Bader charge dependency, leading to much weaker OH* binding.

Even in the absence of any strain effect and without any CO* spectators, a wide variation in band centers (Figure S6 in the Supporting Information) is observed for both Ir and Ru atoms next to the bridge site and the O atoms close to them. The range of band positions observed in the mixed-oxide surfaces ranges both above and below the band position of the metal-*d* band and the O-*p* band of pure IrO_2 and RuO_2, strongly indicating that complex nonlinear ligand effects are in play. It is clear that ligand effects between the chemically similar Ir and Ru atoms are strong and result in electronic structure modification, leading to anomalous behavior in the mixed

DOI: 10.1021/acscatal.7b02914
ACS Catal. 2017, 7, 8502−8513

oxides. The presence of CO* spectators (electron donors) further enhances this unprecedented behavior. These findings show that mixed-oxide catalyst design should explicitly include the electronic structure effects due to metal−metal ligand interaction through the O *p*-band.

Here, such interaction leads to changes in the band positions. For Ir atoms in the oxide electrocatalysts, t_{2g} orbitals are occupied and e_g orbitals are empty.[88] Becuase of the interaction with neighboring Ru atoms, the Ir-atom t_{2g} orbital changes position. For $\beta = 0.29$, the Ir atom has only Ru neighbors. Its t_{2g} orbital increases in energy without CO* coverage, compared to active site Ir atom in pure IrO_2. With CO* coverage, the shift is in the opposite direction. The $\beta = 0.75$ surface has both Ir and Ru atoms as neighbors and the t_{2g} orbital of the Ir atoms shifts even more in the negative direction when CO* spectators are present (see Figure 6). A negative shift of the d-orbital causes weaker binding with the O 2p orbital of the adsorbate.[89]

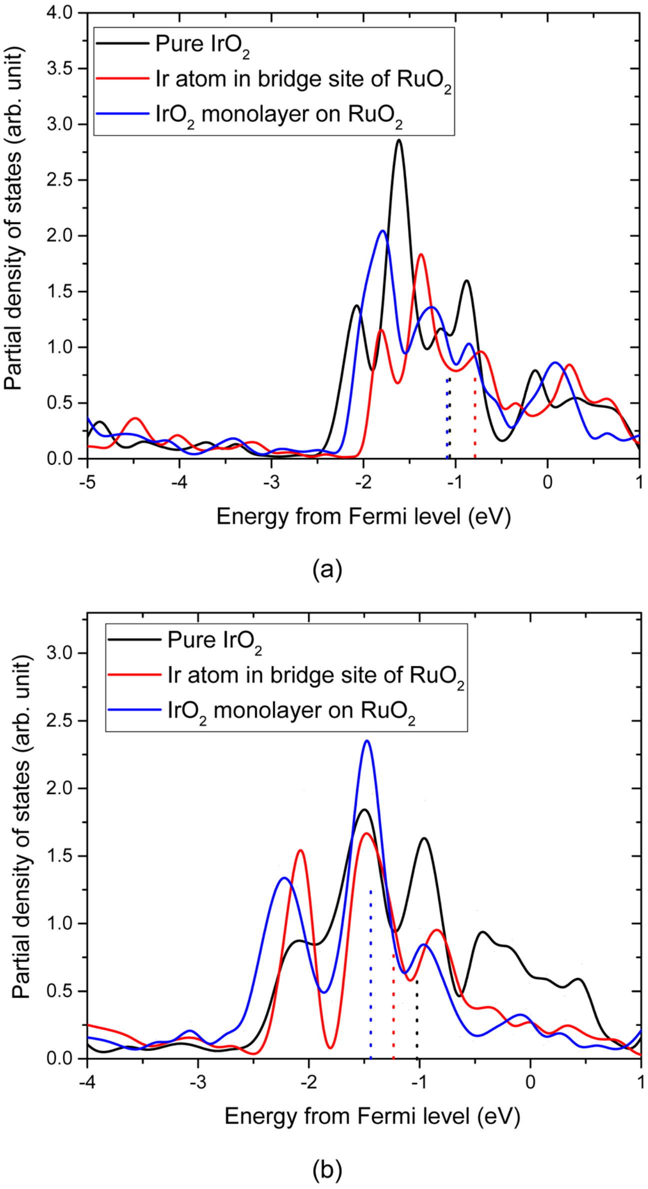

Figure 6. Shift in the t_{2g} orbital of Ir atom from the ligand effect of neighboring Ru atom: (a) no CO* coverage and (b) 50% CO* coverage. The t_{2g}-band centers for the Ir atom are marked.

Because of the strong covalency of the oxide, the O p-orbital also is affected. Differences originating from both the O-atom and metal-atom electronic structure parameters affect the adsorbate binding energy. The intricacy of the intermingled effects results in a complex, nonlinear correlation with the adsorbate binding energy, which is beyond the scope of the model systems under consideration here. Blocking of Kramers Anderson superexchange in the metal−oxygen−metal bond, because of onsite triplet pairing at the Ru t_{2g} orbital might be crucial, although this is speculative, because magnetic effects are not included in this work. Detailed analysis is currently ongoing. The lack of simple correlations of binding energy with either the metal d-band position or the O p-band center position parameter is provided in the Supporting Information.

■ CONCLUSION

RuO_2-based CO2RR electrocatalysts hold great promise for conversion of CO_2 to liquid fuel. The overpotential and selectivity of these catalysts can be further enhanced through control of the CO* coverage and, more importantly, through doping with Ir. In the presence of CO* and OH* spectators (often present under CO2RR conditions), small amounts of Ir substituents are predicted to segregate near the bridge position in the rutile(110) surface.

Bridge sites in surfaces with $\beta = 0.29$, 0.75, or 0.79 show intriguing nonlinear adsorbate binding energies, because of strong ligand effects from neighboring Ru atoms onto the Ir atom, constituting the bridge site. CO* binds much stronger on surfaces with such bridge sites than on the pure IrO_2 and RuO_2 oxides. The CO* adsorbate interaction effects are also more influential for these mixed-oxide surfaces, where, e.g., the CO* interaction leads to weaker OCHO* and OH* binding on these surfaces.

A thermodynamic reaction pathway analysis shows that two elementary steps determine the onset potential for CO2RR, regardless of the chemical nature of the bridge site and CO* spectator coverage: (i) OCHO* protonation and (ii) OH* removal. The CO* interaction weakens the binding energy of OH* for $\beta = 0.75$ or $\beta = 0.29$, such that an onset potential for methanol of −0.2 V RHE is predicted.

We also have shown the universality of OH*/OCHO* and OH*/H_3CO* scaling relations, regardless of CO* coverage, simplifying the analysis of CO2RR activity on CO* coverage mixed-oxide systems. Enhancements of the catalytic activity in mixed oxides come from a concerted ligand and spectator effects, where the mixing of oxides with strong covalent character can lead to remarkable electronic structure effects and binding energy behavior. Through these synergistic effects, the activity for electrochemical conversion of CO_2 to liquid fuel is improved by moving closer to the top of the activity volcano[21] for different products on the previously predicted oxide catalysts (see Figure 7, as well as Figure S7 in the Supporting Information). This new concept of ligand-effect-based manipulation of adsorbate binding can open a door to novel avenues of catalyst engineering, e.g., for oxygen evolution. Ligand effects in oxide catalysts are unexplored, and this work indicates the immense possibility in that.

Unlike metals, where simple interpolation techniques often provide good approximations of the binding energies of key adsorbates, mixed oxides display more-complex electronic structure variations. The increased complexity also provides a unique possibility to design very active catalysts with low levels of cation substitution. Specifically, we propose a monolayer or

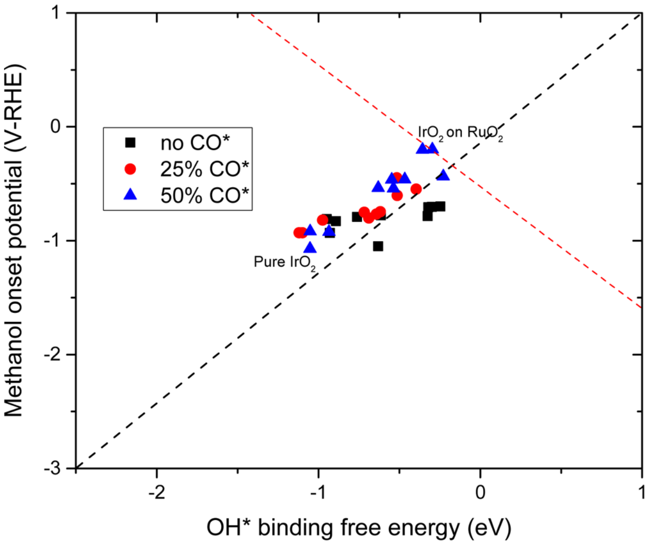

Figure 7. Synergistic effects from ligand interaction and adsorbate−adsorbate interaction as the CO* spectator moves partially CO*-covered mixed Ir−Ru oxide surfaces closer to the top of the volcano for methanol evolution on oxide catalysts. Activity volcanos for different products obtained from our previous work[21] are shown.

less of IrO_2 deposited on the $RuO_2(110)$ surface to be a very good CO2RR catalyst for formic acid and methanol evolution with moderate CO* coverage.

■ ASSOCIATED CONTENT

Supporting Information

The Supporting Information is available free of charge on the ACS Publications website at DOI: 10.1021/acscatal.7b02914.

> Additional explanation for computational methods, visualizations for adsorbate configurations, free-energy plot for all adsorbates on all surfaces and CO* coverages, correlation of β, OH* binding, and important electronic structure parameters (PDF)

■ AUTHOR INFORMATION

Corresponding Author

*Tel.: +45 45 25 82 11. Fax: +45 46 77 57 58. E-mail: heih@dtu.dk.

ORCID

Arghya Bhowmik: 0000-0003-3198-5116

Notes

The authors declare no competing financial interest.

■ ACKNOWLEDGMENTS

Funding from the Lundbeck Foundation (Grant No. R141-2013-A13204) and The Velux Foundations through V-Sustain: The VILLUM Center for the Science of Sustainable Fuels and Chemicals (Grant No. 9455) are gratefully acknowledged. The Niflheim supercomputer at DTU was used for the computations performed in this work.

■ REFERENCES

(1) Lewis, N. S.; Nocera, D. G. *Proc. Natl. Acad. Sci. U. S. A.* **2006**, *103*, 15729−15735.

(2) Olah, G. A.; Goeppert, A.; Prakash, G. K. S. *Beyond Oil and Gas: The Methanol Economy*; Wiley−VCH Verlag GmbH & Co. KGaA: Weinheim, Germany, 2009.

(3) Chu, S.; Cui, Y.; Liu, N. *Nat. Mater.* **2016**, *16*, 16−22.

(4) Ganesh, I. *Renewable Sustainable Energy Rev.* **2014**, *31*, 221−257.

(5) Centi, G.; Perathoner, S. *Catal. Today* **2009**, *148*, 191−205.

(6) Whipple, D. T.; Kenis, P. J. A. *J. Phys. Chem. Lett.* **2010**, *1*, 3451−3458.

(7) Hori, Y.; Kikuchi, K.; Suzuki, S. *Chem. Lett.* **1985**, *14*, 1695−1698.

(8) Hori, Y.; Murata, A.; Takahashi, R. *J. Chem. Soc., Faraday Trans. 1* **1989**, *85*, 2309.

(9) Hori, Y. In *Modern Aspects of Electrochemistry*, Vol. *42*; Springer: New York, 2008; pp 89−189.

(10) Peterson, A. A.; Abild-Pedersen, F.; Studt, F.; Rossmeisl, J.; Nørskov, J. K. *Energy Environ. Sci.* **2010**, *3*, 1311.

(11) Peterson, A. A.; Nørskov, J. K. *J. Phys. Chem. Lett.* **2012**, *3*, 251−258.

(12) Hansen, H. A.; Varley, J. B.; Peterson, A. A.; Nørskov, J. K. *J. Phys. Chem. Lett.* **2013**, *4*, 388−392.

(13) Li, Y.; Sun, Q. *Adv. Energy Mater.* **2016**, *6*, 1600463.

(14) Bandi, A.; Kühne, H. *J. Electrochem. Soc.* **1992**, *139*, 1605.

(15) Bandi, A. *J. Electrochem. Soc.* **1990**, *137*, 2157.

(16) Popic, J. P.; Avramov-Ivić, M. L.; Vuković, N. B. *J. Electroanal. Chem.* **1997**, *421*, 105−110.

(17) Qu, J.; Zhang, X.; Wang, Y.; Xie, C. *Electrochim. Acta* **2005**, *50*, 3576−3580.

(18) Spataru, N.; Tokuhiro, K.; Terashima, C.; Rao, T. N.; Fujishima, A. *J. Appl. Electrochem.* **2003**, *33*, 1205−1210.

(19) Rochefort, D.; Dabo, P.; Guay, D.; Sherwood, P. M. A. *Electrochim. Acta* **2003**, *48*, 4245−4252.

(20) Kasian, O.; Geiger, S.; Stock, P.; Polymeros, G.; Breitbach, B.; Savan, A.; Ludwig, A.; Cherevko, S.; Mayrhofer, K. J. J. *J. Electrochem. Soc.* **2016**, *163*, F3099−F3104.

(21) Bhowmik, A.; Vegge, T.; Hansen, H. A. *ChemSusChem* **2016**, *9*, 3230−3243.

(22) Karamad, M.; Hansen, H. A.; Rossmeisl, J.; Nørskov, J. K. *ACS Catal.* **2015**, *5*, 4075−4081.

(23) Jacobsen, C. J. H.; Dahl, S.; Clausen, B. S.; Bahn, S.; Logadottir, A.; Nørskov, J. K. *J. Am. Chem. Soc.* **2001**, *123*, 8404−8405.

(24) Studt, F.; Sharafutdinov, I.; Abild-Pedersen, F.; Elkjær, C. F.; Hummelshøj, J. S.; Dahl, S.; Chorkendorff, I.; Nørskov, J. K. *Nat. Chem.* **2014**, *6*, 320−324.

(25) Stoerzinger, K. A.; Qiao, L.; Biegalski, M. D.; Shao-Horn, Y. *J. Phys. Chem. Lett.* **2014**, *5*, 1636−1641.

(26) Stoerzinger, K. A.; Diaz-Morales, O.; Kolb, M.; Rao, R. R.; Frydendal, R.; Qiao, L.; Wang, X. R.; Halck, N. B.; Rossmeisl, J.; Hansen, H. A.; Vegge, T.; Stephens, I. E. L.; Koper, M. T. M.; Shao-Horn, Y. *ACS Energy Lett.* **2017**, *2*, 876−881.

(27) Rossmeisl, J.; Qu, Z. W.; Zhu, H.; Kroes, G. J.; Nørskov, J. K. *J. Electroanal. Chem.* **2007**, *607*, 83−89.

(28) Angelinetta, C.; Trasatti, S.; Atanasoska, L. D.; Minevski, Z. S.; Atanasoski, R. T. *Mater. Chem. Phys.* **1989**, *22*, 231−247.

(29) Marshall, A. T.; Haverkamp, R. G. *Electrochim. Acta* **2010**, *55*, 1978−1984.

(30) Lyons, M. E. G.; Floquet, S. *Phys. Chem. Chem. Phys.* **2011**, *13*, 5314−5335.

(31) Kötz, R.; Stucki, S. *Electrochim. Acta* **1986**, *31*, 1311−1316.

(32) Siahrostami, S.; Vojvodic, A. *J. Phys. Chem. C* **2015**, *119*, 1032−1037.

(33) Cheng, J.; Zhang, H.; Chen, G.; Zhang, Y. *Electrochim. Acta* **2009**, *54*, 6250−6256.

(34) Lee, Y.; Suntivich, J.; May, K. J.; Perry, E. E.; Shao-Horn, Y. *J. Phys. Chem. Lett.* **2012**, *3*, 399−404.

(35) Over, H.; Seitsonen, A. P.; Lundgren, E.; Schmid, M.; Varga, P. *J. Am. Chem. Soc.* **2001**, *123*, 11807−11808.

(36) Lister, T. E.; Tolmachev, Y. V.; Chu, Y.; Cullen, W. G.; You, H.; Yonco, R.; Nagy, Z. *J. Electroanal. Chem.* **2003**, *554*−*555*, 71−76.

(37) Doyle, A. D.; Montoya, J. H.; Vojvodic, A. *ChemCatChem* **2015**, *7*, 738−742.

(38) Toftelund, A.; Man, I. C.; Hansen, H. A.; Abild-Pedersen, F.; Bligaard, T.; Rossmeisl, J.; Studt, F. *ChemCatChem* **2012**, *4*, 1856–1861.

(39) Torun, E.; Fang, C. M.; De Wijs, G. A.; De Groot, R. A. *J. Phys. Chem. C* **2013**, *117*, 6353–6357.

(40) Gutsche, C.; Moeller, C. J.; Knipper, M.; Borchert, H.; Parisi, J.; Plaggenborg, T. *J. Phys. Chem. C* **2016**, *120*, 1137–1146.

(41) Wang, H. Y.; Schneider, W. F. *Mol. Simul.* **2012**, *38*, 615–630.

(42) Wang, J.; Fan, C. Y.; Jacobi, K.; Ertl, G. *Surf. Sci.* **2001**, *481*, 113–118.

(43) Karlsson, R. K. B.; Cornell, A.; Pettersson, L. G. M. *J. Phys. Chem. C* **2016**, *120*, 7094–7102.

(44) Xu, J. H.; Jarlborg, T.; Freeman, A. J. *Phys. Rev. B: Condens. Matter Mater. Phys.* **1989**, *40*, 7939–7947.

(45) Butler, S. R.; Gillson, J. L. *Mater. Res. Bull.* **1971**, *6*, 81–89.

(46) Mavrikakis, M.; Hammer, B.; Nørskov, J. *Phys. Rev. Lett.* **1998**, *81*, 2819–2822.

(47) Strasser, P.; Koh, S.; Anniyev, T.; Greeley, J.; More, K.; Yu, C.; Liu, Z.; Kaya, S.; Nordlund, D.; Ogasawara, H.; Toney, M. F.; Nilsson, A. *Nat. Chem.* **2010**, *2*, 454–460.

(48) Escudero-Escribano, M.; Malacrida, P.; Hansen, M. H.; Vej-Hansen, U. G.; Velazquez-Palenzuela, A.; Tripkovic, V.; Schiotz, J.; Rossmeisl, J.; Stephens, I. E. L.; Chorkendorff, I. *Science (Washington, DC, U. S.)* **2016**, *352*, 73–76.

(49) Wang, H.; Xu, S.; Tsai, C.; Li, Y.; Liu, C.; Zhao, J.; Liu, Y.; Yuan, H.; Abild-pedersen, F.; Prinz, F. B.; Nørskov, J. K.; Cui, Y. *Science (Washington, DC, U. S.)* **2016**, *354*, 1031–1036.

(50) Balko, E. N.; Davidson, C. R. *J. Inorg. Nucl. Chem.* **1980**, *42*, 1778–1781.

(51) Wanjala, B. N.; Luo, J.; Loukrakpam, R.; Fang, B.; Mott, D.; Njoki, P. N.; Engelhard, M.; Naslund, H. R.; Wu, J. K.; Wang, L.; Malis, O.; Zhong, C. J. *Chem. Mater.* **2010**, *22*, 4282–4294.

(52) Liao, H.; Fisher, A.; Xu, Z. J. *Small* **2015**, *11*, 3221–3246.

(53) Tang, X.; Li, Y.; Huang, X.; Xu, Y.; Zhu, H.; Wang, J.; Shen, W. *Appl. Catal., B* **2006**, *62*, 265–273.

(54) Di Cosimo, J. I.; Díez, V. K.; Xu, M.; Iglesia, E.; Apesteguía, C. R. J. *J. Catal.* **1998**, *178*, 499–510.

(55) Schoeb, A. M.; Raeker, T. J.; Yang, L.; Wu, X.; King, T. S.; Depristo, A. E. *Surf. Sci. Lett.* **1992**, *278*, L125–L130.

(56) Christoffersen, E.; Liu, P.; Ruban, A.; Skriver, H. L.; Nørskov, J. K. *J. Catal.* **2001**, *199*, 123–131.

(57) Novell-Leruth, G.; Carchini, G.; López, N. *J. Chem. Phys.* **2013**, *138*, 194706.

(58) Garcia-Mota, M.; Vojvodic, A.; Metiu, H.; Man, I. C.; Su, H. Y.; Rossmeisl, J.; Nørskov, J. K. *ChemCatChem* **2011**, *3*, 1607–1611.

(59) Kim, H. Y.; Lee, H. M.; Pala, R. G. S.; Shapovalov, V.; Metiu, H. *J. Phys. Chem. C* **2008**, *112*, 12398–12408.

(60) He, H.; Zapol, P.; Curtiss, L. a. *Energy Environ. Sci.* **2012**, *5*, 6196.

(61) Karlsson, R. K. B.; Cornell, A.; Pettersson, L. G. M. *Electrochim. Acta* **2015**, *180*, 514–527.

(62) Bhowmik, A.; Hansen, H. A.; Vegge, T. *J. Phys. Chem. C* **2017**, *121*, 18333–18343.

(63) Kresse, G.; Joubert, D. *Phys. Rev. B: Condens. Matter Mater. Phys.* **1999**, *59*, 1758–1775.

(64) Hjorth Larsen, A.; Jørgen Mortensen, J.; Blomqvist, J.; Castelli, I. E.; Christensen, R.; Dułak, M.; Friis, J.; Groves, M. N.; Hammer, B.; Hargus, C.; Hermes, E. D.; Jennings, P. C.; Jensen, P. B.; et al. *J. Phys.: Condens. Matter* **2017**, *29*, 273002.

(65) Wellendorff, J.; Lundgaard, K. T.; Møgelhøj, A.; Petzold, V.; Landis, D. D.; Nørskov, J. K.; Bligaard, T.; Jacobsen, K. W. *Phys. Rev. B: Condens. Matter Mater. Phys.* **2012**, *85*, 235149.

(66) Lee, K.; Murray, É. D.; Kong, L.; Lundqvist, B. I.; Langreth, D. C. *Phys. Rev. B: Condens. Matter Mater. Phys.* **2010**, *82*, 081101.

(67) Liu, W.; Carrasco, J.; Santra, B.; Michaelides, A.; Scheffler, M.; Tkatchenko, A. *Phys. Rev. B: Condens. Matter Mater. Phys.* **2012**, *86*, 245405.

(68) Ramalho, J. P. P.; Gomes, J. R. B.; Illas, F. *RSC Adv.* **2013**, *3*, 13085.

(69) Christensen, R.; Hansen, H. A.; Vegge, T. *Catal. Sci. Technol.* **2015**, *5*, 4946–4949.

(70) Nørskov, J. K.; Rossmeisl, J.; Logadottir, A.; Lindqvist, L.; Kitchin, J. R.; Bligaard, T.; Jónsson, H. *J. Phys. Chem. B* **2004**, *108*, 17886–17892.

(71) Zafeiratos, S.; Piccinin, S.; Teschner, D. *Catal. Sci. Technol.* **2012**, *2*, 1787.

(72) Hoffmannová, H.; Okube, M.; Petrykin, V.; Krtil, P.; Mueller, J. E.; Jacob, T. *Langmuir* **2013**, *29*, 9046–9050.

(73) Mayrhofer, K. J. J.; Juhart, V.; Hartl, K.; Hanzlik, M.; Arenz, M. *Angew. Chem., Int. Ed.* **2009**, *48*, 3529–3531.

(74) Shi, C.; O'Grady, C. P.; Peterson, A. a; Hansen, H. a; Nørskov, J. K. *Phys. Chem. Chem. Phys.* **2013**, *15*, 7114–7122.

(75) Back, S.; Kim, J. H.; Kim, Y. T.; Jung, Y. *Phys. Chem. Chem. Phys.* **2016**, *18*, 9652–9657.

(76) Yoo, J. S.; Christensen, R.; Vegge, T.; Nørskov, J. K.; Studt, F. *ChemSusChem* **2016**, *9*, 358–363.

(77) Kuhl, K. P.; Hatsukade, T.; Cave, E. R.; Abram, D. N.; Kibsgaard, J.; Jaramillo, T. F. *J. Am. Chem. Soc.* **2014**, *136*, 14107–14113.

(78) Jovanov, Z. P.; Hansen, H. A.; Varela, A. S.; Malacrida, P.; Peterson, A. A.; Nørskov, J. K.; Stephens, I. E. L.; Chorkendorff, I. *J. Catal.* **2016**, *343*, 215–231.

(79) Abild-Pedersen, F.; Greeley, J.; Studt, F.; Rossmeisl, J.; Munter, T. R.; Moses, P. G.; Skulason, E.; Bligaard, T.; Nørskov, J. K. *Phys. Rev. Lett.* **2007**, *99*, 016105.

(80) Lee, Y.-L.; Kleis, J.; Rossmeisl, J.; Shao-Horn, Y.; Morgan, D. *Energy Environ. Sci.* **2011**, *4*, 3966.

(81) Han, B.; Risch, M.; Lee, Y.-L.; Ling, C.; Jia, H.; Shao-Horn, Y. *Phys. Chem. Chem. Phys.* **2015**, *17*, 22576–22580.

(82) Suntivich, J.; May, K. J.; Gasteiger, H. A.; Goodenough, J. B.; Shao-Horn, Y. *Science (Washington, DC, U. S.)* **2011**, *334*, 1383–1385.

(83) Calle-Vallejo, F.; Inoglu, N. G.; Su, H.-Y.; Martínez, J. I.; Man, I. C.; Koper, M. T. M.; Kitchin, J. R.; Rossmeisl, J. *Chem. Sci.* **2013**, *4*, 1245.

(84) Mattheiss, L. *Phys. Rev. B* **1976**, *13*, 2433–2450.

(85) Daniels, R. R.; Margaritondo, G.; Georg, C. A.; Lévy, F. *Phys. Rev. B: Condens. Matter Mater. Phys.* **1984**, *29*, 1813–1818.

(86) Tang, W.; Sanville, E.; Henkelman, G. *J. Phys.: Condens. Matter* **2009**, *21*, 084204.

(87) Kim, Y. D.; Seitsonen, A. P.; Over, H. *Phys. Rev. B: Condens. Matter Mater. Phys.* **2001**, *63*, 115419.

(88) Sun, W.; Song, Y.; Gong, X.-Q.; Cao, L.; Yang, J. *Chem. Sci.* **2015**, *6*, 4993–4999.

(89) Stamenkovic, V.; Mun, B. S.; Mayrhofer, K. J. J.; Ross, P. N.; Markovic, N. M.; Rossmeisl, J.; Greeley, J.; Nørskov, J. K. *Angew. Chem.* **2006**, *118*, 2963–2967.

Supporting Information: Electrochemical reduction of CO_2 on $Ir_xRu_{(1-x)}O_2$ (110) surfaces

Arghya Bhowmik, Dr. Heine Anton Hansen* and Prof. Dr. Tejs Vegge

Department of Energy Conversion and Storage, Technical University of Denmark, Fysikvej Bldg. 309,

DK-2800 Kgs. Lyngby, Denmark.

E-mail: heih@dtu.dk; Fax: +45 46 77 57 58; Tel: +45 45 25 82 11

Computational details

Simulation parameters

The density functional theory (DFT) based simulation tool Vienna ab-initio simulation package (VASP)[1], is used here. 500 eV cutoff is used for wave functions. The bulk IrO_2 or RuO_2 unit cell Brillouin zone is sampled with a 5×5×7 Monkhorst-Pack k-point mesh and that of the oxide catalyst surface slab is 4×4×1. The catalyst surface model consists of four atomic (metal and oxygen atoms) layer thick slab, which is periodic in x and y direction. The simulation cell dimensions are 6.399 Å × 6.451 Å × 27.902 Å for models with IrO_2 substrate and 6.271 Å × 6.416 Å × 27.831 Å for models with RuO_2 substrate. Due to periodic boundary conditions, 16 Å of vacuum in the z-direction is considered to minimize spurious interlayer interactions. Due to the finite electronic occupation at Fermi energy, a Gaussian smearing of 10 meV is used for the electronic states in all calculations. Optimizations of atomic structures are performed until forces of are less than 0.003 eV/Å. For surfaces, all atoms in the top two atomic layer along with any adsorbates are optimized. For bulk IrO_2 and RuO_2, cell parameter optimization is also done.

The BEEF-vdW[2] exchange correlation functional with the vdW-DF2[3] nonlocal correlation energy and potential is used here to properly represent adsorbate interactions[4,5]. Van der Waals effects are important for larger adsorbate molecules formed in CO_2 reduction[6]. When multiple adsorption geometries are possible, different configurations are evaluated to identify the energetically most favorable one; e.g. the CHO* intermediate, which prefers binding simultaneously through the O and C atoms. For a bridge site between an Ir and a Ru atom, the adsorbate O atom can bind to the Ru atom and C atom to the Ir atom or vice versa (figure SI1).

The adsorption geometry can be such that the Ru-Ir bond is perpendicular to the C-O bond of the CHO* adsorbate. The free energy of the reactant and product molecules are calculated by including zero point energy and finite temperature contributions to the free energy within the quantum mechanical harmonic approximation, as described in previous computational studies of CO2RR on oxide surfaces[7]. Specific parameters for molecular free energy calculations like fugacity and adjustments for systematic DFT errors[8] used in this work have been listed in the supporting information.

Thermodynamics of electrochemical CO2RR

To estimate the change in free energy under an applied potential for elementary proton transfer steps, the reaction thermodynamic are calculated using the computational hydrogen electrode (CHE) model[9]. CHE provides a simple linear model to evaluate the effect of applied potential on the reaction free energy of an elementary electrochemical reaction step[9] at a certain applied potential from the reaction free energy, calculated without explicitly including the potential or the electrolyte system. The model links the reaction free energy of each reduction step involving single proton transfer (ΔG_{step}) to the applied potential (U) by a simple linear relation

$$\Delta \mathrm{G}_{\text{step}}(\mathrm{U}) = \Delta \mathrm{G}_{\text{step}}(\mathrm{U}=0) + \mathrm{eU}$$

Where e is the elementary charge. If a reaction step involving a proton/electron transfer increase the free energy by $\Delta \mathrm{G}_{\text{step}}(\mathrm{U}=0)$ eV, on the reversible hydrogen electrode (RHE) scale, applying $-\Delta \mathrm{G}_{\text{step}}/e$ V-RHE potential, will make the free energy change zero, equilibrating the reaction step. The potential at which all elementary step of a reaction mechanism becomes downhill in free energy (exergonic) is defined as the thermodynamic onset potential. Working with the computational hydrogen electrode model and the RHE scale, large-scale analysis of adsorbate and surfaces becomes manageable.

Adsorbate binding free energies can be used to calculate free energy changes without applied potential $\Delta \mathrm{G}_{\text{step}}(\mathrm{U}=0)$, with respect to the free energy of the reference molecules (CO_2, H_2O, and H_2). For example, OCHO* is a possible reaction intermediate formed after the first proton transfer starting from CO_2. The electronic energy of the catalyst surface is E_* and that of the surface with OCHO* is E_{OCHO^*}. The free energy correction term combining the zero point energy, heat capacity and entropy for the OCHO* adsorbate is $G_{OCHO^*}^{corr}$. The binding free energy of OCHO* is

$$\Delta G_{OCHO^*} = E_{OCHO^*} + G_{OCHO^*}^{corr} - E_* - G_{CO_2} - 0.5 \times G_{H_2}$$

G_{CO_2},G_{H_2O} and $G_{H_2}$are the free energy of CO_2, H_2O and H_2 molecules, respectively. The free energy correction term $G_{OCHO^*}^{corr}$ is calculated on $RuO_2(110)$ surface without spectators and assumed constant irrespective of the spectator coverage or surface chemistry. Finite temperature energy corrections for adsorbates are calculated from the vibrational modes of the adsorbates within the quantum mechanical harmonic approximation. Calculated heat capacity (C_p), entropy as well as zero point energy (E_{ZPE}) are incorporated in the correction term for adsorbates:

$$\mathrm{G}^{corr} = \mathrm{E}_{\mathrm{ZPE}} + \int \mathrm{C_p dT} - \mathrm{TS}$$

The free energies of molecules are calculated within the ideal gas approximation. A previously described method[7,10] has been followed. The specific calculation parameters and energies are provided in the supporting information. Energies of molecular CO_2, COOH* intermediate and molecular H_2 are corrected by +0.3 eV, +0.15 eV and +0.1 eV, respectively, to correct for the systematic DFT errors associated with these species[8].

The change in free energy associated with an elementary reaction step gives the reaction free energy change at 0 V vs RHE. For example, the free energy change for protonation of the H_2CO^* intermediate to H_3CO^* at 0 V vs RHE is

$$\Delta G_{H_2CO^* \rightarrow H_3CO^*} = \Delta G_{H_3CO^*} - \Delta G_{H_2CO^*}$$

The free energy change for protonation of H_3CO^* to methanol is related to the binding free energy of H_2CO^* and reactant H_2 and product CH_3OH.

$$\Delta G_{H_3CO^* \rightarrow CH_3OH} = G_{CH_3OH} - \frac{1}{2} G_{H_2} - \Delta G_{H_3CO^*}$$

The binding energy of CO* spectators has been reported here with respect to the CO molecule rather than CO_2.

$$\Delta G_{CO^*} = E_{CO^*} + G_{CO^*}^{corr} - E_* - G_{\mathrm{CO}}$$

Ir/Ru character ratio

The surfaces are assigned a representative numerical value to indicate how much Ir/Ru-character an adsorbate feels while attached to an active site. This serves as a surrogate variable for mapping binding characteristics and catalytic properties to mixed oxide systems with variable composition. To create a reference point for distribution function analysis, a hydrogen atom is added to the bridge site of the bare oxide surface and geometry optimization is done for the H* and top two atom layers. The partial radial distribution function (RDF) for Ir and Ru atoms are computed up to 12 Å from the H* adsorbate which is comparable to the thickness of the simulation slab. Periodic boundary condition is used while estimating the RDF functions. The Ir distribution curve is denoted $\mathrm{Ir}_{\mathrm{rdf}}(r)$ and that of Ru atoms as $\mathrm{Ru}_{\mathrm{rdf}}(r)$. Furthermore, a proxy variable describing abundance of Ir and Ru atoms ($\mathrm{Ir}_{\mathrm{index}}$ and $\mathrm{Ru}_{\mathrm{index}}$) close to the adsorption site is defined as

$$\mathrm{Ru}_{\mathrm{index}} = \int_0^{12} (12 - \mathrm{r})\mathrm{Ru}_{\mathrm{rdf}}(\mathrm{r})dr$$

$$\mathrm{Ir}_{\mathrm{index}} = \int_0^{12} (12 - \mathrm{r})\mathrm{Ir}_{\mathrm{rdf}}(\mathrm{r})dr$$

Using these indexes, a single unbiased parameter ranging from 0 to 1 is created

$$\eta = \frac{\mathrm{Ir}_{\mathrm{index}}}{\mathrm{Ir}_{\mathrm{index}} + \mathrm{Ru}_{\mathrm{index}}}$$

The β-value indicates how IrO_2 –like the character of the active site is expected to be. Pure RuO_2 surface has β = 0 and pure IrO_2 have β = 1. Surfaces and their β values are listed in **Error! Reference source not found.**.

Table S1: Adsorbate/product cases examined at electron transfer step from 0e⁻ to 8e⁻.

$1\ e^-$	$2\ e^-$	$3\ e^-$	$4\ e^-$
$OHCO^*$, H^*, $COOH^*$	$HCOOH^*$, $CO^*+H_2O(l)$, $HCOOH(aq)$, $H_2(aq)$	H_2COOH^*, $CHO^*+H_2O(l)$, $COH^*+H_2O(l)$	$H_3CO^*+OH^*$, $H_2CO+H_2O(l)$, $O^*+CH_3OH(aq)$, $CHOH^*+H_2O(l)$, $C^*+2H_2O(l)$
$5\ e^-$	$6\ e^-$	$7\ e^-$	$8\ e^-$
$H_3CO^*+H_2O(l)$, $H_2COH^*+H_2O(l)$, $OH^*+CH_3OH(aq)$, $CH^*+2H_2O(l)$	$O^*+CH_4(aq)+H_2O(l)$, $CH_3OH^*+H_2O(l)$, $CH_3OH(aq)+H_2O(l)$, $CH_2^*+2H_2O(l)$	$OH^*+CH_4(aq)+H_2O(l)$, $CH_3^*+2H_2O(l)$	$CH_4(aq)+2H_2O(l)$

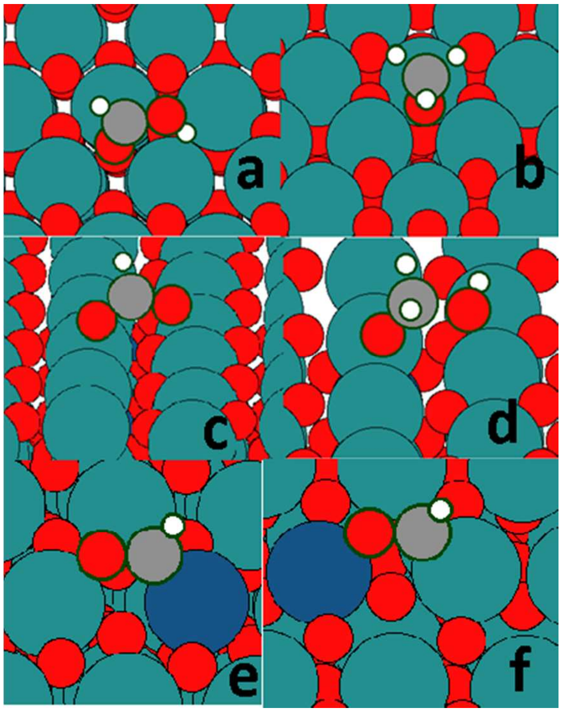

Figure S1: Adsorption geometry of adsorbates (a) HCOOH (b) H_3CO* (c) OCHO* (d) H_2COOH* adsorbates on RuO_2 (110) surface and (e)-(f) CHO* adsorbate in two different configuration on RuO_2 (110) surface with Ir atom substitution close to bridge site*

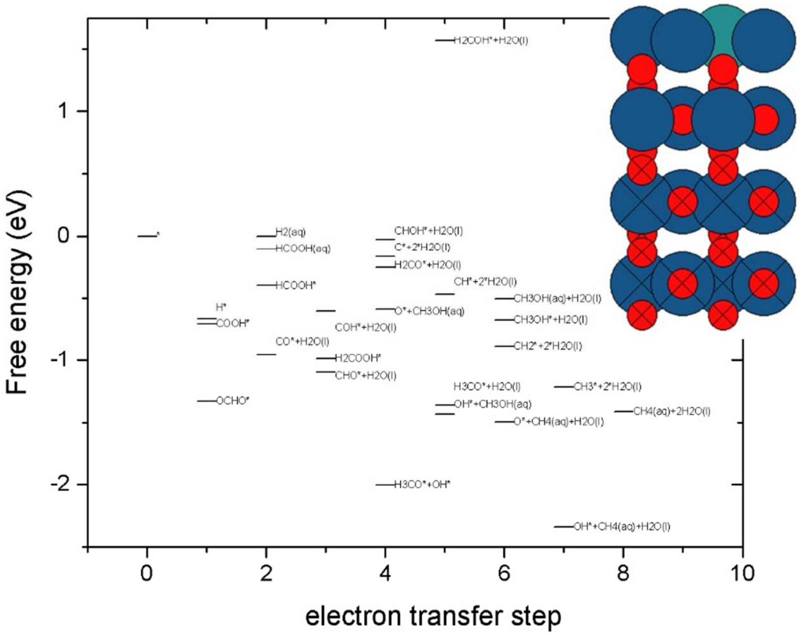

Free energy (eV)
1
0
-1
-2
electron transfer step
0
2
4
6
8
10
*
H2COH*+H2O(l)
H2(aq)
HCOOH(aq)
HCOOH*
H*
COOH*
CO*+H2O(l)
OCHO*
COH*+H2O(l)
H2COOH*
CHO*+H2O(l)
CHOH*+H2O(l)
C*+2*H2O(l)
H2CO*+H2O(l)
O*+CH3OH(aq)
H3CO*+OH*
CH*+2*H2O(l)
H3CO*+H2O(l)
OH*+CH3OH(aq)
CH3OH(aq)+H2O(l)
CH3OH*+H2O(l)
CH2*+2*H2O(l)
O*+CH4(aq)+H2O(l)
CH3*+2*H2O(l)
OH*+CH4(aq)+H2O(l)
CH4(aq)+2H2O(l)

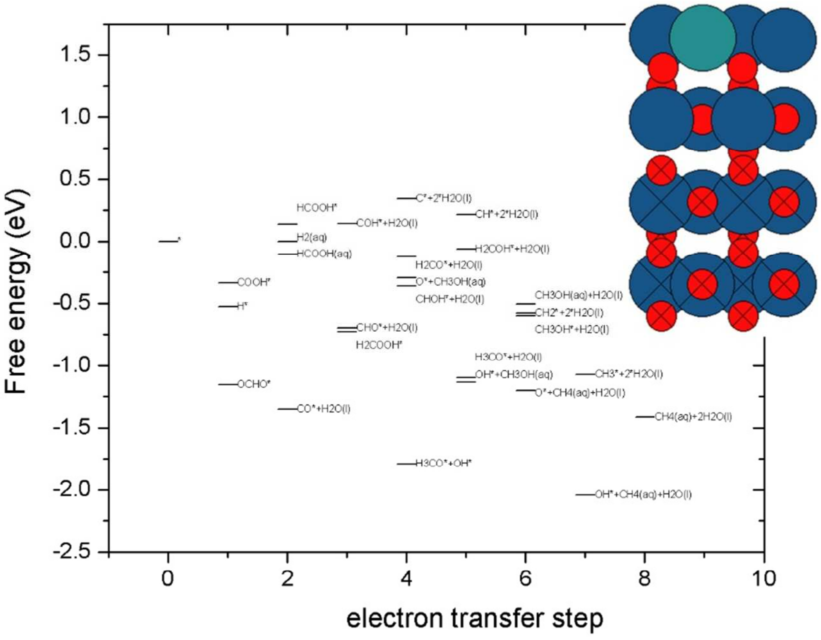

Free energy (eV)
1.5
1.0
0.5
0.0
-0.5
-1.0
-1.5
-2.0
-2.5
electron transfer step
0
2
4
6
8
10
*
COOH*
H*
OCHO*
HCOOH*
H2(aq)
HCOOH(aq)
CO*+H2O(l)
COH*+H2O(l)
CHO*+H2O(l)
H2COOH*
C*+2*H2O(l)
H2CO*+H2O(l)
O*+CH3OH(aq)
CHOH*+H2O(l)
H3CO*+OH*
CH*+2*H2O(l)
H2COH*+H2O(l)
H3CO*+H2O(l)
OH*+CH3OH(aq)
CH3OH(aq)+H2O(l)
CH2*+2*H2O(l)
CH3OH*+H2O(l)
O*+CH4(aq)+H2O(l)
CH3*+2*H2O(l)
OH*+CH4(aq)+H2O(l)
CH4(aq)+2H2O(l)

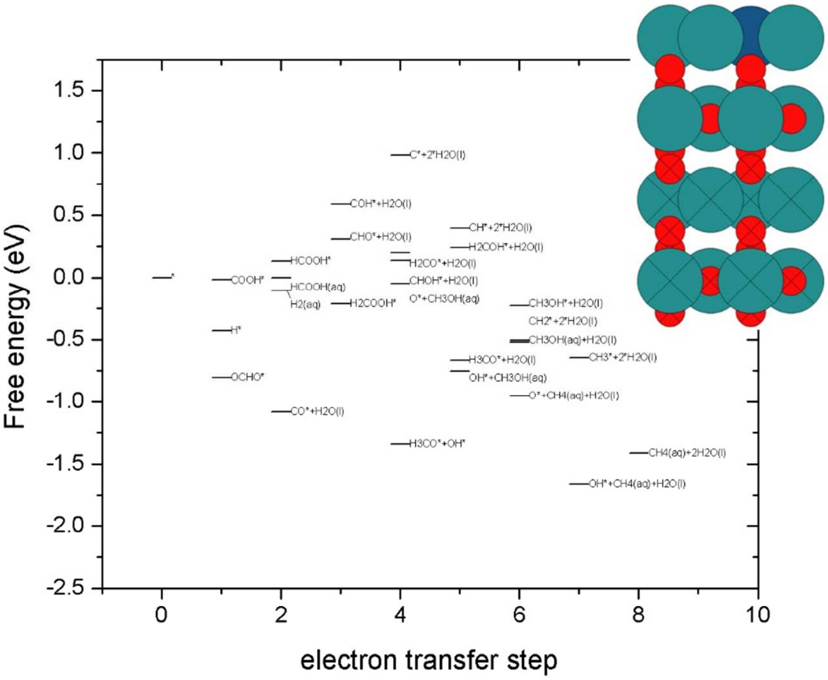
Free energy (eV)
1.5
1.0
0.5
0.0
-0.5
-1.0
-1.5
-2.0
-2.5
0
2
4
6
8
10
electron transfer step
*
COOH*
H*
OCHO*
HCOOH*
HCOOH(aq)
H2(aq)
CO*+H2O(l)
COH*+H2O(l)
CHO*+H2O(l)
H2COOH*
C*+2*H2O(l)
H2CO*+H2O(l)
CHOH*+H2O(l)
O*+CH3OH(aq)
H3CO*+OH*
CH*+2*H2O(l)
H2COH*+H2O(l)
H3CO*+H2O(l)
OH*+CH3OH(aq)
CH3OH*+H2O(l)
CH2*+2*H2O(l)
CH3OH(aq)+H2O(l)
O*+CH4(aq)+H2O(l)
CH3*+2*H2O(l)
OH*+CH4(aq)+H2O(l)
CH4(aq)+2H2O(l)

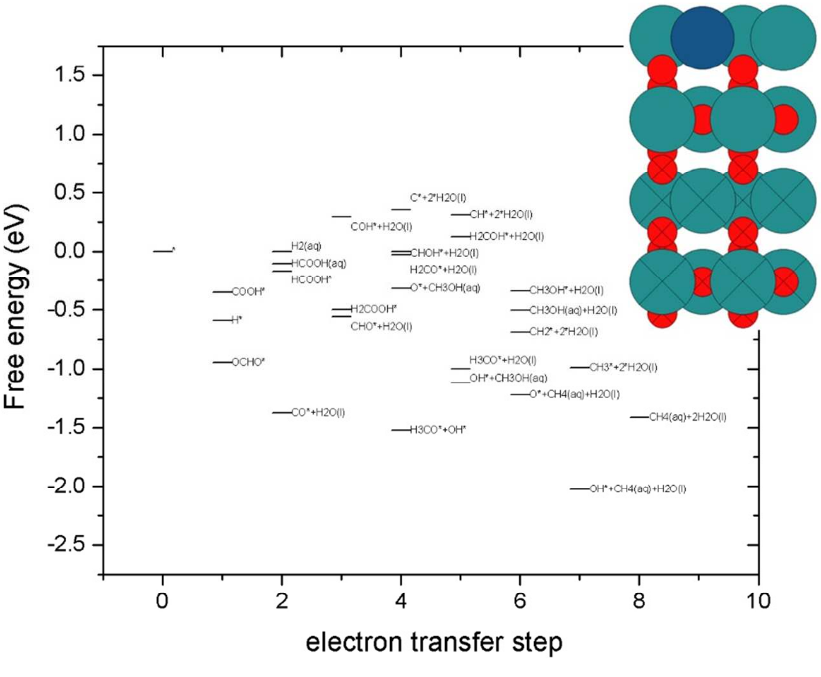
Free energy (eV)
1.5
1.0
0.5
0.0
-0.5
-1.0
-1.5
-2.0
-2.5
0
2
4
6
8
10
electron transfer step
*
COOH*
H*
OCHO*
H2(aq)
HCOOH(aq)
HCOOH*
CO*+H2O(l)
COH*+H2O(l)
H2COOH*
CHO*+H2O(l)
C*+2*H2O(l)
CHOH*+H2O(l)
H2CO*+H2O(l)
O*+CH3OH(aq)
H3CO*+OH*
CH*+2*H2O(l)
H2COH*+H2O(l)
H3CO*+H2O(l)
OH*+CH3OH(aq)
CH3OH*+H2O(l)
CH3OH(aq)+H2O(l)
CH2*+2*H2O(l)
O*+CH4(aq)+H2O(l)
CH3*+2*H2O(l)
CH4(aq)+2H2O(l)
OH*+CH4(aq)+H2O(l)

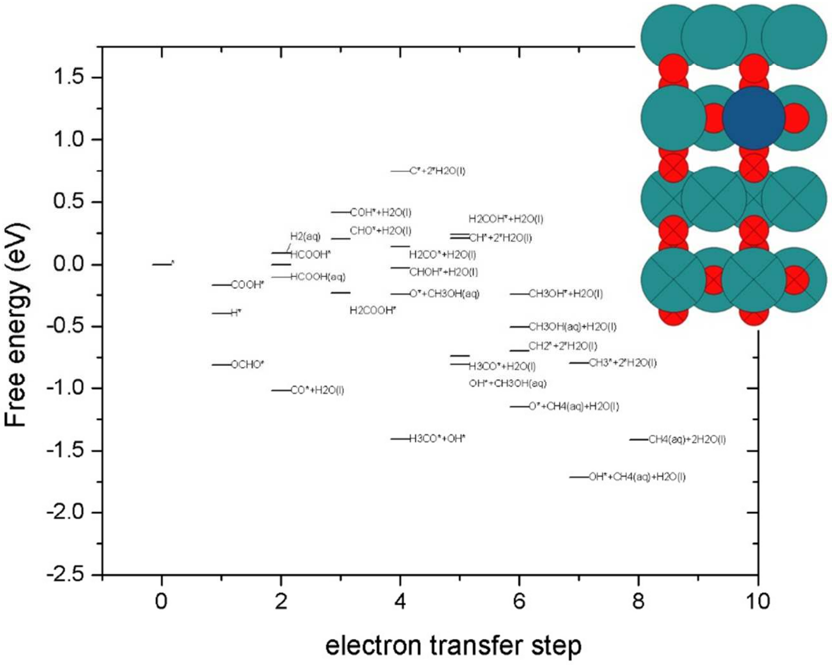
Free energy (eV)
1.5
1.0
0.5
0.0
-0.5
-1.0
-1.5
-2.0
-2.5
0
2
4
6
8
10
electron transfer step
*
COOH*
H*
OCHO*
H2(aq)
HCOOH*
HCOOH(aq)
CO*+H2O(l)
COH*+H2O(l)
CHO*+H2O(l)
H2COOH*
C*+2*H2O(l)
H2CO*+H2O(l)
CHOH*+H2O(l)
O*+CH3OH(aq)
H3CO*+OH*
H2COH*+H2O(l)
CH*+2*H2O(l)
H3CO*+H2O(l)
OH*+CH3OH(aq)
CH3OH*+H2O(l)
CH3OH(aq)+H2O(l)
CH2*+2*H2O(l)
O*+CH4(aq)+H2O(l)
CH3*+2*H2O(l)
OH*+CH4(aq)+H2O(l)
CH4(aq)+2H2O(l)

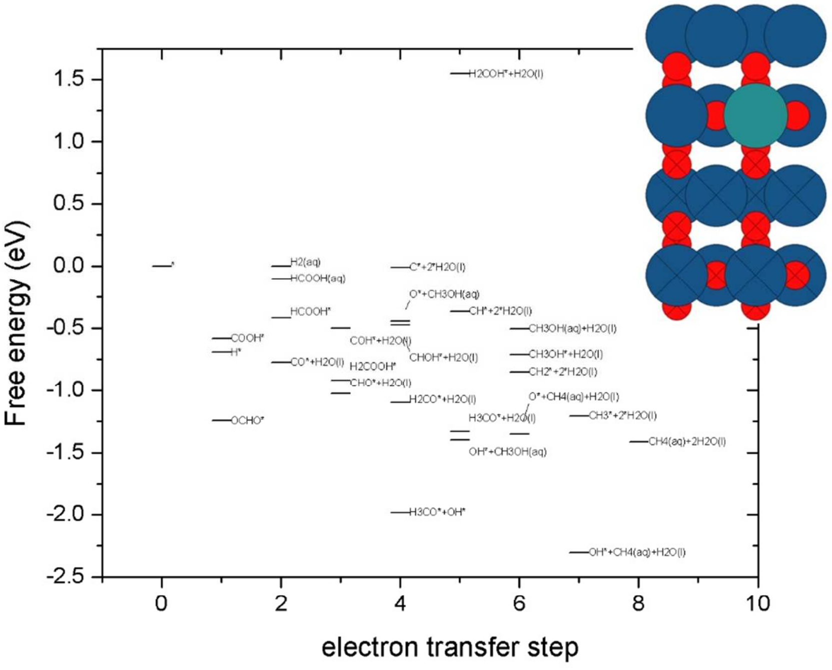
Free energy (eV)
1.5
1.0
0.5
0.0
-0.5
-1.0
-1.5
-2.0
-2.5
0
2
4
6
8
10
electron transfer step
*
COOH*
H*
OCHO*
H2(aq)
HCOOH(aq)
HCOOH*
CO*+H2O(l)
COH*+H2O(l)
H2COOH*
CHO*+H2O(l)
C*+2*H2O(l)
O*+CH3OH(aq)
CHOH*+H2O(l)
H2CO*+H2O(l)
H3CO*+OH*
H2COH*+H2O(l)
CH*+2*H2O(l)
H3CO*+H2O(l)
OH*+CH3OH(aq)
CH3OH(aq)+H2O(l)
CH3OH*+H2O(l)
CH2*+2*H2O(l)
O*+CH4(aq)+H2O(l)
CH3*+2*H2O(l)
OH*+CH4(aq)+H2O(l)
CH4(aq)+2H2O(l)

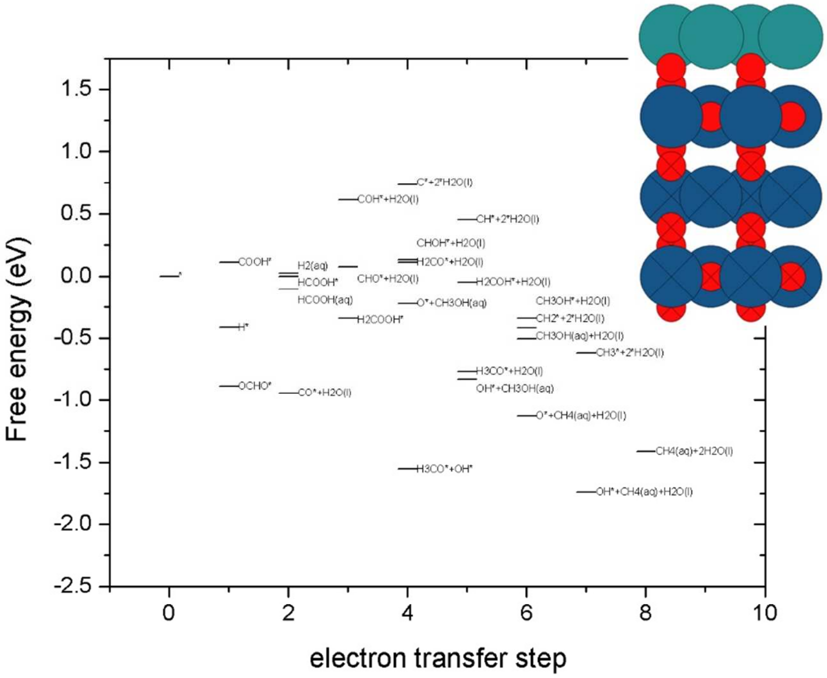

Free energy (eV)
1.5
1.0
0.5
0.0
-0.5
-1.0
-1.5
-2.0
-2.5
0
2
4
6
8
10
electron transfer step
*
COOH*
H*
OCHO*
H2(aq)
HCOOH*
HCOOH(aq)
CO*+H2O(l)
COH*+H2O(l)
CHO*+H2O(l)
H2COOH*
C*+2*H2O(l)
CHOH*+H2O(l)
H2CO*+H2O(l)
O*+CH3OH(aq)
H3CO*+OH*
CH*+2*H2O(l)
H2COH*+H2O(l)
H3CO*+H2O(l)
OH*+CH3OH(aq)
CH3OH*+H2O(l)
CH2*+2*H2O(l)
CH3OH(aq)+H2O(l)
O*+CH4(aq)+H2O(l)
CH3*+2*H2O(l)
OH*+CH4(aq)+H2O(l)
CH4(aq)+2H2O(l)

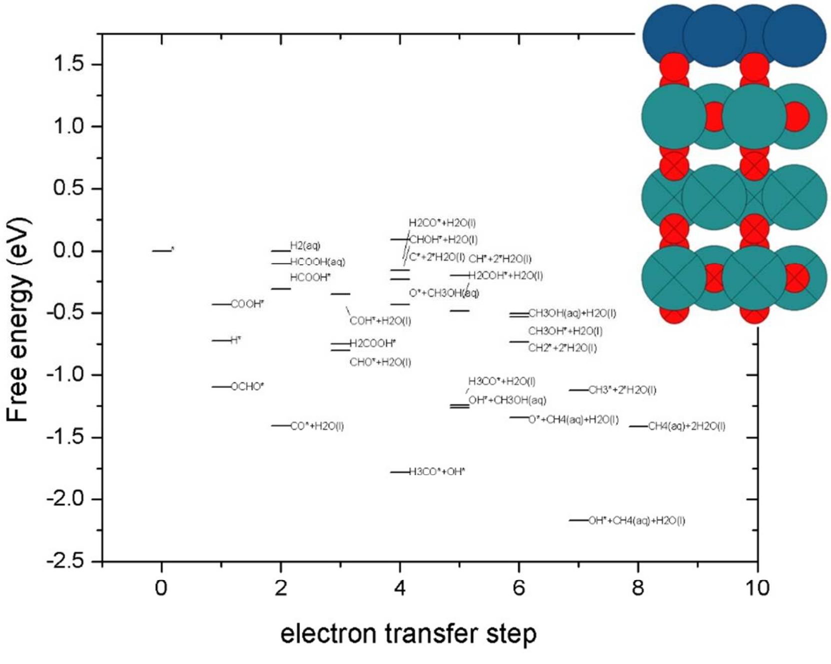

Free energy (eV)
1.5
1.0
0.5
0.0
-0.5
-1.0
-1.5
-2.0
-2.5
0
2
4
6
8
10
electron transfer step
*
COOH*
H*
OCHO*
H2(aq)
HCOOH(aq)
HCOOH*
CO*+H2O(l)
COH*+H2O(l)
H2COOH*
CHO*+H2O(l)
H2CO*+H2O(l)
CHOH*+H2O(l)
C*+2*H2O(l)
O*+CH3OH(aq)
H3CO*+OH*
CH*+2*H2O(l)
H2COH*+H2O(l)
H3CO*+H2O(l)
OH*+CH3OH(aq)
CH3OH(aq)+H2O(l)
CH3OH*+H2O(l)
CH2*+2*H2O(l)
O*+CH4(aq)+H2O(l)
CH3*+2*H2O(l)
CH4(aq)+2H2O(l)
OH*+CH4(aq)+H2O(l)

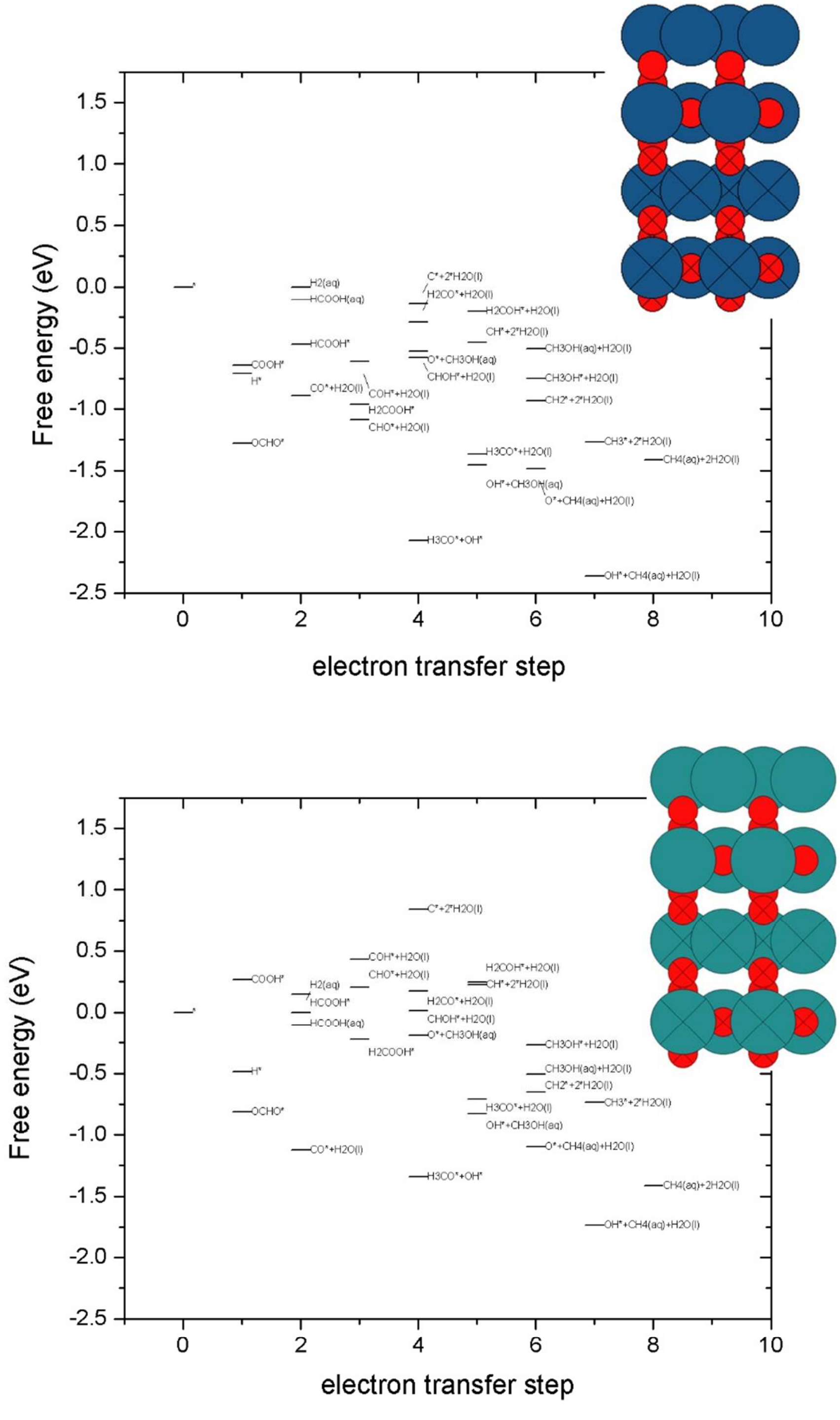

Figure S2: free energy of reaction intermediates and products with reference to CO_2, H_2 and H_2O at 0 V-RHE on all 10 surfaces models with no CO coverage*

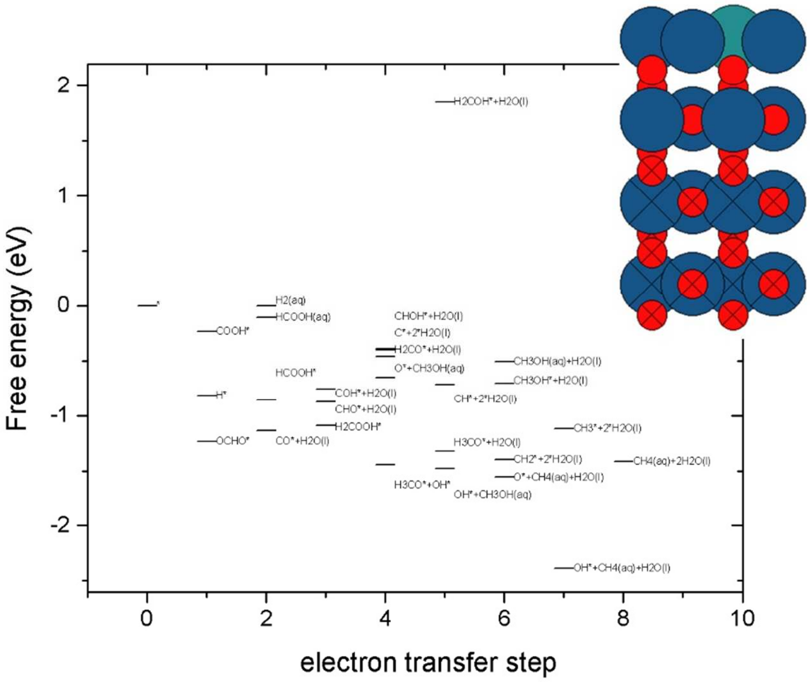

Free energy (eV)
2
1
0
-1
-2
0
2
4
6
8
10
electron transfer step
*
COOH*
H*
OCHO*
H2(aq)
HCOOH(aq)
HCOOH*
CO*+H2O(l)
COH*+H2O(l)
CHO*+H2O(l)
H2COOH*
CHOH*+H2O(l)
C*+2*H2O(l)
H2CO*+H2O(l)
O*+CH3OH(aq)
H3CO*+OH*
H2COH*+H2O(l)
CH*+2*H2O(l)
H3CO*+H2O(l)
OH*+CH3OH(aq)
CH3OH(aq)+H2O(l)
CH3OH*+H2O(l)
CH2*+2*H2O(l)
O*+CH4(aq)+H2O(l)
CH3*+2*H2O(l)
OH*+CH4(aq)+H2O(l)
CH4(aq)+2H2O(l)

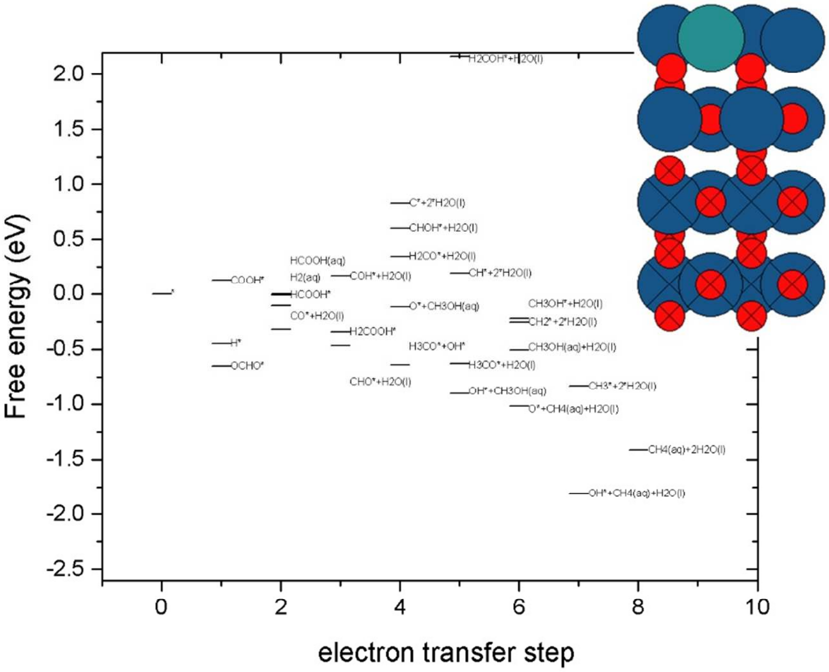

Free energy (eV)
2.0
1.5
1.0
0.5
0.0
-0.5
-1.0
-1.5
-2.0
-2.5
0
2
4
6
8
10
electron transfer step
*
COOH*
H*
OCHO*
HCOOH(aq)
H2(aq)
HCOOH*
CO*+H2O(l)
COH*+H2O(l)
H2COOH*
CHO*+H2O(l)
C*+2*H2O(l)
CHOH*+H2O(l)
H2CO*+H2O(l)
O*+CH3OH(aq)
H3CO*+OH*
H2COH*+H2O(l)
CH*+2*H2O(l)
H3CO*+H2O(l)
OH*+CH3OH(aq)
CH3OH*+H2O(l)
CH2*+2*H2O(l)
CH3OH(aq)+H2O(l)
O*+CH4(aq)+H2O(l)
CH3*+2*H2O(l)
CH4(aq)+2H2O(l)
OH*+CH4(aq)+H2O(l)

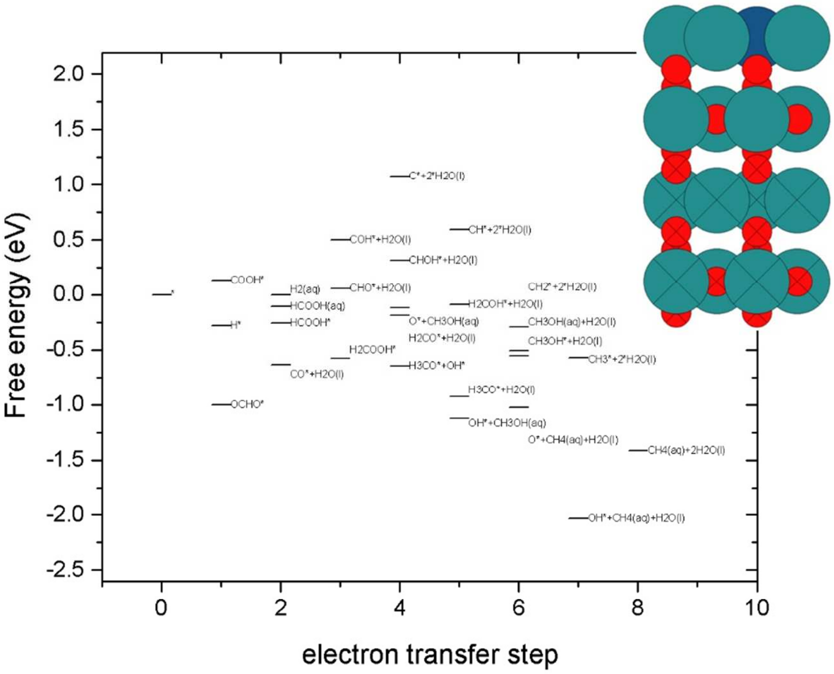
2.0
1.5
1.0
0.5
0.0
-0.5
-1.0
-1.5
-2.0
-2.5
Free energy (eV)
0
2
4
6
8
10
electron transfer step
*
COOH*
H*
OCHO*
H2(aq)
HCOOH(aq)
HCOOH*
CO*+H2O(l)
COH*+H2O(l)
CHO*+H2O(l)
H2COOH*
C*+2*H2O(l)
CHOH*+H2O(l)
O*+CH3OH(aq)
H2CO*+H2O(l)
H3CO*+OH*
CH*+2*H2O(l)
H2COH*+H2O(l)
H3CO*+H2O(l)
OH*+CH3OH(aq)
CH2*+2*H2O(l)
CH3OH(aq)+H2O(l)
CH3OH*+H2O(l)
O*+CH4(aq)+H2O(l)
CH3*+2*H2O(l)
OH*+CH4(aq)+H2O(l)
CH4(aq)+2H2O(l)

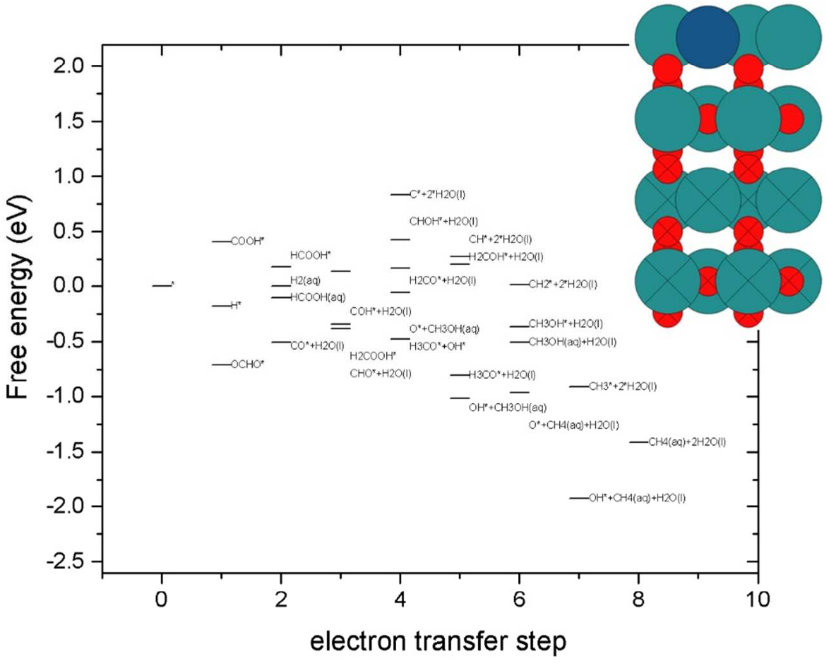
2.0
1.5
1.0
0.5
0.0
-0.5
-1.0
-1.5
-2.0
-2.5
Free energy (eV)
0
2
4
6
8
10
electron transfer step
*
COOH*
H*
OCHO*
HCOOH*
H2(aq)
HCOOH(aq)
CO*+H2O(l)
COH*+H2O(l)
H2COOH*
CHO*+H2O(l)
C*+2*H2O(l)
CHOH*+H2O(l)
H2CO*+H2O(l)
O*+CH3OH(aq)
H3CO*+OH*
CH*+2*H2O(l)
H2COH*+H2O(l)
H3CO*+H2O(l)
OH*+CH3OH(aq)
CH2*+2*H2O(l)
CH3OH*+H2O(l)
CH3OH(aq)+H2O(l)
O*+CH4(aq)+H2O(l)
CH3*+2*H2O(l)
OH*+CH4(aq)+H2O(l)
CH4(aq)+2H2O(l)

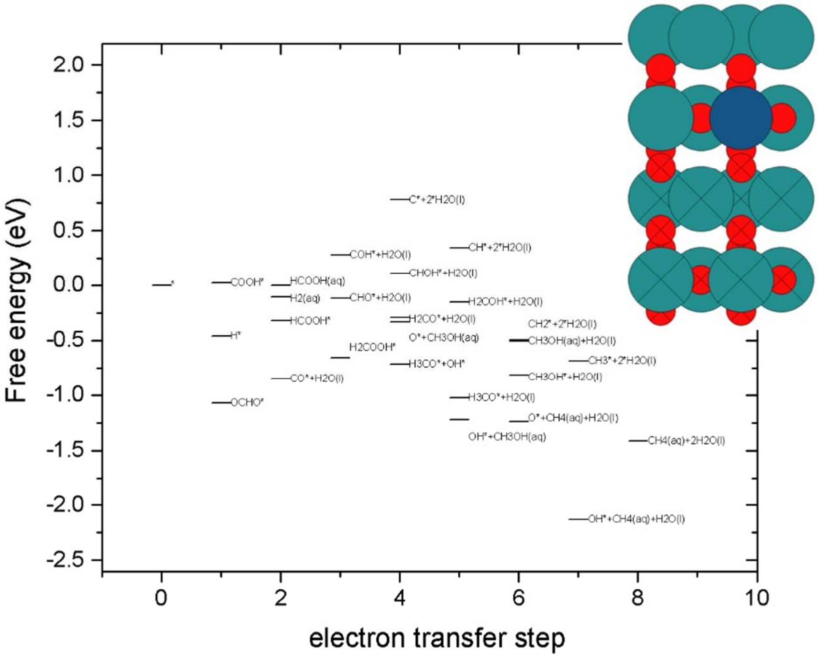
Free energy (eV)
2.0
1.5
1.0
0.5
0.0
-0.5
-1.0
-1.5
-2.0
-2.5
0
2
4
6
8
10
electron transfer step
*
COOH*
H*
OCHO*
HCOOH(aq)
H2(aq)
HCOOH*
CO*+H2O(l)
COH*+H2O(l)
CHO*+H2O(l)
H2COOH*
C*+2*H2O(l)
CHOH*+H2O(l)
H2CO*+H2O(l)
O*+CH3OH(aq)
H3CO*+OH*
CH*+2*H2O(l)
H2COH*+H2O(l)
H3CO*+H2O(l)
OH*+CH3OH(aq)
CH2*+2*H2O(l)
CH3OH(aq)+H2O(l)
CH3OH*+H2O(l)
O*+CH4(aq)+H2O(l)
CH3*+2*H2O(l)
CH4(aq)+2H2O(l)
OH*+CH4(aq)+H2O(l)

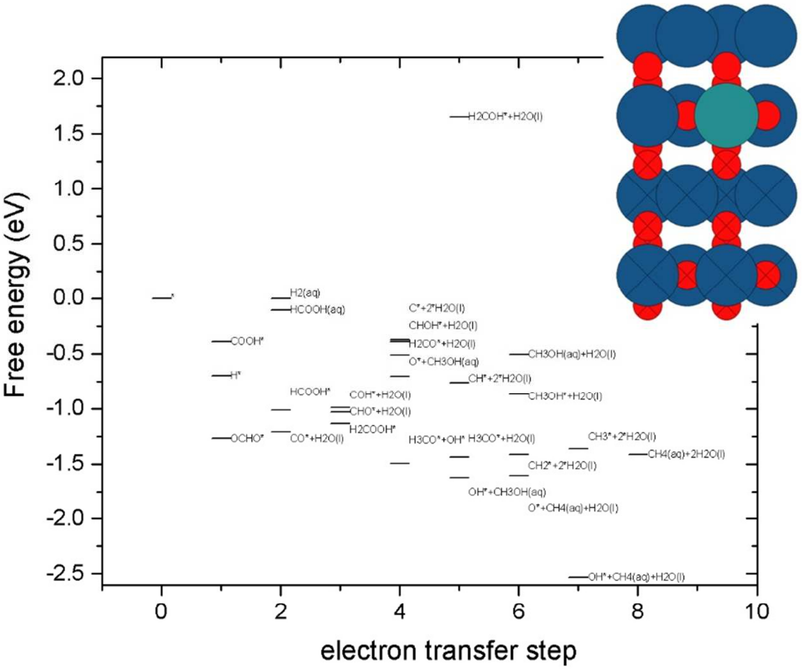
Free energy (eV)
2.0
1.5
1.0
0.5
0.0
-0.5
-1.0
-1.5
-2.0
-2.5
0
2
4
6
8
10
electron transfer step
*
COOH*
H*
OCHO*
H2(aq)
HCOOH(aq)
HCOOH*
CO*+H2O(l)
COH*+H2O(l)
CHO*+H2O(l)
H2COOH*
C*+2*H2O(l)
CHOH*+H2O(l)
H2CO*+H2O(l)
O*+CH3OH(aq)
H3CO*+OH*
H2COH*+H2O(l)
CH*+2*H2O(l)
H3CO*+H2O(l)
OH*+CH3OH(aq)
CH3OH(aq)+H2O(l)
CH3OH*+H2O(l)
CH2*+2*H2O(l)
O*+CH4(aq)+H2O(l)
CH3*+2*H2O(l)
CH4(aq)+2H2O(l)
OH*+CH4(aq)+H2O(l)

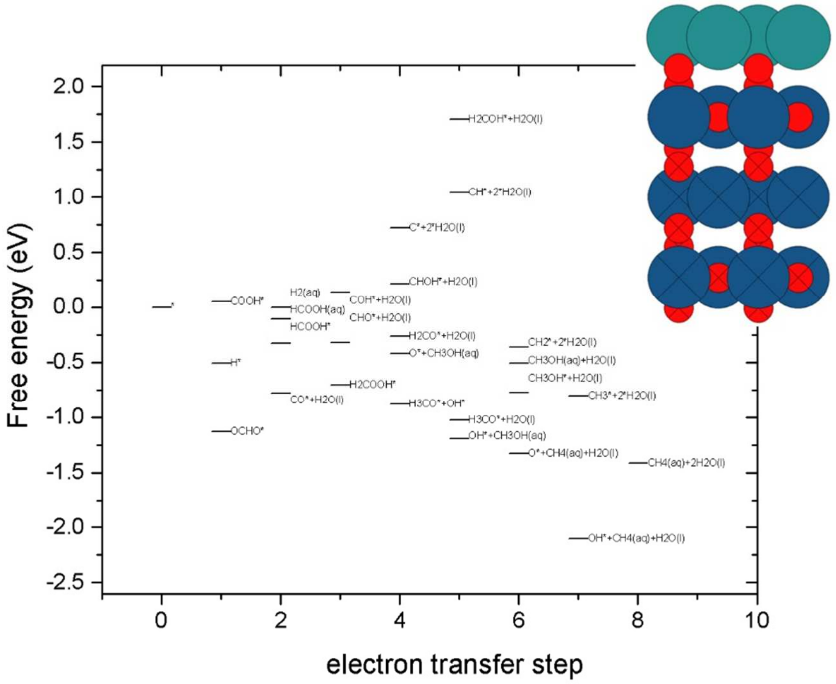

2.0
1.5
1.0
0.5
0.0
-0.5
-1.0
-1.5
-2.0
-2.5
Free energy (eV)
0
2
4
6
8
10
electron transfer step
*
COOH*
H*
OCHO*
H2(aq)
HCOOH(aq)
HCOOH*
CO*+H2O(l)
COH*+H2O(l)
CHO*+H2O(l)
H2COOH*
C*+2*H2O(l)
CHOH*+H2O(l)
H2CO*+H2O(l)
O*+CH3OH(aq)
H3CO*+OH*
H2COH*+H2O(l)
CH*+2*H2O(l)
H3CO*+H2O(l)
OH*+CH3OH(aq)
CH2*+2*H2O(l)
CH3OH(aq)+H2O(l)
CH3OH*+H2O(l)
O*+CH4(aq)+H2O(l)
CH3*+2*H2O(l)
CH4(aq)+2H2O(l)
OH*+CH4(aq)+H2O(l)

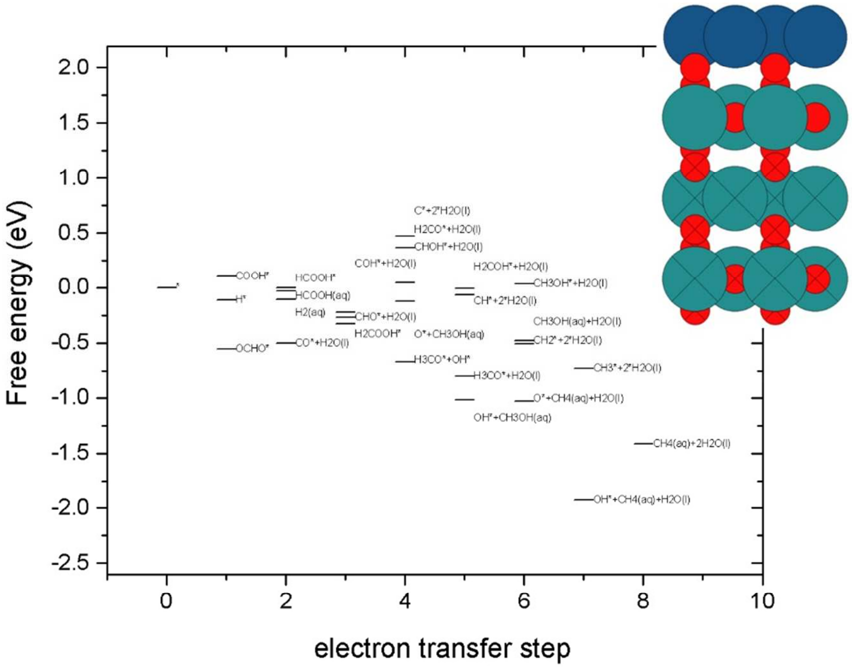

2.0
1.5
1.0
0.5
0.0
-0.5
-1.0
-1.5
-2.0
-2.5
Free energy (eV)
0
2
4
6
8
10
electron transfer step
*
COOH*
H*
OCHO*
HCOOH*
HCOOH(aq)
H2(aq)
CO*+H2O(l)
COH*+H2O(l)
CHO*+H2O(l)
H2COOH*
C*+2*H2O(l)
H2CO*+H2O(l)
CHOH*+H2O(l)
O*+CH3OH(aq)
H3CO*+OH*
H2COH*+H2O(l)
CH*+2*H2O(l)
H3CO*+H2O(l)
OH*+CH3OH(aq)
CH3OH*+H2O(l)
CH3OH(aq)+H2O(l)
CH2*+2*H2O(l)
O*+CH4(aq)+H2O(l)
CH3*+2*H2O(l)
CH4(aq)+2H2O(l)
OH*+CH4(aq)+H2O(l)

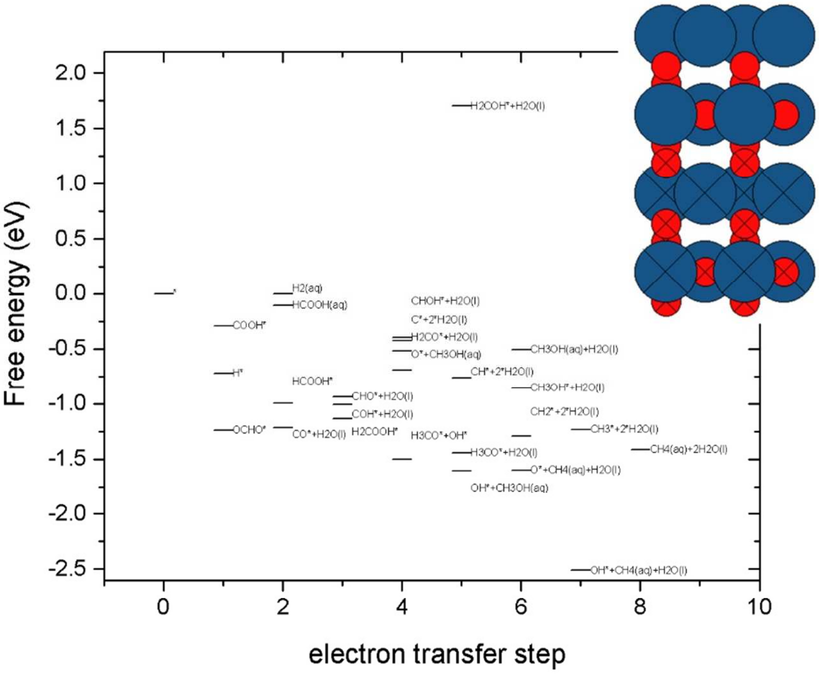

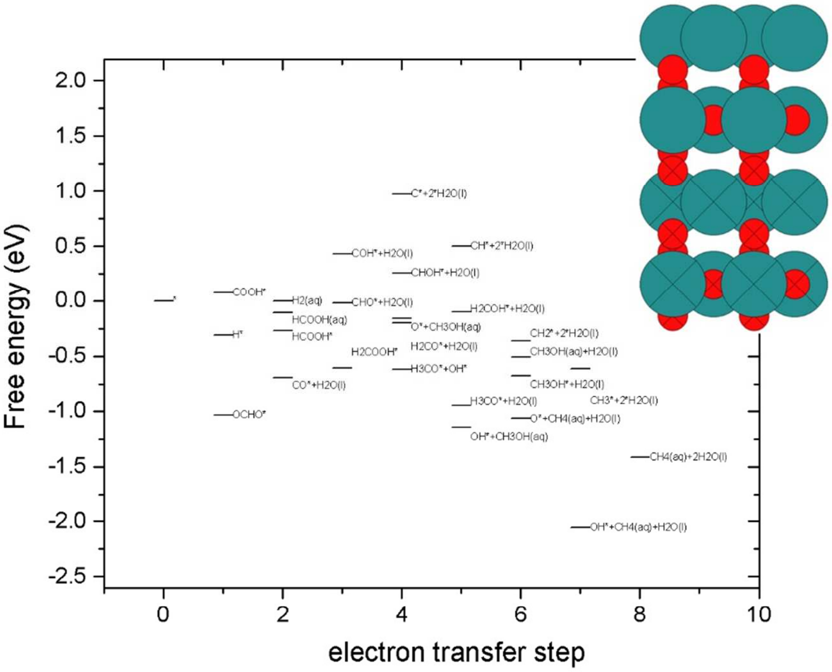

Figure S3: free energy of reaction intermediates and products with reference to CO_2, H_2 and H_2O at 0 V-RHE on all 10 surfaces models with 25% CO coverage*

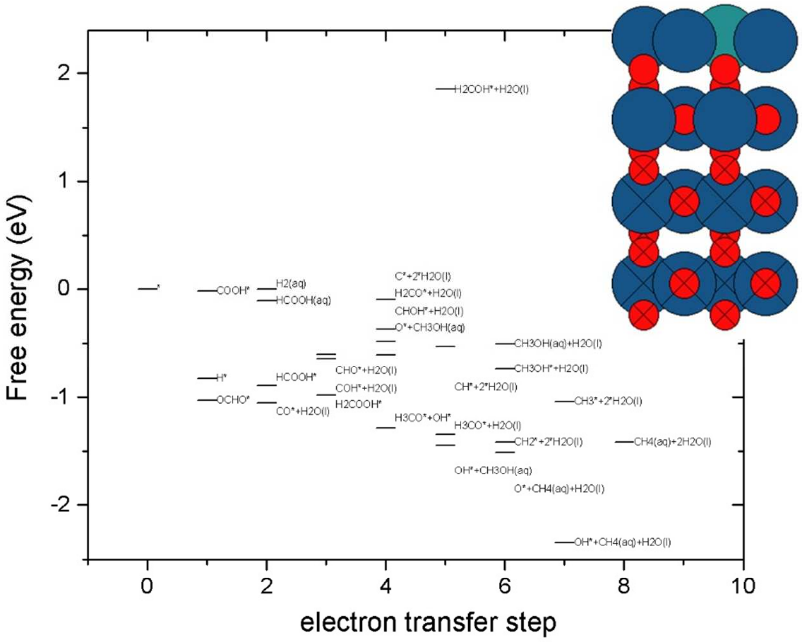
Free energy (eV)
electron transfer step
2
1
0
-1
-2
0
2
4
6
8
10
*
COOH*
H*
OCHO*
H2(aq)
HCOOH(aq)
HCOOH*
CO*+H2O(l)
CHO*+H2O(l)
COH*+H2O(l)
H2COOH*
C*+2*H2O(l)
H2CO*+H2O(l)
CHOH*+H2O(l)
O*+CH3OH(aq)
H3CO*+OH*
H2COH*+H2O(l)
CH*+2*H2O(l)
H3CO*+H2O(l)
OH*+CH3OH(aq)
CH3OH(aq)+H2O(l)
CH3OH*+H2O(l)
CH2*+2*H2O(l)
O*+CH4(aq)+H2O(l)
CH3*+2*H2O(l)
OH*+CH4(aq)+H2O(l)
CH4(aq)+2H2O(l)

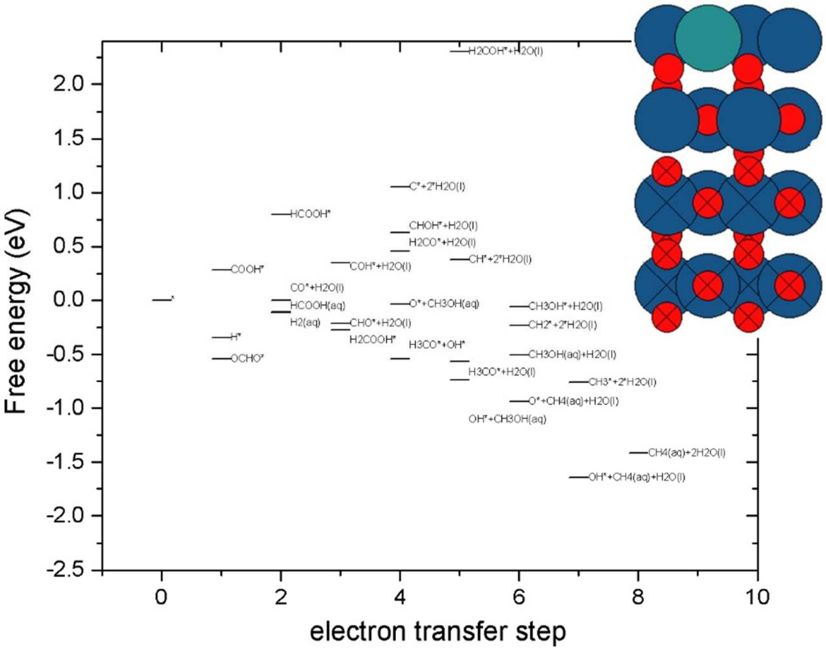
Free energy (eV)
electron transfer step
2.0
1.5
1.0
0.5
0.0
-0.5
-1.0
-1.5
-2.0
-2.5
0
2
4
6
8
10
*
COOH*
H*
OCHO*
HCOOH*
CO*+H2O(l)
HCOOH(aq)
H2(aq)
COH*+H2O(l)
CHO*+H2O(l)
H2COOH*
C*+2*H2O(l)
CHOH*+H2O(l)
H2CO*+H2O(l)
O*+CH3OH(aq)
H3CO*+OH*
H2COH*+H2O(l)
CH*+2*H2O(l)
H3CO*+H2O(l)
OH*+CH3OH(aq)
CH3OH*+H2O(l)
CH2*+2*H2O(l)
CH3OH(aq)+H2O(l)
O*+CH4(aq)+H2O(l)
CH3*+2*H2O(l)
OH*+CH4(aq)+H2O(l)
CH4(aq)+2H2O(l)

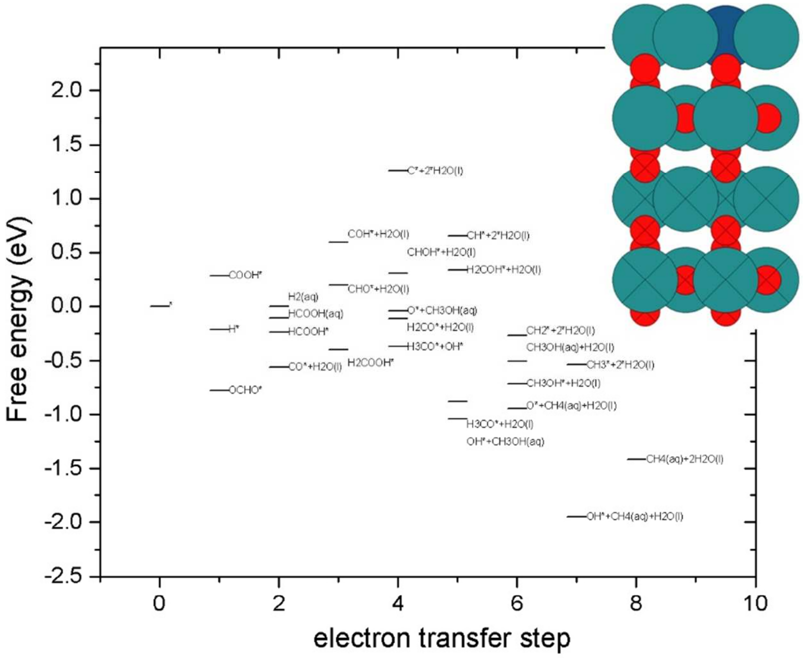

Free energy (eV)
2.0
1.5
1.0
0.5
0.0
-0.5
-1.0
-1.5
-2.0
-2.5
0
2
4
6
8
10
electron transfer step
*
COOH*
H*
OCHO*
H2(aq)
HCOOH(aq)
HCOOH*
CO*+H2O(l)
COH*+H2O(l)
CHO*+H2O(l)
H2COOH*
C*+2*H2O(l)
CHOH*+H2O(l)
O*+CH3OH(aq)
H2CO*+H2O(l)
H3CO*+OH*
CH*+2*H2O(l)
H2COH*+H2O(l)
H3CO*+H2O(l)
OH*+CH3OH(aq)
CH2*+2*H2O(l)
CH3OH(aq)+H2O(l)
CH3*+2*H2O(l)
CH3OH*+H2O(l)
O*+CH4(aq)+H2O(l)
CH4(aq)+2H2O(l)
OH*+CH4(aq)+H2O(l)

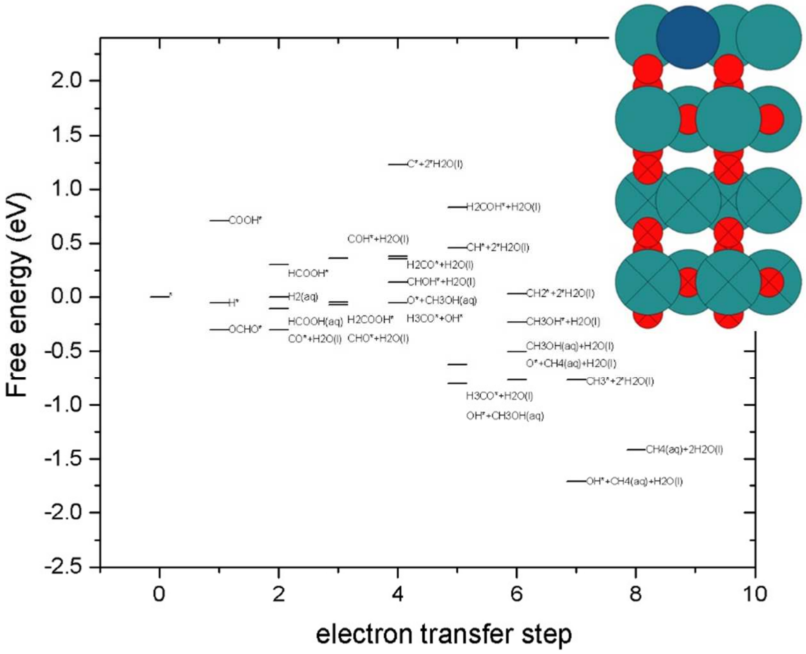

Free energy (eV)
2.0
1.5
1.0
0.5
0.0
-0.5
-1.0
-1.5
-2.0
-2.5
0
2
4
6
8
10
electron transfer step
*
COOH*
H*
OCHO*
HCOOH*
H2(aq)
HCOOH(aq)
CO*+H2O(l)
COH*+H2O(l)
H2COOH*
CHO*+H2O(l)
C*+2*H2O(l)
H2CO*+H2O(l)
CHOH*+H2O(l)
O*+CH3OH(aq)
H3CO*+OH*
H2COH*+H2O(l)
CH*+2*H2O(l)
H3CO*+H2O(l)
OH*+CH3OH(aq)
CH2*+2*H2O(l)
CH3OH*+H2O(l)
CH3OH(aq)+H2O(l)
O*+CH4(aq)+H2O(l)
CH3*+2*H2O(l)
CH4(aq)+2H2O(l)
OH*+CH4(aq)+H2O(l)

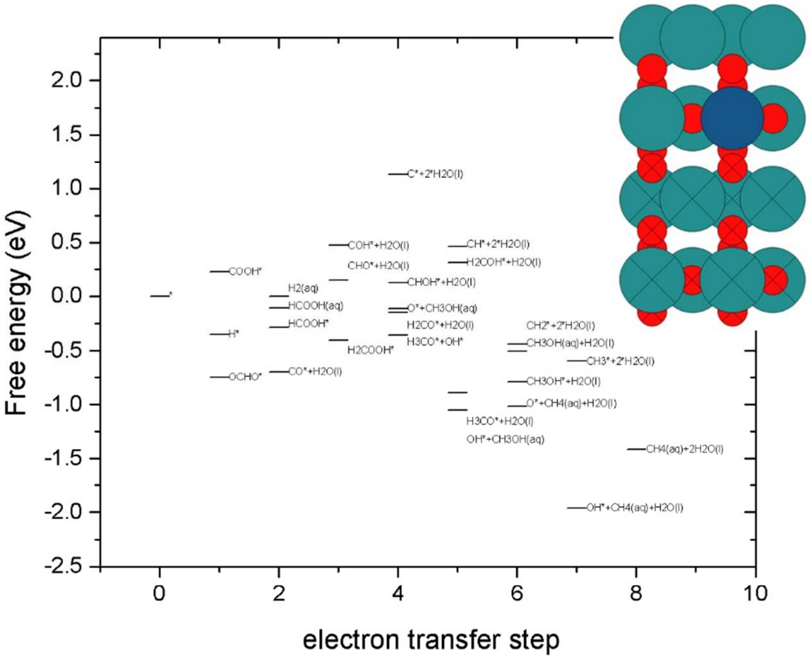
Free energy (eV)
2.0
1.5
1.0
0.5
0.0
-0.5
-1.0
-1.5
-2.0
-2.5
0
2
4
6
8
10
electron transfer step
*
COOH*
H*
OCHO*
H2(aq)
HCOOH(aq)
HCOOH*
CO*+H2O(l)
COH*+H2O(l)
CHO*+H2O(l)
H2COOH*
C*+2*H2O(l)
CHOH*+H2O(l)
O*+CH3OH(aq)
H2CO*+H2O(l)
H3CO*+OH*
CH*+2*H2O(l)
H2COH*+H2O(l)
H3CO*+H2O(l)
OH*+CH3OH(aq)
CH2*+2*H2O(l)
CH3OH(aq)+H2O(l)
CH3OH*+H2O(l)
O*+CH4(aq)+H2O(l)
CH3*+2*H2O(l)
OH*+CH4(aq)+H2O(l)
CH4(aq)+2H2O(l)

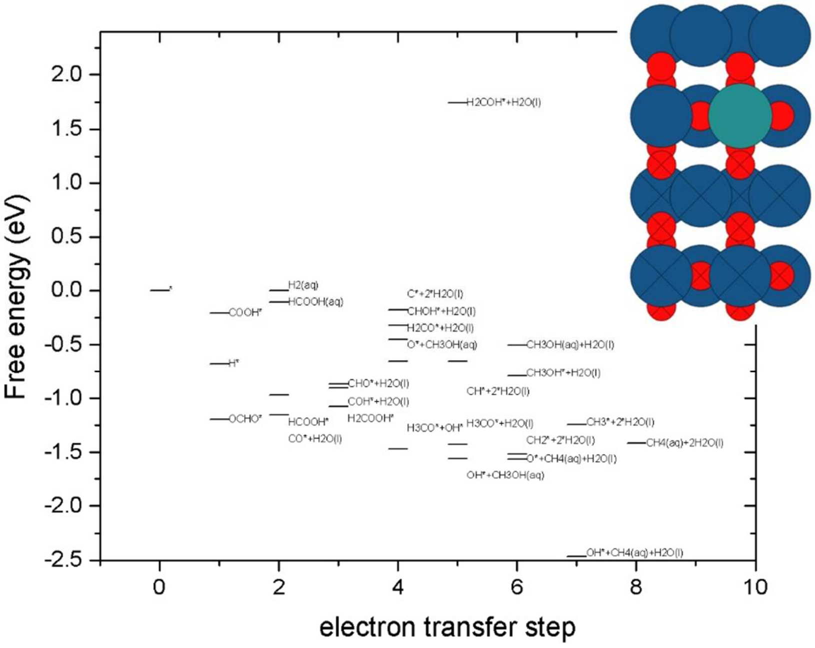
Free energy (eV)
2.0
1.5
1.0
0.5
0.0
-0.5
-1.0
-1.5
-2.0
-2.5
0
2
4
6
8
10
electron transfer step
*
COOH*
H*
OCHO*
H2(aq)
HCOOH(aq)
HCOOH*
CO*+H2O(l)
CHO*+H2O(l)
COH*+H2O(l)
H2COOH*
C*+2*H2O(l)
CHOH*+H2O(l)
H2CO*+H2O(l)
O*+CH3OH(aq)
H3CO*+OH*
H2COH*+H2O(l)
CH*+2*H2O(l)
H3CO*+H2O(l)
OH*+CH3OH(aq)
CH3OH(aq)+H2O(l)
CH3OH*+H2O(l)
CH2*+2*H2O(l)
O*+CH4(aq)+H2O(l)
CH3*+2*H2O(l)
OH*+CH4(aq)+H2O(l)
CH4(aq)+2H2O(l)

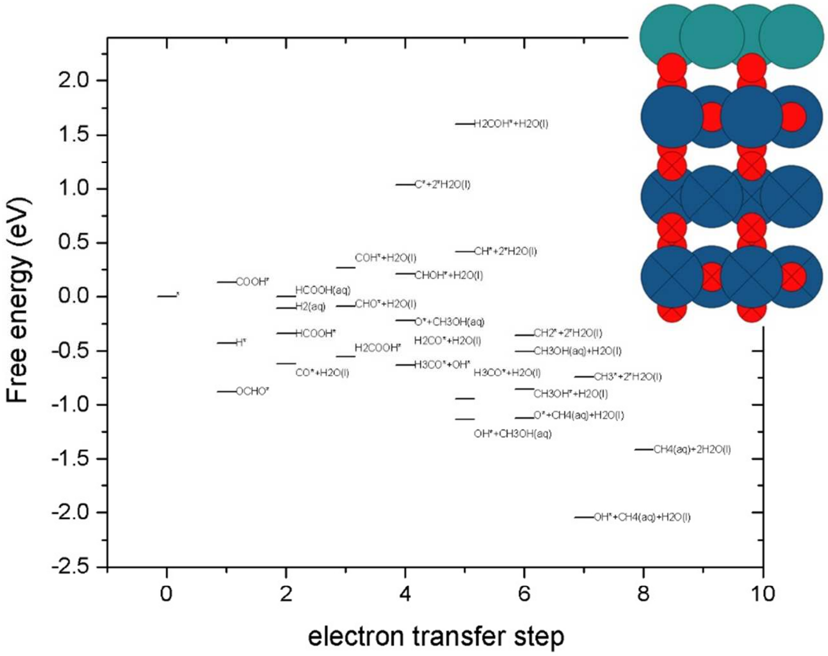

Free energy (eV)
2.0
1.5
1.0
0.5
0.0
-0.5
-1.0
-1.5
-2.0
-2.5
electron transfer step
0
2
4
6
8
10
*
COOH*
H*
OCHO*
HCOOH(aq)
H2(aq)
HCOOH*
CO*+H2O(l)
COH*+H2O(l)
CHO*+H2O(l)
H2COOH*
C*+2*H2O(l)
CHOH*+H2O(l)
O*+CH3OH(aq)
H2CO*+H2O(l)
H3CO*+OH*
H2COH*+H2O(l)
CH*+2*H2O(l)
H3CO*+H2O(l)
OH*+CH3OH(aq)
CH2*+2*H2O(l)
CH3OH(aq)+H2O(l)
CH3OH*+H2O(l)
O*+CH4(aq)+H2O(l)
CH3*+2*H2O(l)
CH4(aq)+2H2O(l)
OH*+CH4(aq)+H2O(l)

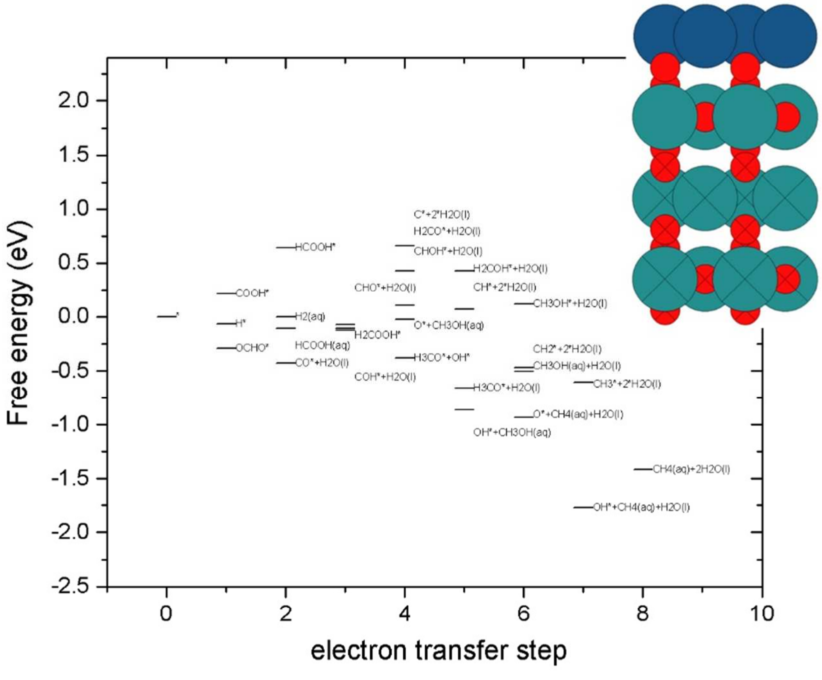

Free energy (eV)
2.0
1.5
1.0
0.5
0.0
-0.5
-1.0
-1.5
-2.0
-2.5
electron transfer step
0
2
4
6
8
10
*
COOH*
H*
OCHO*
HCOOH*
H2(aq)
HCOOH(aq)
CO*+H2O(l)
CHO*+H2O(l)
H2COOH*
COH*+H2O(l)
C*+2*H2O(l)
H2CO*+H2O(l)
CHOH*+H2O(l)
O*+CH3OH(aq)
H3CO*+OH*
H2COH*+H2O(l)
CH*+2*H2O(l)
H3CO*+H2O(l)
OH*+CH3OH(aq)
CH3OH*+H2O(l)
CH2*+2*H2O(l)
CH3OH(aq)+H2O(l)
O*+CH4(aq)+H2O(l)
CH3*+2*H2O(l)
CH4(aq)+2H2O(l)
OH*+CH4(aq)+H2O(l)

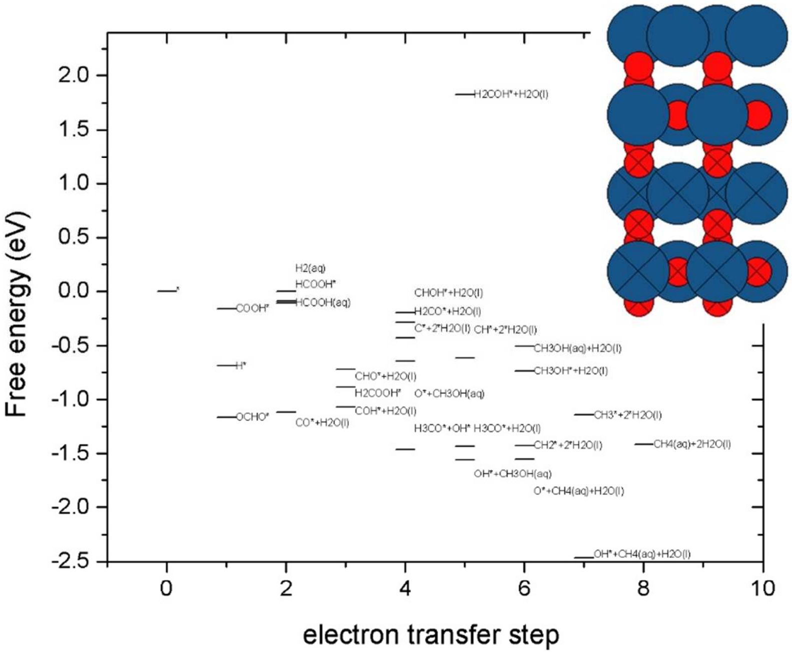

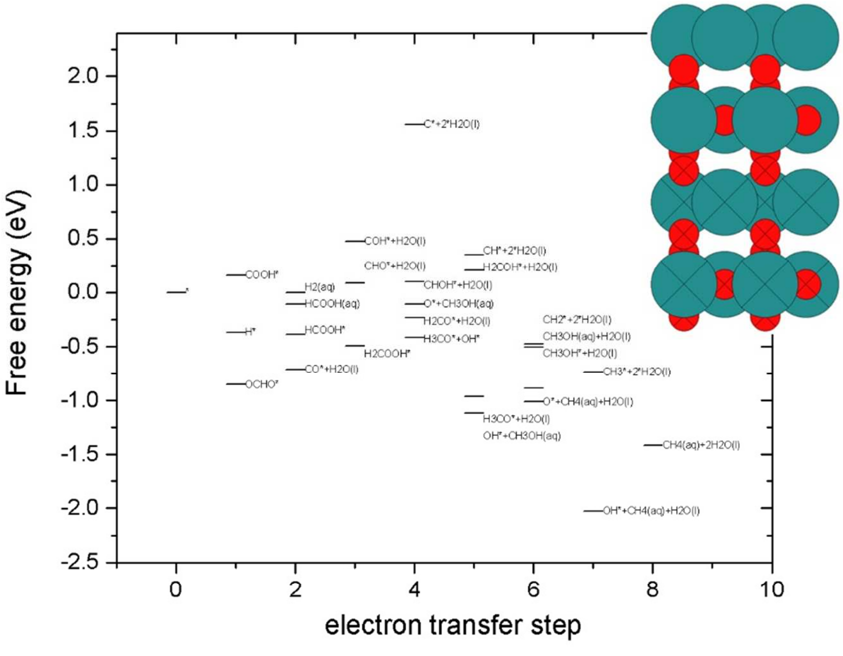

Figure S4: free energy of reaction intermediates and products with reference to CO_2, H_2 and H_2O at 0 V-RHE on all 10 surfaces models with 50% CO coverage*

Table S2: Binding free energy difference of COOH* and OCHO* intermediates formed from CO_2 activation. Lightest share means highest value and darkest is the lowest value (OCHO* more stable).

β	0.00	0.05	0.11	0.25	0.29	0.75	0.79	0.90	0.95	1.00
CO* spectator coverage	OCHO* and COOH* binding free energy difference (eV)									
0%	-1.08	-0.64	-0.78	-1.00	-0.60	-0.67	-0.82	-0.62	-0.66	-0.64
25%	-1.11	-1.10	-1.14	-1.18	-1.12	-0.66	-0.78	-1.00	-0.88	-0.94
50%	-1.01	-0.98	-1.06	-1.01	-1.01	-0.51	-0.83	-1.01	-0.99	-1.00

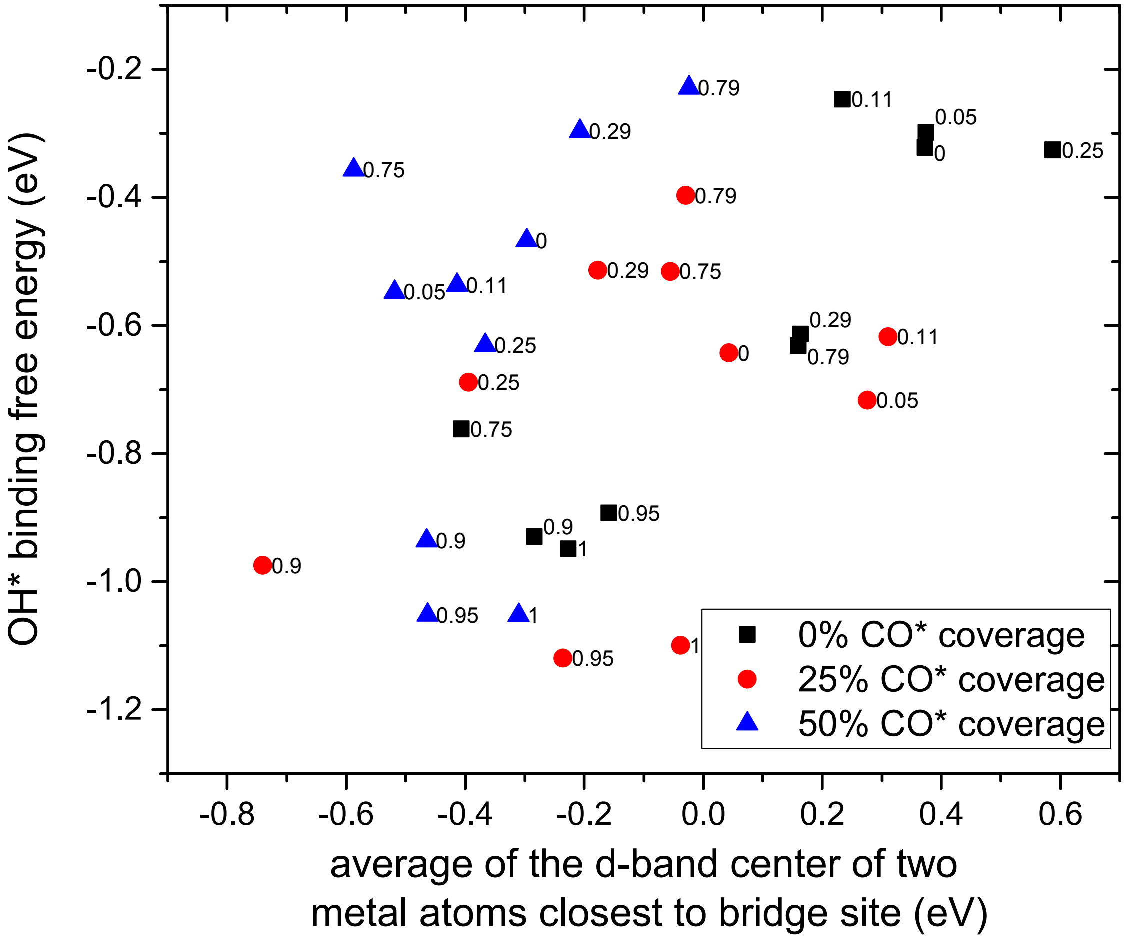

(a)

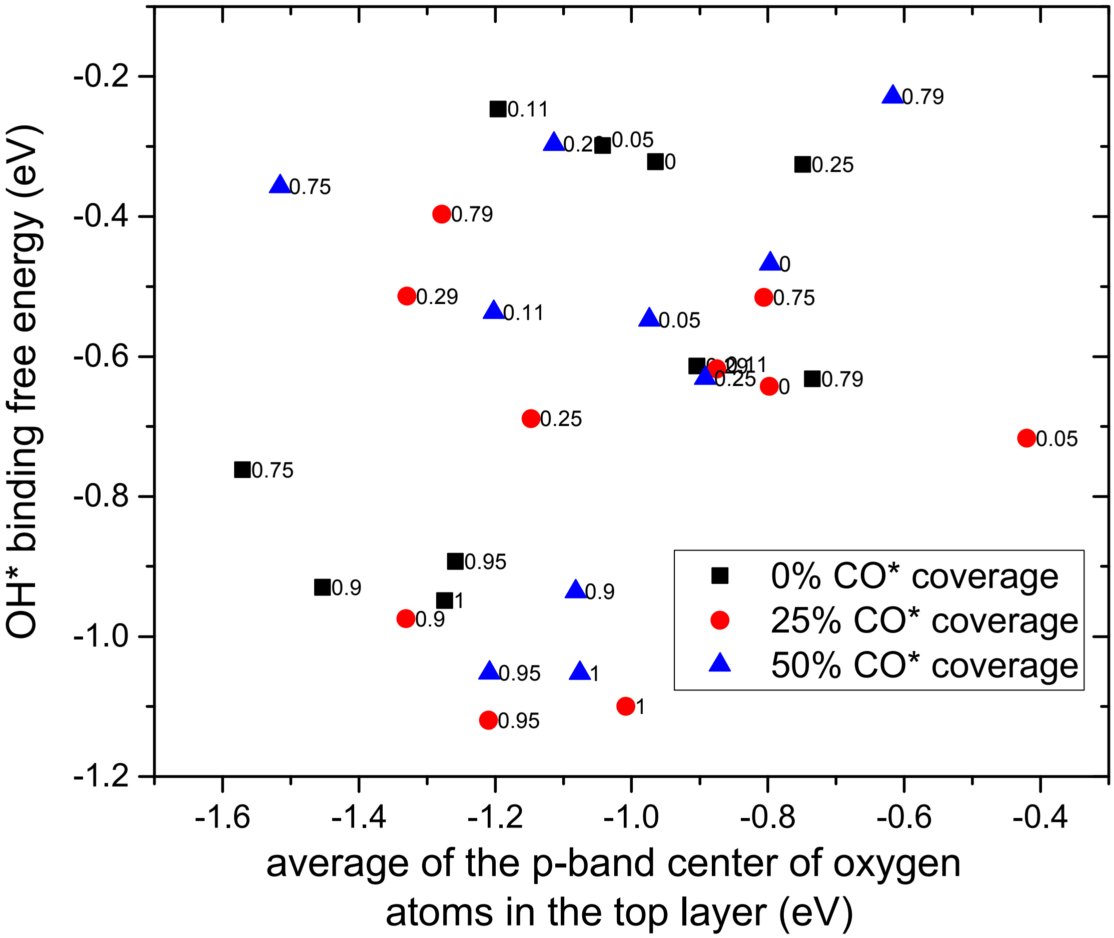

(b)

Figure S5: correlation of OH binding free energy with (a) average d-band position of the two metal atoms closest to the bridge site (b) average p-band position of oxygen atoms in the top layer of the catalyst surfaces. Labels indicate the β value of the surface for which the data point.*

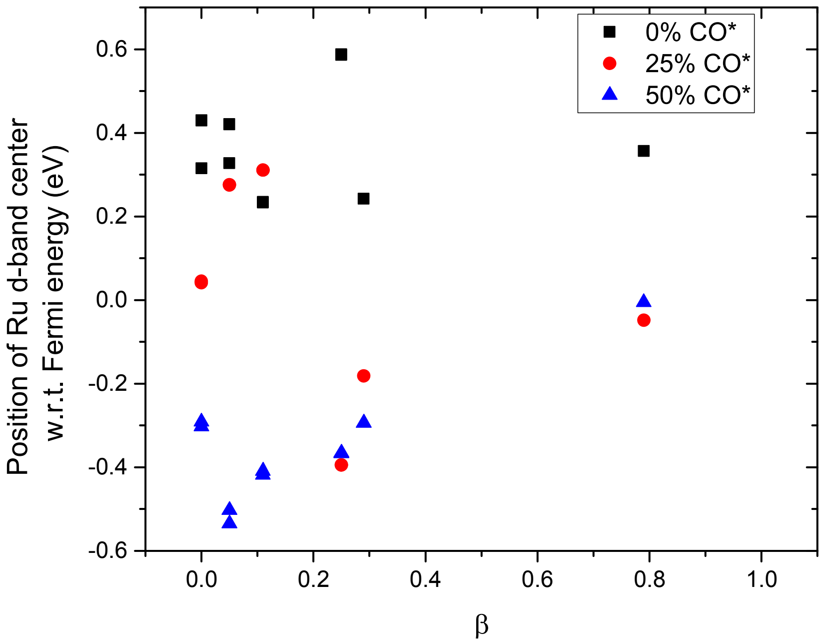
0% CO*
25% CO*
50% CO*
Position of Ru d-band center
w.r.t. Fermi energy (eV)
0.6
0.4
0.2
0.0
-0.2
-0.4
-0.6
0.0
0.2
0.4
0.6
0.8
1.0
β

(a)

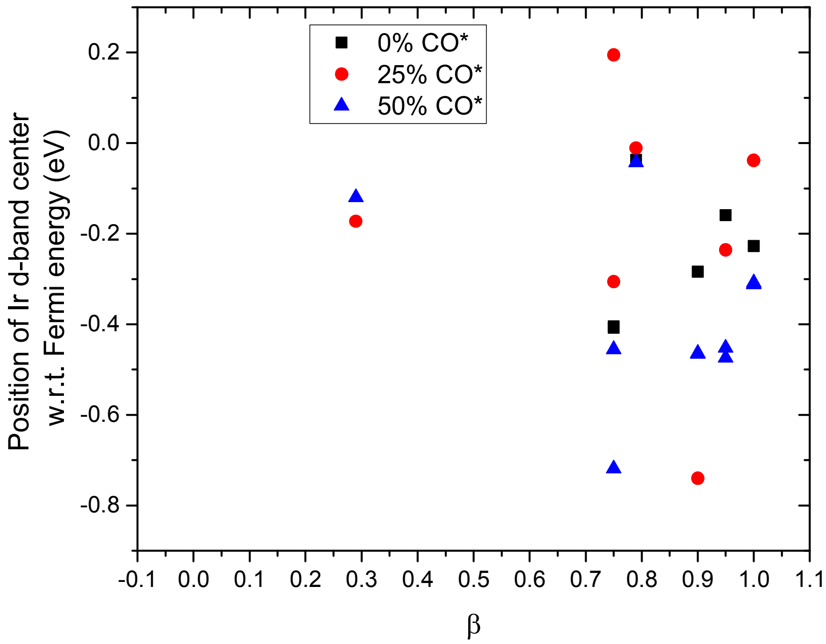
0% CO*
25% CO*
50% CO*
Position of Ir d-band center
w.r.t. Fermi energy (eV)
0.2
0.0
-0.2
-0.4
-0.6
-0.8
-0.1
0.0
0.1
0.2
0.3
0.4
0.5
0.6
0.7
0.8
0.9
1.0
1.1
β

(b)

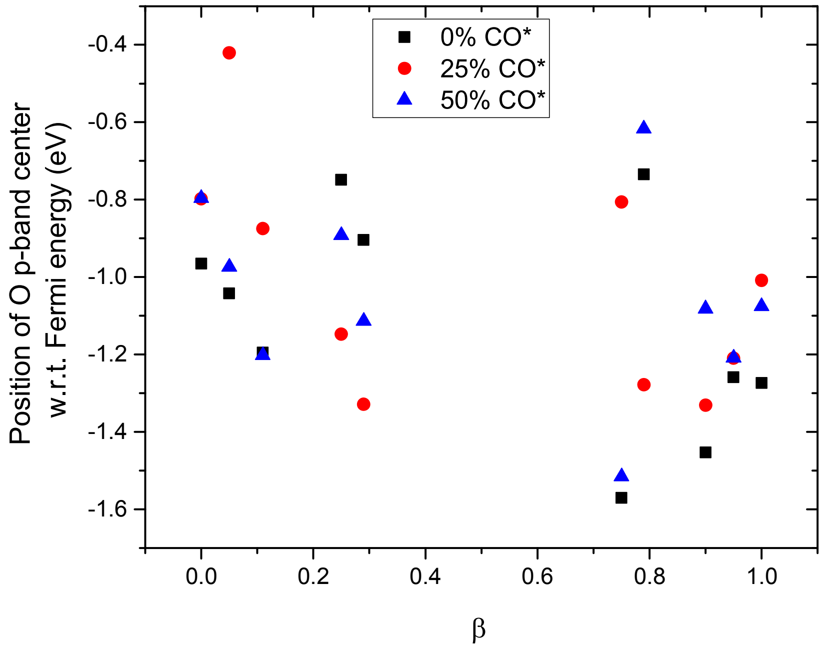

(c)

Figure S6: Modification in the band center for (a) Ru-d electrons (b) Ir d-electrons (c) O-p electrons, due to ligand effects and CO coverage*

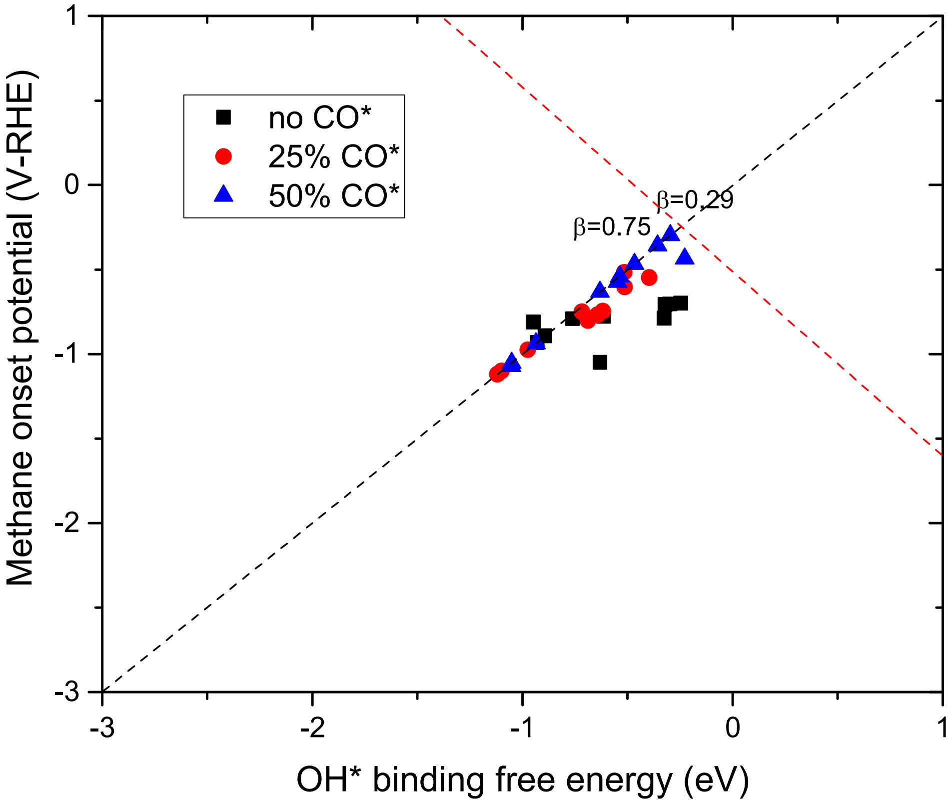

(a)

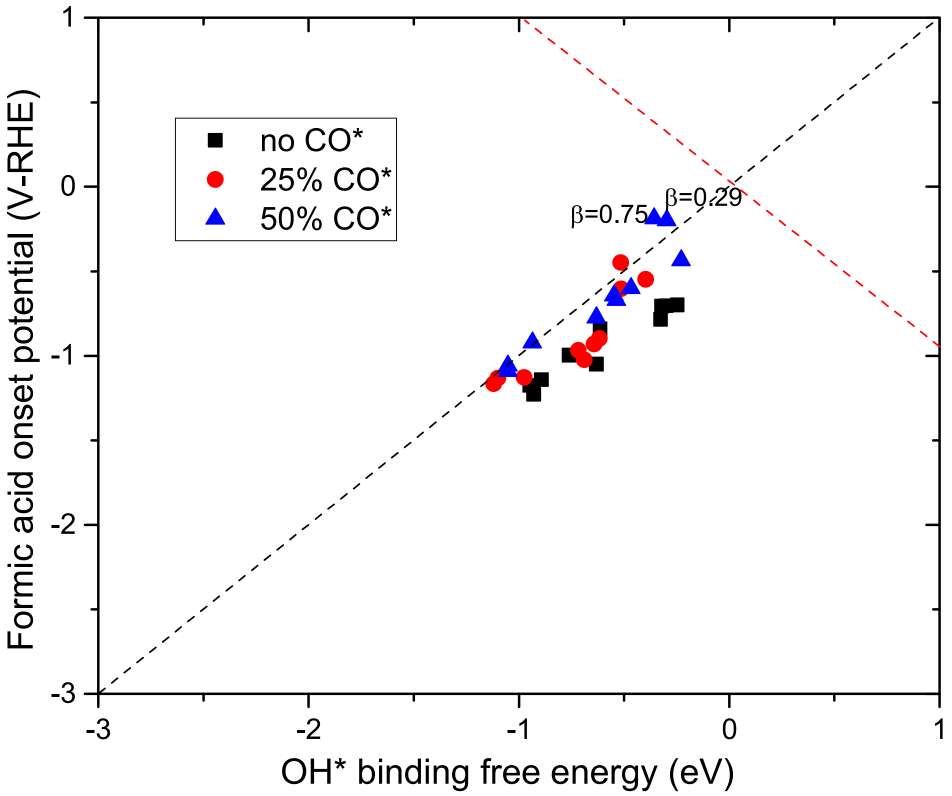

(b)

Figure S7: Effects of ligand interaction and adsorbate-adsorbate interaction from spectating CO moves partially CO* covered mixed Ir-Ru oxide surfaces closer to the top of the volcano for oxide catalysts (a) methane (b) formic acid evolution. Activity volcanos for different products obtained from our previous work[7].*

References:

(1) Kresse, G. *Phys. Rev. B* **1999**, *59*, 1758–1775.

(2) Wellendorff, J.; Lundgaard, K. T.; Møgelhøj, A.; Petzold, V.; Landis, D. D.; Nørskov, J. K.; Bligaard, T.; Jacobsen, K. W. *Phys. Rev. B* **2012**, *85*, 235149.

(3) Lee, K.; Murray, É. D.; Kong, L.; Lundqvist, B. I.; Langreth, D. C. *Phys. Rev. B - Condens. Matter Mater. Phys.* **2010**, *82*, 3–6.

(4) Liu, W.; Carrasco, J.; Santra, B.; Michaelides, A.; Scheffler, M.; Tkatchenko, A. *Phys. Rev. B - Condens. Matter Mater. Phys.* **2012**, *86*, 1–6.

(5) Ramalho, J. P. P.; Gomes, J. R. B.; Illas, F. *RSC Adv.* **2013**, *3*, 13085.

(6) Studt, F.; Abild-Pedersen, F.; Varley, J. B.; Nørskov, J. K. *Catal. Letters* **2013**, *143*, 71–73.

(7) Bhowmik, A.; Vegge, T.; Hansen, H. A. *ChemSusChem* **2016**, *9*, 3230–3243.

(8) Christensen, R.; Hansen, H. A.; Vegge, T. *Catal. Sci. Technol.* **2015**, *5*, 4946–4949.

(9) Nørskov, J. K.; Rossmeisl, J.; Logadottir, A.; Lindqvist, L.; Kitchin, J. R.; Bligaard, T.; Jónsson, H. *J. Phys. Chem. B* **2004**, *108*, 17886–17892.

(10) Hjorth Larsen, A.; Jørgen Mortensen, J.; Blomqvist, J.; Castelli, I. E.; Christensen, R.; Dułak, M.; Friis, J.; Groves, M. N.; Hammer, B.; Hargus, C.; Hermes, E. D.; Jennings, P. C.; Bjerre Jensen, P.; Kermode, J.; Kitchin, J. R.; Leonhard Kolsbjerg, E.; Kubal, J.; Kaasbjerg, K.; Lysgaard, S.; Bergmann Maronsson, J.; Maxson, T.; Olsen, T.; Pastewka, L.; Peterson, A.; Rostgaard, C.; Schiøtz, J.; Schütt, O.; Strange, M.; Thygesen, K. S.; Vegge, T.; Vilhelmsen, L.; Walter, M.; Zeng, Z.; Jacobsen, K. W. *J. Phys. Condens. Matter* **2017**, *29*, 273002.